Study of Heavy Flavours from Muons Measured with the ALICE Detector in Proton-Proton and Heavy-Ion Collisions at the CERN-LHC

X. Zhang

Numéro d'ordre : DU 2240 PCCF T 1201
EDSF : 714

CENTRAL CHINA NORMAL UNIVERSITY
UNIVERSITÉ BLAISE PASCAL

P H D T H E S I S

présentée pour obtenir le grade de

DOCTOR OF UNIVERSITY

Spécialité : Physique Corpusculaire

Par

Xiaoming Zhang

Study of Heavy Flavours from Muons Measured with the ALICE Detector in Proton–Proton and Heavy-Ion Collisions at the CERN-LHC

defended on May 23, 2012

Jury :

Rapporteurs:	B. Erazmus	-	CNRS, CERN, Genève
	G. Martinez Garcia	-	CNRS, SUBATECH, Nantes
Examinateurs:	X. Cai	-	CCNU, Wuhan
	H. Chen	-	USTC, Hefei
	Y. Ma	-	SINAP, Shanghai
Directeurs de thèse:	N. Bastid	-	LPC, Clermont-Ferrand
	P. Crochet	-	LPC, Clermont-Ferrand
	D. Zhou	-	CCNU, Wuhan

分类号_____ 密级_____

UDC _____ 编号_____

华中师范大学

博士学位论文

题目：LHC/ALICE 实验向前区重夸克物理的研究

学位申请人姓名: 张晓明

申请学位学生类别: 全日制博士

申请学位学科专业: 粒子物理与原子核物理

指导教师姓名: 周代翠 教授

菲利普•胡克 资深研究员

妮可•巴斯蒂 教授

博士学位论文

LHC/ALICE 实验向前区重夸克物理的研究

论文作者： 张晓明

指导教师： 周代翠　　教授

菲利普•胡克　资深研究员

妮可•巴斯蒂　教授

学科专业： 粒子物理与原子核物理

研究方向： 高能重离子碰撞实验

华中师范大学物理科学与技术学院

2012 年 5 月

博士学位论文
DOCTORAL DISSERTATION

Université Blaise Pascal

Dissertation

Study of Heavy Flavours from Muons Measured with the ALICE Detector in Proton-Proton and Heavy-Ion Collisions at the CERN-LHC

By

Xiaoming Zhang

Supervisors: Pr. Daicui Zhou

Dr. Philippe Crochet

Pr. Nicole Bastid

Specialty: Particle Physics and Nuclear Physics

Research Area: Heavy-Ion Collision Experiment

College of Physical Science and Technology

Central China Normal University

May 2012

华中师范大学学位论文原创性声明和使用授权说明

原创性声明

本人郑重声明：所呈交的学位论文，是本人在导师指导下，独立进行研究工作所取得的研究成果。除文中已经标明引用的内容外，本论文不包含任何其他个人或集体已经发表或撰写过的研究成果。对本文的研究做出贡献的个人和集体，均已在文中以明确方式标明。本声明的法律结果由本人承担。

作者签名：　　日期：　　年　　月　　日

学位论文版权使用授权书

学位论文作者完全了解华中师范大学有关保留、使用学位论文的规定，即：研究生在校攻读学位期间论文工作的知识产权单位属华中师范大学。学校有权保留并向国家有关部门或机构送交论文的复印件和电子版，允许学位论文被查阅和借阅；学校可以公布学位论文的全部或部分内容，可以允许采用影印、缩印或其它复制手段保存、汇编学位论文。（保密的学位论文在解密后遵守此规定）

保密论文注释：本学位论文属于保密，在 _____年解密后适用本授权书。

非保密论文注释：本学位论文不属于保密范围，适用本授权书。

作者签名：　　导师签名：

日期：　　年　　月　　日　　日期：　　年　　月　　日

本人已经认真阅读“CALIS 高校学位论文全文数据库发布章程”，同意将本人的学位论文提交“CALIS 高校学位论文全文数据库”中全文发布，并可按“章程”中的规定享受相关权益。同意论文提交后滞后：□半年；□一年；□二年发布。

作者签名：　　导师签名：

日期：　　年　　月　　日　　日期：　　年　　月　　日

摘要

宇宙中的可见物质是由那些基本粒子组成的？这些基本粒子间的相互作用又有那些特性？一直是人类不断探寻自然界奥秘的过程中试图解决的最基本也是最关键的问题。

标准模型告诉我们，宇宙中所有的可见物质都是由夸克和轻子构成的，不同种类的玻色子（如光子，胶子等）用以传播它们之间不同种类的相互作用。夸克和轻子被统称为基本粒子。传播相互作用的玻色子被称为规范粒子。通过 Higgs 机制，Yang-Mils 场中的规范粒子通过吃掉由真空对称性破缺而产生的 Goldstone 粒子而获得质量。与此同时，规范粒子和基本粒子间的 Yukawa 耦合使得基本粒子也获得了其在物理真空中的质量（由于对不同基本粒子质量的测量和定义方法不同，其在物理真空中质量的名称也不同，对于夸克，在不太严格的条件下，其在物理真空中的质量可以笼统的称为流质量）。基于标准模型，普通的强子（如构成原子核的质子和中子）都是由夸克组成的，胶子用以传播夸克间的强相互作用。夸克和胶子又被统称为部份子。体现强相互作用的荷被称为色荷。类比于描述电磁相互作用的量子电动力学，用以描述强相互作用的理论被称为量子色动力学（另外，弱相互作用中的荷被称为味荷，早期也存在量子味动力学用以描述弱相互作用，但后来被并入电弱统一理论中）。

众所周知，在量子电动力学中，由于涨落而产生的极化，物理真空可被视为电介质。而在量子色动力学（QCD）中，由于胶子所存在的自相互作用，物理真空中同时存在着色荷的极化和反极化，在通常条件下，其总体效应使得物理真空等价于色导体。与电导体内部不存在净电荷向相对应，在可被视为色导体的物理真空中也不存在自由的色荷。部份子（夸克和胶子）被“囚禁”在强子之中。这一特性被称为色禁闭或夸克“囚禁”。同时，色禁闭也解释了为何到目前为止，在通常条件下从未明确观测到自由的部份子。从另一角度，可以做如下推想：当空间中的色荷距离越来越近，无论是色极化或色反极化都将越来越弱，而在物理真空中出现自由的部份子。也就是说，不同于电磁相互作用和弱相互作用，强相互作用是随着部份子间的距离减小而减弱的，而当部份子间的距离增大时强相互作用会增强。强相互作用的这一特性已在理论上被 QCD 耦合常数对虚度的依赖性的研究所证实，而且随后的大量实验观测也完全符合并肯定了这一理论结论。不仅如此，格点量子色动力学（lQCD）进一步预言了在极端高温和/或高重子数密度的条件下，将发生由普通强子物质相到退禁闭的夸克－胶子－等离子体（QGP）相的强相互作用相变。而且，基于 lQCD 的计算，在低重子数密度的条件下，退禁闭相

变还会伴随着手征对称性的恢复，及在生成的 QGP 内，微扰真空会向物理真空回归，而夸克在强子内的组份质量也会回归到其在物理真空内的流质量。目前，退禁闭的 QGP 物质被认为存在于大爆炸后约 1 μs的早期宇宙，而且现在还存在于中子星内部。基于上述结论，对 QGP 特性的研究，不仅对掌握强相互作用的性质以及宇宙中可见物质的质量产生机制起到非常关键的作用，而且还有助于了解早期宇宙及其演化。因此，对退禁闭相变过程和 QGP 物质特性的研究已成为当前高能物理领域最重要的前沿课题。

高能重离子碰撞是在实验室条件下实现退禁闭相变的唯一途径。在碰撞过程中，首先，两个入射原子核被加速到接近于光速，然后进行碰撞并把它们的绝大部分能量沉积在碰撞区域，使得碰撞区域内具有超高的能量密度而达到发生退禁闭相变的条件，从而在碰撞区域内产生自由的夸克和胶子，及 QGP 物质。随着 QGP 系统的膨胀，其内部温度也迅速降低，而使整个体系回到强子相（强子气）然后形成末态所能观测到的各种粒子。在过去的 30 年中，一系列重离子加速器如 SPS，AGS 和 RHIC 先后被建造，并获得了丰富的实验证据表明 QGP 物质相的存在。其中具有代表性的有：

1. SPS 能区，
   a. 奇异粒子产额的增强以及低质量共振态分布的修正，被解释为手征对称性在退禁闭物质相中的恢复而使得奇异夸克在 QGP 物质中产生阈值的降低;
   b. J/Ψ粒子产额的压低，被认为是粲夸克偶素（$c\bar{c}$）在 QGP 物质里的色 Debye 屏蔽势的作用下熔解而导致的;
2. RHIC 能区，
   a. 光子产额的增高，体现了退禁闭的 QGP 物质的热辐射;
   b. 椭圆流对组份夸克数的标度性，揭示了部份子在 QGP 内的热化自由度;
   c. 高横动量强子谱的压低以及背对背喷注关联的减弱，反映了高横动量部份子在穿越 QGP 物质时，与 QGP 介质发生强相互作用而引起的能量损失。

以上结果充分表明了 QGP 物质的存在，对于当前的研究而言，所面临的问题便是对其特性进行系统而深入的研究。

基于此目的，位于欧洲核子研究中心（CERN）目前世界上最大的大型强子对撞机（LHC）于 2009 年底正式运行，并在 2010 年底首次获取了两体质心能量为 $\sqrt{s_{NN}}=2.76\ TeV$的铅－铅碰撞数据。在 LHC 能区，由于其高出在 RHIC 能区（两

体质心能为$\sqrt{s_{NN}}=200\ GeV$的金－金碰撞）约 15－30 倍的两体碰撞质心能和更重的铅核体系，所形成的 QGP 介质较之 RHIC 能区有更长的存在时间和更大的形成体积，为全面而深入的探索 QGP 物质的特性提供了独特的条件和有利的保障。ALICE，作为 LHC 上四大实验之一，专门致力与高能重离子碰撞物理的研究，及 QGP 物质特性的探索。

在众多反映 QGP 特性的末态探针中，重夸克(粲夸克和美夸克)已其独特的特性而异常重要。绝大部分的重夸克产生与高能重离子碰撞初期的硬散射过程，由于其质量效应，它具有较之其它轻部份子更短的形成时间和更硬的碎裂函数。这一特性导致：一方面，重夸克早与 QGP 物质而形成，并穿越随后形成的 QGP 物质体系，纪录了 QGP 系统各演化阶段的信息；另一方面，其运动学分布又能很好的被其末态强子所反映。基于重夸克的优越特性和在超高能的 LHC 能区丰富的重夸克产额，使得重夸克成为揭示 QGP 物质特性的独特探针。

首先，重夸克在穿越 QGP 体系时与其内部部份子相互作用而导致的能量损失体现了强相互作用的特性。根据标准模型的对称性，理论上预言，胶子的辐射能量损失大于夸克。而较之轻夸克，重夸的胶子辐射会在与其夸克质量相关的锥角内压低，从而导致重夸克辐射能量损失比轻夸克小，这一效应被称为死角效应。核修正因子R_{AA}是反映部份子能量损失的实验观测量。基于重夸克辐射能量损失的死角效应，重味强子的R_{AA}因大于轻强子。但这一现象并未在 RHIC 能区上被观测到。因此，在 LHC 能区对重夸克末态产物R_{AA}的测量有利于深入了解部份子在 QGP 介质内的相互作用特性。更进一步，在 LHC 能区由于丰富的重夸克产额，提供了新的实验观测量，重轻比，即开粲或开美强子的R_{AA}与轻强子的R_{AA}之比。在 LHC 能区，轻强子主要源于胶子的碎裂，而粲夸克的质量（$m_c\approx 1.5\ MeV$）较之其能量可以忽略而表现出轻夸克的特性，于此同时质量较大的美夸克（$m_b\approx 4.5\ MeV$）仍保持其重夸克的性质。根据以上特性，开粲强子与轻强子之间的重轻比体现了部份子能量损失对色荷的依赖性，而开美强子与轻强子间的重轻比进一步反映了部份子能量损失对其质量的依赖关系。根据新近的理论研究，对开美强子和开粲强子间R_{AA}之比的测量不仅能直接的反映夸克能量损失对其质量的依赖还可用以区分描述 QGP 物质的不同理论，是标定 QGP 属性的关键观测量。

另一方面，相变过程的特性，往往体现于其末态产物的集体行为。因此，重夸克末态产物的集体流也是实验中非常重要的观测量。在低横动量区间，重夸克末态产物的集体流揭示了重夸克在 QGP 介质内的热化自由度；在高横动量区间，这一观测量体现的是重夸克能量损失对穿越路径长度的依赖性。更重要的是,表征

QGP 介质的关键量，粘滞系数与熵的比值（η/s），可通过结合重夸克的 R_{AA} 和集体流的实验测量结果而得到。

此外，重夸克的重要性不仅仅体现在重离子碰撞中，在核子－核（pA）和核子－核子（pp）碰撞中，对重夸克末态产物的测量也蕴涵着丰富的物理。在 pA 碰撞中，它是了解各种冷核效应（核遮蔽，内禀横动量增宽以及胶子饱和等）的有利工具；特别是在实验的向前快度区间，它能使对冷核效应的测量达到及小的 Bjorken 分数区间（$x\sim10^{-4}$）。在 pp 碰撞中，对重夸克末态产物的测量不仅为 pA 碰撞和重离子碰撞提供了归一化基准，同时，也是检测微扰量子色动力学（pQCD）的有利工具。在 pQCD 的计算中，重夸克的质量可有效抑制微扰级数的红外发散，从而提高了 pQCD 对重夸克产生截面预言的准确性，这使通过比较重夸克末态产物产生截面的实验测量结果和理论预言成为验证 pQCD 理论的重要手段。

本工作基于 LHC/ALICE 实验的向前区 μ 子谱仪，通过半 μ 子衰变道分别研究铅－铅碰撞和质子－质子碰撞中重夸克的产生。在第一章中，将对 QGP 相变和高能重离子物理做全面的介绍，并讨论已有的典型实验结果以及 LHC 能区优越的实验条件和 ALICE 实验上已获得的重要结果。对重夸克在核子－核子，核子－核以及重离子碰撞中的产生机制和对应物理将在第二章中做系统介绍，同时讨论 ALICE 实验上已获得的通过半电子衰变道和强子衰变道对重夸克产物测量的结果。在正式讨论基于本论文的工作之前，作为工作基础，在第三章和第四章里，将对 ALICE 探测器特别是向前区 μ 子谱仪和 ALICE 实验数据获取和分析的在线和离线环境进行介绍。同时将着重讨论在本工作中我们针对重夸克半 μ 子道测量所开发的数据分析和校正的软件框架。第五章总结了我们在模拟条件下通过单，双 μ 子道测量重味强子产生截面的可行性研究结果，在研究中，我们成功的重建出了模拟所输入的重味强子谱。然后，第六章道第九章将对我们数据分析的过程和结果做着重讨论。第六章，将以质心系能量 $\sqrt{s}=900\ GeV$ 的质子－质子碰撞数据为例，对实验中 ALICE 向前区 μ 子谱仪的性能，实验数据中的背景和对数据的筛选做全面讨论。在质心系能量 $\sqrt{s}=7\ TeV$ 的质子－质子碰撞中对向前区重夸衰变 μ 子的产生截面的测量方案及其结果是第七章的主要论述内容。在误差范围内，我们的测量结果很好的符合了次领头阶的 pQCD 计算的预言，这一结果是首次在此新能区下对 pQCD 理论预言的重夸克产生截面的检验。此外，在这一章的最后，我们还讨论了新的背景减除方案和如何对开粲和开美强子衰变 μ 子组份进行分离的思路。在第八章中，我们首先讨论了铅－铅碰撞数据的基本特性，重点介绍了数据中心度选择的各种方法；随后，运用第七章中的方法，我们给出了在质心系能

量$\sqrt{s}=2.76\ TeV$的质子－质子碰撞中向前区重夸克衰变μ子的产生截面的测量结果，此结果也在误差范围内很好的符合了次领头阶 pQCD 的预言，它将作为我们在此两体碰撞质心能下计算铅－铅碰撞中重夸克衰变μ子的和修正因子的归一化基准；在两体质心能为$\sqrt{s_{NN}}=2.76\ TeV$的铅－铅碰撞中对重夸克衰变μ子核修正因子的计算方案和结果的讨论是这一章重点内容，最后，我们的结果首次反映出重夸克在向前区的压低与中心快度区间相似，这一结论的重要性在于它并不符合之前理论的预言（在向前区由于其部份子密度较之中心区要低，高横动量区间的重夸克压低效应较之中心区要弱），这为理论研究提供了新的方向，也为深入揭示部份子在 QGP 介质内的能量损失机制给出了新的线索。第九章是关于遍举μ子椭圆流的测量，在全面介绍和比较了各种集体流的分析方法之后，我们逐一运用这些方法于数据分析之中，并对它们做出了检验；在误差范围内，不同的分析方法和参考粒子给出了相同结果，而且符合分析的预期；这一工作为我们进一步测量重夸克衰变μ子的集体流和通过结合核修正因子和集体流的测量结果深入揭示 QGP 特性打下了坚实的基础。论文的最后是对我们以上所有相关工作的总结和展望。

关键字：大型强子对撞机（LHC），大型重离子碰撞实验（ALICE），质子－质子碰撞，超相对论重离子碰撞，单μ子，重夸克产生，核修正因子，椭圆流，微扰量子色动力学

Résumé

Les collisions d'ions lourds ultra-relativistes ont pour objectif principal l'étude des propriétés de la matière nucléaire soumise à des conditions extrêmes et de température de densité d'énergie. Les calculs de la ChromoDynamique Quantique (QCD) prédisent dans ces conditions une nouvelle phase de la matière dans laquelle on assisterait au déconfinement des constituants des hadrons en un plasma de quarks et gluons (QGP). Les saveurs lourdes (charme et beauté) sont produites lors de processus durs aux premieres instants de la collision puis traversent le milieu produit durant la collision. Par conséquent, la mesure des quarkonia et des saveurs lourdes ouvertes devrait être particulièrement intéressante pour l'étude des propriétés du système créé aux premiers instants de la collision. On s'attend à ce que les saveurs lourdes ouvertes présentent des sensibilités à la densité d'énergie via les mécanismes de perte d'énergie des quarks lourds dans le milieu et que les quarkonia soient sensibles à la température initiale du système via leur dissociation par écrantage de couleur. La mesure du flot des saveurs lourdes devrait apporter des informations concernant le degré de thermalisation des quarks lourds dans le milieu nucléaire. De plus, l'observable viscosité/entropie pourrait être obtenue en combinant les mesures du facteur de modification nucléaire et de flot. En conséquence, l'étude de la production des quqrkonia et saveurs lourdes ouvertes est un domaine de recherche intensément étudié au niveau experimental et théorique.

Les mesures effectuées au SPS et RHIC ont permis de mettre en évidence plusieurs caractéristiques du milieu produit mais ont aussi laissé plusieurs questions sans réponse. Avec une énergie par paire de nucléon de 15 fois supérieure à celle du RHIC, le LHC entré en fonctionnement fin 2009, a ouvert une nouvelle ère pour l'étude des propriétés du QGP. Un des plus importants aspects de ce domaine en énergie est l'abondante production de quarks lourds utilisés pour la première fois comme sonde de haute statistique du milieu. Le LHC délivra les premières collisions pp à $\sqrt{s} = 0.9$ TeV en octobre 2009 et a atteint l'énergie de $\sqrt{s} = 7$ TeV en mars 2010. Un run pp à $\sqrt{s} = 2.76$ TeV a eu lieu en mars 2011 pendant une durée limitée. Les runs Pb–Pb à $\sqrt{s_{\rm NN}} = 2.76$ TeV ont eu lieu fin 2010 et 2011.

ALICE (A Large Ion Collider Experiment) est l'expérience dédiée à l'étude des collisions d'ions lourds au LHC. ALICE enregiste aussi des collisions pp afin de tester les calculs perturbatifs de QCD dans la région des faibles valeurs de x-Bjorken et de fournir la référence indispensable pour l'étude des collisions noyau–noyau et p–noyau. ALICE enregistrera aussi, début 2013, des collisions p–Pb/Pb-p afin d'étudier les effets nucléaires froids. Les quarkonia et saveurs lourdes ouvertes sont mesurés dans ALICE suivant leur mode de désintégration (di)-muonique, (di)-electronique et hadronique. Cette thèse concerne l'étude des saveurs lourdes ouvertes dans les collisions pp et Pb–Pb avec les muons simples mesurés aux rapidités avant avec le spectromètre à muons d'ALICE.

Le document est structuré comme suit. Le premier chapitre est une introduction à la physique des collisions d'ions lourds et du diagramme de phase de la matière nucléaire. Le deuxième chapitre présente les objectifs de l'étude des saveurs lourdes ouvertes dans les collisions proton–proton, proton–noyau et noyau–noyau. Un

intérêt particulier est porté au domaine en énergie du LHC. Le troisième chapitre est une description du détecteur ALICE et du spectromètre à muons. Le quatrième chapitre présente les systèmes "online" et "offline". Le cinquième chapitre est un résumé des performances du spectromètre à muons pour la mesure des saveurs lourdes ouvertes dans les collisions pp au moyen des muons simples et dimuons. Les chapitres 6 à 9 concernent l'analyse de données. Le sixième chapitre décrit l'analyse des premières collisions pp à $\sqrt{s} = 0.9$ TeV collectées avec ALICE. L'objectif principal était la compréhension de la réponse du détecteur. Ces données ont permis aussi fixer la stratégie d'analyse des saveurs lourdes ouvertes : sélection des événements, optimisation des coupures, différentes sources de bruit de fond à soustraire. Le septième chapitre présente la mesure de la section de production des saveurs lourdes ouvertes dans les collisions pp à $\sqrt{s} = 7$ TeV. La méthode d'analyse est décrite. Cela concerne la sélection des collisions et traces reconstruites dans le spectromètre à muons, la soustraction du bruit de fond (composé principalement de muons issus de la désintégration de pions et kaons primaires), les corrections, la normalisation et la détermination des incertitudes systématiques. Les résultats expérimentaux sont discutés et comparés aux calculs perturbatifs QCD (calculs "Fixed Order Next-to-Leading Log"). Cela concerne les sections efficaces de production des muons issus de la désintégration des saveurs lourdes ouvertes aux rapidités avant ($2.5 < y < 4$) en fonction de la rapidité et de l'impulsion transverse ($p_{\rm t}$). Le huitième chapitre aborde la mesure des muons issus de la désintégration des saveurs lourdes ouvertes dans les collisions Pb–Pb à $\sqrt{s_{\rm NN}} = 2.76$ TeV collectées en 2010. Les effets de milieu nucléaire sont étudiés à partir du facteur de modification nucléaire $R_{\rm AA}$. La référence pp est déterminée à partir de l'analyse des collisions pp à $\sqrt{s} = 2.76$ TeV. Le facteur de facteur modification nucléaire est étudié en fonction de $p_{\rm t}$ et de la centralité de la collision. Pour comparaison, les résultats obtenus à partir de la mesure du facteur de modification nucléaire central sur périphérique ($R_{\rm CP}$) sont aussi présentés. Le neuvième chapitre commence par une revue des différentes méthodes utilisées pour la mesure de la composante de flot elliptique. Les méthodes telles que les cumulants et Lee-Yang Zeroes, permettant de supprimer les effets non-flot, sont détaillées. Des premiers résultats prometteurs concernant la mesure de la composante de flot elliptique des muons sont discutés. Ils sont obtenus avec différentes méthodes et présentés en fonction de $p_{\rm t}$ et de la centralité de la collision. Le manuscript se termine par une conclusion et des perspectives.

mots clés : LHC, expérience ALICE, collisions pp, collisions d'ions lourds ultra-relativistes, muons, production de saveurs lourdes, facteur de modification nucléaire, flot elliptique, calculs pQCD.

Abstract

Ultra-relativistic heavy-ion collisions aim at investigating the properties of strongly-interacting matter at extreme conditions of temperature and energy density. According to quantum chromodynamics (QCD) calculations, under such conditions, the formation of a deconfined medium, the Quark-Gluon Plasma (QGP), is expected. Amongst the most important probes of the properties of the QGP, heavy quarks are of particular interest since they are expected to be produced in hard scattering processes during the early stage of the collision and subsequently interact with the hot and dense medium. Therefore, the measurement of quarkonium states and open heavy flavours should provide essential information on the properties of the system formed at the early stage of heavy-ion collisions. Indeed, open heavy flavours are expected to be sensitive to the energy density through the mechanism of in-medium energy loss of heavy quarks, while quarkonium production should be sensitive to the initial temperature of the system through their dissociation due to color screening. The measurement of the collective flow of heavy flavours provides additional insights on the possible thermalization of heavy quarks in the medium. Furthermore, one of the important medium characteristic, viscosity over entropy (η/s), can be extracted by combining the information from measured nuclear modification factor (related to in-medium energy loss) and the magnitude of the heavy quark flow. In this regard, both quarkonium and open heavy flavour production are a field of intense experimental and theoretical researches.

Despite the work devoted to these studies at SPS and RHIC, several questions are left open. With a nucleus-nucleus center of mass energy nearly 15 times larger than the one reached RHIC, the LHC which started operating in November 2009, provides a new era for studies of interacting matter at high temperature and energy density. One of the most important aspects of this new energy range is the abundant production rate of heavy quarks which are used, for the first time, as high statistics probes of the medium. The LHC delivered the first proton-proton collisions at $\sqrt{s} = 0.9$ TeV in October 2009 and reached its current maximum energy of 7 TeV in March 2010. A short proton–proton run at $\sqrt{s} = 2.76$ TeV, at the same energy than the Pb–Pb run, was performed in March 2011. The first heavy-ion run (Pb–Pb collisions at $\sqrt{s_{\rm NN}} = 2.76$ TeV) took place in November 2010 and the second one end of 2011.

ALICE (A Large Ion Collider Experiment) is the experiment dedicated to the study of heavy-ion collisions at the LHC. ALICE also takes part in the LHC proton–proton program which is of great interest for testing perturbative QCD calculations at unprecedented low Bjorken-x values and for providing the necessary baseline for nucleus–nucleus and proton–nucleus collisions. ALICE will also collect, in the beginning of 2013, p–Pb/Pb–p collisions in order to investigate cold nuclear matter effects. ALICE measures quarkonia and open heavy flavours with (di)-electrons, (di)-muons and through the hadronic channels. This thesis work is devoted to the study of open heavy flavours in proton–proton and Pb–Pb collisions via single muons with the ALICE forward muon spectrometer.

The document is organized as follows. The first chapter consists in a general

introduction on heavy-ion collisions and QCD phase transitions. Chapter 2 summarizes the motivations for the study of open heavy flavours in nucleon–nucleon, nucleon–nucleus and nucleus–nucleus collisions. A particular emphasis is placed on the novelties at the LHC. Chapter 3 gives an overview of the ALICE experiment with a detailed description of the forward muon spectrometer. Chapter 4 gives a short summary of the ALICE online and offline systems. Then the analysis framework (for data and simulations) and in particular the software developed for the study of open heavy flavours is detailed. Chapter 5 summarizes the performance of the ALICE muon spectrometer for the study of the production of open heavy flavours in pp collisions via single muons and dimuons. Chapters 6 to 9 are dedicated to data analysis. Chapter 6 deals with the analysis of first pp collisions at 900 GeV. The main aim was the understanding of the response of the apparatus. These data allowed also to determine the analysis strategy for heavy flavour measurement in the single muon channel: selection of events, optimization of cuts, understanding of the background components in data. Chapter 7 presents the measurement of the production of heavy flavour decay muons in pp collisions at $\sqrt{s} = 7$ TeV. The analysis strategy is described: event and track selection, background subtraction (mainly the contribution of muons from primary pion and kaon decays), corrections, normalization and investigation of the systematic uncertainties. The experimental results are discussed and compared to perturbative QCD calculations (Fixed Order Next-to-Leading Log calculations). That concerns the transverse momentum and rapidity differential production cross sections of muons from heavy flavours decays at forward rapidity ($2.5 < y < 4$). Chapter 8 addresses the measurement of heavy flavour decay muon production in Pb–Pb collisions at $\sqrt{s_{\rm NN}} = 2.76$ TeV collected in 2010. The analysis strategy is presented. In-medium effects are investigated by means of the nuclear modification factor ($R_{\rm AA}$) of muons from heavy flavour decays. The proton–proton reference is obtained from the measurement of the differential production cross section of heavy flavour decay muons at the same center of mass energy. The nuclear modification factor is studied as a function transverse momentum ($p_{\rm t}$) and collision centrality. For comparison, results obtained with the central-to-peripheral nuclear modification factor $R_{\rm CP}$ are also discussed. Chapter 9 gives an overview of the different methods investigated in ALICE for the study of the elliptic flow. In particular, the recent methods which allow to remove non-flow effects like the Q-Cumulants and Lee-Yang Zeroes are detailed. Promising results concerning the inclusive muon elliptic flow as a function of $p_{\rm t}$ and centrality obtained with different flow analysis methods are compared. Finally, summary and outlooks are given.

Keywords: LHC, ALICE experiment, pp collisions, ultra-relativistic heavy-ion collisions, single muons, heavy flavour production, nuclear modification factor, elliptic flow, pQCD calculations

Contents

I Introduction **1**

1 QCD Phase Transition and Heavy Ion Collisions **3**
1.1 History of Standard Model . . . 3
1.1.1 Quark Model . . . 3
1.1.2 Higgs Mechanism . . . 4
1.1.3 Standard Model . . . 5
1.2 Quantum ChromoDynamics . . . 6
1.2.1 QCD Lagrangian . . . 6
1.2.2 Asymptotic Freedom . . . 7
1.2.3 Chiral Symmetry Restoration . . . 8
1.2.4 Ends and New Starts . . . 10
1.3 Quark Gluon Plasma . . . 10
1.3.1 Lattice QCD Predictions . . . 11
1.3.2 QCD Phase Diagram . . . 12
1.4 Heavy Ion Collisions . . . 14
1.4.1 Trace Back to the Big Bang . . . 14
1.4.2 Collision System Evolution . . . 15
1.4.3 Final State Observables . . . 19
1.4.4 Heavy Ion Facilities . . . 21
1.5 Evidence of the Quark Gluon Plasma . . . 22
1.5.1 SPS: First evidences . . . 22
1.5.2 RHIC: Strong Coupled QGP? . . . 24
1.5.3 LHC: Opportunities and Challenges . . . 28

2 Heavy Flavours: a Promising QGP Tomography **33**
2.1 Open Heavy Flavour Hadronic Production . . . 33
2.1.1 Factorization Theorem . . . 33
2.1.2 Bjorken-x in PDFs via Heavy Flavours . . . 35
2.1.3 Partonic Cross Section . . . 38
2.1.4 Hard Fragmentation . . . 40
2.1.5 Comparison with Data . . . 42
2.2 Heavy Flavour Production in A–A Collisions . . . 46
2.2.1 Binary Scaling of Heavy Flavour Production in A–A Collisions 47
2.2.2 Cold Nuclear Effects . . . 50
2.2.3 Hot Nuclear Effects . . . 54
2.3 Heavy Flavours Physics at the LHC . . . 62
2.3.1 Novel Aspects of Heavy Flavours at the LHC . . . 62
2.3.2 Heavy Flavour Measurements with ALICE at the LHC . . . 66

II ALICE Experiment **73**

3 Experimental Apparatus **75**
3.1 ALICE Setup . . . 75
3.2 Central Barrel Detectors . . . 79
3.2.1 Detector Layout . . . 79
3.2.2 Primary Vertex Determination . . . 81
3.2.3 Charged Track Reconstruction . . . 82
3.2.4 Particle Identification . . . 84
3.3 Global Detectors . . . 86
3.4 Forward Muon Spectrometer . . . 90
3.4.1 Design Consideration . . . 90
3.4.2 Front Absorber and Beam Shielding . . . 91
3.4.3 Dipole Magnet . . . 93
3.4.4 Muon Tracker . . . 94
3.4.5 Trigger System . . . 98

4 ALICE Online and Offline **103**
4.1 Online Control System . . . 103
4.1.1 Trigger System (TRG) . . . 103
4.1.2 Data AcQuisition (DAQ) System . . . 105
4.1.3 High-Level Trigger (HLT) . . . 107
4.1.4 Detector and Experiment Control System . . . 109
4.2 ALICE Offline Project . . . 110
4.2.1 ALICE Computing Grid . . . 110
4.2.2 AliRoot Framework . . . 112
4.3 Analysis Framework of MUON . . . 115
4.3.1 Overall View . . . 116
4.3.2 Muon Code for HF Analysis . . . 118

III Measurements of Open Heavy Flavours with the Muon Spectrometer **121**

5 Performance Study of Open HF Measurements **123**
5.1 Analysis Inputs . . . 123
5.1.1 Simulation Strategy . . . 123
5.1.2 Efficiency Correction . . . 125
5.2 Sources of (di)muons from HF . . . 127
5.3 Separation of Charm and Beauty Components . . . 130
5.3.1 Combined Fit . . . 130
5.3.2 Systematic Uncertainties . . . 131
5.4 Calculation of $\mathrm{d}\sigma_{\mathrm{D/B}}/\mathrm{d}p_{\mathrm{t}}(p_{\mathrm{t}} > p_{\mathrm{t}}^{\mathrm{min}})$ . . . 134
5.4.1 Method . . . 134
5.4.2 Systematic Uncertainty on $F^{\mathrm{MC}}_{\mu\leftarrow\mathrm{D/B}}(\phi^{\mu}, p_{\mathrm{t}}^{\mathrm{min}})$ . . . 135

5.4.3 Results . . . 136
5.5 Discussions . . . 137
5.5.1 Statistics Estimates . . . 138
5.5.2 Background Subtraction . . . 140

6 Analysis of pp data at $\sqrt{s} = 900$ GeV 145
6.1 Data Sample and Online Trigger . . . 145
6.2 Offline Event Selection . . . 148
6.2.1 Physics Selection . . . 148
6.2.2 Primary Vertex Selection . . . 150
6.2.3 Effect of the Event Selection on Muon Tracks . . . 151
6.3 Muon Track Selection . . . 153
6.3.1 Matching with MUON trigger tracks . . . 153
6.3.2 Acceptance Cuts . . . 157
6.4 Conclusion: Physics Analysis Cuts . . . 158

7 Heavy Flavour Production in pp Collisions at $\sqrt{s} = 7$ TeV 161
7.1 Data Quality Assurance . . . 161
7.1.1 Quality Assurance for Muon Analysis . . . 161
7.1.2 Results of Data Quality Assurance . . . 163
7.1.3 Pile-up Correction . . . 166
7.2 Data Sample . . . 170
7.2.1 Summary of Statistics . . . 170
7.2.2 Event Normalization . . . 172
7.3 Background Subtraction . . . 176
7.3.1 Strategy . . . 177
7.3.2 Background Estimate . . . 178
7.3.3 Background Normalization . . . 180
7.3.4 Uncorrected Results . . . 183
7.3.5 Systematic Uncertainty . . . 185
7.4 Efficiency Correction . . . 188
7.4.1 Strategy . . . 189
7.4.2 Test of the Efficiency Correction in Simulations . . . 190
7.4.3 Systematic Uncertainty in Data . . . 192
7.5 Comparison with FONLL Predictions . . . 195
7.5.1 Error Propagation for FONLL Predictions . . . 195
7.5.2 Results of the Comparison . . . 198
7.6 Beam Induced Backgroud Rejection . . . 201
7.6.1 Additional Background component in the High p_{t} Region . . . 201
7.6.2 Kinematics Combination . . . 203
7.6.3 Study of $p\times$DCA Observable . . . 210
7.7 Results . . . 218
7.7.1 Summary of the Analysis Strategy . . . 218
7.7.2 Final Results . . . 219
7.8 Discussion . . . 224

7.8.1 Data Based Background Estimate . . . 224
7.8.2 Charm and Bottom Component Separation . . . 227

8 Heavy Flavour Suppression in Pb–Pb Collisions at $\sqrt{s_{\rm NN}} = 2.76$ TeV 229
8.1 Event Trigger Selection . . . 230
8.1.1 Trigger Classes . . . 230
8.1.2 De-bunching . . . 231
8.1.3 Selection Results . . . 232
8.2 Centrality Determination . . . 233
8.2.1 VZERO Amplitude . . . 234
8.2.2 $E_{\rm ZEM}$ *vs.* $E_{\rm ZDC}$ . . . 236
8.2.3 Centrality QA . . . 237
8.2.4 Centrality Scaling Factors . . . 238
8.3 Track Selection . . . 239
8.3.1 Typical Distributions . . . 239
8.3.2 Fake Tracks . . . 240
8.3.3 $p\times$DCA in Pb–Pb Collisions . . . 242
8.3.4 Statistics Summary . . . 246
8.4 Reference from pp Collisions . . . 248
8.4.1 Energy Interpolation . . . 249
8.4.2 Reference from pp Data at 2.76 TeV . . . 252
8.5 Background Estimate . . . 255
8.5.1 Strategy . . . 255
8.5.2 Inputs from Data . . . 257
8.5.3 Convert the Spectra of K/π to the Muon Level . . . 258
8.5.4 Estimate of the Rapidity Extrapolation Factor . . . 265
8.5.5 Yield of Decay Muons in pp Collisions . . . 269
8.6 Efficiency and Uncertainty . . . 270
8.6.1 Efficiency Correction . . . 271
8.6.2 Systematic Uncertainty on the Final Results . . . 273
8.7 Results . . . 276
8.7.1 $R_{\rm CP}$ of Inclusive Muons . . . 276
8.7.2 $R_{\rm AA}$ of Muons from Heavy Flavour Decays . . . 278
8.7.3 Discussions . . . 281

9 Elliptic Flow of Muons in Pb–Pb Collisions at $\sqrt{s_{\rm NN}} = 2.76$ TeV 285
9.1 Flow Analysis Methods . . . 285
9.1.1 Event Plane Method . . . 286
9.1.2 Fit-Q and Scalar Product . . . 291
9.1.3 Cumulant Methods . . . 295
9.1.4 Lee-Yang-Zeroes Methods . . . 304
9.2 Data Analysis Environment . . . 310
9.2.1 Reference Particle Selection . . . 310
9.2.2 Single Muons in the Flow Package . . . 311
9.3 Analysis Configuration . . . 315

9.3.1 Corrections for the Event Plane Method 315
9.3.2 Configurations of Other Methods 323
9.4 Results and Discussions 326
9.4.1 Preliminary Results 326
9.4.2 Discussion 329

Conclusion and Outlooks **331**

IV Appendix **337**

A Publication of "Heavy Flavour decay muon production at forward rapidity in proton–proton collisions at $\sqrt{s} = 7$ TeV" **339**

B Publication of "Production of muons from heavy flavour decays at forward rapidity in pp and Pb–Pb collisions at $\sqrt{s_{\mathrm{NN}}} = 2.76$ TeV" **353**

Bibliography **367**

Publication List **393**

Acknowledgments **395**

List of Figures

1.1 Elementary particles in the Standard Model (left) and the fundamental interactions between them (right) [17]. 5
1.2 QCD running coupling as a function of Q with $\Lambda_{QCD} \approx 200$ MeV [31]. 8
1.3 Constituent quark masses with various current masses of different flavours [32]. 9
1.4 Left: energy density, ε/T^4, versus temperature, T, with 2 light and 1 heavier (strange) quarks [39]. Right: chiral condensation, $< \overline{\Psi}\Psi >$ (Eq. (1.11)), and quark free energy function, $L(f_q)$, (Eq. (1.13)) with their associated susceptibilities, $\chi_{\overline{\Psi}\Psi}$ and χ_L, as a function of temperature, T/T_c [34]. All the results are obtained with $\mu_B = 0$. 12
1.5 Schematic view of the QCD Phase Diagram 13
1.6 Picture presenting the evolutiion of the Universe. 14
1.7 Schematic view of an Heavy Ion Collision [34] 15
1.8 Geometry of the collision in a two-dimension (left panel) and three-dimension plane (right panel). 16
1.9 Characterization of a collision by using the charged particle multiplicity [50]. 16
1.10 CGC Evolution 17
1.11 Hard partons as a tomography of QCD medium. 20
1.12 Ratio between measured J/Ψ yield and expected yield as a function of energy density ε, by assuming the suppression source only comes from ordinary nuclear absorption [92]. 23
1.13 Hyperon production in Pb–Pb collisions normalized to the ratio from p–Be collisions as a function of centrality (expressed by $< N_{wound} >$), measured in the NA57 experiment at the SPS [95]. 24
1.14 Jet Quenching 25
1.15 Left: $R_{AA}(p_t)$ of π^0 in central $(0-10\%)$ and peripheral $(80-92\%)$ Au–Au collisions at $\sqrt{s_{NN}} = 200$ GeV measured by the PHENIX experiment [96], the shaded hands represent the systematic uncertainties on normalization. Right: two particle azimuthal distributions in pp, d–Au and Au–Au collisions measured by the STAR experiment [97]. 26
1.16 p/π^+ and $\overline{p}/\pi^-$ ratios in d–Au [99, 100] and Au–Au [101] collisions measured by the STAR experiment at RHIC. The dotted-dashed line is the ratio $(p+\overline{p})/(\pi^+ + \pi^-)$ measured in e^-–e^+ collisions [102]. The model calculations in central Au–Au collisions [103, 104] are shown in dotted and dashed lines. 27
1.17 Elliptic flow of different hadrons scaled by the number of quark constituents of hadrons. The lower panel shows the ratios between data and a Polynomial fit [106]. 28

1.18 Comparison of the integrated charged hadron elliptic flow as a function of centrality measured in the PHENIX experiment [109] and STAR experiment [110] with VISHNU calculations using **Participant Plane** (**PP**) averaged [108]. 29

1.19 Left: charged particle pseudo-rapidity density per participant in central nucleus-nucleus and non-single diffractive pp ($p\overline{p}$) collisions as a function of $\sqrt{s_{NN}}$ [112]. Right: decoupling time from ALICE (red filled dot) compared to the one obtained for central Au–Au and Pb–Pb collisions at lower energies at the AGS, SPS and RHIC [113]. . . 30

1.20 $v_2(p_t)$ from multi-particle methods in Pb–Pb collisions at $\sqrt{s_{NN}}$ = 2.76 TeV measured in ALICE [114], and compared with the results from the STAR experiment in different centrality classes. 31

1.21 Charged particle R_{AA} as a function of p_t up to 100 GeV/c in Pb–Pb collisions at $\sqrt{s_{NN}}$ = 2.76 TeV measured in the CMS experiment. The results are compared with the R_{AA} of π^0 predicted by WHDG calculations [115]. 31

2.1 Examples of Feynman diagrams: D^+D^- production in $p\overline{p}$ collisions via $gg \rightarrow c\overline{c}$ (left panel) and $D^+ \rightarrow \overline{K}^0\mu\overline{\nu}_\mu$ (right panel). 34

2.2 Left: parton distribution functions in proton from CTEQ 4L with Q^2 = 5 GeV^2 [41]. Right: Bjorken-x as a function of M^2 for particle production in nucleon-nucleon collisions at the SPS, RICH and LHC. The lines correspond to constant rapidity at corresponding energies [129]. 36

2.3 Accessible Bjorken-x range for heavy flavours in Pb–Pb collisions at $\sqrt{s_{NN}}$ = 5.5 TeV (left) and in pp collisions at $\sqrt{s}$ = 14 TeV (right) in the rapidity range that can be measured with ALICE at the LHC [130]. 36

2.4 Enhancement factor $R(p_t, \Delta y)$ for charm quarks (dashed lines) and D (D^0, D^+) mesons (solide lines), with m_c = 1.2 GeV/c^2, $Q^2 = 4m_T^2$ (left panel) and m_c = 1.3 GeV/c^2, $Q^2 = m_T^2$ (right panel) [132]. . . . 37

2.5 Upper plots: Distributions of different fragmentation functions for heavy quarks; middle plots: p_t distributions of open heavy flavour hadrons according to the corresponding fragmentation functions shown in the upper plots and comparisons with the p_t distribution of mother quark which is obtained from HvQMNR predictions [151] for beauty quarks; lower plots: ratios of different hadron p_t distributions to the result obtained with the Peterson fragmentation function. Each case is shown with $< z >= 0.9$ (left), 0.8 (middle) and 0.666 (right) [152]. Note that in the figures $< z >$ is expressed as $< x >$ in the plots. 41

2.6 p_t-differential cross section of open b-hadron production [161] measured by CDF **run II** at Tevatron. Results are compared with FONLL predictions [162]. 43

2.7 Differential cross section measurements for D-mesons in $|y| < 1$ as a function of p_t with CDF II detector at the Tevatron (circles) [163]. The solid curves are the FONLL predictions [164], with the uncertainties indicated by the shaded bands. The dashed curve shown for D^{*+} cross section is the theoretical prediction from Ref. [165] and the dotted lines indicate the corresponding uncertainty. 44

2.8 Left: (a) invariant differential cross sections of electrons from heavy flavour decays measured by PHENIX in pp collisions at $\sqrt{s} = 200$ GeV [166]. The curves are FONLL calculations [167]; (b) ratio of data and FONLL calculations, upper (lower) curve shows the theoretical upper (lower) limit of the FONLL calculations. Right: invariant cross section of $(e^+ + e^-)/2$ from beauty (upper-left) and charm meson (upper-right) decays measured by the STAR collaboration in pp collisions at $\sqrt{s} = 200$ GeV, together with the ratio of the corresponding measurements to FONLL predictions for beauty (lower-left) and charm electrons (lower-right) [168]. 45

2.9 Collision geometry in the transverse plane. 46

2.10 Charm production cross section per nucleon-nucleon collision at mid-rapidity as a function of N_{bin} (or N_{coll}) measured at RHIC in Au–Au collisions at $\sqrt{s_{NN}} = 200$ GeV [177]. 49

2.11 Yield of hard process in Pb–Pb collisions relative to the cross section in nucleon-nucleon collisions, as a function of the impact parameter cut $b < b_c$ [41]. 49

2.12 Illustration of a smoothly matched R_i^A function. 50

2.13 Comparison of the average valence quark, sea quark, and gluon modifications at $Q^2 = 1.69$ GeV^2 ($\sim m_c^2$) for a Pb nucleus, from LO global DGLAP analyses: EKS98, nDS [187], HKN07, EPS08 and EPS09LO. 52

2.14 Same as Fig. 2.13, but for the comparison of NLO global DGLAP analyses: HKN07, nDS and EPS09 NLO at $Q^2 = 1.69$ GeV^2 (upper panel) and 100 GeV^2 (lower panel). 53

2.15 Left: Average values of x and Q^2 of the DIS data from NMC (triangles) and E665 (diamonds), and of x_2 and M^2 of Drell-Yan (DY) dilepton data (squares). The heavy quark mass scales are shown by the horizontal dashed lines. Right: Ratios of gluon distribution functions from different models at $Q^2 = 5$ GeV^2. These two figures are extracted from [188]. 54

2.16 Medium modified fractional energy loss versus Debye mass μ in zeroth order opacity with **Ter-Mikayelian Effect** for up, charm and bottom quarks [195]. 55

2.17 Nuclear modification factor R_{AA} of non-photonic electron measured in d–Au and Au–Au collisions at $\sqrt{s_{NN}} = 200$ GeV with the STAR detector. Extracted from Ref. [201]. 56

2.18 Nuclear modification factor and elliptic flow of non-photonic electrons measured in Au–Au collisions at $\sqrt{s_{\rm NN}} = 200$ GeV with the PHENIX detector. The data are compared to predictions from different Langevin based models (see text). Extracted from [202]. . . . 56

2.19 $R_{\rm AA}$ of non-photonic electron measured in Au–Au collisions at $\sqrt{s_{\rm NN}} = 200$ GeV with the PHENIX experiment. The data are compared with the predictions of the collisional dissociation model. Extracted from [202]. . . . 58

2.20 Prompt electron distribution measured in the 10% most central Au–Au collisions at $\sqrt{s_{\rm NN}} = 130$ AGeV with the PHENIX detector [212]. 60

2.21 Theory comparison of non-photonic electron, v_2, versus $p_{\rm t}$ in Au–Au collisions at $\sqrt{s_{\rm NN}} = 200$ GeV [202] measured with the PHENIX detector [202], see the text for more details. . . . 60

2.22 Production cross sections as a function of the center-of-mass energy for Pb–Pb collisions [221]. . . . 62

2.23 The $p_{\rm t}$-differential production cross section ($\mathrm{d}\sigma/\mathrm{d}p_{\rm t}$) for charm hadron (top left) and bueaty hadron (top left) in pp collisions at $\sqrt{s} = 14$ TeV obtained from MNR predictions [151]. The correspoding botton plots show the components of the uncertainty from quark mass ($m_{\rm Q}$), parton density parametrisation (PDF), fragmentation parameter and the perturbative uncertainty from scale variations on the results [152]. . . . 63

2.24 Heavy-to-light ratios for D mesons (upper plots) and B mesons (lower plots) with a realistic heavy quark mass (plots on the right) and for a case study in which the quark mass dependence of parton energy loss is neglected (plots on the left). Extracted from Ref. [222]. . . . 64

2.25 Predictions of $R^{\rm c}_{\rm AA}(p_{\rm t})/R^{\rm b}_{\rm AA}$ versus $p_{\rm t}$ at LHC energies from fully weakly coupled pQCD calculations and strongly coupled AdS/CFT energy loss models [115]. . . . 65

2.26 $N_{\rm coll}$ ($N_{\rm part}$) dependence of the charmed meson yield at mid-rapidity, $\eta = 0$, and at forward rapidity, $\eta = 2$, in d–Au (Au–Au) collisions [190]. 66

2.27 Schematic representation of $\mathrm{D}^0 \to \mathrm{K}^-\pi^+$ decay with track impact parameter d_0 and pointing angle $\theta_{\rm pointing}$ [41]. . . . 66

2.28 Invariant-mass spectrum of D^0 (left) and D^+ (centre) candidates, and invariant-mass difference, $\Delta m = m(\mathrm{K}\pi\pi) - m(\mathrm{K}\pi)$, for D^{*+} candidates (right) in pp collisions at $\sqrt{s} = 2.76$ TeV measured with ALICE [224]. . . . 67

2.29 Upper: $p_{\rm t}$-differential cross section for prompt D^0, D^+, and D^{*+} mesons in pp collisions at $\sqrt{s} = 2.76$ TeV [224] compared with the scaling of the ALICE measurement at $\sqrt{s} = 7$ TeV [225]. Bottom: ratio of the $\sqrt{s} = 2.76$ TeV cross section and the $\sqrt{s} = 7$ TeV measurement scaling. Results are obtained with ALICE. . . . 67

2.30 Left: average D^0, D^+ and D^{*+} mesons R_{AA} in the $0-7.5\%$ centrality class [227] and charged hadron and pion R_{AA} in the $0-10\%$ centrality class [228, 229]. Right: v_2 of D^0, D^+ and D^{*+} mesons in centrality $30-50\%$ [230] compared to charged hadron v_2 [231]. Results are measured in Pb–Pb collisions at $\sqrt{s_{NN}} = 2.76$ TeV with ALICE. . . . 68

2.31 Inclusive electron yield per minimum bias pp collision as function of p_t at $\sqrt{s} = 7$ TeV in comparison with background electron cocktails for the TPC-TOF/TPC-TRD-TOF analysis (left) and for the TPC-EMCal analysis (right). Lower panels show the ratio of the inclusive electron yield to the background electron cocktail. Results are measured in pp collisions at $\sqrt{s} = 7$ TeV with ALICE [232]. 69

2.32 (a) p_t-differential invariant cross sections of electrons from beauty and from charm hadron decays. The solid (dashed) lines indicate the FONLL predictions [233] (uncertainties). Ratios of the data and the FONLL calculations are shown in (b) and (c) for electrons from beauty and charm hadron decays, respectively. (d) Measured ratio of electrons from beauty and charm hadron decays with error boxes depicting the total uncertainty. Results are measured in pp collisions at $\sqrt{s} = 7$ TeV with ALICE [234]. 70

2.33 p_t-differential R_{AA} (left) and v_2 (right) of electrons from heavy flavour decays in Pb–Pb collisions at $\sqrt{s_{NN}} = 2.76$ TeV measured with ALICE [235]. The results are compared with corresponding ones from PHENIX measurements [202]. 71

3.1 ALICE schematic layout. 76

3.2 Primary vertex resolution in Pb–Pb collisions at $\sqrt{s_{NN}} = 2.76$ TeV as a function of half of the tracklets multiplicity of the event [248]. Data taken in 2010, see text for details. 81

3.3 Left: track prolongation efficiency in ITS for TPC tracks, for the request of ITS-refit only (black) and ITS-refit with at least a point in SPD (red); data from Pb–Pb collisions at $\sqrt{s_{NN}} = 2.76$ TeV in 2010, MC results based on HIJING simulations. Right: transverse impact parameter resolution estimate as a function of p_t for pions, kaons, protons; data from pp collisions at $\sqrt{s} = 7$ TeV in 2010, MC corresponds to PYTHIA simulations with Perugia-0 configuration. . 83

3.4 Top: dE/dx of charged particles *vs.* their momentum, measured by the ITS alone (left) and TPC (right), the lines are a parameterization of the Bethe-Bloch curve. Bottom left: β *vs.* signed momentum in the TOF. Bottom right: HMPID Cherenkov angle *vs.* track momentum, continuous lines represent theoretical Cherenkov angle values *vs.* track momentum. The results correspond to pp collisions at $\sqrt{s} = 7$ TeV. 84

3.5 Left: charge deposit for electrons and pions at a momentum of 2 GeV/c, in pp collisions at $\sqrt{s} = 7$ TeV. Data (symbols) are compared with test beam measurements performed in 2004. Right: TPC dE/dx signal (in units of resolution) relative to the electron Bethe-Bloch lines (shown in the top right panel of Fig. 3.4) for 2 GeV/c tracks and 6 TRD tracklets, with and without electron tagging in the TRD, in pp collisions at $\sqrt{s} = 7$ TeV (2011 data). 85
3.6 Layout of the ALICE muon spectrometer. 88
3.7 Layout of front absorber. 92
3.8 Schema of the beam shielding. 93
3.9 Layout of dipole magnet of the muon spectrometer. 94
3.10 Layout of the tracking station 2 (left) and 4, 5 (right). 95
3.11 General view of the GMS. The red lines present the optical lines. . . 96
3.12 Principle of muon track reconstruction. 97
3.13 Left: scheme of the muon trigger stations MT1 and MT2 with two planes of RPCs on both of them. Right: scheme of a Resistive Plate Chamber (RPC). 99
3.14 Sketch of the track transverse momentum determination by the ALICE muon spectrometer trigger system. 100

4.1 The overall architecture of the ALICE DAQ and the interface to the HLT system [237]. 106
4.2 The six architectural layers of HLT [237]. 108
4.3 Schematic view of the ALICE offline computing tasks in the framework of the tiered MONARC model. Taken from Ref. [273]. 110
4.4 Schematic view of AliRoot framework. 113
4.5 Data Processing Framework of AliRoot 115
4.6 Schematic view of MUON analysis framework [282]. 116
4.7 Schematic view of the analysis tasks for the study of heavy flavours with muon data. 118

5.1 Single muon reconstruction efficiency as a function of p_{t} and η. . . . 125
5.2 The single muon p_{t} distributions (left) and unlike-sign dimuon M_{inv} distributions (right) from PDC06 after efficiency correction. 126
5.3 Reconstructed invariant mass distributions of correlated unlike-sign dimuons from beauty (left) and charm (right) decays in pp collisions at $\sqrt{s} = 14$ TeV. The different sources are displayed. 128
5.4 Reconstructed invariant mass distributions of correlated unlike-sign dimuons from $\mathrm{BB}_{\mathrm{diff}}$ channel (left) and $\mathrm{DD}_{\mathrm{diff}}$ channel (right) decay in pp collisions at $\sqrt{s} = 14$ TeV. The sources corresponding to different pQCD NLO processes of heavy flavour production are shown. 129
5.5 The results of the combined fit for single muon p_{t} distributions (left) and dimuon M_{ivn} distributions (right). 131

5.6 Transverse momentum distributions (upper panels) used for the estimation of systematics uncertainties and ratios of these distributions to the nominal case (lower panels). Shown from left to right are, D-hadrons, B-hadrons, decay muons from D-hadrons and from B-hadrons. All distributions are presented in the acceptance of the ALICE muon spectrometer. 132
5.7 Example of combined fits obtained with biased $f_{\mathrm{c/b}}^{\mu^{\pm}}$ shapes for single muon p_{t} distribution (left) and with biased $f_{\mathrm{c/b}}^{\mu^{-}\mu^{+}}$ shapes for unlike-sign dimuon invariant mass distribution (right). The vertical error bars (smaller than the points for single muon channel) are the statistical ones. 132
5.8 Relative systematic uncertainty on the estimation of single muons from charm (left) and beauty (right) decay *vs.* p_{t}. The different curves correspond to different values of pQCD parameters. 133
5.9 Relative systematic uncertainty on the estimation of unlike-sign dimuons from charm (left) and beauty (right) decay *vs.* M_{inv}. The different curves correspond to different $f_{\mathrm{c/b}}^{\mu^{-}\mu^{+}}$ biased shapes. 133
5.10 Illustration of $F^{\mathrm{MC}}_{\mu\leftarrow\mathrm{D/B}}(\phi^{\mu}, p_{\mathrm{t}}^{\mathrm{min}})$ calculation. 135
5.11 Dependence of $F^{\mathrm{MC}}_{\mu\leftarrow\mathrm{B}}$ (left panel) and $F^{\mathrm{MC}}_{\mu\leftarrow\mathrm{D}}$ (right panel) Monte-Carlo scaling factors on $p_{\mathrm{t}}^{\mathrm{min}}$ for selected muon p_{t} bins and, for different shapes of the B-hadron and D-hadron p_{t} distributions. 136
5.12 B-hadron (left) and D-hadron (right) inclusive production differential cross sections in pp collisions at $\sqrt{s} = 14$ TeV. The results are shown in the forward region: $-4 < \eta^{\mathrm{B(D)}} < -2.5$. The histogram is the input distribution. The points correspond to the reconstructed results from single muon and dimuon channels, respectively. The vertical error bars (smaller than the symbols in most of cases) are the statistical ones. The height and width of the boxes represent the systematic error from the fits and the uncertainty on the determination of $p_{\mathrm{t}}^{\mathrm{min}}$, respectively. 137
5.13 Signal yield (left), signal over background ratio (middle) and significance (right) of the single muon contribution from beauty decay (upper panels) and charm decay (lower panels) for the three scenarios of data taking. 139
5.14 The same as Fig. 5.13, but for dimuons. 140
5.15 Left: p_{t} distribution of reconstructed tracks in the ALICE muon spectrometer in minimum bias pp collisions at $\sqrt{s} = 14$ TeV (PDC08 production); the yields corresponding to the different sources are also plotted. The data are corrected for reconstruction efficiency, for $p_{\mathrm{t}} > 1$ GeV/c. Right: the production mechanisms for different muon track sources. 141
5.16 The some as Fig. 5.15 with the additinal requirements of track-trigger matching (left) and further cut on DCA< 9.3 cm (right). 142

5.17 p_t distribution of reconstructed tracks in the ALICE muon spectrometer in PDC08 with DCA< 9.3 cm are matched with the trigger tracks and muons from primary pion and kaon decays are subtracted. The contribution of muons from open heavy flavour decay contaminated with secondary muons from pion and kaon decays which is obtained by using the vertex method (blue histogram) is compared to the expected distribution (red histogram). 143

6.1 Ratios of events in background triggers to that in CINT1B trigger as a function of the run number (data taking time). 146
6.2 Ratio of events triggered in CMUS1B with respect to that in CINT1B as a function of the run number (data taking time). 146
6.3 The V0 leading time distributions in V0A (left) and V0C (right). The red band shows the time window for beam gas event, and the green band is the time window for beam-beam interaction events. 149
6.4 Event statistics in physics selection. 149
6.5 Left: v_z distributions with and without applying the physics selection. Right: distribution of number of contributors used for the primary vertex reconstruction. Results are obtained from the analysis of pp collisions at $\sqrt{s} = 900$ GeV collected in the end of 2009 with ALICE. 150
6.6 p_t (top left), η (top right), trigger matching (bottom left) and DCA (bottom right) distributions of reconstructed muon tracks with different event selection conditions as labeled inside each plot. Results are from LHC09d data in pp collisions at $\sqrt{s} = 900$ GeV. 152
6.7 DCA distribution of muon tracks without matching with trigger (left) and with matching with trigger (right) after the physics selection is applied to LHC09d data (pp collisions at $\sqrt{s} = 900$ GeV). The results are normalized to unit and compared with the ones from realistic simulations with PYTHIA and PhoJet, under the same conditions. . 154
6.8 DCA distributions of different muon track sources in simulations of pp collisions at $\sqrt{s} = 900$ GeV with PYTHIA (up) and PhoJet (down). The results are presented without matching with trigger (left) and with matching with trigger (right). The realistic detector effects of LHC09d data in pp collisions at $\sqrt{s} = 900$ GeV are included in the simulations. 154
6.9 Momentum p (left), p_t (middle) and η (right) distributions of muon tracks after the physics selection is applied to LHC09d data (pp collisions at $\sqrt{s} = 900$ GeV). The results are shown without the trigger matching (in blue) and with the trigger matching (in red), respectively. 155
6.10 DCA versus η for tracks without trigger matching (left) and with trigger matching (right) after the physics selection is applied to LHC09d data (pp collisions at $\sqrt{s} = 900$ GeV). A sharp p_t of 0.5 GeV/c is applied. 156

6.11 Relative momentum resolution σ_p/p as a function of p of the tracks reconstructed in the MUON spectrometer. Results are from the LHC09d data (pp collisions at $\sqrt{s} = 900$ GeV). 156

6.12 Composition of the front absorber of the ALICE muon spectrometer. 157

6.13 Left: σ_p/p as a function of $R_{\rm abs}$, the corresponding $\pi - \theta_{\rm abs}$ region is mentioned. Right: same as Fig. 6.11, but tracks are separated in different $\pi - \theta_{\rm abs}$ regions: $1^\circ - 2^\circ$ (red), $2^\circ - 3^\circ$ (blue), $3^\circ - 10^\circ$ (green) and $10^\circ - 90^\circ$ (purple). 158

7.1 The ratios of the number of tracker tracks over trigger tracks (top), matched tracks over trigger tracks (middle) and matched tracks over tracker tracks (bottom) as a function of run number in LHC10c period. The black lines show the results in the minimum bias events (CINT1B) and the red lines are the results in the muon trigger events (CMUS1B). 164

7.2 Multiplicity of trigger tracks (top), tracker tracks (middle) and matched tracks (bottom) in minimum bias events from LHC10d. Results are shown as a function of the run number. 165

7.3 Same as Fig. 7.2, but for muon trigger events in LHC10d. 166

7.4 Transverse momentum distributions of reconstructed muon tracks from the events with no identified pile-up vertex (blue) and from the tagged pile-up events (black). To compare the shapes of these two distributions, we scaled them together with the $p_{\rm t}$ distribution in the full event sample (red) according to the integrated yield given by the red line. These results are from the muon triggered events in run 124364 of LHC10d1 where the pile-up effect is large. 167

7.5 Same as the middle plot in Fig. 7.2, the tracker track multiplicity in minimum bias events from LHC10d. The results before the pile-up correction, black line, are compared with the one after the pile-up correction with Eq. (7.8), red line. 169

7.6 Transverse momentum (left) and η (right) distributions of muon tracks in minimum bias events (red) and in muon trigger events (blue) in pp collisions at $\sqrt{s} = 7$ TeV from LHC10c1. The ratios between the corresponding distributions in the minimum bias events and that in the muon trigger event are shown in the bottom panel. 171

7.7 The same as Fig. 7.6, but the distributions are from LHC10d2b. . . . 172

7.8 Normalized muon $p_{\rm t}$ distribution in minimum bias events (labeled as "MB data") and in muon trigger events (labeled as "MU data") with the pile-up correction in LHC10c1 and LHC10d2b, respectively. The results are shown as a function of $p_{\rm t}$ (left) and η (left). The normalization of muon trigger events is done with the multiplicity scaling method. 176

7.9 Transverse momentum distributions of muon track sources without any selection cut (left) and with the standard selection cuts (right) in pp collisions at $\sqrt{s} = 7$ TeV. Results from the LHC10f6a simulations with PYTHIA Perugia-0 tuning and realistic detector configurations correspond to LHC10d2b data sample. 177

7.10 Comparison between the $p_{\rm t}$-shape of primary muons in total η region, $-4 < \eta < -2.5$ (red lines) and the sum from fit results in 5 pseudo-rapidity bins (blue lines). The results are obtained, under the same selection cuts applied to data, from realistic simulations of LHC10d4 (pythia, upper, left), LHC10d4a (PhoJet, upper, right), LHC10f6 (PhoJet, down, left) and LHC10f6a (PYTHIA, down, right). 179

7.11 Upper panels: normalized inclusive $p_{\rm t}$ distributions in $-4 < \eta < -3.7$ in the muon triggered data from LHC10c1 (left) and LHC10d2b (right) with respect to the number muon triggered events. The results are compared to the $p_{\rm t}$ distributions of inclusive muons and primary muons in the corresponding realistic simulations. The simulations are scaled with $S_{\rm MC}$ (Eq. 7.27), obtained in the same η region before normalization with the corresponding number of events applied in the data. Lower panels: ratio between the primary muons and inclusive muons in data and in Monte-Carlo for LHC10c1 (left) and LHC10d2b (right). 180

7.12 The same as Fig. 7.11, in $-3.7 < \eta < -3.4$. 181

7.13 The same as Fig. 7.11, in $-3.4 < \eta < -3.1$. 181

7.14 The same as Fig. 7.11, in $-3.1 < \eta < -2.8$. 182

7.15 The same as Fig. 7.11, in $-2.8 < \eta < -2.5$. 182

7.16 Uncorrected $p_{\rm t}$-differential production cross section of muons from open heavy flavour decays in different η regions. Results from the minimum bias triggered data and muon triggered data in LHC10c1 and LHC10c2 are compared together. The systematics uncertainties are not yet shown. 184

7.17 Uncorrected η-differential production cross section of muons from open heavy flavour decays in $p_{\rm t} > 2$ GeV/c, obtained according to Eq. (7.24). Results from the minimum bias triggered data and muon triggered data in LHC10c1 and LHC10c2 are compared. The systematic uncertainties are not yet shown. 185

7.18 Estimate of $\sigma_{\rm models}$ (left column) and $\sigma_{\rm norm}$ (right column) with LHC10d2b in different η regions, see text for more details. 186

7.19 The ratios of primary muons (left) and secondary muons (right) to the total muons in $0 < p_{\rm t} < 1$ GeV/c (the region we used to calculate the $R_{\rm MC}$) in different simulations. 187

7.20 The two-dimension efficiency correction matrices as a function of $p_{\rm t}$ and η, built with the input of charm quark kinematics from HvQMNR predictions for LHC10c1 (left) and LHC10d2b (right), respectively. . 189

7.21 The efficiency correction for the η (left) and p_t (right) distributions of muons from open charm hadrons in the ideal simulation with PYTHIA ATLAS tuning. The reconstructed distributions are labeled as "reco", the distributions after the efficiency correction are labeled as "corr" and the input distributions are labeled as "kine". The ratio between the corrected distributions and the input distributions are presented in the bottom panels. The correction matrix is built with the charm quark kinematics distributions from HvQMNR predictions as the simulation inputs and under the ideal detector configurations. 190

7.22 Same conditions as in Fig. 7.21, except muons from open beauty hadrons are used as input. 191

7.23 Same conditions as in Fig. 7.21, except taht total muon signals from both open charm and beauty hadrons are used as input. 192

7.24 The efficiency correction matrices made by muons from charm (left) and muons from beauty (right) with the inputs of HvQMNR predictions. The realistic detector configurations corresponding to run 119159 in LHC10c1 are used for these simulations. 192

7.25 Results of efficiency correction in run 119159 from LHC10c1 for minimum bias data (up) and muon triggered data (down), respectively. The efficiency matrix is built with muons from charm with the corresponding realistic detector configurations, as shown in left plot of Fig. 7.24. 193

7.26 Results of efficiency correction in run 119159 from LHC10c1 for minimum bias data (up) and muon triggered data (down), respectively. The efficiency matrix is built with muons from beauty with the corresponding realistic detector configurations, as shown in right plot of Fig. 7.24. 193

7.27 Comparison of the corrected results in run 119159 from LHC10c1 with the correction matrices build by muons from charm (left plot of Fig. 7.24) and that with muons from bottom (right plot of Fig. 7.24), for the minimum bais triggered data (left) and muon triggered data (right), respectively. 194

7.28 The production cross sections of heavy quark pairs (left) and muons from heavy quark decays (right) from FONLL predictions in $-4 < \eta < -2.5$, in pp collisions at $\sqrt{s} = 7$ TeV. 195

7.29 The rescaled ratios of production cross sections with respect to the central values for $c\bar{c}$ (left) and $b\bar{b}$ (right) from FONLL predictions in $-4 < \eta < -2.5$, in pp collisions at $\sqrt{s} = 7$ TeV. 196

7.30 The corrected p_t-differential production cross sections of muons from open heavy flavour decays in LHC10c1, LHC10c2 and LHC10e, in different η regions. The results are compared with the FONLL predictions. In each run period, only the muon triggered data are used. 198

7.31 The corrected η-differential production cross section of muons from open heavy flavour decays in LHC10c1, LHC10c2 and LHC10e, in $p_{\rm t} > 2$ GeV/c. The result are compared with the FONLL predictions. In each run period, only the muon triggered data are used. 199

7.32 Similar as Fig. 7.30, but the comparison with FONLL predictions is presented for LHC10e data, with $p_{\rm t}$ measured up to 15 GeV/c. . . . 200

7.33 The mean values of DCA (left) and tracking χ^2 (right) for reconstructed tracks versus $p_{\rm t}$ bin in five pseudo-rapidity regions. The results are obtained from the muon triggered events in LHC10e with the muon selection cuts. 202

7.34 $\theta_{\rm abs}$ distributions in $-3.1 < \eta < -2.8$ (left) and in $-2.8 < \eta < -2.5$ (right) from the muon triggered data in LHC10e with the muon selection cuts. The results (red lines) are compared with the ones with DCA$<$ 10 cm (blue lines) in each η region. 203

7.35 The distribution of $\eta - \theta_{\rm abs}$ combination from muon triggered events in LHC10e (left) and LHC10d2b (right) with the selection cuts in $p_{\rm t} > 2$ GeV/c, see text for more details. 204

7.36 DCA (in $p_{\rm t} > 2$ GeV/c, left column) and $p_{\rm t}$ (right column) distributions without (red lines) and with (blue lines) the combination cut defined in Eq. (7.34) in five pseudo-rapidity bins. The results are from the muon triggered data in LHC10d2b with the muon selection cuts. 205

7.37 The ratios of the track multiplicity with the muon selection cuts plus the additional combination cut in minimum bias events to that in muon triggered events as a function of $p_{\rm t}$ (left) and η (right). The results are gotten from LHC10e. 206

7.38 Similar as Fig. 7.32, but the results are gotton with the additional combination cut defined in Eq. (7.34). 208

7.39 Same as the left panel of Fig. 7.35, but with the correlation between η and $\theta_{\rm CMS}$ as defined in Eq. (7.35), see text for more details. 209

7.40 The $\eta - \theta_{\rm CMS}$ distributions in $0 < p_{\rm t} < 0.5$ GeV/c (left column), 0.5 GeV/$c < p_{\rm t} <$ 1 GeV/c (middle column) and 1 GeV/$c < p_{\rm t} <$ 2 GeV/c (right column) from the data of muon trigger events in LHC10e (upper plots) and from the simulation of LHC10f6a based on PYTHIA Perugia-0 tuning (lower plots). The results are shown together with the cuts defined in Eq. (7.37) as the bound curves and are obtained after the muon selection cuts in both data and simulations. 210

7.41 The DCA$_{x,\rm vtx}$ (left) and DCA$_{y,\rm vtx}$ (right) distributions with the muon selection cuts for the muon trigger events in LHC10e. 212

7.42 $p\times$DCA (pDCA$_{\rm calib}$ as defined in Eq. (7.47)) versus $p_{\rm t}$ for muon trigger data in LHC10e. The muon selection cuts are applied. 212

7.43 Left: the ratio between the number of tracks in $N \cdot \sigma(p \times \mathrm{DCA})$ cut and the total number of tracks as a function of N in $p_{\mathrm{t}} > 2$ GeV/c. Right: the p_{t} distributions in $N \cdot \sigma(p \times \mathrm{DCA})$ with various values of N, the ratios between the p_{t} distributions with and without the $p \times$ DCA cut are shown in the lower panel. All the results are from muon trigger events in LHC10e with the muon selection cuts. 214

7.44 Similar as Fig. 7.37, but instead of implementing the $\eta - \theta_{\mathrm{abs}}$ cut, the additional cut $p\times$DCA in $5 \cdot \sigma(p \times \mathrm{DCA})$ is used. The results are also compared with those without the $p\times$DCA cut. 215

7.45 Ratio between the p_{t} distributions with $p\times$DCA cut in $5 \cdot \sigma(p \times \mathrm{DCA})$ and without this cut for different muon track sources from simulation from LHC10f6 (left) and LHC10f6a (right). The muon selection cuts are implemented. 216

7.46 The p_{t}-differential production cross section of muons from open heavy flavour decays in pp collisions at $\sqrt{s} = 7$ TeV in five rapidity regions. The analysis is based on the muon triggered data in LHC10e. The gray bands show the predictions from the FONLL predictions. These results are published in Ref. [317]. 221

7.47 The ratio between the measured results in data and the central value of the FONLL predictions, as shown in Fig. 7.46, in five rapidity regions, with the re-scaled errors. These results are published in Ref. [317]. 222

7.48 The differential production cross sections of muons from open heavy flavour decays as a function of p_{t} in $2.5 < y < 4$ (left) and as a function of rapidity y in $2 < p_{\mathrm{t}} < 12$ GeV/c (right). The analysis is based on the muon triggered data in LHC10e. The comparison with the FONLL predictions is also presented. As in Fig. 7.47, the lower panels show the ratio between the measured cross sections and central values of the FONLL predictions, with the re-scaled systematical uncertainties. These results are published in Ref. [317]. 223

7.49 The measured spectra of π^-, $\mathrm{K}^-$and $\overline{\mathrm{p}}$ (left), and π^+, $\mathrm{K}^+$and p (right) in central rapidity region ($|y| < 0.5$) in pp collisions at $\sqrt{s} = 7$ TeV with ALICE. All the results are fitted by the Lévy function, see the text for more details. 224

7.50 Left: the prompt J/Ψ spectra measured in pp collisions at $\sqrt{s} = 7$ TeV from LHCb [320]. Right: the normalized p_{t}-differential spectra of muons from the prompt J/Ψ decay according to the prompt J/Ψ distributions from LHCb (left plot) in different η regions; the ratio between the spectra of muons from the prompt J/Ψ decay and the normalized inclusive muon spectrum measured in pp collisions at $\sqrt{s} = 7$ TeV with the ALICE muon spectrometer is shown in the lower panel of this plot. 226

7.51 Left: Comparison between the results in Fig. 7.46 and those with the background subtraction via the parameterized K/π and J/Ψ distributions measured in data. Right: similar as Fig. 7.47, the ratios between the production cross sections of muons from heavy flavour decays measured in data and the central values of the FONLL predictions. 226

7.52 Similar as Fig. 7.48, but the production cross section of muons from heavy flavour decays based on the background estimate via the parameterized K/π and J/Ψ distributions are added at here. 227

8.1 The correlation between the corrected TDC timing of ZDC C−A and that of ZDC C+A. The results are obtained from minimum bias triggered events. The tails corresponding to the de-bunching collisions are shown in the plot. 231

8.2 Event statistics table in physics selection of run 139036 in LHC10h pass 2, with AliRoot version v5-02-02-AN. 232

8.3 The impact parameter distriubtion in Pb–Pb collisions. 233

8.4 An example of DoubleNBD grid fitting to the VZERO amplitude. . . 233

8.5 The $N_{\rm coll}$ (left) and $N_{\rm part}$ (right) distributions in different centrality classes obtained from the multiplicity distribution in Fig. 8.4. 234

8.6 The combination distribution of corrected ZEM amplitude and $E_{\rm ZDC}$. The results are obtained from minimum-bias triggered events in LHC10h pass 2. The four centrality bins are selected with the VZERO amplitude. 236

8.7 The event distribution as a function of centrality (left) and v_z distribution (right) in LHC10h pass 2. The results are obtained from minimum-bias trigger events. In both cases, the red histogram shows the results after the physics selection and the blue one shows the results with the additional centrality QA selection. 237

8.8 Left: muon track multiplicity distribution as a function of centrality. Right: normalized $p_{\rm t}$ distribution of muon tracks in different centrality classes. The results are obtained with the muon selection cuts listed in each plot and from LHC10h pass 2 data analyzed in April 2011. 239

8.9 The mean values of DCA (left) and tracking χ^2 (right) as a function of $p_{\rm t}$ in different centrality classes. The results are obtained from LHC10h pass 2 data with the muon selection cuts. The corresponding results from pp collisions at $\sqrt{s} = 7$ TeV (from LHC10e pass 2) are also shown. 240

8.10 The $\eta - \theta_{\rm abs}$ correlation of muon tracks with the selection cuts from LHC10h pass 1 in the centrality classes $0 - 20\%$ (left) and $60 - 80\%$ (right), respectively. The red lines show the 3σ limit of the correlation calculated according to Eq. (7.34). 241

8.11 Left: the momentum distributions of muon tracks at different reconstruction steps as labeled in the plot. The p_{CMS} observable defined in Eq. (7.42) is also shown in this plot (black histogram). Right: the v_x and v_y distributions used to correct the DCA_x and DCA_y, as defined in Eq. (7.44). All the distributions are obtained from LHC10h pass 2 data with the selection cuts listed in the plots. 242

8.12 The distributions of DCA_x (left) and DCA_y (right) without the correction of the vertex position (red histograms) and with the vertex correction (blue histograms), according to Eq. (7.44) and with the inputs of v_x and v_y distributions from the right plot of Fig. 8.11. . . 243

8.13 Left: $< \mathrm{DCA}_{x/y,\mathrm{vtx}} >$ with different selection conditions. Right: fits of the $p\mathrm{DCA}_{\mathrm{calib}}$ in two different θ_{abs} regions according to the function in Eq. (7.48). The results are obtained from LHC10h pass 2 data with the selection conditions listed in the plots. 243

8.14 The left and right plots are similar to the upper and lower plots in the right plot of Fig. 7.43. The results are here obtained from LHC10h pass 2 data. 244

8.15 The correlation of $p\mathrm{DCA}_{\mathrm{calib}}$ *vs.* p_{t} in $171^{\circ} < \theta_{\mathrm{abs}} < 177^{\circ}$ (left) and $177^{\circ} < \theta_{\mathrm{abs}} < 178^{\circ}$ (right) from LHC10h pass 2 data with the muon selection cuts. The black lines correspond to $5\sigma_{\mathrm{meas}}(p \times \mathrm{DCA})$ obtained from the fits in the right plot of Fig. 8.13. 245

8.16 Similar as Fig. 8.9, but the results are obtained with the additional $p\times$DCA cut in $5\sigma_{\mathrm{meas}}(p \times \mathrm{DCA})$. 245

8.17 The p_{t} (upper) and DCA (lower) distributions of muon tracks with the standard selection cuts in different centrality classes. The results are obtained from LHC10h pass 2 data which is used for our final analysis. The distributions without the $p\times$DCA cut and those with $p\times$DCA cut are compared. 247

8.18 Left: the interpolation factor for scaling the production cross section of muons from heavy flavour decays from pp collisions at $\sqrt{s} = 7$ TeV to that at $\sqrt{s} = 2.76$ TeV via FONLL calculations. The results are obtained by fixing $\mu_{\mathrm{F}} = \mu_{\mathrm{R}} = \mu_0$, and by varying the masses of charm and beauty quarks in the 9 combinations listed in the plot. The yellow band shows the envelope of the results obtained with all mass combinations. Right: the re-scaled results from the left side plot according to the one with $m_{\mathrm{c}} = 1.5$ GeV/c^2 and $m_{\mathrm{b}} = 4.75$ GeV/c^2. The yellow band shows the envelope of these re-scaled results. It corresponds to the relative uncertainty of the interpolation factor from quark masses. 250

8.19 As in Fig. 8.18, the results are obtained by fixing $m_{\mathrm{c}} = 1.5$ GeV/c^2 and $m_{\mathrm{b}} = 4.75$ GeV/c^2 and by varying the QCD scales in the corresponding 49 combinations. The color lines show the results for charm and beauty choices the with different values of the QCD scales. . . . 250

8.20 The interpolation factor (left) and its re-scaled ratio (right), with the uncertainties on the quark masses and the QCD scales obtained from Fig. 8.18 and Fig. 8.19, respectively. The total uncertainty calculated according to Eq. (8.15) is also shown. 251

8.21 The $\mathrm{d}\sigma_{\mathrm{pp}}^{\mu\leftarrow\mathrm{HF}}/\mathrm{d}p_{\mathrm{t}}|_{2.76\ \mathrm{TeV}}$ calculated according to Eq. (8.13) (in red) and compared with the inclusive muon production cross section in data (in black). See text for more details. 252

8.22 Left: production cross section of muons from heavy flavour decays in pp collisions at $\sqrt{s} = 2.76$ TeV from LHC11a. This was obtained at the end of 2011 according the two scenarios described in the text. The results are also compared with the ones using the energy interpolation (red curve in Fig. 8.21) and FONLL predictions. Right: the ratio between the production cross section of muons from heavy flavour decays in pp collisions at $\sqrt{s} = 2.76$ TeV in the left side plot and that obtained in pp collisions at $\sqrt{s} = 7$ TeV (shown in Fig. 7.48). The interpolation factor in the left plot of Fig. 8.20 using the FONLL calculations is also presented for comparison. 253

8.23 The production cross sections of muons from heavy flavour decays in pp collisions at $\sqrt{s} = 2.76$ TeV from LHC11a. The background is estimated according to both PYTHIA and PHOJET simulations with realistic detector configurations. 254

8.24 Left: the p_{t} spectra of charged pions measured in ALICE central barrel in different centrality bins in Pb–Pb collisions at $\sqrt{s_{\mathrm{NN}}} = 2.76$ TeV. The results are normalized to the number of events and compared with the charged pions spectrum measured in pp collisions under the same conditions. Right: the R_{AA} of charged pions obtained according to the p_{t} spectra in the left plot. The results are compared with the R_{AA} of the measured total charged particles. 257

8.25 R_{AA} of K_s^0 measured in $0-5\%$ (left) and $60-80\%$ (right) centrality classes from ALICE central barrel in Pb–Pb collisions at $\sqrt{s_{\mathrm{NN}}} = 2.76$ TeV. The results are compared to other charged particles as well as to model predictions as labeled in the plots. 258

8.26 The spectra of π^- (left) and π^+ in different centrality classes measured in ALICE central barrel in Pb–Pb collisions at $\sqrt{s_{\mathrm{NN}}} = 2.76$ TeV. The results concern the low p_{t} region where thermal production dominants. The Blast-Wave fits for these spectra are also shown in the plots. 259

8.27 The study of thermal charged pions. See text for more details. 259

8.28 Left: the normalized p_{t} distributions of charged pions in different centrality classes derived from the left plot of Fig. 8.24. Right: the distribution of muons from charged pion decays in $18 < p_{\mathrm{t}} < 20$ GeV/c with a flat p_{t} distribution of the charged pions as input. 260

8.29 The distribution of muons from $\pi^{\pm}$ decays in different mother pions p_{t} regions with a flat p_{t} distribution of the charged pions as input and a cut on the muon production distance of < 130 cm. 261
8.30 Left: the control plot used to get the upper limit of the p_{t} for the mother kaons. See text for more details. Right: the measured kaon spectra in ALICE central barrel in Pb–Pb collisions at $\sqrt{s_{\mathrm{NN}}} = 2.76$ TeV and pp collisions at the same collision energy. The results are extrapolated with a fit using Eq. (1.21). 262
8.31 Muons from pion (left) and kaon (right) decays in $-4 < \eta < -2.5$, with $\rho < 130$ cm and $n_y = 1$. 263
8.32 Left: the R_{AA} of muons in different centrality classes obtained by converting the charged pion spectra in left plot of Fig. 8.28 to the muon level, the error bars show the systematic uncertainties converted from the mother pion spectra. Right: the R_{AA} of muons from kaon decays in different centrality classes, the results are compared of those from pion decays in the corresponding centrality classes. 263
8.33 Left: the R_{AA} of different sources of decay muons in two different centrality classes as labeled in the plot. The results are obtained after all conversion steps in Sec. 8.5.3.2 with the inputs from Fig. 8.29. Right: the double ratio between $R_{\mathrm{AA}}^{\mu\leftarrow\pi}$ and $R_{\mathrm{AA}}^{\mu\leftarrow\mathrm{K}/\pi}$ which is obtained from the left plot in two different centrality classes. 264
8.34 R_{CP} extracted from the inclusive charged particle distributions in different η ranges, and three centrality classes $0-5\%$, $30-40\%$ and $50-60\%$ with respect to a common peripheral sample ($60-80\%$). Statistical errors are shown with vertical lines and the overall systematic uncertainty is shown with gray boxes [330]. 268
8.35 The spectra of decay muons normalized at the cross section level in pp collisions at $\sqrt{s} = 2.76$ TeV, see text for more details. 269
8.36 R_{CP} of inclusive muons as a function of p_{t} in different centrality regions in Pb–Pb collisions at $\sqrt{s_{\mathrm{NN}}} = 2.76$ TeV. The reference is provided by the centrality region $40-80\%$. The results are gotten from LHC10h pass 2 data. 277
8.37 R_{CP} of inclusive muons as a function of the centrality percentage in $p_{\mathrm{t}} > 5$ GeV/c (left) and $p_{\mathrm{t}} > 6$ GeV/c (right) in Pb–Pb collisions at $\sqrt{s_{\mathrm{NN}}} = 2.76$ TeV. The reference is the centrality region $60-80\%$. The results are gotten from LHC10h pass 2 data. 277
8.38 R_{AA} as a function of p_{t} for muons from open heavy flavour decays in centrality classes $0-10\%$ (upper) and $40-80\%$ (lower) measured in ALICE muon spectrometer in Pb–Pb collisions at $\sqrt{s_{\mathrm{NN}}} = 2.76$ TeV [332], see the text for more details. 279
8.39 R_{AA} of muons from open heavy flavour decays as a function of centrality measured in the acceptance of the ALICE muon spectrometer in Pb–Pb collisions at $\sqrt{s_{\mathrm{NN}}} = 2.76$ TeV [332], see the text for more details. 280

8.40 Left: $R_{\rm AA}$ of muons from heavy flavour decays as a function of $p_{\rm t}$ for the centrality $0-10\%$, which is extracted from left plot of Fig. 8.38. Right: $R_{\rm AA}$ of D-mesons as a function of $p_{\rm t}$ for the centrality in $0-7\%$ measured in ALICE central barrel ($|\eta| < 0.5$) [333]. Both results are obtained in Pb–Pb collisions at $\sqrt{s_{\rm NN}} = 2.76$ TeV and compared with the model predictions, see the text for more details. 281
8.41 Left: $R_{\rm AA}$ of muon from heavy flavour decays as a function of centrality gotten from Fig. 8.39. Right: $R_{\rm AA}$ of D-mesons as a function of centrality measured in ALICE central barrel ($|\eta| < 0.5$) [333]. Both results are shown in $p_{\rm t} > 6$ GeV/c. 281
8.42 $R_{\rm AA}$ of muon from heavy flavour decays as a function of centrality gotten from Fig. 8.39 and that of heavy flavour electrons measured in $|\eta| < 0.6$. 282

9.1 The normalized azimuthal distributions of different kinds of RP with the corresponding RP selection cuts or corrections. 310
9.2 The $p_{\rm t}$ (left), η (middle) and ϕ (right) distributions of global tracks without any selection cut. 311
9.3 The $p_{\rm t}$ (left), η (middle) and ϕ (right) distributions of standard global tracks with the selection cuts. 312
9.4 The $p_{\rm t}$ (left) and η (right) dependence of v_2 for the RP from second order GFC method. 312
9.5 The $p_{\rm t}$ (left) and η (right) dependence of v_2 for the RP from the second order QC method. 312
9.6 The $p_{\rm t}$ (left) and η (right) dependence of v_2 for the POI from the second order GFC method. 313
9.7 The $p_{\rm t}$ (left) and η (right) dependence of v_2 for the POI from the second order QC method. 313
9.8 The $p_{\rm t}$ (left), η (middle) and ϕ (right) distributions of muon tracks without any selection cut. 313
9.9 The $p_{\rm t}$ (left), η (middle) and ϕ (right) distributions of muon tracks with standard muon selection cuts. 314
9.10 Left: the azimuthal distribution and its weight distributions of standard TPCsa tracks. Right: the reference elliptic flow as a function of $p_{\rm t}$ for standard TPCsa tracks calculated via the EP method according to Eq. (9.12). Results are obtained from LHC10h pass 2 data. 316
9.11 The 2nd order event plane Ψ_2 distributions for standard TPCsa RP in different centrality classes obtained with the particle weights defined in Eq. (9.89). 317
9.12 The distributions of saturation corrected VZERO amplitude as a function of sector number in different centrality classes. 318
9.13 The distributions of saturation corrected VZERO amplitude as a function of sector number after the event-by-event weighting according to Eq. (9.92) in different centrality classes. 319

9.14 The x (left) and y (right) components of 2nd order Q-vector calculated from VZERO amplitude after the weighting. The results are shown in different centrality classes as labeled in the plots. 319
9.15 The x (left) and y (right) components of 2nd order Q-vector with the re-centering according to Eq. (9.93). The results are shown in different centrality classes as labeled in the plots. 320
9.16 The 2nd order event plane Ψ_2 distributions calculated according the Q-vector after the re-centering with Eq. (9.93) in different centrality classes. The results are shown before the shifting (black histograms) and after the shifting according to Eq. (9.94) (red histograms), respectively. 321
9.17 The 2nd order event-plane resolution for standard TPCsa RP (left) and VZERO RP (right) as a function of centrality. See text for more details. 322
9.18 Left: the 2nd order integrated cumulant $c_2\{2\}$ distributions as a function of centrality with different values of r_0 as labeled in the plot. Right: the integrated cumulant distribution as a function of the cumulant order in different centrality regions. The results are obtained with the standard TPCsa RP. 324
9.19 The integrated Q-cumulant distributions as a function of the cumulant orders in different centrality classes with the standard TPCsa RP. 324
9.20 $|G_n^\theta(ir)|$ as a function of r with the standard TPCsa RP from sum generating function (left) and product generating function (right), respectively. The results are shown in different centrality regions as labeled in each plot. 325
9.21 The same as Fig. 9.20, but with the VZERO RP. 325
9.22 The $p_{\rm t}$-dependence of v_2 for inclusive muons with different analysis methods and different kinds of RP in four centrality classes. 327
9.23 The same as Fig. 9.22, but the results are integrated over $p_{\rm t}$ and shown as a function of centrality. 327
9.24 The mean values of the results in Fig. 9.23 for $p_{\rm t} > 4$ GeV/c. 328

List of Tables

1.1 Global properties of the medium created at SPS, RHIC and LHC energies [111]. From up to bottom, the following quantities are presented: center of mass energy per nucleon pair, charged particle density at mid-rapidity, equilibration time of QGP, ratio of QGP temperature to critical temperature, energy density, QGP life-time, life-time and volume of the system at freeze-out, and baryonic chemical potential 30

2.1 The accessible Bjorken-x values with $c\bar{c}$ and $b\bar{b}$ production at threshold at mid-rapidity ($y = 0$) and different energies. 37

3.1 Summary of the ALICE detector subsystems. Extracted from [237]. . 77
3.2 Summary of the main characteristics of the muon spectrometer. Extracted from [237]. 89

5.1 Heavy flavours and quarkonia production cross sections in pp collisions at $\sqrt{s} = 14$ TeV simulated in PDC06. 124
5.2 Rejection rate of tracks sources with $p_t > 1.5$ GeV/c with matching with the trigger (second column) and, an additional DCA cut of 9.3 cm (third column). 142

6.1 Number of events and reconstructed tracks in the ALICE MUON Spectrometer for each trigger class in LHC09d data. 146

7.1 Statistics used in our analysis of LHC10c1, LHC10d2b and LHC10e. The corresponding number of minimum bias events N^{ev}_{MB} are gotten after the physics selection, the number of tracks in both minimum bias events and muon trigger events (labeled as N^{trk}_{MB} and N^{trk}_{MU}) are gotten after the muon selection cuts discussed in Sec. 6.4. 170
7.2 Simulations used in our analysis for corresponding data taking run periods. 171
7.3 Systematic uncertainties introduced by the procedure used for the subtraction of primary muons. The absolute values of η are used. The systematic uncertainties on normalization are corrected by the $p\times$DCA cut, as it will be discussed in Sec. 7.6.3.2. 188
7.4 The ratio of the corrected results with two independent correction matrices for run 119159 from LHC10c1 for the minimum bias triggered events extracted from lower panel in left plot of Fig. 7.27 in some given p_t regions. 194
7.5 Ratio of the corrected results with two independent correction matrices in run 119159 from LHC10c1 for the muon triggered events extracted from lower panel in right plot of Fig. 7.27 in some given p_t regions. 194

7.6 The number of reconstructed track in the MUON spectrometer with the muon selection cuts in both minimum bias events and muon trigger events, together with the corresponding ratios. The results are gotten with LHC10e data and shown with and without the additional combination cut defined in Eq. (7.34). 207
7.7 The values of $\sigma_{\rm meas}(p \times {\rm DCA})$ in $171^{\circ} < \theta_{\rm abs} < 177^{\circ}$ and $177^{\circ} < \theta_{\rm abs} < 178^{\circ}$ from the muon triggered events in LHC10e with the muon selection cuts. 213
7.8 Values of the parameters in Lévy function (Eq. (7.61)) obtained by fitting the charged K/π spectra shown in Fig. 7.49. 225

8.1 Mean values of number of participants ($< N_{\rm part} >$), number of binary collisions ($< N_{\rm coll} >$) and nuclear overlap function ($< T_{\rm AA} >$) in six centrality classes from Glauber model. Results are offered by ALICE officially. 238
8.2 The values of $\sigma_{\rm meas}(p \times {\rm DCA})$ in $171^{\circ} < \theta_{\rm abs} < 177^{\circ}$ and $177^{\circ} < \theta_{\rm abs} < 178^{\circ}$ in LHC10h pass 2 data extracted from the fit presented in the right plot of Fig. 8.13. 244
8.3 Event statistics in LHC10h pass 2 used for the final analysis. 246
8.4 Muon track statistics in LHC10h pass 2 used for the final analysis. . 246
8.5 The event statistics in the used LHC11a data sample. 252
8.6 The muon-track statistics in the used LHC11a data sample. 253
8.7 The ratios between the efficiency correction of single muons in different centrality regions and the one in $60-80\%$. The results are gotten by embedding the J/Ψ signal in LHC10h data [331]. 272

9.1 The status of the different flow analysis methods with the standard TPCsa RP and the VZERO RP. 326

Part I

Introduction

Chapter 1

QCD Phase Transition and Heavy Ion Collisions

I have always been asked, what is the meaning of my PhD thesis, **heavy ion collisions**, and how to use them in real life? Most of time, it is hard to use simple words to answer these questions, as Stephen Hawking did in his well known report entitled «A Brief History of Time» [1]. Parts of the answer could become as obscure as issues in philosophy for persons who do not have background in this field. I would like to start this thesis with a brief history of elementary particles in the Universe and their interactions in order to fully answer these questions. In general, one starts with the **origin of mass** and **the new phase transition generated by the strong interactions**.

1.1 History of Standard Model

In the beginning of the 20th century, the development of the **Special Relativity** [2] and **Quantum Mechanics** [3, 4, 5, 6] not only led to the global third industrial revolution, but also opened a new era for modern physics.

1.1.1 Quark Model

In 1911, Ernest Rutherford discovered the structure of the atom according to the well known Rutherford scattering experiment [7]. During the period 1930-1940, the only known elementary particles were protons, neutrons, electrons, muons, neutrinos and pions, the latter transfer the nuclear force between nucleons (protons and neutrons). In 1947, the Λ particle was found in cosmic rays beyond expectations, then it follows the discovery of a large number of new particles. Finally, it is worth mentioning that hadrons were not considered as "fundamental" particles.

During the implementation of the classification schemes of hadrons, the unitary spin symmetry was found, and triggered the development of the **Quark Model** [8]. In the Quark Model, the hadrons are composed of the elementary particles, the quarks and gluons (mesons (baryons) are made of two (three) valence quarks) [1]. Each quark has three different kinds of "color" and the gluon (with 8 kinds of "color") exchange the strong interaction, due to the color charge between quarks. Up to now, 6 flavours of quarks (up, down, strange, charm, bottom and top) are

[1] Also, there are sea quarks and gluons in the hadrons. But they are hidden inside the Dirac sea under normal conditions. The main properties of hadrons are reflected by their valence quarks.

found in the nature. The author of the model, Gell-Mann, received the **Nobel Prize** in 1969, after the ${}^{3/2}\Omega^{-}$ baryon (predicted by the model) was discovered at Brookhaven National Laboratory.

1.1.2 Higgs Mechanism

Indeed, the theory of strong interaction was developed before the Quark model. In 1954, Chen-Ning Yang and Robert Mills developed the **Yang-Mills Theory** [9] in order to explain the strong interaction and they extended the gauge theory in abelian groups, *e.g.* **Quantum ElectroDynamics** (**QED**), to non-abelian groups. The basic concept of the Yang-Mills theory is that it requires Lagrangian of the gauge field, which has the global gauge invariance (the additional local gauge invariance). In order the Lagrangian has both global and local gauge invariances, a new gauge field should be introduced. This new gauge field describes the interaction of this system (e.g. the gravitational field is the gauge field used to keep the local Pinkoé transform invariance of special relativity particles and the electromagnetic field is the gauge field used to keep the QED local gauge invariance). A non-abelian gauge field, **Yang-Mills Field**, should be introduced in order to require that particles in local compact semi-simple Lie groups (*e.g.* SU($\mathcal{N}$) group for strong interaction) transform invariance. The non-abelian nature explains that the Yang-Mills field has the self-interaction, and also includes automatically the isospin. However, as in all gauge theories, particles in the Yang-Mills field are massless, which means that the strong interaction has long range effects, which had never been oberved experimentally.

The Yang-Mills theory allows to obtain the interaction term in the Lagrangian of the system but it is assumed that particles are massless. Where is the mass coming from or what is the origin of the mass? This puzzle was **partly** solved in 1960.

In order to go further, we first introduce a theorem derived from condensed matter physics,

Goldstone's Theorem*: since a system with Lagrangian has invariance under a continuous group with n group parameters, G_n, and its Lagrangian in the ground state is invariance under group G_m ($m < n$); $n-m$ bosons with vanished rest mass, energy-momentum and spin, G bosons, will be produced, after spontaneously symmetry breaking [10].*

The G bosons were discovered in BCS mechanism [11] and elucidated by Jeffrey Goldstone in 1961. Furthermore, A. Salam and S. Weinberg implemented this theorem in quantum field theory in 1962 [12].

In 1964, Peter Higgs introduced the unification of G bosons and gauge field, which explained the origin of mass of elementary particles. The massless gauge field has only two horizontal polarization degree of freedom, while the massive field should have an additional longitudinal polarization degree of freedom, this new degree of freedom corresponds to the G bosons. The **Higgs Mechanism** [13], endows gauge bosons in a gauge theory with mass through absorption of G-bosons after the symmetry is spontaneously broken.

With the Higgs mechanism, all the gauge theory (including the Yang-Mills the-

ory) can be massive. In 1967 and 1968, S. Weinberg and A. Salam used it and unified the **Electroweak Model** [14, 15]. During 1972-1974, the **Standard Model** (modern form [16] of **Quantum Chromodynamics**) which is the theory describing electromagnetic, weak and strong interactions is developed.

1.1.3 Standard Model

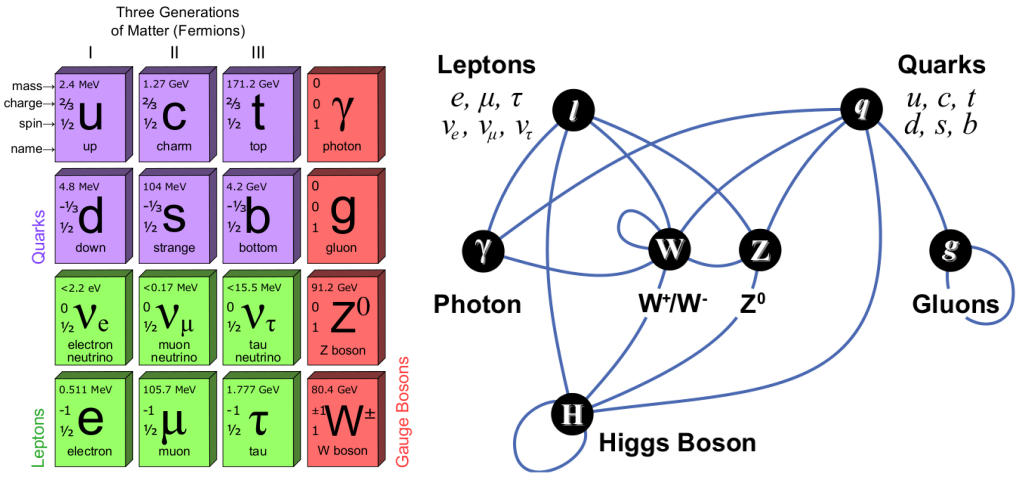

Figure 1.1: Elementary particles in the Standard Model (left) and the fundamental interactions between them (right) [17].

In the Standard Model, the elementary fermions are classified in three families of leptons and three families of quarks, as shown in left side of Fig. 1.1. The i-th family of left-hand fermions is merged in SU(2) doublets, and the right-hand fermions are merged in SU(2) singlets. If one uses the Yang-Mills theory and one requires the Lagrangian invariance under SU(2)⊗U(1), a three-component weak-isospin vector $\vec{W}_\mu$ and a weak-isospin scalar B_μ need to be introduced. The first two components of $\vec{W}_\mu$ are charged $W^\pm_\mu$, while W^3_μ and B_μ are neutral. They are related to the intermediate vector boson Z_μ and photon A_μ,

$$\begin{pmatrix} A_\mu \\ Z_\mu \end{pmatrix} = \begin{pmatrix} \cos\theta_W & -\sin\theta_W \\ \sin\theta_W & \cos\theta_W \end{pmatrix} \cdot \begin{pmatrix} B_\mu \\ W^3_\mu \end{pmatrix}, \tag{1.1}$$

where θ_W is the Weinberg angle (angle by which spontaneous symmetry beaking rotates W^0).

After spontaneous symmetry breaking via the Higgs mechanism with the appropriate θ_W angle, $W^\pm$ and Z^0 become massive by keeping the photon massless. The fermions (quarks and leptons) obtain their masses via the Yukawa coupling with the Higgs scalar field. Parity is conserved for the electromagnetic interaction, while for the weak interaction, the non-conservation of parity is satisfied automatically. Photons, $W^\pm$ and Z^0 plus gluons, the gauge bosons in the Standard Model, carry the electromagnetic, weak and strong interactions by exchanging charge, flavour

and color between the quarks and leptons (right panel of Fig. 1.1). Gluons have the self-interactions due to the non-abelian nature of QCD.

In 1973, neutral weak currents due to Z^0 exchange were discovered at **CERN** (**European Organization for Nuclear Research** [2]) [18, 19, 20]. Glashow, Salam, and Weinberg shared the **1979 Nobel Prize in Physics** after these discoveries. In 1983, $W^{\pm}$ and Z^0 were discovered experimentally according to the masses predicted by the Standard Model. An other model predicts the Higgs particle (neutral scalar boson). Recently, the ATLAS and CMS collaborations presented a clear evidence for the production of neutral boson with a measured mass of $125-126$ GeV$/c^2$ [21, 22]. This observation is compatible with the production and decay of the standard model Higgs boson.

The fundamental interactions in microscopic world, introduced by the Yang-Mills theory, are described by the electro-weak model and QCD (Quantum ChromoDynamics). The Standard Model includes all these interactions [3]. What an harmony world! It looks like our story about the origin of mass could end here$\cdots$ But all of the wonderful stories are full with twists and turns. We just played the overture, the bigger dark clouds are waiting for us$\cdots$

1.2 Quantum ChromoDynamics

Quantum ChromoDynamics (QCD) is the gauge field theory of SU(3)$\otimes$SU(2)$\otimes$U(1). It describes the strong interaction between colored quarks and gluons which constitute the hadrons according to the Standard Model. To continue our story about the origin of mass, let us start with the introduction on the general properties of QCD. Then we will find that this story overlaps with an other story about the phase transition between hadronic matter and a new matter phase.

1.2.1 QCD Lagrangian

The Lagrangian in QCD is [23],

$$\mathcal{L} = \sum_q \overline{\psi}_{q,a}(i\gamma^\mu\partial_\mu\delta_{ab} - g_{\rm s}\gamma^\mu t^C_{ab}\mathcal{A}^C_\mu - m_a\delta_{ab})\psi_{q,b} - \frac{1}{4}F^A_{\mu\nu}F^{A,\mu\nu}. \qquad (1.2)$$

In Eq. (1.2), γ^μ are Dirac γ-matrices; $\psi_{q,b}$ are quark field spinors, where, q and a are the quark flavour and color indexes, a runs between $a = 1 \rightarrow N_{\rm c} = 3$; $\mathcal{A}^C_\mu$ are gluon fields with C running between $C = 1 \rightarrow N_{\rm c}^2 - 1 = 8$; m_q are quark masses generated via the Higgs mechanism and $g_{\rm s}$ (or $\alpha_{\rm s} = g_{\rm s}/4\pi$) is the QCD coupling constant; $m_{\rm q}$ and $g_{\rm s}$ (or $\alpha_{\rm s}$) are two fundamental parameters in QCD; t^C_{ab} are 8 generators of SU(3) group. The field tensor $F^A_{\mu\nu}$ is given by,

$$F^A_{\mu\nu} = \partial_\mu\mathcal{A}^A_\nu - \partial_\nu\mathcal{A}^A_\mu - g_{\rm s}f_{ABC}\mathcal{A}^B_\mu\mathcal{A}^C_\nu, \qquad (1.3)$$

[2] the abbreviation "CERN" is according to its old name in French, **Conseil Européen pour la Recherche Nucléaire.**

[3] There still are questions beyond the Standard Model like quantization of gravitation, dark matter and dark energy, but they concern grand macro physics.

where the definition of SU(3) structure constants, f_{ABC}, is

$$[t^A, t^B] = i f_{ABC} \cdot t_C. \tag{1.4}$$

Two useful constants, the color Casimir factors $C_{\rm F}$ and $C_{\rm A}$, are defined via the color algebra relations,

$$\begin{aligned} t^A_{ab} \cdot t^A_{bc} &= \delta_{ac} C_{\rm F} \quad (C_{\rm F} \equiv \frac{N_{\rm c}^2 - 1}{2N_{\rm c}} = \frac{4}{3}), \\ f^{ACD} \cdot f^{BCD} &= \delta_{AB} C_{\rm A} \quad (C_{\rm A} \equiv N_{\rm c} = 3). \end{aligned} \tag{1.5}$$

$C_{\rm F}$ and $C_{\rm A}$ are associated with the gluon emission from quark and gluon emission from gluon, respectively.

The last non-abelian term in Eq. (1.3) reflects the gluon self-interactions. It governs a very important property of QCD, the **Asymptotic Freedom**.

1.2.2 Asymptotic Freedom

In analogy with **QED** (**Quantum ElectroDynamics**), due to the quantum fluctuations, QCD vacuum is like a polarizable medium. Gluons can create the virtual quark-antiquark ($\rm q\overline{q}$) pairs in vacuum, as the uncharged photons create e^-e^+ pairs in QED. This screens the color charge in the QCD vacuum can be considered as a color dielectric ($\varepsilon_0^{\rm c} > 1$) [4] and color diamagnetic ($\mu_0^{\rm c} < 1$) medium according to the Lorentz invariance,

$$\varepsilon_0^{\rm c} \cdot \mu_0^{\rm c} = 1. \tag{1.6}$$

Also, due to self-interactions of gluons via color charge exchange, the QCD vacuum becomes a magnetized medium. As a consequence, QCD vacuum behaves as a color paramagnetic, $\mu_0^{\rm c} > 1$ [24]. With Lorentz invariance condition (Eq. (1.6)), the QCD vacuum is a color conductor ($\varepsilon_0^{\rm c} < 1$). As there is no net electric charge inside an electric conductor, free color charge cannot appear in the QCD vacuum. This is why only hadrons, but not their quark constituents, are found in the nature.

Due to the color anti-screening in QCD vacuum, the interactions between $\rm q\overline{q}$ pairs will become stronger while separating. But one can imagine that, when the distance between them is close to zero ($r \to 0$), the quantities $\varepsilon_0^{\rm c}$, $\mu_0^{\rm c} \to 1$ and the interaction between $\rm q\overline{q}$ becomes weak. This leads to the running property of the QCD coupling. This property is described in the renormalization group equation under the framework of **perturbative QCD** (**pQCD**) [23]:

$$\mu_{\rm R}^2 \frac{{\rm d}\alpha_{\rm s}}{{\rm d}\mu_{\rm R}^2} = \beta(\alpha_{\rm s}) = -\sum_{n=0}^{\infty} b_n \alpha_{\rm s}^{n+2}, \tag{1.7}$$

where, $\alpha_{\rm s}$ is the coupling constant and $\mu_{\rm R}$ is the QCD renormalization scale. First terms of the sum in β function (b_n, in Eq. (1.7)) can be found in [23]. More details

[4] By analogy with the dielectric constant ε_0 and permeability μ_0 in QED, $\varepsilon_0^{\rm c}$ and $\mu_0^{\rm c}$ denote the color dielectric constant and color permeability in QCD, respectively.

are given in [25, 26, 27, 28]. A solution of Eq. (1.7) considering only first term of the sum (b_0), under the assumption $\mu_R^2 \simeq Q^2$ is [29, 30]:

$$\alpha_s(Q^2) = \frac{12\pi}{(33 - 2n_f)\ln(Q^2/\Lambda_{QCD}^2)}, \tag{1.8}$$

where, Q^2 is the virtuality related to the momentum transfer in a given process, n_f is the number of light flavours with $m_q \ll Q$ and, Λ_{QCD} is the non-perturbative QCD scale corresponding to an α_s value where pQCD cannot be used. Eq. (1.8) is confirmed by experiments, as shown in Fig. 1.2, and David J. Gross, H. David Politzer and Frank Wilczek awarded the **2004 Nobel Prize in Physics**.

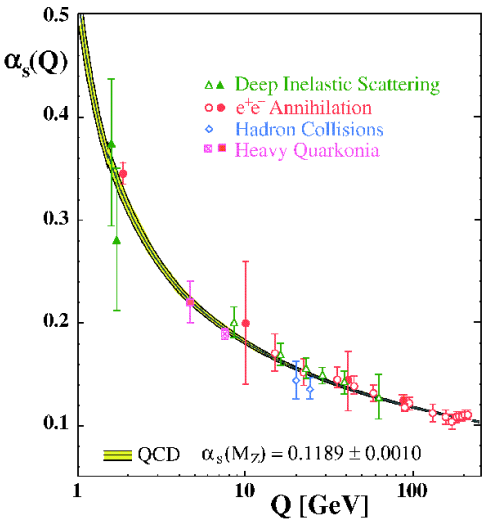

Figure 1.2: QCD running coupling as a function of Q with $\Lambda_{QCD} \approx 200$ MeV [31].

Eq. (1.8) reveals that, due to the small value of Q^2 in normal world, the coupling between quarks and gluons is very large since they are confined in the hadrons. On the contrary, for processes with high momentum transfer, α_s becomes small, free quarks and gluons behave as free particles in the QCD vacuum: this is the well known "asymptotic freedom" (or deconfinement). It is worth pointing out that in processes with large momentum transfer, where α_s is small, the **Chiral Symmetry** in the QCD Lagrangian, Eq. (1.2), will be broken. This aspect points out to the origin of mass, the starting point of our story!

1.2.3 Chiral Symmetry Restoration

According to the Standard Model, the mass of quarks is generated via Yukawa coupling with Higgs field and, hadrons are composed by quarks and gluons. In principle, in the ground state, the mass of a given hadron should correspond to the one of its valence quarks. For instance, for pion mesons ($\pi^{\pm}$ and π^0), which are composed of u and d quarks, the masses are $m_{\pi^{\pm}} \approx 140$ MeV/c^2 and $m_{\pi^0} \approx 135$ MeV/c^2. However the current masses [5] of u and d quarks are only $m_u = 1.7 - 1.3$ MeV/c^2 and $m_d = 4.1 - 5.8$ MeV/c^2, which are very small relative to the

[5] The mass of quarks is a very complicate item. The masses of light quarks, here u, d and s, generated by the Higgs mechanism are named "current" masses; for heavy flavours, c and b, the corresponding masses are named "running" masses. The "current" or "running" masses are distinguished by their quark "constituent" mass, which will be introduced later. Also there is the "bare" mass of quarks, and it gives the relation between the "current" or "running" mass [32].

mass of pions. Where is the additional mass of pions coming from? To answer this question, we should go back to the QCD Lagrangian (Eq. (1.2)).

By considering the first two flavours in Eq. (1.2), u and d, and ignoring the quark mass terms (masses of u and d are small) one obtains:

$$\mathcal{L} = \sum_{q=\mathrm{u,d}} \overline{\psi}_{q,a}(i\gamma^{\mu}\partial_{\mu}\delta_{ab} - g_{\mathrm{s}}\gamma^{\mu}t^{C}_{ab}\mathcal{A}^{C}_{\mu})\psi_{q,b} - \frac{1}{4}F^{A}_{\mu\nu}F^{A,\mu\nu}. \tag{1.9}$$

Eq. (1.9) is invariant under the **Chiral Transformation**,

$$\psi \rightarrow e^{i\alpha\gamma^{5}}\psi, \tag{1.10}$$

where α is the generator of SU(2) group. This means that, with vanishing masses, quarks travel with the speed of light, their helicity (h, the projection of spin along the motion direction) has two eigenstates $h = \pm 1/2$ corresponding to the right- and left-hand particles. Also, due to the total angular momentum conservation, the interactions with gluons will not change the helicity of quarks [33]. In this case, particles with opposite parity must be degenerated in mass, even the small values of m_{u} and m_{d} break slightly this **Chiral Symmetry**, *e.g.* the triplet $\rho(770)$ and $\mathrm{a}_1(1260)$. But in the real life, $m_{\rho(770)} \approx 755.5$ MeV/c^2 and $m_{\mathrm{a}_1(1260)} \approx 1230$ MeV/c^2 are very different, the chiral symmetry is strongly broken. The chiral symmetry breaking indicates that the masses of u and d quarks are not as small as their current masses in the QCD vacuum, then their speed is far from the speed of light. This leads to the chirality flip.

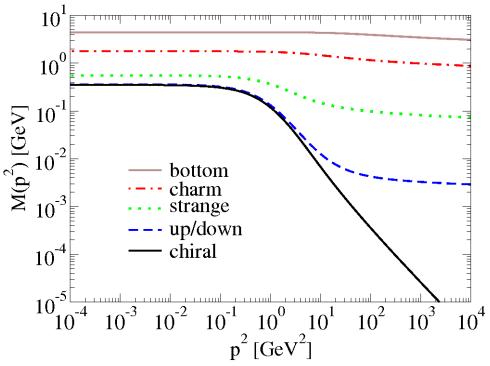

Figure 1.3: Constituent quark masses with various current masses of different flavours [32].

Presently, due to the strong coupling between quarks, the QCD vacuum is non-vanishing, it is defined as the **chiral condensation** [34],

$$< \overline{\psi}\psi > \equiv < 0|\overline{\psi}_{\mathrm{L}}\psi_{\mathrm{R}} + \overline{\psi}_{\mathrm{R}}\psi_{\mathrm{L}}|0 > \neq 0, \tag{1.11}$$

where, $\psi_{\mathrm{L/R}}$ are the spinors for left- and right-hand particles. Eq. (1.11) denotes the **Chiral Symmetry Spontaneous Breaking** in QCD vacuum, and describes the flip of the chirality as, *e.g.* a right-hand particle annihilates in vacuum via ψ_{R}, leaving $\overline{\psi}_{\mathrm{L}}$ to create a left-hand particle with the same momentum. The left- and right-handed particle pair plays the same role as the Cooper-pair in the BCS theory [35]. In analogy with the BCS theory, $< \overline{\psi}\psi >$ explains the energy gap between the physics vacuum and QCD vacuum. This energy gap generates the additional constituent mass for quarks even with vanishing current masses [36],

$$M(p^2) = \frac{2}{3}\pi^2\gamma_{\mathrm{m}}\frac{-<\overline{\psi}\psi>}{(\frac{1}{2}\ln\frac{p^2}{\Lambda^2_{\mathrm{QCD}}})^{1-\gamma_{\mathrm{m}}}} \text{ (current quark mass } m_{\mathrm{q}} \rightarrow 0), \tag{1.12}$$

where, p is the quark momentum in the quark propagator and $\gamma_{\rm m} = 12/(11N_{\rm c}-2n_{\rm f})$. Eq. (1.12) presents a general property: when the quark momentum increases, with large momentum transfer and $\alpha_{\rm s}$ decreases (Fig. 1.2), the constituent mass in the quark propagator becomes smaller. Considering the finite quark current mass effect and the evolution of $<\overline{\psi}\psi>$, the full relation between the quark constituent mass and its momentum given by the Dyson-Schwinger formalism [37] is shown in Fig. 1.3.

Results in Fig. 1.3 reveal that, 99% of u and d masses and a very large part of the mass of s are generated by the chiral symmetry spontaneous breaking, and the chiral symmetry is restored with large momentum transfer. Since the normal matter in the Universe is constituted by the nucleons (protons, p(udd) and neutrons, n(uud)) almost all the visible Universe is created by this effect [6].

1.2.4 Ends and New Starts

The origin of mass has been intensively discussed within the framework of the Standard Model. However, some trivial aspects, like the chiral symmetry spontaneous breaking which also affects the Goldstone theorem and generates the so-called pseudo-Goldstone particles as pions, are not detailed. But this does not affect following conclusion: in the framework of the Standard Model, where the mass of elementary particles is generated by the Higgs mechanism, additionally, in the non-perturbative structure of QCD vacuum, the quarks obtain the additional constituent mass, and it dominates in almost all the visible Universe.

In the framework of QCD (Eq. (1.2)), following properties can be extracted: both asymptotic freedom and chiral symmetry restoration occur with large momentum transfer. This indicates that in the high energy regime, QCD should allow to study the properties of a new phase of matter and reveal the mystery of the Universe just after the **Big Bang**!

1.3 Quark Gluon Plasma

In Sec. 1.2.2, we learnt that, with larger momentum exchange or small distance between partons the strong interaction becomes weaker, and free partons are present in the vacuum. The increase of the momentum exchange or the decrease of the distance between partons is equivalent to heat or compress the normal hadronic matter. This indicates that, by continuing to heat or compress, a transition between normal hadronic matter and a new matter phase composed of free quarks and gluons with weak interactions between them is expected. In analogy to the **electromagnetic plasma**, which is composed of separated ions and electrons gas, this new matter phase is named: **Quark-Gluon-Plasma** (**QGP**). In addition to the onset

[6] In the prospect of **Precision Cosmology**, the so-called dark energy and dark matter contribute at $\sim 72\%$ and $\sim 24\%$ of the whole energy density in the Universe, respectively. The rest $\sim 4\%$ of the visible part of the Universe is created by the Standard Model particles. In the context of this thesis, we only focus on the part of the Universe described by the Standard Model.

of deconfinement, the chiral symmetry should be restored [7].

1.3.1 Lattice QCD Predictions

Due to long distance particle correlations during the **QCD phase transition** (phase transition between hadronic matter and QGP), the perturbative calculations fail in describing such process. Also, the chiral symmetry comes from the non-perturbative property of the QCD vacuum. In order to get rid of these problems, lattice calculations, **Lattice QCD** (**lQCD**) [38], were implemented to solve the QCD equations from first principle calculations.

In lQCD, the QCD Lagrangian is introduced on discrete Euclidean space-time lattices. The quarks are located on the lattice vertices, and gluons travel along the lines between the vertices to exchange the strong force. It uses the Feynman path integral to deal with the parton propagator, while the system temperature is treated by the statistical mechanics. The physics results could be estimated by extrapolating the calculations with different lattice sizes to the continuum case (infinitesimal lattice size).

Despite lQCD calculations still have problems to treat the finite baryon chemical potential (in case of $\mu_{\mathrm{B}} > 0$), several results have already been obtained under this framework for what concerns the prediction of the QCD phase transition at high temperature. This has been done by decreasing the size of space-time lattice and using realistic values of light quark masses.

The left panel of Fig. 1.4 shows the energy density ε/T^4 *vs.* temperature T for 2 light plus 1 heavier (strange) quarks with $\mu_{\mathrm{B}} = 0$, as calculated from recent lQCD calculations with physical dynamic quark masses [39]. The main uncertainty comes from the quark flavour number. By assuming the QGP is an equilibrated ideal gas, the contribution from heavy quarks (c, b and t) is suppressed by the Boltzmann factor $\exp(-m_{\mathrm{c,b,t}}/T)$, the case of $2+1$ flavours seems to be close to the real mass spectrum. There is a large "jump" in energy density around a critical temperature $T_{\mathrm{c}} \simeq 173$ MeV [40]. The sharp increase of the energy density indicates a phase transition from the hadronic matter to the deconfined QGP. This can be easily understood assuming, 2-flavour (u and d) scenario and $\mu_{\mathrm{B}} = 0$. In this case, before the phase transition there is the *a priori* equilibrated pion gas satisfying Stefan-Boltzmann statistics, the energy density is proportional to the number of degree of freedom $n_{\mathrm{dof}} = 3$ (for $\pi^{\pm}$ and π^0 triplet) of the system. When the QCD phase transition occurs, the number of degree of freedom of the system rises to $n_{\mathrm{dof}} = n_{\mathrm{g}} + 7/8(n_{\mathrm{q}} + n_{\bar{\mathrm{q}}}) = 37$ [41] (the factor 7/8 accounts for the differences between

[7] This is easy to understand when we continue to heat the hadronic matter. If the QGP is present, quarks are highly excited and get large momentum during their propagation. According to Eq. (1.12) their constituent mass decreases and the chiral symmetry is restored. But if we continue to compress the hadronic matter, it is a little bit complicated. In this direction, under some conditions, the chiral condensation, Eq. (1.11), would decrease and chiral symmetry restoration occurs in QGP; in some cases, the QGP could be created while the chiral symmetry restoration is absent. We will present some predictions concerning this "high density" QGP (also named **Quark Matter**). Since this is not directly related to the topic of this thesis, we will not mention the details of the chiral symmetry restoration conditions in the "high density" QGP.

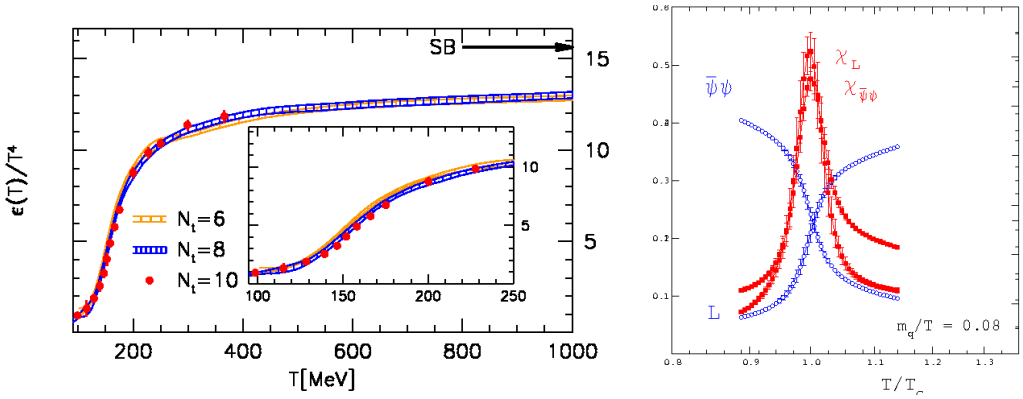

Figure 1.4: Left: energy density, ε/T^4, versus temperature, T, with 2 light and 1 heavier (strange) quarks [39]. Right: chiral condensation, $<\overline{\Psi}\Psi>$ (Eq. (1.11)), and quark free energy function, $L(f_{\rm q})$, (Eq. (1.13)) with their associated susceptibilities, $\chi_{\overline{\Psi}\Psi}$ and $\chi_{\rm L}$, as a function of temperature, $T/T_{\rm c}$ [34]. All the results are obtained with $\mu_{\rm B} = 0$.

the Bose-Einstein, for gluons, and Fermi-Dirac, for quarks, statistics). The energy density $\varepsilon_{\rm SB}/T^4$ in QGP from Stefan-Boltzmann predictions with $T_{\rm c} = 173$ MeV is compared with the lQCD results, and is higher than that from lQCD calculations at a temperature close to $T_{\rm c}$. This indicates that at $T \sim T_{\rm c}$, interactions between partons are still present in the QGP and it cannot be treated as an ideal gas.

An other hint for a QCD phase transition is shown in the right plot of Fig. 1.4 [34]. The quark free energy function is

$$L \propto \exp(-f_{\rm q}/T), \tag{1.13}$$

where $f_{\rm q}$ is the quark free energy. It increases sharply from a small value to a finite number around $T_{\rm c}$. This reflects the energy variation of an isolated colored source from confinement (divergence) to deconfinement (given value). Also, the chiral condensate $<\overline{\Psi}\Psi>$ is restored around the same value of $T_{\rm c}$. Both the susceptibilities [8] $\chi_{\overline{\Psi}\Psi}$ and χ_L, which reflect how strong are the thermodynamical observable fluctuations, are maximum around $T_{\rm c}$. This illustrates that the deconfinement phase transition is always associated with the chiral phase transition at $\mu_{\rm B} = 0$. The chiral condensate $<\overline{\Psi}\Psi>$ could be treated as an order parameter for the QCD phase transition.

1.3.2 QCD Phase Diagram

At a temperature around $T_{\rm c}$, with $\mu_{\rm B} = 0$, the susceptibilities exhibit a clear maximum but do not diverge. A similar trend is evidenced for the order parameters, L and $<\overline{\Psi}\Psi>$ (Fig. 1.4, right panel). Instead of a first order phase transition, the

[8] The definition of susceptibility for an observable m is $\chi_m = < m^2 > - < m >^2$.

lQCD predicts the QGP formation as a crossover at $\mu_B = 0$. Since lQCD calculations have problems to deal with $\mu_B > 0$, the **Bag Model** [42], which describes the QCD phase transition with a finite value of μ_B, is used and suggests a first order phase transition for all values of μ_B [43]. By combining the results from lQDC and Bag Model, a **Critical End Point** (**CEP**), which ends the phase bound of first order transition with a crossover behaviour, appears in the (T, μ_B) plane. This representation is the so-called **QCD Phase Diagram**.

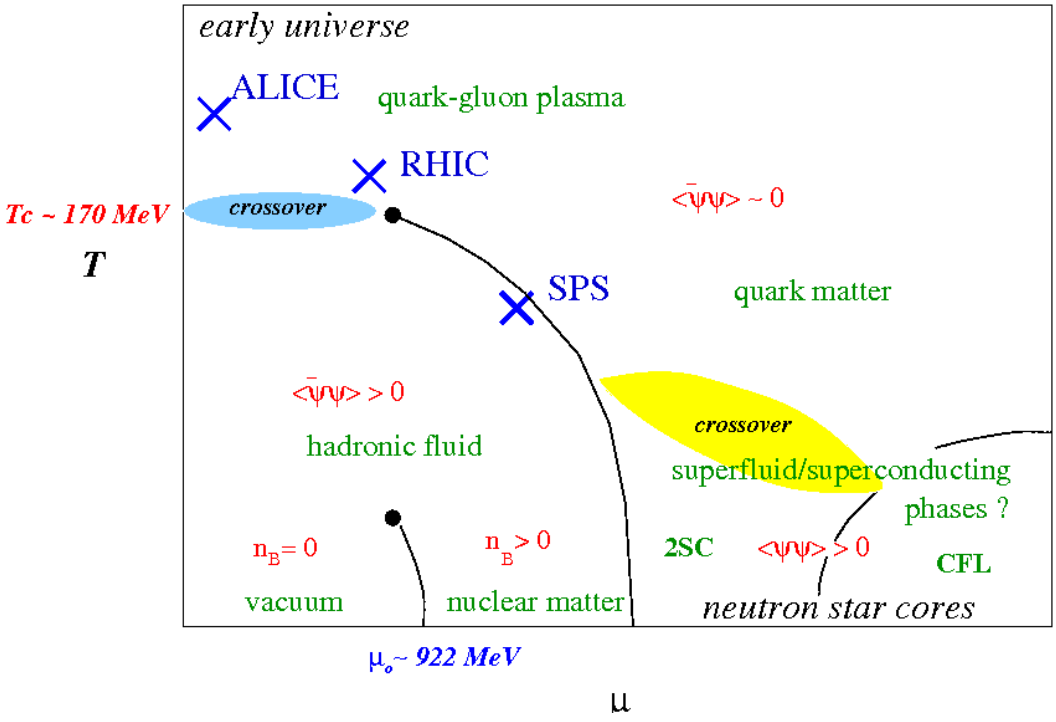

Figure 1.5: Schematic view of the QCD Phase Diagram

Fig. 1.5 shows the QCD Phase Diagram. In the region $\mu_B \gtrsim 992$ MeV, corresponding to the normal nuclear matter, by increasing its temperature (heating), the nuclear matter will change into the hadronic gas phase, which is mainly composed of pions, excited protons and neutrons. When the temperature is still increasing, quarks and gluons will exit from hadrons and form the QGP. When the value of μ_B decreases, the first order phase transition from hadron gas to QGP becomes the crossover. The phase matter transition is rapid and continuous at the CEP. In the QGP, the chiral condensate is also restored and $< \overline{\Psi}\Psi > \sim 0$.

An other way to achieve the strong interaction phase transition in the QCD phase diagram is the compression of nuclear matter (by increasing μ_B). With different temperatures, the phase transition could not always meet the crossover region, and the chiral condensation $< \overline{\Psi}\Psi >$ would not always be restored. This shows that the QCD phase structure is more complicated. More details can be found in [44].

It is worth noticing that the QCD phase diagram is displayed in the plane $(T/T_c,$

μ_B/T_c). Some attempts to determine T_c are presented in [45].

1.4 Heavy Ion Collisions

The QCD phase diagram (Fig. 1.5) allows to extract the main properties of the QCD phase transition. In particular, the lines along the T axis at $\mu_B = 0$, in this QCD phase diagram, describe the evolution of the early Universe after the Big Bang.

1.4.1 Trace Back to the Big Bang

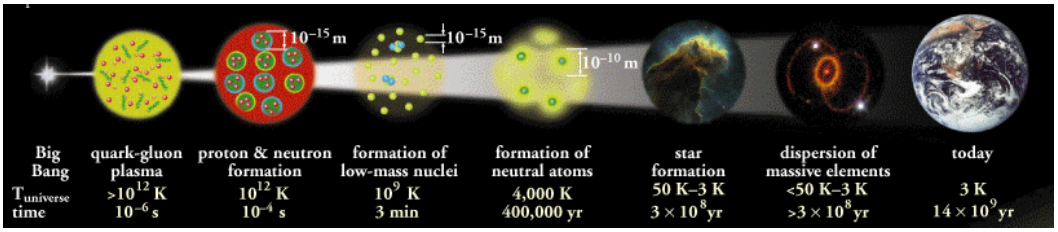

Figure 1.6: Picture presenting the evolutiion of the Universe.

Under the prospect of the Big Bang Model [46], after the electro-weak transition, which happened at $t \sim 10^{-11}$ s after the Big Bang, the Universe was filled with free quarks and gluons. Then, the temperature went down during the expansion. At $t \simeq 10^{-4}$ s after the Big Bang, the temperature reached the critical temperature T_c and the transition between deconfinement phase and hadronic phase occurs. Today's Universe was created after a lengthy evolution from the hadronic phase in the early Universe (Fig. 1.6). The thermodynamical and hydrodynamical properties of the deconfinement matter before the phase transition, such as the initial conditions, influenced this evolution. In the **Mechanical Concept**, one could say that the present Universe was determined in $t \lesssim 10^{-4}$ s, after the Big Bang where free quarks and gluons governed the Universe.

A systematic study of the evolution of the deconfinement phase is mandatory not only for understanding the properties of the strong interaction and the dynamic mass generating mechanism via chiral symmetry spontaneous breaking, but also for tracing back the Universe just after the Big Bang!

Then, a question arises: under the normal nuclear matter conditions, how to create or where to find the deconfinement matter phase with $t > T_c \simeq 200$ GeV ($\mathcal{O}(10^{12}$ Kelvin)$)$? **Ultra-Relativistic Heavy Ion Collisions** have been proposed as the factory of QGP production in laboratory. These collisions deposit a sufficiently huge energy density in the colliding region to create the "Big Bang matter", QGP, which filled the whole Universe a few microseconds after the Big Bang [47, 48, 49]. The observables measured in the final stage of the collisions carry the information from each step of the collision, as the microwave background gives the information from early Universe. Ultra-relativistic collisions allow to trace back

the Universe after the Big Bang and to answer some questions which cannot be addressed by any conceivable astronomical observables with telescopes and satellites. I am proud to say that, this is the topic of my PhD thesis!

1.4.2 Collision System Evolution

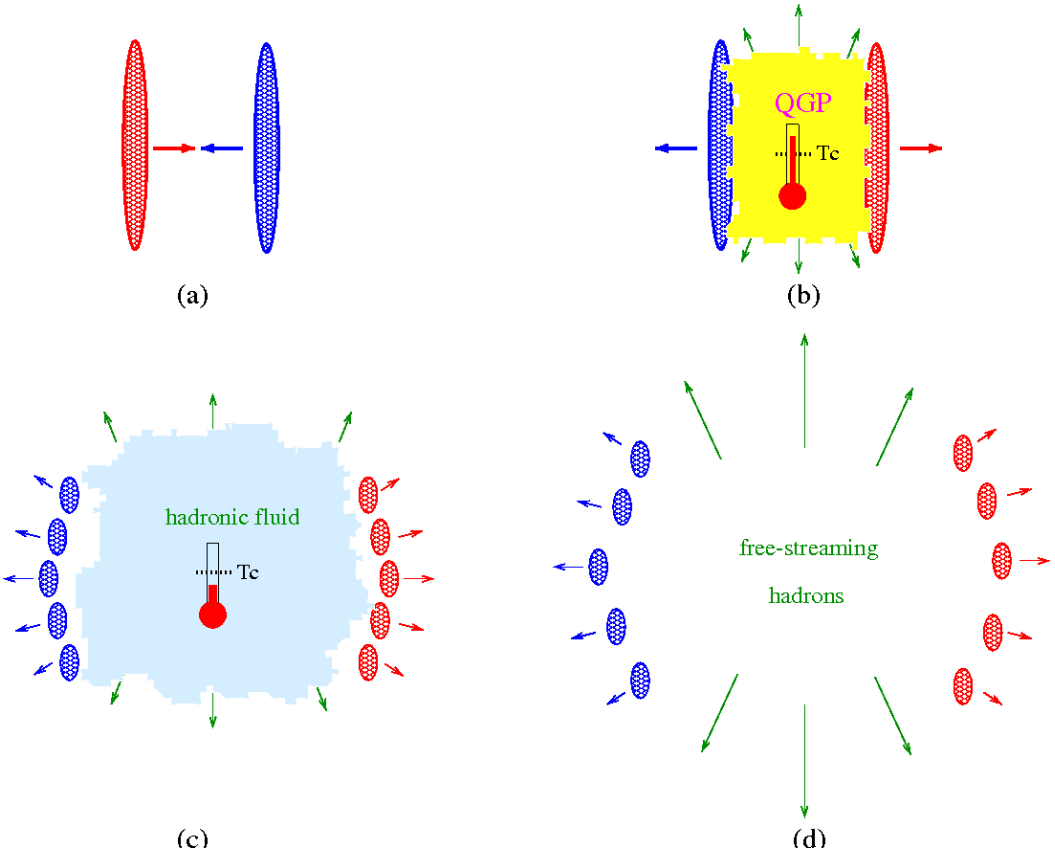

Figure 1.7: Schematic view of an Heavy Ion Collision [34]

Before to focus on the extraordinary heavy ion collision experiments, two questions should be ascertained:

- is the QGP formed during the collisions?
- if it is the case, how to extract its properties via final observables?

In order to address these open issues, it is very important to understand the evolution of the system.

As shown in Fig. 1.7, the whole evolution of heavy ion collisions can be classified into four periods. First, we discuss the characterization of a collision.

1.4.2.1 Collision Geometry

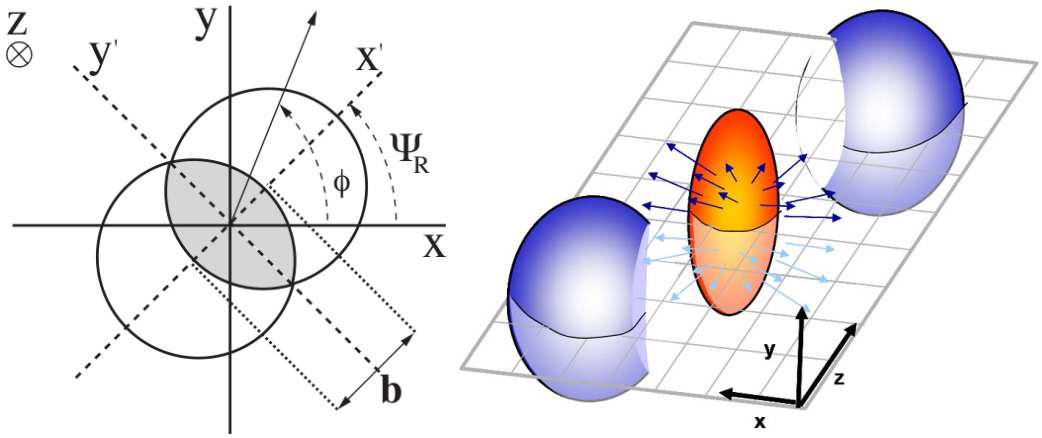

Figure 1.8: Geometry of the collision in a two-dimension (left panel) and three-dimension plane (right panel).

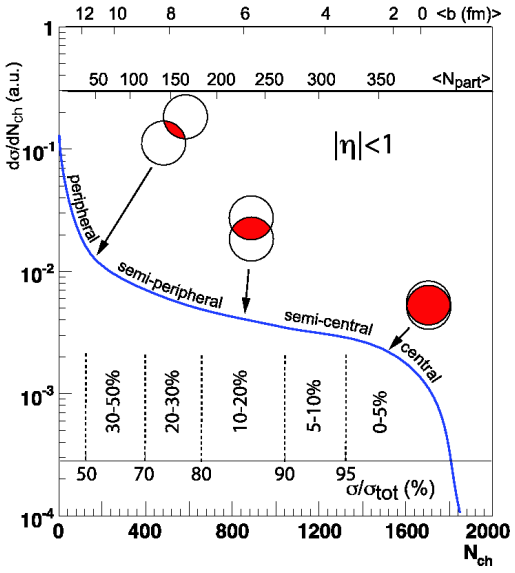

Figure 1.9: Characterization of a collision by using the charged particle multiplicity [50].

If one considers an heavy ion collision, as shown in Fig. 1.8, the **Impact Parameter** $\vec{b}$ is a vector starting from the center of one nucleus and pointing to the center of an other nucleus. The plane which contains the impact parameter and the beam direction (z-axis in the laboratory coordinate system) is defined as the **Reaction Plane** of the collision as shown in the right plot of Fig. 1.8. The angle between the reaction plane and x-axis defines the reaction plane angle $\Psi_{\rm R}$. In the x-y plane, $\Psi_{\rm R}$ is the azimuth of the reaction plane. The directions parallel and perpendicular to the reaction plane are defined as the in-plane and out-of-plane directions, respectively.

Collisions are classified into different centrality classes according to the length of impact parameter: $|\vec{b}| = 0$ defines the most central collisions (two nuclei collide head-on); when $|\vec{b}| \simeq R_{\rm A} + R_{\rm B}$ ($R_{\rm A}$ and $R_{\rm B}$ are the radii of two incoming nuclei), the collisions are peripheral (two nucleus rub shoulders). Since $|\vec{b}|$ can not measured directly, collisions are classified according to their degree of centrality by using observables which are expected to exhibit a strong correlation with $|\vec{b}|$. Amongst these observables, one can mention the charged particle multiplicity.

As shown in Fig. 1.9, the charged particle multiplicity distribution ($\mathrm{d}\sigma/\mathrm{d}N_{\mathrm{ch}}$) is used to define centrality classes by binning the distribution according to the fraction of the total integral. In a given centrality class, $< N_{\mathrm{part}} >$ is defined as the mean number of participating nucleons, and $< N_{\mathrm{coll}} >$ is used to express the mean number of binary nucleon-nucleon collisions. Both $< N_{\mathrm{part}} >$ and $< N_{\mathrm{coll}} >$ are two important quantities to characterize a collision, as well as the reaction plane angle Ψ_{R}.

Additionally, in the most central collisions ($|\vec{b}| \simeq 0$), the overlap region of the two nuclei (named as almond, as shown in red in Fig. 1.9) is symmetric. When $|\vec{b}|$ increases, the collisions become more and more peripheral, and the almond becomes more and more asymmetric. The initial conditions affect the evolution of the system as it will be discussed hereafter. The changing of the almond with collision centrality classes effects the initial conditions of collisions and drives the evolution of the created medium in the collisions, as we are going to mention.

1.4.2.2 Initial Stage of Collisions

In the initial stage of the collisions, Fig. 1.7 (a), the two nucleus are accelerated with ultra-relativistic velocities, and become as two "pancakes" due to the Lorentz contraction as a factor $\gamma = E/m$ (E is the beam energy per nucleon and m is the mass of nucleon). At such energies, the nucleons inside the nuclei are highly excited. In this case, not only the valence quarks but also the sea quarks and gluons become visible. The **Parton Distribution Functions** (**PDFs**) in the nucleus, which govern the initial conditions of the evolution of the system, are modified by the **Nuclear Initial State Effects** (or **Cold Nuclear Effects**). Presently, there are two mainstream models used to describe the initial conditions.

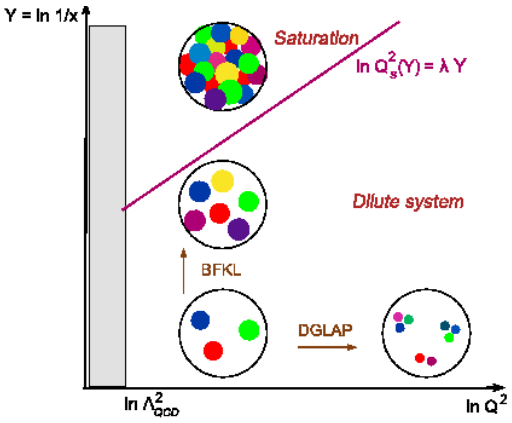

Figure 1.10: CGC Evolution

The **Glauber Model** [51] considers nuclei-nuclei (A–A) collisions as the superpostion of binary nucleon-nucleon collisions weighted by the binary inelastic scattering cross section, $\sigma_{\mathrm{NN}}^{\mathrm{inel}}$. With the inputs from the nucleon distribution in the given nuclei and $|\vec{b}|$, it returns the probability of binary collisions as a function of the position (x, y) inside the overlapping region, and also $< N_{\mathrm{part}} >$ and $< N_{\mathrm{coll}} >$ calculated via the "Glauber Monte-Carlo" (GMC) approach [52]. Cold nuclear effects are mainly described by shadowing/anti-shadowing [53, 54, 55] and intrinsic transverse momentum (k_{t}) broadening [56] in PDFs of the nucleons.

An other model intensively used, is the **Color Glass Condensate** (**CGC**) theory [57]. Without going into details, the CGC treats the system at the parton

level, directly. In the small Bjorken-x region, gluon bremsstrahlung is dominant in QCD and follows a DGLAP evolution [58, 59, 60]. The gluon density is described as,

$$\alpha_s^p \ln^m(1/x) \ln^n(Q^2). \tag{1.14}$$

One clearly sees that at large Q^2 and small Bjorken-x values, the gluon density increases very sharply, according to Eq. (1.14). In a finite nucleus volume, the low Bjorken-x gluons will merge together and their density will saturate according to the BFKL evolution [61, 62, 63], as shown in Fig. 1.10. The gluon saturation modifies the PDFs in the high energy nucleus and also leads to parton shadowing. Some Monte-Carlo approaches are used to implement the CGC model, as the so-called MC-KLN [64] and rcBK [65]. As compared to the Glauber based initial conditions, the CGC model gives smaller scale and larger initial state fluctuations.

1.4.2.3 Fireball

Under initial conditions just discussed, the two nuclei collide. The evolution of the collision is summarized in Fig. 1.7 (b). Hard processes with large momentum transfer, $Q \gg 1$ GeV, occur during parton scattering at the very beginning of the collisions at $\tau \approx 1/Q$. Then, the spectators escape form the interaction region and the participants deposit their energy in the fireball. This leads to a rapid increase of the entropy which could lead to thermalization (Fig. 1.7 (b)). At high energy density, the created fireball behaves as a Quark Gluon Plasma (QGP) [9]. After that, the temperature of the fireball goes down due to the rapid expansion of the system. When the critical temperature T_c is reached, a transition from QGP to hadronic phase is observed (Fig. 1.7 (c)). Quarks and gluons are again confined into hadrons (Fig. 1.7 (c)). Then, at the **Chemical Freeze-Out** the chemical composition of the system is frozen.

In the theoretical side, the QGP medium is characterized by the physical quantities as:

- opacity N, number of scatterings by the particle in a medium thickness L;
- Debye mass m_D, related to the typical momentum exchange with the medium;
- transport coefficient $\hat{q}$, the energy transferring per unit length in medium;

as well as its temperature T, gluon density dN_g/dy (or energy density ε) and viscosity η *etc.* In the experimental side, all the physical quantities of the medium can be extracted via the final state observables (to be mentioned in Sec. 1.4.3). If the system energy is sufficiently important, the interactions between hadrons could also form a thermal equilibrium state until the **Thermal Freeze-Out** appears due to the decrease of the temperature.

[9] Fig. 1.5 shows that the chiral symmetry is always restored at small μ_B values reached in the QGP. In ultra-relativistic heavy ion collisions, the participants are confined in the interaction region. As displayed in Fig. 1.5, the μ_B values reached in our energy range of interest (SPS, RHIC, LHC) satisfy the conditions for chiral symmetry restoration.

Finally, the kinematic distributions are fixed: this is the **Kinetic Freeze-Out**. At this moment the fireball desintegrates and hadrons escape from them. Then, the resonances and highly excited states decay to stable particles that can be measured (Fig. 1.7 (d)).

1.4.3 Final State Observables

The fireball created during the collision produces **Hot Nuclear Effects** [10] at the partonic level. Since hard and soft partons are generated in different stages of the collision with different mechanisms and do not have the same energy, they suffer different hot nuclear effects. The whole picture of the fireball evolution could be reverted by combining the information of the final state observables from both soft and hard partons.

1.4.3.1 Global Observables and Collective Flow

Soft partons, which evolve as the fireball, are very sensitive to the initial conditions (thermodynamical and hydrodynamical properties) and to the fluctuations in the fireball. Their overall behaviour is reflected into the final state global observables, such as final state particle distributions, correlations and event-by-event fluctuations.

Amongst them, the collective flow components which describe the correlations between **Particles Of Interest** (**POI**) in the final state of the collisions, are very important global observables.

In the final state, the flow can be both parallel and perpendicular to the beam direction and is called longitudinal flow and transverse flow, respectively. The origin of the flow could due to different reasons: initial conditions of the collisions and/or pressure gradient in the created fireball, *etc.*. In general, the longitudinal flow is mainly affected by the expansion of the fireball along the beam direction and is governed by the variation of the fireball energy density as function of the rapidity [66]. The transverse flow is of particular interest. It is proposed to probe the hydrodynamical properties and the **Equation of State** (**EOS**) of the medium [67].

If one considers a non-central collision as shown in Fig. 1.8, after the collision, the created fireball is anisotropic, the invariant cross section of final state particles can be written in terms of a Fourier expansion relative to the reaction plane:

$$E\frac{\mathrm{d}^3\sigma}{\mathrm{d}^3\vec{p}} = \frac{\mathrm{d}^2\sigma}{2\pi p_\mathrm{t}\mathrm{d}p_\mathrm{t}\mathrm{d}y}[1 + \sum_{n=1}^{\infty} 2v_n \cos n(\phi - \Psi_\mathrm{R})], \tag{1.15}$$

where $\vec{p}$, p_t, y and ϕ are the 3-momentum, transverse momentum, rapidity and azimuth of the particles. Note that the sine terms vanish since the fireball is symmetric

[10] Normally, hot nuclear effects refer to the ones due to the QGP medium. Anyhow, the hadronic gas also affects the final state observables. Since the interactions in hadronic gas are much smaller than that in QGP, the effects from hadronic gas are always smaller as compared to those from QGP.

with respect to the reaction plane. The Fourier coefficient of n-th order given by

$$v_n = < \cos n(\phi - \Psi_{\mathrm{R}}) >, \tag{1.16}$$

corresponds to the n-th order flow component.

The first order coefficient, v_1, is the directed flow and is related to the overall shift of the particle distribution in the transverse plane.

A non vanishing value of v_2, the elliptic flow component, indicates a larger pressure gradient (with respect to the outside vacuum) in the in-plane direction than in the out-of-plane direction. This initial pressure gradient anisotropy explains the anisotropic azimuthal distribution of final state particles. Hence, more particles are pushed and emitted from the in-plane direction than from the out-of-plane direction. Several quantities, like the temperature and viscosity of QGP, can be extracted by measuring v_2 of soft particles in the low p_{t} region. In the high p_{t} region, v_2 reflects the pass length dependence of hard probe energy loss (see Sec. 1.4.3.2). v_3, the triangular flow, is affected by the asymmetry of the colliding system or the fluctuations of the system. The rectangular flow, v_4, is mostly observed in the rapidity window close to the center of mass. Finally, the squeeze-out effect, quantified by v_2, characterizes a preferred emission of particles in the out-of-plane direction.

1.4.3.2 Hard Probes

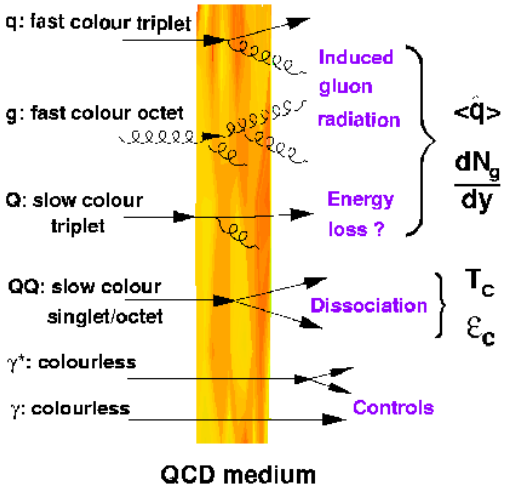

Figure 1.11: Hard partons as a tomography of QCD medium.

Hard partons are created in the early time of the collision and carry large energy. They will loss their energy through their propagation in the QGP medium via interactions with soft partons in the medium [68]. This is the so-called quenching effect. The energy loss, ΔE, depends on the temperature, coupling strength and thickness (L) of pass length of the medium. The hard process of their production can be predicted in the pQCD framework. Hard partons are valuable tools for the tomography of the QGP, as shown in Fig. 1.11. From the theoretical side, quenching effects are estimated by using two approaches: one is based on pQCD calculations by assuming weak coupling (small α_{s}) between partons in the QGP medium and the other one is based on the super string theory, and can deal with large α_{s}, where the perturbative expansion is not valid.

In perturbative calculations, the in-medium energy loss is classified into collisional and radiative terms,

$$\Delta E = \Delta E_{\rm col} + \Delta E_{\rm rad}. \tag{1.17}$$

The collisional energy loss [69, 70, 71, 72] which is due to elastic scattering, drives the linear dependence between $\Delta E_{\rm col}$ and L, and the logarithmic $\Delta E_{\rm col}$ dependence on initial parton energy. The medium induced gluon radiation is responsible for the radiative energy loss of hard partons [73, 74, 75, 76, 77]. In this case, $\Delta E_{\rm rad}$ shows a the typical L^2 dependence, the relation between $\Delta E_{\rm rad}$ and parton initial energy is more complicated than that of the collisional energy loss because of the LPM (Landau-Pomeranchuk-Migdal) effect [78]. Some phenomenological approaches as BDMPS/ASW [79], AMY [80, 81], DGLV [82] and HT [83, 84] are developed to connect these pQCD calculations of hard parton energy loss with experimental observables. The differences between these models mainly come from the treatment of the relationship between relevant QCD scales and space-time profile of the medium.

The calculations of the parton energy loss in a strong coupling QCD system are derived from the string theory, which describes in a 5-dimensional **Anti de Sitter** (**AdS**) space times, a 5-dimensional sphere ($AdS_5 \times S_5$). The 4-dimensional boundary of this space is equivalent to a **Conformal Field Theory** (**CFT**), *e.g.* the SU(4) strong coupled Super Symmetric Yang-Mills (SYM) gauge theory with duality of supergravity in a curved space-time. By virtue of this duality, the analytical gravity calculations can holographically map out to non-perturbative QCD. Hence this dual theory is named as **AdS/CFT** [85]. Within this framework, the parton energy loss is calculated with the medium temperature equal to the black hole Hawking temperature [86, 87, 88].

Hard partons will fragment into hadron jets at the surface of the QGP medium. Some hadrons in the jets could still interact with the hadron gas subsequently and further modify their distributions. The final state observables from hard partons, jets and leading particles, which take the largest energy/momentum fraction, are called hard probes. They allow to study in particular the medium modified fragmentation function, suppression of high $p_{\rm t}$ particles and back-to-back correlations.

1.4.4 Heavy Ion Facilities

The development of heavy-ion accelerators began at the Berkeley Bevalac (USA) in 1975 and latter at Saturne (Saclay, France). After that, several experiments were operated at various facilities:

1987 – 1994 : heavy-ion collisions were studied at the **AGS** (**Alternating Gradient Synchrotron**) of **BNL** (**Brookhaven National Laboratory**) at $\sqrt{s_{\rm NN}} <$ 14.2 GeV;

1986 – 2003 : heavy ion collisions were studied at the CERN/**SPS** (**Super Proton Synchrotron**) at $\sqrt{s_{\rm NN}} \sim 19$ GeV;

1994 – 2003 : seven experiments have been operated at the SPS (Pb nuclei were accelerated up to $\sqrt{s_{\rm NN}} \sim 17$ GeV);

2000 – *now* : **RHIC** (**Relativistic Heavy Ion Collider**) entered in service at the BNL and delivered Au–Au collisions up to $\sqrt{s_{\rm NN}} = 200$ GeV. Four experiments: PHENIX, STAR, BRAHMS, PHOBOS are operated at this facility;

2009–now : CERN/**LHC** (**Large Hadron Collider**) entered in service in 2009 and delivered Pb–Pb collisions at $\sqrt{s_{\rm NN}} = 2.76$ TeV in 2010 (nearly 14 times larger than that reached at RHIC), opening a new era for studying the properties of strongly interacting matter under extreme thermodynamical conditions!

There also are running heavy-ion programs at lower energies: the **SIS** facility (**SchwerIonen Synchrotron**) located at **GSI** (**Gesellschaft für Forschung SchwerIonen**) accelerates heavy ions at a maximum energy of about 2 AGeV. A new project, the **CBM** experiment (**Compressed Baryonic Matter**) at GSI/**FAIR** (**Facility for Antiproton and Ion Research**) is presently in preparation. One can also mention the **NICA** experiment in development at Dubna facility. These experiments are dedicated to the study of the QCD phase transition at high $\mu_{\rm B}$ and low T. The complementary results between different experiments operated at different energies could help to scan the CEP in the QCD phase diagram and clarify the whole picture of the QCD phase transition.

1.5 Evidence of the Quark Gluon Plasma

Abundant evidences of QGP have been obtained with heavy ion experiments at SPS and RHIC. A new era for the systematic study of the properties of the QGP, the understanding of the mass origin and the investigation of the early Universe is opened. The mysteries of the nature are being unveiled.

1.5.1 SPS: First evidences

The various experiments operated at the SPS collected O–O, S–S, In–In and Pb–Pb collisions in a wide energy range from 40 AGeV to 158 AGeV. Proton–proton and p–A collisions were also measured in this energy range, in order to provide the baseline for the study of nuclei-nuclei collisions. Many observables are in favour of the QGP formation in heavy ion collisions. In the following, we focus on two observables: J/Ψ production and strangeness production.

1.5.1.1 J/Ψ Anomalous Suppression

The anomalous suppression of J/Ψ production with respect to the Drell-Yan dimuon yield when considering the normal nuclear absorption, was measured in NA38, NA50 and NA60 experiments with different collision systems at the SPS [89]. The measured J/Ψ yield normalized to the expected yield by assuming the suppression source only comes from ordinary nuclear absorption in different systems is

shown in Fig. 1.12. In order to compare the suppression patterns in different colliding systems, the results are shown as a function of the energy density reached in each collision system at the local thermal equilibration time, estimated within the Bjorken scenario [47] as,

$$\varepsilon = \frac{1}{S_\perp \tau} \frac{\mathrm{d}E}{\mathrm{d}y}|_{y=0}, \tag{1.18}$$

where $S_\perp$ is the size of almond region in transverse plane and τ is the system lifetime. The sudden decrease of the ratio in $\varepsilon \gtrsim 2.5$ GeV/fm^3 (Fig. 1.12) is clearly in disagreement with the predictions from hadronic models [90]. This trend strongly supports that the QGP is formed in this region [91].

As predicted in [93], similarly to the electromagnetic plasma, in the QGP, where the color charges are liberated, the charge potential between two partons is expected to be screened at a distance beyond the Debye length λ_D. Hadrons with radii $r > \lambda_\mathrm{D}$, as $\mathrm{c\bar{c}}$ and $\mathrm{b\bar{b}}$ bound states, are expected not to be bound in the QGP. This effect explains that the quark pairs lose their correlations and flow with independent trajectories. In Fig. 1.12, the non-anomalous J/Ψ suppression at small ε indicates that the deconfinement was not formed with such low energy densities; at $\varepsilon \simeq 2.5$ GeV/fm^3, the increase of the anomalous suppression with ε illustrates that the J/Ψ bound state is melt in the present QGP medium due to the color charge screening, and the screening length λ_D increases with the energy density of the QGP since more and more free color charges appear.

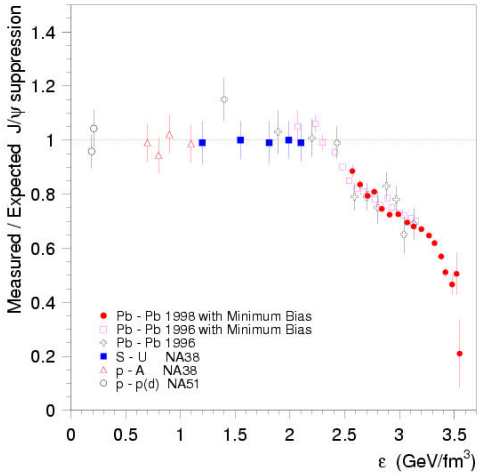

Figure 1.12: Ratio between measured J/Ψ yield and expected yield as a function of energy density ε, by assuming the suppression source only comes from ordinary nuclear absorption [92].

1.5.1.2 Hyperon Enhancement

As mentioned in Sec. 1.2.3, the deconfinement phase transition is always associated with the chiral symmetry restoration. In the QGP, the threshold production of a $\mathrm{s\bar{s}}$ pair is reduced from it mass constituent $m_{\mathrm{s\bar{s}}}^{\mathrm{cont}} \simeq 600$ MeV/c^2 to it current/bare mass $m_{\mathrm{s\bar{s}}}^{bare} \simeq 300$ MeV/c^2 (Fig. 1.3), which is half of the energy required to produce the $\mathrm{s\bar{s}}$ pair in hadronic interactions. This leads to an increase of the yield of (multi-)strange baryons (hyperons) in the deconfinement medium, as compared to that in the hadronic matter [94].

The results in Fig. 1.13 show that the hyperon production increases in Pb–Pb collisions, in comparison to that in p–Be and p–Pb collisions, where the QGP is not expected to be produced. This enhancement is a direct evidence for the

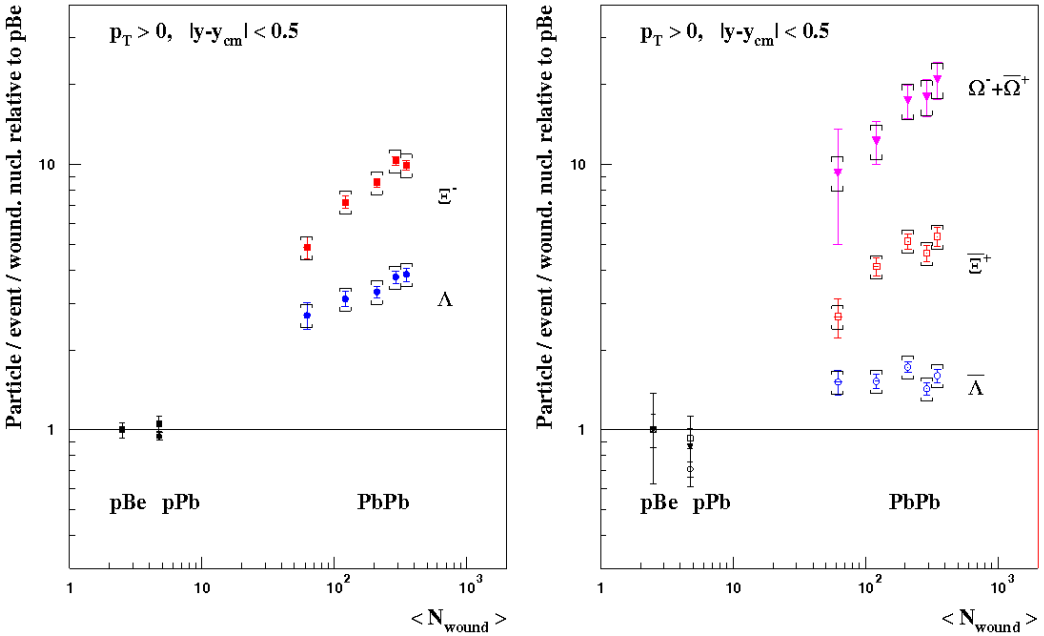

Figure 1.13: Hyperon production in Pb–Pb collisions normalized to the ratio from p–Be collisions as a function of centrality (expressed by $< N_{\text{wound}} >$), measured in the NA57 experiment at the SPS [95].

chiral symmetry restoration, and illustrates that a deconfined medium is created at SPS energies. The increase of the enhancement, with the strangeness content, $\varepsilon(\Lambda) < \varepsilon(\Xi) < \varepsilon(\Omega)$ [11], confirms this picture.

1.5.2 RHIC: Strong Coupled QGP?

The anomalous J/Ψ suppression and hyperon enhancement discovered at SPS could be an evidence of the QGP formation. At RHIC energies, in Au–Au collisions at a center of mass energy of $\sqrt{s_{\text{NN}}} = 200$ GeV, which is more than 10 times larger than that at SPS energies, the produced collisions are well above the threshold of the deconfinement phase transition. On one hand, the QGP at RHIC energies has a longer life-time, its properties could be better reflected in the collective behaviour of the global observables; on the other hand, the production cross section of hard probes increases significantly, letting them become experimentally accessible.

1.5.2.1 Hard Probe Quenching

As mentioned in section 1.4.3.2, due to quenching, hard partons, which have large initial energy, lose their energy in the QGP medium before they fragment into hadron jets. This leads to a decrease of the particle yields in the high p_{t} region in the final stage of the collision, with respect to the situation where there is no

[11] Here ε expresses the enhancement of the strangeness particles

quenching at parton level. Experimentally, this effect is measured via the nuclear modification factor,

$$R_{\rm AA}(p_{\rm t}) = \frac{1}{< N_{\rm coll} >} \frac{{\rm d}\sigma_{\rm AA}/{\rm d}p_{\rm t}}{{\rm d}\sigma_{\rm pp}/{\rm d}p_{\rm t}}, \tag{1.19}$$

which is the ratio between the particle production cross section normalized to the binary nucleon-nucleon collisions via $< N_{\rm coll} >$ in A–A collisions and the production cross section for the corresponding particles in pp collisions where the QGP is not formed. The measured $R_{\rm AA}$ of π^0 in Au–Au collisions at $\sqrt{s_{\rm NN}} = 200$ GeV by the PHENIX experiment at RHIC is shown in Fig. 1.15, left panel [96]. One can observe that, there is a strong suppression of high $p_{\rm t}$ π^0 ($p_{\rm t} \gtrsim 4$ GeV/c) in central collisions ($0 - 10\%$) with respect to pp collisions. This phenomenon indicates that the QGP medium was formed in central collisions and hard partons are quenched inside it, while in the peripheral collisions ($80 - 92\%$) the suppression is small (peripheral collisions can be considered as a superposition of pp collisions).

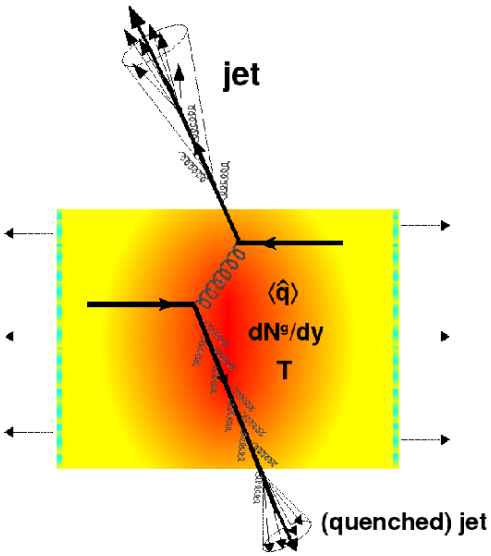

Figure 1.14: Jet Quenching

During hard processes, hard partons are always produced in back-to-back pairs. If there is no quenching, as in pp and d–Au collisions, the produced hard parton pairs could fragment into two back-to-back hadron jets. In this case, if we choose one of the leading particles in one of these two jets as the trigger particle and build the correlated azimuthal distribution for other particles according to this particle (${\rm d}N/{\rm d}\Delta\phi$), there could be two back-to-back peaks in this distribution, as shown in Fig. 1.15 (right panel), in the case of pp and d–Au collisions. The nearside peak is composed from the associated particles of this trigger particle in the same jet and the way-side peak comes from the particles in the corresponding opposite jet. But with quenching effect, as shown in Fig. 1.14, if a hard parton pair is created near the surface of the QGP medium, one of them would just cross the medium surface and with almost no energy loss will fragment into a jet similarly as in pp collisions, while another parton could pass almost the whole medium region and suffer the quenching inside the medium. In this case, the nearside peak in the two particle correlated azimuthal distribution does not change too much, as compared to pp collisions, but the away-side peak could become wider due to multi-scatterings of the opposite parton or it could disappear because the opposite parton losses all its energy in the medium. This phenomenon is shown in Fig. 1.15 (right panel) for Au–Au collisions, and compared with pp and d–Au collisions. One can see that the two particle azimuthal correlations disappear at away-side, in central Au–Au collisions ($0 - 20\%$).

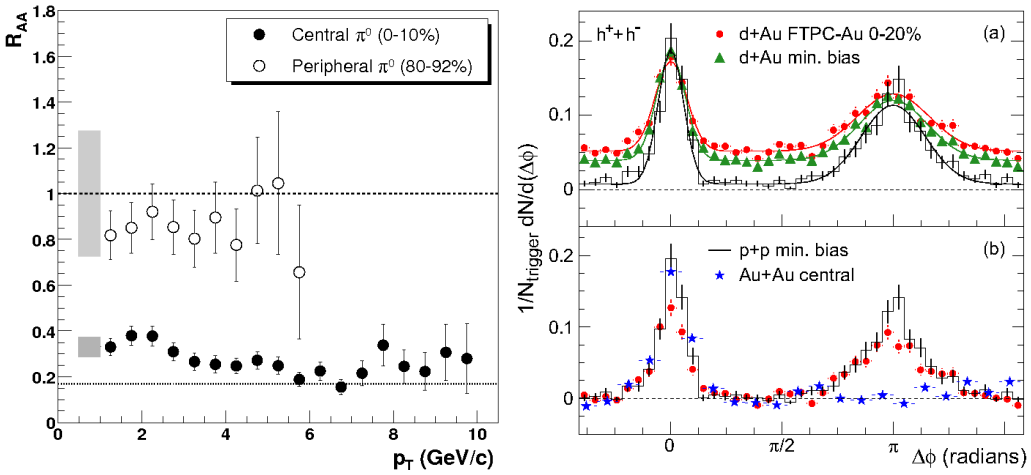

Figure 1.15: Left: $R_{\mathrm{AA}}(p_{\mathrm{t}})$ of π^0 in central $(0-10\%)$ and peripheral $(80-92\%)$ Au–Au collisions at $\sqrt{s_{\mathrm{NN}}} = 200$ GeV measured by the PHENIX experiment [96], the shaded hands represent the systematic uncertainties on normalization. Right: two particle azimuthal distributions in pp, d–Au and Au–Au collisions measured by the STAR experiment [97].

1.5.2.2 Fragile Probes?

If we look into more details to the results presented in Fig. 1.15, we can notice that, in the $0-10\%$ central collisions, π^0 are strongly suppressed by a factor of about 5 in $p_{\mathrm{t}} \gtrsim 4$ GeV/c ($R_{\mathrm{AA}} \simeq 0.2$). Even in the 20% most central collisions, the disappearance of back-to-back correlations indicates that almost all of opposite partons have lost all their energy and are absorbed in the medium. Both effects illustrate that the quenching strength or the interactions in the QGP medium are very strong. In this case, it is difficult for hard partons to escape from the central region of the QGP medium, due to strong quenching effects. Therefore, only partons emitted near the surface of the medium can survive, as predicted in Ref. [98]. This is the so-called "surface emission".

One way to check the surface emission mechanism is to study probes with different colors. As predicted in [82], the coupling of gluons is stronger than that of light quarks in QGP medium. If the hard probes are sensitive to the medium properties, the suppression factor of gluon jets would be larger than that of quark jets. On the opposite side, if the suppression is controlled by the surface emission, its color dependence will be lost. At RHIC energies, the gluon jet contribution to protons is significantly larger than to pions, as predicted in [105] and also measured in [101]. Fig. 1.16 shows the ratios of p/π^+ and $\overline{\mathrm{p}}/\pi^-$ in central $(0-12\%)$ and peripheral $(60-80\%)$ Au–Au collisions at $\sqrt{s_{\mathrm{NN}}} = 200$ GeV compared with the results in d–Au collisions at the same binary center of mass energy. The measurements were performed in the STAR experiment at RHIC. One can notice that, all ratios become identical, in $p_{\mathrm{t}} \gtrsim 6$ GeV/c, and higher than the model predictions [103, 104]. This

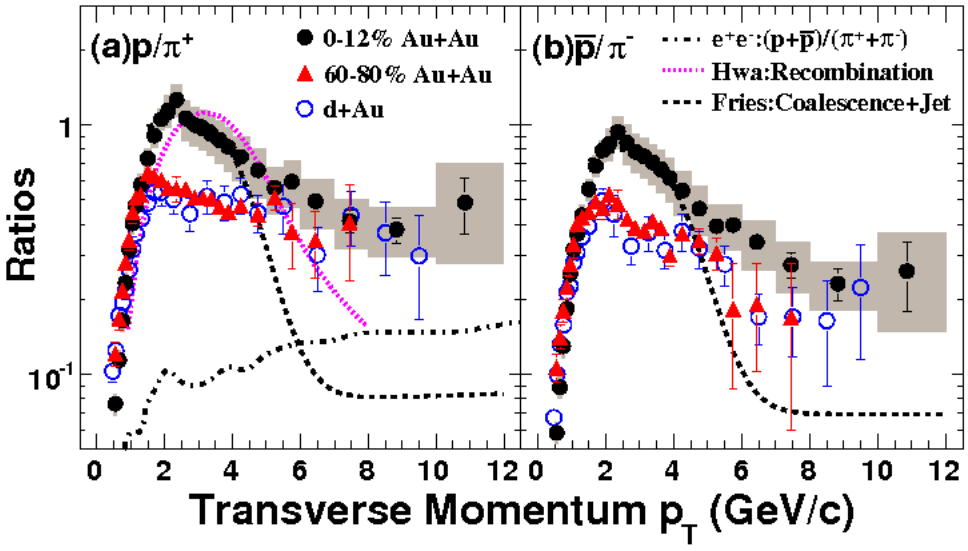

Figure 1.16: p/π^+ and $\overline{p}/\pi^-$ ratios in d–Au [99, 100] and Au–Au [101] collisions measured by the STAR experiment at RHIC. The dotted-dashed line is the ratio $(p+\overline{p})/(\pi^+ + \pi^-)$ measured in e^-–e^+ collisions [102]. The model calculations in central Au–Au collisions [103, 104] are shown in dotted and dashed lines.

indicates that the suppression is not sensitive to the color of the probes. One possible explanation is that the suppression of high p_t particles is governed by surface emission due to the strong coupling inside the QGP medium, and the hard probes become fragile because they can not carry information of the QGP medium.

1.5.2.3 Elliptic Flow and Quark-Gluon Plasma

Even if is well known that the QGP was created at RHIC, a lot of work remains to be done in order to understand its properties. Please take easy! We should not forget an other powerful tool: the flow, as emphasized in Sec. 1.4.3.1. In the low p_t region, different components of flow can be observed due to the collective behaviour of all the particles from the fireball. They are sensitive to the initial conditions, hydrodynamics and degree of freedom inside the fireball. Amongst all flow measurements at RHIC, an interesting result which is worth to be introduced (Fig. 1.17), is v_2 from different hadron species scaled by the number of quark constituents (nQ) of hadrons as a function of p_t scaled by nQ, in Au–Au collisions at $\sqrt{s_{NN}} = 200$ GeV [106]. It can be observed that v_2 of all these hadrons fall into the universal nQ scaling in the region $p_t/\text{nQ} > 0.6$ GeV/c. This implies that, in the intermediate p_t region, the final hadrons are formed by coalescence of their quark constituents when the partonic phase hadronizes. Once more, this provides the evidence of deconfinement in the early stage of the collisions at RHIC energies.

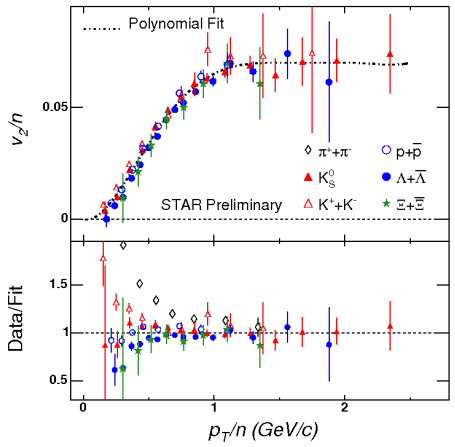

Figure 1.17: Elliptic flow of different hadrons scaled by the number of quark constituents of hadrons. The lower panel shows the ratios between data and a Polynomial fit [106].

Also, the flow measurement allows to extract one of the key parameters, the ratio of shear viscosity to entropy η/s which is used to determine the damping rate of QGP. In AdS/CFT [86], this parameter is $\eta/s \geq 1/4\pi$. This relation is true in any thermal field theory according to the Heisenberg uncertainty principle. Since $\eta/s \sim \tau_{\rm mft}\varepsilon$, where $\tau_{\rm mft}$ is the typical mean free time of a quasiparticle and ε is the average energy per particle, η/s should be much larger than $1/4\pi$ in a weakly coupled system because the mean free time $\tau_{\rm mft}$ is larger (*e.g.* for water under normal conditions $\eta/s \simeq 380 \cdot 1/4\pi$). On the contrary, if the value of η/s is close to $1/4\pi$, the coupling in the system should be more stronger.

The charged hadron elliptic flow as a function of centrality (Fig. 1.18), measured in Au–Au collisions at $\sqrt{s_{\rm NN}} = 200$ GeV at RHIC is compared with hybrid calculations which describe the QGP via the relativistic viscous fluid dynamics and implement microscopic Boltzmann cascade for the late hadronic re-scatterings [107]. These calculations use both the Glauber model and CGC theory to describe the initial conditions. The comparison with data, gives the range for the ratio of shear viscosity to entropy in $1 < 4\pi(\eta/s) < 2.5$ and the temperature of QGP in $T_{\rm c} < T \lesssim 2T_{\rm c}$ at RHIC [108]. The value of η/s extracted from the flow measurement is very close to $1/4\pi$ and this indicates that the coupling inside the QGP medium at RHIC is very strong.

Finally, by combining results from hard probes and flow, a picture of strong coupled QGP (sQGP) is coming out at RHIC energies. This picture is against the prime expectations for the QGP: according to the asymptotic freedom, the interactions between partons should be weak in the deconfinement phase, and the QGP could behave as the ideal gas. But at RHIC, the results seem to indicate that the medium is a quark and gluon soup instead of an ideal gas. Is this the essential attribute of the QGP, or just the tip of the iceberg$\cdots$

1.5.3 LHC: Opportunities and Challenges

The first heavy ion run at the LHC took place end of 2010. With a center of mass energy $\sqrt{s_{\rm NN}} = 2.76$ TeV, which has never been reached before, the LHC brings a revolution in high energy heavy ion physics.

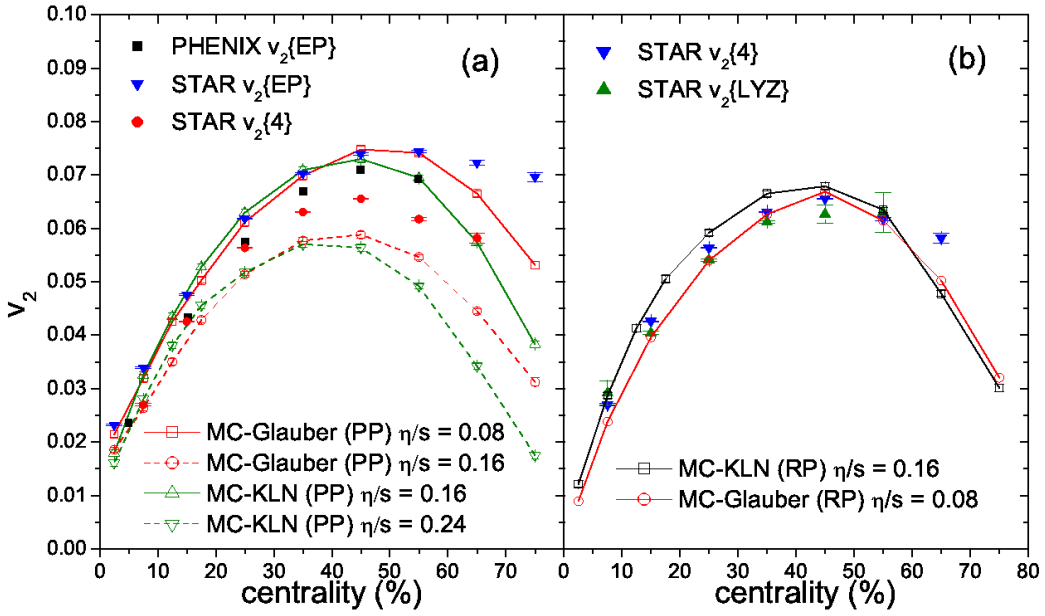

Figure 1.18: Comparison of the integrated charged hadron elliptic flow as a function of centrality measured in the PHENIX experiment [109] and STAR experiment [110] with VISHNU calculations using **Participant Plane** (**PP**) averaged [108].

1.5.3.1 Bulk Properties

The measurement of the charged particle pseudo-rapidity density $\mathrm{d}N_{\mathrm{ch}}/\mathrm{d}\eta$, which constrains the mechanisms of particle production is used to estimate the initial energy density. This is the first step in the characterisation of the system produced at the LHC. The interplay between hard parton-parton scattering processes and soft processes is also reflected by the energy and system size dependence of $\mathrm{d}N_{\mathrm{ch}}/\mathrm{d}\eta$. The red filled dot in Fig. 1.19 (left panel) is the charged particle pseudo-rapidity density per participant, $\mathrm{d}N_{\mathrm{ch}}/\mathrm{d}\eta/0.5 < N_{\mathrm{part}} >$, measured in Pb–Pb collisions at $\sqrt{s_{\mathrm{NN}}} = 2.76$ TeV in ALICE [112]. It shows an increase of $\mathrm{d}N_{\mathrm{ch}}/\mathrm{d}\eta$ by a factor 2.2 at the LHC, as compared to that in Au–Au collisions at $\sqrt{s_{\mathrm{NN}}} = 200$ GeV at RHIC. This indicates that the initial energy density is significantly higher at the LHC than that at the RHIC.

Experimentally, in the final stage of the collisions, the expansion time and the spatial extent of the fireball at hadron decoupling are accessible with intensity interferometry measurements via the Hanbury-Brown-Twiss (HBT) analysis approach [116, 117]. The hadron decoupling time τ_{f} as a function of $\mathrm{d}N_{\mathrm{ch}}/\mathrm{d}\eta$ in various energies is shown in Fig. 1.19 (right panel). The red filled dot measured with ALICE data has been obtained with two-pion Bose-Einstein correlations [113]. The comparison with the results at lower energies show that the largest hadron decoupling time is measured at the LHC. For pions, it exceeds 10 fm/c which is 40% larger than at RHIC. This indicates that the lifetime of the QGP is larger at the

facility	SPS	RHIC	LHC
system	Pb–Pb	Au–Au	Pb–Pb
$\sqrt{s_{\rm NN}}$ (GeV)	17	200	2760
$\mathrm{d}N_{\rm ch}/\mathrm{d}y\|_{y=0}$	500	850	1600*
$\tau^0_{\rm QGP}$ (fm/c)	1	0.2	0.1
$T_{\rm QGP}/T_{\rm c}$	1.1	1.9	$3.0-4.2$
ε (GeV/fm^3)	3	5	$15-60$
$\tau_{\rm QGP}$ (fm/c)	≤ 2	$2-4$	≥ 10
$\tau_{\rm f}$ (fm/c)	~ 10	$20-30$	$\sim 10^*$
$V_{\rm f}$ (fm^3)	$\sim 10^3$	$\sim 10^4$	$\sim 10^5$
$\mu_{\rm B}$ (MeV)	250	20	1

Table 1.1: Global properties of the medium created at SPS, RHIC and LHC energies [111]. From up to bottom, the following quantities are presented: center of mass energy per nucleon pair, charged particle density at mid-rapidity, equilibration time of QGP, ratio of QGP temperature to critical temperature, energy density, QGP life-time, life-time and volume of the system at freeze-out, and baryonic chemical potential

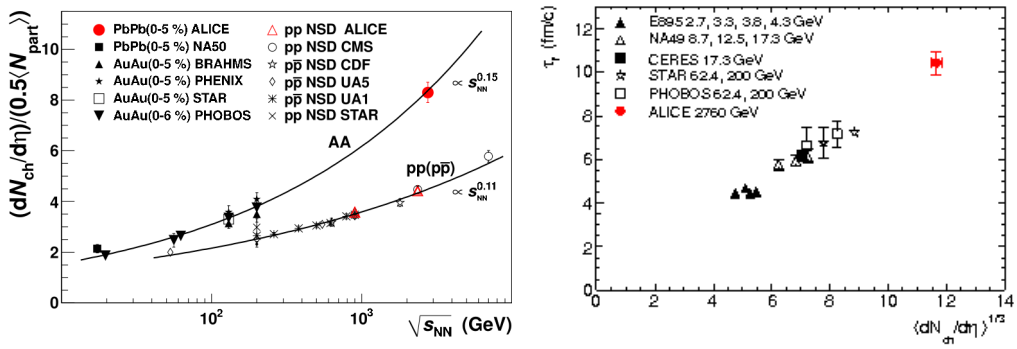

Figure 1.19: Left: charged particle pseudo-rapidity density per participant in central nucleus-nucleus and non-single diffractive pp (p$\overline{\rm p}$) collisions as a function of $\sqrt{s_{\rm NN}}$ [112]. Right: decoupling time from ALICE (red filled dot) compared to the one obtained for central Au–Au and Pb–Pb collisions at lower energies at the AGS, SPS and RHIC [113].

LHC than at the RHIC.

Tab. 1.1 [12] summarizes the main global properties from SPS, RHIC and LHC. All

[12] At LHC energies, the parameters with * are from the newest measurements, others are obtained via model predictions in Pb–Pb collisions at $\sqrt{s_{\rm NN}} = 5.5$ TeV.

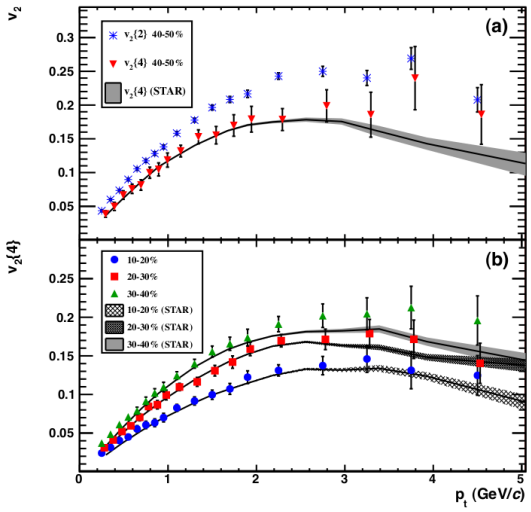

Figure 1.20: $v_2(p_t)$ from multi-particle methods in Pb–Pb collisions at $\sqrt{s_{NN}}$ = 2.76 TeV measured in ALICE [114], and compared with the results from the STAR experiment in different centrality classes.

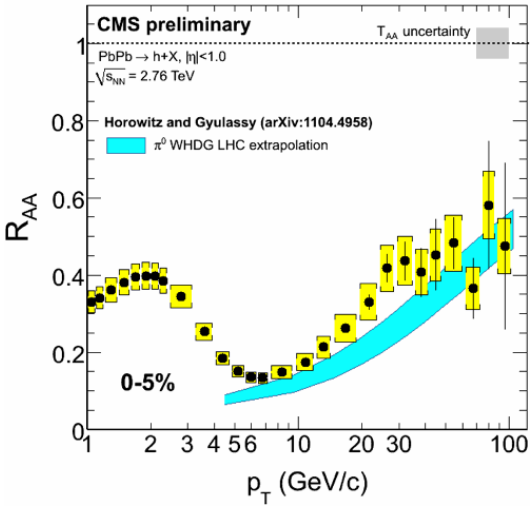

Figure 1.21: Charged particle R_{AA} as a function of p_t up to 100 GeV/c in Pb–Pb collisions at $\sqrt{s_{NN}}$ = 2.76 TeV measured in the CMS experiment. The results are compared with the R_{AA} of π^0 predicted by WHDG calculations [115].

the numbers show that the LHC produces the closest conditions of the early Universe after the Big Bang and offers the opportunities to study the deconfinement matter!

1.5.3.2 Strong Coupled or Perturbative?

Following the train of thought that was used for discussing the results at RHIC, one should use hard probes and global observables to study the properties of the QGP created at the LHC.

The elliptic flow measured in Pb–Pb collisions at $\sqrt{s_{NN}}$ = 2.76 TeV in ALICE is presented in Fig. 1.20 [114] and compared with the measurements in Au–Au collisions at $\sqrt{s_{NN}}$ = 200 GeV made by the STAR Collaboration at RHIC. This figure shows that $v_2(p_t)$ at the LHC is similar to the one measured at RHIC. If one refers to the discussion in Sec. 1.5.2.3, one expects no obvious change for η/s from RHIC to the LHC with a zero order estimate. In other words, even if the conditions are better for the creation of the QGP at the LHC, the properties of the created deconfined medium are almost the same than at RHIC, they support a strong coupled liquid (sQGP). This outcome has been predicted two years ago [118], but you will find that the situation is not so straightforward immediately.

With a sQGP, the perturbative description would fail at LHC energies. But is it like this? Let us look at Fig. 1.21, which shows the charged particle $R_{AA}(p_t)$ measured at CMS up to p_t = 100 GeV/c. This observable tends to increase as p_t increases in the region $p_t \gtrsim 10$ GeV/c. According to perturbative calculations [76],

with an opacity expansion of the medium, the parton energy loss is,

$$< \Delta E > \propto \ln E. \tag{1.20}$$

In pp collisions, where there is no energy loss mechanism, the high $p_{\rm t}$ particle spectrum can be described as

$$\frac{{\rm d}N}{{\rm d}p_{\rm t}} \propto \frac{1}{p_{\rm t}^{n}}; \tag{1.21}$$

then, in A–A collisions, the energy loss can lead to an overall shift for the high $p_{\rm t}$ particle spectrum of $< \Delta E >$ and we get,

$$R_{\rm AA}(p_{\rm t}) \propto (1 - \frac{< \Delta E >}{p_{\rm t}})^{n}, \tag{1.22}$$

where $< \Delta E > /p_{\rm t} \sim \ln p_{\rm t}/p_{\rm t}$, according to Eq. (1.20). By fitting the pp data, we get the power law n in Eq. (1.21). Then, by using Eq. (1.22), the increase trend of $R_{\rm AA}$ in the high $p_{\rm t}$ region can be estimated with pQCD calculations, as done in Ref. [115]. It works very well with $n + 1 \sim 5$ at the LHC. Does this means that pQCD works at the LHC or is there still a sQGP?

It is too early to conclude about the properties of the QGP created at the LHC. The biggest QCD factory in the world, the LHC, continues to create deconfined matter. Our protagonists: the heavy quarks, are going to appear on the scene. In the next chapter, we shall see that heavy quarks are powerful tools to answer the opened questions from RHIC and LHC.

Chapter 2

Heavy Flavours: a Promising QGP Tomography

The heavy flavour (HF, charm (c) and beauty (b)) saga began in 1974, with the experimental discovery of J/Ψ ($c\overline{c}$ bound state) [119, 120]. Soon after, open charm baryons Λ_c^+ and open charm mesons $D^{0\pm}$ were measured in 1975 [121] and 1976 [122, 123], respectively. In parallel to the charm story, the elementary particle picture was enriched by Υ ($b\overline{b}$ bound state) discovered in 1977 [124], and the first observations of open beauty baryons Λ_b and mesons $B^{0\pm}$ were presented in 1981 [125] and 1983 [126], respectively.

Due to their heavy masses, heavy flavours are not only promising probes for the QGP medium but also powerful tools to test the QCD framework. Additionally, at LHC energies, the Drell-Yan signal is expected to be negligible. Instead of measuring the Drell-Yan process, the measurement of open heavy flavour production is the most natural normalization for charmonia and bottomonia at the LHC.

In order to illustrate the motivations for heavy flavour measurements, we begin with the heavy flavour production in nucleon-nucleon collisions.

2.1 Open Heavy Flavour Hadronic Production

In nucleon-nucleon collisions, heavy quarks are produced by pairs via hard scatterings, with virtuality threshold $Q \sim 2m_Q$ ($\sim$ 3 GeV for charm and $\sim$ 9.5 GeV for beauty). According to the asymptotic freedom (Sec. 1.2.2), the QCD running coupling α_s is small in heavy flavour production and allows to use pQCD predictions.

2.1.1 Factorization Theorem

Experimentally, heavy flavours are measured in the hadronic channel (H_Q) or via their decay leptons in the final state, as illustrated in Fig. 2.1. Heavy quark hadronic production can be calculated, in nucleon-nucleon collisions, in the pQCD framework according to the factorization theorem [127],

$$\frac{\mathrm{d}\sigma^{NN\to H_Q X}}{\mathrm{d}p_t}(\sqrt{s_{NN}}, m_Q, \mu_F^2, \mu_R^2) = \sum_{i,j=q,\overline{q},g} f_i(x_1, \mu_F^2) \otimes f_j(x_2, \mu_F^2) \otimes \frac{\mathrm{d}\hat{\sigma}^{ij\to Q(\overline{Q})\{n\}}}{\mathrm{d}\hat{p}_t}(\alpha_s(\mu_R^2), \mu_R^2, \mu_F^2, m_Q, x_1 x_2 s_{NN}) \otimes D_Q^{H_Q}(z), \tag{2.1}$$

with corrections of the order of $\mathcal{O}(\Lambda_{QCD}/\max(m_Q, p_t))$ which are suppressed with heavy flavour masses and/or with large p_t.

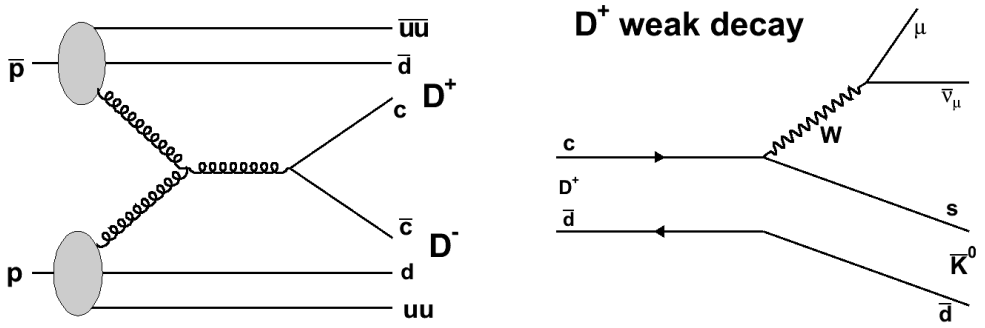

Figure 2.1: Examples of Feynman diagrams: D^+D^- production in $p\overline{p}$ collisions via $gg \to c\overline{c}$ (left panel) and $D^+ \to \overline{K}^0\mu\overline{\nu}_\mu$ (right panel).

In Eq. (2.1), the sum runs over all subprocesses for open heavy flavour hadron production. Each term corresponds to a given process in H_Q production (see example in Fig. 2.1, left panel).

1. In the initial stage of nucleon-nucleon collisions, two partons (i and j) are extracted from each nucleon with momentum fractions $x_{i/j}$ according to the probabilities given by the parton distribution functions $f_{i/j}(x_{i/j}, \mu_F^2)$, where i/j reflects the species of partons (q, $\overline{q}$ or g) and μ_F is the factorization scale. As for the renormalization factor μ_R, μ_F is an unphysical parameter in QCD, which is introduced to describe the QCD higher order corrections due to gluon radiation. Parton Distribution Functions (PDFs) evolve with Q^2 up to μ_F^2 through DGLAP equations [58].

2. Then, heavy flavours are produced during hard scatterings between the two extracted partons with virtuality $Q \sim x_1 x_2 s_{NN}$. At this step, where $m_Q > \Lambda_{QCD}$, the elementary partonic cross section $d\hat{\sigma}^{ij\to Q(\overline{Q})\{n\}}/d\hat{p}_t$ (where $\hat{p}_t$ is quark transverse momentum) up to a given perturbative order n, is related to the interactions at high Q^2 and can be computed by pQCD in terms of α_s^k (k evolves up to the perturbative order n).

3. After a heavy quark is formed, it will interact with other partons and fragment into an open heavy flavour hadron. $D_Q^{H_Q}(z)$ is the heavy quark fragmentation function which represents the probability for the scattered heavy quark to materialize as an hadron H_Q with momentum fraction $z = p^{H_Q}/p^Q$.

The whole procedure of open heavy flavour hadronic production (Fig. 2.1, left panel) is characterized by three quantities: $f_{i/j}(x, \mu_F)$ PDFs, partonic cross section $d\hat{\sigma}^{ij\to Q(\overline{Q})\{n\}}/d\hat{p}_t$ and fragmentation function $D_Q^{H_Q}(z)$, corresponding to the three steps just discussed. To get the final results, one should calculate their convolutions in Eq. (2.1). Due to the large mass of heavy quarks, each of these three steps for open heavy flavour hadron production has its special properties that are different

from those for light flavours. All these properties make the heavy flavour observables in the final state more interesting than that from light flavours, even in nucleon-nucleon collisions. Before to apply the convolution calculations in Eq. (2.1), one should study into detail each step to understand which relevant information can be obtained via heavy flavour final state observables.

2.1.2 Bjorken-x in PDFs via Heavy Flavours

The parton distribution functions are measured in deep inelastic scatterings as $ep \to eX$. Once the initial conditions of the nucleon structure are experimentally determined at a given Q, PDFs can be predicted by pQCD via the DGLAP evolution [60]. At present, the most widely used PDFs are the CTEQ PDFs sets [128].

It is interesting to constrain PDFs in the low Bjorken-x range in nucleon-nucleon collisions to test the pQCD calculations. Furthermore, measuring the nuclear modified PDFs (nPDFs) down to low Bjorken-x values is very important for understanding the whole picture of cold nuclear effects, as mentioned in Sec. 1.4.2.2. One of the advantages of heavy flavours is that they allow to access small Bjorken-x range in (n)PDFs, in particular with high center-of-mass collision energy and/or large (pseudo)-rapidity.

We start with a simple case: $\mathrm{Q\overline{Q}}$ production through the leading order gluon-gluon fusion $\mathrm{gg} \to \mathrm{Q\overline{Q}}$ in nucleon-nucleon collisions. By ignoring the parton intrinsic transverse momentum in the nucleons, the four-momenta of the two incoming gluons can be written as $(x_1, 0, 0, x_1)\sqrt{s_{\mathrm{NN}}}/2$ and $(x_2, 0, 0, -x_2)\sqrt{s_{\mathrm{NN}}}/2$ and we get

$$M^2_{\mathrm{Q\overline{Q}}} = x_1 x_2 s_{\mathrm{NN}}, \tag{2.2}$$

$$y_{\mathrm{Q\overline{Q}}} = \frac{1}{2}\ln\frac{E + p_{\mathrm{z}}}{E - p_{\mathrm{z}}} = \frac{1}{2}\ln\frac{x_1}{x_2}, \tag{2.3}$$

with virtuality at $\mathrm{Q\overline{Q}}$ production threshold. Then the Bjorken-x values of these two initial gluons are

$$x_1 = \frac{M_{\mathrm{Q\overline{Q}}}}{\sqrt{s_{\mathrm{NN}}}}\exp(+y_{\mathrm{Q\overline{Q}}}), \qquad x_2 = \frac{M_{\mathrm{Q\overline{Q}}}}{\sqrt{s_{\mathrm{NN}}}}\exp(-y_{\mathrm{Q\overline{Q}}}). \tag{2.4}$$

These results, Eq. (2.4), will not change in symmetric nucleus-nucleus collisions. According to Eq. (2.4), at LHC energies, in pp collisions at $\sqrt{s_{\mathrm{NN}}} = 7$ TeV, one can access Bjorken-x values down to $x \sim 4 \cdot 10^{-4}$ for charm quarks in the mid-rapidity region.

Tab. 2.1 shows the accessible Bjorken-x range corresponding to $\mathrm{c\overline{c}}$ and $\mathrm{b\overline{b}}$ production at threshold in the mid-rapidity region ($y = 0$) at different energies, as calculated from Eq. (2.4). The Bjorken-x regime relevant for charm production at the LHC $\mathcal{O}(10^{-4})$ is about two and three orders of magnitude lower than that at RHIC and SPS, respectively. To get a clear comparison of the accessible Bjorken-x region for heavy flavours at RHIC and LHC, the parton distribution functions $xf(x, Q^2)$ in proton from CTEQ 4L [131] are shown in Fig. 2.2 (left panel) with the corresponding achieved Bjorken x range, at $Q^2 = 5$ GeV^2 corresponding to $\mathrm{c\overline{c}}$

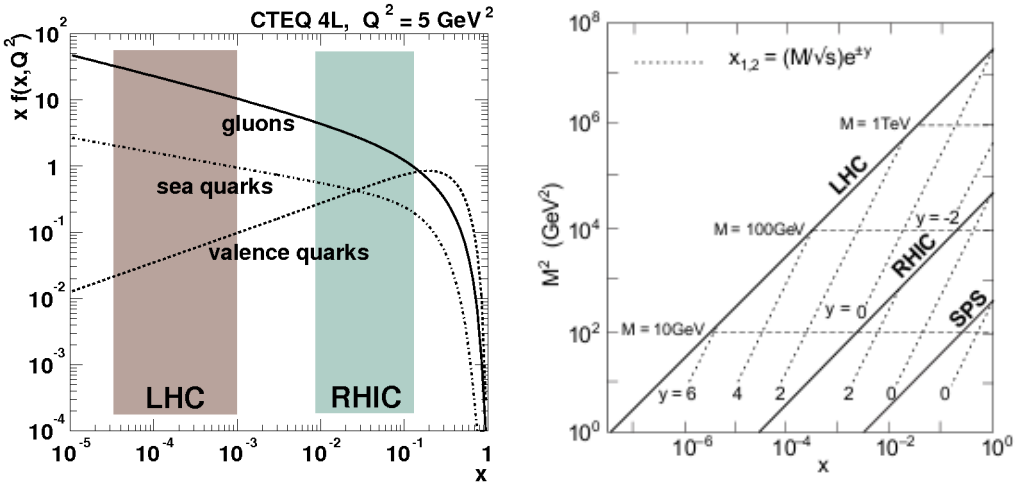

Figure 2.2: Left: parton distribution functions in proton from CTEQ 4L with $Q^2 = 5$ GeV^2 [41]. Right: Bjorken-x as a function of M^2 for particle production in nucleon-nucleon collisions at the SPS, RICH and LHC. The lines correspond to constant rapidity at corresponding energies [129].

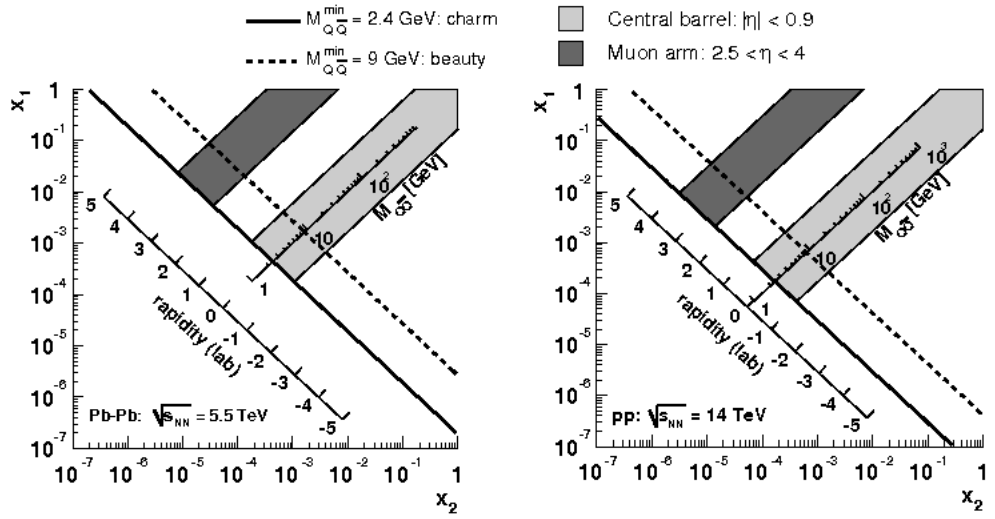

Figure 2.3: Accessible Bjorken-x range for heavy flavours in Pb–Pb collisions at $\sqrt{s_{\rm NN}} = 5.5$ TeV (left) and in pp collisions at $\sqrt{s} = 14$ TeV (right) in the rapidity range that can be measured with ALICE at the LHC [130].

production at threshold. It sorts out that, due to the higher beam energies delivered at the LHC than at the RHIC, heavy quarks allow to probe the low Bjorken-x region dominated by gluons at the LHC.

It is worth mentioning that as the rapidity increases, one will be able to in-

machine	SPS	RHIC	LHC	LHC	LHC	LHC
system	Pb–Pb	Au–Au	Pb–Pb	Pb–Pb	pp	pp
$\sqrt{s_{\rm NN}}$ (TeV)	0.017	0.2	2.76	5.5	7	14
charm	$\simeq 10^{-1}$	$\simeq 10^{-2}$	$\simeq 8 \cdot 10^{-4}$	$\simeq 4 \cdot 10^{-4}$	$\simeq 4 \cdot 10^{-4}$	$\simeq 2 \cdot 10^{-4}$
beauty	-	-	$\simeq 4 \cdot 10^{-3}$	$\simeq 2 \cdot 10^{-3}$	$\simeq 1 \cdot 10^{-3}$	$\simeq 6 \cdot 10^{-4}$

Table 2.1: The accessible Bjorken-x values with $c\overline{c}$ and $b\overline{b}$ production at threshold at mid-rapidity ($y = 0$) and different energies.

vestigate unprecedented low Bjorken-x values, as shown in Fig. 2.2 (right panel). Fig. 2.3 shows the regions in the (x_1, x_2) plane covered by charm and beauty in the ALICE acceptance, in Pb–Pb collisions at $\sqrt{s_{\rm NN}} = 5.5$ TeV (left panel) and in pp collisions at $\sqrt{s} = 14$ TeV (right panel). In this figure, the points with constant invariant mass lie on hyperbola $x_1 \cdot x_2 = m^2_{\rm Q\overline{Q}}/s_{\rm NN}$ (straight lines in logarithmic scale) and the points with constant rapidity lie on straight lines $x_1 = x_2 \exp(+y_{\rm Q\overline{Q}})$. In the acceptance of the ALICE forward MUON spectrometer, $-4 < \eta < -2.5$, the accessible Bjorken-x range will be down to $\mathcal{O}(10^{-6})$, which is lower by two orders of magnitude than that can be accessed in the ALICE Central Barrel acceptance, as depicted in Fig. 2.3. The measurement of heavy flavours in the forward rapidity region at the LHC offers unique opportunity to measure PDFs down to extremely low Bjorken-x values which have not been achieved in the past.

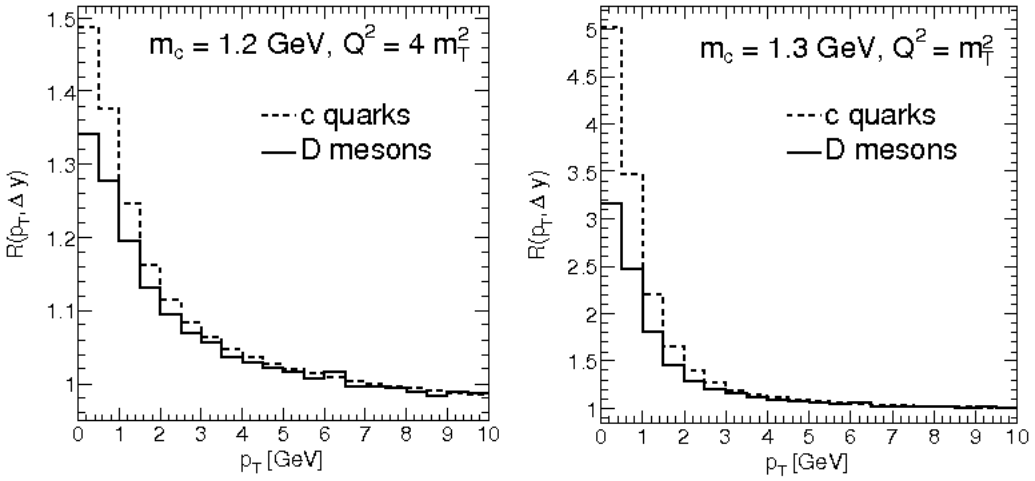

Figure 2.4: Enhancement factor $R(p_{\rm t}, \Delta y)$ for charm quarks (dashed lines) and D ($\rm D^0$, $\rm D^+$) mesons (solide lines), with $m_{\rm c} = 1.2$ GeV/c^2, $Q^2 = 4m_{\rm T}^2$ (left panel) and $m_{\rm c} = 1.3$ GeV/c^2, $Q^2 = m_{\rm T}^2$ (right panel) [132].

At LHC energies, heavy quarks are preferentially produced in the initial fusion of gluons ($\rm gg \rightarrow Q\overline{Q}$) rather than in the interactions $\rm q\overline{q} \rightarrow Q\overline{Q}$ [133]. In the Bjorken-x range, which is achieved by heavy flavours at the LHC, the density of gluons is close

to saturation in the available phase space, leading to gluon recombination gg $\rightarrow$ g as described in the CGC picture. This effect is taken into account in the non-linear term in DGLAP evolution [134]:

$$\partial f_{\mathrm{g}}(x, Q^2)/\partial \ln Q^2 = [\mathrm{DGLAP}, \mathcal{O}(f_{\mathrm{g}})] - \mathcal{O}(f_{\mathrm{g}}). \tag{2.5}$$

Eq. (2.5) allows a higher gluon density at small Q^2, and implies modified gluon distribution function for heavy flavour production even in nucleon-nucleon collisions. This also indicates a possible enhancement of heavy quark pairs in the low p_{t} region at the LHC [135], as shown in Fig. 2.4 in the case of charm quarks.

2.1.3 Partonic Cross Section

The partonic cross section of heavy quark production is validated by pQCD calculations for virtuality equal to heavy quark mass. This will bring tight constraints on the phase space. In some cases, one will need to implement a resummation technique for the calculation of both the inclusive and differential partonic production cross section of heavy flavours.

2.1.3.1 Inclusive Cross Section

In the calculations of the inclusive partonic cross section for heavy flavours, the remnant long-distance dynamics in hard scattering functions can become large when the phase space near partonic threshold is dominated by pQCD higher order corrections [136, 137]. This effect always implies that each order of α_{s} is accompanied by logarithmic terms as a coefficient $\sim (\alpha_{\mathrm{s}} \ln \tau)^n$ (τ is an arbitrary order parameter) when the perturbative series end up. A general way to treat this problem is to use the **Fix Order** (**FO**, with a given power n) cross section to different orders of logarithmic terms which include the long-distance dynamics correction with the general resummation form [138]. For any order of n, the resummed inclusive partonic cross section can be expressed as [139]:

$$\hat{\sigma}^{ij\rightarrow \mathrm{Q}(\overline{\mathrm{Q}})}(\alpha_{\mathrm{s}}(\mu^2), \mu^2, m_{\mathrm{Q}}, \hat{s}) = \frac{\alpha_{\mathrm{s}}(\mu^2)}{m_{\mathrm{Q}}^2} \sum_{n=0}^{\infty} (4\pi\alpha_{\mathrm{s}}(\mu^2))^n \sum_{k=0}^{n} f_{nk}^{ij}(\xi) \ln^k \frac{\mu^2}{m_{\mathrm{Q}}^2} \tag{2.6}$$

by assuming $\mu_{\mathrm{R}} = \mu_{\mathrm{F}} = \mu$, where $\xi = \hat{s}/4m_{\mathrm{Q}}^2 - 1$ with $\hat{s} = x_i x_j s_{\mathrm{NN}}$ as defined in Eq. (2.1), $f_{nk}^{ij}(\xi)$ are series of dimensionless scaling functions and depend only on ξ, and the order parameter $\tau = \mu^2/m_{\mathrm{Q}}^2$.

In Eq. (2.6), $n = 0$ gives the **Leading Order** (**LO**) cross section with $\mathcal{O}(\alpha_{\mathrm{s}})$ or the Born term and $n = 1$ ($\mathcal{O}(\alpha_{\mathrm{s}}^2)$) corresponds to the **Next-to-Leading Order** (**NLO**) cross section. With a given fixed order n and using $k = n$ one obtains the **Leading Logarithm** (**LL**) terms. The **Next-to-Leading Logarithm** (**NLL**) terms are obtained by adding to the LL terms the $k = n - 1$ terms. A recent calculation of the total cross section to Next-to-Next-to-Next Leading Order (N^{2}LO) and Next-to-Next-to-Next Leading Logarithm (N^{2}LL) has been presented in [138]. However they can be applied only near the partonic threshold. As charm and beauty

production at LHC energies is well above the threshold, it will not be affected by long-distance dynamics effects and resummation calculations can be used.

2.1.3.2 Differential Cross Section

Gluon emission should be treated with soft and collinear limits in the calculation of the differential cross section. As it will be discussed in the following, due to their large masses, heavy quarks are treated differently as compared to light quarks. For the light quarks, soft gluon emission is considered in the factorization and evolution of PDFs. The hard scale given by the heavy quark mass acts as a cutoff on collinear singularities even with $\hat{p}_{\rm t} \to 0$. Therefore, the introduction of the renormalization scale $\mu_{\rm R}$ is no longer needed in case of heavy quarks. Also, the gluon emission from heavy quarks contributes as a power expansion in the strong coupling constant $\alpha_{\rm s} \ln \hat{p}_{\rm t}/m_{\rm Q}$ in the cross section, which is evaluated as a renormalization scale near the heavy quark mass. This term is not dangerous at low and intermediate $\hat{p}_{\rm t}$. Due to the presence of heavy quark mass $m_{\rm Q}$, the perturbative expansion in terms of $\alpha_{\rm s}$ can be done. But with large values of $\hat{p}_{\rm t}$, $\ln \hat{p}_{\rm t}/m_{\rm Q}$ can bias the pQCD calculations of the cross section.

In this case, with NLO calculations [1], the differential cross section which can be schematically written as

$$\frac{{\rm d}\hat{\sigma}}{{\rm d}\hat{p}_{\rm t}} = \alpha_{\rm s}^2[\alpha_0 + s(\frac{m_{\rm Q}}{\hat{p}_{\rm t}})] + \alpha_{\rm s}^3[\alpha_1 \ln \frac{\hat{p}_{\rm t}}{m_{\rm Q}} + \beta_0 + s(\frac{m_{\rm Q}}{\hat{p}_{\rm t}})] + \mathcal{O}(\alpha_{\rm s}^4 \ln^2 \frac{\hat{p}_{\rm t}}{m_{\rm Q}}), \qquad (2.7)$$

is not reliable at high $\hat{p}_{\rm t}$. In Eq. (2.7), α_i and β_i ($i = 0$ and/or 1) depend $\hat{s}$ (on center of mass energy), $\hat{p}_{\rm t}$, $\mu_{\rm R}$ and $\mu_{\rm F}$. $s(m_{\rm Q}/\hat{p}_{\rm t})$ stands for the terms suppressed by powers of $m_{\rm Q}/\hat{p}_{\rm t}$ in the large $\hat{p}_{\rm t}$ limit and/or vanishing value of $m_{\rm Q}$. One approach was adopted in order to deal with these logarithmic enhanced terms. They are estimated with the first neglected LL terms $\mathcal{O}(\alpha_{\rm s}^4 \ln^2 \hat{p}_{\rm t}/m_{\rm Q})$ in Eq. (2.7) by choosing $\mu_{\rm R}$ and $\mu_{\rm F}$ of the order of $\hat{p}_{\rm t}$ [140]. However, this method gives large uncertainties at very large value of $\hat{p}_{\rm t}$.

An improved way is to consider the correlations from the resumed LL and NLL terms via the fragmentation function formalism which was used for light quarks [141],

$$\frac{{\rm d}\hat{\sigma}}{{\rm d}\hat{p}_{\rm t}} = \alpha_{\rm s}^2 \sum_{l=0}^{\infty} a_l \alpha_{\rm s}^l \ln^l \frac{\hat{p}_{\rm t}}{m_{\rm Q}} + \alpha_{\rm s}^3 \sum_{k=0}^{\infty} b_k \alpha_{\rm s}^k \ln^k \frac{\hat{p}_{\rm t}}{m_{\rm Q}} + \mathcal{O}(\alpha_{\rm s}^4 \alpha_{\rm s}^m \ln^m \frac{\hat{p}_{\rm t}}{m_{\rm Q}}). \qquad (2.8)$$

As for α_i and β_i in Eq. (2.7), the coefficients a_l and b_k depend on $\hat{s}$, $\hat{p}_{\rm t}$, $\mu_{\rm R}$ and $\mu_{\rm F}$. The drawback of this method is that, with the massless formalism, all contributions from $s(m_{\rm Q}/\hat{p}_{\rm t})$ terms are excluded in Eq. (2.8).

The FO calculations (Eq. (2.7)) introduce large uncertainties for high $\hat{p}_{\rm t}$ and resummation formalism up to NLL. Eq. (2.8) does not include the contributions from $s(m_{\rm Q}/\hat{p}_{\rm t})$ terms. Then, a reasonable consideration is to match the FO and

[1] In Eq. (2.6), the inclusive partonic cross section of heavy quark production starts at LO with $\mathcal{O}(\alpha_{\rm s})$, and the NLO term corresponds to $\mathcal{O}(\alpha_{\rm s}^2)$. But for differential cross section calculation, the LO starts with $\mathcal{O}(\alpha_{\rm s}^2)$ and NLO up to $\mathcal{O}(\alpha_{\rm s}^3)$.

NLL calculations together as the so-called FONLL (Fixed-Order Next-to-Leading Logarithm) formalism [142],

$$\mathrm{FONLL} = \mathrm{FO} + (\mathrm{NLL} - \mathrm{FOM0}) \times G(m_{\mathrm{Q}}, \hat{p}_{\mathrm{t}}), \tag{2.9}$$

where, the function $G(m_{\mathrm{Q}}, \hat{p}_{\mathrm{t}})$ is used to correct the effect from $s(m_{\mathrm{Q}}/\hat{p}_{\mathrm{t}})$ terms, its limit is

$$\lim_{m_{\mathrm{Q}}/\hat{p}_{\mathrm{t}} \to 0} G(m_{\mathrm{Q}}, \hat{p}_{\mathrm{t}}) = 1, \tag{2.10}$$

and FOM0 is the massless limit of FO calculations in Eq. (2.7),

$$\mathrm{FOM0} = \alpha_{\mathrm{s}}^2 \cdot \alpha_0 + \alpha_{\mathrm{s}}^3 [\alpha_1 \ln \frac{\hat{p}_{\mathrm{t}}}{m_{\mathrm{Q}}} + \beta_0]. \tag{2.11}$$

By subtracting the fixed terms already present in FO calculations from the NLL formalism (Eq. (2.8)), the term (NLL − FOM0) in Eq. (2.11) is an approximation of the contributions from only the logarithmic mass terms in Eq. (2.8), and avoid double counting. To choose the appropriate formalism of series a_l and b_k we take, $a_0 = \alpha_0$, $a_1 = \alpha_1$ and $b_0 = \beta_0$. Then, Eq. (2.7) and Eq. (2.8) can be matched in FONLL formalism (Eq. (2.9)) as,

$$\begin{aligned}\frac{\mathrm{d}\hat{\sigma}}{\mathrm{d}\hat{p}_{\mathrm{t}}} =& \alpha_{\mathrm{s}}^2 [a_0 + s(\frac{m_{\mathrm{Q}}}{\hat{p}_{\mathrm{t}}})] + \alpha_{\mathrm{s}}^3 [a_1 \ln \frac{\hat{p}_{\mathrm{t}}}{m_{\mathrm{Q}}} + b_0 + s(\frac{m_{\mathrm{Q}}}{\hat{p}_{\mathrm{t}}})] \\ &+ (\alpha_{\mathrm{s}}^2 \sum_{l=2}^{\infty} a_l \alpha_{\mathrm{s}}^l \ln^l \frac{\hat{p}_{\mathrm{t}}}{m_{\mathrm{Q}}} + \alpha_{\mathrm{s}}^3 \sum_{k=1}^{\infty} b_k \alpha_{\mathrm{s}}^k \ln^k \frac{\hat{p}_{\mathrm{t}}}{m_{\mathrm{Q}}}) \times G(m_{\mathrm{Q}}, \hat{p}_{\mathrm{t}}) \\ &+ \mathcal{O}(\alpha_{\mathrm{s}}^4 \alpha_{\mathrm{s}}^m \ln^m \frac{\hat{p}_{\mathrm{t}}}{m_{\mathrm{Q}}}) + \mathcal{O}(\alpha_{\mathrm{s}}^4 \cdot s(\frac{m_{\mathrm{Q}}}{\hat{p}_{\mathrm{t}}})).\end{aligned} \tag{2.12}$$

This approach overcomes the logarithm enhancement in FO calculations and also corrects the contributions from $s(m_{\mathrm{Q}}/\hat{p}_{\mathrm{t}})$ terms in NLL resummation. It is one of epidemic theory on heavy flavour production cross section estimate. Also, the resummation formalism guarantees the accuracy of pQCD predictions for heavy flavour production cross sections. The measurement of heavy flavour observables in nucleon-nucleon collisions will allow to test the pQCD framework.

2.1.4 Hard Fragmentation

The fragmentation which treats the desintegration of quarks and gluons into hadrons, is a non-perturbative process in QCD. For light quarks, the QCD factorization theorem [143, 144] allows to factorize these non-perturbative effects into universal fragmentation functions (FF) together with the partonic cross section,

$$\int \frac{\mathrm{d}z}{z} \frac{\mathrm{d}\hat{\sigma}^{ij \to k}}{\mathrm{d}p_{\mathrm{t}}^{\mathrm{h}}} (\frac{p_{\mathrm{t}}^{\mathrm{h}}}{z}, \mu) D_k^{\mathrm{h}}(z, \mu), \tag{2.13}$$

where, i, j and k are the light partons, $p_{\mathrm{t}}^{\mathrm{h}} = z \cdot \hat{p}_{\mathrm{t}}$ is the transverse momentum of light hadrons h, the artificial factorization scale μ is a non-physical quantity of

both partonic cross sections and fragmentation functions. The process of fragmentation is different for heavy quarks. Due to their large masses that act as a cutoff for the collinear singularities which appear in higher orders in perturbative calculations, the perturbative calculations of heavy quark production and non-perturbative fragmentation functions are separated, as in Eq. (2.1).

The average value of the fragmentation fraction z of heavy quarks in Eq. (2.1), is estimated as [145, 146]:

$$< z > \simeq 1 - \frac{\Lambda_{\rm H}}{m_{\rm Q}}. \tag{2.14}$$

Since the heavy quark mass $m_{\rm Q}$ is much larger than the hadronic scale $\Lambda_{\rm H}$, Eq. (2.14) indicates that the non-perturbative fragmentation function for heavy quarks should be very hard. This behaviour is derived from various phenomenological models of the non-perturbative heavy quark fragmentation functions as: Kartvelishvili-Likhoded-Petrov [147], Bowler [148], Peterson-Schlatter-Schmitt-Zerwas [149] and Collins-Spiller [150].

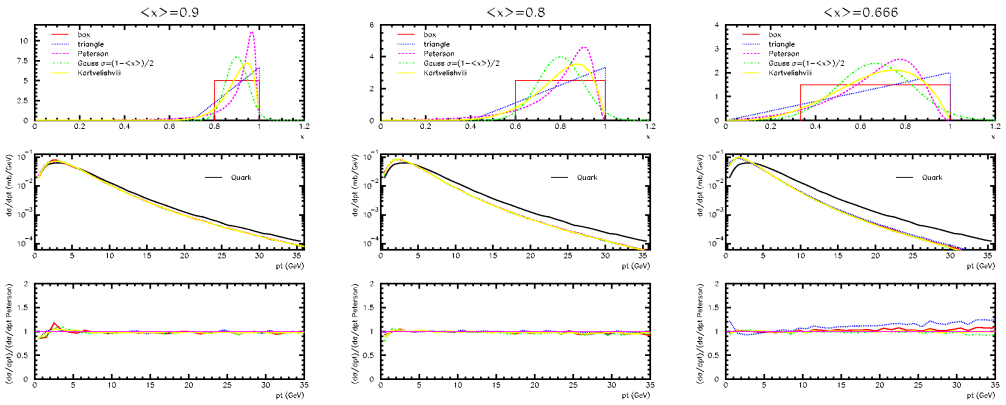

Figure 2.5: Upper plots: Distributions of different fragmentation functions for heavy quarks; middle plots: $p_{\rm t}$ distributions of open heavy flavour hadrons according to the corresponding fragmentation functions shown in the upper plots and comparisons with the $p_{\rm t}$ distribution of mother quark which is obtained from HvQMNR predictions [151] for beauty quarks; lower plots: ratios of different hadron $p_{\rm t}$ distributions to the result obtained with the Peterson fragmentation function. Each case is shown with $< z >= 0.9$ (left), 0.8 (middle) and 0.666 (right) [152]. Note that in the figures $< z >$ is expressed as $< x >$ in the plots.

Upper plots of Fig. 2.5 display the open heavy flavour hadron distributions with different test fragmentation functions of heavy quarks, with different values of $< z >$ mentioned on the figures. The corresponding $p_{\rm t}$ distributions at hadron level with different test fragmentation functions are shown in middle plots of Fig. 2.5. The results are compared to the $p_{\rm t}$ distribution of the mother quark, obtained from the HvQMNR predictions for beauty quark [151]. The lower plots in Fig. 2.5 show the ratios of different hadron $p_{\rm t}$ distributions to the result obtained with the Peterson

fragmentation function. Two important features can be extracted from this figure:

1. with $< z >= 0.8$ and $< z >= 0.9$ which are the typical values for charm and beauty, respectively, the p_{t} distributions at hadron level are very similar with those at quark level whatever test fragmentation functions are used. This is due to the fact that fragmentation functions of heavy flavours are very hard (large $< z >$ values) and that the p_{t} distributions at quark level can be very well described by the measured p_{t} distributions at hadron level;

2. with different test fragmentation functions and different $< z >$ values, the p_{t} distributions at hadron level are very close to each other even for $< z >= 0.666$. Due to the large quark mass, the measured p_{t} distributions of open heavy flavour hadrons are insensitive to the detailed shape of $D(z)$ which is controlled by non-perturbative effects.

2.1.5 Comparison with Data

Due to the large heavy quark masses and harder fragmentation functions, even with the non-perturbative fragmentation process, the measurement of open heavy flavour hadrons in the final stage of the collision can reflect the properties of their mother heavy quarks and also serve as an important test of pQCD calculations. From the experimental side, the measurement of heavy flavour observables in pp collisions is mandatory as a baseline for the interpretation of results concerning heavy flavour production in nucleon-nucleus and nucleus-nucleus collisions to test the so-called cold and hot nuclear effects, respectively. In particular, the comparison of heavy flavour production in nucleon-nucleon collisions and nucleus-nucleus collisions allows to evidence and study the properties of QGP.

2.1.5.1 Tevatron

The Fermilab Tevatron is a proton-antiproton collider (1 km radius superconducting synchrotron). The two beams collide at two interaction points, where the CDF and DØ detectors are located.

One of the first measurements of b quark production cross section in hadronic collisions was done in the UA1 collaboration (at SPS) in $\mathrm{p\overline{p}}$ collisions at $\sqrt{s} =$ 630 GeV [153, 154]. The results show an agreement with NLO pQCD predictions including all the mass effects [155, 140] within a 40% rather large theoretical uncertainty.

After that, the CDF collaboration at the Tevatron performed a measurement of the b-quark production cross section in the **run 0** ($\mathrm{p\overline{p}}$ collisions at $\sqrt{s} = 1.8$ TeV) via the exclusive decay channel $\mathrm{B}^{\pm} \rightarrow \mathrm{J/\Psi K}^{\pm}$ [156] but the results are larger than the NLO predictions by a factor ~ 6. The disagreement between data and model calculations, in constract to what was observed at $\sqrt{s} = 630$ GeV, was attributed to the different Bjorken-x range at these two beam energies and to the uncertainties on PDFs. In 2002, the CDF Collaboration published the results for the exclusive B^{+} meson production cross section with the **run I** data sample (same beam energy

as in the **run 0**) and found that the ratio between data and central value of NLO predictions was 2.9 ± 0.5. At this time, the theoretical predictions were updated with new sets of input PDFs (MRST [157] and CTEQ 5M [158]) and were increased by almost a factor of 2.

The disagreement between data and NLO predictions for b-quark production cross section has been also presented in the DØ collaboration at the Tevatron which published their first results in 1995 [159]. The data have been re-analysed in 2000 (correction of $B \to J/\Psi$ family) and the results from DØ are still significantly higher than the updated NLO predictions [160].

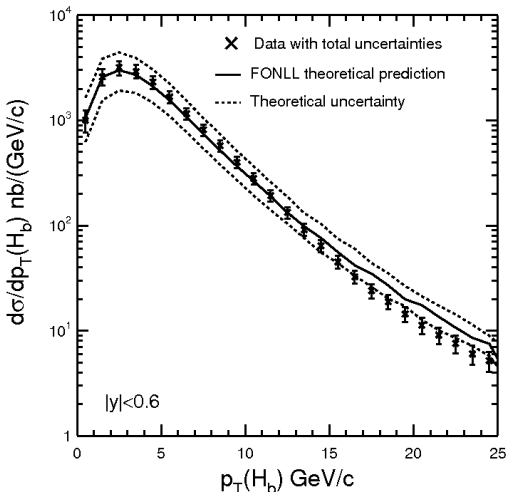

Figure 2.6: p_t-differential cross section of open b-hadron production [161] measured by CDF **run II** at Tevatron. Results are compared with FONLL predictions [162].

This disagreement between data and theory at Tevatron energies triggered improvements in both experimental and theoretical side. In 1998, the FONLL calculations mentioned in Sec. 2.1.3.2 were developed. Soon after, the CDF collaboration measured the inclusive B-meson production cross section by correcting the $B \to J/\Psi$ cross section with Monte Carlo simulations (CDF **run II** data for $p\bar{p}$ collisions at $\sqrt{s} = 1.96$ TeV). The results are presented in Fig. 2.6 [161] and compared with FONLL predictions [162]. After almost 10 years of improvements on the experimental and theoretical side, the b-hadron production cross section shown in Fig. 2.6 lies well within the theoretical uncertainty band and is finally in very good agreement with the FONLL predictions.

However, charm productiom is still not well reproduced by the calculations as shown in Fig. 2.7 [163]. This figure displays the open charm hadrons, D^0, D^{*+}, D^+ and D_s^+ p_t-differential production cross sections reconstructed via the corresponding hadronic decay channels:

$$D^0 \to K^-\pi^+$$
$$D^{*+} \to D^0\pi^+$$
$$D^+ \to K^-\pi^+\pi^+$$
$$D_s^+ \to \phi\pi^+$$

and measured in CDF **run II** data. The comparison with FONLL predictions [164] (shaded bands in Fig. 2.7), indicates that the data are systematically higher than the theoretical calculations.

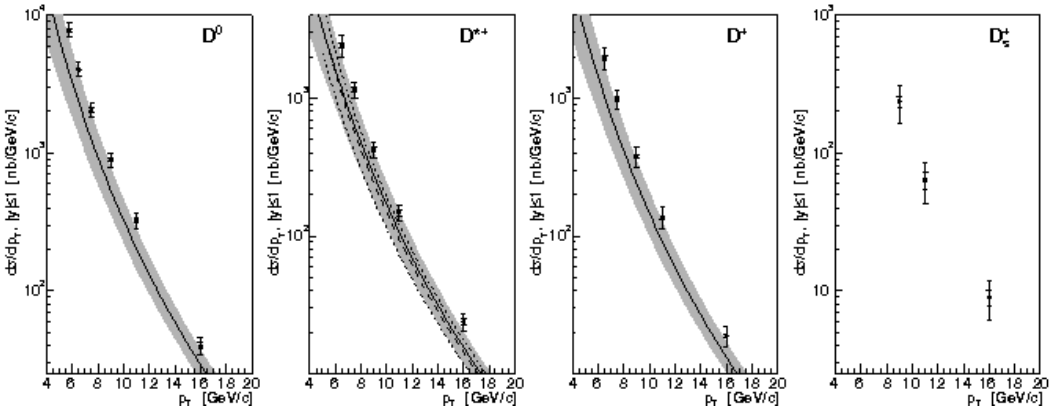

Figure 2.7: Differential cross section measurements for D-mesons in $|y| < 1$ as a function of p_t with CDF II detector at the Tevatron (circles) [163]. The solid curves are the FONLL predictions [164], with the uncertainties indicated by the shaded bands. The dashed curve shown for D^{*+} cross section is the theoretical prediction from Ref. [165] and the dotted lines indicate the corresponding uncertainty.

2.1.5.2 RHIC

Due to a lower center of mass energy (pp collisions at $\sqrt{s} = 130$ or 200 GeV) with respect to the Tevatron, the production cross sections of heavy flavours at RHIC are smaller than measured at Tevatron. The heavy flavour measurements at RHIC mainly focus on charm production, which is done by detecting D-mesons either through their semi-leptonic decays or via their hadronic channels. That offers a good chance to investigate the mentioned problem of pQCD predictions for charm quark production at the Tevatron in this "low" energy range.

Among many heavy flavour measurements at RHIC, Fig. 2.8 (left panel) shows the invariant differential cross section of electrons from heavy flavour decays measured by PHENIX in pp collisions at $\sqrt{s} = 200$ GeV [166] at mid-rapidity. Two independent analysis methods, "cocktail" method [169] and "converter" method [170], are used in the low and high p_t region, respectively. The lower panel presents the ratio between data and FONLL predictions (red points) with the systematic uncertainties displayed by yellow bands [167]. The upper and lower curves are the two limits of the theoretical uncertainties. One clearly sees that, the data points are located at the upper limit of the FONLL predictions within uncertainties, and the difference between data and theory in this measurement is around one σ, which is consistent with the results at the Tevatron (Fig. 2.7) [2].

Recently, in 2011, the STAR collaboration at RHIC published the newest non-photonic electron measurement in pp collisions at $\sqrt{s} = 200$ GeV with data from

[2] In Fig. 2.7, only the open charm contributions are considered, while in Fig. 2.8 (left panel) the non-photonic electrons include both charm and bottom components. But according to FONLL predicitons [167], the total production cross section of non-photonic electrons is dominated by the charm component.

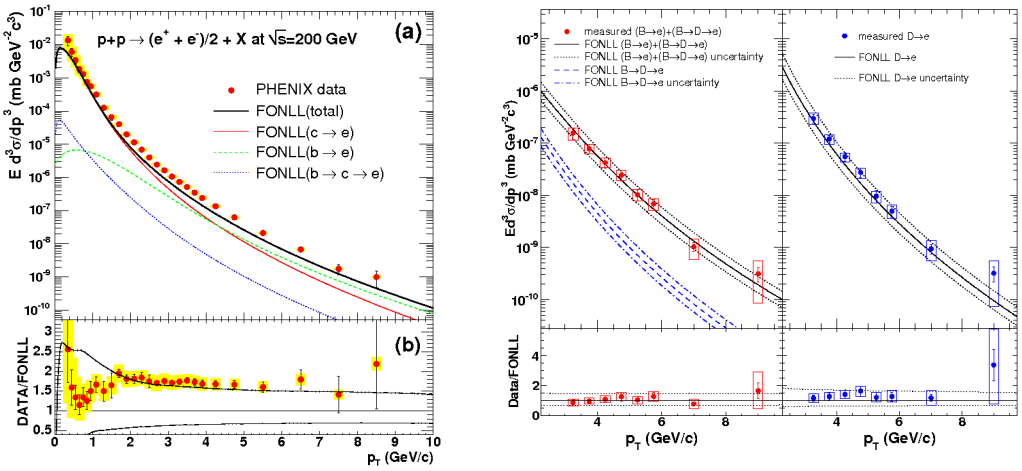

Figure 2.8: Left: (a) invariant differential cross sections of electrons from heavy flavour decays measured by PHENIX in pp collisions at $\sqrt{s} = 200$ GeV [166]. The curves are FONLL calculations [167]; (b) ratio of data and FONLL calculations, upper (lower) curve shows the theoretical upper (lower) limit of the FONLL calculations. Right: invariant cross section of $(e^+ + e^-)/2$ from beauty (upper-left) and charm meson (upper-right) decays measured by the STAR collaboration in pp collisions at $\sqrt{s} = 200$ GeV, together with the ratio of the corresponding measurements to FONLL predictions for beauty (lower-left) and charm electrons (lower-right) [168].

Run2005 and **Run2008**, where charm and beauty components have been unraveled [168]. The results are shown in Fig. 2.8 (right panel), together with the ratios of corresponding measurements to FONLL predictions [167]. The total non-photonic electron production is consistent with the measurements from the PHENIX Collaboration (Fig. 2.8 left [166]), and the charm and beauty components are separated via the differences in their respective azimuthal distributions with respect to the corresponding charged hadrons by using the method described in [171]. In these newest results, not only the data points for beauty component but also the ones for charm component are inside the uncertainty bands of the FONLL predictions. It is the first time that a so good agreement between data and theory predictions of heavy flavours production for both beauty and charm is achieved! There also exists measurements of muons from heavy flavour decays in the forward rapidity region from the PHENIX collaboration. The results are underestimated by the model calculations.

Now, can we say that large part of the contradictions in heavy flavour hadronic production between data and theory are solved? Of course, the answer is **"NO"**! First, all the experimental results listed above have still large uncertainties as well as the ones concerning the theoretical predictions. Moreover, the forward rapidity needs a particular interest. Also, the theoretical predictions need to be validated at higher energies. In particular, it has been already debated whether charm quarks

are heavy enough to be reliablely treated by the pQCD framework at higher energies [172]. All of these aspects illustrate the need and importance to measure the heavy flavour production at LHC energies!

2.2 Heavy Flavour Production in A–A Collisions

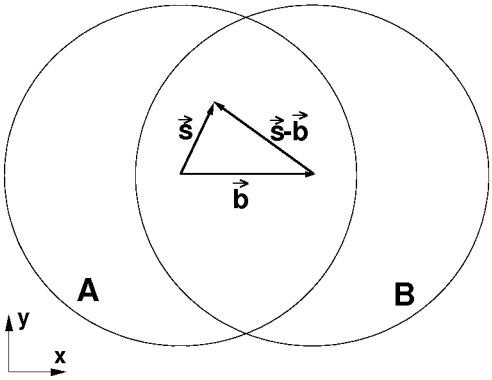

Figure 2.9: Collision geometry in the transverse plane.

Heavy quarks are important probes of the hot and dense matter formed in heavy ion collisions. Due to their large masses, their dominant production mechanism is restricted to parton-parton hard scatterings collisions in the early stage of A–A collisions. Also, due to the large virtuality threshold ($Q \sim 2m_{\mathrm{Q}}$, as mentioned in Sec. 2.1) for heavy quark pair production in hard scatterings, heavy flavours are produced in the early stage of nucleus-nucleus collisions (formation time for $\mathrm{c\bar{c}}$ pair production is $\tau \sim 1/Q \simeq 0.08$ fm/c). As a consequence, they are created before the QGP formation. Then, they pass through the fireball, and suffer the full evolution of the system. After that, they are expected to fragment into hadrons at the phase bound of the QGP medium because of their hard fragmentation functions. Open heavy flavour hadrons are expected to be sensitive to the energy density of the system through the mechanism of in-medium energy loss of heavy quarks. Also, if the initial temperature of the medium is high enough, there is a probability to produce heavy flavours inside the it. Heavy flavours created by this kind of thermal mechanism are very sensitive to the initial temperature of the system. This is an other promising way to extract the initial conditions of the fireball via their final state observables. When the temperature of system goes down due to the fireball expansion, the heavy flavour production gets frozen. Thus, heavy flavours created via hard processes in the early stage of the collisions give a very clean tomography of the QGP medium.

To illustrate how to extract the medium information via the final state observables from heavy flavours, we first introduce the pure binary scaling for extrapolating the heavy flavour production from nucleon-nucleon collisions to nucleus-nucleus collisions without any nuclear effect. Then we introduce the nuclear effects step by step to see how they affect the final observables related to heavy flavours.

2.2.1 Binary Scaling of Heavy Flavour Production in A–A Collisions

Ultra-relativistic heavy ion collisions can be treated as a superposition of independent nucleon-nucleon collisions [173]. In the absence of nuclear effects, the open heavy flavour differential yield in the final state of nucleus-nucleus interactions can be obtained by scaling the yield in nucleon-nucleon collisions with the number of binary collisions $< N_{\rm coll} >$ as,

$$\frac{\mathrm{d}^2 N_{\rm AA}^{\rm HF}}{\mathrm{d}p_{\rm t} dy} =< N_{\rm coll} > \times \frac{\mathrm{d}^2 N_{\rm NN}^{\rm HF}}{\mathrm{d}p_{\rm t} dy}. \tag{2.15}$$

As defined in Sec. 1.4.2.1, $< N_{\rm coll} >$ depends on the centrality class which can be described by the collisional impact parameter $\vec{b}$. Considering the two incoming nucleus A and B (as shown in Fig. 2.9) with $N_{\rm A}$ and $N_{\rm B}$ the corresponding numbers of nucleons, the maximum number of binary nucleon-nucleon collisions during the interactions between these two nucleus could be achieved when each nucleon in the nuclei A collides with all of nucleons in nuclei B. This leads to:

$$m = N_{\rm A} \cdot N_{\rm B}. \tag{2.16}$$

Using $\mathcal{P}(n, \vec{b})$ to determine the probability of having n binary nucleon-nucleon collisions in a given nucleus-nucleus event with impact parameter $\vec{b}$, $< N_{\rm coll} >$ is given by the mean value of n

$$< N_{\rm coll} > (\vec{b}) = \sum_{n=0}^{m} n\mathcal{P}(n, \vec{b}). \tag{2.17}$$

According to the **Binomial Theorem**, $\mathcal{P}(n, \vec{b})$ can be written as

$$\mathcal{P}(n, \vec{b}) = C_n^m p^n(\vec{b})[1 - p(\vec{b})]^{m-n}, \tag{2.18}$$

where $p(\vec{b})$ is the probability to have one binary collision. To obtain the expression of $p(\vec{b})$, one should consider the following steps: (i) get two nucleons in nuclei A and B at position $(\vec{s}_{\rm A/B}, z_{\rm A/B})$ with the probability density $\rho_{\rm A/B}(\vec{s}_{\rm A/B}, z_{\rm A/B})$; (ii) define $t(\vec{s})$ as the probability density for having a binary collision between two nucleons when one baryon is located at a distance $\vec{s}$ relative to an other baryon. With the inelastic nucleon-nucleon collision cross section $\sigma_{\rm NN}^{\rm inel}$, the binary collision probability is given by $t(\vec{s}) \cdot \sigma_{\rm NN}^{\rm inel}$; (iii) with a given $\vec{b}$, the probability $p(\vec{b})$ to have one binary collision between nuclei A and B (Eq. (2.18)) is

$$p(\vec{b}) = \int \mathrm{d}\vec{s}_{\rm A}\mathrm{d}z_{\rm A}\rho_{\rm A}(\vec{s}_{\rm A}, z_{\rm A})\mathrm{d}\vec{s}_{\rm B}\mathrm{d}z_{\rm B}\rho_{\rm B}(\vec{s}_{\rm B}, z_{\rm B})t(\vec{s}_{\rm A} + \vec{s}_{\rm B} - \vec{b}) \cdot \sigma_{\rm NN}^{\rm inel}. \tag{2.19}$$

The nuclear density function $\rho(\vec{s}, z)$ can be described by the **Woods-Saxon** profile [174],

$$\rho(\vec{s}, z) = \rho_0 \frac{1 + \omega \cdot (s/R)^2}{1 + \exp[(s - R)/z]}, \tag{2.20}$$

where, $s = |\vec{s}|$, ρ_0 is a normalization factor, ω is the allowed center non-regularity for a given nuclei and R is the nucleus radius. For a Pb nucleus (we measure Pb–Pb collisions at the LHC), the Woods-Saxon parameters in Eq. (2.20) are [175]: $\rho_0 = 0.16$ fm^{-3}, $\omega = 0$ and $R = 6.624$ fm.

As treated in the Glauber model [176], $t(\vec{s})$ is usually a δ function (the collision geometry is shown in Fig. 2.9) and Eq. (2.19) can be written as

$$p(\vec{b}) = \sigma_{\rm NN}^{\rm inel} \cdot \int {\rm d}\vec{s} \cdot T_{\rm A}(\vec{s}) T_{\rm B}(\vec{s} - \vec{b}) \equiv \sigma_{\rm NN}^{\rm inel} \cdot T_{\rm AB}(\vec{b}). \tag{2.21}$$

In Eq. (2.21), $T_{\rm AB}$ is the so-called thickness function or nuclear overlap function and is given by:

$$T_{\rm AB} \equiv \int {\rm d}\vec{s} \cdot T_{\rm A}(\vec{s}) T_{\rm B}(\vec{s} - \vec{b}), \tag{2.22}$$

where $T_i(\vec{s})$ is the thickness function of a nucleus i ($i = {\rm A}, {\rm B}$),

$$T_i(\vec{s}) = \int {\rm d}z_i \cdot \rho(\vec{s}_i, z_i). \tag{2.23}$$

By combining Eq. (2.17), (2.18) and (2.21), one can get

$$< N_{\rm coll} > (\vec{b}) = m \cdot \sigma_{\rm NN}^{\rm inel} \cdot T_{\rm AB}(\vec{b}). \tag{2.24}$$

Finally with Eq. (2.24) and Eq. (2.15) one can obtain the yield of open heavy flavours in the final stage of the collision, if there is no nuclear effect.

Fig. 2.10 shows the charm production cross section per nucleon-nucleon collision at mid-rapidity as a function of the number of binary collisions $N_{\rm coll}$ (denoted as $N_{\rm bin}$ in this figure) measured at RHIC [177]. This result illustrates that, with nuclear effects, the integrated production cross section of charm quarks still follows the binary scaling,

$$\int {\rm d}p_{\rm t}{\rm d}y \frac{{\rm d}^2 N_{\rm AA}^{\rm HF}}{{\rm d}p_{\rm t}{\rm d}y} = m \cdot \sigma_{\rm NN}^{\rm inel} \cdot T_{\rm AB}(\vec{b}) \times \int {\rm d}p_{\rm t}{\rm d}y \frac{{\rm d}^2 N_{\rm NN}^{\rm HF}}{{\rm d}p_{\rm t}{\rm d}y}, \tag{2.25}$$

at RHIC energies. The nuclear effects modify the shape of heavy flavour distributions and do not affect the normalization. It also confirms that, at RHIC energies, the dominant mechanism of heavy flavour production in A–A collisions is hard scatterings in the initial stage of the collisions.

An other important information is to get the number of hard processes (*e.g.* the processes for heavy flavour production) per triggered event in nucleus-nucleus collisions,

$$N_{\rm AB}^{\rm hard} = \frac{\sigma_{\rm AB}^{\rm hard}}{\sigma_{\rm AB}^{\rm inel}} \equiv R \cdot \sigma_{\rm NN}^{\rm hard}, \tag{2.26}$$

where $\sigma_{\rm AB}^{\rm inel}$ and $\sigma_{\rm AB}^{\rm hard}$ are the inelastic and hard cross section in nucleus-nucleus collisions, $\sigma_{\rm NN}^{\rm hard}$ is the measured cross section in nucleon-nucleon collisions for hard processes. R is defined as the scaling factor between $\sigma_{\rm NN}^{\rm hard}$ and $N_{\rm AB}^{\rm hard}$ and it depends on the collision centrality. To obtain the scaling factor R which is very important

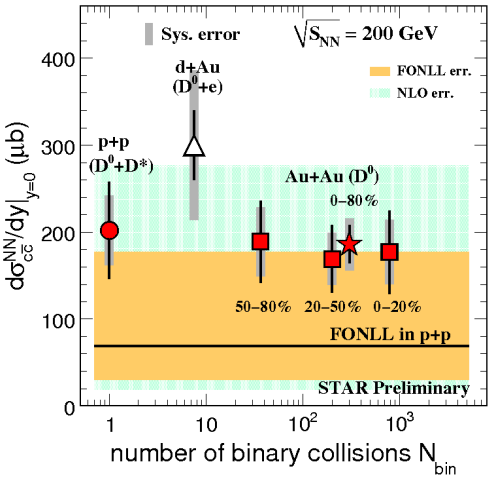

Figure 2.10: Charm production cross section per nucleon-nucleon collision at mid-rapidity as a function of $N_{\rm bin}$ (or $N_{\rm coll}$) measured at RHIC in Au–Au collisions at $\sqrt{s_{\rm NN}} = 200$ GeV [177].

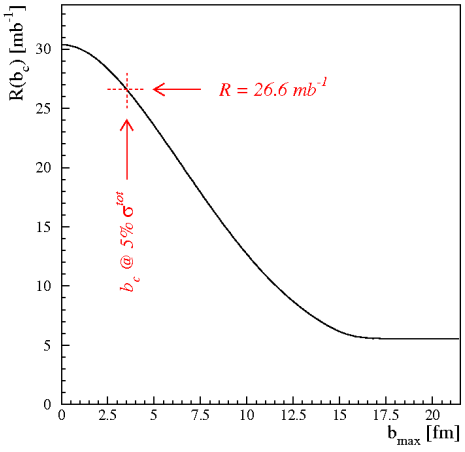

Figure 2.11: Yield of hard process in Pb–Pb collisions relative to the cross section in nucleon-nucleon collisions, as a function of the impact parameter cut $b < b_{\rm c}$ [41].

for the evaluation of the systematic uncertainty on the normalization of the heavy flavour production cross section in A–A collisions, we should first determine $\sigma_{\rm AB}^{\rm inel}$ and $\sigma_{\rm AB}^{\rm hard}$. The differential inelastic cross section in nucleus-nucleus collisions is given by the probability that at least one binary collision occurs at a given impact parameter $\vec{b}$,

$$\frac{{\rm d}\sigma_{\rm AB}^{\rm inel}}{{\rm d}\vec{b}} = \sum_{n=1}^{m} \mathcal{P}(n,\vec{b}) = 1 - [1 - \sigma_{\rm NN}^{\rm inel} \cdot T_{\rm AB}(\vec{b})]^m. \tag{2.27}$$

Therefore, from Eq. (2.27), the total inelastic cross section corresponding to the collision of nuclei A and B is

$$\sigma_{\rm AB}^{\rm inel}(\vec{b}_{\rm c}) = \int_0^{\vec{b}_{\rm c}} {\rm d}\vec{b} \cdot \{1 - [1 - \sigma_{\rm NN}^{\rm inel} \cdot T_{\rm AB}(\vec{b})]^m\}. \tag{2.28}$$

Using $\sigma_{\rm NN}^{\rm hard}$ instead of $\sigma_{\rm NN}^{\rm inel}$ in Eq. (2.28), one gets the total cross section of hard processes as,

$$\begin{aligned}
\sigma_{\rm AB}^{\rm hard}(\vec{b}_{\rm c}) &= \int_0^{\vec{b}_{\rm c}} {\rm d}\vec{b} \cdot \{1 - [1 - \sigma_{\rm NN}^{\rm hard} \cdot T_{\rm AB}(\vec{b})]^m\} \\
&= \int_0^{\vec{b}_{\rm c}} {\rm d}\vec{b} \cdot \{1 - [1 - m \cdot \sigma_{\rm NN}^{\rm hard} \cdot T_{\rm AB}(\vec{b}) + \mathcal{O}((\sigma_{\rm NN}^{\rm hard} \cdot T_{\rm AB}(\vec{b}))^2)]\} \\
&\simeq \int_0^{\vec{b}_{\rm c}} {\rm d}\vec{b} \cdot m \cdot \sigma_{\rm NN}^{\rm hard} \cdot T_{\rm AB}(\vec{b}),
\end{aligned} \tag{2.29}$$

where the approximation of small $\sigma_{\rm NN}^{\rm hard}$ has been considered as the last calculation step. By using Eq. (2.28) and (2.29) into the definition of the scaling factor R

(Eq. (2.26)), one can deduce that

$$R(\vec{b}_c) = \frac{\int_0^{\vec{b}_c} d\vec{b} \cdot m \cdot T_{AB}(\vec{b})}{\int_0^{\vec{b}_c} d\vec{b} \cdot \{1 - [1 - \sigma_{NN}^{inel} \cdot T_{AB}(\vec{b})]^m\}}, \tag{2.30}$$

is a function of $\vec{b}_c$. Fig. 2.11 shows $R(\vec{b}_c)$ in Pb–Pb collisions. As an example, one can find that for the 5% most central Pb–Pb collisions, N_{AB}^{hard} is obtained by multiplying the elementary cross section by 26.6 mb^{-1}.

2.2.2 Cold Nuclear Effects

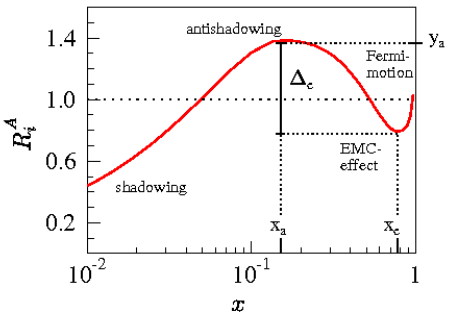

Figure 2.12: Illustration of a smoothly matched R_i^A function.

Bound nucleons (protons, p, and neutrons, n) in nucleus have different properties from the free ones due to the interactions and correlations inside the nucleus. In particular, in heavy ion collisions, final state observables are affected by the initial state nuclear effects (the so-called cold nuclear effects, as mentioned in Sec. 1.4.2.2) because they modify the initial collision conditions. Many mechanisms are introduced to describe these effects. First experimental evidence for cold nuclear effects has been discussed in 1982 [178]. It is believed that, different mechanisms will drive different cold nuclear effects in different Bjorken-x regions, and they are often grouped into the experimental ratios of PDFs of nucleons in nucleus (**Nuclear PDFs, nPDFs**) $f_i^A(x, Q^2)$ and PDFs in free nucleons $f_i^N(x, Q^2)$,

$$R_i^A(x, Q^2) = \frac{f_i^A(x, Q^2)}{f_i^N(x, Q^2)}, \tag{2.31}$$

where i is the parton specie index (valence quark, sea quark or gluon). Fig. 2.12 shows a typical shape of $R_i^A(x, Q^2)$. According to this shape, the whole Bjorken-x region is separated into different regions with following cold nuclear effects:

- shadowing, $x \lesssim 0.1$, $R_i^A(x, Q^2) < 1$,;
- anti-shadowing, $0.1 \lesssim x \lesssim 0.3$, $R_i^A(x, Q^2) > 1$;
- EMC effect [179], $0.3 \lesssim x \lesssim 0.7$, a depletion in $R_i^A(x, Q^2)$;
- Fermi motion [180], an excess towards $x \to 1$ and beyond.

There were two kinds of earlier studies for the nPDFs description based on a global DGLAP fits to the data: one is **EKS98** set [181, 182] and the other one is **HKM** set [183].

In EKS98, the parton distributions in the bound protons, inside the nucleus, are defined through the modifications of the corresponding distributions in the free protons via $R_i^{\rm A}$, as presented in Eq. (2.31). As for free nucleons, for isocalar nuclei the parton distributions of bound neutrons are obtained through isospin symmetry,

$$f_{\rm u(\bar{u})}^{\rm n/A} = f_{d(\bar{d})}^{\rm p/A} \qquad \text{and} \qquad f_{\rm d(\bar{d})}^{\rm n/A} = f_{u(\bar{u})}^{\rm p/A}, \tag{2.32}$$

and this is a good approximation for all kinds of nuclei. To simplify the determination of input nuclear effects for valence quarks, $R_{\rm V}^{\rm A}(x,Q^2)$, and for sea quarks, $R_{\rm S}^{\rm A}(x,Q^2)$, one assumes:

$$\begin{aligned} R_{\rm V}^{\rm A}(x,Q_0^2) \approx & R_{\rm u/V}^{\rm A}(x,Q_0^2) \approx R_{\rm d/V}^{\rm A}(x,Q_0^2) \\ R_{\rm S}^{\rm A}(x,Q_0^2) \approx & R_{\rm \bar{u}/S}^{\rm A}(x,Q_0^2) \approx R_{\rm \bar{d}/S}^{\rm A}(x,Q_0^2) \approx R_{\rm \bar{s}/S}^{\rm A}(x,Q_0^2). \end{aligned} \tag{2.33}$$

These ratios are calculated at $Q^2 = Q_0^2 = m_{\rm c}^2 \simeq 2.25$ GeV^2 as initial conditions of DGLAP evolution. Thus, only three independent initial ratios, $R_{\rm V}^{\rm A}(x,Q_0^2)$, $R_{\rm S}^{\rm A}(x,Q_0^2)$ and the nuclear modifications for gluons $R_{\rm G}^{\rm A}(x,Q_0^2)$ should be determined at $Q^2 = Q_0^2$. These three initial ratios are determined in different Bjorken-x regions up to higher scales $Q^2 > Q_0^2$ via the LO DGLAP evolution. As shown in [181], $R_i^{\rm A}(x,Q^2)$ from EKS98 parametrization can be used together with any LO set of free proton PDFs like GRVLO [184] and CTEQ4L [185]. But the best overall fit for the determination of the input initial ratio in EKS98 has so far been done iteratively in such a way that the scale evolved distributions are consistent with data.

Differently from the ESK98 set, in the HKM analysis, nPDFs are defined as the average distributions of each flavour i in a nucleus:

$$f_i^{\rm A}(x,Q^2) = (Z/A) f_i^{\rm p/A}(x,Q^2) + (1-Z/A) f_i^{\rm n/A}(x,Q^2), \tag{2.34}$$

and evolved with the initial condition,

$$f_i^{\rm A}(x,Q_0^2) = \omega_i(x,A,Z) f_i^{\rm N}(x,Q_0^2), \tag{2.35}$$

at $Q^2 = Q_0^2 = 1$ GeV^2 with the average PDFs in free nucleons,

$$f_i^{\rm N}(x,Q^2) = (Z/A) f_i^{\rm p}(x,Q^2) + (1-Z/A) f_i^{\rm n}(x,Q^2), \tag{2.36}$$

and the initial nuclear modification,

$$\omega_i(x,A,Z) = 1 + (1 - \frac{1}{A^{1/3}}) \frac{a_i(A,Z) + b_i x + c_i x^2}{(1-x)^{n_i}}, \tag{2.37}$$

where $a_i(A,Z)$, b_i, c_i and n_i are the parameters used for the global fit. An improvement of the HKM method is that, relative to the EKS98 set, the extraction of the initial nuclear modification $\omega_i(x,A,Z)$ at $Q^2 = Q_0^2$ is done by implementing a χ^2 minimization procedure. But the drawback of HKM is that, shadowing effects are underestimated because the initial conditions are obtained from a fit to the DIS (deep inelastic scattering) data.

The updated version of EKS98 is the so-called **EPS08** [54]. It uses d–Au data measured at RHIC for the initial condition determination and uses a minimum χ^2 fit procedure. The NLO DGLAP evolution is included in the **EPS09** [55] analysis (as well in the updated version of HKM set with DGLAP evolution up to NLO named **HKN07** [186] analysis). The comparisons of the average valence and sea quark, and gluon modification for Pb nucleus, $R_{\rm V}^{\rm Pb}$, $R_{\rm S}^{\rm Pb}$ and $R_{\rm G}^{\rm Pb}$, at different values of Q^2 for both LO and NLO nPDFs are shown in Fig. 2.13 and Fig. 2.14, respectively. The results are from [55]. According to these results, there are less shadowing effects in the HKM (or HKN07) sets than that in EKS98 (or EPS08/09) sets in the small Bjorken-x region, in particular for gluons. Also, one can observe that the EMC effect is not observed clearly with HKN07, with both the LO and NLO DGLAP evolutions.

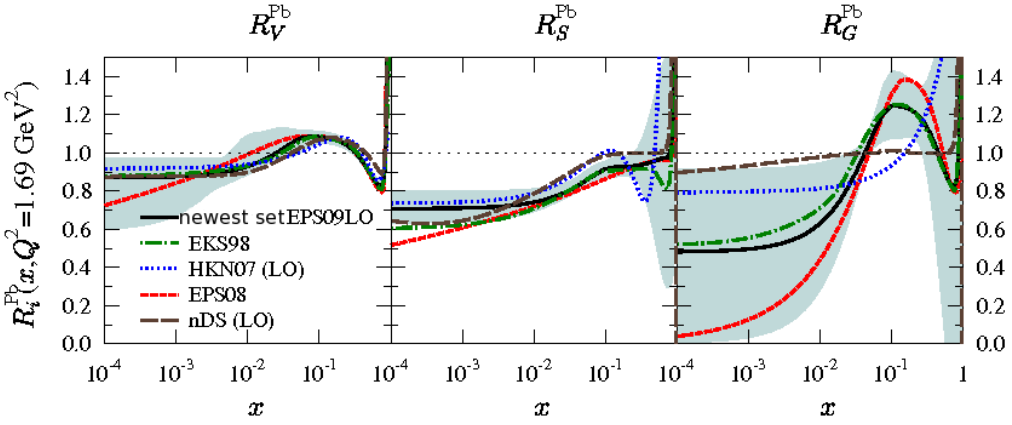

Figure 2.13: Comparison of the average valence quark, sea quark, and gluon modifications at $Q^2 = 1.69$ GeV^2 ($\sim m_{\rm c}^2$) for a Pb nucleus, from LO global DGLAP analyses: EKS98, nDS [187], HKN07, EPS08 and EPS09LO.

As shown in Fig. 2.15 (left panel), at different energies, the final state heavy flavour observables probe different regions of Bjorken-x. In particular, at the LHC, the data could constrain the deep shadowing region due to the very small value of Bjorken-x that can be accessed. The hard probes (like heavy flavours) at RHIC and LHC will provide very important constraints on the nPDFs where the DGLAP evolution is expected to be applicable. The expected gluon saturation limits for proton and Pb nucleus estimated in [189] are shown in Fig. 2.15, left panel. With the presented limits, the chances of measuring the effects of non-linearities in the evolution through open charm production in p–A (the same in A–A) collisions at RHIC would seem marginal; however at the LHC, the systematic measurements of the staturation effects in nuclear gluon distributions through open heavy flavours could be possible. Fig. 2.15 (right panel) shows $R_{\rm G}^{\rm A}$ as a function of Bjorken-x at $Q^2 = (2m_{\rm c}^2) \simeq 5$ GeV^2 (corresponding to the threshold of $\rm c\bar{c}$ production) obtained

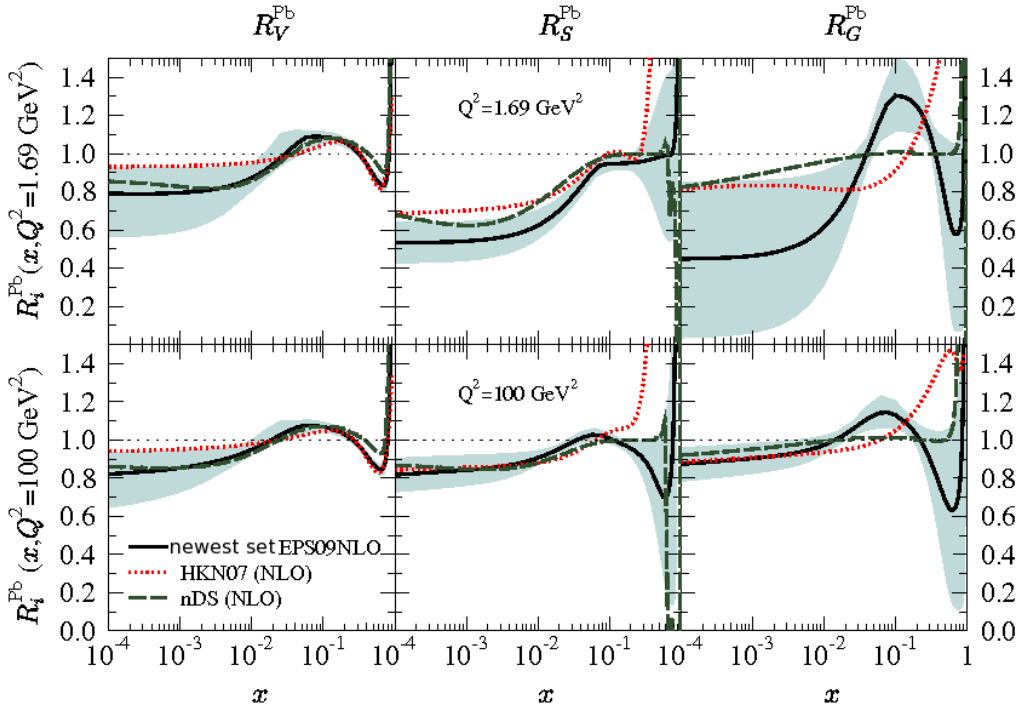

Figure 2.14: Same as Fig. 2.13, but for the comparison of NLO global DGLAP analyses: HKN07, nDS and EPS09 NLO at $Q^2 = 1.69$ GeV^2 (upper panel) and 100 GeV^2 (lower panel).

from different models. The bands represent the ranges of Bjorken-x for $c\bar{c}$ production with $|y| < 0.5$ at RHIC ($\sqrt{s} = 200$ GeV) and LHC ($\sqrt{s} = 5.5$ TeV).

The gluon saturation has been also studied in the CGC framework. In this approach, open charm is expected to obey a $N_{\rm part}$ ($\sqrt{N_{\rm part}}$) scaling in A–A (or p–A) collisions instead of the $N_{\rm coll}$ scaling at energies higher than the RHIC ones, or reached at forward rapidity at RHIC [190], where smaller Bjorken-x are probed by charm and the saturation scale is expected to exceed the mass of charm quark. In this case, the mechanism of heavy quark production should be similar to that of light partons: heavy partons at small Bjorken-x are not independent, and the factorization theorem cannot be applied. In addition, the CGC also suggests that, the open charm meson spectrum should be much harder than that predicted by collinear factorization calculation at high energy. This is due to the fact that the intrinsic transverse momentum $k_{\rm t}$ becomes of the order of $Q_{\rm s}$ ($Q_{\rm s} \gg \Lambda_{\rm QCD}$) which rather larger than $\Lambda_{\rm QCD}$.

Additionally, cold nuclear effects not only modify the PDFs of free nucleons but also lead to a broadening of the intrinsic transverse momentum $k_{\rm t}$ for partons, the $k_{\rm t}$ **Broadening Effect** [191], due to the Brownian motion of the partons inside the nucleus. For heavy quarks, as argued in [192], the $k_{\rm t}$ broadening effect could play

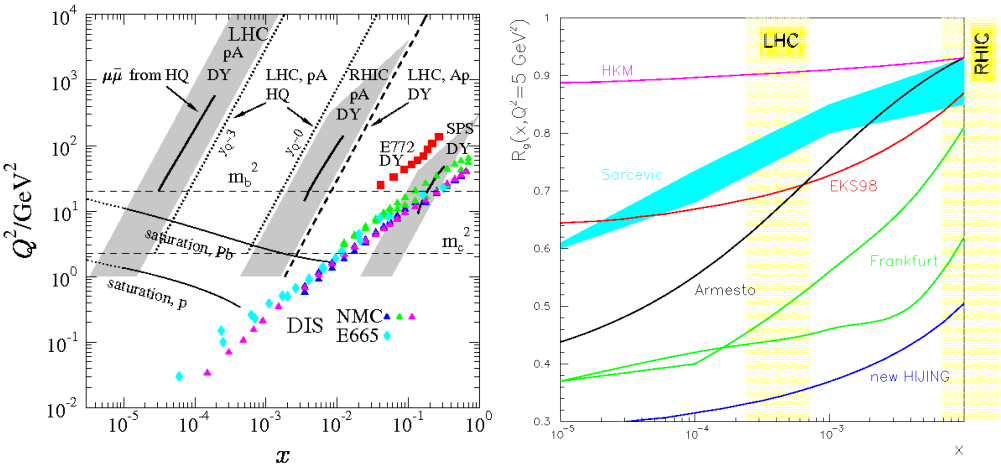

Figure 2.15: Left: Average values of x and Q^2 of the DIS data from NMC (triangles) and E665 (diamonds), and of x_2 and M^2 of Drell-Yan (DY) dilepton data (squares). The heavy quark mass scales are shown by the horizontal dashed lines. Right: Ratios of gluon distribution functions from different models at $Q^2 = 5$ GeV^2. These two figures are extracted from [188].

an important role in the angular dependence of gluon emission.

2.2.3 Hot Nuclear Effects

As discussed in Sec. 1.4.3.2, heavy flavours created in the early stage of nucleus-nucleus collisions via hard scatterings will pass through the QCD medium formed in these collisions and loss their energy due to the interactions between partons inside the medium. It was predicted that, the dominant in-medium energy loss mechanism for heavy flavours is gluon radiation or "**gluonbremstrahlung**". Recently, the results of heavy flavour measurements at RHIC along with model predictions have opened new possibilities to investigate other interaction mechanisms such as collisional energy loss, in-medium fragmentation and collective motion due to thermalization of heavy quarks.

In this section, we will discuss different in-medium interaction mechanisms of heavy flavours based on the observables measured at RHIC. We will finish with the new heavy flavour observables that can be investigated at LHC energies.

2.2.3.1 Radiative Energy Loss

Dead Cone Effect Due to the mass effect, the radiation energy loss of heavy quarks is different from that of light quarks in the nuclear medium. One of the differences is the suppression due to gluon bremsstrahlung from massive quarks at small angle [193],

$$\theta_0 = m_Q/E, \tag{2.38}$$

where $m_{\rm Q}$ and E are the mass and initial energy of heavy quarks. This is the so-called **Dead Cone Effect**. Dokshitzer and Kharzeev proposed that due to the dead cone effect reducing the medium induced gluon radiation, the suppression of leading open heavy flavour hadron production rates is reduced and gluon radiating spectrum by massive quarks $\mathrm{d}P_{\rm HQ}$ can be obtained by using the radiative spectrum of massless quarks $\mathrm{d}P_{\rm LQ}$ times a suppression factor $F(k_{\rm t}, m_{\rm Q}, E)$, related to the transverse momentum of gluon ($k_{\rm t}$), mass and energy of heavy quarks. This factor is named dead cone factor [194],

$$\mathrm{d}P_{\rm HQ} = \mathrm{d}P_{\rm LQ} \cdot F(k_{\rm t}, m_{\rm Q}, E) = \mathrm{d}P_{\rm LQ} \cdot (1 + \frac{\theta_0^2}{\theta^2})^{-2} = \mathrm{d}P_{\rm LQ} \cdot (\frac{k_{\rm t}^2}{k_{\rm t}^2 + x^2 m_{\rm Q}^2}). \quad (2.39)$$

where ω is the energy of the radiated gluon, $\theta = k_{\rm t}/\omega$ is the radiative angle of the gluon relative to the motion direction of the heavy quark and $x = \omega/E$ is the energy fraction taken by the radiated gluon.

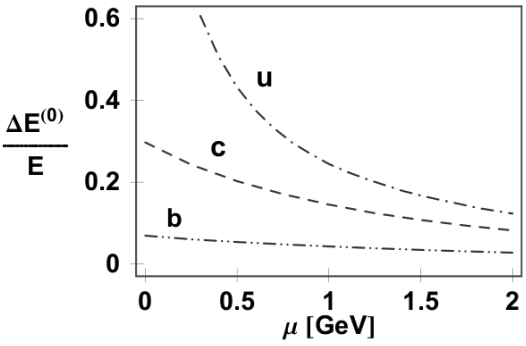

Figure 2.16: Medium modified fractional energy loss versus Debye mass μ in zeroth order opacity with **Ter-Mikayelian Effect** for up, charm and bottom quarks [195].

The simple factorization formalism, Eq. (2.39), was confirmed in [196] by expanding the gluon radiative spectrum of heavy quarks using the BDMPS model [79] via both single hard scattering and multiple soft scattering approximations under the medium absence limit. A complete understanding of the medium induced gluon radiative behaviour of heavy quarks requires detailed calculations of in-medium effects. Fig. 2.16 [195] shows the comparison of the medium modified fractional energy loss as a function of Debye mass μ in zeroth order opacity by considering the in-medium **Ter-Mikayelian Effect** [197] for heavy flavours between up, charm and bottom quarks, by choosing the mass of charm and beauty as $m_{\rm c} = 1.5$ GeV/c^2 and $m_{\rm b} = 4.5$ GeV/c^2, respectively. The medium effects are introduced via the Debye mass μ, the vacuum corresponds to $\mu = 0$ and the increase of μ value denotes that medium effects become more and more important. One can observe in this figure that, the radiative energy loss of light quarks and charm quarks is more sensitive to the medium effects than that of beauty quarks.

An interesting question is: what is the mass dependence of heavy quark radiative energy loss in the QCD medium? Also, is Eq. (2.39) still valid when considering medium effects? We studied these issues some years ago [198] with the radiative gluon spectrum of massless quarks from GLV opacity expansion calculations [76] with the dead cone factor $F(k_{\rm t}, m_{\rm Q}, E)$ as given by Eq. (2.39) and $\mathrm{d}P_{\rm HQ}^{\rm DG} = \mathrm{d}P_{\rm LQ}^{\rm GLV} \cdot$

$F(k_t, m_Q, E)$. Finally, we compare the numerical results of dP_{HQ}^{DC} with the radiative gluon spectrum of charm quarks obtained also under the GLV opacity expansion framework [199]. Our results show that, the factorization formalism (Eq. (2.39)) is still valid for charm quarks to describe the in-medium radiative energy loss at both RHIC and LHC energies. Furthermore, we extended the comparison to beauty quarks [200] and found that the deviations between the radiative gluon spectrum of massless quarks from factorization formalism and that from pQCD calculations increase with the quark mass. The differences between these two approaches are about 40% in the region of beauty quark mass ($4.2\ \mathrm{GeV}/c^2 < m_b < 4.8\ \mathrm{GeV}/c^2$). This clearly illustrates that the study of quark mass dependence of heavy quark in-medium energy loss is very important and interesting from the experimental side (more detailed discussion about this issue will be presented in Sec. 2.3.1).

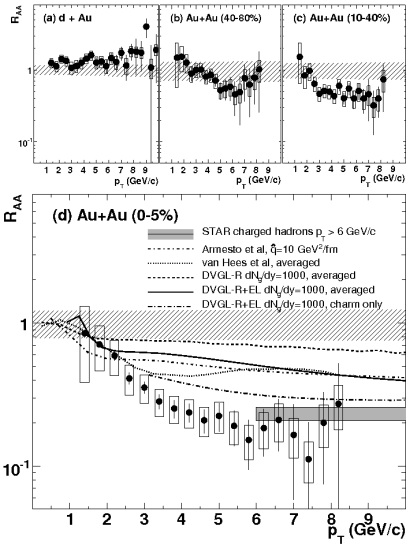

Figure 2.17: Nuclear modification factor R_{AA} of non-photonic electron measured in d–Au and Au–Au collisions at $\sqrt{s_{NN}} = 200$ GeV with the STAR detector. Extracted from Ref. [201].

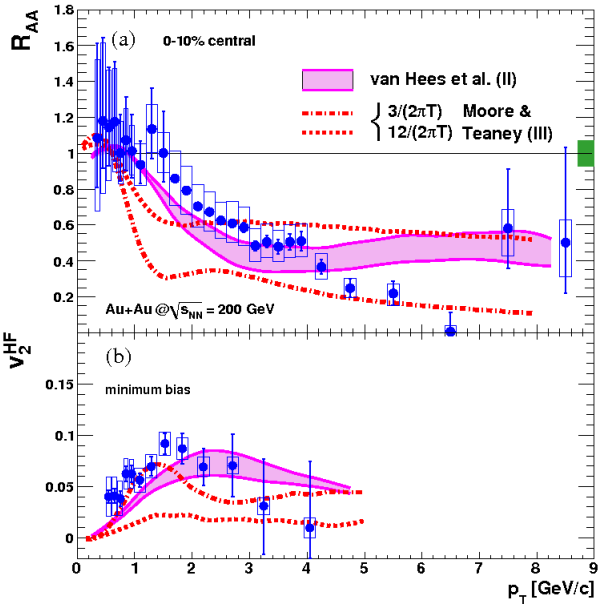

Figure 2.18: Nuclear modification factor and elliptic flow of non-photonic electrons measured in Au–Au collisions at $\sqrt{s_{NN}} = 200$ GeV with the PHENIX detector. The data are compared to predictions from different Langevin based models (see text). Extracted from [202].

Comparisons with data There are two independent sets of calculations for heavy quarks in-medium radiative energy loss, one is based on BDMPS framework [79] and the other one relies on the DGLV opacity expansion framework [195], as just mentioned. Both approaches predicted the dead cone effect of heavy flavour radiative energy loss and shown consistent results. For the comparison of these predictions with data, one should also consider cold nuclear effects in A–A collisions on the experimental final state observables. Different inputs of initial state conditions (dis-

cussed in Sec. 1.4.2.2 and Sec. 2.2.2) will introduce uncertainties in the theoretical predictions.

Fig. 2.17 (a) shows the nuclear modification factor $R_{\rm AA}$ of non-photonic electrons measured in d–Au collisions at $\sqrt{s_{\rm NN}}$ = 200 GeV with the STAR detector. Since the initial state energy density is not sufficient to create the deconfinement medium in the final state of d–Au collisions, the measured $R_{\rm AA}$ mainly reflects cold nuclear effects for the Au nucleus. A $R_{\rm AA}$ value of unit, in $p_{\rm t} > 2$ GeV/c, means that, cold nuclear effects for high $p_{\rm t}$ non-photonic electron spectrum are very small. Therefore, the deviations between the high $p_{\rm t}$ non-photonic electron spectrum in Au–Au collisions and that in pp collisions, as shown in Fig. 2.17 (b) and Fig. 2.17 (c), are mainly due to hot nuclear effects from the QCD medium.

The comparisons of the non-photonic electron $R_{\rm AA}$ from STAR data and that from different theoretical predictions are presented in Fig. 2.17 (d). In this plot, the lines labeled as "Armesto et al" and "DVGL-R" refer to the predictions of the non-photonic electron $R_{\rm AA}$ considering that the heavy flavour in-medium radiative energy loss at RHIC energies is based on BDMPS calculations and DGLV opacity expansion calculations, respectively. Both charm and beauty components of non-photonic electrons are considered in these two predictions. One observes that these predictions overestimate the $R_{\rm AA}$ of non-photonic electrons. A possible explanation is that, in addition to the radiative energy loss mechanism, other mechanisms could lead to in-medium energy loss of heavy flavours.

2.2.3.2 Collisional Energy Loss

Since the radiative energy loss mechanism cannot explain the high $p_{\rm t}$ non-photonic electron suppression in Au–Au collisions at RHIC, as shown in Fig. 2.17 (d), the in-medium collisional energy loss mechanism of heavy flavours has been considered. The first study was presented in [203]: it was found that, with a set of medium parameters relevant to RHIC energies, the transport coefficients $\hat{q}$ [3] for radiative and collisional energy of the heavy flavours are comparable. Therefore, the collisional energy loss of heavy flavours cannot be neglected in the study for the in-medium quenching of heavy flavours. In fact, due the large masses of heavy flavours, the measured $p_{\rm t}$ region at RHIC energies does not cover high $p_{\rm t}$ values. In this case, one cannot argue that the radiative energy loss mechanism dominates over the elastic collisional one for the heavy flavours. This is similar to the energy loss of electrons in QED: the ionization energy loss is the dominant effect with low electron energy, while photon bremsstrahlung mainly contributes in the higher energy region; at intermediate energy, both phenomena are comparable.

DGLV Approach Calculations of heavy flavour in-medium energy loss by considering both radiative and collisional contributions under the DGLV framework are developed in [82]. The results from these predictions are labeled as "DVGL-R+EL" in Fig. 2.17 (d). The comparison with data shows that the heavy flavour in-medium

[3] The definition of $\hat{q}$ is the average squared transverse momentum transferred to the parton.

energy loss is still underestimated, even with the additional collisional mechanism. What is interesting to notice is that, the model predictions are in better agreement with data if only the contribution from charm component in the total non-photonic electron spectrum is considered, as shown by the line labeled as "DVGL-R+EL, charm only" in Fig. 2.17 (d). This behavior suggested that the relative contribution of charm and beauty components used in the model calculations was incorrect. As shown in Fig. 2.16, charm quarks are expected to loss more energy than that of beauty quarks in the QCD medium. The predictions of the R_{AA} for total non-photonic electron are sensitive to the input fractions of the input charm and bottom components. However, recent measurements by the PHENIX collaboration [204] suggest that the fraction of charm and beauty components is comparable to what was used in the BDMPS and DGLV calculations (see also Fig. 2.8). Finally, the disagreements between data and different predictions suggest that other mechanisms of heavy flavours in-medium energy should be considered.

Thermal Scattering A Langevin based model which aims at describing the elastic scatterings between heavy flavours and QCD medium has been developed [205]. The interactions in the Langevin model are exclusively elastic collisions and it is a good approximation for quarks which are not ultra-relativistic in the center of mass frame of the collisions. In this model, heavy flavours are placed in a thermal medium and it is asumed that in-medium interactions of heavy flavours can be described by uncorrelated momentum kicks. The diffusion coefficient $D \propto 1/T$ is introduced to describe the elastic $2 \rightarrow 2$ scattering processes $\mathrm{qH_Q} \rightarrow \mathrm{qH_Q}$ and $\mathrm{gH_Q} \rightarrow \mathrm{gH_Q}$. The thermalization of heavy flavours in the QCD medium is predicted in this approach, hence the collective motion of heavy flavours (like the heavy flavour elliptic flow as we shall discuss in Sec. 2.2.3.4) can also be derived in this model. As for the collisional dissociation mechanism, this model can also explain qualitatively the large suppression of non-photonic electrons at RHIC, as shown in Fig. 2.18 (a). But the drawback of this model is that, it fails to simultaneously describe both the measured R_{AA} and v_2 with a single value of the diffusion coefficient (Fig. 2.18 (b)).

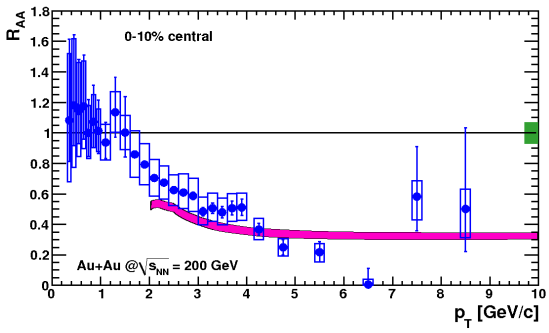

Figure 2.19: R_{AA} of non-photonic electron measured in Au–Au collisions at $\sqrt{s_{\mathrm{NN}}} = 200$ GeV with the PHENIX experiment. The data are compared with the predictions of the collisional dissociation model. Extracted from [202].

An other Langevin based model [206], also predicts strong suppression for non-photonic electron measured in Au–Au collisions at RHIC, by evaluating heavy flavour rescattering in the expanding fireball via resonance excitation of D and B-

like states in the medium above the critial temperature. The introduction of the mediated resonances in the QGP leads to a substantial reduction of the equilibration time scales, making this model as a promising approach for an explanation of the large energy loss and elliptic flow of heavy flavours, as shown in Fig. 2.18.

Collisional Dissociation As suggested in [207], the collisional dissociation of heavy quarkonia in the QCD medium might be a possible explanation for J/Ψ suppresion in heavy ion collisions. Under this assumption, the pQCD dynamics of open charm and beauty production is investigated by extending the GLV approach to $q\bar{q}$ states, and to derive the medium induced dissociation probability for D and B mesons traveling through the QCD medium [208]. This mechanism predicts that heavy flavours fragment inside the nuclear matter and open heavy flavours are further suppressed by collisional dissociation inside the QGP.

This QGP induced dissociation mechanism shows a large B hadron suppression which can be comparable to or larger than that of D hadrons in $p_t \lesssim 10$ GeV/c. This is due to the significantly smaller formation time for open beauty with respect to that for open charm: the fragmentation and/or dissociation process occur at a much faster rate for B-hadrons and explain the strong suppression. This is not predicted by other models. In this case, the collisional dissociation model gives larger suppression for the total non-photonic electron production and agrees with data better, as shown in Fig. 2.19.

2.2.3.3 Other Energy Loss Mechanisms

Many other mechanisms were developed to describe the heavy flavour in-medium energy loss. In the following, we mention the ones which agree with the data measurements at RHIC energies.

- In [209], one assumes a modification of open charm hadron chemical composition in the most central heavy ion collisions, in particular, an enhancement of the Λ_c production. This leads to a R_{AA} of non-photonic electrons smaller than one, due to a smaller semi-leptonic decay branching ratio of charm baryons compared to charm mesons, and also a softer spectrum of the electrons from charm baryons;

- In [210], the pQCD running coupling constant in collisional energy loss calculations is considered and the Debye mass is changed in a hard thermal loop calculation. However, the radiative energy loss is not included in this model;

- In [211], the authors predicted an universal bound for the energy of a parton escaping strongly coupled matter in $\mathcal{N} = 4$ SUSY Yang-Mills theory under the AdS/CFT framework, with some assumptions about the evolution of gauge field in heavy ion collisions.

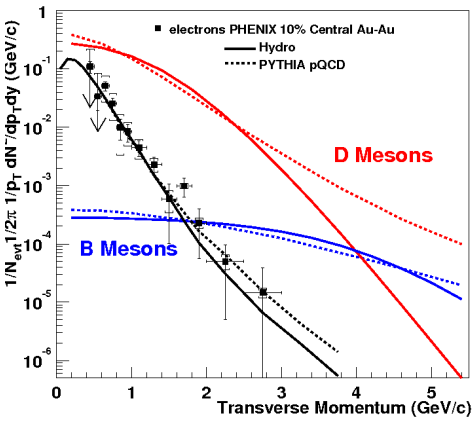

Figure 2.20: Prompt electron distribution measured in the 10% most central Au–Au collisions at $\sqrt{s_{\rm NN}}$ = 130 AGeV with the PHENIX detector [212].

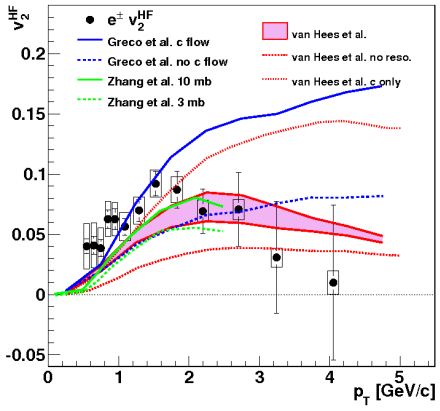

Figure 2.21: Theory comparison of non-photonic electron, v_2, versus $p_{\rm t}$ in Au–Au collisions at $\sqrt{s_{\rm NN}}$ = 200 GeV [202] measured with the PHENIX detector [202], see the text for more details.

2.2.3.4 Collective Flow

The motivation for the measurement of the heavy flavour collective flow was triggered by the studies shown in Fig. 2.20 [212]. The invariant multiplicity distribution as a function of $p_{\rm t}$ for non-photonic electrons, measured in central Au–Au collisions at $\sqrt{s_{\rm NN}}$ = 130 AGeV in the PHENIX Collaboration, is compared with the combined beauty and charm components from two opposite scenarii: the pQCD based PYTHIA and thermal hydrodynamical models. Both models show a good agreement with the data. The agreement between data and PYTHIA indicates that the factorization theorem (Eq. (2.1)) can be applied for heavy flavour production, and hence that heavy flavours have large mean free path in the QCD medium. On the other hand, data are well reproduced by the thermal hydrodynamical model, suggesting that a local equilibrium of heavy flavours with zero mean free path in the medium is achieved. As mentioned in this publication, the measurement of the non-photonic electron in the high $p_{\rm t}$ region with much higher statistics could help to differentiate these two scenarii. The measurement of non-zero flow for heavy flavours would be an important test of these models.

From the theoretical side, the parton covariant transport theory [213] was used to estimate the collective flow of heavy flavours. This model treats the evolution of the parton phase density with the $2 \rightarrow 2$ elastic and inelastic scatterings and the finite mean free path (λ) of heavy flavours is interpolated between cases of free streaming ($\lambda \rightarrow \infty$) and ideal hydrodynamics ($\lambda \rightarrow 0$). In this case, it can predict the collective flow for heavy flavours in both low $p_{\rm t}$ and high $p_{\rm t}$ regions, since the assumptions of vanishing mean free path and local thermal equilibrium are no longer satisfied in the high $p_{\rm t}$ region.

To compare the theoretical predictions with experimental observables, the hadronization process should be considered. Two main mechanisms are used to take into account the hadronization of heavy flavours: the fragmentation process and the coalescence (recombination) process. As discussed in Sec. 2.1.4, in the fragmentation picture, the hadrons obtain momenta from their mother partons via $p_{\rm t}^{\rm H} = z \cdot p_{\rm t}^{\rm Q}$. Since the fragmentation functions $D(z)$ of heavy flavours are very hard, $z \to 1$ (see Fig. 2.5). In this picture the collective flow at hadron level is essentially the same as at quark level [214]. The independent fragmentation picture is expected to prevail in the high $p_{\rm t}$ region [215]. The coalescence scenario, which can be implemented in the low $p_{\rm t}$ region, treat the constituent momentum fraction z as [216]:

$$z_i = \frac{m_i}{m_\alpha + m_\beta} \text{ (for mesons)}, \qquad z_i = \frac{m_i}{m_\alpha + m_\beta + m_\gamma} \text{ (for baryons)}, \tag{2.40}$$

where m_i is the effective mass of constituent quark and the indices α, β and γ refer to the quarks inside the hadrons. According to Eq. (2.40), the collective flow v_n for open heavy flavours can be calculated as,

$$v_n^{\rm M}(p_{\rm t}) \simeq \sum_{i=\alpha,\beta} v_{n,i}(z_i p_{\rm t}) \quad \text{and} \quad v_n^{\rm B}(p_{\rm t}) \simeq \sum_{i=\alpha,\beta,\gamma} v_{n,i}(z_i p_{\rm t}) \tag{2.41}$$

for mesons and baryons, respectively.

The elliptic flow v_2 of non-photonic electrons measured in Au–Au collisions at $\sqrt{s_{\rm NN}} = 200$ GeV with PHENIX is compared to model predictions in Fig. 2.21. The lines labeled as "Greco *et al.*" come from the predictions of the model presented in [217]. This is an improved version of the coalescence model [216]. In these calculations, open heavy flavour hadrons are formed from heavy quark coalescence with thermal light flavours which also carry the collective expansion characteristics. This is a more realistic scenario than the fragmentation based calculations presented in [214]. The lines with the additional labels "c flow" and "no c flow" corresponding to sets of non-vanishing and vanishing values of charm flow in Eq. (2.41), respectively. Within this scenario, the predictions with charm flow are in better agreement with the data than that without charm flow. This indicates the thermalization of charm quarks in the QCD medium. The lines labeled as "Zhang *et al.*" are the predictions from the hybrid model [218], using the HIJING Monte-Carlo generator [219] as an initial condition followed by a parton cascade and finally treating the hadronization with parton coalescence model. The results are presented with the parton scattering cross section $\sigma_{\rm p} = 3$ mb and 10 mb, respectively.

Additionally, the predictions in [206], already discussed in Fig. 2.18 (b), are also presented in Fig. 2.21. As mentioned in Sec. 2.2.3.2, this model describes simultaneously the large energy loss and elliptic flow of non-photonic electrons with the diffusion coefficient $D(2\pi T) \sim 4 - 6$ [220]. This coefficient, as obtained from pQCD calculations with three light flavours, is related to η (shear viscosity), ε (energy density) and p (pressure of the medium) through

$$D \sim 6 \cdot \frac{\eta}{\varepsilon + p}, \qquad (2.42)$$

with

$$\varepsilon + p = Ts + \mu_{\mathrm{B}} n_{\mathrm{B}} \approx Ts, \qquad (2.43)$$

This is valid in the baryon free region (with the vanishing value of baryon chemical potential μ_{B} and baryon density n_{B}). The key parameter is the shear viscosity over entropy density (mentioned in Sec. 1.5.2.3) and is estimated as $\eta/s \sim (1.33-2)/4\pi$ at RHIC energies according to the measured R_{AA} and v_2 of non-photonic electrons. This value is close to the KKS limit $\eta/s \geq 1/4\pi$ [86] and is consistent with the estimates from other observables at RHIC (like the flow of charged hadrons, fluctuations *ect.*, and see [202] for more details). This is an additional evidence for the strongly coupled QGP at RHIC.

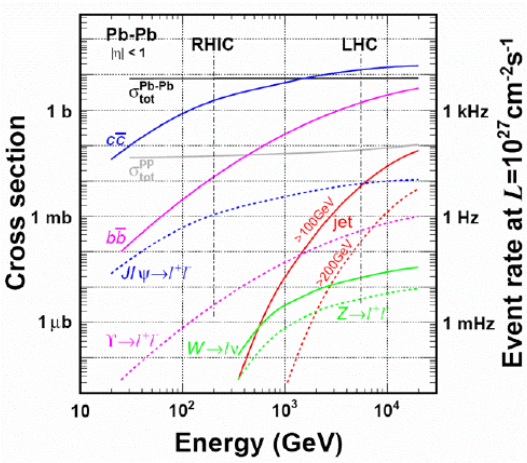

Figure 2.22: Production cross sections as a function of the center-of-mass energy for Pb–Pb collisions [221].

2.3 Heavy Flavours Physics at the LHC

As already mentioned, heavy flavours are very promising probes for the study of the properties of the QCD medium formed in the high energy heavy ion collisions. Moreover the measurement in pp and p–A collisions will allow to test pQCD calculations and nuclear modified PDFs, respectively. At LHC energies, heavy flavours are produced with high rate. This allows to investigate new powerful observables for the tomography of the QCD medium.

2.3.1 Novel Aspects of Heavy Flavours at the LHC

There are many novel aspects for heavy flavour physics at the LHC. Due to the large production rates of heavy flavours at LHC energies, as shown in Fig. 2.22, the final state heavy flavour observables are measured with high statistics. Also, the measurements can be extended to the high p_{t} region. This gives the unique chance to separate the open charm and open beauty components and restrict the large uncertainty on the pQCD predictions of the heavy quark productions (as an example shown in Fig. 2.23 the results from HvQMNR predictions [151, 152]) [4]. What is more, the new observables are accessible such as the double ratio between the nuclear modification factor of open heavy flavours $R_{\mathrm{AA}}^{\mathrm{D(B)}}$ and that of light hadrons $R_{\mathrm{AA}}^{\mathrm{h}}$, the

[4] A detail illustration of the uncertainties on pQCD predictions of the heavy quark productions will be given in Sec. 7.5.1.

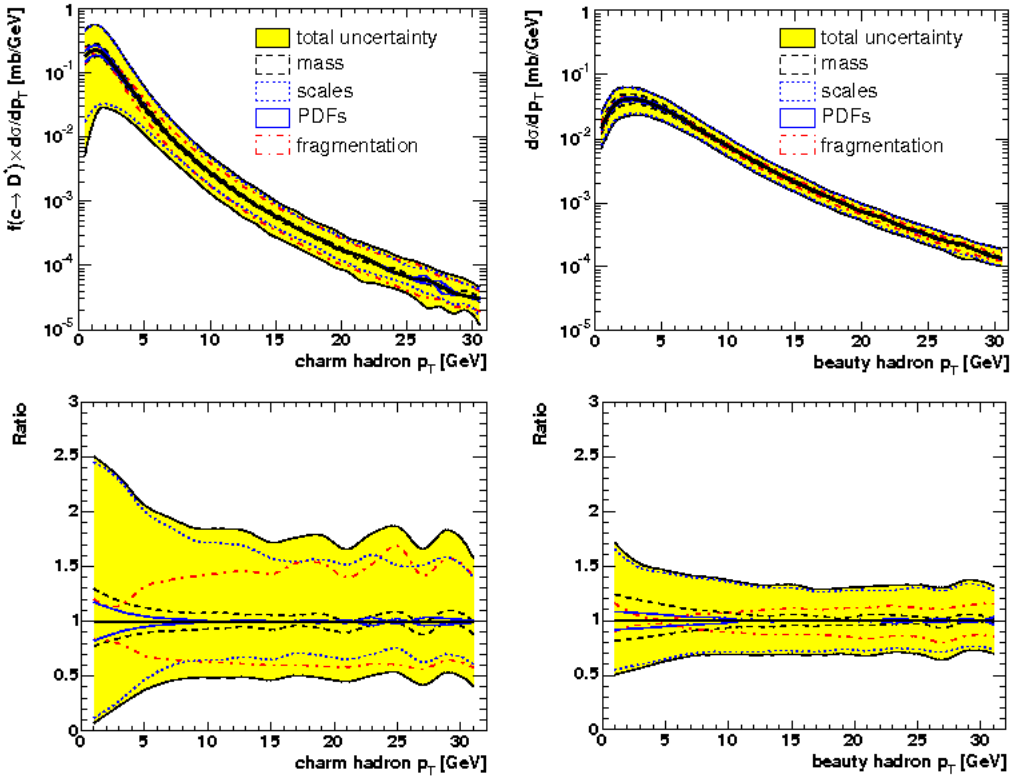

Figure 2.23: The $p_{\rm t}$-differential production cross section ($\mathrm{d}\sigma/\mathrm{d}p_{\rm t}$) for charm hadron (top left) and bueaty hadron (top left) in pp collisions at $\sqrt{s}$ = 14 TeV obtained from MNR predictions [151]. The correspoding botton plots show the components of the uncertainty from quark mass ($m_{\rm Q}$), parton density parametrisation (PDF), fragmentation parameter and the perturbative uncertainty from scale variations on the results [152].

so-called **Heavy-to-Light Ratios**,

$$R_{\rm D(B)/h}(p_{\rm t}) = \frac{R_{\rm AA}^{\rm D(B)}(p_{\rm t})}{R_{\rm AA}^{\rm h}(p_{\rm t})}. \tag{2.44}$$

The latter allows to test the color charge and mass dependence of parton in-medium energy loss, as proposed in Ref. [222]. In the region $p_{\rm t} \gtrsim 10$ GeV/c, since the mass of charm quarks $m_{\rm c} \simeq 1.2$ GeV/c^2 is negligible with respect to their momentum, charm quarks behave as light quarks; but the beauty quarks with $m_{\rm b} \simeq 4.8$ GeV/c^2, still keep their massive behavior. However, since light hadron yields are dominated by gluon parents, the heavy-to-light ratio of D mesons is a sensitive probe of the color charge dependence of parton energy loss. In contrast, due to the larger b quark mass, the medium modification of B mesons in the same kinematical regime provides a sensitive test of the mass dependence of parton energy loss.

As discussed in [203] (see Sec. 2.2.3.2), the gluon radiation dominates the heavy

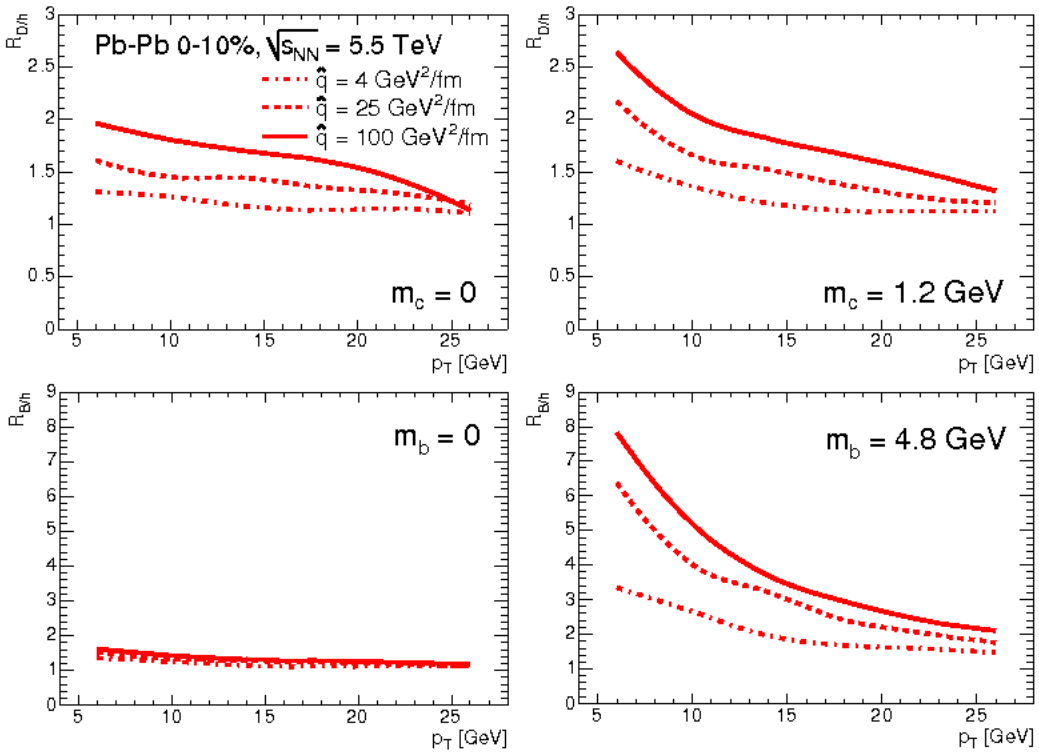

Figure 2.24: Heavy-to-light ratios for D mesons (upper plots) and B mesons (lower plots) with a realistic heavy quark mass (plots on the right) and for a case study in which the quark mass dependence of parton energy loss is neglected (plots on the left). Extracted from Ref. [222].

quark in-medium energy loss. According to BDMPS calculations with infinite path length limit, $L \to \infty$, the mean parton in-medium radiative energy loss can be expressed as [223],

$$< \Delta E > \propto \alpha_s C_R < \hat{q} > L^2, \tag{2.45}$$

where C_R is the color Casimir factor, which is $C_F = 4/3$ for quarks and $C_A = 3$ for gluons (see Eq. (1.5)). Thus, the mean energy loss of gluons is larger than that of quarks by a factor of $C_A/C_F = 9/4$. Fig. 2.24 shows the predictions of the heavy-to-light ratio for D and B mesons in the 10% most central Pb–Pb collisions at $\sqrt{s_{NN}} = 5.5$ TeV at the LHC by considering the radiative energy loss under the BDMPS framework. One clearly sees that the heavy-to-light ratio of open charm hadrons does not depend on the mass of charm quark in $p_t \gtrsim 10$ GeV/c. The ratio reflects the color charge dependence of the parton energy loss in the high p_t region. Its measurement should allow to test the ratio of the color Casimir factor for quarks and for gluons. On the other hand, the strong mass dependence of the heavy-to-light ratio for B-hadrons, shown in lower plots of Fig. 2.24, signs the additional mass effect on the parton in-medium energy loss. In this case, the double retio between the R_{AA} of D-hadrons to that of B-hadrons, $R^c_{AA}(p_t)/R^b_{AA}$ versus p_t, allows to isolate the

information of the mass dependence of the quark in-medium energy loss, which is a quite important and interesting issue, as mentioned in Sec. 2.2.3.1.

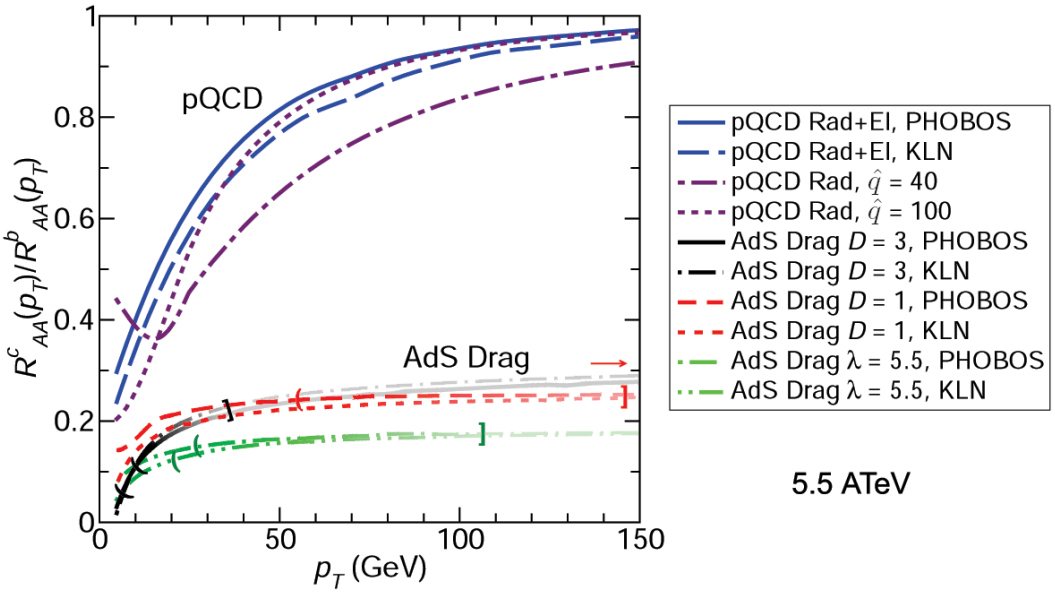

Figure 2.25: Predictions of $R^{c}_{AA}(p_t)/R^{b}_{AA}$ versus p_t at LHC energies from fully weakly coupled pQCD calculations and strongly coupled AdS/CFT energy loss models [115].

Furthermore, as mentioned in Sec. 1.5.3.2, one of the challenges at the LHC is to determine if the QGP created at these energies is a strongly coupled medium or a weakly coupled one, in other words, if the QGP at LHC is an ideal gas or a perfect liquid. As proposed in [115], the measurement of the double ratio $R^{c}_{AA}(p_t)/R^{b}_{AA}(p_t)$ in the high p_t region will provide valuable evidence of dominant energy loss mechanism in the QCD medium. Fig. 2.25 shows the predictions of $R^{c}_{AA}(p_t)/R^{b}_{AA}(p_t)$ from pQCD based calculations and from AdS/CFT based calculations. These two models give a different p_t behaviour of this double ratio, in particular in the high p_t range. The pQCD calculations predict a rapid rise to unit when p_t increases because the mass of both charm and beauty is negligible with sufficiently large energy and the pQCD predictions become insensitive to the mass of the parent parton. On the other hand, AdS/CFT drag results suggest a nearly p_t independent ratio significantly below the unit at approximately the ratio of the quark masses, m_c/m_b. The measurement of the D-to-B double ratio should allow either to validate pQCD calculations (weakly coupled QGP) or AdS/CFT predictions (strongly coupled QGP).

An other aspect of heavy flavour physics, which is worth to mention, is that, as mentioned in Sec. 2.2.2, according to the CGC predictions [190], due to the gluon saturation in the initial state of the collisions, in the forward rapidity region at the RHIC or at the LHC, the N_{coll} scaling of the heavy flavour production in A–A collisions, Fig. 2.10, is no longer valid (left plot of Fig. 2.26). The open charm is expected to follow a N_{part} ($\sqrt{N_{part}}$) scaling in A–A(or p–A) collisions, as shown

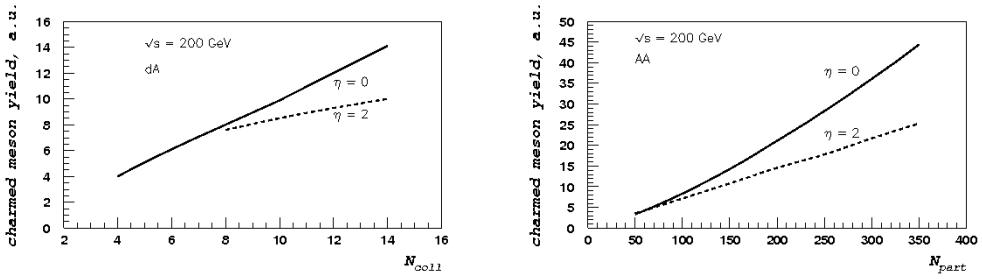

Figure 2.26: $N_{\rm coll}$ ($N_{\rm part}$) dependence of the charmed meson yield at mid-rapidity, $\eta = 0$, and at forward rapidity, $\eta = 2$, in d–Au (Au–Au) collisions [190].

in right plot of Fig. 2.26. Checking the violation of the $N_{\rm coll}$ scaling for integrated heavy flavour production cross section at LHC energies, in particular at forward region, should allow to get information on the gluon saturation in the initial state of the collision and to understand the magnitude of the collective flow, which is very sensitive to the initial conditions of the collisions.

2.3.2 Heavy Flavour Measurements with ALICE at the LHC

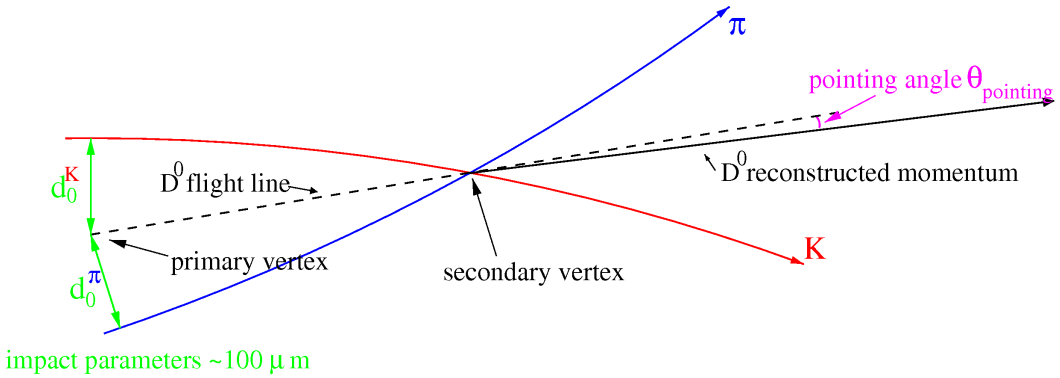

Figure 2.27: Schematic representation of $\mathrm{D}^0 \rightarrow \mathrm{K}^-\pi^+$ decay with track impact parameter d_0 and pointing angle $\theta_{\rm pointing}$ [41].

ALICE is the detector dedicated to the physics of heavy ion collisions at the LHC. The ALICE experiment measures heavy flavour production at mid-rapidity through the semi-electronic decay channel and in a more direct way through D mesons, and at forward rapidity through the semi-muonic decay channel. The measurements are presently performed both in pp and Pb–Pb collisions. This thesis concerns the heavy flavour measurements via the semi-muonic decay channel. Hereafter, is a summary of the results obtained in the mid-rapidity region.

2.3.2.1 Reconstruction of D Mesons

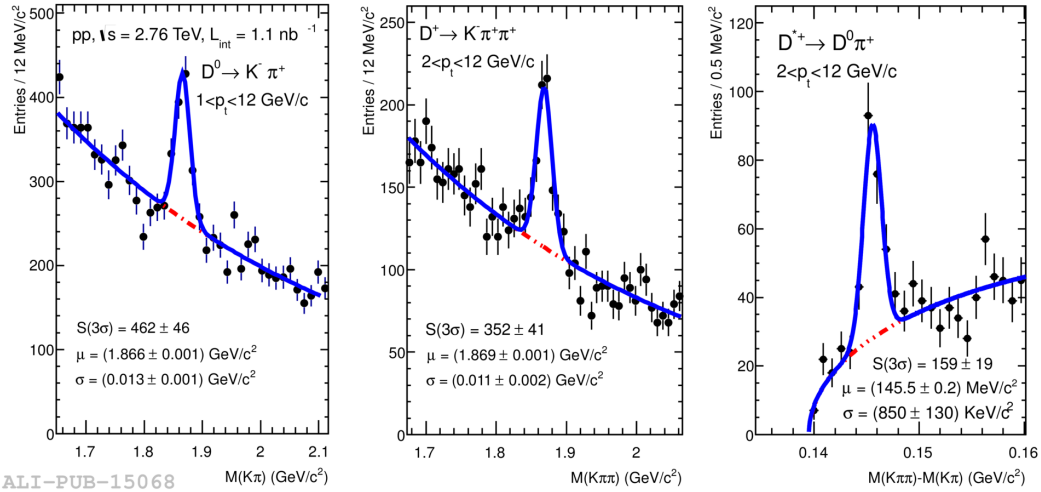

Figure 2.28: Invariant-mass spectrum of D^0 (left) and D^+ (centre) candidates, and invariant-mass difference, $\Delta m = m(K\pi\pi) - m(K\pi)$, for D^{*+} candidates (right) in pp collisions at $\sqrt{s} = 2.76$ TeV measured with ALICE [224].

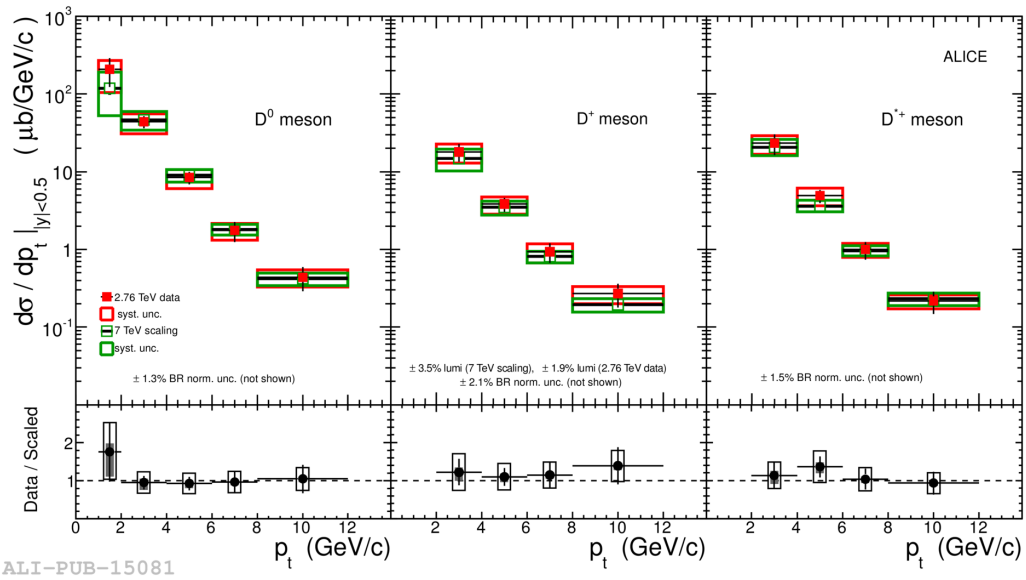

Figure 2.29: Upper: p_{t}-differential cross section for prompt D^0, D^+, and D^{*+} mesons in pp collisions at $\sqrt{s} = 2.76$ TeV [224] compared with the scaling of the ALICE measurement at $\sqrt{s} = 7$ TeV [225]. Bottom: ratio of the $\sqrt{s} = 2.76$ TeV cross section and the $\sqrt{s} = 7$ TeV measurement scaling. Results are obtained with ALICE.

D mesons are measured in the ALICE Central Barrel via the reconstruction of their hadronic decay channels. As an example, a schematic view of $D^0 \to K^-\pi^+$ decay, is presented in Fig. 2.27. The reconstruction is based on a set of cuts on the impact parameter $d_0^{K/\pi}$ between two opposite sign tracks for K and π. Then, the condition for the D^0 to point back to the primary vertex is applied by imposing a cut on the angle (pointing angle $\theta_{\rm pointing}$) defined by the momentum vector of D^0 candidate and the line connecting the primary and secondary vertex. Finally, the D^0 signals are extracted by fitting the invariant mass distribution of $K^-\pi^+$ combinations, with the optimised set of cuts. With the similar strategy, the D^+ (D^-) and D^{*+} (D^{*-}) mesons are reconstructed via $D^+ \to K^-\pi^+\pi^+$ and $D^{*+} \to D^0\pi^+$ channels, respectively. Fig. 2.28 shows the invariant-mass spectrum of $D^0+\overline{D}^0$ (left) and $D^+ + D^-$ (centre) candidates, and invariant-mass difference, for $D^{*+} + D^{*-}$ candidates (right) in pp collisions at $\sqrt{s} = 2.76$ TeV measured with ALICE [224]. The clear visible in each plot gives the clear D-meson signals. The corresponding $p_{\rm t}$-differential production of D-mesons in $p_{\rm t}$ up to 12 GeV/c are shown in Fig. 2.29 [224] according to the strategy just discussed. Recently, ALICE published the additional measurement of the production cross section of D_s meson in pp collisions at $\sqrt{s} =$ 7 TeV, via the cascade decay process $D_s^+ \to \phi\pi^+$, $\phi \to K^-K^+$, more details can be found in [226].

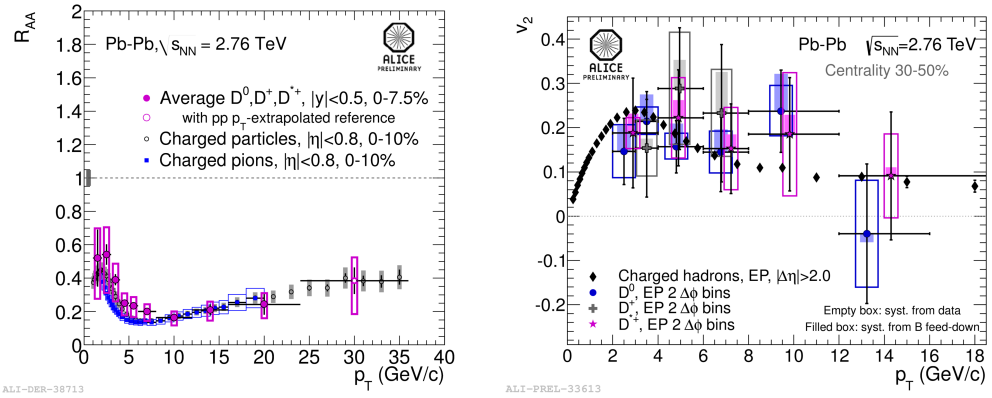

Figure 2.30: Left: average D^0, D^+ and D^{*+} mesons $R_{\rm AA}$ in the $0-7.5\%$ centrality class [227] and charged hadron and pion $R_{\rm AA}$ in the $0-10\%$ centrality class [228, 229]. Right: v_2 of D^0, D^+ and D^{*+} mesons in centrality $30-50\%$ [230] compared to charged hadron v_2 [231]. Results are measured in Pb–Pb collisions at $\sqrt{s_{\rm NN}} =$ 2.76 TeV with ALICE.

In Pb–Pb collisions, the D-meson signals can be extracted by applying the same strategy as the one used in pp collisions. The left plot of Fig. 2.30 shows the $p_{\rm t}$-differential $R_{\rm AA}$ averaged over D^0, D^+ and D^{*+} mesons in Pb–Pb collisions at $\sqrt{s_{\rm NN}} = 2.76$ TeV measured with ALICE [227]. The result is compared with $R_{\rm AA}$ of light charged hadrons and pions [228, 229]. The comparison shows that, the $R_{\rm AA}$ of D-mesons is slightly larger than the one of charged particles and $\pi^\pm$, $R_{\rm AA}^{\rm D} > R_{\rm AA}^{\rm h^\pm}$,

in $p_{\mathrm{t}} \lesssim 10$ GeV/c. This result indicates the in-medium energy loss of charm quarks is smaller than that of the light partons in this p_{t} region, which is consistent with the discussion about the dead cone effect of heavy quark energy loss in Sec. 2.2.3.1. The right plot of Fig. 2.30 is the comparison between the v_2 of D^0, D^+ and D^{*+} mesons [230] and that of light hadrons [231] measured in Pb–Pb collisions at $\sqrt{s_{\mathrm{NN}}} =$ 2.76 TeV with ALICE. In this plot, a non-zero v_2 of D-mesons is measured and this value is comparable with that of light hadrons.

2.3.2.2 Non-Photonic Electron Measurement

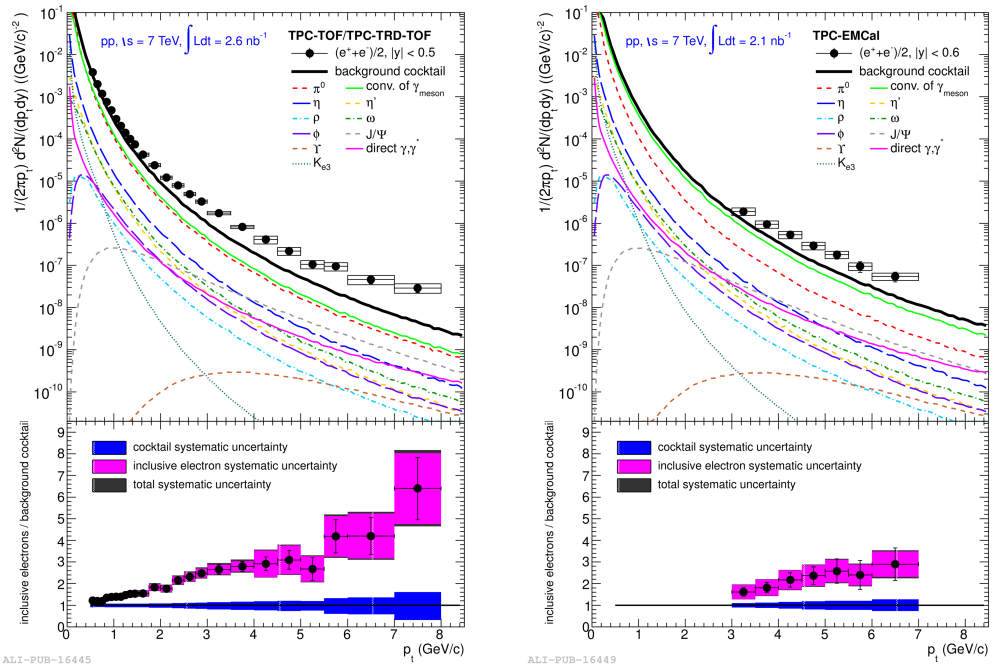

Figure 2.31: Inclusive electron yield per minimum bias pp collision as function of p_{t} at $\sqrt{s} = 7$ TeV in comparison with background electron cocktails for the TPC-TOF/TPC-TRD-TOF analysis (left) and for the TPC-EMCal analysis (right). Lower panels show the ratio of the inclusive electron yield to the background electron cocktail. Results are measured in pp collisions at $\sqrt{s} = 7$ TeV with ALICE [232].

The strategy for measuring the non-photonic electron production cross sections is based on the cocktail technique, as shown in Fig. 2.31. The background electron cocktails for the TPC-TOF/TPC-TRD-TOF analysis and for the TPC-EMCal analysis are shown in the left and right plots of Fig. 2.31, respectively [232] [5]. In the lower panels of Fig. 2.31, the deviations between the unit and the ratios of the inclusive electron yield to the background electron cocktail indicate the contribution

[5]The TPC, TRD, TOF and EMcal are detectors located in ALICE central barrel. The description of the ALICE detectors will be given in Chap. 3.

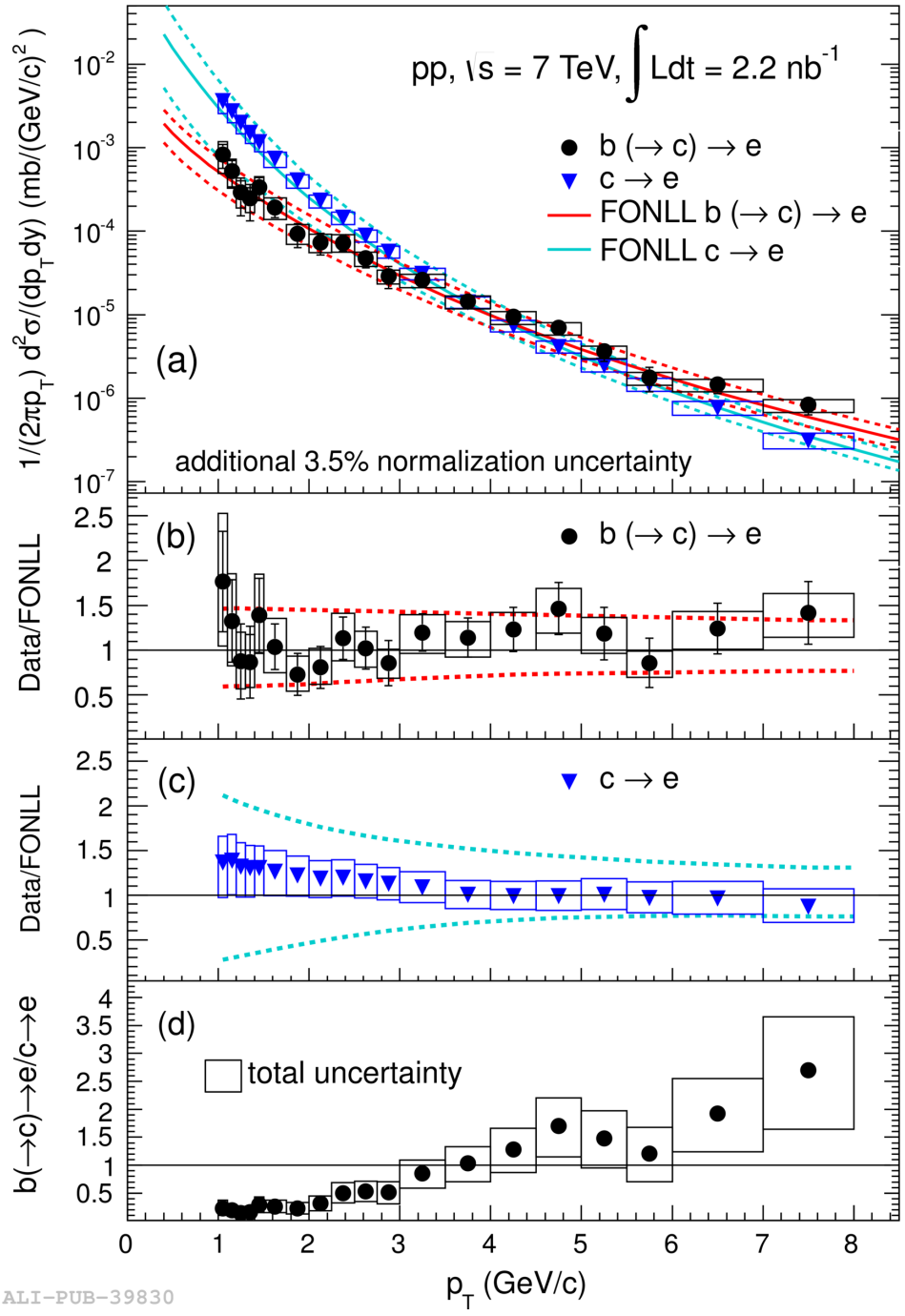

Figure 2.32: (a) p_{t}-differential invariant cross sections of electrons from beauty and from charm hadron decays. The solid (dashed) lines indicate the FONLL predictions [233] (uncertainties). Ratios of the data and the FONLL calculations are shown in (b) and (c) for electrons from beauty and charm hadron decays, respectively. (d) Measured ratio of electrons from beauty and charm hadron decays with error boxes depicting the total uncertainty. Results are measured in pp collisions at $\sqrt{s} = 7$ TeV with ALICE [234].

from the heavy flavour elections. In this case, the non-photonic electron spectrum is obtained by subtracting the cocktail sources from the inclusive electron spectrum. Furthermore, the beauty component in the non-photonic electron spectrum, which is very important for the calculation of the heavy-to-light ratio and D-to-B ratio as mentioned in Sec. 2.3.1, can be measured based on the displacement of the decay vertex from the collision vertex.

With the discussed strategy, Fig. 2.32 shows the p_{t}-differential invariant cross sections of electrons from beauty and from charm hadron decays in pp collisions at $\sqrt{s} = 7$ TeV measured with ALICE [234]. And we can clearly see that, both the production cross section of electrons from charm decays and that of electrons from beauty decays are well in agreement with the FONLL predictions [233] with in uncertainties.

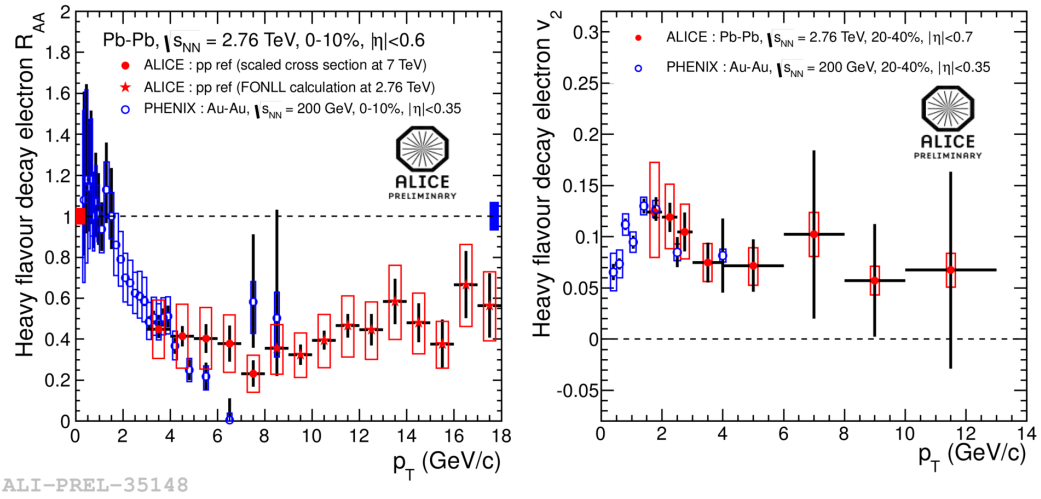

Figure 2.33: p_{t}-differential R_{AA} (left) and v_2 (right) of electrons from heavy flavour decays in Pb–Pb collisions at $\sqrt{s_{\mathrm{NN}}} = 2.76$ TeV measured with ALICE [235]. The results are compared with corresponding ones from PHENIX measurements [202].

The p_{t}-differential R_{AA} and v_2 of electrons from heavy flavour decays measured in Pb–Pb collisions at $\sqrt{s_{\mathrm{NN}}} = 2.76$ with ALICE is shown in the left and right plots of Fig. 2.33, respectively [235]. The corresponding measurements from PHENIX [202] are also presented. We can find that, the magnitude of R_{AA} and v_2 of the heavy flavour electrons are comparable at these two energies. And the measurements with ALICE will give richer information of the heavy flavour production in heavy-ion collisions, due to the higher p_{t} reached at the LHC energies.

2.3.2.3 Discussion

The published and preliminary results of R_{AA} and v_2 of D mesons and non-photonic electrons measured in (semi-)central Pb–Pb collisions at $\sqrt{s_{\mathrm{NN}}} = 2.76$ TeV as well as their production cross sections measured in pp collisions at $\sqrt{s} = 7$ TeV

or 2.76 TeV performed the high precision of heavy flavour measurements via the hadronic decay and semi-electronic decay channels with ALICE, thanks for the high track momentum and position resolution and the high efficiency for hadron and electron identification in the ALICE Central Barrel. All of the results were discussed gave a deep understanding of the properties of the deconfinement matter at the LHC energies. They also provided an important test of the pQCD calculations in this new energy domain.

But there is an important aspect which is worth to be mentioned. All the above excellent results are obtained in the mid-rapidity region. Based on rigorous scientific spirit, there will be no final conclusion presented until the researches are extended to the forward region. As emphasized, initial conditions are different in the mid-rapidity and forward regions. Also, the longitudinal expansion of the QCD medium will introduce new properties of the final state observables measured in the forward region. In the following, we are going to present the heavy flavour measurements in the forward region with the ALICE MUON spectrometer, and discuss the advantages in both detection and physics aspects.

Part II

ALICE Experiment

Chapter 3

Experimental Apparatus

ALICE (A Large Ion Collider Experiment) is the heavy-ion detector at the CERN LHC, which is designed to address the physics of strongly interacting matter (the quark-gluon plasma) at extreme values of energy density and temperature in nucleus-nucleus collisions. It allows a comprehensive study of hadrons, electrons, muons, and photons produced in the heavy-ion collisions (*e.g.* Pb–Pb), up to the highest multiplicities anticipated at the LHC. The physics programme also includes collisions with lighter ions and at lower energy, in order to vary energy density and interaction volume, as well as dedicated proton-nucleus and proton-proton runs.

First conceptual ideas for a heavy-ion detector at the LHC were formulated in a workshop, at the end of 1990 [236]. The experiment was approved in 1997, and the expected detector performance based on detailed simulations, are summarized in the Physics Performance Report [221, 133]. Presently, the ALICE collaboration is composed of 1200 members from 132 institute in 36 countries.

3.1 ALICE Setup

As all experiments dedicated to heavy-ion physics, ALICE is addressing a broad range of observables which were typically covered at previous accelerators (AGS, SPS, RHIC) by several specialized experiments The schematic layout of ALICE is shown in Fig. 3.1 The apparatus is made of three parts.

Central Barrel Detectors The central part covers the pseudo-rapidity range $-0.9 < \eta < 0.9$ (polar angles $45^{\circ} < \theta < 135^{\circ}$). It is embedded in the large L3 solenoid magnet [238]. From the inside out, the Central Barrel contains the **Inner Tracking System** (**ITS**) made of six planes of high resolution silicon pixel (**SPD**), drift (**SDD**) and strip (**SSD**) detectors, the cylindrical **Time-Projection Chamber** (**TPC**), the **Transition Radiation Detector** (**TRD**), the **Time-Of-Flight** (**TOF**), the **High Momentum Particle Identification Detector** (**HMPID**) based on **Ring Imaging Cherenkov** technique and two electromagnetic calorimeters: the **PHOton Spectrometer** (**PHOS**) and the **ElectroMagnetic CALorimeter** (**EMCal**). All detectors except HMPID, PHOS, and EMCal cover the full azimuth. They allow for primary vertex reconstruction, charged particles tracking over a momentum range from $\sim$ 10 MeV/c to $\sim$ 100 GeV/c and **Particle Identification** (PID) for charged hadrons, electrons and photons.

Global Detectors Several smaller detectors, the **Zero Degree Calorimeter** (**ZDC**), the **Photon Multiplicity Detector** (**PMD**), the **Forward Multi-**

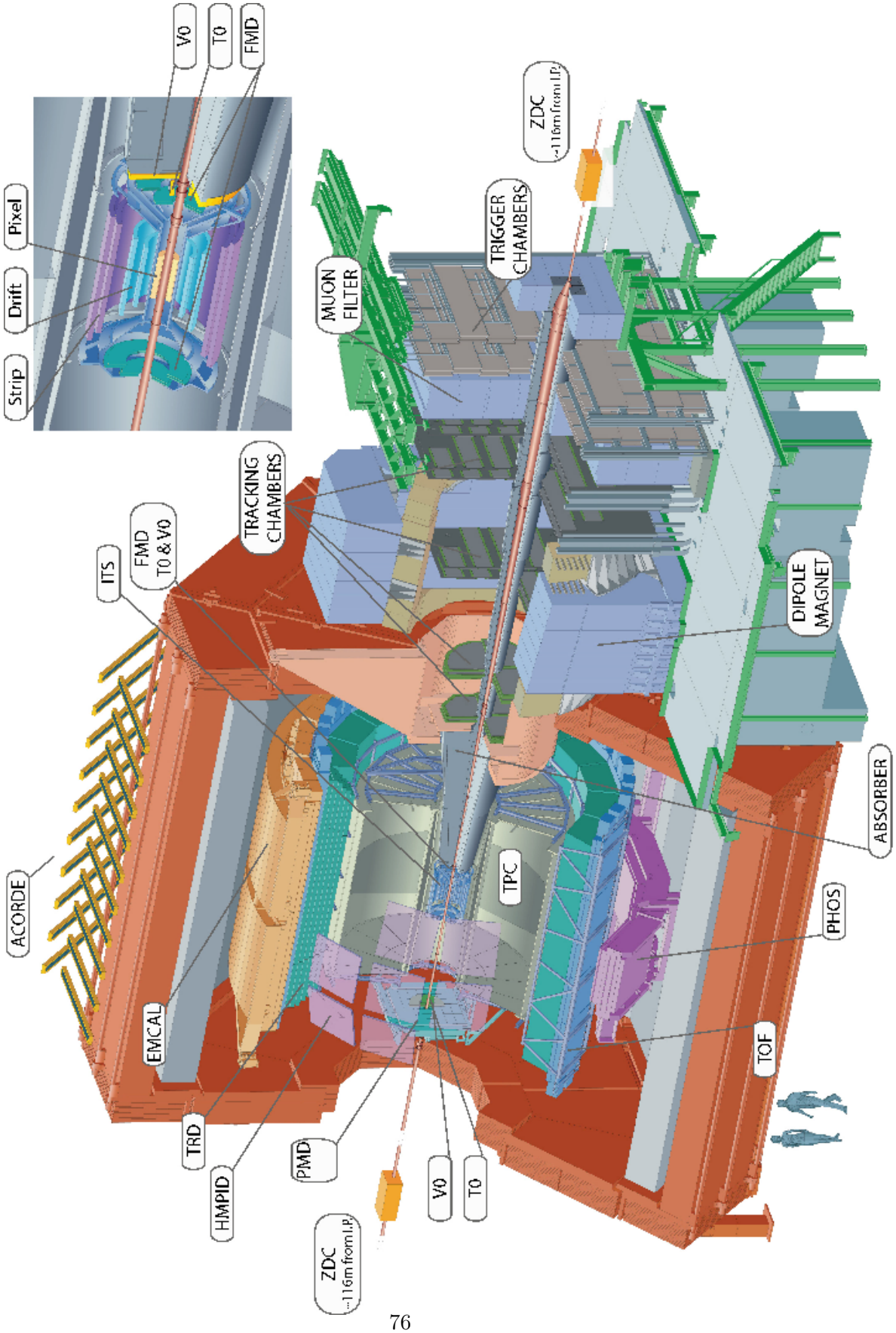

Figure 3.1: ALICE schematic layout.

Detector	Acceptance (η, ϕ)	Position (m)	Dimension (m^2)	Channels
ITS layer 1,2 (SPD)	± 2, ± 1.4	0.039, 0.076	0.21	9.8 M
ITS layer 3,4 (SDD)	± 0.9, ± 0.9	0.150, 0.239	1.31	133 000
ITS layer 5,6 (SSD)	± 0.97, ± 0.97	0.380, 0.430	5.0	2.6 M
TPC	± 0.9 at $r = 2.8$ m ± 1.5 at $r = 1.4$ m	0.848, 2.466	readout 32.5 m^2 Vol. 90 m^3	557 568
TRD	± 0.84	2.90, 3.68	716	1.2 M
TOF	± 0.9	3.78	141	157 248
HMPID	± 0.9, $1.2^\circ < \phi < 58.8^\circ$	5.0	11	161 280
PHOS	± 0.12, $220^\circ < \phi < 320^\circ$	4.6	8.6	17 920
EMCal	± 0.7, $80^\circ < \phi < 187^\circ$	4.36	44	12 672
ACORDE	± 1.3, $-60^\circ < \phi < 60^\circ$	8.5	43	120
Muon spectrometer				
Tracking station 1	$-2.5 < \eta < -4$	-5.36	4.7	1.08 M
Tracking station 2		-6.86	7.9	
Tracking station 3		-9.83	14.4	
Tracking station 4		-12.92	26.5	
Tracking station 5		-14.22	41.8	
Trigger station 1		-16.12	64.6	21 000
Trigger station 2		-17.12	73.1	
ZDC:ZN	$\lvert\eta\rvert < 8.8$	± 116	2×0.0049	10
ZDC:ZP	$6.5 < \lvert\eta\rvert < 7.5$	± 116	2×0.027	10
ZDC:ZEM	$4.8 < \eta < 5.7$ $-16^\circ < \phi < 16^\circ$ and $164^\circ < \phi < 169^\circ$	7.25	2×0.027	10
PMD	$2.3 < \eta < 3.7$	3.64	2.59	2 221 184
FMD disc 1	$3.62 < \eta < 5.03$	inner: 3.2	0.266	51 200
FMD disc 2	$1.7 < \eta < 3.68$	inner: 3.2		
FMD disc 3	$-3.4 < \eta < -1.7$	outer: 0.752 inner: -0.628 outer: -0.752		
V0A	$2.8 < \eta < 5.1$	3.4	0.548	32
V0C	$-1.7 < \eta < -3.7$	-0.897	0.315	32
T0A	$4.61 < \eta < 4.92$	3.75	0.0038	12
T0C	$-3.28 < \eta < -2.97$	0.727	0.0038	12

Table 3.1: Summary of the ALICE detector subsystems. Extracted from [237].

plicity Detector (**FMD**) as well as the **T0** and **V0** detectors are located at forward and backward pseudo-rapidity regions. They are used for global event characterization (like centrality determination, multiplicity measurement, and event plane reconstruction in heavy-ion collisions) and triggering purposes.

Muon Spectrometer The ALICE forward muon arm is primarily designed to heavy-quark resonances (J/Ψ and Υ families) with a mass resolution sufficient to separate all sub-states as well as to measure open heavy flavour semi-muonic decays. In addition, the detector allows to investigate the production of weak interaction probes ($W^{\pm}$ and Z^0) and low mass resonances (ρ, ω and ϕ). It is located at small angles ($2^{\circ} < \theta < 9^{\circ}$, $-4 < \eta < -2.5$) in order to provide a good acceptance down to zero transverse momentum and a manageable background from hadron decays. It consists of a composite absorber, a beam shield, a large dipole magnet with a 3 Tm field integral placed outside the L3 magnet, and ten planes of very thin, high-granularity, cathode strip tracking stations. A second muon filter at the end of the spectrometer and four planes of **Resistive Plate Chambers** (**RCP**) are used for muon identification and triggering. The analysis which is presented in this thesis is based on the ALICE forward muon spectrometer. A more detailed description of the detector layout and of its tracking and trigger algorithms is given in Sec. 3.4

The apparatus is completed by an array of scintillators, **ALICE COsmic Ray DEtector** (**ACORDE**), on top of the L3 magnet, used to trigger on cosmic rays. Tab. 3.1 summarizes the acceptance and location of the various detection elements.

ALICE has been optimized in order to cope a with charged particle density of about $dN/d\eta = 4000$, anticipated in central Pb–Pb collisions at the moment of its design, but tested with simulations up to twice that amount. The tracking was made particularly safe and robust by using mostly three dimensional hits information with many points (up to 150) in a moderate field of 0.5 T. Most detector systems were installed and ready for data taking by mid 2008 when the LHC was scheduled to start operation, with the exception of parts of PHOS (1 out of 5 modules installed), TRD (4 out of 18), PMD, and EMCal (its construction started in 2008). These detectors have been completed for the Pb–Pb run of 2010 and later on.

The physics program with ALICE includes a number of measurements such as:

- particle multiplicity, spectra and correlations;
- event-by-event fluctuations;
- jets;
- direct photons;
- di-leptons;
- heavy quark and quarkonium production;
- low mass resonances;
- $W^{\pm}$ and Z^0 bosons.

3.2 Central Barrel Detectors

The ALICE central barrel is composed of three sets of detector systems: the main tracking system (ITS and TPC) mainly used for the reconstruction of primary vertex and charged tracks as well as particle identification; the particle identification system (TRD, TOF and HMPID) used to separate charged kaons, pions, protons and electrons in a wide p_t range; the electromagnetic calorimeters (PHOS and EMCal) allowing the measurement and reconstruction of neutral particles (photon, π^0 and η *etc.*). In this section, after a brief overview of these detectors, we give a short description of the algorithms developed for the reconstruction of the interaction vertex and tracks. We also present some detector performance for particle identification.

3.2.1 Detector Layout

Inner Tracking System (ITS) [239, 240] The ITS consists of six cylindrical layers of silicon detectors, with a radius between 3.9 cm and 43 cm. Pixel, drift and strip detectors (SPD, SDD and SSD) have been chosen for the two innermost, the two intermediate and the two outer layers, respectively. The SPD covers $|\eta| < 2$ and $|\eta| < 1.4$ for the inner and outer layers, respectively. This allows to provide, together with the forward detectors, a continuous coverage in rapidity for charged particles multiplicity measurements. The six layers will operate together with the central detectors at low frequency (about 100 Hz), while the Silicon Pixel Detector (SPD) can run at higher rate (about 1 kHz) to provide the vertex information for events triggered by the forward muon spectrometer. The main aim of the ITS is to provide precise track and vertex reconstruction close to the interaction point.

Time Projection Chamber (TPC) [241] The TPC is the main tracking detector in the ALICE central barrel. It is designed to provide charged particle momentum measurements up to $p_t = 100$ GeV/c, with good particle identification and vertex determination in the high multiplicity environment of Pb–Pb collisions. The simultaneous detection of high and low momentum particles is achievable with a low magnetic field (≤ 0.5 T). The Time Projection Chamber is made of a cylindrical field cage and is filled with 90^3 m^3 of $Ne/CO_2/N_2$. It is composed of 18 trapezoidal sectors. Multi-wire proportional chambers with cathode pad readout are mounted on them. It has an inner radius of about 85 cm and an outer one of about 250 cm, with a total length of about 500 cm. The 88 μs drift time is the limiting factor for the luminosity in p-p collisions.

The TPC allows to measure charged particles from $p_t = 100$ MeV/c to 100 GeV/c. The study of soft hadronic observables requires a resolution of 1% for momenta between 100 MeV/c and 1 GeV/c, while the detection of hard probes requires a 10% resolution for tracks with $p_t = 100$ GeV/c. The latter can be achieved by using the TPC in combination with the ITS and the TRD. The resolution on the relative momentum between two particles, necessary for the study of two-particle correlations, has to be better than 5 MeV/c. It is worth noting that the TPC can

provide particle identification by $\mathrm{d}E/\mathrm{d}x$ measurement from the low momentum region up to few tens of GeV/c, in combination with the TOF, the TRD and the ITS.

Transition Radiation Detector (TRD) [242, 243] The TRD provides electron identification for momenta greater than 1 GeV/c, where the pion rejection capability through energy loss measurement in the TPC is no longer sufficient. It is used with the TPC and the ITS in order to measure the production of light and heavy vector meson resonances, and of open charm and beauty thanks to the good impact parameter resolution of the ITS. A similar technique can be used to separate the directly produced J/Ψ mesons from those arising from B-hadron decays. The TRD consists of 18 sectors of 6 layers each with a 5 fold segmentation along the beam direction, for a total of $18 \times 5 \times 6 = 540$ detector modules. Each module consists of a radiator of 4.8 cm thickness, a multi-wire proportional readout chamber with cathode pad readout. The TRD increases the ALICE pion rejection capabilities by a factor of 100 for electron momenta above 3 GeV/c and allows a mass resolution of 100 MeV/c^2 at the Υ region for $B = 0.4$ T.

Time Of Flight (TOF) [244, 245] The TOF allows for particle identification in the intermediate momentum range, from 0.2 to 2.5 GeV/c. Coupled with the ITS and the TPC it provides identification of pions, kaons and protons. Its large coverage requires the use of a gaseous detector. Multi-gap Resistive Plate Chambers were chosen, providing an intrinsic time resolution of better than 40 ps and an efficiency close to 100%. The detector is segmented in 18 sectors in ϕ and 5 segments in z. It is located at a radius between 370 cm and 399 cm and has a length of 745 cm.

High Momentum Particle Identification Detector (HMPID) [246] The detector is dedicated to inclusive measurements of identified hadrons with $p_{\mathrm{t}} >$ 1 GeV/c and extend π/K (K/p) separation to 3 (5) GeV/c. The HMPID has a pseudo-rapidity acceptance of $|\eta| < 0.6$ and an azimuthal coverage of about 58°, corresponding to 5% of the central barrel phase space. The detector is based on proximity focusing Ring Imaging Cherenkov counters and consists of seven modules of about 1.5×1.5 m^2 for each.

PHOton Spectrometer (PHOS) [247] The high resolution electromagnetic spectrometer provides photon identification as well as neutral meson identification through the di-photon decay channel. It can be used also as a fast trigger. The PHOS is a single arm spectrometer including a highly segmented electromagnetic calorimeter made of lead-tungstenate crystals coupled to Avalanche Photo-Diode followed by a low-noise preamplifier, and a charged particle veto detector consisting of a Multi-Wire Proportional Chamber with cathode-pad readout. The spectrometer, positioned at the bottom of the ALICE setup at a distance of 460 cm from the interaction point, covers a pseudo-rapidity range of $|\eta| < 0.12$ and 100° in azimuthal angle.

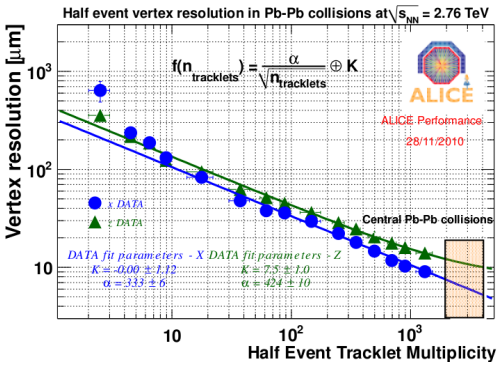

Figure 3.2: Primary vertex resolution in Pb–Pb collisions at $\sqrt{s_{\rm NN}} = 2.76$ TeV as a function of half of the tracklets multiplicity of the event [248]. Data taken in 2010, see text for details.

ElectroMagnetic Calorimeter (EMCal) [249] The EMCal enhances the ALICE capabilities for jet quenching measurements. It enables triggering on high energy jets, reduces significantly the measurement bias for jet quenching studies, improves jet energy resolution and increases existing ALICE capabilities to measure high momentum photons and electrons. The EMCal is placed between the ALICE space-frame, supporting the entire central detectors, and the magnet coils. The azimuthal acceptance covered (107°) is limited by the PHOS and the HMPID. The chosen technology is a layered Pb-scintillator sampling calorimeter with alternating layers of 1.44 mm of lead and 1.76 mm of polystyrene scintillator with longitudinal wavelength-shifting fiber light collection. The EMCal covers $-0.7 < \eta < 0.7$ and is positioned in opposite side of the PHOS calorimeter.

3.2.2 Primary Vertex Determination

The reconstruction of the primary vertex is based on the information provided by the SPD, which constitutes the two innermost layers of the ITS. The pairs of reconstructed points are selected in these two layers, which are close in azimuthal angle in the transverse plane. The z-position of the primary vertex is estimated by using a linear extrapolation. A similar procedure is also performed in the transverse plane. Due to the bending in the magnetic field, the linear extrapolation is an approximation; however, thanks to the short distances from the interaction point, the x- and y-coordinates of the primary vertex are determined with a sufficient precision to be used as constraints in the first tracking pass. This estimate of the primary vertex position is then used to correct the measurement of the z-coordinate, for effects due to an off-axis position of the interaction point in the transverse plane. For well focused beams one can determine the transverse position of the interaction point averaging over many events, provided that the beam position is sufficiently stable in time.

The resolution on the position of the primary vertex $\sigma_{\rm vtx}$ depends on the track multiplicity $n_{\rm trklet}$, *i.e.* on the charged-particle density as [237],

$$\sigma_{\rm vtx} = \frac{\alpha}{\sqrt{n_{\rm trklet}}} \oplus K. \tag{3.1}$$

In Fig. 3.2 the resolution of x- and z-coordinate of the primary vertex reconstruction

with the fitting function from Eq. (3.1) are shown. The resolution of the vertexer is obtained by dividing the tracklets of the event in two random samples and reconstructing two vertices for the two samples. The difference between these two vertices is the measurement of the resolution as a function of the half tracklet multiplicity. For charged-particle densities in central heavy-ion collisions, a vertex-position resolution on the 10 μm level is obtained and in pp collisions ($n_{\mathrm{trklet}} \simeq 6-7$) the vertex resolution ~ 150 μm. This measurement of the primary-vertex position is used as an input for the tracking.

After track reconstruction, the position of the primary vertex is then recalculated using the measured track parameters.

3.2.3 Charged Track Reconstruction

The basic method employed for track finding and fitting is the Kalman filter [250]. This method relies on the determination, for each track, of a set of initial seed values for the track parameters and their covariance matrix. In ALICE this seeding is done using the space points reconstructed in TPC twice: the first time assuming that the track originated from the primary vertex and the second one assuming that the track originated elsewhere (decay, secondary interaction, *etc.*). The combination of the space points starts from a few outermost pad rows using, in the first pass, the primary vertex position as a constraint. The procedure is repeated several times, choosing a set of pad rows closer and closer to the centre of the TPC. The Kalman filter essentially consists of the following steps:

1. propagate the state vector of the track parameters and their covariance matrix to the next pad row;

2. add to the inverted covariance matrix, which represents the information matrix of the knowledge of the track parameters at that point, a noise term to represent the information loss due to stochastic processes like multiple scattering and energy loss fluctuations;

3. the track information will be updated, if the filter finds in the new pad row a space point compatible with the track prolongation.

Then, repeat the seeding a second time without the primary vertex constraint.

After this step, the tracks are propagated to the outer layers of the ITS (ITS-refit) in two independent passes, first imposing the primary vertex position as a constraint, and then without this condition. Both sets of track parameters are stored for further analysis. Whenever more than one space-point candidate is found within the search window around the prolongation of a track (a half-width of four standard deviations is typically used), all possible assignments are used as different hypotheses and are followed independently towards the innermost ITS layer. In this way each TPC track can have several candidate paths throughout the ITS. A decision is made only at the end, based on the sum of the χ^2 along the track-candidates' path in the ITS. Optionally, layer skipping and cluster sharing between

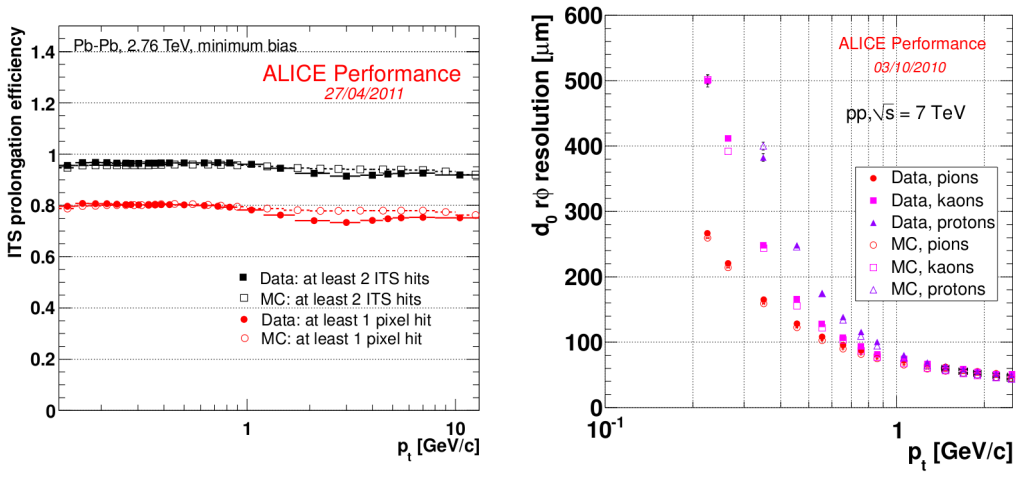

Figure 3.3: Left: track prolongation efficiency in ITS for TPC tracks, for the request of ITS-refit only (black) and ITS-refit with at least a point in SPD (red); data from Pb–Pb collisions at $\sqrt{s_{\rm NN}} = 2.76$ TeV in 2010, MC results based on HIJING simulations. Right: transverse impact parameter resolution estimate as a function of $p_{\rm t}$ for pions, kaons, protons; data from pp collisions at $\sqrt{s} = 7$ TeV in 2010, MC corresponds to PYTHIA simulations with Perugia-0 configuration.

tracks are allowed, in which case a weight factor is introduced in the χ^2 sum. The left plot in Fig. 3.3 shows the track prolongation efficiency in the ITS for TPC tracks, for the request of ITS-refit only (black) and ITS-refit with at least a point in SPD (red), the additional requirement for at least one point in SPD helps to reject the fake tracks which represent $\sim 20\%$, as estimated from data.

When the ITS tracking is completed, the Kalman filter is reversed and follows the track from the inner ITS layers outwards. Starting with much more precise track parameters than during the first step, the improperly assigned points (outliers), now, can be eliminated. Then we continue following the tracks beyond the TPC, assigning space points in the TRD, and matching the tracks with hits in the TOF, minimum-ionizing clusters in the HMPID. Finally, the Kalman filter will be reversed one last time to refit all tracks from the outside inwards, in order to obtain the values of the track parameters at or nearby the primary vertex. Optionally, an additional track-finding step using only points from the ITS would be proceeded, after having removed all the ITS space points already assigned to tracks. This is useful for finding tracks that have not been seeded in the TPC.

The track parameters obtained both with and without the primary vertex constraint are stored for all tracks, in order to allow for the subsequent analysis of short lived particle decays (such as charm and beauty decays) taking place very close to the primary vertex. The main performance parameter for such studies is the resolution in the impact parameter (the distance between the primary vertex and the track prolongation to the point of closest approach to the primary vertex). This res-

olution depends both on the precision of the primary vertex position determination and on the precision of the determination of the track parameters. The right plot in Fig. 3.3 shows transverse impact parameter ($d_0(r\phi)$) resolution estimations for charged pions, kaons and protons, obtained in pp collisions at $\sqrt{s} = 7$ TeV, taken in 2010. This is done using the ITS-refit and 2 points in SPD, and the primary vertex was reconstructed using the beam constraint.

3.2.4 Particle Identification

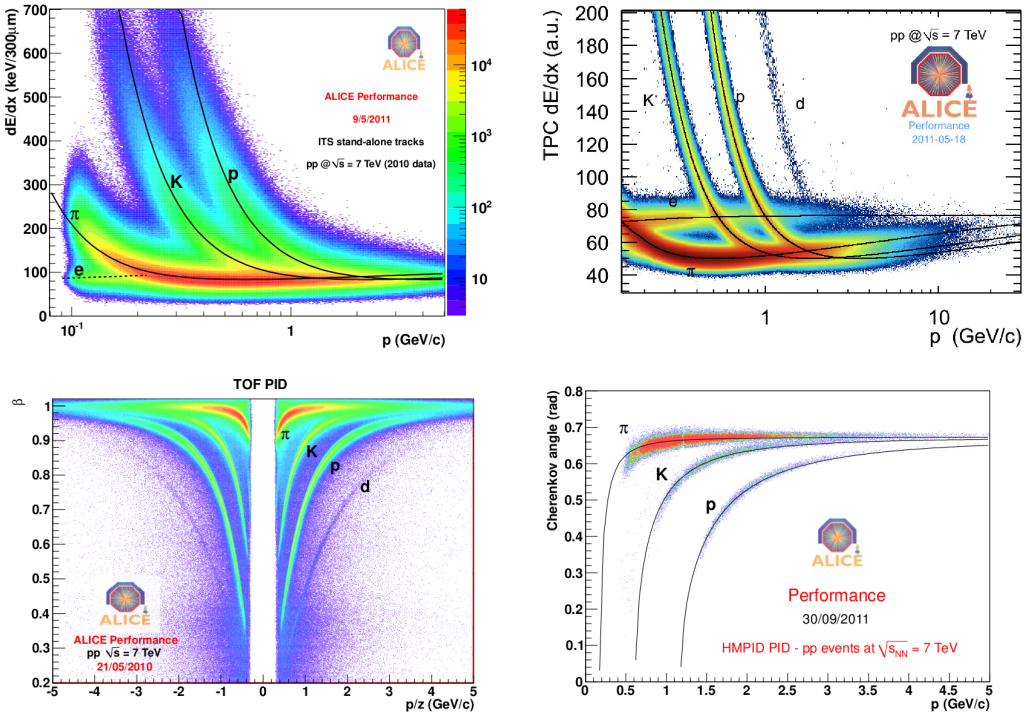

Figure 3.4: Top: dE/dx of charged particles *vs.* their momentum, measured by the ITS alone (left) and TPC (right), the lines are a parameterization of the Bethe-Bloch curve. Bottom left: β *vs.* signed momentum in the TOF. Bottom right: HMPID Cherenkov angle *vs.* track momentum, continuous lines represent theoretical Cherenkov angle values *vs.* track momentum. The results correspond to pp collisions at $\sqrt{s} = 7$ TeV.

In the ALICE central barrel, charged particle identification is done with the ITS, TPC, TRD, TOF and HMPID detectors, each of them having a different momentum-dependent performance. The best results are achieved by combining the information they provide individually. Particle identification is performed in two steps: during the first step, the information from each detector is used to assign to every track a set of probabilities, one for each particle type; then, the information from the individual detectors is combined in the second PID step.

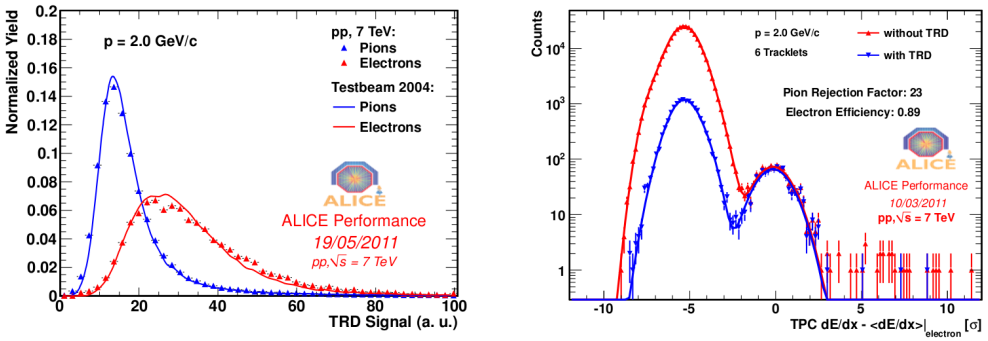

Figure 3.5: Left: charge deposit for electrons and pions at a momentum of 2 GeV/c, in pp collisions at $\sqrt{s} = 7$ TeV. Data (symbols) are compared with test beam measurements performed in 2004. Right: TPC dE/dx signal (in units of resolution) relative to the electron Bethe-Bloch lines (shown in the top right panel of Fig. 3.4) for 2 GeV/c tracks and 6 TRD tracklets, with and without electron tagging in the TRD, in pp collisions at $\sqrt{s} = 7$ TeV (2011 data).

Four layers of the ITS (two silicon-drift and two silicon-strip detector layers) provide signal amplitude information, which can be used for PID in the low-momentum range by measuring ionization energy loss dE/dx. This is estimated as a truncated mean (using the two or three lowest amplitude signals out of four) in order to minimize the influence of Landau fluctuations. The resulting plot is shown in the top left panel of Fig. 3.4 for pp collisions at $\sqrt{s} = 7$ TeV. The resolution of the ITS dE/dx measurement is about 11%, which allows for good π/K separation up to 450 MeV/c and for good p/K separation up to about 1 GeV/c.

As in the ITS, the dE/dx measurement in TPC uses the truncated mean of the 65% lowest-amplitude pad-row samples. The estimated resolution of the dE/dx measurement depends slightly on the charged-particle density; it changes from 5.5% for pp events to 6.5% for central Pb–Pb collisions according to the simulations. Fig. 3.4 (top, right) shows the particle identification for tracks measured in the TPC in pp collisions at 7 TeV. Typically, the separation power (expressed as number of standard deviations) for different pairs of particle species starts with excellent separation in the region below the particle masses; increasing the momentum, the separation progressively worsen, and decreases to zero, at the value of momentum where the Bethe-Bloch curves for the two particles cross each other.

The measurement of dE/dx in the TRD contributes to charged-particle PID in the same momentum range as for the TPC. Although the ionization in the TRD gas (based on xenon) is larger than that in the TPC (based on neon), the TRD dE/dx measurement is only a complement to the TPC measurement, because of the limited TRD track length L (the resolution scales as $\sqrt{L}$). The precision on the dE/dx measurement in the TRD is estimated to be 18−20%. The TRD provides the main source of information for electron identification in ALICE, and can also give

electron-identification information at the trigger level. For electrons, the average charge deposit is higher due to the additional contribution from the absorption of bremsstrahlung transition radiation in the drift gas, as shown in the left panel of Fig. 3.5. The electrons in the TRD can be tagged via the likelihood method [1], which is expected to reject pions by a factor of 100 or better, for 90% electron detection efficiency. The TPC $\mathrm{d}E/\mathrm{d}x$ signal relative to the electron Bethe-Bloch lines (the left and right peaks correspond to the contribution from charged pions and electrons, respectively) for 2 GeV/c tracks and 6 TRD track-lets, with and without electron tagging in the TRD, is shown in the right panel of Fig. 3.5.

As introduced above, charged-particle identification based on the $\mathrm{d}E/\mathrm{d}x$ measurements (in ITS and TPC) performs well in the $1/\beta^2$ [2] region and, for gas-based detectors, in the multi-GeV region. However, this technique inevitably leaves a hole in the momentum range around the minimum of the ionizing losses (*i.e.* between 0.9 and 3 GeV/c). In the ALICE experiment this range is covered by the TOF detector, that is able to measure a particle's arrival time with a precision of about 80 ps. During the last tracking pass in the Kalman filter, the integral of the particle's time-of-flight for different mass hypotheses are computed, and compared with the TOF measurement smeared by the response function. In this way, one can obtain the TOF track probabilities for the different particle species. The TOF detector allows to extend, on a track-by-track basis, the kaon/pion separation out to $2.5-3$ GeV/c and the proton/kaon separation out to $3.5-4$ GeV/c, as shown in the bottom left panel of Fig. 3.4.

Finally, the HMPID is used to further extend the momentum range for charged-particle identification, although in a limited acceptance, by distinguishing the Cherenkov angles of different particle species, albeit only within a limited acceptance. The expected performance is shown in the bottom right panel of Fig 3.4, where the momentum dependence of the Cherenkov angle is plotted for different particle species. As can be seen, the HMPID is able to identify protons up to 5 GeV/c.

Additionally, an excellent photon-detection capability is provided by the PHOS and EMcal. The EMCal also opens the possibility of triggering on high-transverse-momentum jets and allows us to improve the measurement of the jet energy including the neutral component.

3.3 Global Detectors

As shown in Tab. 3.1, a set of small angle detectors, located in the forward and backward rapidity regions, are used to deliver global information like centrality and event plane in A-A collisions as well as multiplicity and trigger decisions in both A-A and pp collisions. A short description of their layout is presented below.

[1] The details for likehood method are introduced in [133].
[2] β is the relativistic velocity in **Natural System of Units**, $c = \hbar = 1$.

Zero Degree Calorimeter (ZDC) [251] The ZDC provides a centrality estimation and is used for triggering in Pb–Pb collisions, and allows to reject electromagnetic interactions. The ZDC measures the energy carried in the forward direction (at zero degrees relative to the beam direction) by non-interacting (spectator) nucleons. The detector consists of two sets of hadronic calorimeters (for neutron and protons), placed on both sides of the interaction point, at 116 m from it. The system is completed by two electromagnetic calorimeters (ZEM), both placed at about 7 m from the interacting point (in the side opposite to the muon spectrometer), which allow to resolve ambiguities in the determination of the centrality.

The neutron calorimeter (ZN) is placed between the beam pipes and has the most severe geometrical constraints: the transverse dimensions have to be smaller than 7 cm, requiring a very dense "passive" material (tungsten). The proton calorimeter (ZP) is placed externally to the beam pipe and is made with a less dense material (lead). The ZN, segmented in four regions, can also provide an estimate of the reaction plane.

The electromagnetic calorimeter (ZEM), made of lead and quartz fibers, is designed to measure the energy of particles, mostly photons generated from π^0 decays, at forward rapidities ($4.8 < \eta < 5.7$). Differently from the ZN and ZP, the ZEM fibers are oriented at 45° in order to maximize the detector response. The ZDCs cannot provide an L0 trigger [3], since they are located too far from the interaction point, but they can provide an essential L1 trigger for centrality.

Photon Multiplicity Detector (PMD) [252] It is a pre-shower detector measuring the multiplicity and spatial ($\eta - \phi$) distribution of photons on an event-by-event basis, in the forward region ($2.3 < \eta < 3.7$). It can also provide estimates for the transverse electromagnetic energy and the reaction plane. The PMD is placed at about 360 cm from the interaction point (ZDC: ZEM side). It consists of two identical planes of detectors, made of gas proportional counters with honeycomb structure and wire readout, with a $3X_0$ thick lead converter in between them: the front detector plane is used as charged particle veto while the detector plane behind the converter is the pre-shower plane and registers hits from both photons and charged hadrons.

Forward Multiplicity Detector (FMD), T0 and V0 [253] The FMD provides a charged particle multiplicity information in the pseudo-rapidity range $-3.4 < \eta < -1.7$ (muon spectrometer side) and $1.7 < \eta < 5.1$ (PMD side). The FMD is composed of three rings (1 inner, 2 inner and outer, and 3 inner and outer). Each detector ring consists of 10 (for an inner ring) or 20 (for an outer ring) silicon sensors. The full FMD contains 51200 silicon strips to be readout. The design ensures, together with the ITS inner pixel layer, a full pseudo-rapidity coverage in

[3] The "fast" part of the ALICE trigger is split into two levels: a Level 0 (L0) signal which reaches detectors at 1.2 μs, but which is too fast to receive all the trigger inputs, and a Level 1 (L1) signal sent at 6.5 μs which picks up all remaining fast inputs. Details about triggers will be presented in the next chapter.

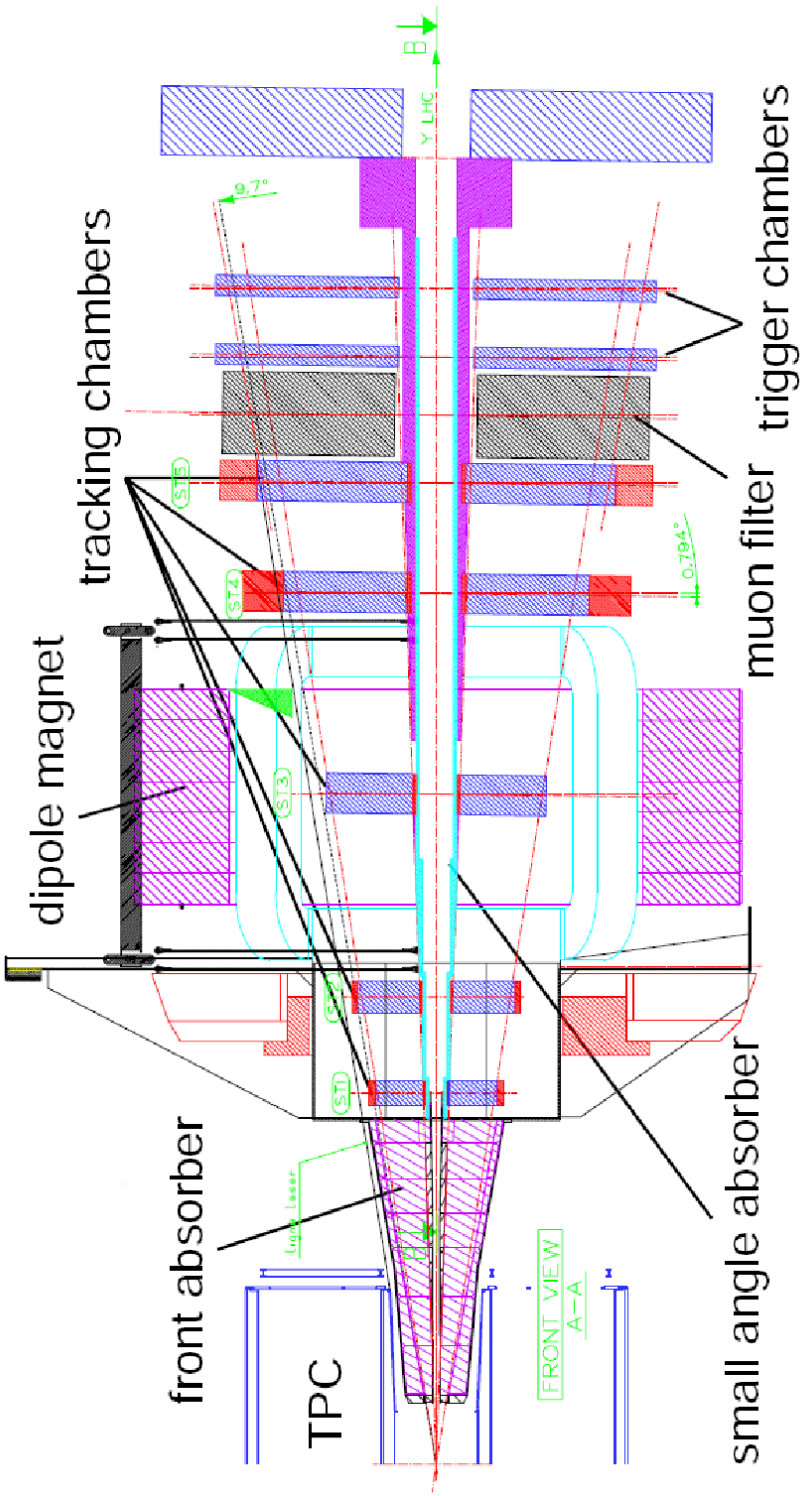

Figure 3.6: Layout of the ALICE muon spectrometer.

Muon Detection	
polar, azimuthal angle coverage	$171^{\circ} < \theta < 178^{\circ}$, 360°
minimum muon momentum	4 GeV/c
pseudo-rapidity coverage	$-4 < \eta < -2.5$
Front Absorber	
longitudinal position (from IP)	$-5030 < z - 900$ mm
total thickness (materials)	$\sim 10\lambda_{\rm int}$, $\sim 60X_0$ (carbon-concrete-steel)
Dipole Magnet	
nominal magnetic field, field integral	0.67 T, 3 Tm
free gap between poles	$2.972 - 3.956$ m
overall magnet length	4.97 m
longitudinal position (from IP)	$-z = 9.94$ m (centre of the dipole coils)
Tracking Chambers	
no. of stations, no. of planes of station	5, 2
longitudinal position of stations	$-z = 5357, 6860, 9830, 12920, 14221$ mm
anode-cathode gap (equal to wire pitch)	2.1 mm for st. 1, 2.5 mm for st. $2-5$
gas mixture	80%Ar/20%CO_2
pad size st. 1 (bending plane)	4.2×6.3, 4.2×12.6, 4.2×25.2 mm^2
pad size st. 2 (bending plane)	5×7.5, 5×15, 5×30 mm^2
pad size st. 3, 4 and 5 (bending plane)	5×25, 5×50, 5×100 mm^2
max. hit dens. st. $1-5$ (central Pb–Pb×2)	$5.0, 2.1, 0.7, 0.5, 0.6 \cdot 10^{-2}$hits/cm^2
spatial resolution (bending plane)	$\simeq 70$ μm
Tracking Electronics	
total no. of FEE channels	1.08×10^6
shaping amplifier peaking time	1.2 μs
Trigger Chambers	
no. of stations, no. of planes of station	2, 2
longitudinal position of stations	$-z = 16120, 17120$ mm
total no. of RPCs, total active surface	72, ~ 140 m^2
gas gap	single, 2 mm
electrode material and resistivity	Bakelite$^{\rm TM}$, $\rho = 2 - 8 \times 10^9$ Ωcm
gas mixture	Ar/$C_2H_2F_4$/i-buthane/SF_6 (50.5/41.3/7.2/1)
pitch of readout strips (bending plane)	10.6, 21.2, 42.5 mm (for trigger st. 1)
max. strip occupancy bend. (non bend.) plane	3% (10%) in central Pb–Pb
max. hit rate on RPCs	3 (40) Hz/cm^2 in Pb–Pb (Ar–Ar)
Trigger Electronics	
total no. of FEE channels	2.1×10^4
no. of local trigger cards	$234 + 8$

Table 3.2: Summary of the main characteristics of the muon spectrometer. Extracted from [237].

the range $-3.4 < \eta < 5.1$, and an overlap between the FMD and the ITS pixel system of about 0.2 pseudo-rapidity units.

The T0 consists of two arrays of Cherenkov counters, with a time resolution better than 50 ps, asymmetrically placed at 72.7 cm (muon spectrometer side) and 375 cm (PMD side) from the interaction vertex, with a pseudo-rapidity coverage of $-3.28 < \eta < -2.97$ and $4.61 < \eta < 4.92$, respectively. It is designed to provide a T0 signal for the TOF detector, to measure the vertex position with a precision of ± 1.5 cm, thus providing a L0 trigger when the position is within the preset values, and can generate minimum bias and multiplicity triggers.

The V0 is made of two arrays of scintillators, located 90 cm (muon spectrometer side) and 340 cm (PMD side) from the interaction point. Each detector is segmented into 32 elementary counters distributed in 4 rings and 8 sectors, with a pseudo-rapidity coverage of $-3.7 < \eta < -1.7$ and $2.8 < \eta < 5.1$. The V0 is used for triggering, centrality selection and participates in the luminosity measurement.

3.4 Forward Muon Spectrometer

In ALICE, the muon detection is performed in the pseudo-rapidity region $-4 < \eta < -2.5$ (with the muon spectrometer [254, 255]. With this detector, the complete spectrum of heavy-quark vector-meson resonances (i.e. J/Ψ, Ψ', Υ, Υ' and Υ''), as well as the low-mass resonances, can be measured in the $\mu^-\mu^+$ decay channel. The simultaneous measurement of all quarkonium species with the same apparatus allows a direct comparison of their production rate as a function of different parameters such as transverse momentum and collision centrality. In addition to vector mesons, the unlike-sign dimuon continuum up to masses around 10 GeV/c^2 can be measured. Since at LHC energies the continuum is expected to be dominated by muons from the semi-leptonic decay of open charm and open beauty, it is possible to study the production of open heavy flavours with the muon spectrometer. Additionallly, heavy-flavour production in the region $-2.5 < \eta < -1$ should be accessible through measurement of $e - \mu$ coincidences [256], where the muon is detected in the muon spectrometer and the electron in the TRD. Finally, $W^{\pm}$ and Z^0 can be also measured with the muon spectrometer.

3.4.1 Design Consideration

As the accuracy of dimuon measurements is statistics limited (at least for the Υ family), the geometrical acceptance of the spectrometer was chosen as large as possible. In addition, a large acceptance down to zero p_{t} is required for measuring direct J/Ψ production. At high p_{t} a large fraction of J/Ψ is produced via b-decay [257]. Tevatron measurements [161] indicate that the contribution from b-decay to the total J/Ψ yield is $\simeq 10\%$ for $p_{\mathrm{t}} < 3 - 4$ GeV/c and increases linearly to $\simeq 40\%$ for p_{t} around $15 - 18$ GeV/c. Since muon identification in the heavy-ion environment is only feasible for muon momenta above about 4 GeV/c because of the large amount of material (absorber) required to reduce the flux of hadrons, measurement of low-p_{t}

charmonia is possible only at small angles (*i. e.* at large rapidities) where muons are Lorentz boosted.

A resolution of 100 MeV/c^2 in the 10 GeV/c^2 dimuon invariant-mass region is needed to resolve the Υ, Υ' and Υ'' resonances. This requirement determined the bending strength of the spectrometer magnet as well as the spatial resolution of the muon tracking system. In addition, multiple scattering is minimized by a careful optimization of the absorber and very thin detector planes. The tracking and trigger detectors of the spectrometer have to cope with the high particle multiplicity of heavy-ion collisions at LHC energies and have therefore a high granularity. The spectrometer is also equipped with a selective dimuon trigger system to match the maximum trigger rate [258].

The muon spectrometer is designed to detect muons in the polar angular range $171^{\circ} - 178^{\circ}$. This interval, a compromise between acceptance and detector cost, corresponds to the pseudo-rapidity range of $-4 < \eta < -2.5$. This allows the study of heavy quarks in a region complementary to the one explored by the ALICE central barrel and by other LHC experiments, like ATLAS and CMS. The layout of the muon spectrometer is shown in Fig. 3.6. The spectrometer consists of the following components: a passive front absorber to absorb hadrons and photons from the interaction vertex; a high-granularity tracking system of 10 detection planes; a large dipole magnet; a passive muon-filter wall, followed by four planes of trigger chambers; an inner beam shield to protect the chambers from primary and secondary particles produced at large rapidities.

The main challenge for the muon spectrometer results from the high particle multiplicity per event rather than from the event rate, which is quite small. This was taken into account both in the design of the absorbers (which have to provide strong absorption of the hadron flux coming from the interaction vertex) and of the detectors (which must be able to sustain the remaining high multiplicity). The main parameters of the muon spectrometer are summarized in Tab. 3.2. They have been optimized by means of simulations with a high multiplicity (an extra factor of two larger than that predicted by HIJING). It is important to note that the muon spectrometer relies on the V0 detector as a fast interaction trigger to make the system more robust against background from beam-gas interactions in particular during the proton-proton run at nominal beam intensity [259]. A High-Level Trigger (HLT) for dimuons will reduce, by a factor four to five, the need in bandwidth and data storage.

3.4.2 Front Absorber and Beam Shielding

The ALICE muon spectrometer design was driven by the requirement of coping with a high multiplicity scenario anticipated in Pb–Pb collisions: about 7000 particles produced in the spectrometer acceptance and about 6000 particles intercepting the beam-pipe in the region $-7 < \eta < -4$. The latter interact with the pipe and introduce additional background particles in the acceptance.

The front absorber reduces the forward flux of charged particles by at least two orders of magnitude and decreases the background of muons from the decay of

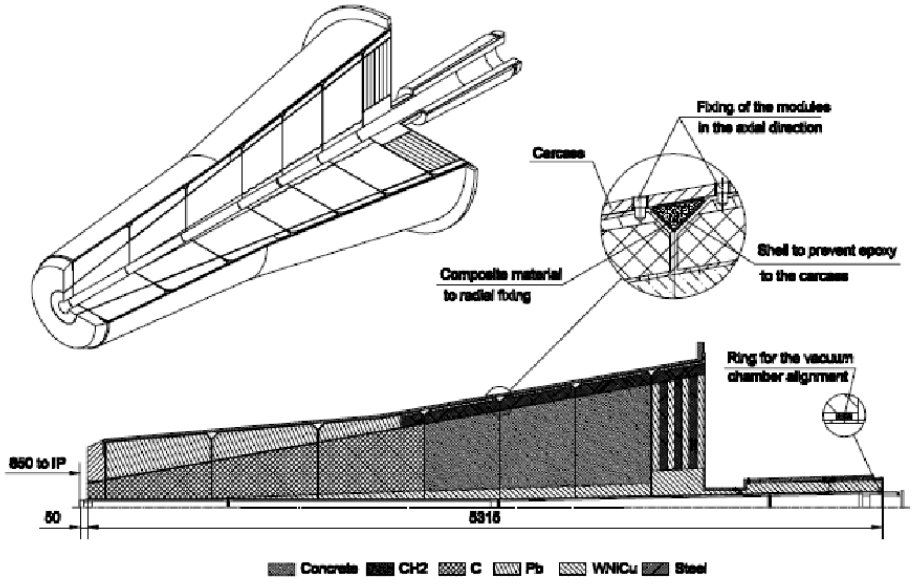

Figure 3.7: Layout of front absorber.

pions and kaons by limiting the free path for primary π/K. This can be achieved by minimizing the distance between the absorber and the vertex, compatibly with the dimension of the inner tracker and the position of the multiplicity counters: the minimal value imposed by such constraints is 90 cm.

The front abasorber has a 4.13 m length ($\sim$ 10 $\lambda_{\rm int}$) and is placed inside the L3 magnet, at 90 cm from the interaction point. The absorber design and composition are optimized to provide good shielding capabilities and a limited multiple scattering which should not compromise the spectrometer mass resolution. This can be achieved by using low-Z material in the absorber layers close to the vertex and high-Z shielding materials in the central part near to the tracking chambers. Therefore, the central part close to the interaction point is made of carbon and concrete, while the central part close to the tracking chambers is composed of lead and tungsten. The inner (outer) shield is composed of lead and tungsten (high density materials). The absorber is completed by a combination of concrete and carbon, as shown in Fig. 3.7. It is worth noting that the use of very dense material at the end of the absorber has an important consequence for the tracking. Since the multiple scattering in this layer is large (about $35X_0$) whereas the distance to the first tracking chamber is small (30 cm), the muon production angle is better defined when the position measurement in the first chamber is combined with the position of the interaction vertex, determined by the ITS.

The small-angle beam shield, as shown in Fig. 3.8, is made of dense materials (tungsten, lead and stainless steel) encased in a 4 cm thick stainless steel envelope. The latter is "pencil-shaped": it follows the 178° acceptance line up to a maximum radius of 30 cm and then stays constant up to the end of the spectrometer. The inner

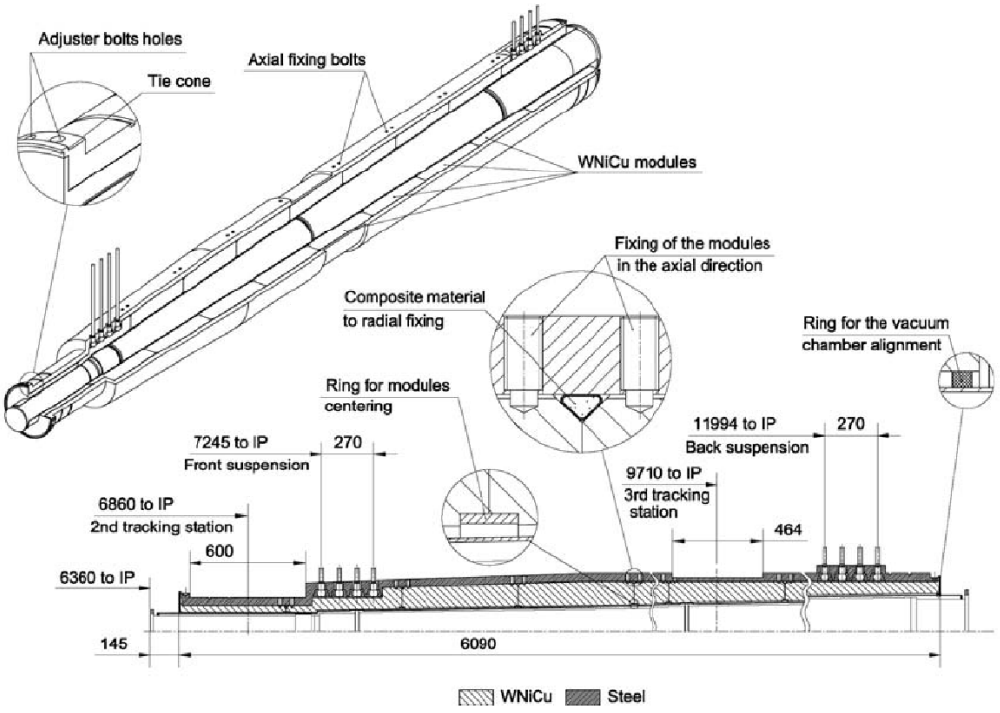

Figure 3.8: Schema of the beam shielding.

cone opens up till the end of the muon arm ("open geometry" configuration). Within the absorber, the beam shield absorbs primary particles in the region $-5 < \eta < -4$.

3.4.3 Dipole Magnet

The dipole magnet [260], shown in Fig. 3.9, is placed 7 m from the interaction vertex, at some 10 cm distance from the L3 solenoid. The size (free gap between poles 3.5 m, height of the yoke 9 m, total weight about 900 t) is defined by the requirements on the angular acceptance of the spectrometer. The magnetic flux density ($B_{\rm nom} = 0.67$ T, 3 Tm field integral between IP and muon filter) is defined by the requirements on the mass resolution. It provides an horizontal magnetic field perpendicular to the beam axis. The polarity can be inverted.

The magnet yoke is constructed from 28 low-carbon steel modules made for cost reasons from existing steel stacks which consist of 3 cm thick steel sheets welded to each other. The vertical poles are oriented at an angle of 9° with respect to the vertical symmetry plane leaving a free gap between the poles of $2.972-3.956$ m. The two Saddle type coils have semi-cylindrical coil ends. They are constructed from hollow aluminum conductor with square cross-section of 25.5 cm^2 and an internal hole for cooling with demineralised water at a rate of some 130 m^3/hr. Each coil is assembled from 3 sub-coils with 4 layers of 14 turns each. They delimit the overall length of the magnet to 5 m. The distance of the centre of the dipole yoke from the

interaction vertex is 9.87 m.

The magnet was installed in its final position on a 3 m high reinforced concrete platform. The close distance between the solenoid magnet and the dipole leads to a strong magnetic force (estimated at 120 t) between the two magnets. Measurements, at full power, do not indicate any displacement of the magnet structures. The stray field in the vicinity of the magnet attenuates rather rapidly to less than 50 Gauss at the level of the gangways.

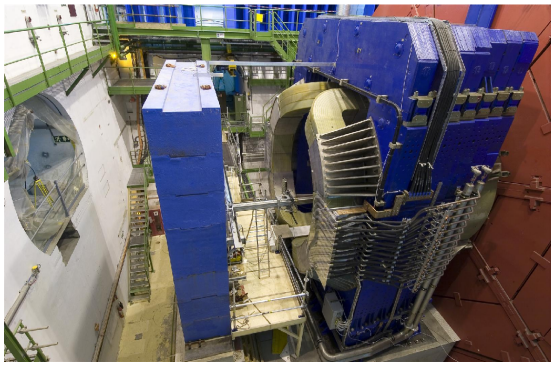

Figure 3.9: Layout of dipole magnet of the muon spectrometer.

3.4.4 Muon Tracker

The muon tracking system includes 5 tracking stations with the **The Geometry Monitoring System** (**GMS**) together to ensure a high track position and momentum resolution. After the description of the muon tracking system, the algorithm for the muon track reconstruction will be discussed, in this section.

3.4.4.1 Tracking Chambers

The tracking chamber design was driven by two main constraints: to achieve the spatial resolution of 100 μm necessary for an invariant mass resolution of 100 MeV/c^2 at the Υ mass and to operate in a maximum hit density of about 5×10^{-2} cm^{-2} expected in central Pb–Pb collisions. The resolution along the non-bending plane (parallel to the magnetic field), should be better than about 2 mm to allow an efficient track finding. An additional constraint is imposed by the large area (about 100 m^2) covered by the tracking system.

All these requirements can be full filled by the use of **Multi-Wire Proportional Chambers** (**MWPC**) with cathode pad readout. The detectors are arranged in five stations: two are placed before, one inside and two after the dipole magnet. Each station is made of two chamber planes, with two cathode planes each, which are readout in order to provide bi-dimensional information. The segmentation of the cathode pads is designed to keep the occupancy at a 5% level: since the hit density decreases with the distance from the beam pipe, larger pads are used at larger radii. This enables to keep the total number of channels at about one million.

Multiple scattering of the muons in the chamber is minimized by using composite material, such as carbon fibers. The chamber thickness corresponds to about $0.03X_0$. Although based on standard MWPC design, the individual chambers have been adapted to meet the particular constraints on the different tracking stations.

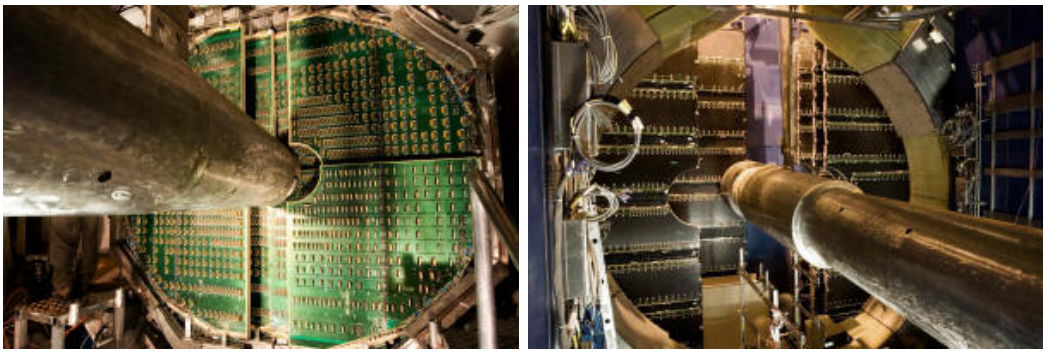

Figure 3.10: Layout of the tracking station 2 (left) and 4, 5 (right).

The first two are based on a quadrant structure [261]. The readout electronics is distributed over the surface, as displayed in the left panel of Fig. 3.10. For the other stations a slat architecture was chosen, with the electronics implemented on the side of the slats, as shown in right plot of Fig. 3.10. The slats overlap to avoid dead zones in the detector.

For all stations the front-end electronics is based on a 16-channel chip called **MANAS** (**Multiplexed ANAlogic Signal processor**) including the functionality of charge amplifier, filter, shaper and track and hold. The signal digitization is performed on board. The channels of four of these chips are fed into a 12-bits ADC, read out by the **Muon Arm Readout Chip** (**MARC**), whose functionalities include zero suppression. The entire chain is mounted on a front-end board, the **MAnas NUmérique** (**MANU**): the 1.08 million channels of the tracking system are treated by about 17000 MANU cards.

The **Protocol for the ALICE Tracking CHamber** (**PATCH**) buses provide the connection between the MANUs and the **Cluster ReadOut Concentrator Unit System** (**CROCUS**) crate. Each chamber is readout by two CROCUS, which concentrate and format the data, transfer them to the DAQ [4] and dispatch the trigger signals, coming from the **Central Trigger Processor** (**CTP**). These crates allow also the control of the FEE and of the calibration processes.

3.4.4.2 The Geometry Monitoring System (GMS)

The requirement of a mass resolution of 1% at the mass of the Υ introduces strong constraints on the alignment of the tracking chambers. During the installation phase the chambers are positioned according to theodolite measurements and with photogrammetry, with a spatial accuracy of few tenths of a millimeter [262]. At the beginning of each data taking period, dedicated runs without magnetic field are carried out in order to align the ten tracking chambers with straight muon tracks, thus determining the initial geometry of the system. However, after switching on the magnet and electronic power supplies, such initial positioning is disturbed by the

[4] DAQ is the Data AcQuisition System, which is described in the next chapter.

forces of the L3 and dipole magnetic fields, as well as by the thermal expansion of the chambers and their support. The displacements and deformations are measured and recorded during data taking by the Geometry Monitoring System (GMS), with a resolution better than 40 μm.

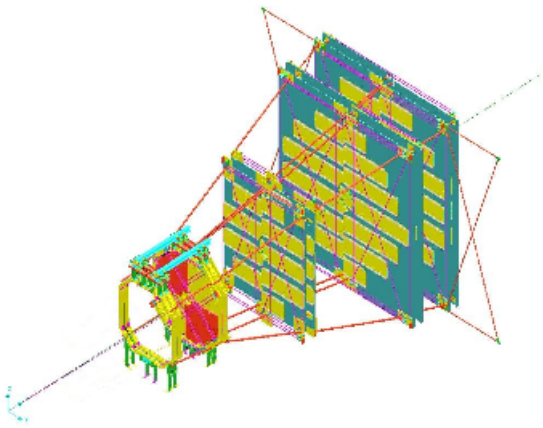

Figure 3.11: General view of the GMS. The red lines present the optical lines.

The GMS is an array of about 460 optical sensors which are placed on platforms located at each corner of the tracking chambers. Two different types of optical devices were used: the **Boston CCD Angle Monitor** (**BCAM**) and the Proximity [263]. In both cases the image of an object is projected on a CCD sensor through a lens: the analysis of the captured image provides a displacement measurements. The most relevant difference between the devices is represented by the luminosity object used: a pair of point-like LEDs for the long range system BCAM and a coded mask for the short distance system Proximity.

The BCAM are used to monitor the relative longitudinal distance between two neighboring chambers in different stations, the flatness of the chamber supports and the absolute displacement of the entire spectrometer, through eight optical lines linking chamber 9 to the ALICE cavern walls. The longitudinal distance between two chambers of the same station is measured by the Proximity device. The resulting optical lines are shown in Fig. 3.11.

3.4.4.3 Muon Track Reconstruction

With the Raw data as input, the cluster-finder algorithm associates clusters to the detector digits, and later the tracking algorithm deals with the reconstruction to evaluate the muon tracks, their trajectory and associated properties. The cluster-finder algorithm begins with the information of the digits and fits the charge induced on the pads of the CPCs by the charged particles with a Mathieson-function-based expression [264]. Thus the clusters coordinates can be extracted from those fits. The tracking algorithm takes as input the clusters information. In the ALICE muon spectrometer two independent algorithms for track reconstruction have been developed. One is based on the Kalman filter, and the other is based on the traditional tracking algorithms that fit the position of the track associated clusters to reconstruct the track. The Kalman filter is the default option in our reconstruction algorithm. For both of the methods, the restrictions applied in tracking procedure are:

- first estimation of track momenta should be 3 GeV/$c < p <$ 3 TeV/c;

- cut χ^2 at both the cluster and track levels;
- the reconstructible track should include 1 over 2 clusters on stations 1, 2 and 3 and 3 over 4 clusters on stations 4 and 5.

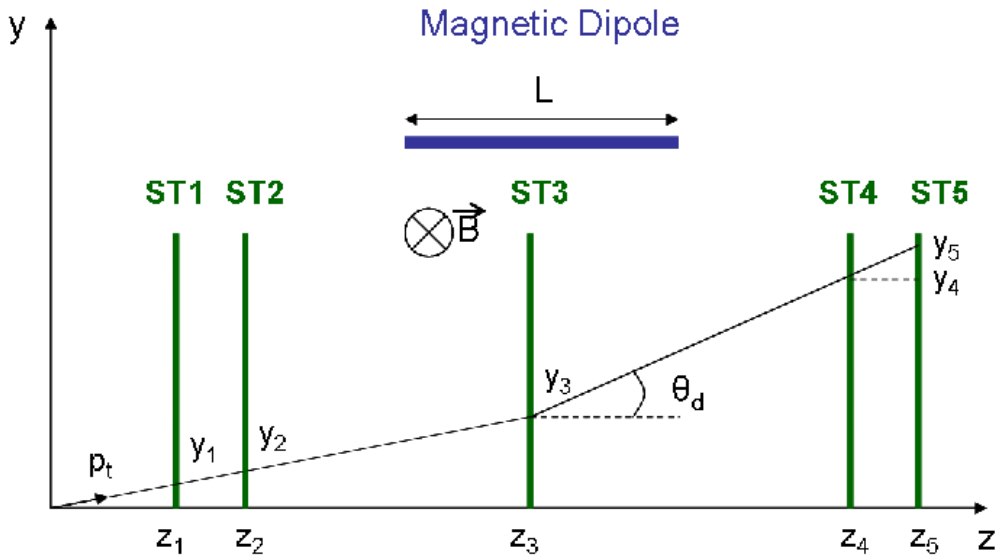

Figure 3.12: Principle of muon track reconstruction.

The track reconstruction starts from the two last tracking stations (stations 4 and 5) because they are less subject to background due to soft particles escaping the front absorber. The algorithm begins linking cluster pairs on stations 4 and 5 (independently) and creating segments by joining the two clusters position by a straight line. Those segments are extrapolated in the magnetic field to the vertex position, as shown in Fig. 3.12, to have a first estimate of the track parameters (position, slope and inverse bending momentum and corresponding errors). The track momentum, p, is calculated through the usual Lorentz-law derived relationship in the case of having only a magnetic field perpendicular to the particle momenta:

$$\vec{F} = \frac{\mathrm{d}\vec{p}}{\mathrm{d}t} = q(\vec{E} + \vec{v} \times \vec{B}), \tag{3.2}$$

where q is the charge of muon, $\vec{v}$ is the velocity, $\vec{E}$ and $\vec{B}$ are the electric and magnetic field of the dipole. With Eq. (3.2) one can obtain the relation between the guessed track momentum p and the radius of curvature R by using:

$$p[\mathrm{GeV}/c] = 0.3[\mathrm{T}] \times R[\mathrm{cm}] = 0.3[\mathrm{T}] \times \frac{L[\mathrm{cm}]}{\theta_{\mathrm{d}}}, \tag{3.3}$$

where L is the length of the magnet and

$$\theta_{\mathrm{d}} = \frac{y_5 - y_4}{z_5 - z_4} - \frac{y_2 - y_1}{z_2 - z_1}, \tag{3.4}$$

as the geometry described in Fig. 3.12. Here comes the first restriction of both tracking algorithms: tracks with $p < 3$ GeV/c or $p > 3$ TeV/c calculated by Eq. (3.3) are rejected.

The second step is to consider as departure the guessed track from station 5 (station 4) clusters and extrapolate it to the station 4 (station 5). The algorithm searches for at least one cluster on that station that could be associated to the track (condition of 3/4 clusters on stations 4 and 5). The restriction applied to associate clusters to tracks is a χ^2 cut. The Kalman based reconstruction algorithm considers all clusters that pass the criteria, while the traditional one usually considers the best associated cluster, the one with the lowest χ^2. Once a cluster is associated, the track parameters are re-calculated. The Kalman algorithm uses the Kalman filter procedure, and the traditional algorithm needs to fit again the associated clusters to evaluate the new parameters. The next step is the track extrapolation to station 3. As before, a χ^2 cut is imposed as cluster selection criteria and a χ^2 cut on the track is also applied. A minimum of one cluster has to be associated to the track for it to be considered (condition of 1/2 clusters on station 3) and then the track parameters are re-evaluated. The remaining tracks are now extrapolated to station 2 and later to station 1. The selection criteria are the same: the χ^2 cut on the clusters and the track and a minimum of 1 associated cluster on both stations (condition of 1/2 clusters on stations 1 and 2).

After the full reconstruction of the tracks in the tracking stations, one gets the first reconstructed track parameters: the **uncorrected track parameters**. Then their parameters can be extrapolated in two ways:

- by taking into account both the energy loss and Coulomb scatterings, the Badier-Branson correction is used. It allows the correction of the parameters of the track points to the vertex position measured by the SPD. This gives the **track parameters related to vertex**. This method consists of calculating the deviation angle from the most probable position of the muon to the end of the absorber, the radiation length of the material and the vertex position. Note that the distribution of the energy loss is very large (~ 4 GeV) and very asymmetric, thus, even if the energy loss is corrected on average, the fluctuations are important. The corrections described in this item are of particular interest for the study of muon from heavy flavour decays that decay near the vertex;

- by taking into account only the energy loss. This calculation allows the **Distance of Closest Approach** (**DCA**) analysis and the study of background noise when muons are produced far from the interaction point; the track parameters determined in this case are called the **parameters related to DCA**.

3.4.5 Trigger System

The design of the muon trigger system allows to reduce hadron background which punch through the front absorber by requiring the tracks reconstructed in the muon traker to match the corresponding hits in the two trigger stations (the

iron filter between the muon tracker and the muon trigger stops almost all of punch through hadrons). The muon trigger delivers different type of (di)muon triggers at hardware level to reduce the background and improve the signals. In the following, we introduce the general structure of the muon trigger system as well as the trigger decision.

3.4.5.1 Design Layout

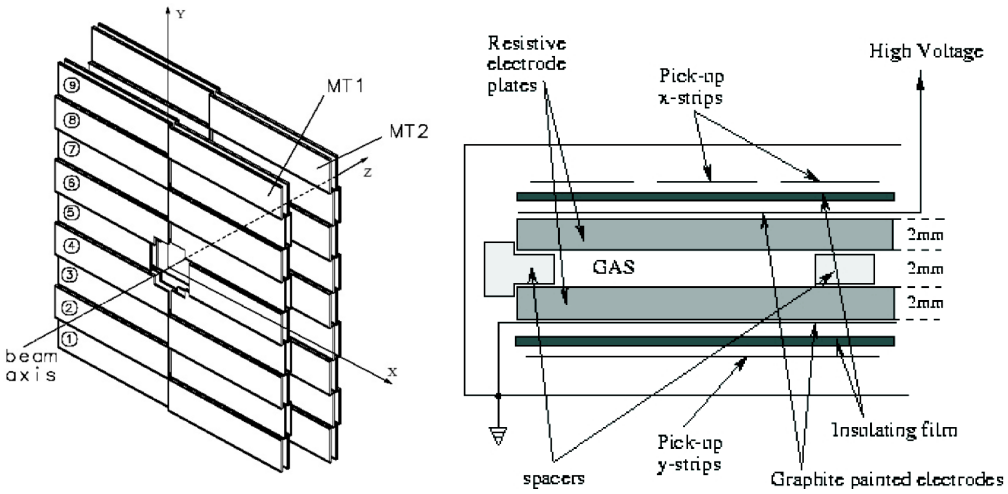

Figure 3.13: Left: scheme of the muon trigger stations MT1 and MT2 with two planes of RPCs on both of them. Right: scheme of a Resistive Plate Chamber (RPC).

The trigger system of the ALICE muon spectrometer consists of two trigger stations (MT1 and MT2) located at about 16 m from the interaction point and 1 m apart from each other, placed behind an iron muon filter, as shown in the left panel of Fig. 3.13. The muon filter has a thickness of 120 cm. It is located between the muon tracker and the trigger stations and corresponds to 7.2 interaction lengths. It allows to select muon tracks because it stops low-energy background particles and hadrons passing through the front absorber (or produced in this absorber).

Each station is composed of two planes of 18 **Resistive Plate Chambers** (**RPCs**). RPCs are large area detectors, made up of high resistivity ($\sim 3-9\times 10^9$ Ωm) Bakelite electrodes separated by 2 mm wide gas gap. The surface of the Bakelite foils on the gap side is painted with linseed oil, while the external surface is painted with graphite, with one layer connected to the high voltage and the other to the ground (right plot in Fig. 3.13). The signal is picked up by read-out strips connected with **the Front-End Electronics** (**FEE**), which basically consists of a leading-edge discriminator stage followed by a shaper. The strips are placed on both sides of the chambers, in order to provide a bi-dimensional information. The horizontal strips measure the bending deviation due to the dipole magnetic field,

while vertical strips measure the non-bending direction. The two layers of read-out pads are therefore called “bending” and "non-bending" plane, respectively.

The signals coming from the FEE, consisting in the x and y fired strip patterns of the four detection planes, are sent to the local trigger electronics. The whole system is divided in 234 detection areas, each of them associated with a local trigger board. The local board density reflects the strip segmentation which is finer in the region close to the beam pipe, where a higher particle multiplicity is expected: in particular, moving from the beam pipe outwards, the strip pitch is about 1, 2 and 4 cm in the bending plane and about 2 and 4 cm in the non-bending plane.

The spatial resolution is better than 1 cm, the chamber response is fast, the signal rises about 2 ns and the time resolution is 1-2 ns.

3.4.5.2 Trigger Decision

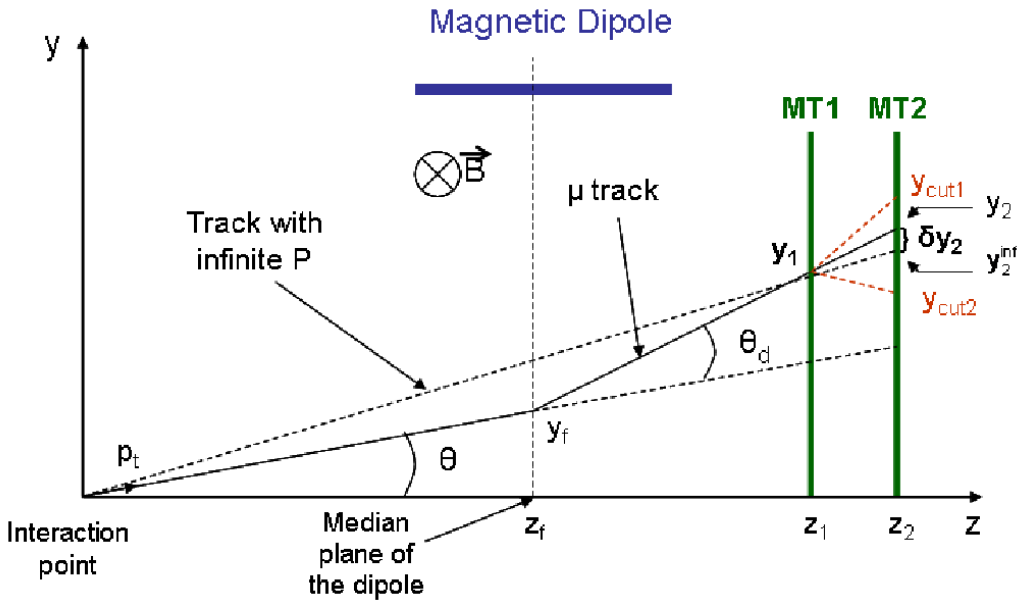

Figure 3.14: Sketch of the track transverse momentum determination by the ALICE muon spectrometer trigger system.

The trigger decision in the ALICE muon spectrometer is taken by the muon trigger chambers (RPCs). The trigger system is able to select in about 650 ns candidate muons or dimuon tracks (like-sign or unlike-sign) above a certain transverse momentum. Note that this p_t cut is justified to reduce the background of muons from pion and kaon decays, which is predominant at low p_t region. The selection of candidate tracks is done by an algorithm at the electronics level. Roughly, the algorithm takes the measured position on the first trigger station, that corresponds to (y_1, z_1) in Fig. 3.14. It considers a straight line trajectory for the track with origin in the interaction vertex, and evaluates which is the deviation of the mea-

sured position in the second trigger station (y_2, z_2) with respect to this straight line trajectory. The measured deviation in the Y plane (bending plane), labeled as δy_2 in the figure, should be smaller than a certain cut, δY_2-cut, which corresponds to the p_t cut [258]. The track deviation angle, θ_d, is calculated by means of

$$\theta_d = \frac{1}{z_f}\left(\frac{z_1 y_2 - z_2 y_1}{z_2 - z_1}\right) \tag{3.5}$$

where z_f is the z coordinate of the dipole. Thus using the small angle approximation the track transverse momentum can be obtained through

$$p_t \simeq qLB\frac{z_2 - z_1}{z_1}\frac{\sqrt{x_f^2 + y_f^2}}{\delta y_2}, \qquad y_f = y_1\frac{z_f}{z_1} - \delta y_2\left(\frac{z_1 - z_f}{z_2 - z_1}\right) \tag{3.6}$$

B and L are the dipole magnetic field and length, as shown in Fig. 3.14.

To fulfil the design requirements the trigger system disposes of a three-level electronics. First the local cards with a decision time of 250 ns treat the information coming from a portion of the detector surface and provide a "local trigger", deciding whether: there is no trigger, there is trigger for positive particles, there is trigger for negative particles, or trigger with no deviation. Secondly the regional cards collect the local cards information and evaluate if there is one candidate track (with which sign), or two or more candidate tracks like-sign or unlike-sign. Finally, the global card gathers regional cards information and provide five trigger signals that will be sent to the Central Trigger Processor. The five possible muon input trigger signals for the CPT are:

- like-sign dimuon candidate of low p_t: PairLikeLPt trigger,
- like-sign dimuon candidate of high p_t: PairLikeHPt trigger,
- unlike-sign dimuon candidate of low p_t: PairUnlikeLPt trigger,
- unlike-sign dimuon candidate of high p_t: PairUnlikeHPt trigger,
- single muon candidate of low or high p_t: SingleLPt or SingleHPt triggers.

In particular, there are two trigger p_t cuts: the low p_t cut and the high p_t cut that correspond to a p_t threshold of 1 GeV/c and 2 GeV/c respectively. These cuts are not sharp, the intrinsic trigger efficiency is not an ideal step function. In fact they are associated to the p_t value for which the trigger efficiency attains 50%. The efficiency increases sharply and reaches a plateau of about 99% (98%) at 3 (5) GeV/c for the low (high) p_t trigger cut [258]. Those p_t cuts combined with the possibility that the trigger offers to disentangle particles' charge permits to define the five trigger signals. Notice that when the trigger has difficulties to identify the particle charge sign it considers both signs to avoid any trouble. The low p_t cut is optimized for the J/Ψ physics and the high p_t cut for the Υ physics. Moreover there is also a minimum cut on p_t that is defined by the maximum deviation that the local electronics can afford. This cut is labeled as All p_t cut and corresponds to about

0.5 GeV/c. Note that a p_{t} threshold of 4.2 GeV/c has been recently implemented for $W^{\pm}$ study.

The CTP receives the trigger signals from detectors, coordinates their information and decides whether the whole trigger conditions identify that an 'interesting' event takes place. This decision is taken while considering the physics characteristics of the events, which define a certain combination of detectors that should trigger, and the available band-width. In [265] details about the different trigger configurations defined at the present time can be found. Once we got a trigger signal from the CTP, the tracking and trigger stations are readout and the information is saved in the form of raw data.

Chapter 4

ALICE Online and Offline

This chapter is devoted to the presentation of the data treatment chain, from data taking at the detector level, via offline data reconstruction to data analysis. It includes three parts. In the first part, the detector online system (trigger, Data Acquisition, High Level Trigger and Detector and Experiment Control) is described. In the second part, we expose the offline components associated to the experiment. These are the offline computing model and the general offline framework. Most of the content of these two parts are taken from Ref. [237]. In the third part, we describe the offline analysis framework for muon data. After an overall description of the framework, more details are given on the offline which has been developed for the analysis presented in this thesis.

4.1 Online Control System

During the data taking, the first task is to determine if there is a interaction according to the information received by the **Trigger system** (**TRG**) from some fast detectors. Then the TRG should make a decision according to detectors which have to be recorded via the **Data AcQuisition** (**DAQ**) system. Meanwhile, the **High Level Trigger** (**HLT**) is used optionally to reduce the data volume and select the interesting physics events. Of course, the cooperations of TRG, DAQ and HLT cannot be achieved without the **Detector Control System** (**DCS**) and **Experiment Control System** (**ECS**). All these modules constitute the online control system for the data taking in ALICE [266] [1].

4.1.1 Trigger System (TRG)

The ALICE **Central Trigger Processor** (**CTP**) [267, 268] is designed to select events having a variety of features at rates which can be downscaled to suit the physics requirements and the restrictions imposed by the bandwidth of the DAQ system, and the HLT. The challenge for the ALICE trigger is to make optimum use of the component detectors, which are busy for widely different periods following a valid trigger, and to perform trigger selection in a way which is optimized for several different running modes: ion (Pb–Pb and several lighter systems), pA and pp, varying by almost two orders of magnitude in counting rate.

The triggers in ALICE are based on the following operational principle: a number of detector systems (*eg.* V0, T0, PHOS, TRD, MUON spectrometer, *etc.*) each

[1] Some of them, like the DCS, not only make sense during data taking, but also are activated when there is no beam.

providing a number of logic trigger signals (trigger classes) characterize a specific measurement in this particular detector (*e.g.* multiplicity, high p_t, muon pair, *etc.*). These logical signals are sent to the CTP, as the trigger inputs. They are combined by logical operations inside a FPGA [2] to form the different physics triggers (*e.g.* minimum-bias or central collision, dimuon event, $\cdots$). In addition, the CTP takes care of downscaling, pile-up protection, ready status of different detectors and read-out memories, trigger priority, and finally synchronization with the LHC machine clock cycle, as distributed by the **Trigger Timing and Control** (**TTC**) system [269, 270].

Another particular feature of the ALICE trigger is the possibility to dynamically configure groups of detectors that participate in the readout of any given event. For instance, while the TPC is constrained to relatively low trigger rates, both because of drift time and data volume, the MUON spectrometer can record events at a much higher rate. When it makes sense to do so in order to improve statistics for specific physics channels, groups of detectors, called trigger clusters, are read out separately and at higher rate.

The output trigger signal is sent to a number of **Local Trigger Unit**s (**LTU**s), typically one for each sub-detector, where they are further processed according to the different detector needs and finally sent back to the detector **Front-End Electronics** (**FEE**).

For coping with the large multiplicities in Pb–Pb collisions (interaction rate 8 kHz at luminosity $\mathfrak{L} = 10^{30}$ cm^{-2}s^{-1}), and also because of use of some 'slow' detectors (the TPC drift time can reach up to about 100 μs), some of the FEE in ALICE is not pipe-lined but await for a trigger before processing or digitizing the detector signals. The trigger is organized into three different levels, L0, L1, and L2, which have different latencies, due to the different arrival times of the trigger inputs and the stringent timing requirements of the detectors. In some detectors the front-end electronics requires a strobe very early, and a first trigger decision must be delivered 1.2 μs after the collision takes place. As some trigger detectors are not able to send their input in time, the 'fast' logic is divided into two stages: every decision which can be achieved in 1.2 μs is used to make the L0 decision, and the detectors which require longer contribute to the L1 decision, which arrives at the detectors after 6.5 μs. Note that the CTP decision is made in 100 ns, with the rest of the L0 latency coming from the generation time for the trigger input signals and from the cable delays. The third step, the L2 decision, comes after the end of the drift time in the TPC, i.e. at about 88 μs. The main purpose of this third step is to wait for the end of the past-future pile-up protection. The read-out of the detector electronics into the optical data link is initiated only upon receipt of a positive L2 decision. As mentioned in Sec. 3.4.5.2, the five trigger classes (trigger signals) from MUON spectrometer contribute to the L0 decision.

In addition ALICE uses a very fast interaction 'pre-trigger', which is derived from the multiplicity arrays (V0, T0) and fed directly to the TRD within ≤ 200 ns in order to activate the TRD electronics. Only if the TRD pre-trigger is sent, the

[2] FPGA: Field-Programmable Gate Array, more details can be find in Wikipedia: FPGA.

TRD is ready to accept triggers, or to be read out. Therefore, the confirmatory TRD pre-trigger signal (interaction detected AND TRD in ready state) is a prerequisite for any class for which TRD triggers or readout are required.

In general, the input data handled by the ALICE CTP is global, in the sense that the CTP does not correlate specific geometrical regions in different detectors. However, for given applications it might not be necessary to record data from all regions of the detector, but only from given azimuthal sectors, with an obvious saving in the overall data volume. The boundaries between these different azimuthal sectors, which define **Regions-of-Interest** (**RoI**), line up in the larger central detectors TPC, TRD and TOF, and equivalent boundaries could be imposed in software in the ITS. If a given trigger detector can identify an azimuthal sector as being the one carrying the information giving rise to the trigger (*e.g.* the presence of a high p_t electron), it is foreseen that a flag can be set to identify the sectors of interest. These can then be treated in a special way, *e.g.* by selecting only those sectors for readout to DAQ, or by treating them differently in the HLT.

When several trigger classes are running concurrently, it becomes necessary to adjust the rates at which they are read out to reflect the physics requirements and the overall DAQ bandwidth. These factors may dictate rates quite different from the natural interaction rates. Studies of data flow through the front end and DAQ systems show that with the current choices for numbers of front end buffers, saturation of front end data storage can be avoided, but without further action temporary data storage in the DAQ can become saturated, with a relaxation time of the order of seconds. This phenomenon would particularly affect rare processes, as these would find the available bandwidth for data recording utilized by more common processes. To avoid this problem, all trigger classes are classified into two groups: those corresponding to rare processes and those corresponding to common processes. Initially all activated trigger classes can generate triggers. On a signal from the DAQ, sent when the occupied temporary storage exceeds some preset 'high water mark', the common classes are temporarily disabled, thus ensuring continued available bandwidth for rare processes. When the available temporary storage has gone below some corresponding 'low water mark' the common classes are again enabled. Owing to the long relaxation time, timing is not critical, and software signals are adequate for toggling the suppression of common classes.

4.1.2 Data AcQuisition (DAQ) System

ALICE will study a variety of (physics) observables, using different beam conditions. A large number of trigger classes will be used to select and characterize the events. The function of the DAQ system is to realize the data flow from the detector up to the data storage, including the data flow to and from the HLT farm as well as sub-event and complete event building. The DAQ system also includes software packages for raw data integrity and system performance monitoring and overall control of the DAQ system.

The architecture of the data acquisition is shown in Fig. 4.1. The detectors receive the trigger signals and the associated information from the CTP, through a

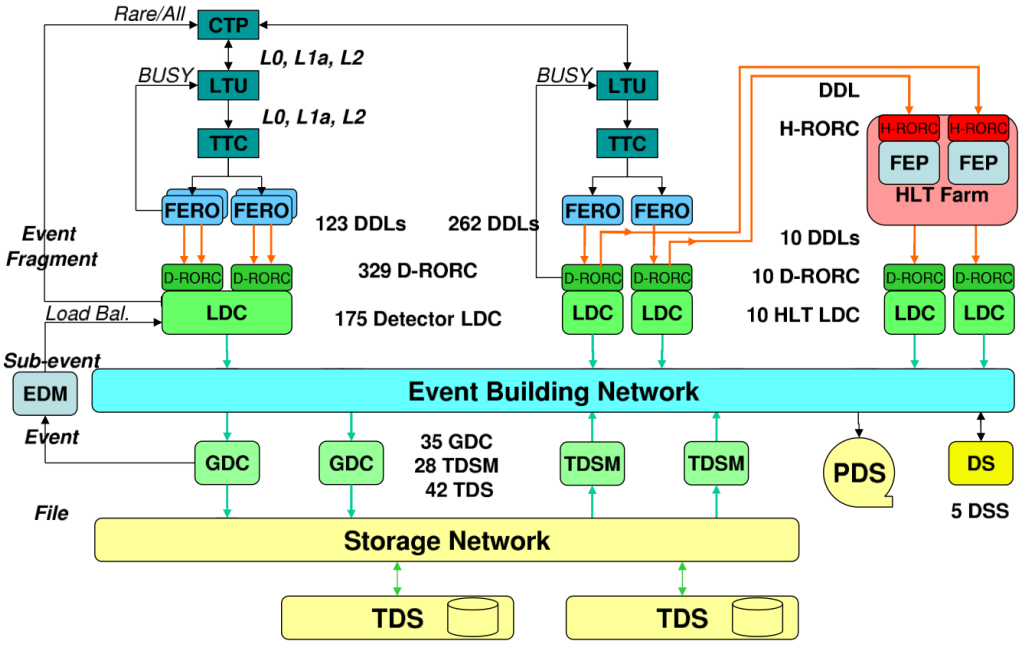

Figure 4.1: The overall architecture of the ALICE DAQ and the interface to the HLT system [237].

dedicated LTU interfaced to a TTC system. The **Front-End Read-Out** (**FERO**) electronics of the detectors is interfaced to the ALICE-standard **Detector Data Links** (**DDL**) and used both for the transfer of physics data from the detector to the DAQ and for the transfer of control commands and configuration parameters in the opposite direction. The data produced by the detectors (event fragments) are injected on the DDLs using the same standard protocol. The fact that all the detectors use the DDL is one of the major architectural features of the ALICE DAQ.

At the receiving side of the DDLs there are PCI-X based electronic modules, called '**DAQ Readout Receiver Card**' (**D-RORC**). The D-RORCs are hosted by the front-end machines (commodity PCs), called **Local Data Concentrator**s (**LDC**s). Each LDC can handle one or more D-RORCs. The D-RORCs perform concurrent and autonomous **Direct Memory Access** (**DMA**) transfers into the LDCs' memory, with minimal software intervention. The event fragments originated by the various D-RORCs are logically assembled into sub-events in the LDCs. The CTP receives a busy signal from each detector. This signal can be generated either in the detector FERO's or from all the D-RORCs of a detector. The role of the LDCs is to ship the sub-events to a farm of machines (also commodity PCs) called **Global Data Collector**s (**GDC**s), where the whole events are built (from all the sub-events pertaining to the same trigger). The GDCs archive the data over the storage network as data files of a fixed size to the **Transient Data Storage** (**TDS**). During a run period, each GDC produces a sequence of such files and registers them in the **Alice Environment** (**AliEn**) software [271].

Another major architectural feature of the ALICE DAQ is the event builder, which is based upon an event-building network. The sub-event distribution is driven by the LDCs, which decide the destination of each sub-event. This decision is taken by each LDC independently from the others (no communication between the LDCs is necessary), but it is synchronized among them by a data driven algorithm, designed to share fairly the load on the GDCs. The **Event-Destination Manager** (**EDM**) broadcasts information about the availability of the GDCs to all LDCs. The role of the GDCs is to collect the sub-events and assemble them into whole events. The GDCs also feed the recording system with the events that eventually end up in **Permanent Data Storage** (**PDS**).

In DAQ all hardware elements are coherently driven and controlled by the **DAQ software framework** (**DATE**). The DATE controls and synchronizes the processes running in the LDCs and the GDCs. It can run on an LDC, a GDC or another computer. The monitoring programs receive data from the LDC or GDC streams. They can be executed on any LDC, GDC or any other machine accessible via the network. The fundamental requirement for a detailed, real-time assessment of the DAQ machines (LDCs and GDCs), for the usage of the system resources, and for the DATE performance is addressed by the **DAQ performance monitoring software** (**AFFAIR**) package. AFFAIR gathers performance metrics from the LDCs and GDCs and performs the centralised handling of them. In addition, DAQ also includes other monitoring and control applications: **DAQ framework for the Monitoring Of Online Data** (MOOD) and **DAQ framework for the Automatic MOnitoRing Environment** (AMORE), which are used to handle the detector status, online and offline data stream, *etc.*.

4.1.3 High-Level Trigger (HLT)

The High Level Trigger [272] combines and processes the full information from all major detectors in a large computer cluster. It receives a copy of all relevant raw data via DDLs and the '**HLT Readout Receiver Card**' (**H-RORC**) into the **Front-End Processors** (**FEP**). The generated data and decisions are transferred to dedicated LDCs. Its task is to select the most relevant data from the large input stream and to reduce the data volume by well over an order of magnitude in order to fit the available storage bandwidth while preserving the physics information of interest. Therefore on-line processing is advised in order to select relevant events or sub-events and to compress the data without losing their physics content. The overall physics requirements of the HLT are categorized as follows:

trigger accept or reject events based on detailed online analysis;

select select a physics region of interest (RoI) within the event by performing only a partial readout;

compress reduce the event size without loss of physics information by applying compression algorithms on the accepted and selected data.

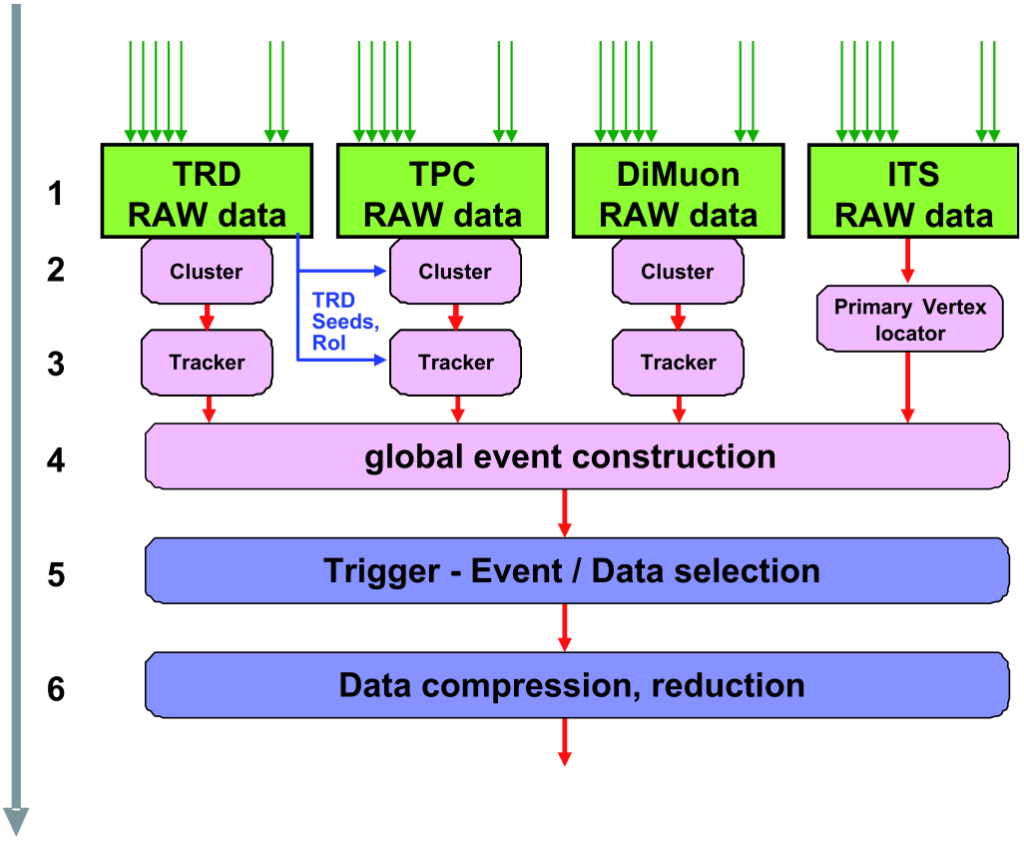

Figure 4.2: The six architectural layers of HLT [237].

The HLT implements a processing hierarchy as shown in Fig. 4.2. The raw data of all ALICE detectors are received via 454 DDLs at layer 1. The first processing layer performs basic calibration and extracts hits and clusters (layer 2). The third layer reconstructs the event for each detector individually. Layer 4 combines the processed and calibrated information of all detectors and reconstructs the whole event. Using the reconstructed physics observables layer 5 performs the selection of events or regions of interest, based on run specific physics selection criteria. The selected data is further subjected to complex data compression algorithms.

In order to meet the high computing demands, the HLT consists of a PC farm of up to 1000 multi-processor computers. The data processing is carried out by individual software components running in parallel on the nodes of the computing cluster. In order to keep inter-node network traffic to a minimum and for the means of parallelisation, the HLT data processing follows the natural hierarchical structure. Local data processing of raw data is performed directly on the **Front-End Processors** (**FEPs**), hosting the H-RORCs. Global data processing, with already reduced data, is done on the compute nodes. The trigger decision, **Event Summary Data** (**ESD**) of reconstructed events and compressed data are transferred back to the DAQ via the HLT output DDLs.

4.1.4 Detector and Experiment Control System

The primary task of the **Detector Control System** (**DCS**) is to ensure safe and correct operation of the ALICE experiment. It will provide configuration, remote control, and monitoring of all experimental equipment. Unlike most of the other online systems, the DCS is supposed to be operational, throughout all operational phases of the experiment, including shutdown periods, putting strong requirements on availability and reliability. In order to ensure a coherent control system and limit the resources needed to develop it, commonalities across the sub-detectors are exploited and common solutions are developed and used wherever possible.

The hardware architecture is divided into three layers: the supervisory layer (PCs) provides the user interface and the connection to disk servers or ALICE external systems; the intermediate control layer (PCs and PLCs) will collect and process information from the lowest (field) layer via field buses or the Local Area Network and forward them to the supervisor (and vice versa). The field layer contains all field devices (e.g. power supplies), sensors and actuators.

The software architecture is built as a tree-like structure representing the structure of sub-detectors, their sub-systems and devices. The basic building blocks for implementation of the controls hierarchy are Control Units (that model the behaviour and interactions between components) and Device Units (that drive the equipment to which they correspond). Like ECS, DAQ, and HLT, the DCS uses an implementation based on **Finite-State Machines** (**FSMs**). These provide an intuitive and convenient mechanism to model the functionality and behaviour of a component. The architecture allows for the implementation of hierarchies of FSM working in parallel providing rule-based automation and error recovery.

The software framework is based on the commercial **SCADA** (**Supervisory Controls And Data Acquisition**) system PVSSII. The communication with the experiment's equipment can use a direct interface to PVSSII as well as alternatives based on industrial standards (OPC) or a specific CERN development (DIM).

As well as controlling all sub-detector equipment, the DCS will also be the interface to the various external services needed for the operation of the experiment such as gas, cooling, electricity, safety, *etc.*.

The **Experiment Control System** (**ECS**) provides a unified view of the experiment and a central point from where all operations are initiated and controlled. It also has to allow independent concurrent activities on parts of the experiment (at the detector level) by different operators. Finally, it has to coordinate the operations of the specific control systems active on a lower level: the detector control, the trigger control, the DAQ run control and the High-Level Trigger control.

Two categories are used to model operations, namely the Activity Domain and the Detector. They are interrelated in the experiment, forming a two-dimensional space upon which the ECS operates. Each Activity Domain extends across the Detectors and, conversely, partitioning the system in independent sets of Detectors implies cutting across all the Activity Domains.

At the centre of the ECS is a database, where all resources are described. The **Experiment Control Agent** (**ECA**) is a utility that facilitates the manipulation

of the database. Resources are allocated by the **Partition Control Agent** (**PCA**), whichs creates a working environment for the **Detector Control Agent** (**DCA**), in such a way that only allocated resources are seen by the sub-systems.

The technology is implemented via FSMs, which provide an intuitive way of representing a behavioral model of a real object and provide a natural way for communication, based on the control of objects located in a remote Activity Domain.

4.2 ALICE Offline Project

The role of the Offline Project is the development and operation of the framework for data processing. This includes tasks such as simulation, reconstruction, calibration, alignment, visualization and analysis. These are the final steps of the experimental activity, which aimed at interpreting the data collected by the experiment and at extracting the physics content. In a large and complex experiment as ALICE, this implies the development and operation of a quite diverse set of environments.

4.2.1 ALICE Computing Grid

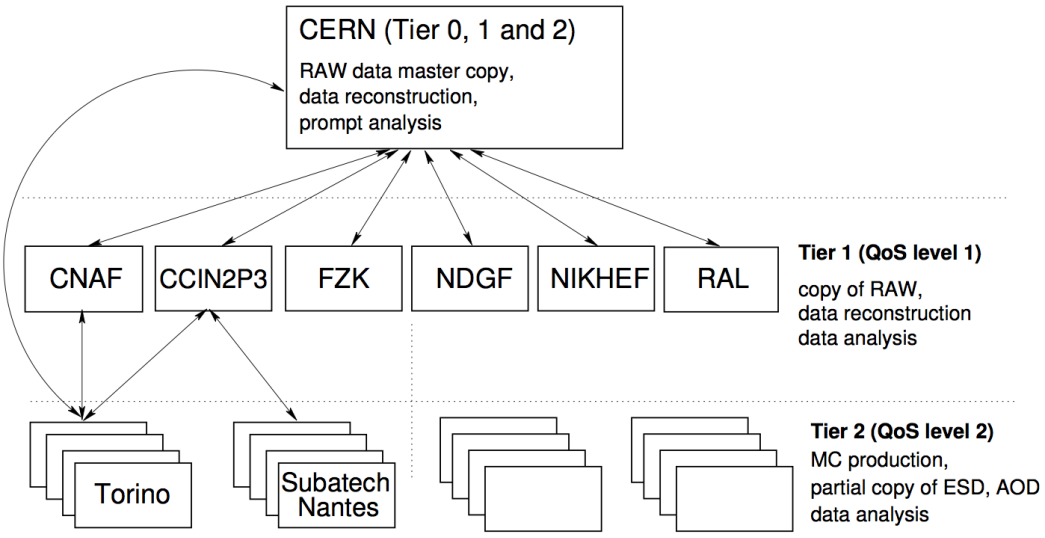

Figure 4.3: Schematic view of the ALICE offline computing tasks in the framework of the tiered MONARC model. Taken from Ref. [273].

The distributed computing infrastructure serving the ALICE experimental programme (also the other experiments at LHC) is coordinated by the **Worldwide LHC Computing Grid** (**WLCG**) project. The WLCG computing infrastructure is, by nature, highly hierarchical, as shown in Fig. 4.3. All real data originate from CERN, with a very large computing centre called Tier-0. Large regional computing

centers, called Tier-1, share with CERN the roles of a safe storage of the data on high reliably storage media and to perform the bulk of the organized processing of the data. Smaller centers, called Tier-2, are logically clustered around the Tier-1's. The main difference between the two kind of centers is the availability of high-reliability mass-storage media at Tier-1's. Tier-2's use the 'closest' Tier-1 to store the data that they produce. The major role of Tier-2's is simulation and end-user (sometimes also called chaotic) analysis.

Within the WLCG structure, a centre, to qualify as a Tier-1 or Tier-2, has to sign and follow up the corresponding, **Service Level Agreement** (**SLA**), which specifies **Quality-Of-Service** (**QoS**) and intervention delays. Smaller centres, corresponding to a departmental computing centre and sometimes called Tier-3's, contribute to the computing resources but there is no definite role or definition for them.

The data processing strategy and the Tier computing centers hierarchy derive from the **Monarch model** [274]. During proton-proton collisions the data, recorded at an average rate of 100 MB/s, are written by the DAQ on a disk buffer at the CERN (Tier-0) computing centre, where the following four activities proceed in parallel on the RAW data:

1. copy to the CASTOR tapes;

2. export to the Tier-1 centers to have a second distributed copy on highly-reliable storage media and to prepare for the successive reconstruction passes that will be processed in the Tier-1 centers;

3. first pass processing at the Tier-0 centre, this includes: reconstruction, production of calibration and alignment constants and scheduled analysis;

4. fast processing of selected sets of data, mainly calibration, alignment, reconstruction and analysis on the CERN **Analysis Facility** (**CAF**) [275].

During nucleus-nucleus runs, as the rate of data acquisition is so high that an excessive amount of computing resources and network bandwidth would be necessary for quasi-online processing. Therefore the processing of the nucleus-nucleus RAW data proceeds as follows:

1. registration of the RAW data in CASTOR;

2. partial export to the Tier-1 centers to allow remote users to examine the data locally;

3. partial first pass processing at the Tier-0 centre to provide rapid feedback on the offline chain;

4. fast processing, mainly calibration, alignment, reconstruction and analysis on the CAF.

The implementation of the above model relies on a distributed computing infrastructure enabled by Grid Middleware. Since 2001, ALICE developed a set of Middleware services, AliEn [276], which implements the above model. With the development of various large Middleware projects, it became possible to replace some of these services with the services offered by these projects. In the resulting architecture, the user interacts with the Grid via the AliEn **User Interface** (**UI**), and the services are offered by a combination of AliEn Middleware, providing high-level or ALICE specific services, and the Middleware installed on the computing centre, providing basic services. The key components and services of the AliEn are:

authentication & **authorization** this allows the user to access the Grid to analysis the data and submit the jobs for simulation and analysis;

job management this part includes the auditing services and workload management, to validate the jobs on Grid and optimizes the queue of jobs by taking into account job requirements based on input files, CPU time, architecture, disk space, *etc.*; the workload management service can modify the job's JDL [3] entry by adding or elaborating requirements based on the detailed information it gets from the system like the exact location of the dataset and replicas, client and service capabilities. When a job requires several files, the workload management systems 'splits' the job in several sub-jobs, each of them dealing with files that are co-located at the same **Storage Element** (**SE**);

file catalogues input and output associated with any job is registered in the AliEn **File Catalogue** controled by the **Data management**; a virtual file system in which a file or a file collection (data set) is identified by a **GloballyUnique IDentifier** (**GUID**); file catalogue does not own the files, it only keeps an association between the **LogicalFileName** (**LFN**) and (possibly more than one) **Physical File Name** (**PFN**) on a real file or mass storage system; PFNs describe the physical location of the files and include the name of the AliEn storage element and the path to the local file; the system supports file replication and caching and uses file location information to schedule jobs for execution.

AliEn also includes the **Application Programming Interface** (**API**) services to provide an AliEn interface in ROOT (see Sec. 4.2.2), as well as the Information and Monitoring services used to check and publish the status of Grid under the MonALISA [4] framework [278].

4.2.2 AliRoot Framework

The ALICE offline framework, AliRoot [279], is shown schematically in Fig. 4.4 [5] Its implementation is based on Object-Oriented techniques for programming and, as

[3] The AliEn user interface uses the **Condor ClassAds** [277] as a **Job Description Language** (**JDL**).

[4] MonALISA=MONitoring Agents using a Large Integrated Services Architecture

[5] Before 2012, the ALICE collaboration had 4 **Physics Working Group**s (**PWG**s):

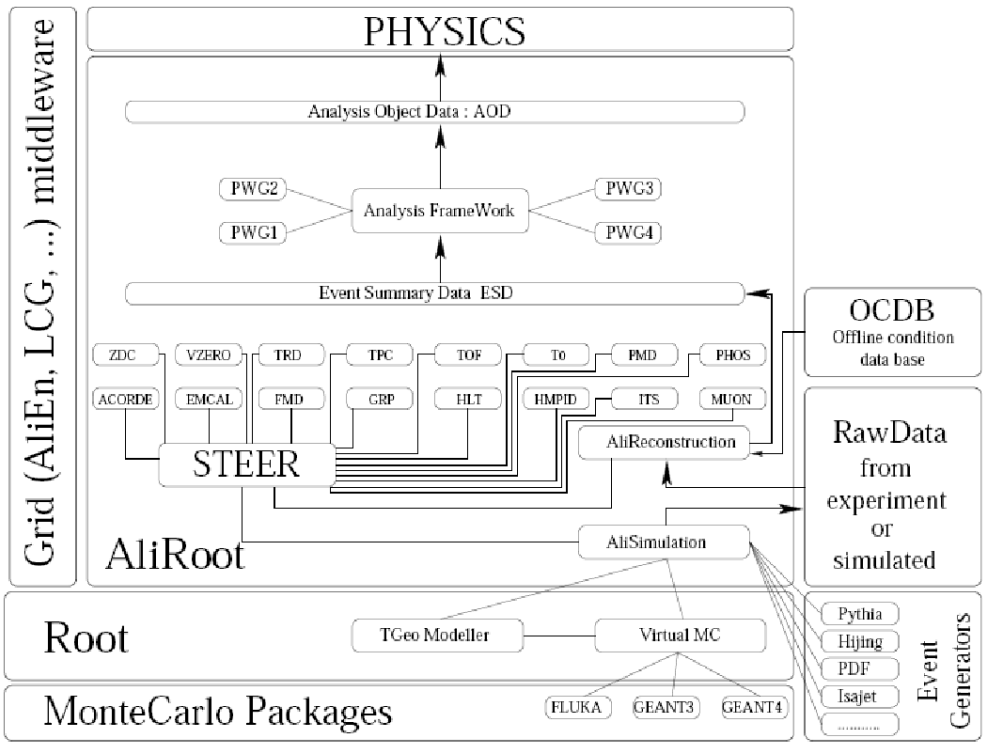

Figure 4.4: Schematic view of AliRoot framework.

PWG1 ALICE Detector Performance,

PWG2 Soft Physics,

PWG3 Heavy Flavour an quarkonia,

PWG4 High p_t and Photons,

as shown in Fig. 4.4. PWG3-MUON is one sub-group under the PWG3 which focus on the open heavy flavours measurements via (di)muons, the quarkonia and vector bosons (low mass resonances, $W^{\pm}$ and Z^0) studies according to their dimuon decays. Since 2012, due to the increasing physics topics in the ALICE collaboration, the physics working groups are splitted from 4 to 8:

PWG-PP Physics Performance,

PWG-CF Correlations Fluctuations and Bulk,

PWG-DQ Dileptons and Quarkonia,

PWG-HF Heavy Flavour,

PWG-GA Gamma (γ, photo) and π^0,

PWG-LF Light Flavour spectra,

PWG-JE Jets,

PWG-UP Utra-peripheral, Diffractive, Cosmics and pp First Physics.

The old PWG3-MUON, is now separated in four sub-groups:

PWG-DQ-LMmumu Low Mass dimuon,

a supporting framework, on the ROOT system [280], complemented by the AliEn system which gives access to the computing Grid. These fundamental technical choices result in one single framework, entirely written in C++, with some external programs (hidden to the users) still in FORTRAN.

The AliRoot framework is used for simulation, alignment, calibration, reconstruction, visualisation and analysis of the experimental data. AliRoot has been in continuous development since 1998. In the preparation phase, before the start of data taking, it was used to evaluate the physics performance of the full ALICE detector and to assess the functionality of the framework towards the final goal of extracting physics from the data. The role of the AliRoot framework is shown schematically in Fig. 4.5. The kinematics tree containing, for example, the physics processes at the parton level and the results of the fragmentation (primary particles) is created by event generators. The data produced by the event generators contain full information about the generated particles: type, momentum, charge, and mother-daughter relationship. During the transport, the response of the detectors to each crossing particle is simulated. The hits (energy deposition at a given point and time) are stored for each detector. The information is complemented by the so called 'track references' corresponding to the location where the particles are crossing user defined reference planes. The hits are converted into digits taking into account the detector and associated electronics response function. Finally, the digits are stored in the specific hardware format of each detector as raw data. At this point the reconstruction chain as implemented for the real data is activated. To evaluate the software and detector performance, simulated events are processed through the whole cycle and finally the reconstructed particles are compared to the Monte Carlo generated ones.

The basic design features of the AliRoot framework are re-usability and modularity. Modularity allows replacement of well defined parts of the system with minimal or no impact on the rest. For example, it is possible to change the event generator or the transport Monte Carlo without affecting the user code. Elements of the framework are made modular by defining an abstract interface to them. The codes from the different detectors are independent so that different detector groups can work concurrently on the system while minimizing the interference. The adopted development strategy can handle design changes in production code for cases when new elements are introduced. Re-usability is the protection of the investment made by the programming physicists of ALICE. This investment is preserved by designing a modular system and by making sure that the maximum amount of backward compatibility is maintained while the system evolves.

The ROOT framework, upon which AliRoot is developed, provides an environ-

PWG-DQ-Jpsi2mumu $J/\Psi \rightarrow \mu^{-}\mu^{+}$,

PWG-DQ-Upsilon2mumu $\Upsilon \rightarrow \mu^{-}\mu^{+}$,

PWG-HF-HFM Heavy Flavour Muons.

The analysis for this four new sub-groups are all based on the data from ALICE MUON Spectrometer, and there still are some common tasks shared between them. In order to facilitate the analysis we keep still them together, as in Fig. 4.6.

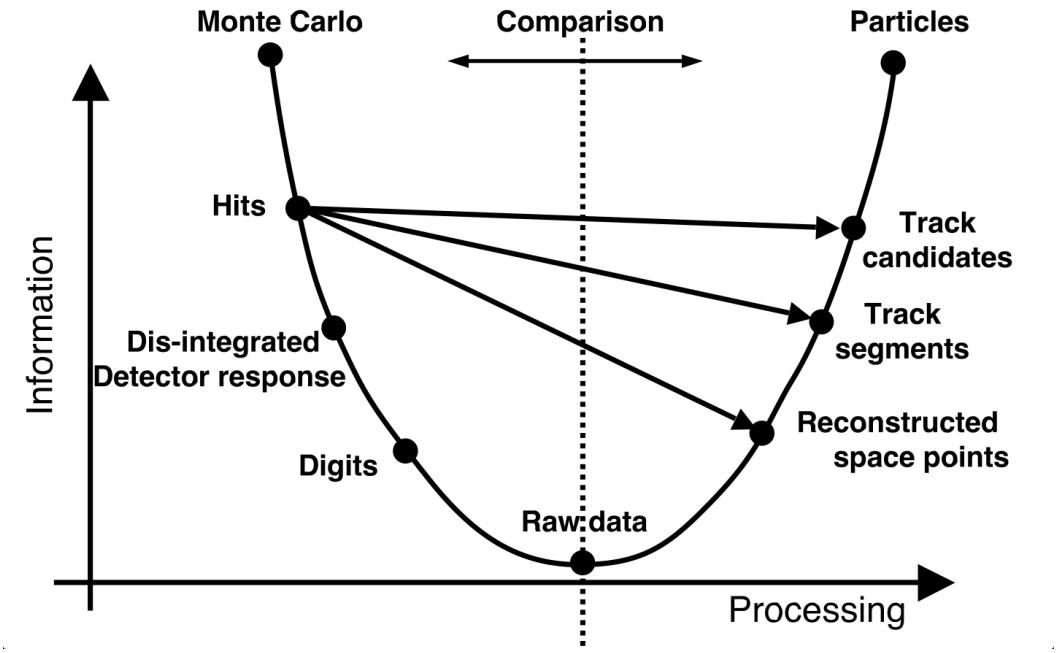

Figure 4.5: Data Processing Framework of AliRoot

ment for the development of software packages for event generation, detector simulation, event reconstruction, and data analysis. The ROOT system was extended with ALICE specific classes and libraries grouped in modules. These libraries are loaded dynamically and the contained classes share the same services with the native ROOT classes, including object browsing, I/O, dictionary and so on. The ROOT system is interfaced with the Grid Middleware in general and, in particular, with the ALICE-developed AliEn system. In conjunction with the PROOF [281] system, which extends ROOT capabilities on parallel computing systems and clusters, this provides a distributed parallel computing platform for large-scale production and analysis.

4.3 Analysis Framework of MUON

Analysis is the final operation performed on the data and the one finally destined to extract physics information. In the ALICE Computing Model, the analysis starts from the ESD produced during the reconstruction step. Analysis tasks produce **Analysis Oriented Data** (**AOD**) with standard content condensed from the ESD as well as AODs for specific analyses. Further analysis passes can start from condensed AODs.

An analysis framework (**AliAnalysis**) was developed for end-user analysis. The **AliAnalysis** is based on **TSelector** and **TTask** classes in ROOT, it was implemented such that the user code is independent of the used computing scheme (local, PROOF or Grid). It also allows to include Monte Carlo information into the analy-

sis chain so that it can be used for efficiency and acceptance correction studies. The analysis framework permits the splitting of each analysis into a tree of dependent tasks. Each task is data oriented: it registers the required input data and publishes its output. The optimization of the execution chain is done after the registration of all tasks included in the analysis.

4.3.1 Overall View

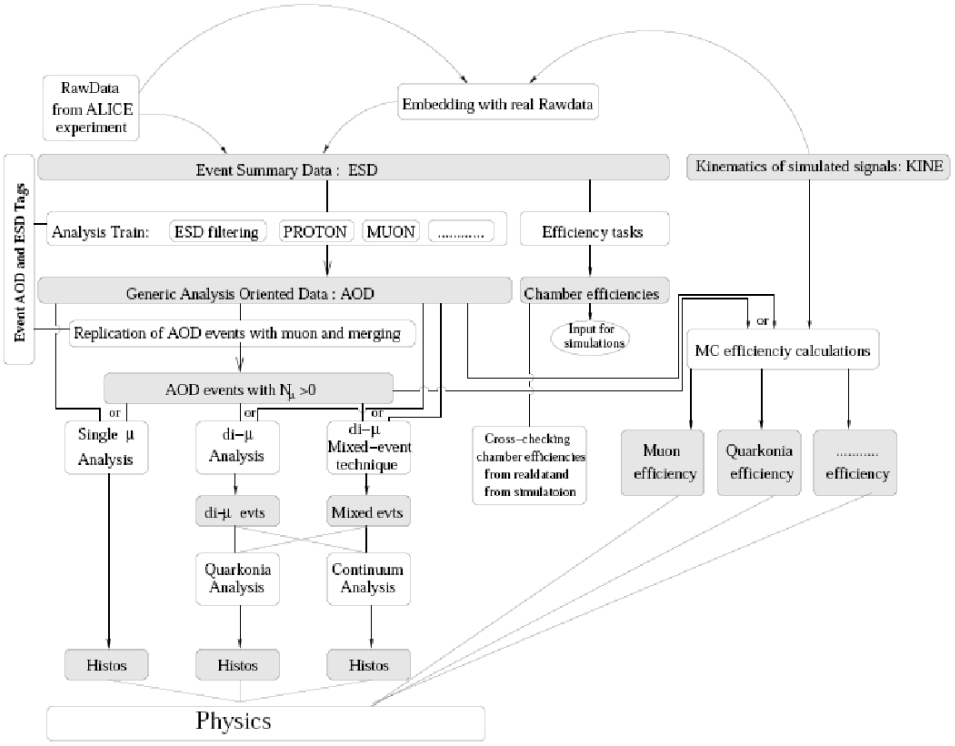

Figure 4.6: Schematic view of MUON analysis framework [282].

Fig. 4.6 shows the schematic view of the MUON analysis framework, extracted from [282]. To illustrate this framework more clearly, we classify it into three independent analysis chains: the filter & tag chain, the analysis chain and the correction chain. The filter & tag chain provide the inputs for the analysis chain, and the final physics results are gotten by merging the outputs from the analysis chain and correction chain together.

The filter chain starts from the ESD, obtained by reconstructing the RAW data with the calibration and alignment. There are two basic filter tasks named **AliAnalysisTaskESDfilter** and **AliAnalysisTaskESDMuonFilter** used to extract the physics information from the ESD and fill them into the AOD, according to the cuts set in the filters. The **AliAnalysisTaskESDfilter** filters the ESD event

except the MUON one. It records the information which will be directly used for the physics analysis from the AOD. Also, during the filter procedure, there will be the pre-construction for some physics observables, like jets, multi-body decay and cascade decay, *etc.*, and these results will be recorded in the corresponding branches of the AOD tree.

The filter will both reduce the size of the AOD and make the analysis based on the AOD more straightforward. On the other hand, the muon analysis just needs inputs from the MUON spectrometer, SPD, V0 (T0) and ZDC. It is independent on the other detectors in the central barrel [6]. Also, not all the events include the muon tracks (in particular in proton-proton collisions); as mentioned in Sec. 3.4.5.2, the MUON spectrometer can take data alone with other detectors and build the MUON triggered events. In this case the ESD MUON filter, **AliAnalysisTaskESDMuonFilter**, is separated from the global filter. It can be run both with the global filter to build the full AOD event and alone to only fill the information for muon analysis in the AOD. Additional, for muon analysis, there is another filter, to record events which have at least one or two muon tracks in the AOD and build the MuonAOD and/or diMuonAOD. This filter will decrease the file size further and make the (di)muon analysis faster. Normally, the filter tasks are run on the ALICE official train, several parallel tasks can also be run together with them to make the detectors QA, to give preliminary distributions and to create the special AODs similar as the (di)MuonAOD for special physics. The events tag (like event multiplicity, number of tracks in special detectors) is build in this step. They are used to select the interesting events for the analysers.

The analysis chain can be presented both in the ALICE official train and by individual analysers. The tasks in the analysis chain, normally, are created by the individual analysers for their specific physics requirements. As a example, we will give a detailed introduction for our muon analysis task, in the next section (Sec. 4.3.2).

The correction chain are used to get the correction efficiency for the final observables. The correction efficiency for a given final observable includes two parts, the reconstruction efficiency and the acceptance efficiency. The reconstruction efficiency depends on the dead channels of the detector read out, the misalignment *etc.*. The first task to build the efficiency is to record these informations in the **Offline Calibration Data-Base** (**OCDB**), for simulating the detector response in the next step. The detector occupancy will also affect the reconstruction efficiency. The probability of different particles overlapping in the same detector region increases with the event multiplicity. This effect becomes more important in Pb–Pb collisions. One way to study the occupancy dependent reconstruction efficiency is to embed the simulated physics signal with the OCDB built from data into the real RAW data with different multiplicities and to perform the reconstruction for these embedding events. The occupancy dependent efficiency, then, is gotten by measuring the re-

[6] As mentioned in Sec. 3.4, the study of electron–muon coincidences needs the combination of the information from both MUON spectrometer and the central barrel detectors. Therefore, one needs both the special trigger during the data taking and the independent filter to exact the signals.

construction efficiency for the embedding signals. The acceptance efficiency is due to the cuts used during the analysis. The estimate of this efficiency could be very sensitive to the input shapes of the signal used for the simulation. The efficiency matrix can be obtained via an iterative approach [283], but this needs a large cost of CPU time. During our analysis, we choose an alternative method to estimate this efficiency, the detailed illustration will be presented in the corresponding section of our analysis later.

4.3.2 Muon Code for HF Analysis

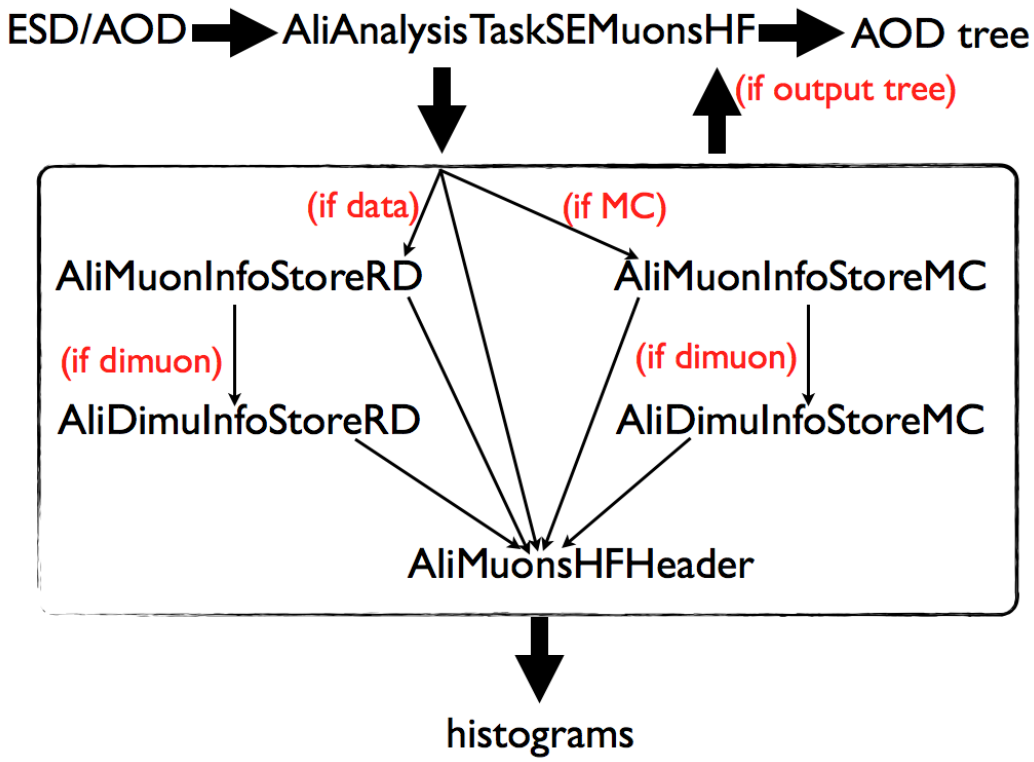

Figure 4.7: Schematic view of the analysis tasks for the study of heavy flavours with muon data.

The physics topic presented in this thesis is the measurement of open heavy flavours via their single muon and/or dimuon decay channels in the ALICE MUON spectrometer. The design of the analysis code should satisfy this physics purpose.

As shown in Fig. 4.6, ESDs are created after data reconstruction. The ESD filter transfers the information from ESDs to AODs. Generally, the analysis is encouraged from AODs because, thanks to their small size, the analysis is more straightforward and faster. However, in some cases, the analysis has to be carried out at the ESD level:

- AODs are usually produced a bit later than ESDs. Therefore, in order to have a quick look at the data, it is sometimes mandatory to analysis the ESDs;
- after filtering, AODs do not include all information present at the ESD level. It is therefore sometimes useful to analyze the ESDs in order, for instance, to understand the background level in the data and to establish a strategy to remove this background by means of cuts on variables stored in the ESDs;
- in some cases, ESDs are not converted to AODs in order to save additional CPU time. This mostly happens for simulated data.

For the three reasons above, it is required that the analysis code must be able to treat both ESDs and AODs as input.

The analysis code should also be able to treat Monte-Carlo data at two levels: reconstructed data (like for real data) and MC truth. This is particularly important in order to build efficiency correction matrices. This requires that, depending on whether the analysis is based on data or simulations and according to the outputs from the analysis task, the structure can change dynamically in order to only include the reconstructed information or include simultaneously the additional MC truth information.

These requirements are essential for the analysis using single muon and dimuon channels. In order to save CPU time and to optimize the size of the output data, one generally studies the single muon channel and the dimuon channel independently. The analysis tasks should therefore be able to run in three different modes: single muon analysis, dimuon analysis or both.

The muon analysis code design is shown in Fig. 4.7. In order to fulfill all above requirements, it includes six modules:

AliAnalysisTaskSEMuonsHF the main task to implement the ALICE analysis framework;

AliMuonInfoStoreRD extracts and stores the muon tracks information from data, and implement the single muon selection cuts;

AliDimuInfoStoreRD combines the single muon information stored in AliMuonInfoStoreRD into dimuon pairs. In order to avoid to use again of the storage ressources, it just saves the hyperlinks to the corresponding two single muons. The methods for calculating the dimuon pair kinematics and for implementing the dimuon pair selection cuts are performed in this module;

AliMuonInfoStoreMC is derived from AliMuonInfoStoreRD, and deals with simulated inputs. The reconstructed information saved in AliMuonInfoStoreRD is in the same form as that from reconstructed (real) data. The additional MC truth information is extracted and stored in this module. It includes a method to distinguish muons originating from different sources. This makes use of a switch allowing to loop over the muon mothers at parton level. Note that the use of this switch is restricted to proton-proton simulated data where

there is at most one heavy quark pair generated in each event. In Pb–Pb collisions, where several heavy quark pairs are produced, it would require too many loops and would increase the CPU time significantly;

AliDimuInfoStoreMC similar to AliMuonInfoStoreMC but it is derived from AliDimuInfoStoreRD. It saves the two hyperlinks to the AliMuonInfoStoreMC objects. The methods for identifying different dimuon sources are implemented here;

AliMuonsHFHeader extracts and stores the information at event level, like the event trigger mask, vertex position and collision centrality *etc.*. It is also used to collect the information stored in the single muon or dimuon InfoStore to fill the (di)muon distribution histograms according to the corresponding running mode with the (di)muon selection cuts set in the (di)muon InfoStore.

The whole analysis chain includes the following steps:

1. the nature of the inputs (ESDs or AODs) is determined in AliAnalysisTaskSE-MuonsHF automatically;
2. the input event is pushed into AliMuonsHFHeader. It extracts and saves the information at event level;
3. loop over the muon tracks and record their information with AliMuonInfoS-toreRD or AliMuonInfoStoreMC, depending if the input is data or simulation;
4. if the dimuon mode is required, additional loops to combine the MuonInfo-StoreRD/MC in DimuInfoStoreRD/MC are activated in AliAnalysisTaskSE-MuonsHF;
5. finally, all actived InfoStore modules are pushed in AliMuonsHFHeader, where the distributions of (di)muons are filled according to the selection cuts at both event level and (di)muon level.

The five modules in the box shown in Fig. 4.7 construct a ROOT tree containing the muon event. If the corresponding switch is turned on, the tree level events will be written to the output as a external AOD tree, which can be read by the standard AOD class, **AliAODEvent**, for the local analysis. This analysis task has been implemented in the ALICE official analysis train, as shown in Fig. 4.6. It is run and allows to get the distribution of (di)muons on a weekly basis. As outputs based on trees or n-tuples are forbidden to save disk storage, the flag for output the "own" AOD tree is turned off in the official analysis train. Our specific analysis is fully based on these "own" AODs.

In addition, in order to measure the flow of muons from heavy flavour decays, we also updated the ALICE flow analysis framework. It will be introduced in Sec. 9.2.2.

Part III

Measurements of Open Heavy Flavours with the Muon Spectrometer

Chapter 5

Performance Study of Open HF Measurements

The capabilities of the ALICE muon spectrometer for reconstructing the open B-hadron production cross section in Pb–Pb collisions at $\sqrt{s_{\rm NN}} = 5.5$ TeV was studied in [284]. Here, we discuss the performance of the ALICE muon spectrometer to measure the inclusive production differential cross sections of both the open charm and the open beauty hadrons from single muons and unlike-sign dimuons in pp collisions at $\sqrt{s} = 14$ TeV. These studies were started 2008 and finished before the first data taking period with ALICE in December 2009. We start with a simple (clean) case by considering that the background is perfectly subtracted. This also allows to test the algorithms to disentangle charm and beauty components and to convert the production cross section at the (di)muon level to the one at the hadron level. Then a realistic background will be considered in order to discuss the muon sources and possible methods for background subtraction. The results related to this analysis are published in two ALICE internal notes [285, 286].

5.1 Analysis Inputs

In order to prepare the full analysis chain for the measurement of the open heavy flavour hadron cross section in pp collisions at $\sqrt{s} = 14$ TeV, realistic high statistics simulated data were required. For this purpose we used a high statistics simulation produced within **Physics Data Challenge 2006** (**PDC06**) via the Computing Grid.

5.1.1 Simulation Strategy

The PDC06 sample is based on full AliRoot simulations of pp collisions, including the response of the detector via GEANT3 [287], from generation to reconstruction and production of Event Summary Data (ESD). Each event consists of a cocktail with a minimum bias event from PYTHIA Monte-Carlo generator [288] and quarkonium signals: J/ψ, ψ', Υ(1S), Υ(2S), and Υ(3S) (it has been checked that quarkonium production in the used PYTHIA version, PYTHIA 6.2, was negligible). PYTHIA events were generated with the global QCD process option **MSEL**= 1, the so-called **ATLAS tuning** for multiple interactions [289] and the CTEQ5L set of parton distribution functions [158]. The main parameter that should be optimized in PYTHIA is the $p_{\rm t}^{\rm hard}$ threshold. A minimum $p_{\rm t}^{\rm hard}$ of 2.76 GeV/c is in particular mandatory to reproduce the $p_{\rm t}$ distribution of $\rm c\bar{c}$ pairs of NLO pQCD

calculations implemented in the HvQMNR program [151]. In such conditions, as shown in Tab. 5.1, the charm production cross section is underestimated by a factor of about two whereas the beauty production cross section agrees within errors with NLO HvQMNR calculations [133]. The input production cross sections of charmonium and bottomonium states (also shown in Tab. 5.1) have been provided by the **Colour Evaporation Model** (**CEM**) [290]. They include direct production and feed-down from higher mass resonances. Note that it has been shown that the CEM predictions are in agreement with the experimental data at Tevatron energies for bottomonium production and underestimate the charmonium cross sections by about a factor of two [291]. The rapidity distributions of the different quarkonium states are obtained from a parameterization of the CEM predictions whereas the p_{t} distributions are an extrapolation to $\sqrt{s} = 14$ TeV of the ones measured by the CDF experiment at $\sqrt{s} = 1.96$ TeV. Finally, the default **Lund String Model** [292] included in PYTHIA is used for the hadronisation.

	$\mathrm{c\overline{c}}$	$\mathrm{b\overline{b}}$	J/ψ	ψ'	$\Upsilon(1S)$	$\Upsilon(2S)$	$\Upsilon(3S)$
σ (μb)	5677	490	49.44	7.67	0.989	0.502	0.228

Table 5.1: Heavy flavours and quarkonia production cross sections in pp collisions at $\sqrt{s} = 14$ TeV simulated in PDC06.

In order to reduce the computing time and to accumulate sufficient statistics for large muon p_{t} or high dimuon invariant mass (M_{inv}) studies, a software trigger is applied at the generation level. It requires a minimum muon multiplicity (at least one or two muons, respectively) in the acceptance of the muon spectrometer and a p_{t} threshold of 0.5 GeV/c on each muon. With this trigger at software level, the background of muons from light hadron decays (mainly pions and kaons) is suppressed strongly. This is due to the fact that in the AliRoot simulation framework, for a better emulating the detector response, the decays of the short-life and long-life particles are treated differently. The life-time of open heavy flavour hadrons ($c_\tau = 311.8$ μm for D-hadrons and $c_\tau \simeq 500$ μm for B-hadrons typically) is very short and they treated as short-time particles in the simulation. The decay of this kind of particles is played by the internal decayer at the generation level before pushing all particles into the transport code (*eg.* GEANT). If a semi-muonic decay of open heavy flavour hadrons occurs in a given simulated event and the muon satisfies the p_{t} threshold, it will be recorded and pushed into the transport code to finish the whole decay chain. On the other hand, the life-time of pions ($c_\tau = 7.9$ m) and kaons ($c_\tau = 3.7$ m) is quite large. Pions and kaons are treated as long-life particles in the simulations. Their decay is handled by the external decayer in the transport code but not at the generation level. In this case, if there are only pions and/or kaons generated in a given event but no open heavy flavour hadrons, this event will be rejected by the trigger at software level since the semi-muonic decay of pions and kaons is not present in this stage. According to this principle, almost all events without the semi-muonic decay of open heavy flavours in the acceptance of muon

spectrometer are rejected by the trigger at the software level.

In addition to the muon spectrometer, the response of the sub-detectors, V0, T0, SPD, TOF, ZDC, FMD and PHOS, which are required for other physics topics are also simulated. Finally, a total number of about $1 \cdot 10^6$ ($2.5 \cdot 10^6$) pp events with single muon (dimuon) software trigger are available for the analysis. The simulations cost $\sim$ 1400 and $\sim$ 17000 CPU days for single muon and dimuon productions, respectively, and used $\sim$ 1.3 TB disk space for the storage.

5.1.2 Efficiency Correction

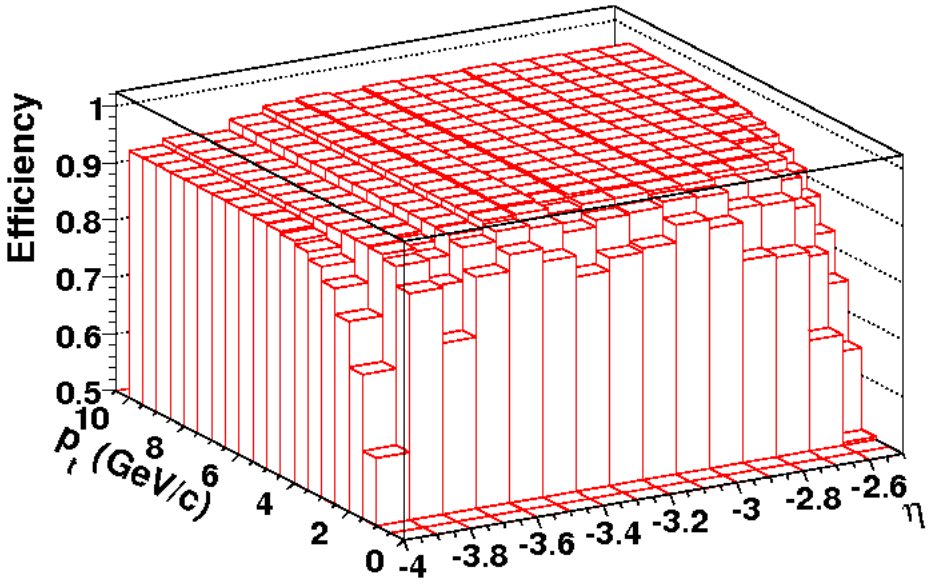

Figure 5.1: Single muon reconstruction efficiency as a function of p_t and η.

The reconstruction efficiency correction for single muons is performed by means of full AliRoot simulations modeling the full response of the muon spectrometer. It is evaluated using an iterative procedure. The process first consists in simulating an uniform muon p_t distribution in the acceptance of the muon spectrometer. Then, the same reconstruction procedure as for PDC06 data is applied to these simulated data. The reconstruction efficiency is determined by computing the ratio of reconstructed muon tracks to the simulated ones. For the next iteration, a weight technique allows to use a realistic p_t distribution, similar to the one from PDC06 production, for the final reconstruction efficiency correction. A detailed description of the procedure can be found in [293]. The resulting reconstruction efficiency as a function of p_t and pseudo-rapidity (η), without trigger consideration, is displayed in Fig. 5.1. One can notice that in the acceptance of the ALICE muon spectrometer ($-4 < \eta < -2.5$)

and for $p_{\mathrm{t}} > 2$ GeV/c, the global reconstruction efficiency amounts to about 95%.

The implementation of this efficiency correction for single muons is straightforward. It consists in weighting each muon track with the inverse of the efficiency $1/eff(p_{\mathrm{t}}, \eta)$ corresponding to the given muon track located in the (η, p_{t}) plane. In the dimuon M_{inv} distribution, the correction is done by weighting the given dimuon pair with $1/eff(p_{\mathrm{t},1}, \eta_1) \times 1/eff(p_{\mathrm{t},2}, \eta_2)$ from individual tracks 1 and 2, respectively. The correlations between the two muons are not taken into account in the correction of the dimuon M_{inv} distribution.

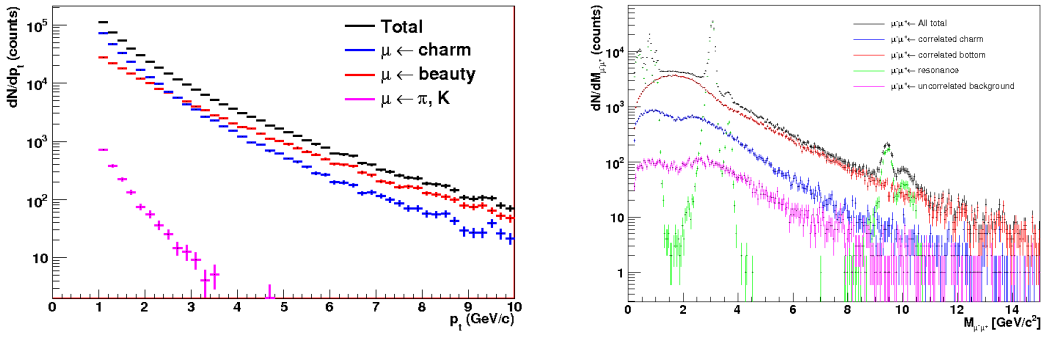

Figure 5.2: The single muon p_{t} distributions (left) and unlike-sign dimuon M_{inv} distributions (right) from PDC06 after efficiency correction.

Fig. 5.2 shows the single muon p_{t} distributions (left) and unlike-sign dimuon M_{inv} distributions (right) from PDC06, after the efficiency correction is applied. A sharp p_{t} cut of 1 GeV/c is used in the single muon p_{t} spectrum in order to remove the bias for the muon trigger threshold of $p_{\mathrm{t}} > 0.5$ GeV/c at generation level. In the case of the dimuon M_{inv} distributions, in addition to the acceptance cuts ($-4 < \eta < -2.5$ and $p > 4$ GeV/c a p_{t} threshold of 1.5 GeV/c is applied on the reconstructed muon tracks. The resonance components include: low mass resonances (η, ρ/ω and ϕ), charmonia (J/Ψ, Ψ') and bottomonium states. Note that in addition to prompt J/Ψ and Ψ', also those from B-hadron decays are taken into account in the corresponding resonance signals. The combinatorial background includes uncorrelated unlike-sign muon pairs from charm and beauty decay and from the decay of light hadrons. Since the PYTHIA setting used in the PDC06 simulation underestimates the charm production cross section by a factor of ~ 2 (Tab. 5.1), as compared to the NLO pQCD calculations, the charm components in (di)muon distributions have been scaled accordingly. Due to the (di)muon trigger at the software level, the background of muons from light hadrons (mainly, pions and kaons) is strongly suppressed in both the single muon p_{t} distribution and dimuon M_{inv} distribution. As a consequence, the single muon p_{t} spectrum is dominated by muons from D and B hadrons and, dimuons from open beauty decays is the main component in the dimuon M_{inv} spectrum. Finally, the statistics available in the PDC06 production allows to exploit the muon p_{t} distribution up to ~ 10 GeV/c

and the dimuon $M_{\rm inv}$ distribution up to ~ 15 GeV/c^2.

5.2 Sources of (di)muons from HF

In the following, we will ignore the background in both the single muon $p_{\rm t}$ distribution and the dimuon $M_{\rm inv}$ distribution [1] and we will focus on the components of muon from the decays D and B hadrons. Then these two components will be separated via a combined fit. Before to apply the combined fit, it is important to understand how to describe the shapes of the different muon components. The situation is a little bit easier with the single muon $p_{\rm t}$ distribution. Heavy quarks are produced in hard scattering processes. According to pQCD, the cross section in this process follows a power law: $\mathrm{d}\sigma/\mathrm{d}p_{\rm t} \propto 1/p_{\rm t}^{n}$ (as in Eq. 1.21). Then, the single muon distributions from both open charm and open beauty hadrons can be described by a power law:

$$f_{\rm c/b}^{\mu^{\pm}} = \frac{A}{(B^2 + p_{\rm t}^2)^n}, \tag{5.1}$$

The additional parameters A and B are used to parameterize the effects from the fragmentation and decay processes. The shape of the dimuon $M_{\rm inv}$ distributions from open heavy flavours is more complicated. In order to find the appropriate shape functions, we should perform a detailed study of the dimuon sources from open heavy flavours. There are two ways to form a correlated dimuon pair from open heavy flavours: the decay pair mode and the decay chain mode. For instance, regarding the beauty production, in addition to the direct semi-muonic decay $\mathrm{B} \to \mu\nu_{\mu}\mathrm{X}$, second generation muons can also originate from cascade decay $\mathrm{B} \to \mathrm{DX}$, $\mathrm{D} \to \mu\nu_{\mu}\mathrm{X}^{'}$. If we consider a B^{+} and a $\overline{\mathrm{B}^{0}}$ originating from a correlated $\mathrm{b\overline{b}}$ pair, they suffer the following decay chains:

$$\begin{aligned} &\mathrm{B}^{+} \to \overline{\mathrm{D}^{0}}\mu_{1}^{+}\nu_{\mu},\ \overline{\mathrm{D}^{0}} \to \mu_{2}^{-}\mathrm{X}^{'}, \\ &\overline{\mathrm{B}^{0}} \to \mathrm{D}^{+}\mu_{3}^{-}\overline{\nu_{\mu}},\ \mathrm{D}^{+} \to \mu_{4}^{+}\mathrm{X}^{''}. \end{aligned} \tag{5.2}$$

When we focus on unlike-sign dimuon pairs, the B decay can produce dimuons in different ways:

- a combination of muons, $\mu_1^+\mu_2^-$ and $\mu_3^-\mu_4^+$, from same B-hadron through a D-hadron decay, this is the $\mathrm{BD}_{\rm same}$ channel;
- two muons from primary B decays, $\mu_1^+\mu_3^-$, called as $\mathrm{BB}_{\rm diff}$;
- two muons from the secondary decay feed down from open beauty to open charm production, $\mu_2^-\mu_4^+$, called as secondary $\mathrm{DD}_{\rm diff}$.

[1] In the single muon $p_{\rm t}$ distribution, background is mainly composed of muons from light hadrons, the contribution from resonances is negligible since their production cross section is much smaller than that of open heavy flavours; the background in the dimuon $M_{\rm inv}$ distribution includes contributions from both light hadron decays, uncorrelated background and from resonances, as shown in right plot of Fig. 5.2.

In addition, the $\mu_1^+\mu_4^+$ and $\mu_2^-\mu_3^-$ give the like-sign dimuon pairs called as BD_{diff}. Moreover, mixing in B^0-$\overline{B^0}$ can produce the correlated like-sign BB_{diff} and secondary DD_{diff} channels. Similarly to the B decays, open D hadrons can produce unlike-sign correlated dimuons via primary DD_{diff} and D-chain (D decays to μ with a light hadron, this light hadron further decays to a μ with opposite charge with respect to the primary muon from D decays).

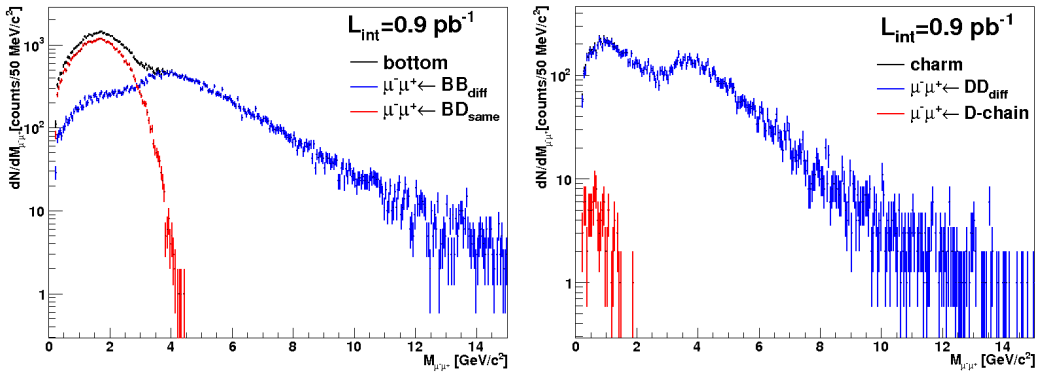

Figure 5.3: Reconstructed invariant mass distributions of correlated unlike-sign dimuons from beauty (left) and charm (right) decays in pp collisions at $\sqrt{s} = 14$ TeV. The different sources are displayed.

Fig. 5.3 (left) displays correlated unlike-sign dimuons from beauty decay originating from different sources. The secondary DD_{diff} component is included in the BB_{diff} as they originate from two correlated b quarks. In the low M_{inv} region, both muons originate mainly from the BD_{same} channel and, in the high M_{inv} region, each muon comes from the direct decay or indirect decay (via a D-hadron) of a B-hadron (BB_{diff} channel). Correlated unlike-sign dimuons from charm decay are produced mainly through the DD_{diff} channel, as shown in right plot of Fig. 5.3. Indeed, the component of unlike-sign dimuons from the D-chain channel is negligible. This is due to the decay process of the light hadrons (mainly pions and kaons) coming from D-hadrons suppressed by the front absorber of the muon spectrometer. Due to their long life time, a very large fraction of them ($\sim 90\%$) are stopped inside the front absorber before they decay to muons.

Furthermore, the different pQCD NLO processes of the heavy flavour production allow to separate the BB_{diff} and DD_{diff} components into more classes. Fig. 5.4 shows the pQCD processes associated with BB_{diff} channel (left) and DD_{diff} channel (right). In the low M_{inv} region, gluon splitting and flavour excitation processes are responsible for the production of unlike-sign dimuons from beauty decay in the BB_{diff} channel while, at high M_{inv} pair creation becomes the dominant production process. Similar trends are evidenced in the DD_{diff} channel. In particular, the gluon splitting process populates significantly the low M_{inv} region and explains the structure in the M_{inv} distribution of correlated unlike-sign dimuons from charm decay.

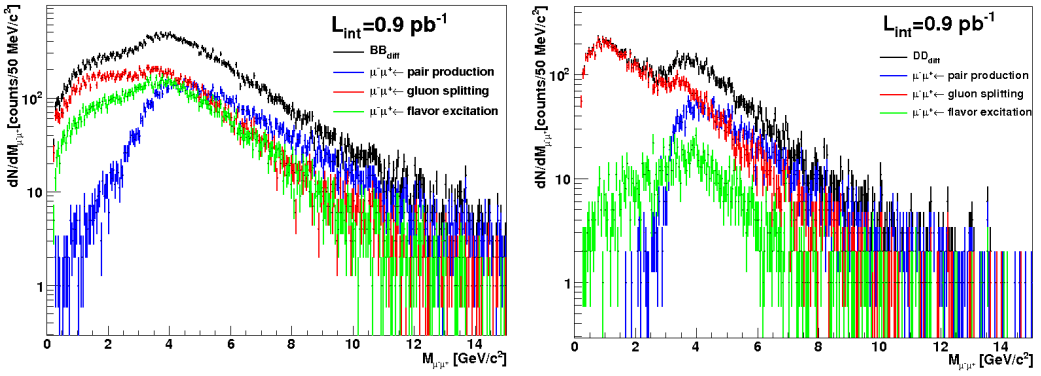

Figure 5.4: Reconstructed invariant mass distributions of correlated unlike-sign dimuons from $\mathrm{BB_{diff}}$ channel (left) and $\mathrm{DD_{diff}}$ channel (right) decay in pp collisions at $\sqrt{s} = 14$ TeV. The sources corresponding to different pQCD NLO processes of heavy flavour production are shown.

After the detailed description of all the sources in the dimuon M_{inv} spectrum of muons from open charm and beauty hadrons, we can choose the proper functions to describe the shapes of these two distributions. In case of the dimuon M_{inv} spectrum of open beauty hadrons, as shown in left plot of Fig. 5.3, the peak in the low M_{inv} region ($\mathrm{BD_{same}}$) can be described by a Gaussian:

$$\mathrm{gaus}(x, x_0, \sigma) = \exp[-\frac{1}{2}(\frac{x - x_0}{\sigma})^2], \tag{5.3}$$

where x_0 and σ^2 are the mean and variance of the Gaussian distribution. Then, the $\mathrm{BB_{diff}}$ component with a wider width is described by a Gaussian plus a tail function as:

$$\mathrm{tail}(x, x_0, a, b, n) = \frac{1 + a \cdot (x - x_0)}{[b^2 + (x - x_0)^2]^n}, \tag{5.4}$$

with parameters x_0, a, b and n. This tail function is used to handle the trend of the distribution in the high M_{inv} region. By adding the three distributions, we get the shape function of the M_{inv} distribution of dimuons from B-hadrons as:

$$\begin{aligned} f_{\mathrm{b}}^{\mu^-\mu^+} &= B_1 \cdot \mathrm{gaus}(M_{\mathrm{inv}}, b_1, b_2) \\ &+ B_2 \cdot [\mathrm{gaus}(M_{\mathrm{inv}}, b_3, b_4) + B_3 \cdot \mathrm{tail}(M_{\mathrm{inv}}, b_5, b_6, b_7, b_8)]. \end{aligned} \tag{5.5}$$

The parameters B_1, B_2 and B_3 are used to for the normalization of the different components, and together with the parameters $b_1 \sim b_8$, Eq. (5.5) has a total number of 11 parameters. The dimuon M_{inv} spectrum of open charm hadrons is mainly composed by the $\mathrm{DD_{diff}}$ channel. As shown in right plot of Fig. 5.4, the peak in the low M_{inv} region comes from the gluon splitting process and the peak in the middle M_{inv} region originates from the combination of the pair production and flavour excitation processes. We used two independent Gaussians to describe them, and the tail function (Eq. (5.4)) is introduced to describe the behaviour of the spectrum

in the high $M_{\rm inv}$ region, as in the case of dimuons from B-hadron decays. The final shape function of dimuon from open charm hadrons is fitted with:

$$\begin{aligned} f_{\rm c}^{\mu^-\mu^+} &= D_1 \cdot {\rm gaus}(M_{\rm inv}, c_1, c_2) \\ &+ D_2 \cdot {\rm gaus}(M_{\rm inv}, c_3, c_4) \\ &+ D_3 \cdot {\rm tail}(M_{\rm inv}, c_5, c_6, c_7, c_8)]. \end{aligned} \tag{5.6}$$

Similarly to Eq. (5.5), Eq. (5.6) also has 11 parameters ($D_1 \sim D_3$ and $c_1 \sim c_8$).

5.3 Separation of Charm and Beauty Components

With the corresponding shapes for charm and beauty components of single muon $p_{\rm t}$ distribution (Eq. (5.1)) and those of dimuon $M_{\rm inv}$ distribution (Eq. (5.5) and (5.6)), now, we focus on the separation of open charm and beauty components in both single muon and dimuon spectra via a combined fit. Since this method is model dependent, a particular emphasis will be also placed on the estimate of the systematic errors. Note that for that study the muon $p_{\rm t}$ distributions from PDC06 have been fitted and extrapolated up to 20 GeV/c. The statistics in both single muon and dimuon distributions corresponds to an integrated luminosity of 1 pb^{-1}.

5.3.1 Combined Fit

We exploit here a method which allows to unravel, via a combined fit, the charm and beauty components from the total muon distribution in a self-consistent way. This technique is applied to both the single muon $p_{\rm t}$ distribution and to the unlike-sign dimuon $M_{\rm inv}$ distribution. The corresponding distribution shapes of (di)muons from charm and beauty decay are assumed to be known but their amplitudes are left as free parameters. This means, we use Eq. (5.1) and, Eq. (5.5) and (5.6) to fit the corresponding (di)muon distributions from open charm and beauty at the generation level, and obtain all parameters of the shape functions. Once the parameters are obtained, the shape functions are noramlized to unit. The total muon or dimuon distribution is fitted with:

$$F^{\mu^\pm/\mu^-\mu^+} = D_{\mu^\pm/\mu^-\mu^+} \cdot f_{\rm c}^{\mu^\pm/\mu^-\mu^+} + B_{\mu^\pm/\mu^-\mu^+} \cdot f_{\rm b}^{\mu^\pm/\mu^-\mu^+}, \tag{5.7}$$

where, $f_{\rm c}^{\mu^\pm/\mu^-\mu^+}$ ($f_{\rm c}^{\mu^\pm/\mu^-\mu^+}$) are given by Eq. (5.1) for single muons and by Eq. (5.5) and (5.6) for the dimuon case, and are normalized to unit. The parameters $D_{\mu^\pm/\mu^-\mu^+}$ and $B_{\mu^\pm/\mu^-\mu^+}$, in Eq. (5.7), are the corresponding amplitudes for charm and beauty components.

Indeed, the total number of (di)muons, $T_{\mu^\pm/\mu^-\mu^+} = D_{\mu^\pm/\mu^-\mu^+} + B_{\mu^\pm/\mu^-\mu^+}$, from heavy flavour decays is known in both simulations and experimental data [2]. Therefore Eq. (5.5) can be also written as:

$$F^{\mu^\pm/\mu^-\mu^+} = (T_{\mu^\pm/\mu^-\mu^+} - B_{\mu^\pm/\mu^-\mu^+}) \cdot f_{\rm c}^{\mu^\pm/\mu^-\mu^+} + B_{\mu^\pm/\mu^-\mu^+} \cdot f_{\rm b}^{\mu^\pm/\mu^-\mu^+}, \tag{5.8}$$

[2] In case of real data, to get $T_{\mu^\pm/\mu^-\mu^+}$, the background subtraction should be performed. We are going to discuss some procedures for the background subtraction in Sec. 5.5.2.

and one is left with only one parameter, the beauty amplitude $B_{\mu^{\pm}/\mu^{-}\mu^{+}}$. In order to avoid this constraint, we introduce the ratio $R_{\mu^{\pm}/\mu^{-}\mu^{+}} = B_{\mu^{\pm}/\mu^{-}\mu^{+}}/D_{\mu^{\pm}/\mu^{-}\mu^{+}}$ into the total fitting function (Eq. (5.7)). In addition, by imposing $R_{\mu^{\pm}/\mu^{-}\mu^{+}}$ in a given expected range can help to reduce the systematic errors of the combined fit. Finally, the total fitting function becomes

$$F^{\mu^{\pm}/\mu^{-}\mu^{+}} = (T_{\mu^{\pm}/\mu^{-}\mu^{+}} - B_{\mu^{\pm}/\mu^{-}\mu^{+}}) \cdot (f_{\rm c}^{\mu^{\pm}/\mu^{-}\mu^{+}} + R_{\mu^{\pm}/\mu^{-}\mu^{+}} \cdot f_{\rm b}^{\mu^{\pm}/\mu^{-}\mu^{+}}). \quad (5.9)$$

In this formula, R = B/C is assumed to be known from Monte-Carlo, but its amplitude is left as a free parameter allowed to vary within 60% around the nominal value.

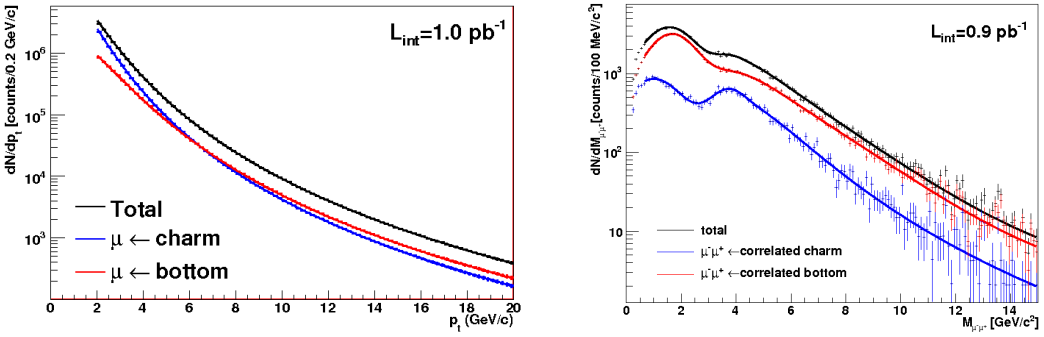

Figure 5.5: The results of the combined fit for single muon $p_{\rm t}$ distributions (left) and dimuon $M_{\rm ivn}$ distributions (right).

Fig. 5.5 shows the result of the combined fit for single muon $p_{\rm t}$ distributions (left) and dimuon $M_{\rm inv}$ distributions (right). The quality of the fit is very good, for both single muon and dimuon cases, since the number of (di)muons from beauty and charm decay extracted from the fits differs only by less than 1% from the corresponding number of (di)muons in the histogram.

5.3.2 Systematic Uncertainties

In order to evaluate the systematic uncertainty on the measured muon yields from charm and beauty decays, we have used the inputs provided in the report from the joined HERA-LHC group [152]. This consists of theoretical predictions on B-hadron and D-hadron rapidity (y) and $p_{\rm t}$ dependent production cross sections calculated in the framework of NLO pQCD with different choices for the quark masses, the QCD factorisation and renormalisation scales, the fragmentation functions and the parton distribution functions. As these predictions are available for B-hadrons and D-hadrons only, the corresponding y and $p_{\rm t}$ distributions have been parameterized [3] and used in order to produce the distributions of decay muons. These $p_{\rm t}$ distributions are shown in Fig. 5.6 together with their ratio with respect to the

[3] These parameteriszations are available in AliRoot.

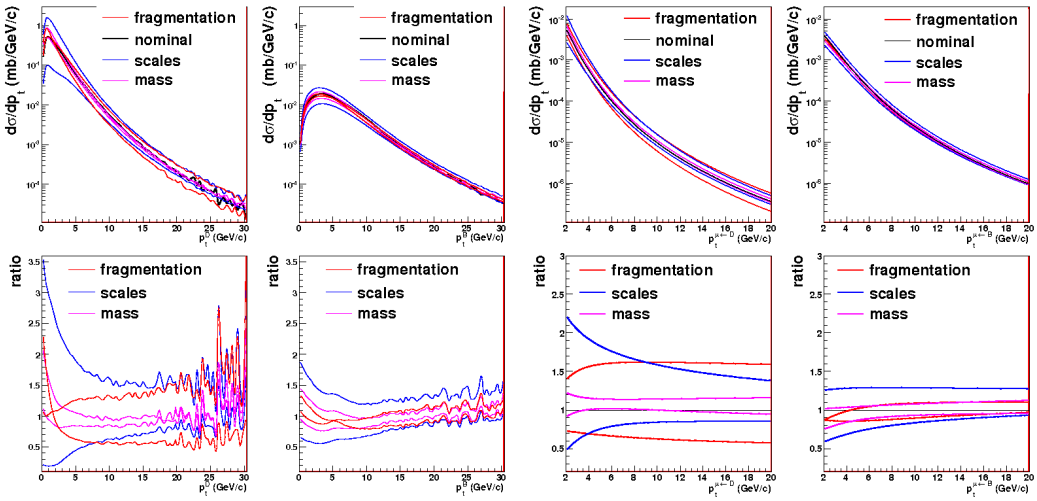

Figure 5.6: Transverse momentum distributions (upper panels) used for the estimation of systematics uncertainties and ratios of these distributions to the nominal case (lower panels). Shown from left to right are, D-hadrons, B-hadrons, decay muons from D-hadrons and from B-hadrons. All distributions are presented in the acceptance of the ALICE muon spectrometer.

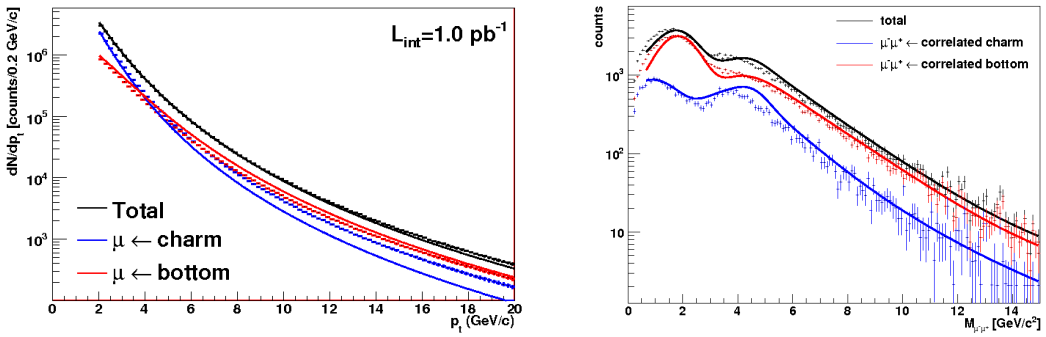

Figure 5.7: Example of combined fits obtained with biased $f_{\mathrm{c/b}}^{\mu^{\pm}}$ shapes for single muon p_{t} distribution (left) and with biased $f_{\mathrm{c/b}}^{\mu^{-}\mu^{+}}$ shapes for unlike-sign dimuon invariant mass distribution (right). The vertical error bars (smaller than the points for single muon channel) are the statistical ones.

nominal case. Note that for each parameter, only the p_{t} distributions which give the largest deviation as compared to the baseline are displayed. They allow to extract biased $f_{\mathrm{c}}^{\mu^{\pm}}$ and $f_{\mathrm{b}}^{\mu^{\pm}}$ shapes which are then used as inputs to fits similar to the ones shown in Fig. 5.5 (left panel). As the theoretical predictions are available for single hadron distributions only, the systematic uncertainty on the number of dimuons is based on $f_{\mathrm{c}}^{\mu^{-}\mu^{+}}$ and $f_{\mathrm{b}}^{\mu^{-}\mu^{+}}$ shapes biased "by hand" in a reasonable way. Examples

of fits with biased $f_{\mathrm{c/b}}^{\mu^{\pm}/\mu^{-}\mu^{+}}$ shapes are shown in Fig. 5.7.

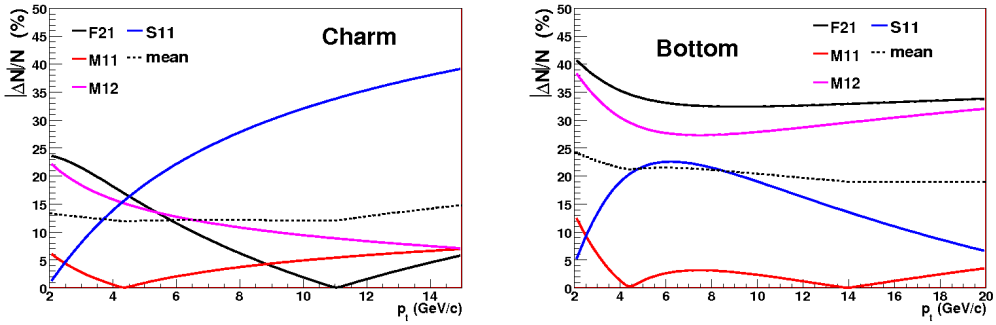

Figure 5.8: Relative systematic uncertainty on the estimation of single muons from charm (left) and beauty (right) decay *vs.* p_{t}. The different curves correspond to different values of pQCD parameters.

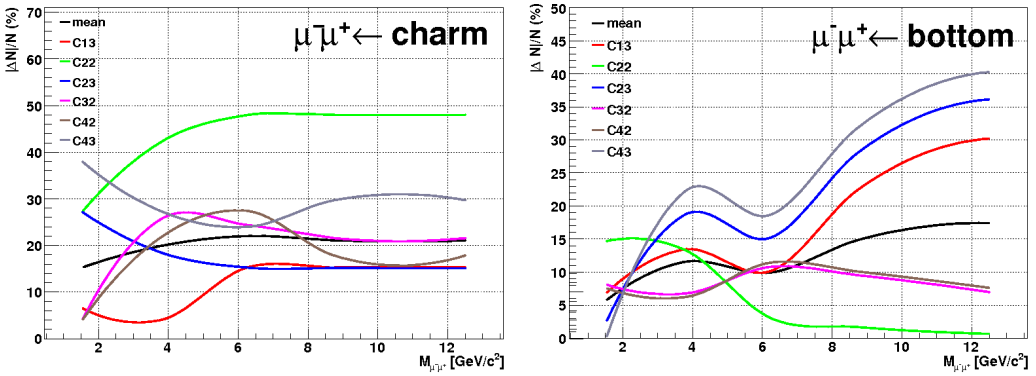

Figure 5.9: Relative systematic uncertainty on the estimation of unlike-sign dimuons from charm (left) and beauty (right) decay *vs.* M_{inv}. The different curves correspond to different $f_{\mathrm{c/b}}^{\mu^{-}\mu^{+}}$ biased shapes.

The relative systematic uncertainty is calculated according to

$$\Delta N/N = \frac{|N_{\mathrm{fit}}^{\mu^{\pm}/\mu^{-}\mu^{+}} - N_{\mathrm{get}}^{\mu^{\pm}/\mu^{-}\mu^{+}}|}{N_{\mathrm{get}}^{\mu^{\pm}/\mu^{-}\mu^{+}}}, \tag{5.10}$$

where $N_{\mathrm{fit}}^{\mu^{\pm}/\mu^{-}\mu^{+}}$ and $N_{\mathrm{get}}^{\mu^{\pm}/\mu^{-}\mu^{+}}$ are the number of (di)muons extracted from the fit and from the original histogram in each p_{t} (M_{inv}) bin, respectively. This relative systematic uncertainty is shown in Fig. 5.8 and 5.9 and, they have been obtained by combining available f_{c} and f_{b} biased shapes. The χ^2 per degree of freedom gives a good indication about the fit quality and allows to constrain the systematics. Only fits with a χ^2 per degree of freedom smaller than 100 are considered. Beyond that

limit, the quality of fits is very bad. The mean value (black curves in Fig. 5.8 and 5.9) shows that this uncertainty is nearly independent of the muon $p_{\rm t}$ and of the dimuon $M_{\rm inv}$. Based on these results, we assume in the following that this systematic uncertainty reaches $\sim 15\%$ and $\sim 20\%$ for single muons from charm and beauty decay and, $\sim 20\%$ and $\sim 15\%$ for dimuons from charm and beauty decay.

5.4 Calculation of $\mathrm{d}\sigma_{\rm D/B}/\mathrm{d}p_{\rm t}(p_{\rm t} > p_{\rm t}^{\rm min})$

The measured (di)muon production differential cross section, from the combined fits, can directly be compared to theoretical predictions provided the calculations take into account fragmentation and decay. In this section, we go further and apply a method which allows to convert this (di)muon production differential cross section to the corresponding hadron production differential cross section.

5.4.1 Method

The B-hadron and D-hadron production $p_{\rm t}$-differential cross sections can be extracted from the single muon $p_{\rm t}$ distribution and from the unlike-sign dimuon $M_{\rm inv}$ distribution using the method developed by the UA1 collaboration [294, 154] and further used by CDF [295] and D0 [160] collaborations at the Tevatron. This is done by correcting for branching ratio and decay kinematics the single muon and unlike-sign dimuon production cross sections measured within a given (di)muon parameter kinematic space ϕ^{μ} through:

$$\begin{aligned}\sigma_{\rm D/B}(p_{\rm t} > p_{\rm t}^{\rm min}) &= \sigma_{\mu\leftarrow{\rm D/B}}(\phi^{\mu}) \times F^{\rm MC}_{\mu\leftarrow{\rm D/B}}(\phi^{\mu}, p_{\rm t}^{\rm min}) \\ &= \frac{N_{\mu\leftarrow{\rm D/B}}(\phi^{\mu})}{\int \mathfrak{L}\cdot \mathrm{d}t} \times F^{\rm MC}_{\mu\leftarrow{\rm D/B}}(\phi^{\mu}, p_{\rm t}^{\rm min}),\end{aligned} \tag{5.11}$$

where, $N_{\mu\leftarrow{\rm D/B}}(\phi^{\mu})$ is the efficiency corrected (di)muon yield, and $\int \mathfrak{L}\cdot \mathrm{d}t$ is the integrated luminosity.

In Eq. (5.11), the scaling factor $F^{\rm MC}_{\mu\leftarrow{\rm D/B}}(\phi^{\mu}, p_{\rm t}^{\rm min})$ from the Monte-Carlo is defined as:

$$F^{\rm MC}_{\mu\leftarrow{\rm D/B}}(\phi^{\mu}, p_{\rm t}^{\rm min}) = \frac{\sigma_{\rm D/B}(p_{\rm t} > p_{\rm t}^{\rm min})}{\sigma_{\rm D/B}(\phi^{\mu})}. \tag{5.12}$$

It is the ratio of the B(D)-hadron cross section in the forward region ($-4 < \eta^{\rm B(D)} < -2.5$) with $p_{\rm t}^{\rm B(D)} > p_{\rm t}^{\rm min}$ to the cross section of B(D)-hadrons decaying to a final state containing a (di)muon within the parameter space ϕ^{μ}. The muon parameter space (ϕ^{μ}) is defined by a $p_{\rm t}$ range, a η range ($-4 < \eta < -2.5$), a momentum range ($p > 4$ GeV/c) and a $M_{\rm inv}$ range (for the dimuon channel). For a given ϕ^{μ}, $F^{\rm MC}_{\mu\leftarrow{\rm D/B}}(\phi^{\mu}, p_{\rm t}^{\rm min})$ depends on $p_{\rm t}^{\rm min}$. It is also worth pointing out that the branching ratio is taken into account in $F^{\rm MC}_{\mu\leftarrow{\rm D/B}}(\phi^{\mu}, p_{\rm t}^{\rm min})$.

$F^{\rm MC}_{\mu\leftarrow{\rm D/B}}(\phi^{\mu}, p_{\rm t}^{\rm min})$ is determined in a rather straight forward way by means of high statistics Monte-Carlo simulations. Fig. 5.10 shows an example of $F^{\rm MC}_{\mu\leftarrow{\rm D/B}}(\phi^{\mu}, p_{\rm t}^{\rm min})$ calculation. In this figure, the area labeled as S_1 corresponds

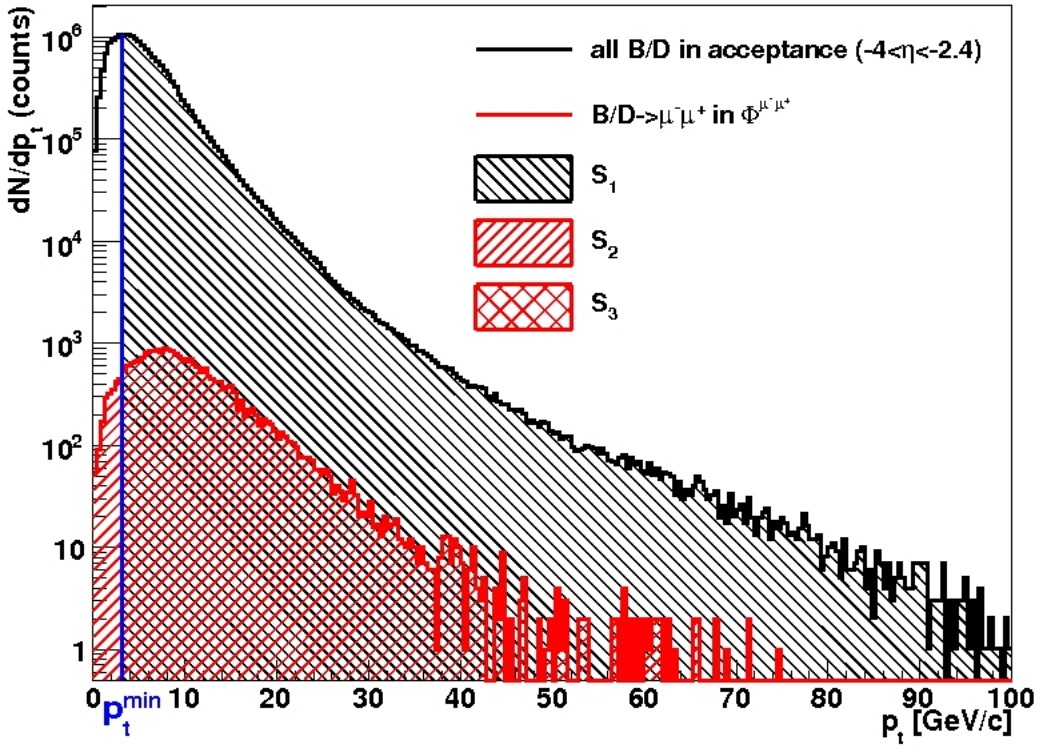

Figure 5.10: Illustration of $F^{\rm MC}_{\mu\leftarrow {\rm D/B}}(\phi^\mu, p_{\rm t}^{\rm min})$ calculation.

to $\sigma_{\rm D/B}(p_{\rm t} > p_{\rm t}^{\rm min})$, S_2 is $\sigma_{\rm D/B}(\phi^\mu)$ and $S_3 = \sigma_{\rm D/B}(\phi^\mu, p_{\rm t} > p_{\rm t}^{\rm min})$. As defined in Eq. (5.12), $F^{\rm MC}_{\mu\leftarrow {\rm D/B}}(\phi^\mu, p_{\rm t}^{\rm min}) = S_1/S_2$. The value of $p_{\rm t}^{\rm min}$ is determined by the condition $S_3/S_2 \simeq 90\%$: that is to say that 90% of accepted D(B)-hadrons that give a (di)muon in ϕ^μ have a $p_{\rm t}$ larger than that value.

5.4.2 Systematic Uncertainty on $F^{\rm MC}_{\mu\leftarrow {\rm D/B}}(\phi^\mu, p_{\rm t}^{\rm min})$

The Monte-Carlo scaling factor, $F^{\rm MC}_{\mu\leftarrow {\rm D/B}}(\phi^\mu, p_{\rm t}^{\rm min}) = S_1/S_2$, contains two sources of systematic uncertainty: the uncertainty on the semi-muonic decay branching ratios; the dependence of $F^{\rm MC}_{\mu\leftarrow {\rm D/B}}(\phi^\mu, p_{\rm t}^{\rm min})$ on the shape of the B(D)-hadron $p_{\rm t}$ distribution. The former is about 3% and is negligible with respect to the errors already present at the (di)muon level (Sec. 5.3.2). The latter has been evaluated for the single muon channel by means of PYTHIA simulations discussed in Sec. 5.3.2 and $F^{\rm MC}_{\mu\leftarrow {\rm D/B}}(\phi^\mu, p_{\rm t}^{\rm min})$ has been calculated over a broad range in $p_{\rm t}^{\rm min}$. Fig. 5.11 displays the resulting systematic uncertainty on $F^{MC}_{\mu\leftarrow {\rm D/B}}(\phi^\mu, p_{\rm t}^{\rm min})$ for some selected single muon $p_{\rm t}$ bins. The results clearly indicate that there is an optimal value of $p_{\rm t}^{\rm min}$ for which the dependence of $F^{\rm MC}_{\mu\leftarrow {\rm D/B}}(\phi^\mu, p_{\rm t}^{\rm min})$ on the shape of the B (D)-hadron $p_{\rm t}$ distribution used in the simulations becomes negligible. This optimal value selects about 90% of the B(D)-hadrons that give a muon in a ϕ^μ phase space. The resulting systematic error introduced on the calculation of $F^{\rm MC}_{\mu\leftarrow {\rm B(D)}}$ is of a few % (less than

5%) and thus is also negligible with respect to the systematic uncertainty on the extracted muon yields. The same definition of $p_{\mathrm{t}}^{\mathrm{min}}$ is used to determine the Monte-Carlo scaling factor in the unlike-sign dimuon channel. Note that we have observed that the parameterization used for the estimation of $F^{\mathrm{MC}}_{\mu^+\mu^-\leftarrow\mathrm{B(D)}}$ does not provide a consistent description of the correlation in the dimuon spectrum, in particular for beauty. Therefore a correction was applied. This consists in a renormalization of the number of correlated dimuons originating from two quarks to the one originating from the same quark in the quark-antiquark pair. This renormalization has been done according to PYTHIA simulations.

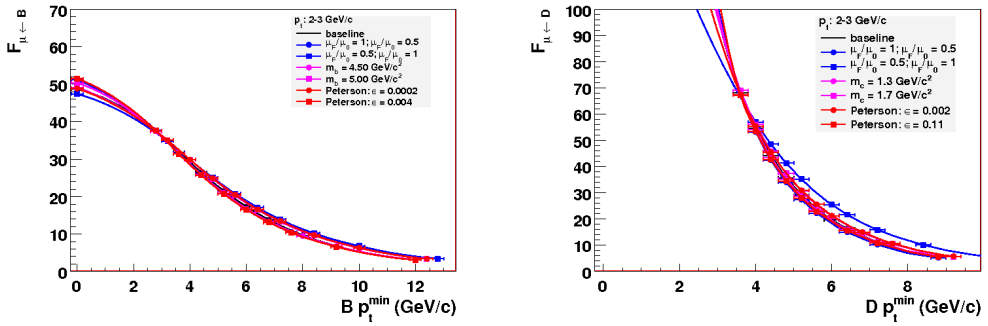

Figure 5.11: Dependence of $F^{\mathrm{MC}}_{\mu\leftarrow\mathrm{B}}$ (left panel) and $F^{\mathrm{MC}}_{\mu\leftarrow\mathrm{D}}$ (right panel) Monte-Carlo scaling factors on $p_{\mathrm{t}}^{\mathrm{min}}$ for selected muon p_{t} bins and, for different shapes of the B-hadron and D-hadron p_{t} distributions.

With present statistics accumulated in the Monte-Carlo simulations, relative statistical errors on $F^{\mathrm{MC}}_{\mu\leftarrow\mathrm{B(D)}}$ range between 0.2% and 4% (0.4% and 6%) for beauty (charm) signal. In the dimuon channel, the corresponding relative statistical errors run from about 1% to 7% (8% to 13%) for beauty (charm) component. Note that such error still can be further reduced, in particular for the dimuon analysis, as it does not depend on the statistics in the PDC06 data but only on the Monte-Carlo simulation used for computing $F^{\mathrm{MC}}_{\mu\leftarrow\mathrm{B/(D)}}$.

5.4.3 Results

The expected performance of the ALICE muon spectrometer for the measurement of the beauty and charm inclusive production differential cross sections in pp collisions at $\sqrt{s} = 14$ TeV is summarized in Fig. 5.12. It depicts the reconstructed B-hadron (left) and D-hadron (right) inclusive production differential cross sections as a function of $p_{\mathrm{t}}^{\mathrm{min}}$ in the single muon channel (squares) and in the unlike-sign dimuon channel (triangles). A nice agreement between single muon and unlike-sign dimuon analysis is evidenced. The results indicate that the input distribution (red curve) is well reconstructed over a large p_{t} range going from about 2 GeV/c to 25 GeV/c (3 GeV/c to 15 GeV/c) for beauty (charm) component. With our analysis cuts, one reconstructs in the ALICE muon spectrometer acceptance about 82% (84%) of the

beauty production cross section in the single muon (dimuon) channel with respect to the total production cross section in the ALICE muon spectrometer acceptance. The corresponding reconstructed charm production cross section amounts to only 17% and 34% in the single muon and dimuon channel, respectively.

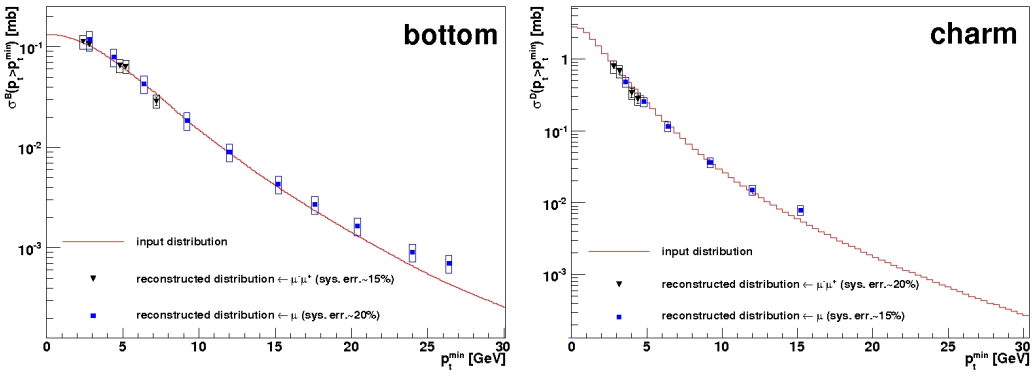

Figure 5.12: B-hadron (left) and D-hadron (right) inclusive production differential cross sections in pp collisions at $\sqrt{s} = 14$ TeV. The results are shown in the forward region: $-4 < \eta^{\mathrm{B(D)}} < -2.5$. The histogram is the input distribution. The points correspond to the reconstructed results from single muon and dimuon channels, respectively. The vertical error bars (smaller than the symbols in most of cases) are the statistical ones. The height and width of the boxes represent the systematic error from the fits and the uncertainty on the determination of $p_{\mathrm{t}}^{\mathrm{min}}$, respectively.

The total statistical uncertainty includes the statistical error on the (di)muon yield and on the Monte-Carlo scaling factor. We remind that the relative statistical error on the muon yield is negligible even at high p_{t} and is less than 2% for both beauty and charm component. This error amounts to about 2.5% (5%) for the unlike-sign dimuon yield from beauty (charm) decay in the highest M_{inv} range. The present relative statistical error on $F^{\mathrm{FM}}_{\mu\leftarrow\mathrm{B/D}}$ does not exceed more than 6% and 13% in the single muon and in the unlike-sign dimuon analysis, respectively. We stress that such error still can be reduced, provided that more statistics is accumulated in the Monte-Carlo simulation. Therefore, the main source of errors is the systematic from the fit (height of boxes). This systematic error exhibits a nearly constant value with p_{t} or M_{inv} of about 15% or 20%, depending on the physics channel. Additional systematic uncertainties on the branching ratio (3%) and on the nucleon-nucleon inelastic cross section (5%) are not displayed.

5.5 Discussions

We have reported on the ability of the ALICE muon spectrometer for the measurement of the B-hadron and D-hadron inclusive production differential cross sections, via single muons and unlike-sign dimuons, in pp collisions at $\sqrt{s} = 14$ TeV. The results indicate that the measurements could be carried out over a wide p_{t} range.

Systematic errors are expected not to exceed 20%. The measurements represent a crucial benchmark for pQCD calculations and are essential for the understanding of the corresponding results in Pb-Pb collisions.

But before to apply the whole strategy to the data, there are two key points that are worth to be mentioned:

- the validation of the combined fit in Sec. 5.3.1 should be supported by sufficiently high statistics. In particular for the single muon $p_{\rm t}$ distributions, the shapes of the distributions for both muons from D and B hadrons can be described by Eq. (5.1). The only evidence that could ensure the separation of these components is the crossing point in the single muon $p_{\rm t}$ distribution for charm and beauty components (around $4 \sim 8$ GeV/c, left plot in Fig. 5.5). Therefore the statistics in data should allow to investigate a higher $p_{\rm t}$ range;

- in the present analysis, we assume that all background is subtracted perfectly. In data analysis, we should understand the sources of background and investigate different methods for their subtraction.

5.5.1 Statistics Estimates

In the following, we perform statistics estimates for different options of data taking. This is done considering three scenarios of luminosity ($< \mathfrak{L} >$) and data-taking time (t):

- $< \mathfrak{L} >= 1 \cdot 10^{30}$ cm^{-2}s^{-1}, $t = 10^6$ s, $N_{\rm pp} = 7.0 \cdot 10^{10}$ (scenario 1);
- $< \mathfrak{L} >= 3 \cdot 10^{30}$ cm^{-2}s^{-1}, $t = 10^6$ s, $N_{\rm pp} = 2.1 \cdot 10^{11}$ (scenario 2);
- $< \mathfrak{L} >= 3 \cdot 10^{30}$ cm^{-2}s^{-1}, $t = 10^7$ s, $N_{\rm pp} = 2.1 \cdot 10^{12}$ (scenario 3);

$N_{\rm pp}$ is the corresponding number of pp collisions assuming that the pp inelastic cross section is 70 mb. The scenario 3 is the so-called nominal run.

We examine in Fig. 5.13, for the three scenarios of data taking, the $p_{\rm t}$ dependence of the signal yield (left panel), signal over background ratio (middle panel) and significance (right panel) corresponding to the muon contribution from beauty (upper panels) and charm (lower panels) decays. The expected statistics is obtained just by scaling the muon yields from PDC06 with the ratio of the number of pp collisions in a given scenario to that of PYTHIA events. We have checked that in the $p_{\rm t}$ range of interest ($p_{\rm t} > 2$ GeV/c), the rates of single muons from beauty and charm decays do not exceed the expected single muon trigger rate of 225 Hz [258]. Note that the muon trigger rates should not exceed 1 kHz in order to keep the dead-time of muon event readout to a low value and such a rate fits the bandwidth of the ALICE muon High Level Trigger. Background includes muons from charm (beauty) decay for the beauty (charm) component. A large statistics of muons from both beauty and charm decay is expected over a wide $p_{\rm t}$ range, even in the first scenario. As a consequence the relative statistical uncertainty is small. In the first scenario and at $p_{\rm t} = 20$ GeV/c, it remains smaller than 1.9% (2.2%) for beauty (charm)

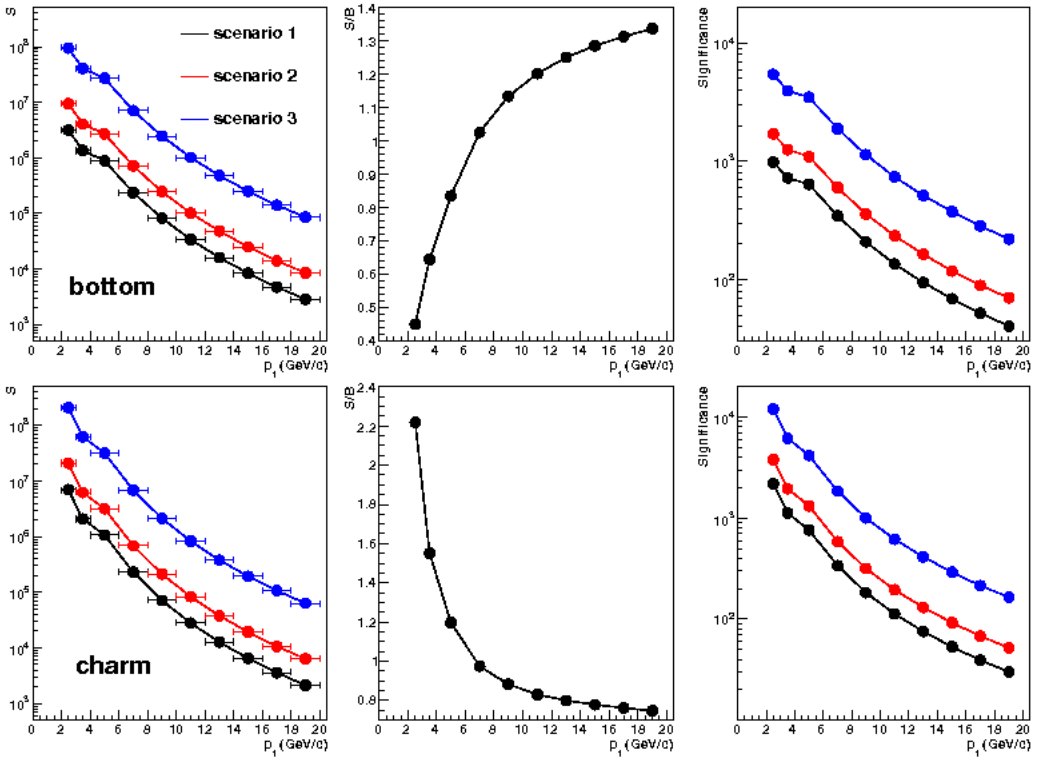

Figure 5.13: Signal yield (left), signal over background ratio (middle) and significance (right) of the single muon contribution from beauty decay (upper panels) and charm decay (lower panels) for the three scenarios of data taking.

contribution. The signal over background ratio (S/B) of the beauty component as a function of $p_{\rm t}$ rises strongly from about 0.4 to 1.2 in the $p_{\rm t}$ range $2 \sim 10$ GeV/c and, tends to saturate at 1.3 for $p_{\rm t} > 12$ GeV/c. S/B ratio of the charm component decreases as $p_{\rm t}$ increases and is about 0.8 for $p_{\rm t} > 12$ GeV/c. The beauty and charm significances are very good over the all $p_{\rm t}$ range, even in the first scenario.

The yields of unlike-sign dimuons from beauty and charm decay are summarized in Fig. 5.14, where the corresponding S/B ratios and significances are also given. Results are displayed in five $M_{\rm inv}$ regions going from 0.6 GeV/c^2 to 15 GeV/c^2 and, for same scenarios of data taking as in the single muon analysis. The statistics of correlated unlike-sign dimuons from beauty decay and corresponding significances are good. The statistics will be high enough to allow the measurement of the B-hadron production differential cross section in the unlike-sign dimuon channel, even in the first scenario of data taking. The S/B ratio is always greater than one. It decreases strongly from $\sim$ 3.9 to 2.3 at low $M_{\rm inv}$ ($0.6 \sim 4$ GeV/c^2) and then increases significantly up to $\sim$ 3.4 in the $M_{\rm inv}$ range $4 \sim 15$ GeV/c^2. The decrease of S/B ratio in the low $M_{\rm inv}$ region is due to the peculiar shape of the charm signal (right plot in Fig. 5.5). The statistics of unlike-sign dimuons from charm decay and corresponding significances are also quite good over the whole $M_{\rm inv}$ range. However,

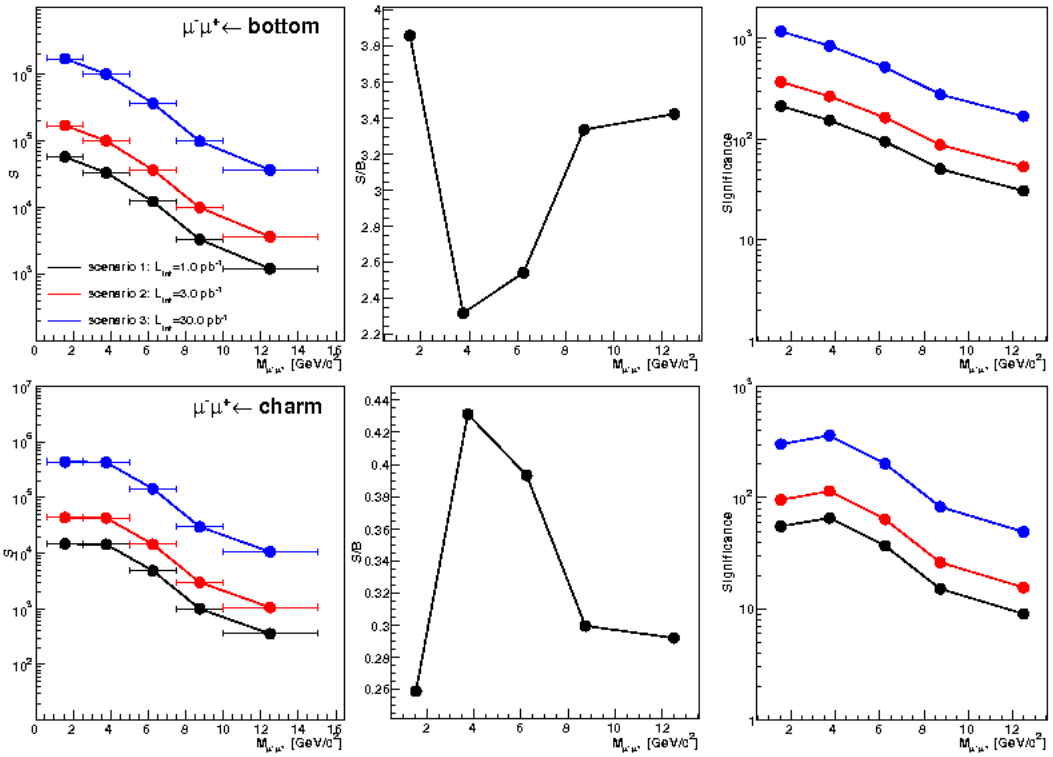

Figure 5.14: The same as Fig. 5.13, but for dimuons.

one observes that the measurement of the charm signal suffers from limited statistics in the first scenario, in particular in the highest $M_{\rm inv}$ bin. As expected, the S/B ratio of the charm contribution as a function of $M_{\rm inv}$ exhibits the opposite behaviour as compared to the beauty component and is always smaller than one.

5.5.2 Background Subtraction

In order to study the background components in the inclusive muon $p_{\rm t}$ spectrum, we focus on the analysis of the minimum bias simulation of pp collisions at $\sqrt{s} =$ 14 TeV, performed within the **Physics Data Challenge 2008** (**PDC08**). Fig. 5.15 depicts the $p_{\rm t}$ distribution of reconstructed tracks in the acceptance of the ALICE muon spectrometer (left plot), with the corresponding production mechanisms (right plot). The correction for reconstruction efficiency [285, 296] is applied to the data for $p_{\rm t} > 1$ GeV/c. The different contributions to this distribution are also displayed.

- muons from charm decay (blue histogram) and beauty decay (red histogram);
- muons from primary light hadron decay, mainly π and K, (green histogram);
- muons from the decay of secondary light hadrons produced mainly inside the front absorber (cyan histogram);

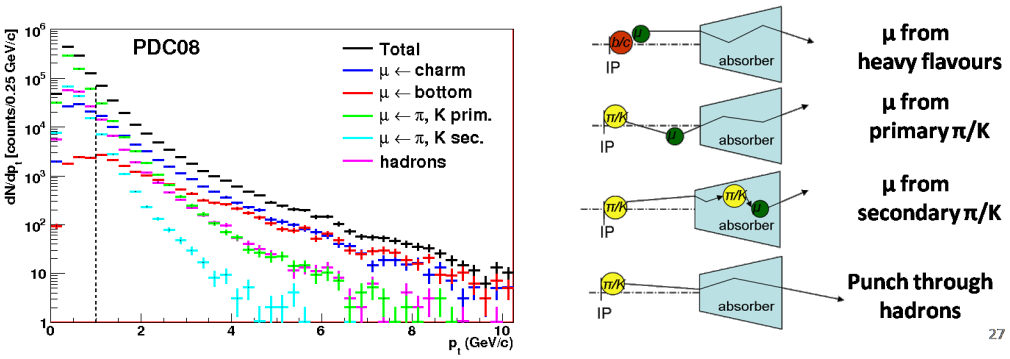

Figure 5.15: Left: p_{t} distribution of reconstructed tracks in the ALICE muon spectrometer in minimum bias pp collisions at $\sqrt{s} = 14$ TeV (PDC08 production); the yields corresponding to the different sources are also plotted. The data are corrected for reconstruction efficiency, for $p_{\mathrm{t}} > 1$ GeV/c. Right: the production mechanisms for different muon track sources.

- hadrons mis-identified as muons (punch-through hadrons, magenta histogram).

These components exhibit different features which are going to be exploited in the following to unravel signal and background. In particular, one can remark that the muon yield from light hadron decay is the main source of background in the muon spectrometer. It dominates the low p_{t} range of the muon distribution up to about $p_{\mathrm{t}} = 2$ GeV/c, decreases steeply for increasing p_{t} and becomes negligible for $p_{\mathrm{t}} \gtrsim 6$ GeV/c. The signal (muons from heavy flavour decay) prevails over the background contributions for $p_{\mathrm{t}} \gtrsim 3$ GeV/c.

As shown in Fig. 5.16 (left panel), part of the background can be suppressed by requiring that the reconstructed track matches the track reconstructed in the trigger system. We observe that thanks to the low p_{t} trigger threshold of about 0.5 GeV/c, the particle yield below that value is strongly reduced but is not completely suppressed since this cut is not a sharp one. In $p_{\mathrm{t}} > 1.5$ GeV/c, almost all punch-through hadrons (98%) are suppressed while the yield of muons from primary light hadron decay and secondary light hadron decay is reduced by about 4% and 6%, respectively. Also, the signal is little affected by this condition since one rejects about 4% of muons from both beauty and charm decay. Moreover, it is still possible to enhance the differences between yields of muons from background and those from heavy flavour decay by using the **Distance of Closest Approach** (**DCA**). The DCA is defined as the distance between the extrapolated muon track and the interaction vertex, in the plane perpendicular to the beam direction and containing the vertex. The influence of a cut on this observable is illustrated on Fig. 5.16 (right). By removing tracks associated with large DCA values (DCA$>$ 9.3 cm), one strongly reduces the yield of muons from secondary light hadron decay (by about 40%) while keeping the signal rejection rate at a low level. Tab. 5.2 summarizes the effect of the

DCA cut on the rejection rate of tracks in the tracking system matched with the trigger track. In these conditions, the number of muons from the decay of secondary light hadrons is reduced by about 50% and the one from primary light hadron decay is suppressed by about 12%, only. One observes a loss in the beauty (charm) signal of about 7% (8%).

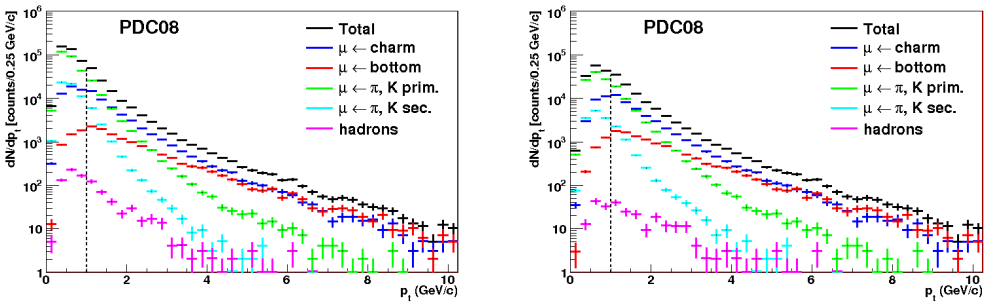

Figure 5.16: The some as Fig. 5.15 with the additinal requirements of track-trigger matching (left) and further cut on DCA< 9.3 cm (right).

Sources	% of rejected tracks with matching	% of rejected tracks with matching & DCA
bottom	4.0	7.0
charm	4.0	8.0
primary K/π	4.0	12.0
secondary K/π	6.0	49.0
punch through hadrons	98.0	99.0

Table 5.2: Rejection rate of tracks sources with $p_{\rm t} > 1.5$ GeV/c with matching with the trigger (second column) and, an additional DCA cut of 9.3 cm (third column).

Furthermore, the remaining muon component from primary light hadron decay can be fully suppressed by using the distribution of primary vertex longitudinal coordinate $z_{\rm v}$, provided by the SPD. Such method has been successfully tested with fast simulations of Pb-Pb collisions at $\sqrt{s_{\rm NN}} = 5.5$ TeV and with full simulations of pp collisions at $\sqrt{s} = 14$ TeV as reported in [297, 298].

In short, the muon two-dimensional distribution on $z_{\rm v}$ and $p_{\rm t}$ is fitted in each $p_{\rm t}$ bin with the function:

$$f(z_{\rm v}, p_{\rm t}) = \frac{1}{\sqrt{2\pi}\sigma} \exp[\frac{-(z_{\rm v}-\mu)^2}{2\sigma^2}] \cdot [\alpha(p_{\rm t})|z_{\rm abs} + \Delta z_i - z_{\rm v}| + \beta(p_{\rm t})]. \qquad (5.13)$$

This function reflects the gaussian distribution of the vertex position multiplied by the linear dependence between the vertex and the front absorber of the muon

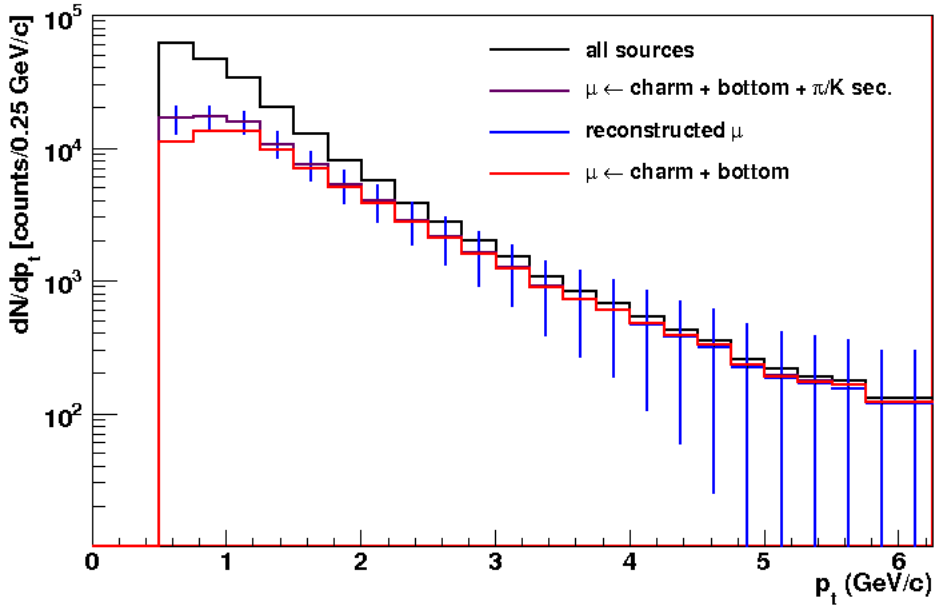

Figure 5.17: p_{t} distribution of reconstructed tracks in the ALICE muon spectrometer in PDC08 with DCA$<$ 9.3 cm are matched with the trigger tracks and muons from primary pion and kaon decays are subtracted. The contribution of muons from open heavy flavour decay contaminated with secondary muons from pion and kaon decays which is obtained by using the vertex method (blue histogram) is compared to the expected distribution (red histogram).

spectrometer. It depends on four parameters: the gaussian mean (μ) and standard deviation (σ) and, the straight line slope ($\alpha(p_{\mathrm{t}})$) and intercept ($\beta(p_{\mathrm{t}})$). The quantity $|z_{\mathrm{abs}} + \Delta z_i - z_{\mathrm{v}}|$ is the free path that pions and kaons can travel before interaction since z_{abs} is the distance between the origin and the front absorber and Δz_i is the mean path traveled by pions and kaons in the absorber before interaction, respectively. The parameter $\beta(p_{\mathrm{t}})$ which gives the contribution of muons from beauty and charm decays biased by the yield of muons from secondary pion and kaon decays is displayed as a function of p_{t} in Fig. 5.17. The results show that the p_{t} distribution of muons from open heavy flavours contaminated by the yield of secondary muons from pion and kaon decays ($\beta(p_{\mathrm{t}})$ parameter, blue histogram) is well reconstructed. However, one can notice that $\beta(p_{\mathrm{t}})$ is affected by large uncertainties, in particular at high p_{t} where the background contribution is small. This trend is expected since the uncertainty is correlated to the statistical error (large at high p_{t}) on the slope parameter $\alpha(p_{\mathrm{t}})$, the latter being related to the yield of muons from the decay of primary pions and kaons.

In addition, in Ref. [297] it was suggested that, the secondary muons can be further subtracted by matching the muon tracks with the FMD since the secondary muons are generated inside the front absorber of muon spectrometer after the tracks

pass through the FMD. But the acceptance of the FMD in the forward region ($-3.4 < \eta < -2.01$ and $-2.29 < \eta < -1.7$, see Sec. 3.3) is not fully compatible with the one of the muon spectrometer ($-4 < \eta < -2.5$). In the overlap region ($-3.4 < \eta < -2.5$), it has been shown that the heavy flavour yield can be successfully extracted in pp collisions, assuming a perfect efficiency of the FMD. The method, still needs to be validated in Pb–Pb collisions, due to the increase of the FMD occupancy which will affect the matching efficiency.

The background in the dimuon $M_{\rm inv}$ distribution contains two parts: the resonances and the uncorrected components. The subtraction of resonances is done in a direct way due to clear peaks aroung the nominal mass. They are subtracted via a combined fitting with resonances shape functions (Gaussian or Crystal Ball [299]) and exponential function for the continuum. The like-sign pair technique and the event-mixing technique can be used to separate the correlated and uncorrelated dimuon components, as mentioned in Ref. [256].

Chapter 6

Analysis of pp data at $\sqrt{s} = 900$ GeV

The first physics pp run at the LHC took place end of 2009, at $\sqrt{s} = 900$ GeV. The main aim of the analysis of these data is the understanding of the apparatus and data properties. The performance of the MUON spectrometer for the detection of muon tracks is presented. Most of the muon selection cuts were fixed via the study of the track characteristics. Some very important basic concepts, like the event trigger classes and the principle of the physics event selection will also be introduced. The understanding of these basic concepts, is very important for the analysis of pp data at $\sqrt{s} = 7$ TeV that will be used for the measurement of heavy flavour decay muons.

The study and/or understanding of the properties of the data cannot be done without comparisons with realistic simulations. Two sets of simulations named LHC10a3 (based on PYTHIA event generator) and LHC10a4 (based on PhoJet [300] event generator) with V0, SPD and MUON spectrometer, are used in our analysis. Realistic residual mis-alignment, realistic status of the front-end electronics and of MUON trigger configuration are included in these simulations.

6.1 Data Sample and Online Trigger

The pp data at $\sqrt{s} = 900$ GeV have been collected during the LHC09d run period and the analysis is done with the second reconstruction pass (pass2). The number of events and tracks in the MUON Spectrometer for each event trigger class are listed in Tab. 6.1.

As shown in Tab. 6.1, 7 event trigger classes were implemented during this data taking period. They belong to three kinds of triggers.

Beam crossing trigger (CBEAMB) This trigger allows to check whether the beams are crossing the ALICE detectors or not, but it does not sign interactions. This explains why we collected ~ 151 M triggered events and just one track reconstructed in the MUON tracking chambers;

Minimum bias trigger (CINT1) Differently from the beam crossing trigger, the minimum bias trigger checks both the beam crossing and the interactions. It requires at least a hit in either one of the V0 counters (V0A and V0C) or at

trigger classes	events	tracks in MUON Spectrometer
CBEAMB-ABCE-NOPF-ALL	150748	1
CINT1B-ABCE-NOPF-ALL	202685	1514
CINT1C-ABCE-NOPF-ALL	26653	5
CINT1A-ABCE-NOPF-ALL	29189	125
CINT1-E-NOPF-ALL	8067	0
CMUS1B-ABCE-NOPF-MUON	893	484
CMUS1A-ABCE-NOPF-MUON	99	37
no triggered (not physics event)	4807	0
total	422182	1665

Table 6.1: Number of events and reconstructed tracks in the ALICE MUON Spectrometer for each trigger class in LHC09d data.

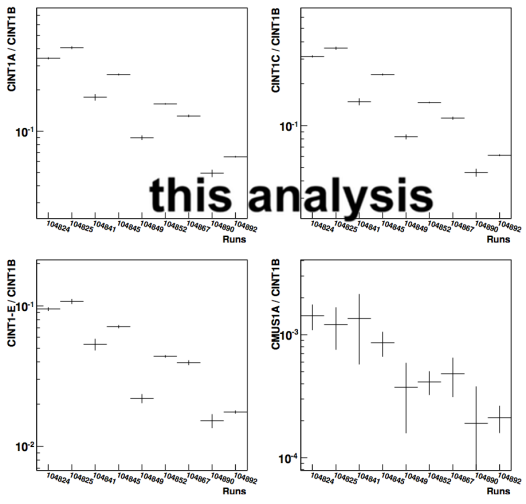

Figure 6.1: Ratios of events in background triggers to that in CINT1B trigger as a function of the run number (data taking time).

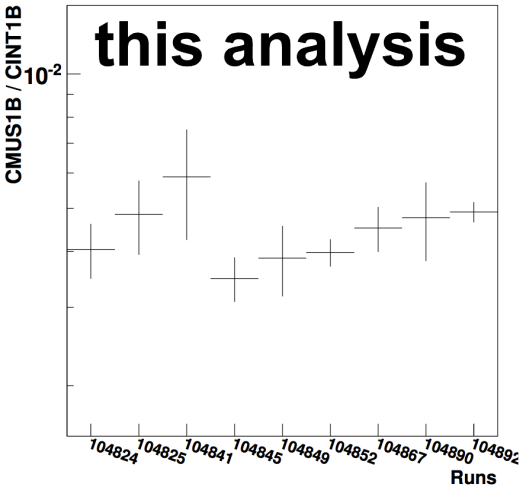

Figure 6.2: Ratio of events triggered in CMUS1B with respect to that in CINT1B as a function of the run number (data taking time).

least a hit in one of the SPD layers [1]. This is done online according to the information received by the CTP from these sub-detectors (as mentioned in Sec. 4.1.1). In order to ensure that the hits in SPD and/or V0 are from the interactions, the beam crossing conditions are also checked. CINT1B is the minimum bias trigger with two injected beams from both side of the ALICE interaction point and it indicates there are two beams crossing each other and making an interaction in ALICE. Although the CINT1A and CINT1C trigger events satisfy the minimum bias trigger conditions, the beam is injected from only one side, side-**A** (PMD side) or side-**C** (MUON Spectrometer side). Finally, CINT1-E triggers correspond to minimum bias events without any beam injection (empty beam). With these background trigger events (CINT1A, CINT1C and CINT1-E), hits in the trigger detectors could be attributed to beam gas interactions (for CINT1A and CINT1C) and noise in the front-end electronics (for CINT1A, CINT1C and CINT1-E). It is worth to notice that, even in CINT1B, the minimum bias trigger decision could also be made in the two situations just mentioned, with a coincidence between signals from the two beam pickup counters. Then, a further offline selection should be applied at software level to reject this background in CINT1B events (the offline event selection will be discussed in Sec. 6.2.1).

Single muon trigger (CMUS1) In addition to the minimum bias trigger conditions, the single muon trigger requires at least one track, above a p_{t} threshold of $\sim$ 0.5 GeV/c, triggered in the MUON trigger stations according to the decision algorithm introduced in Sec. 3.4.5.2. As for the CINT1 trigger, the CMUS1B is the single muon trigger with two injected beams from both side of the ALICE interaction point, and CMUS1A corresponds to the single muon trigger with only beam from side-**A**. The further offline event selection also should be applied to these trigger events in order to reject the remaining background in CMUS1B triggered events.

The string "NOPF" in each trigger class means that the triggers have the Pass-Future (PF) protection used to reject pile-up events. The last string "ALL" or "MUON" in each trigger class is the name of the trigger cluster. The trigger cluster is a group of detectors read for a given trigger. The included detectors in each trigger cluster can change from a data taking period to another one, depending on the detector status, run luminosity and system (pp collisions or Pb–Pb collisions). If one sums over the number of different type of events (Tab. 6.1), the result is not equal to the total number of events since some events are triggered by several trigger classes.

It is quite interesting to see how different triggers evolved with the data taking time. Fig. 6.1 shows the ratio of events in the background triggers, CINT1A (top,

[1] The trigger selection conditions implemented are the only way to define the interactions, these conditions could change according to run status and special requirements. During our analysis, we only use this definition to determine the interactions in pp collisions. With the increase of multiplicity in Pb–Pb collisions, the definition of the interaction determination will change and this will be discussed in Chap. 8.

left), CINT1C (top, right), CINT-E (bottom, left) and CMUS1A (bottom, right), with respect to that in the minimum bias trigger CINT1B, as a function of run number. The run number increases with the data taking time, then, the trends in Fig. 6.1 illustrate how the background evolved during the data taking. As one can observe, the background conditions improved considerably from the first to the last run by almost one order of magnitude. However, the ratio of CMUS1B over CINT1B remains constant during the data taking period, as shown in Fig. 6.2. This indicates that the status of the muon trigger is stable during data taking.

Both minimum bias triggered data (CINT1B) and muon triggered data (CMUS1B) have been used in our muon analysis. In principle, by requiring at least one triggered track in each event, the multiplicity of the muon tracks should be much higher in muon triggered events than that in minimum bias triggered events and one should collect more statistics in the muon triggered events. Since the statistics in the muon triggered events is too small in the 900 GeV data sample, the following analysis has been carried out with minimum bias triggered events.

6.2 Offline Event Selection

As mentioned, after the online event selection at the hardware level, there is still some background in the physics triggered events, like CINT1B triggered events. In this case, an offline trigger selection should be implemented to reject the remaining background events. In this section, we start with the principle of the offline event selection, then particular event selection conditions needed for the muon analysis will be studied.

6.2.1 Physics Selection

The offline physics event selection or the so-called physics selection includes following steps: reproduce the online trigger at software level, remove beam gas in V0 leading time windows and background identification.

Hardware and software offline triggers We can have incorrect trigger decisions at hardware level due to the response and noise of the front-end electronics. Therefore, it is important to reproduce the trigger conditions at the offline level in order to reject background.

V0 leading time Fig. 6.3 shows the event leading time distribution in V0A (left) and V0C (right). There are two visible peaks in both distributions, and they correspond to beam-beam interactions (red bands, labeled as BB) and beam gas (green bands, labeled as BG). The events will be identified as beam gas events and will be rejected if the leading time in any one of the beam gas windows of V0A or V0C.

Background identification In parallel to the determination of the V0 leading time, background can be further identified according to the global event character-

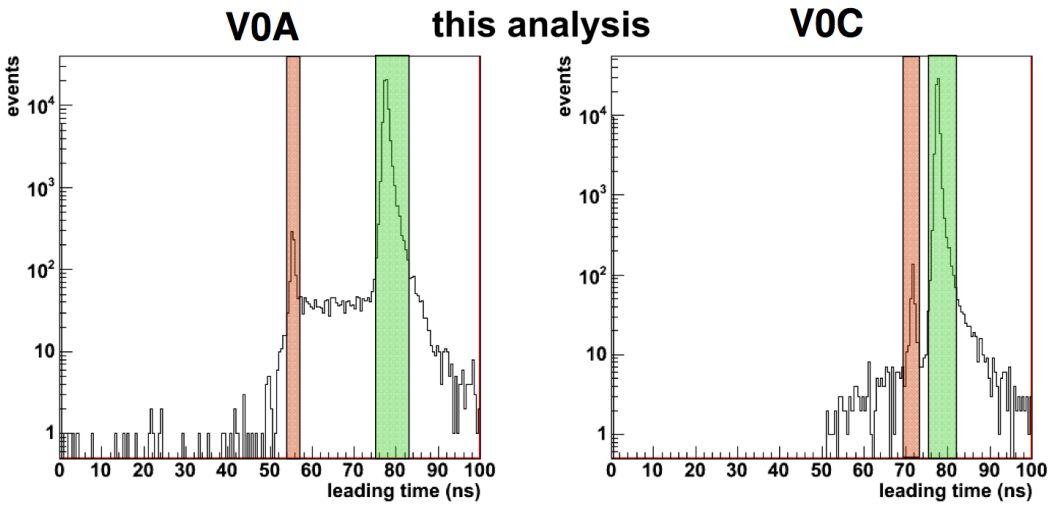

Figure 6.3: The V0 leading time distributions in V0A (left) and V0C (right). The red band shows the time window for beam gas event, and the green band is the time window for beam-beam interaction events.

istics. This identification is done according to the correlation between the tracklets and clusters in SPD and the azimuthal cut to build a SPD tracklet pointing to the beam axis during the reconstruction of the interaction vertex along z-axis [301]. More details about the background identification can be found in [302].

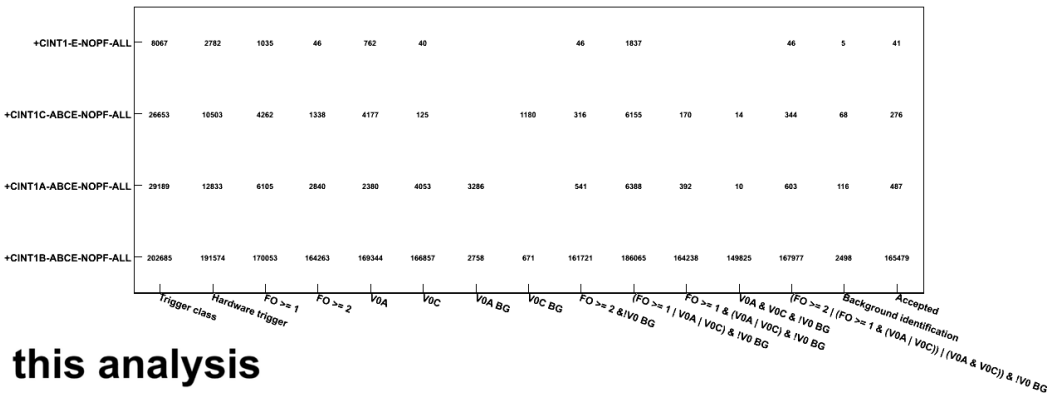

Figure 6.4: Event statistics in physics selection.

Fig. 6.4 shows the statistics of the physics selection in our data sample. The label "FO" is the number of hits in SPD; "V0A" means at least one hit in V0A detector and located in the beam-beam interaction leading time window (green band in left plot of Fig. 6.3), "V0ABG" means that events are located in the leading time window of beam gas in V0A detector (red band in left plot of Fig. 6.3). The definitions of "V0C" and "V0CBG" are the same as "V0A" and "V0ABG". If the event is labeled

either as "V0ABG" or "V0CBG", it is also labeled as "V0BG". According to the above definitions, the minimum bias trigger condition is given by:

$$(\mathrm{FO} >= 2)|(\mathrm{FO} >= 1\&(\mathrm{V0A}|\mathrm{V0C}))|(\mathrm{V0A}\&\mathrm{V0C}), \tag{6.1}$$

at software level.

Here, we define the physics selected events as the events which pass the offline software trigger (as defined in Eq. (6.1)) and are not labeled as "V0BG", as listed in the third column, in the right side of Fig. 6.4. As we can see, almost all the CINT-E events are rejected under the physics selected conditions. This shows that, the incorrect trigger decisions due to the front-end electronics are rejected effectively by reproducing the online trigger at software level.

In the physics selected events, the background is further identified according to the background identification conditions. The results are shown in the second column in the right side of Fig. 6.4. After subtracting these background events from the physics selected events, finally, we get the physics accepted events, as listed in the first column in the right side of Fig. 6.4. The physics accepted events in CINT1B trigger class are the inputs for our muon analysis.

6.2.2 Primary Vertex Selection

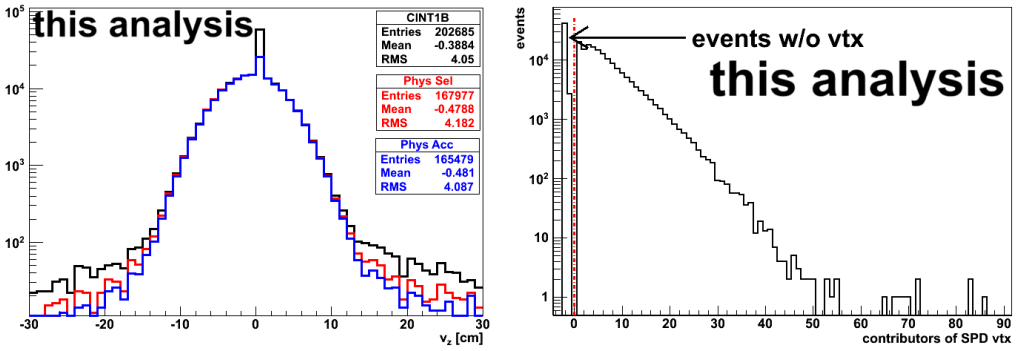

Figure 6.5: Left: v_z distributions with and without applying the physics selection. Right: distribution of number of contributors used for the primary vertex reconstruction. Results are obtained from the analysis of pp collisions at $\sqrt{s} = 900$ GeV collected in the end of 2009 with ALICE.

After the understanding of the physics selection, one will see how typical distributions are affected by the physics selection. The v_z distributions from CINT1B events without any cut (black line, labeled as "CINT1B"), in the physics selected events (red line, labeled as "Phys Sel") and in the physics accepted events (blue line, labeled as "Phys Acc") gotten from LHC09d data in pp collisions at $\sqrt{s} = 900$ GeV are presented in the left plot of Fig. 6.5. One can observe that, there is a peak around $v_z = 0$. This peak corresponds to events without reconstructed primary vertex, since the vertex position for these events is set at the origin of the global

coordinate system $(0, 0, 0)$. The physics selection conditions can reject part of these events. But these events are insensitive to the additional conditions of the physics accepted events. Also, some events with reconstructed v_z position far from the center of the ALICE detectors ($v_z = 0$) are rejected in the final physics accepted data sample.

As illustrated in Sec. 3.4.4, the last step of the muon track reconstruction is to relate the reconstructed muon tracks to the primary vertex and correct the track kinematics. This correction is very important to obtain the distribution of muons from heavy flavour decays, since these muons are produced at the interaction point [2]. For events without primary vertex, the muon track kinematics is corrected using $(0, 0, 0)$ for the vertex position. In this case the spectrum of muons from heavy flavour decays is not correct. To minimize this effect, we proposed to reject the muon tracks in the events without primary vertex in our further analysis. This rejection is done by requiring the number of contributors of primary vertex larger than zero. The vertex contributor is the SPD tracklets of all reconstructed tracks in the central barrel used to determine the position of the vertex. If the vertex reconstruction fails a negative value of number of contributors will be set [301]:

$= -2$ absence of reconstructed points in SPD;

$= -1$ impossible to build suitable tracklets.

The right plot of Fig. 6.5 shows the distribution of number of primary vertex contributors. The events located in the region of number of contributors< 0 are without reconstructed primary vertex.

It is worth to notice that, here we just reject muon tracks in the event without reconstructed primary vertex. If these events pass the physics selection, they are still counted in the minimum bias events. In our further analysis, we keep these events to count the total number of minimum bias events for the physics spectrum normalization.

6.2.3 Effect of the Event Selection on Muon Tracks

Fig. 6.6 shows the p_t (top left), η (top right), trigger matching (bottom left) and DCA (bottom right) distributions of reconstructed muon tracks with different event selection conditions as labeled inside each plot. The results are obtained from LHC09d data in pp collisions at $\sqrt{s} = 900$ GeV.

After physics selection (the physics accepted events, labeled as "Phys Acc" in the plots), a large fraction of reconstructed muon tracks are removed in the high p_t region. Since the physics selection is used to reject the beam gas background, these tracks that are removed in the high p_t region are mainly from beam gas events. As mentioned in Sec. 1.5.3.2 and Sec. 5.2, the p_t distribution of physics tracks follows a power law, and it decreases sharply with p_t, while the tracks in the beam gas events are insensitive with p_t. In this case, the fraction of beam gas tracks is larger

[2] Indeed, the typical decay lengths for D hadrons is ~ 100 μm and for B hadrons is $\sim 500\mu$m, but they are negligible with respect to the resolution of the DCA of muon tracks, Sec. 6.3.

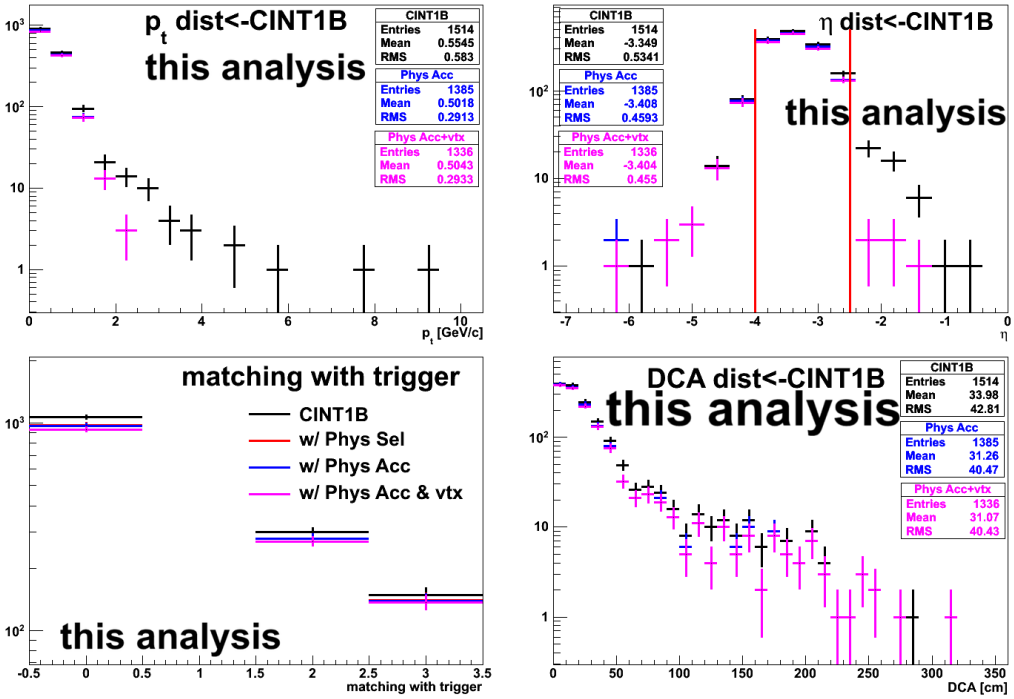

Figure 6.6: p_t (top left), η (top right), trigger matching (bottom left) and DCA (bottom right) distributions of reconstructed muon tracks with different event selection conditions as labeled inside each plot. Results are from LHC09d data in pp collisions at $\sqrt{s} = 900$ GeV.

in the high p_t region than in the low p_t region. In the η distribution, the physics selection mainly rejects tracks outside the acceptance of the MUON spectrometer (in particular, in the region $\eta > -2.5$), indicating that there is a large fraction of beam gas tracks located in this region [3]. Also p_t and η distributions are not very sensitive with the additional requirement of reconstructed primary vertex in the physics accepted data sample (labeled as "Phys Acc+Vtx" or "Phys Acc & Vtx" in the plots).

In the trigger matching distribution, the tracks that are not matched with the muon trigger are labeled as 0, 1 means that the track is matched with the all p_t trigger, the labels 2 and 3 express that the track is matched with the low p_t (not high p_t trigger) and high p_t trigger, respectively [4]. In this data sample, the low p_t trigger is set as all p_t, so when the tracks match the all p_t trigger, it is replaced by

[3] According to the strategy of the muon tracks reconstruction, mentioned in Sec. 3.4.4, the final tracks kinematics is given after relating the track to the primary vertex. In this case, the kinematics for tracks not produced at the interaction point is incorrect. This is why we can find a large number of tracks reconstructed in the MUON spectrometer but with the pseudo-rapidity outside the acceptance of the spectrometer.

[4] The different p_t trigger thresholds are mentioned in Sec. 3.4.5.2. Here, low and high p_t threshold is 0.5 GeV/c and 1 GeV/c, respectively

the low p_t trigger and explains why the bin of all p_t trigger matching is empty. One can observe that the effect of the physics selection is visible both for tracks with and without trigger matching; and the effect of the additional reconstructed vertex requirement is also small, in particular for tracks matched with the muon trigger. In the physics analysis, it will be required that the tracks are matched with the muon trigger tracks. In this case, the effect from the vertex cut for the tracks matched with the muon trigger is negligible, and we don't need to do further correction for this vertex cut in our physics analysis.

Finally, when we look at the DCA distributions, the effect of the vertex cut is visible in the region of large DCA values. The DCA determination in these events is incorrect. As a consequence, the DCA distribution is wide for tracks reconstructed in these events.

6.3 Muon Track Selection

In this section, we will introduce two important track selection cuts to be used in our physics analysis:

matching with trigger This cut was already studied in Sec. 5.5.2 with simulated data. It is studied here with data;

cut at the end of front absorber This cut has been introduced during the study of the track resolution.

6.3.1 Matching with MUON trigger tracks

Fig. 6.7 shows the normalized DCA distributions of muon tracks without requiring matching with trigger (left) and with matching with trigger (right) after the physics selection is applied to LHC09d pp data at $\sqrt{s} = 900$ GeV. The distribution is compared with the one from realistic simulations with PYTHIA and PhoJet as event generators, under the same conditions. Before requiring the matching with the trigger, one can notice that, there is a bump located in the large DCA region in both data and simulations. The bump disappears after requiring matching with the trigger. In both cases, the trends of the DCA distributions in data are well reproduced by the simulations, indicating that the bump in both data and simulations is due to the same effect.

Fig. 6.8 shows the DCA distributions from realistic simulations with PYTHIA (up) and PhoJet (down) used for the comparison with experimental results from Fig. 6.7. In order to explain the bump in the large DCA region, the different muon track sources are plotted. When we do not require the trigger matching (Fig. 6.8, left plots), both PYTHIA and PhoJet simulations reproduce the bump in the high DCA region which is due to punch-through hadrons. After the trigger matching (Fig. 6.8, right plots), the bump disappears since almost all punch-trough hadrons are rejected (they are stopped in the iron wall). This study confirms the results in Tab. 5.2 from the performance study with PDC08 simulations.

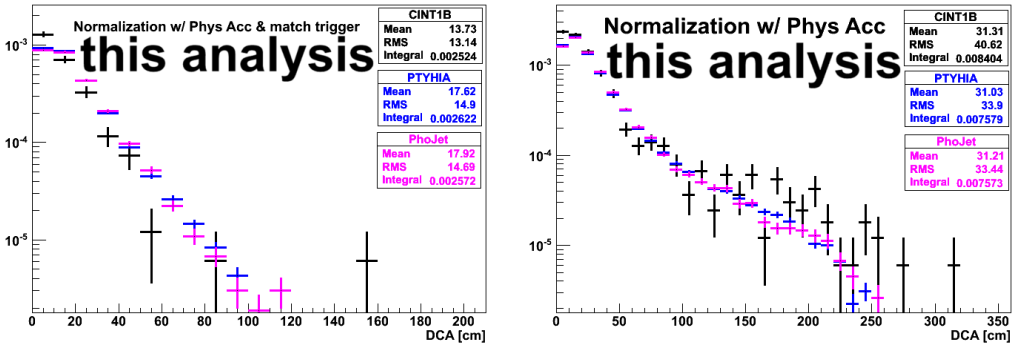

Figure 6.7: DCA distribution of muon tracks without matching with trigger (left) and with matching with trigger (right) after the physics selection is applied to LHC09d data (pp collisions at $\sqrt{s} = 900$ GeV). The results are normalized to unit and compared with the ones from realistic simulations with PYTHIA and PhoJet, under the same conditions.

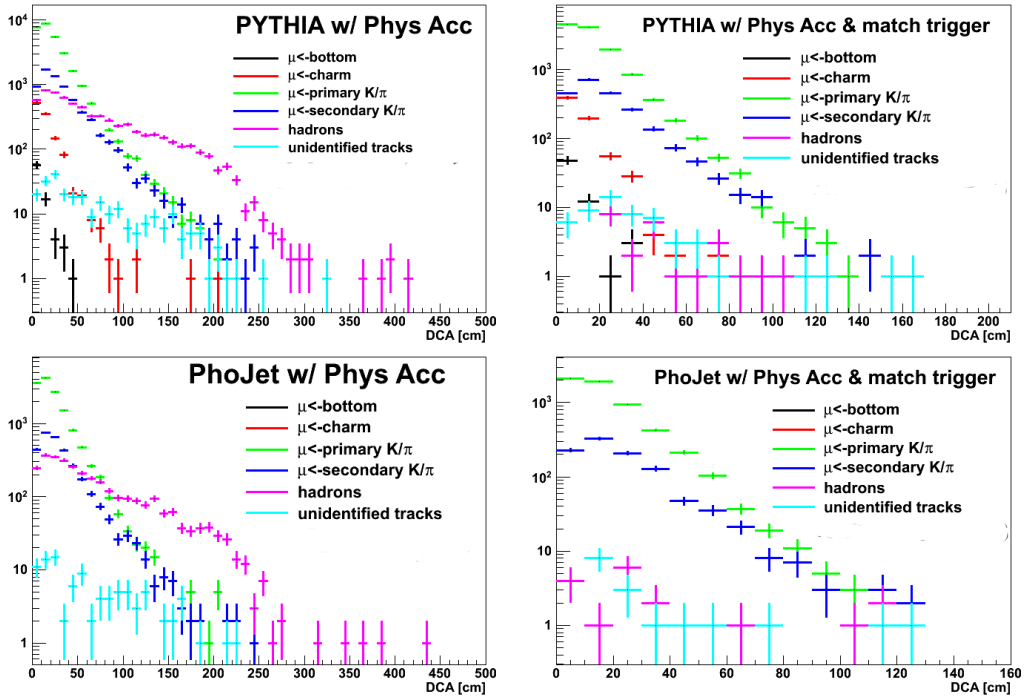

Figure 6.8: DCA distributions of different muon track sources in simulations of pp collisions at $\sqrt{s} = 900$ GeV with PYTHIA (up) and PhoJet (down). The results are presented without matching with trigger (left) and with matching with trigger (right). The realistic detector effects of LHC09d data in pp collisions at $\sqrt{s} = 900$ GeV are included in the simulations.

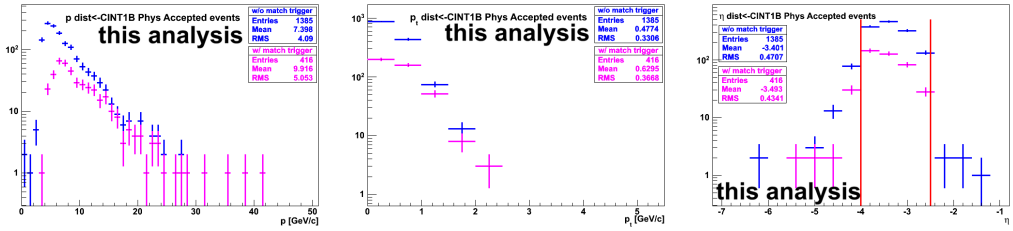

Figure 6.9: Momentum p (left), p_{t} (middle) and η (right) distributions of muon tracks after the physics selection is applied to LHC09d data (pp collisions at $\sqrt{s} =$ 900 GeV). The results are shown without the trigger matching (in blue) and with the trigger matching (in red), respectively.

The effect of the trigger matching on different muon observables is shown in Fig. 6.9. From left to right, one can find the momentum p, p_{t} and η distributions. The results are obtained from LHC09d data for pp collisions at $\sqrt{s} = 900$ GeV. In each plot, the distribution without the trigger matching condition (blue) is compared with that with the trigger matching condition (red). By looking into more detail, following comments can be made:

- the spectrum in low momentum region is strongly affected by the trigger matching,
- the trigger matching condition shifts the peak in the momentum distribution to higher momenta.

Since the trigger matching rejects the hadronic component, this explains the shape of the momentum distribution in the low momentum region. As mentioned in Sec. 3.4.4 the average energy loss of muons inside the front absorber is ~ 3 GeV; when they pass through the muon filter (the iron wall in front of the muon trigger system, as shown in Fig. 3.6) there is an additional average energy loss of ~ 1 GeV for muons inside the iron wall. This additional energy loss is responsible for the strong suppression in the low momentum region and the momentum shift to higher momenta. Then, the trigger matching rejects not only punch-through hadrons but also removes the low energy tracks. The suppression of low p_{t} tracks can also be explained by these two effects. In the η distribution, a huge part of tracks outside the acceptance of the spectrometer is rejected by the trigger matching, since the region outside the spectrometer acceptance is dominated by hadrons. In addition, after the trigger matching, the yields decrease as η varies from -4 to -2.5, although higher multiplicities are measured at mid-rapidity than at forward rapidity. This is due to the trigger matching efficiency which decreases as η varies from -4 to -2.5 since the momentum resolution becomes worse [258].

The other effect of the trigger matching is to remove tracks produced in the beam shield. Fig. 6.10 shows DCA versus η for tracks without trigger matching (left) and with trigger matching (right) after the physics selection is applied to LHC09d data (pp collisions at $\sqrt{s} = 900$ GeV). The p_{t} cut of 0.5 GeV/c is implemented. Under

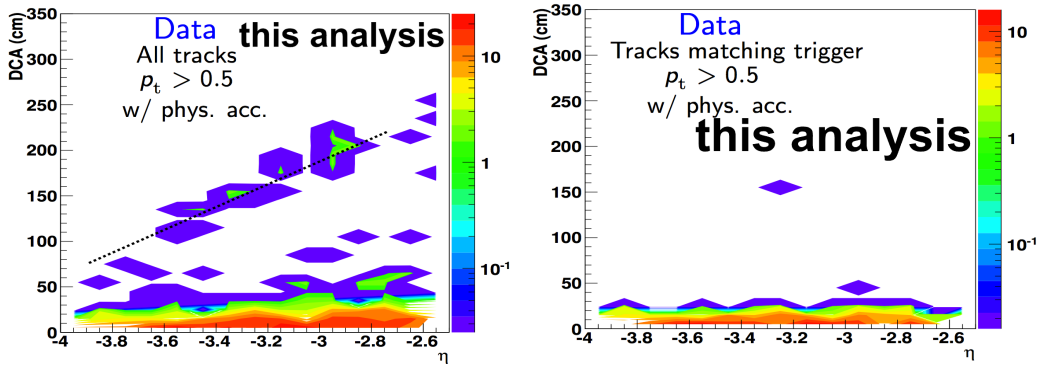

Figure 6.10: DCA versus η for tracks without trigger matching (left) and with trigger matching (right) after the physics selection is applied to LHC09d data (pp collisions at $\sqrt{s} = 900$ GeV). A sharp p_t of 0.5 GeV/c is applied.

the small angle approximation, there is a linear relation between η and DCA of tracks produced inside the beam shield. According to this linear relation, it is easy to identify this component in the left plot of Fig. 6.10. The disappearance of this component (right plot of Fig. 6.10) shows the ability of the trigger matching to reject the tracks produced in the beam shield [5].

Finally, I prefer to go back to Fig. 6.8 and mention something that is not related to the trigger matching. Comparing with Fig. 5.16, there is an additional source labeled as "unidentified tracks" in Fig. 6.8. These tracks are not produced by particles but by the incorrect hit combination during the track reconstruction in the MUON spectrometer, and they are fake tracks. As shown in Fig. 6.8 (right), after trigger matching, the fake track component is also negligible. But in Pb–Pb collisions, with the increasing multiplicity and tracking chamber occupancy, a large fraction of fake tracks will be reconstructed. The rejection of fake tracks in Pb–Pb collisions is very important.

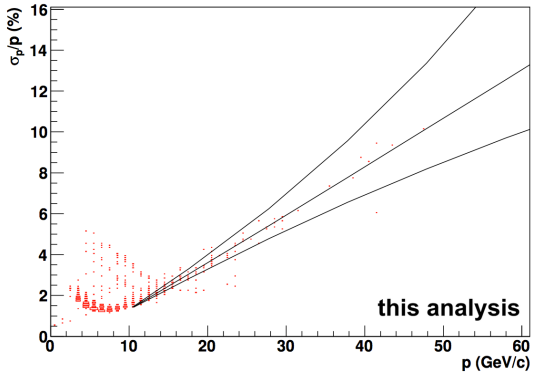

Figure 6.11: Relative momentum resolution σ_p/p as a function of p of the tracks reconstructed in the MUON spectrometer. Results are from the LHC09d data (pp collisions at $\sqrt{s} = 900$ GeV).

[5] As we will see, the trigger matching can reject part of the tracks produced in beam shield, but not all. The remaining part has a large effect in the high p_t region, and several new approaches will be developed to further separate this component.

6.3.2 Acceptance Cuts

The relative momentum resolution σ_p/p as a function of p, for tracks reconstructed in the MUON spectrometer, is shown in Fig. 6.11 for LHC09d data (pp collisions at $\sqrt{s} = 900$ GeV). First, σ_p/p decreases with the momentum in the low momentum region, and it increases with p in the high momentum region. This trend is well understood. In the low momentum region, σ_p/p is mainly affected by the multi-scattering of low energy tracks when they cross the detector chambers. With the increase of p, this multi-scattering effect becomes smaller and explains the decrease of σ_p/p with momentum. On the other hand, in the high momentum region, σ_p/p is limited by the cell size of the detector chambers. In a given magnet field, the smaller chamber cell size is required to ensure the track position resolution for high energy tracks, and to calculate their curvature in this magnet field and momentum. With a fixed chamber cell size, σ_p/p decreases with the momentum.

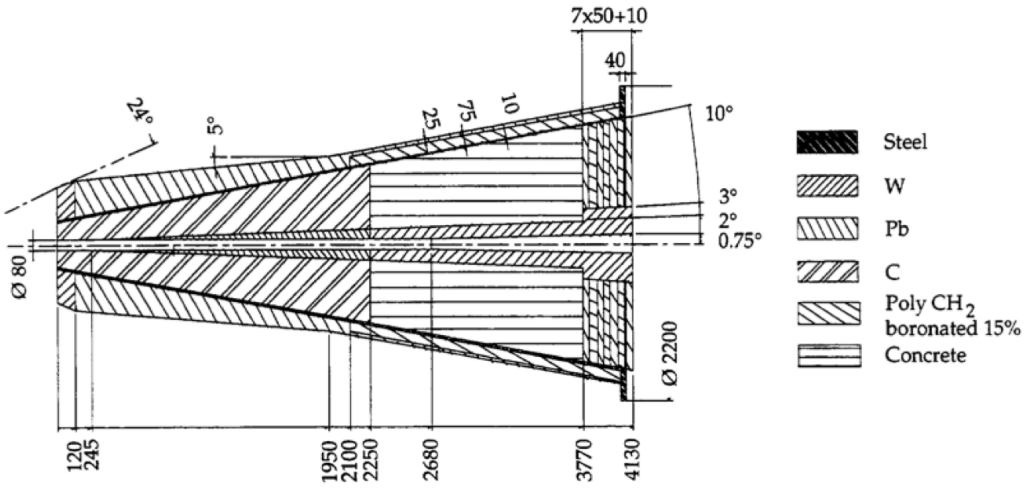

Figure 6.12: Composition of the front absorber of the ALICE muon spectrometer.

When looking into detail to Fig. 6.11, we can see that the momentum dependence on σ_p/p can be identified in different components, in particular, in the low momentum region. This indicates that not all tracks have the same multi-scattering behaviour. For a given particle specie, its multi-scattering behaviour is different in different material. As the front absorber is built with different materials, as shown in Fig. 3.7 the different components in the σ_p/p distribution could be due to particles crossing different material region of the front absorber and suffering different multi-scatterings.

To confirm this hypothesis, we can first look at the front absorber depicted in Fig. 6.12. We can see that, the different materials in the end of the front absorber are classified into different angle regions. This angle is defined as the polar angle at the end of the front absorber in the ALICE global coordinate system. We denote

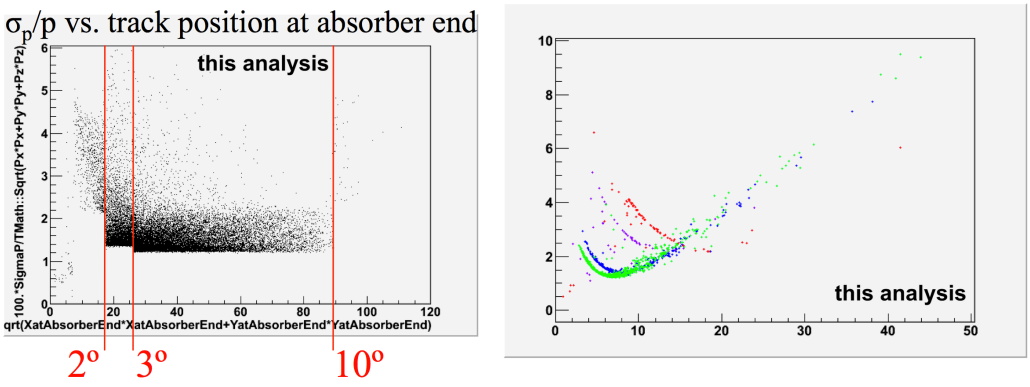

Figure 6.13: Left: σ_p/p as a function of $R_{\rm abs}$, the corresponding $\pi - \theta_{\rm abs}$ region is mentioned. Right: same as Fig. 6.11, but tracks are separated in different $\pi - \theta_{\rm abs}$ regions: $1^\circ - 2^\circ$ (red), $2^\circ - 3^\circ$ (blue), $3^\circ - 10^\circ$ (green) and $10^\circ - 90^\circ$ (purple).

this polar angle as $\theta_{\rm abs}$, and define the radius at the end of front absorber as,

$$R_{\rm abs} = L_{\rm abs} \cdot \tan\theta_{\rm abs}, \tag{6.2}$$

where $L_{\rm abs} = 505$ cm is the distance between the end of front absorber and the origin of the ALICE global coordinate system. In Fig. 6.13 (left panel), one can see that, σ_p/p is different from one $R_{\rm abs}$ (or $\theta_{\rm abs}$) region to an other. Fig. 6.13 (right panel) shows σ_p/p versus p in different $\theta_{\rm abs}$ regions (it corresponds to the different components in Fig. 6.11).

Finally, to avoid the effect from different materials in the front absorber in our further single muon analysis, we apply a cut $171^\circ < \theta_{abs} < 178^\circ$ (or 17.6 cm$< R_{\rm abs} <$ 80 cm) according to the geometry of the front absorber. This $\theta_{\rm abs}$ (or $R_{\rm abs}$) cut is combined with the usual η cut, $-4 < \eta < -2.5$. They represent the accpetance cuts.

6.4 Conclusion: Physics Analysis Cuts

Now it is time to make a conclusion about what we learnt from the analysis of the 900 GeV pp data:

- the analysis should be performed with physics triggered events. For the muon analysis, it could be minimum bias events or muon triggered events;
- to further reject the background in the physics triggered events, the offline physics selection should be implemented;
- after the physics selection, the vertex cut is used to remove the muon tracks in the events without the reconstructed primary vertex to minimize the bias from the correction of the track kinematics, but these events are taken into account in the total number of minimum bias events;

- the trigger matching is required to reject punch-through hadrons , small energy tracks and part of tracks produced in the beam shield;
- the cut $171^{\circ} < \theta_{\rm abs} < 178^{\circ}$ [6] or 17.6 cm$< R_{\rm abs} <$ 80 cm is used to avoid the effects from different materials in the front absorber, and with the cut $-4 < \eta < -2.5$ they constitute the acceptance cuts.

Due to the careful study of 900 GeV data, all event and track cuts will be implemented in the analysis of pp collisions at 7 TeV. They are mandatory for a pre-subtraction of the background. This will make the analysis of 7 TeV data more straightforward. Our main task in the analysis of the 7 TeV data will be the subtraction of muons from primary light hadron decays and secondary muons produced inside the front absorber in order to extract the spectrum of muons from open heavy flavour hadron decays.

[6] Since the analysis of the data token in 2011, the cut on $\theta_{\rm abs}$ have been changed to $170^{\circ} < \theta_{\rm abs} < 178^{\circ}$. In this thesis, we use the old cut on $\theta_{\rm abs}$ since the data aanlysed were collected in 2009-2010.

Chapter 7

Heavy Flavour Production in pp Collisions at $\sqrt{s} = 7$ TeV

The detailed analysis of pp data at $\sqrt{s} = 900$ GeV, presented in Chap. 6, allows to discuss the analysis of pp collisions at $\sqrt{s} = 7$ TeV in a straightforward way. During 2010, data have been taken in a total of six periods corresponding to different conditions of beam and detector operation. The periods are named LHC10b, LHC10c, LHC10d, LHC10e, LHC10f and LHC10g. LHC10f and LHC10g correspond to the high luminosity runs. The analysis in this chapter is based on the data from LHC10c, LHC10d and LHC10e for which the statistics is sufficient to extract the production cross section of muons from open heavy flavour decays. The data in LHC10c and LHC10d are used to test the analysis strategy. The final results are obtained with the data from LHC10e for which the high statistics allows to reach muon p_{t} up to about 12 GeV. Finally, data from LHC10c and LHC10d are used to cross-check the results obtained with LHC10e.

7.1 Data Quality Assurance

The event and track selection strategy was discussed in Sec. 6.4. Before implementing all these selections, the data **Quality Assurance** (**QA**) should be studied to choose the correct data sample for our analysis.

7.1.1 Quality Assurance for Muon Analysis

The data quality assurance for muon analysis includes two parts. The first one is the global data QA and the second one is specific to the MUON spectrometer.

First, let us look how to determine the global QA. A given data taking period is the result of several independent runs. The global QA is used to identify and reject the bad runs with the following conditions:

- During the data taking, different types of runs are recorded according to different needs, like, detector calibration, luminosity measurement *etc.*. The runs taken for the physics analysis are labeled as "PHYSICS" in the physics partition. The first step of the global QA is to select these runs according to the information in the log-book which has been filled during data taking.
- Then, for a given run, the two following conditions:
  - data taking duration$>$ 10 min,

– total sub-events> 5000

are set to check whether the data taking status of this run was stable or not;

- With the selected stable physics runs, the beam status and the beam energy should also be checked. In pp collisions at $\sqrt{s} = 7$ TeV, the beam energy should be $\sqrt{s}/2 = 3500$ GeV, If beam energy is not equal to this value or the beam status is not labeled as "stable", this run should be removed.

- After checking the status of the data taking and of the injected beams, the status of the DAQ system (like, whether the data are recorded in GDC correctly or not) should also be checked.

- For the muon analysis, we have the additional following special requirements:

  – both the MUON trigger stations and the V0 detector should be included in the trigger detectors,

  – the readout detectors should include the MUON trigger and tracker stations as well as the V0, SPD and ZDC.

  The status of all above detectors should not be labeled as "bad" in the logbook.

- Finally, the current in L3 magnet and the magnet dipole should be correct and stable, otherwise, the track momentum will be determined incorrectly.

It is worth noticing that, in some cases, we will find a run passing all above selection conditions, but its global data quality may be labeled as "bad" in the **Run Condition Table** (**RCT**) [303]. This can be due to many reasons, like the TPC is not included in the readout detectors (in this case, there is no effect for the muon analysis). To avoid any further trouble, it is quite important to also take into account the information from the detector experts. After the global QA selections, we should inspect the conditions of the MUON tracker and trigger stations more closely, for each run, to determine whether this run can be used for the analysis or not. For the MUON tracker system, we consider following situations for a given run:

- the detector configuration is nominal and no major problem is observed, the average number of clusters per track per chamber is above 0.9, this run is usable for physics analysis;

- the detector configuration is lower that the nominal one, thus the tracking efficiency is slightly reduced and the average number of clusters per track and per chamber is above 0.75 (but below 0.9), this run still can be used for physics analysis;

- the detector configuration is not nominal, for instance a DDL is missing or a high occupancy in one detector element has appeared, the average number of clusters per track and per chamber is below 0.75, thus the tracking efficiency is modified. However if the tracking efficiency can be simulated correctly, this run can be still usable for physics analysis;

- if the detector configuration is not nominal and the tracking efficiency is not understood, then this run is not usable for physics analysis.

Similarly, the QA definition for the MUON trigger system starts by checking the detector configuration for a given run. If the configuration is nominal and the full system is included in the trigger and readout detectors (or just small part of the system is missing but the trigger efficiency is still under control), then this run is usable for physics analysis. If the configuration of the trigger system is not nominal, (problems occurring during data taking or the single muon or dimuon trigger is not set correctly) then, of course, the corresponding runs have to be rejected from the data sample for physics analysis.

7.1.2 Results of Data Quality Assurance

Here, we do not attempt to show all the QA plots in each data taking period. We just list some typical examples to illustrate how we selected the correct data samples for our analysis.

Before to show the results, some definitions for the muon tracks have to be added. The MUON spectrometer includes two parts: the tracking stations and the trigger stations. During the data taking, these two parts record the data independently. Then, the reconstructed tracks in the MUON spectrometer are classified into three classes:

tracker track this corresponds to a track which is reconstructed in the tracking stations, no matter it is tagged by the trigger stations or not, and we say that it "contains the tracker data";

trigger track this corresponds to a track which is tagged by the trigger stations, no matter it is reconstructed in the tracking stations or not, and we say that it "contains the trigger data";

matched track if a given track contains both the tracker data and the trigger data, we labeled this track as the "matched track".

According to these definitions, the matched tracks correspond to tracks reconstructed in the tracking system and matched with the corresponding one in the trigger system. Also, the tracker tracks are the ones we used in the analysis and the matched tracks are the ones of the tracker tracks with the all p_{t} trigger matching ($p_{\mathrm{t}} > 0.5$ GeV/c).

7.1.2.1 QA of LHC10c

Fig. 7.1 shows the ratios of the number of tracker tracks over trigger tracks (top), matched tracks over trigger tracks (middle) and matched tracks over tracker tracks (bottom) as a function of the run number in LHC10c period. The black lines correspond to minimum bias events (CINT1B) and the red ones correspond to muon trigger events (CMUS1B). In the bottom plot, the ratio between the number

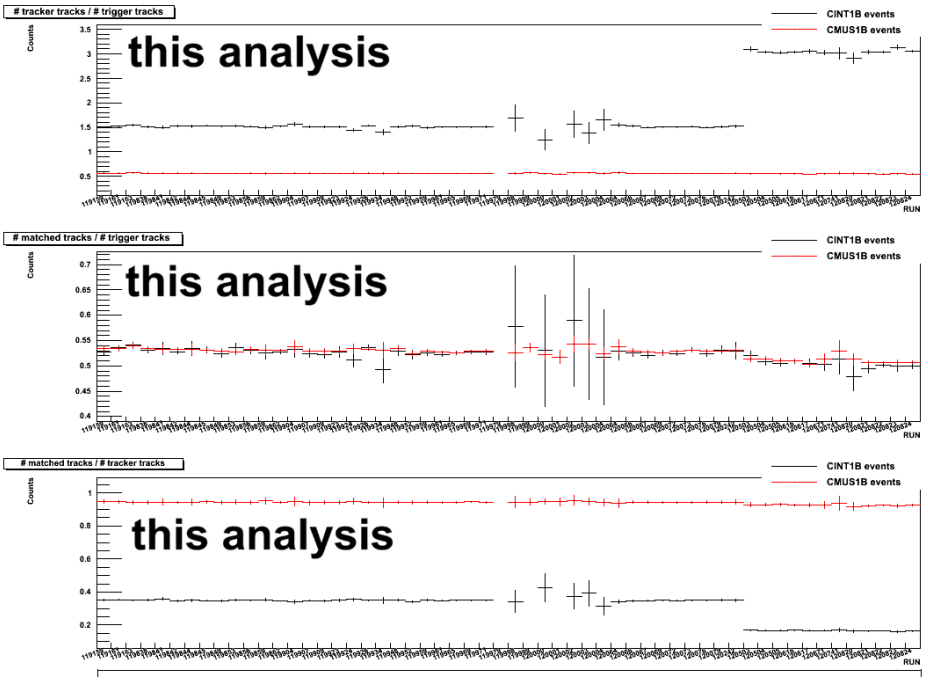

Figure 7.1: The ratios of the number of tracker tracks over trigger tracks (top), matched tracks over trigger tracks (middle) and matched tracks over tracker tracks (bottom) as a function of run number in LHC10c period. The black lines show the results in the minimum bias events (CINT1B) and the red lines are the results in the muon trigger events (CMUS1B).

of matched tracks over the number of tracker tracks is shown. This represents the trigger matching efficiency. One can find that, the trigger matching efficiency is almost flat in the first part of this plot in both minimum bias events and muon trigger events. This means that the detector status is stable during these runs. It drops to $\sim$ 50% in the last part of this period for minimum bias events. The decrease of the trigger matching efficiency indicates that the status of the trigger system was changed in the last runs. It was still stable according to the trigger matching efficiency which shows a flat behaviour. This results from the fact that half of the electronics of the trigger stations was not read out.

After having applied the QA selections defined in Sec. 7.1.1, we separate good runs in LHC10c into two parts: the part with the full trigger stations is named as LHC10c1 and the part with half of the trigger stations is named as LHC10c2. During our analysis, to avoid the bias in the efficiency correction for the half of the trigger stations, we just used the data in LHC10c1.

7.1.2.2 QA of LHC10d

The multiplicity of trigger tracks, tracker tracks and matched tracks in LHC10d is shown in Fig. 7.2 and Fig. 7.3 for minimum bias events and muon trigger events,

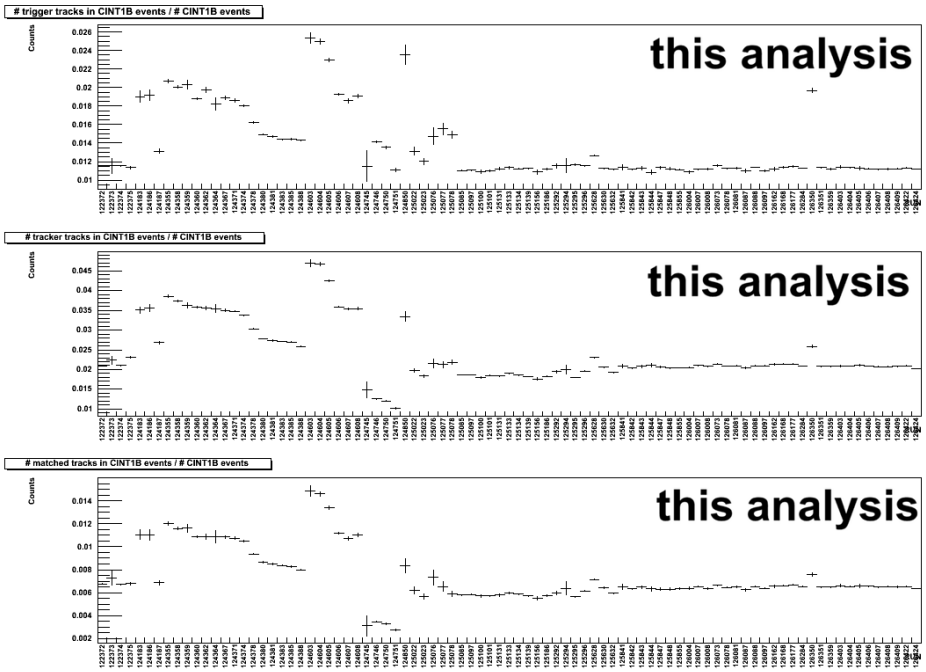

Figure 7.2: Multiplicity of trigger tracks (top), tracker tracks (middle) and matched tracks (bottom) in minimum bias events from LHC10d. Results are shown as a function of the run number.

respectively. From these two figures. One can notice that there is a region with large multiplicity fluctuations located for the runs in the middle of this period. For sure, these runs should be rejected as they correspond to an unstable detector status.

After excluding the unstable runs, for minimum bias events, the multiplicities for the different kinds of tracks are systematically higher in the first part of the period than in the last part. However, for the muon triggered events, the multiplicities for the different kinds of tracks are similar over the whole period. Since the muon trigger events require at least a trigger track, this allows to reject tracks from background events. The different evolution behavior of the track multiplicities in the minimum bias events and the muon trigger events indicates that there is a visible fraction of background events included in the first runs of LHC10d period. The CTP information indicates that, due to the higher beam intensity in these runs, the pile-up effect is larger. According to this, we separate the LHC10d period into two parts, the first part with high beam intensity and pile-up is called as LHC10d1, the other one with low beam intensity and low pile-up is called as LHC10d2.

If one looks at the multiplicity distribution in LHC10d2 a little bit carefully, then one can find that, the multiplicities in the first runs are slightly lower than that in the rest of the period. This is due to 7 tracking chambers that are missing during the data taking of these runs. Furthermore, according to the different status of the tracking stations, the LHC10d2 has been separated as LHC102a with 7 track-

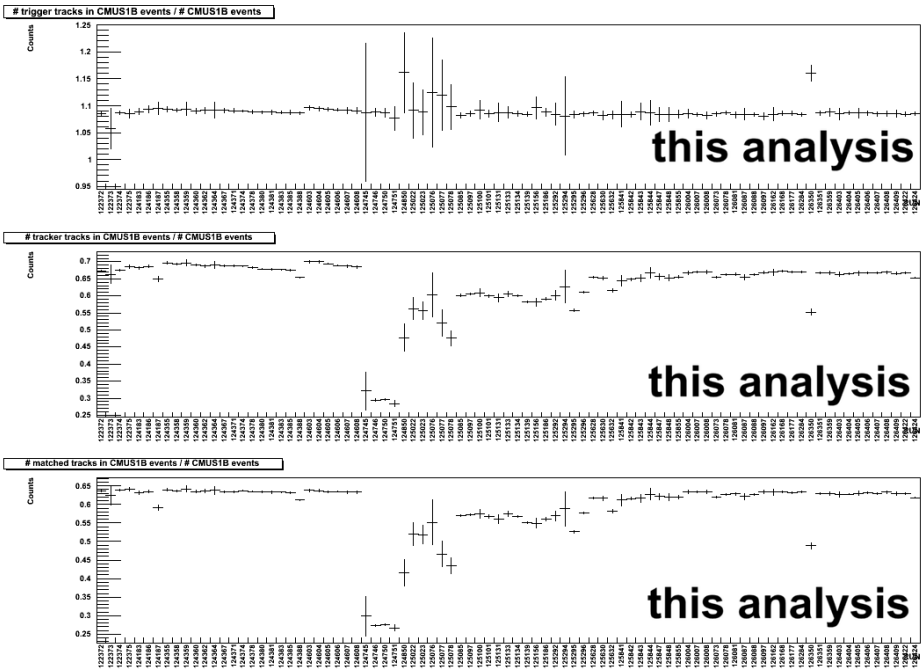

Figure 7.3: Same as Fig. 7.2, but for muon trigger events in LHC10d.

ing chambers missing and LHC10d2b with full tracking chambers. To avoid bias from the pile-up correction in high beam intensity runs and bias for the efficiency correction for the runs with missing 7 tracking chambers, we focus on the analysis of the data sample LHC10d2b.

In addition, the QA for the LHC10e is similar as the one done in LHC10c and LHC10d. Nothing particular needs to be mentioned for that period.

7.1.3 Pile-up Correction

Since there is no post-future protection settled during the data taking, the pile-up effect is always present in different run periods, and sometimes, it was particularly large, as in LHC10d1 period. The pile-up events make bias on the normalization of data. In order to get the correct normalization in our final results, the pile-up effect, anyhow, should be corrected. There are two different methods that can be used to get the pile-up information from data. One method characterizes the pile-up events by identifying the pile-up vertex in the reconstructed events; the other one is based on the estimate of the mean number of collision events in each beam crossing. Now, we are going to introduce these two methods.

7.1.3.1 Pile-up Vertex Identification

The first place to identify the pile-up vertex is during the estimate of the vertex position according to the SPD tracklets. In this step, with a given set of cuts, not

all the reconstructed tracklets in SPD are pointing to the same vertex. The main vertex (the primary vertex candidates) is tagged as the one with largest contributors. Then, remaining vertex candidates for which the contributors not point to the main vertex are identified as the pile-up vertex candidates. Then, after the whole event reconstruction, the information of these pile-up vertex candidates will be recorded in the ESD/AOD as well as that of the primary vertex.

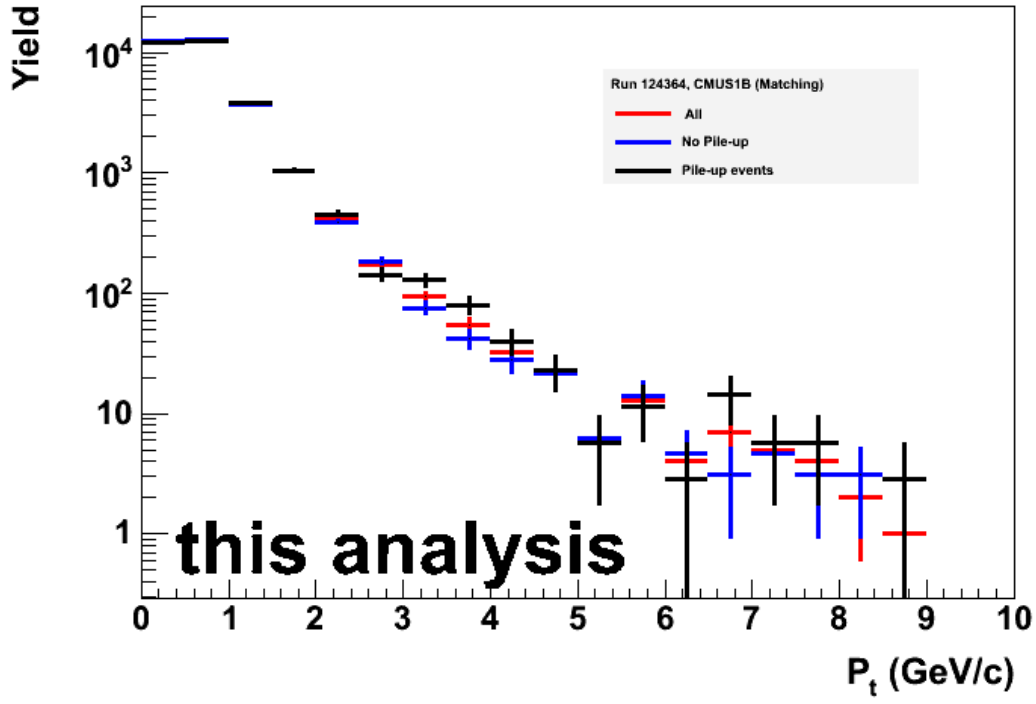

Figure 7.4: Transverse momentum distributions of reconstructed muon tracks from the events with no identified pile-up vertex (blue) and from the tagged pile-up events (black). To compare the shapes of these two distributions, we scaled them together with the p_{t} distribution in the full event sample (red) according to the integrated yield given by the red line. These results are from the muon triggered events in run 124364 of LHC10d1 where the pile-up effect is large.

In each reconstructed event, one can loop over the pile-up vertex candidates and identify the pile-up vertices according to the following cuts:

- the number of contributors of the pile-up vertex should be larger than a given threshold, which depends on the event multiplicity;
- the reconstructed pile-up candidate should be located inside the estimated collision diamond region, otherwise, it is not produced by a physics collision;
- the distance between the pile-up candidate and the primary vertex should be larger than a given value which is determined by the position resolution of

these two vertices in order to be sure that, they are not from the same collision event.

If the total number of pile-up vertices, which passed above cuts in a given event is larger than one, then this event will be tagged as pile-up event.

Fig. 7.4 shows the p_t distribution of muon tracks from the events with no identified pile-up vertex (blue) and that from the identified pile-up events (black) in muon triggered events from run 124364 located in LHC10d1 where the pile-up effect is large. To compare their shapes, they are scaled together according to the yields from the total number of events (red). In this figure, one can see that the p_t distributions of the muon tracks from both the pile-up events and no pile-up events are similar, indicating that these two kinds of events include the same physics content. We do not need to separate them, if we just want to extract the physics distribution. But when we want to convert yields into a cross section, it is important to count the correct number of minimum bias collisions.

The drawback of this method is that, we do not know exactly the efficiency for the pile-up vertex identification according to the above cuts. In this case, neither the cut of tagged pile-up events which will also reduce our statistics nor the correction of the number of minimum bias collisions with the number of identified pile-up vertex can be used in our analysis. The reason is the unknown pile-up identification efficiency which will make a bias in the normalization.

7.1.3.2 Pile-up Factor Estimate

The pile-up can also be described in a mathematical side of view.

In a given data taking period, the number of crossing beams is given by the CBEAMB trigger, and is named as N_{CBEAMB}, the number of minimum bias collisions is triggered by the L0 minimum bias trigger before the trigger selection, is named as $N_{\mathrm{MB}}^{\mathrm{L0b}}$ [1]. If there is always pile-up in the triggered minimum bias collisions, $N_{\mathrm{MB}}^{\mathrm{L0b}}$ does **NOT** give the number of collisions but gives the number of triggered data with **At Least** one collision occurring. Then, the ratio $N_{\mathrm{MB}}^{\mathrm{L0b}}/N_{\mathrm{CBEAMB}}$ does **NOT** provide the probability to have one collision, but this is the probability to have **At Least** one collision:

$$P(n \geq 1) = \frac{N_{\mathrm{MB}}^{\mathrm{L0b}}}{N_{\mathrm{CBEAMB}}}. \tag{7.1}$$

To get the real number of collisions in N_{CBEAMB} beam crossing, the corresponding N_{CBEAMB} should be corrected with the mean number of collisions in one beam crossing (or the probability to have one collision).

The probability to have n collisions is given by Poisson distribution:

$$p(n, m) = \frac{m^n}{n!} e^{-m}, \tag{7.2}$$

[1] As mentioned in Chap. 4, there are three different level of triggers applied during the data taking, L0, L1 and L2. For each trigger, the trigger rates are taken into account before and after the trigger selection, respectively. For example, we use L0a and L0b to denote the trigger rates at L0 before and after the trigger selection, the same naming rule is applied to L1 and L2 triggers.

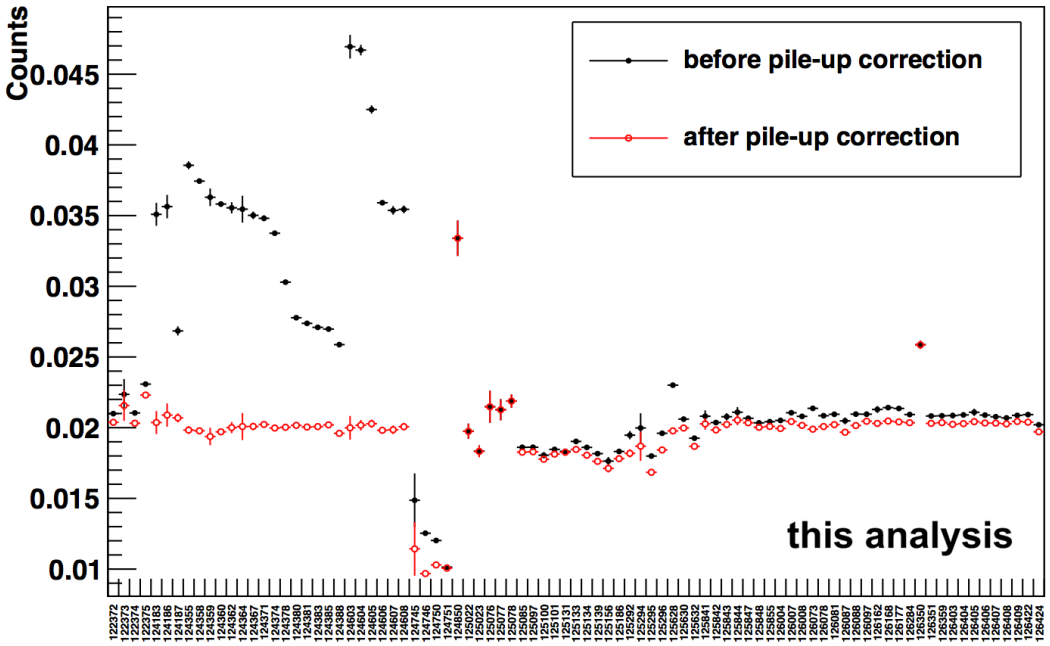

Figure 7.5: Same as the middle plot in Fig. 7.2, the tracker track multiplicity in minimum bias events from LHC10d. The results before the pile-up correction, black line, are compared with the one after the pile-up correction with Eq. (7.8), red line.

where m is the mean of the distribution. Eq. (7.2) satisfied the normalization condition:

$$\sum_{n=0}^{\infty} p(n,m) = 1. \tag{7.3}$$

According to the definition of Eq. (7.1), we have,

$$P(n \geq 1) = \sum_{n=1}^{\infty} p(n,m) = \sum_{n=0}^{\infty} p(n,m) - p(0,m) = 1 - e^{-m} = \frac{N_{\mathrm{MB}}^{\mathrm{L0b}}}{N_{\mathrm{CBEAMB}}}, \tag{7.4}$$

and get,

$$m = \ln \frac{N_{\mathrm{CBEAMB}}}{N_{\mathrm{CBEAMB}} - N_{\mathrm{MB}}^{\mathrm{L0b}}}. \tag{7.5}$$

Finally, the mean number of collisions in one beam crossing or the probability to have one collision is given by,

$$< n_{\mathrm{coll}} >= \frac{\sum_{n=1}^{\infty} n \cdot p(n,m)}{\sum_{n=1}^{\infty} p(n,m)} = \frac{\sum_{n=0}^{\infty} n \cdot p(n,m) - 0 \cdot p(0,m)}{\sum_{n=1}^{\infty} p(n,m)}. \tag{7.6}$$

Assuming m is the mean of Poisson distribution and the relation in Eq. (7.4), we have,

$$< n_{\mathrm{coll}} >= \frac{m}{P(n \geq 1)} = \frac{N_{\mathrm{CBEAMB}}}{N_{\mathrm{MB}}^{\mathrm{L0b}}} \ln \frac{N_{\mathrm{CBEAMB}}}{N_{\mathrm{CBEAMB}} - N_{\mathrm{MB}}^{\mathrm{L0b}}}. \tag{7.7}$$

Then, in N_{CBEAMB} beam crossing, the number of minimum bias collisions is given by:

$$N_{\mathrm{MB}}^{\mathrm{corr}} =< n_{\mathrm{coll}} > N_{\mathrm{MB}}^{\mathrm{L0b}} = N_{\mathrm{CBEAMB}} \cdot \ln \frac{N_{\mathrm{CBEAMB}}}{N_{\mathrm{CBEAMB}} - N_{\mathrm{MB}}^{\mathrm{L0b}}}. \tag{7.8}$$

In Eq. (7.8), both N_{CBEAMB} and $N_{\mathrm{MB}}^{\mathrm{L0b}}$ evolve with the data taking time t, $N_{\mathrm{MB}}^{\mathrm{corr}}$ is also a function of t, and the pile-up correction (Eq. (7.8)) should be implemented to data run by run. Fig. 7.5 shows the multiplicity of tracker tracks in minimum bias events from LHC10d, the results before and after the pileup correction (with Eq. (7.8)) are presented with black and red histograms, respectively. One can notice that, after the pile-up correction, there is a reduction in the tracker track multiplicity, especially for LHC10d1 period, where the pile-up effect is large, and the multiplicities in LHC10d1 and LHC10d2b are consistent with each other and stable with the data taking time. This is because Eq. (7.8) gives a stable way to estimate the real number of minimum bias collisions in the pile-up events. We choose this method for the pile-up correction in the following analysis.

7.2 Data Sample

Before to go through the physics analysis, I would like to show the statistics and typical distributions in our used data samples. With the pile-up correction, we can normalize the minimum bias events. But in the normalization of muon triggered events sample, we should first know its equivalent statistics in the minimum bias collisions. This issue will also be discussed in this section.

7.2.1 Summary of Statistics

run period	reconctruction pass	$N_{\mathrm{MB}}^{\mathrm{ev}}$	$N_{\mathrm{MB}}^{\mathrm{trk}}$	$N_{\mathrm{MU}}^{\mathrm{trk}}$
LHC10c1	2	$\sim$ 56 M	$\sim$ 362 k	$\sim$ 848 k
LHC10d2b	2	$\sim$ 97 M	$\sim$ 549 k	$\sim$ 2.1 M
LHC10e	2	$\sim$ 120 M	$\sim$ 761 k	$\sim$ 6.7 M

Table 7.1: Statistics used in our analysis of LHC10c1, LHC10d2b and LHC10e. The corresponding number of minimum bias events $N_{\mathrm{MB}}^{\mathrm{ev}}$ are gotten after the physics selection, the number of tracks in both minimum bias events and muon trigger events (labeled as $N_{\mathrm{MB}}^{\mathrm{trk}}$ and $N_{\mathrm{MU}}^{\mathrm{trk}}$) are gotten after the muon selection cuts discussed in Sec. 6.4.

Tab. 7.1 summarizes the statistics used in our analysis, all the numbers are obtained after the event and muon track selection cuts discussed in Sec. 6.4. Also the number of minimum bias events are corrected for pile-up with Eq. (7.8). In this table, one can notice that, the ratios between number of tracks in the muon trigger events and that in the minimum bias events increase with the run periods:

run period	simulation	generator
LHC10c1	LHC10d4 LHC10d4a	PYTHIA Perugia-0 PhoJet
LHC10d2b	LHC10f6 LHC10f6a	PhoJet PYTHIA Peruia-0
LHC10e	–	–

Table 7.2: Simulations used in our analysis for corresponding data taking run periods.

this shows that the data taking rate for the muon trigger events become higher and higher during data taking. In particular, the statistics of tracks in the muon trigger events in LHC10e is more than 3 times larger than the sum of those in LHC10c1 and LHC10d2b. With such high statistics, this data sample allows to extract muons from heavy flavour decays up to 12 GeV/c, and our final results are gotton from this data sample.

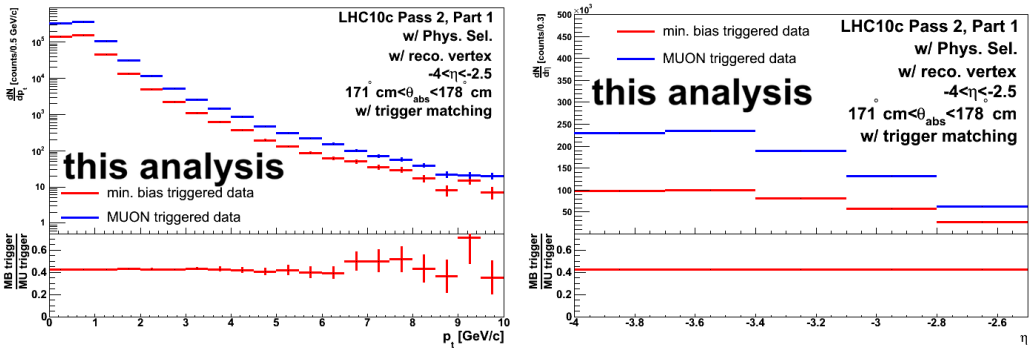

Figure 7.6: Transverse momentum (left) and η (right) distributions of muon tracks in minimum bias events (red) and in muon trigger events (blue) in pp collisions at $\sqrt{s} = 7$ TeV from LHC10c1. The ratios between the corresponding distributions in the minimum bias events and that in the muon trigger event are shown in the bottom panel.

Fig. 7.6 and 7.7 show the $p_{\rm t}$ and η distributions after all selection cuts in pp collisions at $\sqrt{s} = 7$ TeV from LHC10c1 and LHC10d2b, respectively. In each case, the results from minimum bias trigger events (red) and that from muon trigger events (blue) are compared together with the ratios between the distributions in these two kinds of data samples, as presented in the bottom panel for each plot. The $p_{\rm t}$ reach in LHC10c1 is ~ 10 GeV/c, and in the LHC10d2b, with higher statistics, the measured $p_{\rm t}$ goes up to ~ 15 GeV/c. An other interesting result to be mentioned, is that after all the selection cuts, the ratios between the distribution in minimum bias events and that in the muon trigger events are almost independent of $p_{\rm t}$ and/or η in

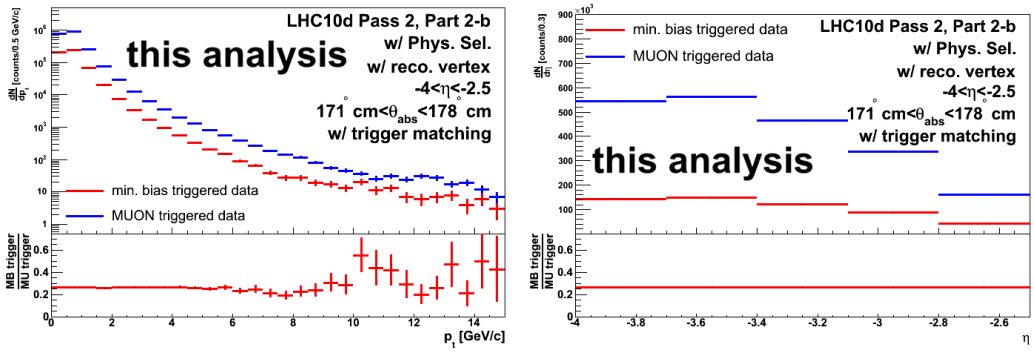

Figure 7.7: The same as Fig. 7.6, but the distributions are from LHC10d2b.

both data samples. In the following we will see that, this property is very important to normalize the muon triggered events. Also, the decrease of data taking rates for the muon triggered events with respect to that of minimum bias events makes these ratios decreasing from ~ 0.4 to ~ 0.3 from LHC10c1 to LHC10d2b.

Similarly to what has been done in pp collisions at $\sqrt{s} = 900$ GeV, there are several sets of realistic simulations used for the analysis for each run period. Tab. 7.2 lists the simulations used in our analysis with their corresponding data taking periods. The main part of the analysis presented in this chapter was finished in the beginning of 2011, and at that time, no simulations for LHC10e anchor runs were available. Then, the simulations used in the analysis of LHC10e data are the LHC10f6 and LHC10f6a for anchor runs of LHC10d. Also, for historical reason, there is a simulation with the ideal detector configuration with PYTHIA ATLAS tuning used in our analysis from time to time.

7.2.2 Event Normalization

The normalization of the distribution in minimum bias events is straightforward,

$$\frac{\mathrm{d}^2\sigma^{\mu}}{\mathrm{d}p_{\mathrm{t}}\mathrm{d}\eta} = \frac{1}{\mathrm{pileup} \times N_{\mathrm{MB}}^{\mathrm{ev}}} \times \frac{1}{\varepsilon} \times \frac{\mathrm{d}^2 N_{\mathrm{MB}}^{\mathrm{trk}}}{\mathrm{d}p_{\mathrm{t}}\mathrm{d}\eta} \times \sigma_{\mathrm{pp}}^{\mathrm{MB}}, \tag{7.9}$$

where, pileup $\times N_{\mathrm{MB}}^{\mathrm{ev}}$ is the pile-up corrected number of minimum bias events, $N_{\mathrm{MB}}^{\mathrm{trk}}$ is the number of muon tracks in the considered data sample, $\sigma_{\mathrm{pp}}^{\mathrm{MB}}$ is the minimum bias cross section in pp collisions under the given center of mass energy and ε is the correction efficiency which we will mention later. In ALICE, $\sigma_{\mathrm{pp}}^{\mathrm{MB}}$ is derived from the cross section of the so-called "V0AND" events, which is a sub-sample of the minimum bias events and measured via van der Meer scan [304]. The V0AND triggered events correspond to coincidence signals in the two VZERO detectors. The ratio between the cross section of V0AND events and minimum bias events is the percentage of minimum bias events with the L0a trigger input fired and satisfying V0AND conditions. Its value is 0.87 and remains stable within 1% over the analyzed

data taking period. In this case, we get,

$$\sigma_{\rm pp}^{\rm MB} = \frac{\sigma_{\rm pp}^{\rm V0AND}}{0.87} = 62.3 \pm 2.5 \text{ (syst.) mb}, \tag{7.10}$$

where the statistical uncertainty is negligible. With all the inputs, there is no difficulty to implement Eq. (7.9) to normalize the minimum bias events. But Eq. (7.10) can not be used to estimate the corresponding number of minimum bias events for a given muon triggered data sample. There are two methods that we proposed to used for the normalization of muon triggered events: one scales the events with special triggers to the minimum bias triggered events according to the information in CTP, the other one estimates the corresponding minimum bias events for a given muon triggered data sample according to the event multiplicity. Now we give a short introduction for both of them.

7.2.2.1 CTP Scalers

We can say that, the beam luminosity $\mathfrak{L}$ is a constant in a short data taking interval t, then for any kind of triggers, the triggered number of events before and after different level of triggers $N^{\rm ev}({\rm L}i{\rm b})$ and $N^{\rm ev}({\rm L}i{\rm a})$ $(i = 0, 1, 2)$ in the interval t are given by:

$$\begin{aligned}
N^{\rm ev}({\rm L0b}) &= \mathfrak{L}\sigma_0 t, \\
N^{\rm ev}({\rm L0a}) &= \mathfrak{L}\sigma_0 (t - \Delta t^{\rm DD} - \Delta t_0^{\rm PF}), \\
N^{\rm ev}({\rm L1b}) &= \mathfrak{L}\sigma_1 (t - \Delta t^{\rm DD} - \Delta t_0^{\rm PF}), \\
N^{\rm ev}({\rm L1a}) &= \mathfrak{L}\sigma_1 (t - \Delta t^{\rm DD} - \Delta t_1^{\rm PF}), \\
N^{\rm ev}({\rm L2b}) &= \mathfrak{L}\sigma_2 (t - \Delta t^{\rm DD} - \Delta t_1^{\rm PF}), \\
N^{\rm ev}({\rm L2a}) &= \mathfrak{L}\sigma_2 (t - \Delta t^{\rm DD} - \Delta t_2^{\rm PF}),
\end{aligned} \tag{7.11}$$

where, $\Delta t^{\rm DD}$ is the detector dead time and it depends on the related triggers (*eg.* minimum bias trigger and muon trigger) according to the detectors used for the trigger decision, $\Delta t_i^{\rm PF}$ and σ_i $(i = 0, 1, 2)$ are the past future protection and triggered cross section at different level of triggers, respectively. According to Eq. (7.11), we can write:

$$\sigma_1 = \frac{N^{\rm ev}({\rm L1b})}{N^{\rm ev}({\rm L0a})}\sigma_0 \qquad \sigma_2 = \frac{N^{\rm ev}({\rm L2b})}{N^{\rm ev}({\rm L1a})}\sigma_1, \tag{7.12}$$

and

$$\sigma_2 = \frac{N^{\rm ev}({\rm L2b})}{N^{\rm ev}({\rm L1a})} \cdot \frac{N^{\rm ev}({\rm L1b})}{N^{\rm ev}({\rm L0a})}\sigma_0. \tag{7.13}$$

According to the ALICE trigger configurations in pp collisions, we have,

$$N^{\rm ev}({\rm L2a}) = N^{\rm ev}({\rm L2b}) = N^{\rm ev}({\rm L1a}) = N^{\rm ev}({\rm L1b}) = N^{\rm ev}({\rm L0a}) \neq N^{\rm ev}({\rm L0b}), \tag{7.14}$$

then, we get,

$$\sigma_2 = \sigma_1 = \sigma_0. \tag{7.15}$$

In this case, for a given trigger type, we do not need to distinguish its cross section in different trigger levels. Also, the number of events and tracks that we used in the analysis are from L2a trigger, and they are equal to those coming from L0a trigger according to Eq. (7.14). We need to notice that, even if our starting point is for a given time interval t, all the relations we get now are independent of the data taking time.

Now let go back to the normalization of the muon triggered events. If we forget the pile-up effect for a moment, the production cross section of muons in the muon triggered events can be expressed as:

$$\begin{aligned}\frac{\mathrm{d}^2\sigma^{\mu}}{\mathrm{d}p_{\mathrm{t}}\mathrm{d}\eta} &= [\frac{1}{N^{\mathrm{ev}}_{\mathrm{MU}}} \times \frac{1}{\varepsilon} \times \frac{\mathrm{d}^2 N^{\mathrm{trk}}_{\mathrm{MU}}}{\mathrm{d}p_{\mathrm{t}}\mathrm{d}\eta}]_{\mathrm{L2a}} \times \sigma^{\mathrm{MU}}_{\mathrm{pp}} \\ &= [\frac{1}{N^{\mathrm{ev}}_{\mathrm{MU}}} \times \frac{1}{\varepsilon} \times \frac{\mathrm{d}^2 N^{\mathrm{trk}}_{\mathrm{MU}}}{\mathrm{d}p_{\mathrm{t}}\mathrm{d}\eta}]_{\mathrm{L0a}} \times \sigma^{\mathrm{MU}}_{\mathrm{pp}},\end{aligned} \tag{7.16}$$

where the definitions of all terms the same as those in Eq. (7.9), the subscript L2a means that the terms in the square bracket come from the L2a trigger and they are equal to those in L0a trigger.

To get the muon cross section in Eq. (7.16), we need to know the value of $\sigma^{\mathrm{MU}}_{\mathrm{pp}}$ in pp collisions. According to Eq. (7.11), in a given time interval t we have

$$N^{\mathrm{ev}}_{\mathrm{MB}}(\mathrm{L0b}) = \mathfrak{L}\sigma^{\mathrm{MB}}_{\mathrm{pp}}t, \qquad N^{\mathrm{ev}}_{\mathrm{MU}}(\mathrm{L0b}) = \mathfrak{L}\sigma^{\mathrm{MU}}_{\mathrm{pp}}t, \tag{7.17}$$

then, we get,

$$\sigma^{\mathrm{MU}}_{\mathrm{pp}} = \frac{N^{\mathrm{ev}}_{\mathrm{MU}}(\mathrm{L0b})}{N^{\mathrm{ev}}_{\mathrm{MB}}(\mathrm{L0b})} \cdot \sigma^{\mathrm{MB}}_{\mathrm{pp}}. \tag{7.18}$$

Indeed, what we get from the van der Meer scan is the cross section of "V0AND" events under the minimum bias trigger. The cross sections of minimum bias events $\sigma^{\mathrm{MB}}_{\mathrm{pp}}$ and the one in V0AND events $\sigma^{\mathrm{V0AND}}_{\mathrm{pp}}$ obey the relation:

$$\sigma^{\mathrm{MB}}_{\mathrm{pp}} = \frac{N^{\mathrm{ev}}_{\mathrm{MB}}(\mathrm{L0a})}{N^{\mathrm{ev}}_{\mathrm{V0AND}}(\mathrm{L0a})} \cdot \sigma^{\mathrm{V0AND}}_{\mathrm{pp}}. \tag{7.19}$$

Finally, putting Eq. (7.18) and (7.19) back to Eq. (7.16), we get the full formula used for the muon triggered event normalization based on the CTP scalers,

$$\begin{aligned}\frac{\mathrm{d}^2\sigma^{\mu}}{\mathrm{d}p_{\mathrm{t}}\mathrm{d}\eta} &= [\frac{1}{N^{\mathrm{ev}}_{\mathrm{MU}}} \times \frac{1}{\varepsilon} \times \frac{\mathrm{d}^2 N^{\mathrm{trk}}_{\mathrm{MU}}}{\mathrm{d}p_{\mathrm{t}}\mathrm{d}\eta}]_{\mathrm{L0a}} \times \frac{N^{\mathrm{ev}}_{\mathrm{MU}}(\mathrm{L0b})}{N^{\mathrm{ev}}_{\mathrm{MB}}(\mathrm{L0b})} \times \frac{N^{\mathrm{ev}}_{\mathrm{MB}}(\mathrm{L0a})}{N^{\mathrm{ev}}_{\mathrm{V0AND}}(\mathrm{L0a})} \cdot \sigma^{\mathrm{V0AND}}_{\mathrm{pp}} \\ &= [\frac{1}{N^{\mathrm{ev}}_{\mathrm{V0AND}}} \times \frac{1}{\varepsilon} \times \frac{\mathrm{d}^2 N^{\mathrm{trk}}_{\mathrm{MU}}}{\mathrm{d}p_{\mathrm{t}}\mathrm{d}\eta}]_{\mathrm{L2a}} \times \frac{N^{\mathrm{ev}}_{\mathrm{MU}}(\mathrm{L0b})}{N^{\mathrm{ev}}_{\mathrm{MU}}(\mathrm{L0a})} \times \frac{N^{\mathrm{ev}}_{\mathrm{MB}}(\mathrm{L0a})}{N^{\mathrm{ev}}_{\mathrm{MB}}(\mathrm{L0b})} \cdot \sigma^{\mathrm{V0AND}}_{\mathrm{pp}}.\end{aligned} \tag{7.20}$$

The relation $N^{\mathrm{ev}}_{\mathrm{V0AND}}(\mathrm{L02}) = N^{\mathrm{ev}}_{\mathrm{V0AND}}(\mathrm{L22})$ is used in the last step of Eq. (7.20).

Eq. (7.20) is derived in a short time interval t during the data taking; to implement it, all the scaler numbers in this formula should be gotten from the integrals over the data taking time, and the pile-up correction should also be added in this

procedure. The drawbacks for this method are: it needs to validate the minimum bias trigger and the so called V0AND trigger together with the muon trigger in the same data taking period, and it is complicated to be implemented with the muon trigger alone. Also, the final information in Eq. (7.20) is based on the condition of Eq. (7.14), and cannot work when the trigger configurations are changed (*eg.* in Pb–Pb collisions).

7.2.2.2 Multiplicity Scaling

To overcome the drawbacks of the CTP scaler method, we can treat the muon triggered event normalization in a more easy way. Let us go back to the starting point again, when the cross section of minimum bias events is measured (according to the V0AND cross section via the van der Meer scan). For the normalization of the muon triggered events, we need to estimate the equivalent number of minimum bias collisions for a given muon triggered data sample. This estimate can be done by noticing that, with a fixed center of mass collision energy, the multiplicity of the muon tracks should not be changed in the minimum bias collisions, regardless this collision is triggered by the minimum bias trigger or the muon trigger. This property is validated by Fig. 7.6 and 7.7. After all analysis cuts, the ratios between distributions in minimum bias events and that in muon trigger events are independent with p_{t} or η in a given run period. This means that the different event triggers can be treated as the scales for the muon track multiplicity.

We denote the equivalent number of minimum bias collisions for a given muon triggered data sample with $N^{\mathrm{ev}}_{\mathrm{MU}}$ muon triggered events and $N^{\mathrm{trk}}_{\mathrm{MU}}$ muon tracks as $N^{\mathrm{ev}}_{\mathrm{MB=MU}}$. It should satisfy the following relation:

$$M^{\mu} = \frac{N^{\mathrm{trk}}_{\mathrm{MB}}}{N^{\mathrm{ev}}_{\mathrm{MB}}} = \frac{N^{\mathrm{trk}}_{\mathrm{MU}}}{N^{\mathrm{ev}}_{\mathrm{MB=MU}}}, \tag{7.21}$$

where $N^{\mathrm{trk}}_{\mathrm{MB}}$ is the number of muon tracks in the minimum bias data sample with $N^{\mathrm{ev}}_{\mathrm{MB}}$ the minimum bias triggered events and M^{μ} the muon track multiplicity in the minimum bias collisions. Thus, similarly as Eq. (7.9), the normalization of muon triggered events is,

$$\begin{aligned} \frac{\mathrm{d}^2\sigma^{\mu}}{\mathrm{d}p_{\mathrm{t}}\mathrm{d}\eta} &= \frac{1}{N^{\mathrm{ev}}_{\mathrm{MB=MU}}} \times \frac{1}{\varepsilon} \times \frac{\mathrm{d}^2 N^{\mathrm{trk}}_{\mathrm{MU}}}{\mathrm{d}p_{\mathrm{t}}\mathrm{d}\eta} \times \sigma^{\mathrm{MB}}_{\mathrm{pp}} \\ &= \frac{1}{\mathrm{pileup} \times N^{\mathrm{ev}}_{\mathrm{MB}}} \times \frac{N^{\mathrm{trk}}_{\mathrm{MB}}}{N^{\mathrm{trk}}_{\mathrm{MU}}} \times \frac{1}{\varepsilon} \times \frac{\mathrm{d}^2 N^{\mathrm{trk}}_{\mathrm{MU}}}{\mathrm{d}p_{\mathrm{t}}\mathrm{d}\eta} \times \sigma^{\mathrm{MB}}_{\mathrm{pp}}. \end{aligned} \tag{7.22}$$

The pile-up correction is included in the last step of Eq. (7.22).

By comparing with Eq. (7.20), the implementation of Eq. (7.22) is more straightforward in the physics analysis and do not need to use the additional CTP information. Also, this method can be extrapolated to Pb–Pb collisions directly. With these advantages, we adopt this method to normalize the muon triggered events in our following analysis.

Fig. 7.8 shows the normalized p_{t} distributions of inclusive muon tracks as a function of p_{t} (left) and η (right) after the pile-up correction in minimum bias events

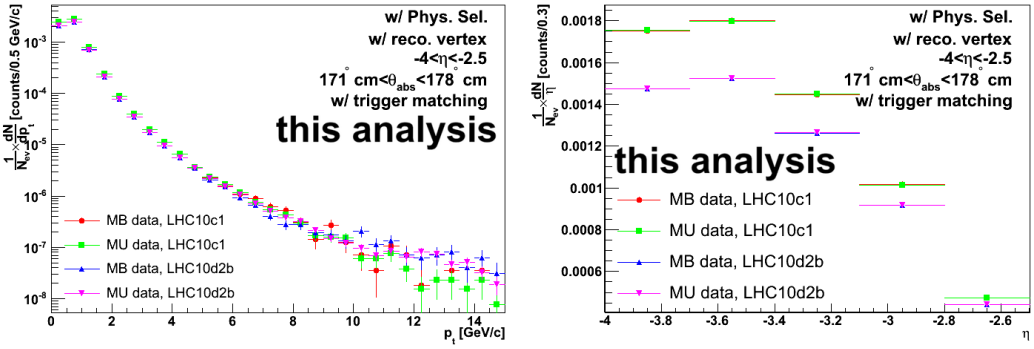

Figure 7.8: Normalized muon p_{t} distribution in minimum bias events (labeled as "MB data") and in muon trigger events (labeled as "MU data") with the pile-up correction in LHC10c1 and LHC10d2b, respectively. The results are shown as a function of p_{t} (left) and η (left). The normalization of muon trigger events is done with the multiplicity scaling method.

and muon trigger events, respectively. The muon triggered events are normalized with the multiplicity scaling method, and the results from LHC10c1 are compared with those from LHC10d2b. For a given run period, both the minimum bias event sample and muon triggered event sample give similar multiplicity distributions. In these two distributions, in particular in the η distribution, one can notice that, the multiplicity of muon tracks in LHC10c1 is higher than that in LHC10d2b. This is due to the fact that the efficiency correction is not implemented yet. The difference between these two run periods comes from the different tracking efficiencies.

7.3 Background Subtraction

The first step of background subtraction is to identify the background components. This can be done by means of realistic simulations. In this section, we start by looking at the muon sources after the event and muon selection cuts defined in Sec. 6.4. Then, we present the strategy for background subtraction according to what we learned in Monte-Carlo.

Since in the final results, we would like to show the differential production cross sections of muons from open heavy flavour decays both as a function of p_{t} and as a function of η, the total acceptance ($-4 < \eta < -2.5$) was divided into five pseudo-rapidity bins, of bin size 0.3: $-4 < \eta < -3.7$, $-3.7 < \eta < -3.4$, $-3.4 < \eta < -3.1$, $-3.1 < \eta < -2.8$ and $-2.8 < \eta < -2.5$. Then, the background subtraction and all the other analysis steps are presented in each pseudo-rapidity bin in order to get the corresponding p_{t}-differential production cross sections: $\mathrm{d}\sigma^{\mu\leftarrow\mathrm{HF}}/\mathrm{d}p_{\mathrm{t}}(\eta)$. Next, we add them together,

$$\frac{\mathrm{d}\sigma^{\mu\leftarrow\mathrm{HF}}}{\mathrm{d}p_{\mathrm{t}}}(-4<\eta<-2.5) = \sum_{\eta} \frac{\mathrm{d}\sigma^{\mu\leftarrow\mathrm{HF}}}{\mathrm{d}p_{\mathrm{t}}}(\eta), \tag{7.23}$$

to get the p_{t}-differential production cross section in the total acceptance $\mathrm{d}\sigma^{\mu\leftarrow\mathrm{HF}}/\mathrm{d}p_{\mathrm{t}}(-4 < \eta < -2.5)$, and integrate the p_{t}-differential production cross sections in each η bin,

$$\frac{\mathrm{d}\sigma^{\mu\leftarrow\mathrm{HF}}}{\mathrm{d}\eta} = \int \mathrm{d}p_{\mathrm{t}} \cdot \frac{\mathrm{d}\sigma^{\mu\leftarrow\mathrm{HF}}}{\mathrm{d}p_{\mathrm{t}}}(\eta), \tag{7.24}$$

to get the η-differential production cross section $\mathrm{d}\sigma^{\mu\leftarrow\mathrm{HF}}/\mathrm{d}\eta$.

7.3.1 Strategy

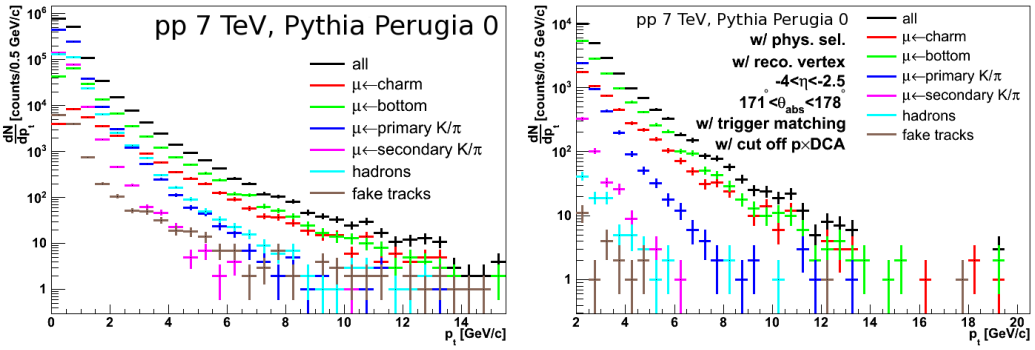

Figure 7.9: Transverse momentum distributions of muon track sources without any selection cut (left) and with the standard selection cuts (right) in pp collisions at $\sqrt{s} = 7$ TeV. Results from the LHC10f6a simulations with PYTHIA Perugia-0 tuning and realistic detector configurations correspond to LHC10d2b data sample.

Fig. 7.9 shows the p_{t} distributions of different sources for tracks reconstructed in the MUON spectrometer, without any selection cuts (left) and with the standard selection cuts [2] (right) from LHC10f6a simulations with PYTHIA (Perugia-0 tuning). This simulation corresponds to pp collisions at $\sqrt{s} = 7$ TeV, and the realistic detector configurations of LHC10d2b data are used. As one can see, comparing with the spectrum without any selection cut (left plot in Fig. 7.9), almost all the hadron and fake track (the unidentified track) components are removed after all the selection cuts (right plot in Fig. 7.9); also, the fraction of muons produced inside the front absorber [3] is $\lesssim 3\%$ with respect to the total inclusive muon distribution in $p_{\mathrm{t}} > 2$ GeV/c, and it can be neglected in this p_{t} region. In this case, when we focus

[2] The cuts listed in the right plot of Fig. 7.9 are named standard muon selection cuts. In addition to the analysis cuts at the event and track level we introduced in Sec. 6.4, there is an additional p×DCA cut. At present, our following analysis still uses the analysis cuts listed in Sec. 6.4. As we will see, the p×DCA cut is used to remove the beam gas background, especially in the high p_{t} region, and will not change the conclusions obtained without this cut.

[3] All the different muon sources have been already mentioned. We remind that muons produced in the front absorber are called "secondary muons", since they mainly come from the interactions of charged kaons and pions with the materials in the frond absorber, they are labeled as "$\mu \leftarrow$ secondary K/π". The muons from the primary light hadrons and resonances are called as the "primary muons", since they are mainly originating from charged kaon and pion decays. They can

on $p_t > 2$ GeV/c, the only main background component that we should consider is primary muons.

To subtract the primary muons in the inclusive muon spectrum, we used the following strategy:

- extract the p_t-shapes of primary muons from realistic simulations with different models under the same selection cuts which are applied in data in each of pseudo-rapidity bin,
- normalize the p_t-shapes of primary muons to the data to estimate the background in data;
- the uncorrected spectrum of muons from open heavy flavours decay are obtained after subtracting the estimated primary muon background from data.

The systematic uncertainty on each step should be taken into account carefully.

7.3.2 Background Estimate

The first step for the background subtraction is to extract the shape of primary muons from different predictions under the same selection cuts applied to the data. As shown in the right plot of Fig. 7.9, after all the selection cuts, the statistics of primary muons is not large enough to estimate the background in the high p_t region ($p_t > 8$ GeV/c) in the simulations. One can imagine that, when we separate it into five pseudo-rapidity bins, the statistics will be even smaller in each η region. Also, it needs large CPU time and disk storage to increase the statistics in the simulations since we should run the full analysis chain from generation until reconstruction. To save CPU time and disk storage, we used the function described in Eq. (5.1) to fit the p_t-shapes of primary muons in a given η region. Then the extrapolation to higher p_t is performed. This procedure should be DONE very carefully, since fitting and extrapolation could introduce additional bias in our background estimate. As shown in Fig. 7.10, to validate the stability of this procedure, we perform following checks (for each simulation):

1. fit the primary muon p_t-spectrum in the five individual pseudo-rapidity regions, and sum the fitting results in each of these regions together to get the get the fitting spectrum in the total η region (blue lines);
2. fit the p_t-spectrum of the primary muons again but in the total η region (red lines);
3. compare the results from above two steps to see how different they are.

According to the results in Fig. 7.10, the comparison between the fit of the p_t-shape of primary muons in the total η region ($-4 < \eta < -2.5$) and the sum over

be also labeled "$\mu \leftarrow$ primary K/π" or "decay muons". Also, the unidentified tracks can be labeled as "fake tracks". So next time, when you see different labels in the so many incoming beautiful figures, I wish you can understand what are they.

the fit results in five individual pseudo-rapidity bins from realistic simulations of LHC10d4 (pythia, upper, left), LHC10d4a (PhoJet, upper, right), LHC10f6 (PhoJet, down, left) and LHC10f6a (PYTHIA, down, right) with the same selection cuts applied to data, shows that the fit results from step 1 and 2 are in agreement, and that the extrapolation is stable. Due to the statistics limitation, as in LHC10d4a, these two kinds of fit results exhibit some differences in the high p_{t} region. This difference can be treated as the systematic uncertainty on the background extrapolation. However, since the background in this p_{t} region is much smaller than the signal (the muon from open heavy flavour decays), the total inclusive muon spectrum is almost insensitive on the observed difference. This systematic uncertainty is neglected in our final systematic uncertainty. With higher statistics in the simulations, as LHC10f6 and LHC10f6a, the difference between these two kinds of fit results disappears.

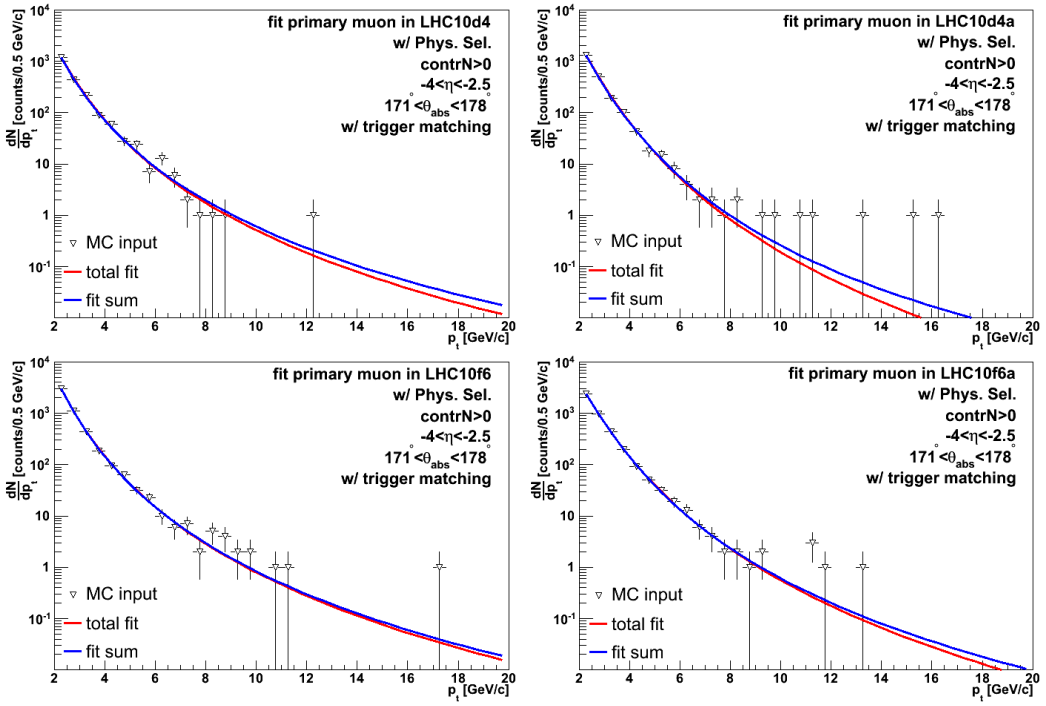

Figure 7.10: Comparison between the p_{t}-shape of primary muons in total η region, $-4 < \eta < -2.5$ (red lines) and the sum from fit results in 5 pseudo-rapidity bins (blue lines). The results are obtained, under the same selection cuts applied to data, from realistic simulations of LHC10d4 (pythia, upper, left), LHC10d4a (PhoJet, upper, right), LHC10f6 (PhoJet, down, left) and LHC10f6a (PYTHIA, down, right).

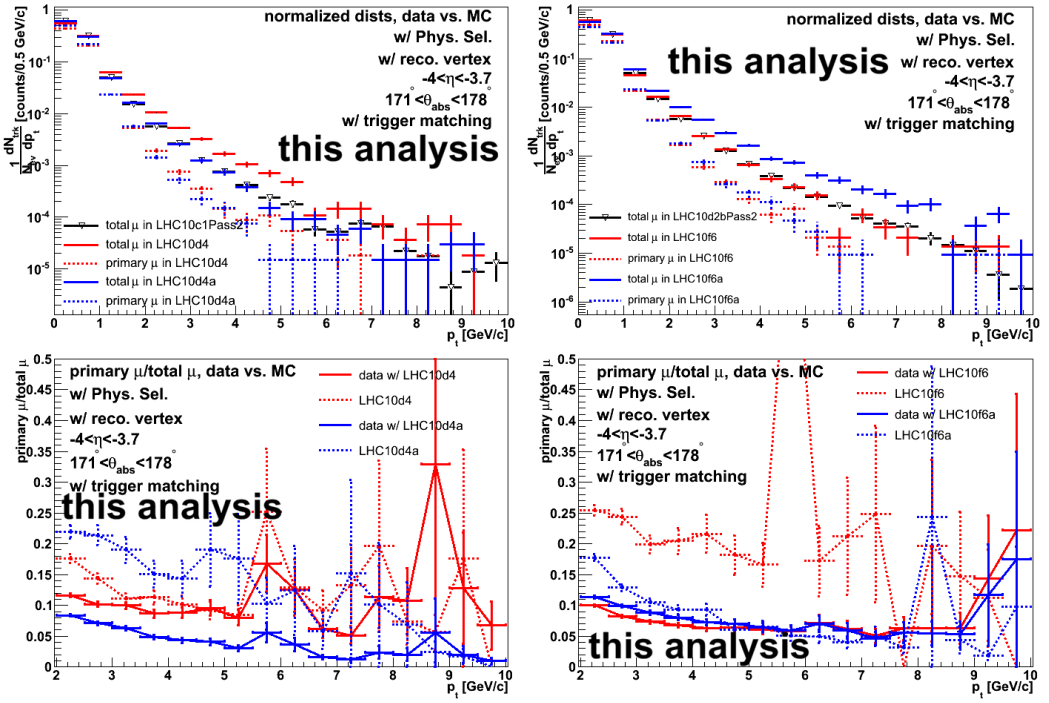

Figure 7.11: Upper panels: normalized inclusive p_{t} distributions in $-4 < \eta < -3.7$ in the muon triggered data from LHC10c1 (left) and LHC10d2b (right) with respect to the number muon triggered events. The results are compared to the p_{t} distributions of inclusive muons and primary muons in the corresponding realistic simulations. The simulations are scaled with S_{MC} (Eq. 7.27), obtained in the same η region before normalization with the corresponding number of events applied in the data. Lower panels: ratio between the primary muons and inclusive muons in data and in Monte-Carlo for LHC10c1 (left) and LHC10d2b (right).

7.3.3 Background Normalization

Before to describe the background normalization, we give the following definition:

$$N_{\mathrm{RD/MC}}^{\text{inclusive/primary }\mu}(\text{low } p_{\mathrm{t}}, \Delta\eta) = \int_{\Delta\eta} \mathrm{d}\eta \int_{0}^{1\ \mathrm{GeV}/c} \mathrm{d}p_{\mathrm{t}} \frac{\mathrm{d}^2 N_{\mathrm{RD/MC}}^{\text{inclusive/primary }\mu}}{\mathrm{d}p_{\mathrm{t}}\mathrm{d}\eta}, \quad (7.25)$$

which expresses the number of inclusive or primary muon tracks counted in $0 < p_{\mathrm{t}} < 1$ GeV/c in a given η region, $\Delta\eta$, in the event sample from data (RD) or Monte-Carlo (MC). After having obtained the background shapes from simulations, the normalization of background to data is done according to the assumption: in the low p_{t} region (here, we use $0 < p_{\mathrm{t}} < 1$ GeV/c) where the background from primary muons dominates, in both data and Monte-Carlo, the ratio of yield of primary muons to that of inclusive muons is the same in a given $\Delta\eta$ region:

$$R_{\mathrm{MC}}(\Delta\eta) = \frac{N_{\mathrm{MC}}^{\text{primary }\mu}(\text{low } p_{\mathrm{t}}, \Delta\eta)}{N_{\mathrm{MC}}^{\text{inclusive }\mu}(\text{low } p_{\mathrm{t}}, \Delta\eta)} = \frac{N_{\mathrm{RD}}^{\text{primary }\mu}(\text{low } p_{\mathrm{t}}, \Delta\eta)}{N_{\mathrm{RD}}^{\text{inclusive }\mu}(\text{low } p_{\mathrm{t}}, \Delta\eta)}, \quad (7.26)$$

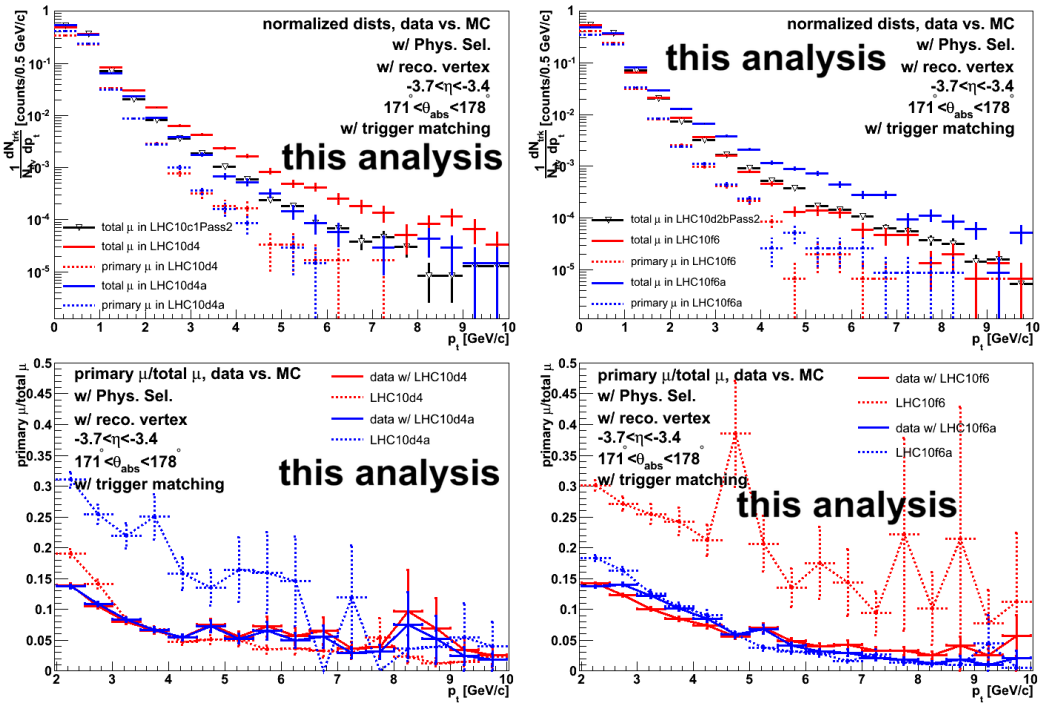

Figure 7.12: The same as Fig. 7.11, in $-3.7 < \eta < -3.4$.

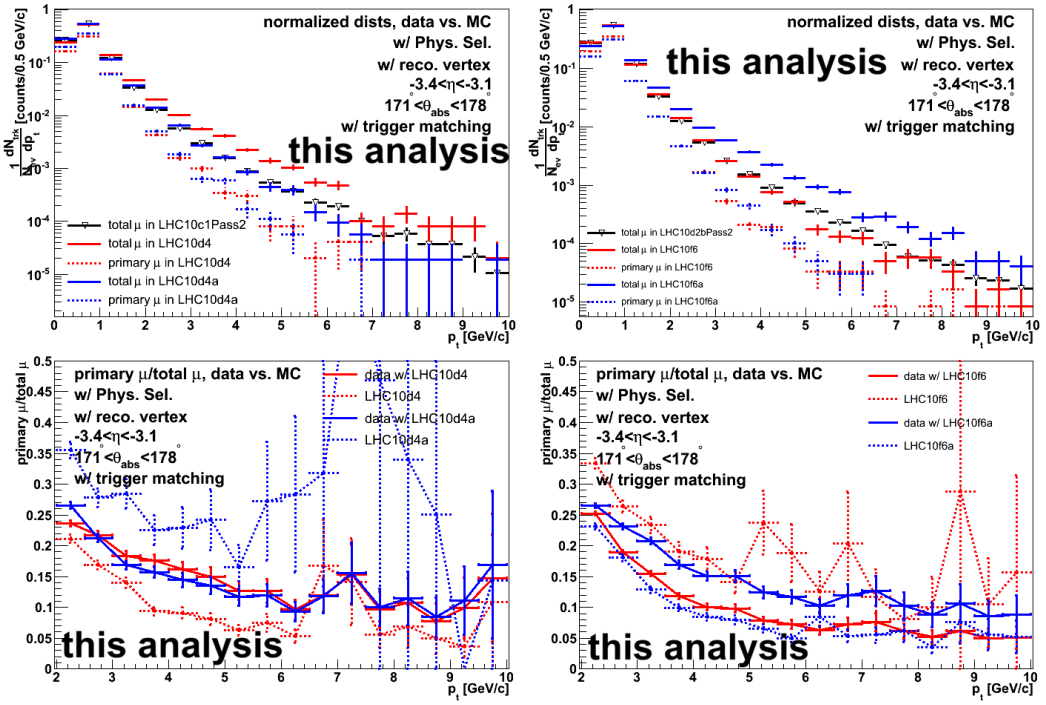

Figure 7.13: The same as Fig. 7.11, in $-3.4 < \eta < -3.1$.

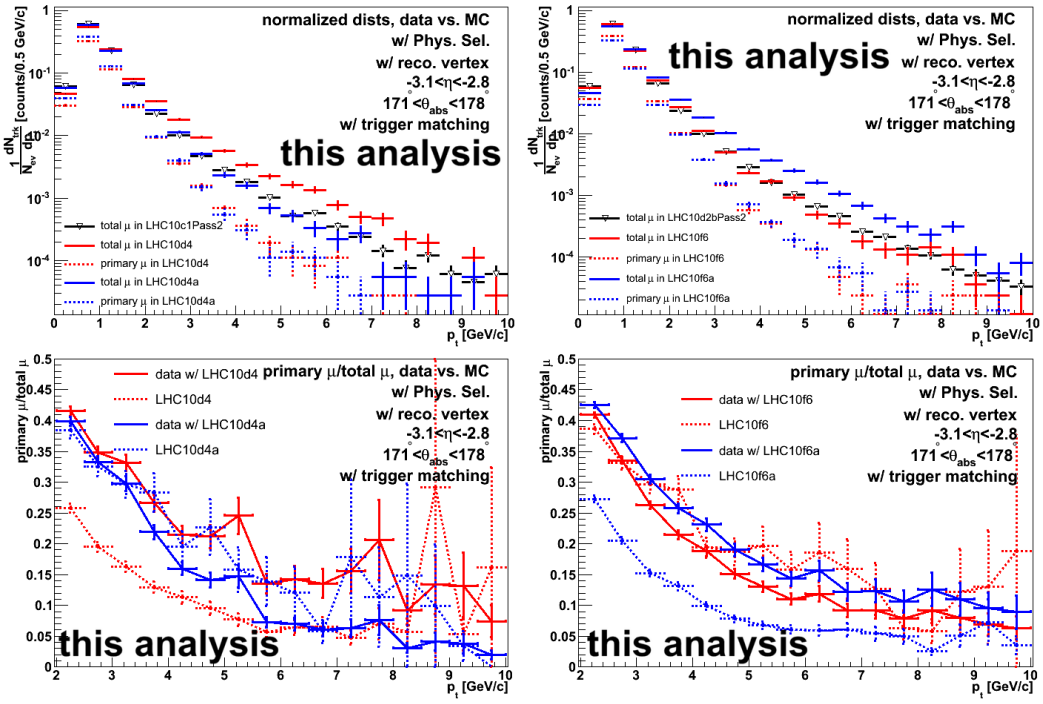

Figure 7.14: The same as Fig. 7.11, in $-3.1 < \eta < -2.8$.

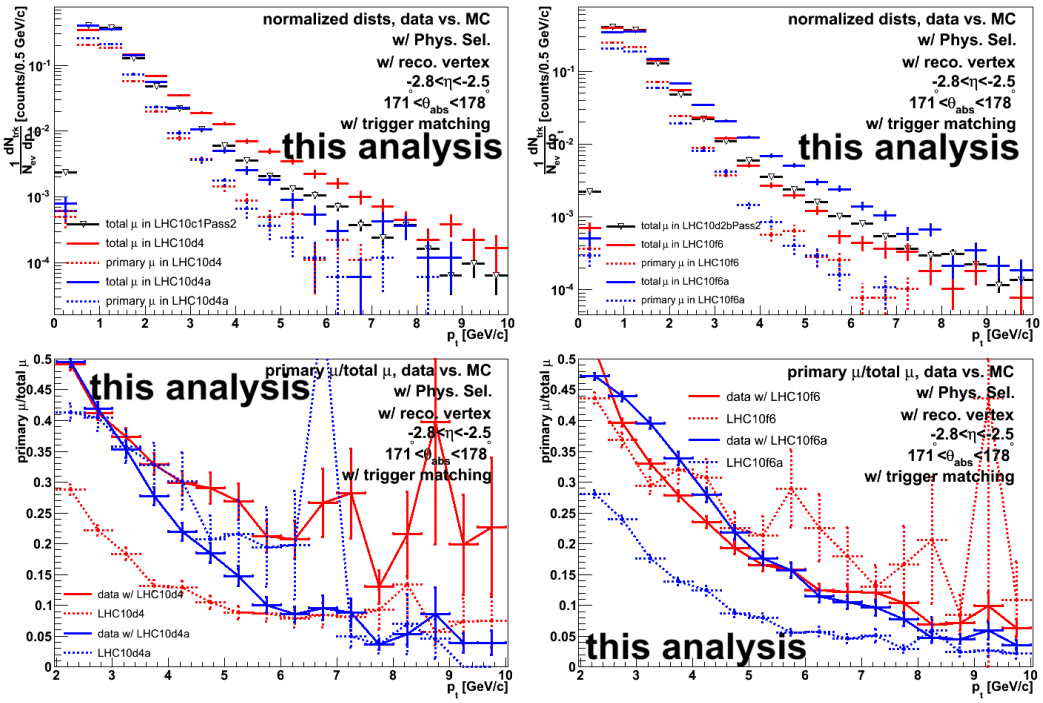

Figure 7.15: The same as Fig. 7.11, in $-2.8 < \eta < -2.5$.

In Eq. (7.26), $N_{\mathrm{MC}}^{\mathrm{primary}\ \mu}(\text{low}\ p_{\mathrm{t}}, \Delta\eta)$, $N_{\mathrm{MC}}^{\mathrm{inclusive}\ \mu}(\text{low}\ p_{\mathrm{t}}, \Delta\eta)$ and $N_{\mathrm{RD}}^{\mathrm{inclusive}\ \mu}(\text{low}\ p_{\mathrm{t}}, \Delta\eta)$ can be obtained from the used event sample in simulation or data directly, according to the definition in Eq. (7.25). With the obtained value of $R_{\mathrm{MC}}(\Delta\eta)$ from the used Monte-Carlo sample, $N_{\mathrm{RD}}^{\mathrm{primary}\ \mu}(\text{low}\ p_{\mathrm{t}}, \Delta\eta)$, the number of primary muons in the used data sample in $\Delta\eta$ and low p_{t} region, can be estimated according to Eq. (7.26).

In this case, we scale $N_{\mathrm{MC}}^{\mathrm{primary}\ \mu}(\text{low}\ p_{\mathrm{t}}, \Delta\eta)$ in the used simulation sample to $R_{\mathrm{MC}}(\Delta\eta) \times N_{\mathrm{RD}}^{\mathrm{inclusive}\ \mu}(\text{low}\ p_{\mathrm{t}}, \Delta\eta)$ with the factor:

$$S_{\mathrm{MC}}(\Delta\eta) = R_{\mathrm{MC}}(\Delta\eta) \times \frac{N_{\mathrm{RD}}^{\mathrm{inclusive}\ \mu}(\text{low}\ p_{\mathrm{t}}, \Delta\eta)}{N_{\mathrm{MC}}^{\mathrm{primary}\ \mu}(\text{low}\ p_{\mathrm{t}}, \Delta\eta)} = \frac{N_{\mathrm{RD}}^{\mathrm{inclusive}\ \mu}(\text{low}\ p_{\mathrm{t}}, \Delta\eta)}{N_{\mathrm{MC}}^{\mathrm{inclusive}\ \mu}(\text{low}\ p_{\mathrm{t}}, \Delta\eta)}. \quad (7.27)$$

Then the scaling factor $S_{\mathrm{MC}}(\Delta\eta)$, defined in Eq. (7.27) is used to scale the extracted primary muon yield in a given $\Delta\eta$ (as shown in Fig. 7.10) to the data sample in order to estimate the yield of primary muons in data.

Fig. 7.11 to 7.15 show the comparisons of the normalized inclusive muon p_{t} distributions in muon triggered data and that in the corresponding realistic simulations in five pseudo-rapidity bins, the normalized p_{t} distributions of primary muons in each $\Delta\eta$ bin are also presented and the ratios between primary muons and inclusive muons in data and simulations are given. The simulations are scaled with S_{MC} defined in Eq. (7.27), before the normalization to the same number of events in the data. In this case, the primary muon distribution depicted in these figures is the estimated primary muon component in data. In general, the shape of inclusive muons produced by PYTHIA (Perugia-0 tuning) are closer to that in data than the one produced by PhoJet. But after the background normalization, both generators give similar estimated fractions of primary muons with respect to data. The difference in the estimated primary muon fractions via these two generators is due to the differences for R_{MC} and primary muon shapes between PYTHIA and PhoJet, and it will be taken into account in the final systematic uncertainty.

7.3.4 Uncorrected Results

After scaling the primary muon yields in the corresponding realistic simulations to the used data samples, LHC10c1 and LHC10d2b, respectively, the background fraction is estimated in the data. After background subtraction in both minimum bias events and muon triggered events, the expected yields of muons from open heavy flavour decays are obtained in these two kinds of triggered events. By using Eq. (7.9) and (7.22), with the value of $\sigma_{\mathrm{pp}}^{\mathrm{MB}}$ from Eq. (7.10) to normalize the results in minimum bias events and muon triggered events, respectively, without the efficiency correction, we obtained the results shown in Fig. 7.16 and 7.17. For both LHC10c1 and LHC10d2b, we have the two corresponding realistic simulations (as listed in Tab. 7.2). The background subtraction for each of these data sample is realized with its two realistic simulations independently, and the final results are given by the central value of the expected signal cross sections, according to the two estimated primary muon yields from different simulations. The systematic uncertainties are not included.

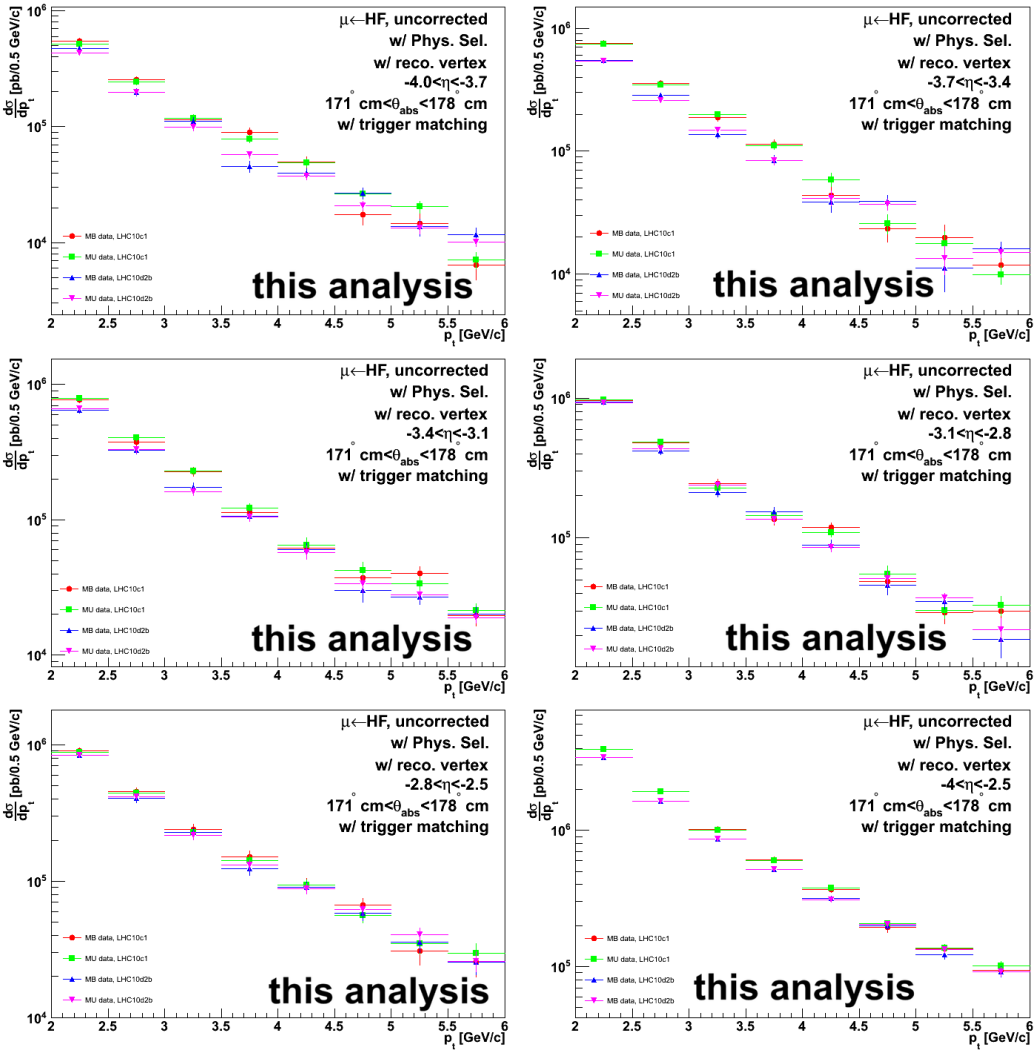

Figure 7.16: Uncorrected p_{t}-differential production cross section of muons from open heavy flavour decays in different η regions. Results from the minimum bias triggered data and muon triggered data in LHC10c1 and LHC10c2 are compared together. The systematics uncertainties are not yet shown.

Fig. 7.16 (bottom, right) shows the uncorrected p_{t}-differential production cross sections of muons from open heavy flavour decays in the total acceptance ($-4 < \eta < -2.5$), obtained by adding the results in five pseudo-rapidity bins according to Eq. (7.23). The results in Fig. 7.17, uncorrected η-differential production cross sections of muon signals in $p_{\mathrm{t}} > 2$ GeV/c, are obtained by integrating the p_{t}-differential production cross sections in each pseudo-rapidity bin according to Eq. (7.24).

In each run period, the minimum bias events and the muon triggered events give the same results, this validates the strategy used in our analysis for event and background normalization. The differences in the results from LHC10c1 and that

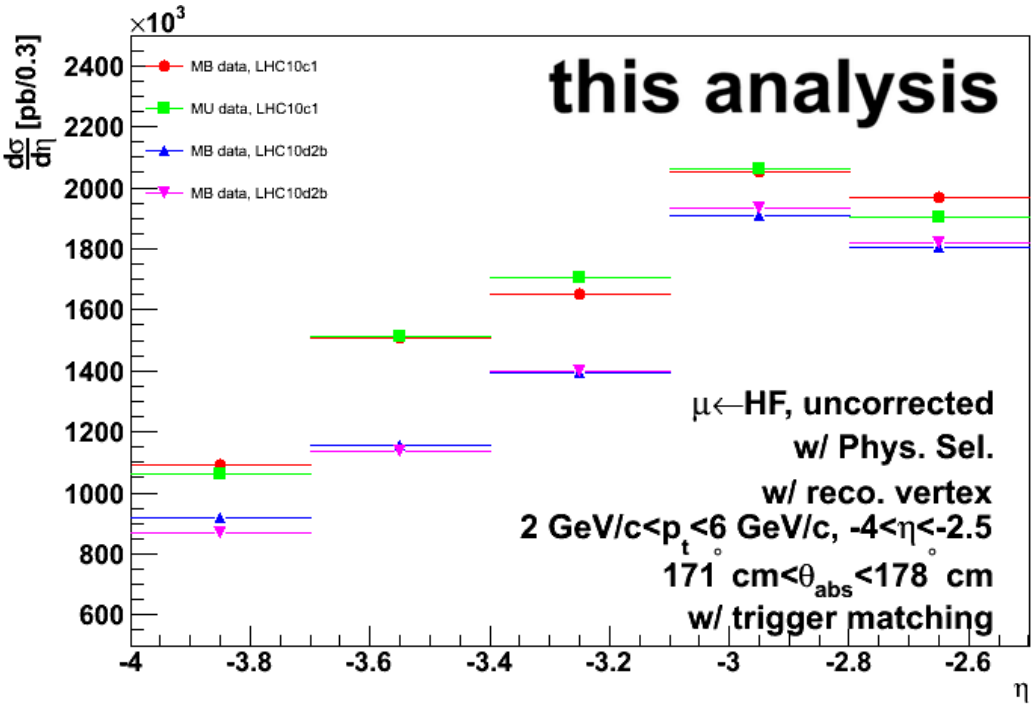

Figure 7.17: Uncorrected η-differential production cross section of muons from open heavy flavour decays in $p_{\rm t} > 2$ GeV/c, obtained according to Eq. (7.24). Results from the minimum bias triggered data and muon triggered data in LHC10c1 and LHC10c2 are compared. The systematic uncertainties are not yet shown.

from LHC10d2b are caused by the different tracking efficiencies in these two run periods.

7.3.5 Systematic Uncertainty

As mentioned, the background from primary muons is estimated from realistic simulations using different models. We used the fitting procedure to extract the background shapes in different models. The systematic uncertainty on this procedure, as discussed in Sec. 7.3.2, is $< 1\%$ and can be ignored. The systematic uncertainty on background subtraction, $\sigma_{\rm bkg}$, includes two parts: one comes from the different background shapes in different models $\sigma_{\rm models}$, and the other one is related to the background normalization $\sigma_{\rm norm}$.

We start with the estimate of $\sigma_{\rm models}$. This is quite straightforward: we get $p_{\rm t}$ spectrum in data after the background subtraction, which corresponds to the spectrum of muons from open heavy flavour decays, with different simulations in different η regions; then, we calculate the mean value of the spectrum in each $p_{\rm t}$ and η bin and this average spectrum gives the central value of the muon signal; the systematic uncertainty from models is given by the deviations between the spectrum with the two used independent simulations and the average spectrum, as shown in

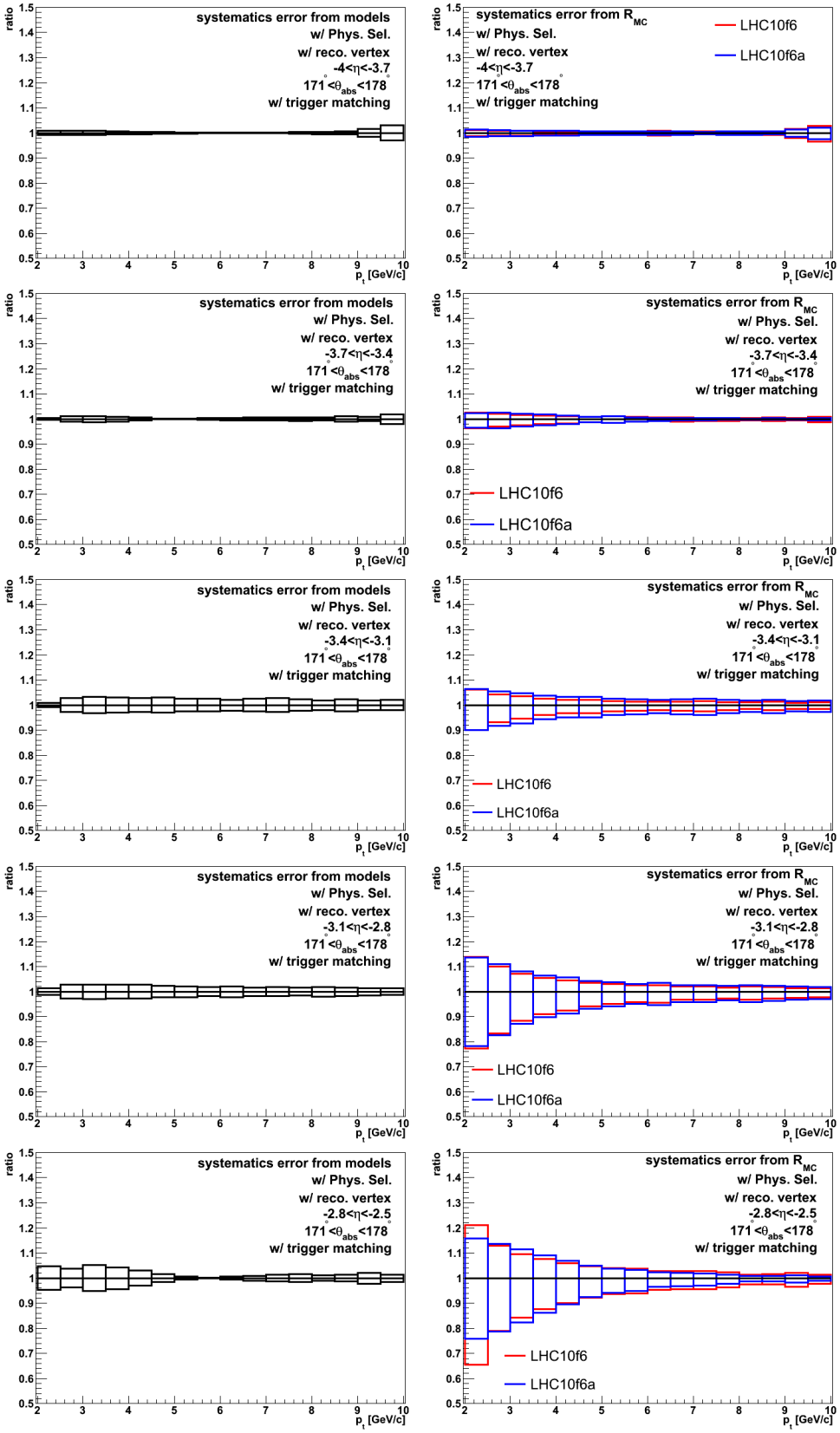

Figure 7.18: Estimate of σ_{models} (left column) and σ_{norm} (right column) with LHC10d2b in different η regions, see text for more details.

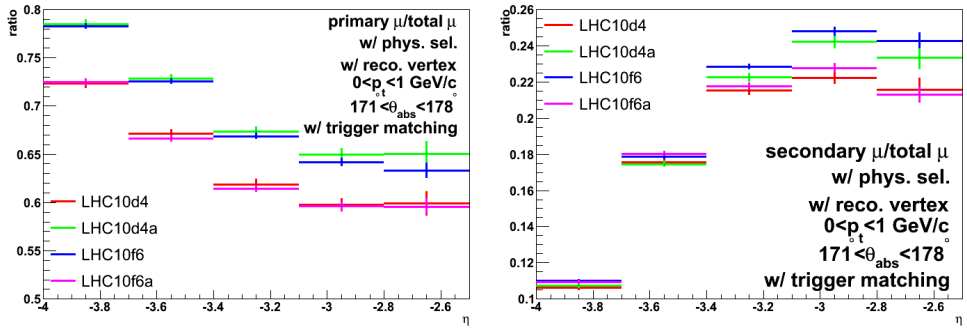

Figure 7.19: The ratios of primary muons (left) and secondary muons (right) to the total muons in $0 < p_{\rm t} < 1$ GeV/c (the region we used to calculate the $R_{\rm MC}$) in different simulations.

the left column of Fig. 7.18. This kind of systematic uncertainty is small. In this case, in a given η region, we use the maximum deviation in the $p_{\rm t}$ spectrum to estimate $\sigma_{\rm models}$ in this η bin.

Concerning the estimate of $\sigma_{\rm norm}$, the situation is a little bit complicated. The transport process in all the used Monte-Carlo samples is provided by GEANT3 transport code. The yield of the secondary muons is sensitive to different transport models (like GEANT4 [305] and Fluka [306]). In the most pessimistic case, the differences of the yield of secondary muons with different transport codes is within 100%. To estimate $\sigma_{\rm norm}$, in each of used model, we change the yield of secondary muons in 100% (this means that we consider no secondary muons or two times more secondary muons) and we re-calculate $R_{\rm MC}$ in Eq. (7.26). Then we implement the new values of $R_{\rm MC}$ in Eq. (7.27) to get the new scaling factors $S_{\rm MC}$ for the background. The deviations between the results from the new $S_{\rm MC}$ and the central value of the spectrum of signal muons, as shown in right column of Fig. 7.18, give the estimated $\sigma_{\rm norm}$ in each $p_{\rm t}$ and η bin. Differently from $\sigma_{\rm models}$, the systematic uncertainty on the background normalization $\sigma_{\rm norm}$ depends both on $p_{\rm t}$ and η. We extract the values of the maximum deviations in each $p_{\rm t}$ and η bin between different used models as $\sigma_{\rm norm}$ in this given region.

The final values that we used for both $\sigma_{\rm model}$ and $\sigma_{\rm norm}$ are summarized in Tab. 7.3. The observed trends can be explained by looking at the results from Fig. 7.19. This figure displays the ratios of primary muons (left) and secondary muons (right) to the total muons in the region we used to calculate the $R_{\rm MC}$ ($0 < p_{\rm t} < 1$ GeV/c) in different simulations. Despite these ratios are not the same in different simulations, they show a systematic trend:

- the ratio between primary muon yield to the total muon yield in $0 < p_{\rm t} < 1$ GeV/c (R) decreases with $|\eta|$, this is due to the mean energy loss $< p^{\rm cut} > \simeq 3$ GeV/c, then,

$$< p_{\rm t}^{\rm cut} > = < p^{\rm cut} > \sin\theta, \tag{7.28}$$

  increases with the polar angle θ, in small $|\eta|$ region, $\sin\theta$ increases and more

	σ_{model}	σ_{norm}						
		p_{t} (GeV/c)						
		$2-2.5$	$2.5-3$	$3-3.5$	$3.5;4.0$	$4-4.5$	$4.5-5$	>5
$2.5<\eta<2.8$	7%	34%	22%	20%	16%	12%	10%	6%
$2.8<\eta<3.1$	5.5%	22%	18%	14%	12%	10%	8%	6%
$3.1<\eta<3.4$	4.5%	10%	9%	8%	7%	6%		
$3.4<\eta<3.7$	3.0%	6%						
$3.7<\eta<4.0$	2.0%	4%						

Table 7.3: Systematic uncertainties introduced by the procedure used for the subtraction of primary muons. The absolute values of η are used. The systematic uncertainties on normalization are corrected by the $p\times$DCA cut, as it will be discussed in Sec. 7.6.3.2.

tracks are rejected in the low p_{t} region;

- the ratio between secondary muon yield to the total muon yield decreases with $|\eta|$ in $0 < p_{\text{t}} < 1$ GeV/c due to the secondary muons produced inside the front absorber, relating them to the primary vertex makes a systematic decrease of their $|\eta|$ value.

If the ratio of primary muon yield to total muon yield decreases with $|\eta|$ in the low p_{t} region, this means that the fraction of primary muons is small in large $|\eta|$ region, then the background subtraction is more and more insensitive with the shape of primary muons when $|\eta|$ decreases. On the contrary, the decrease of the ratio between the secondary muon yield to the total muon yield makes the re-calculated value of R_{MC} more and more sensitive to the secondary muon component when $|\eta|$ decreases. By combining all effects, finally, we get the trends shown in Tab. 7.3.

7.4 Efficiency Correction

The correction efficiency includes two aspects: the detection efficiency related to the reconstruction efficiency from the given reconstruction algorithm (like the Kalman Filter) and the dead channels in the detector cells or the readout electronics *etc.*; the acceptance efficiency, which is introduced by the cuts implemented during the analysis. For muon tracks, the correction efficiency is determined by following factors:

- the tracking efficiency, which is one kind of detection efficiency, it is from the track reconstruction in the tracking chambers, and it depends on the chamber occupancy which related to the input track multiplicity;

- the trigger matching efficiency, which includes both acceptance efficiency and detection efficiency components. On one hand, the trigger matching can be

treated as a p_{t} cut for the reconstructed tracks, on the other hand, there is also an efficiency for matching the tracker tracks to the corresponding trigger tracks;

- the efficiency to correct for the θ_{abs} cut which is one kind of acceptance cut: we use $171^{\circ} < \theta_{\mathrm{abs}} < 178^{\circ}$ to avoid the different material effects in the front absorber. Part of reconstructed tracks in the pseudo-rapidity acceptance are rejected by this cut, and this should be corrected in the final results.

The basic task of the efficiency correction for our analysis, is to take into account all the above factors.

7.4.1 Strategy

The following efficiency correction strategy is used:

1. get the kinematic distributions of heavy quarks from theoretical predictions (here we use the results from HvQMNR calculations [172]) as simulation inputs);

2. play the heavy quark hadronization and semi-muonic decay under the AliRoot framework with realistic detector effects according to the corresponding data taking period;

3. reconstruct the simulated muon tracks from heavy flavours under the realistic reconstruction conditions in data;

4. the ratio between the distributions of reconstructed muon tracks with the same selection cuts used in data and the input muon distributions from open heavy flavour decays gives the correction efficiency including all above efficiency sources.

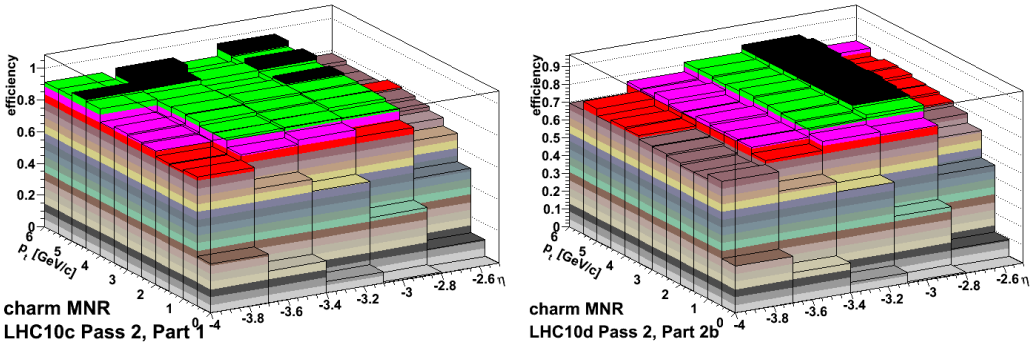

Figure 7.20: The two-dimension efficiency correction matrices as a function of p_{t} and η, built with the input of charm quark kinematics from HvQMNR predictions for LHC10c1 (left) and LHC10d2b (right), respectively.

Fig. 7.20 shows the two-dimension efficiency correction matrices as a function of p_{t} and η with the charm quark kinematics from HvQMNR predictions as the input for LHC10c1 (left) and LHC10d2b (right), respectively. In order to study the bias introduced by the efficiency correction, the estimate of the systematic uncertainty of the correction is also quite important. The systematic uncertainty estimate is investigated with several independent test procedures.

7.4.2 Test of the Efficiency Correction in Simulations

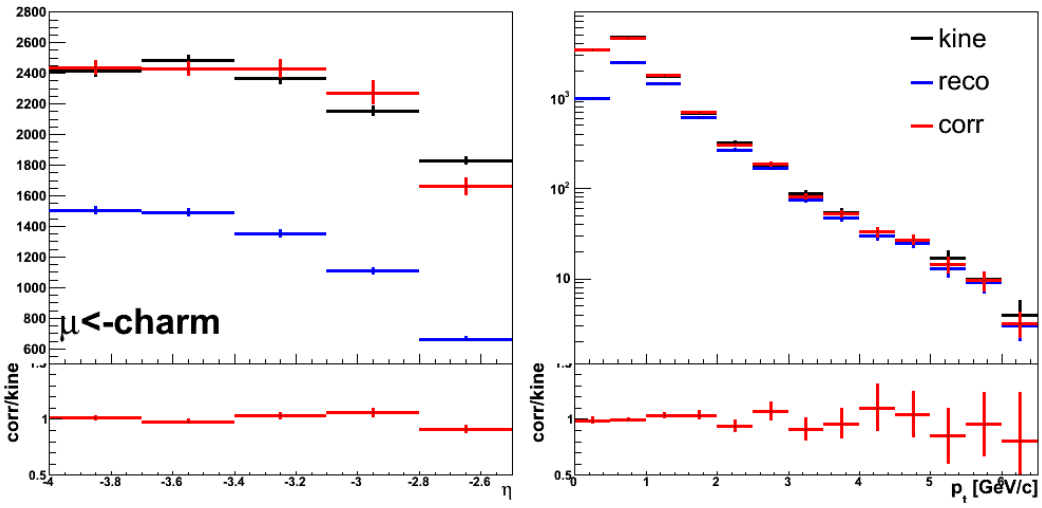

Figure 7.21: The efficiency correction for the η (left) and p_{t} (right) distributions of muons from open charm hadrons in the ideal simulation with PYTHIA ATLAS tuning. The reconstructed distributions are labeled as "reco", the distributions after the efficiency correction are labeled as "corr" and the input distributions are labeled as "kine". The ratio between the corrected distributions and the input distributions are presented in the bottom panels. The correction matrix is built with the charm quark kinematics distributions from HvQMNR predictions as the simulation inputs and under the ideal detector configurations.

First, we should check whether the efficiency correction is reliable or not. This can be done easily in simulations, with following steps:

1. prepare a two-dimension efficiency matrix as a function of p_{t} and η built with the charm quark kinematics distributions from HvQMNR predictions as simulation inputs;

2. use it to correct the p_{t} and η distributions of muons from open charm hadrons in another independent simulation (here we use the results from the simulation with PYTHIA ATLAS tuning);

3. compare the corrected results and the input distributions.

For this study, here we just use the ideal detector configurations in the simulations. As shown in Fig. 7.21, the input signal distributions are well reproduced by the corrected spectrum, except that there are some differences in the η distribution. This difference is caused by the efficiency estimate in the low p_{t} region. Due to the energy loss of muons in the front absorber and muon filter, the efficiency of muon tracks is very small. As shown in [307], with a p_{t} cut ($p_{\mathrm{t}} > 2$ GeV/c) the conditions in the η distribution are strongly improved. The results in Fig. 7.21 allow to conclude that, the corrected spectrum reproduces the input distribution and the correction strategy is reliable.

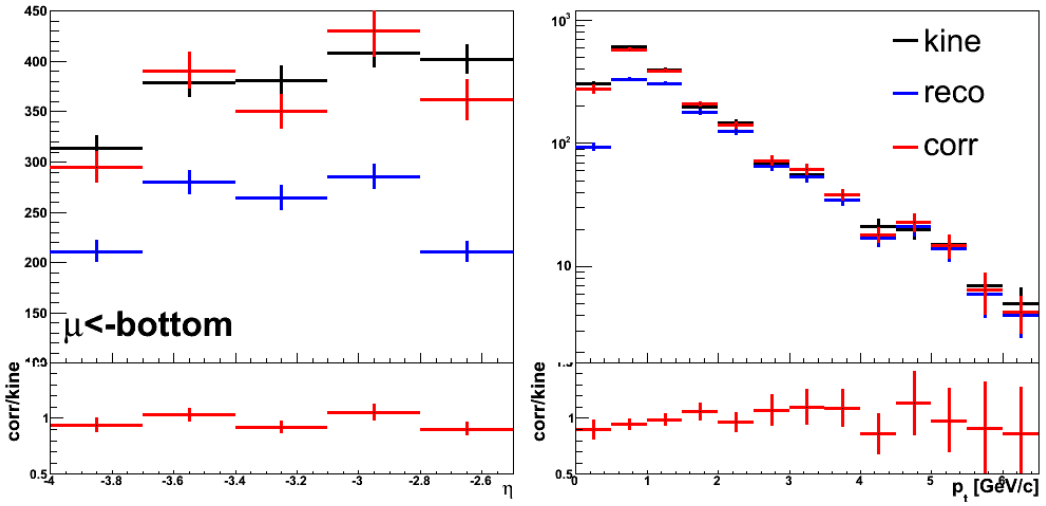

Figure 7.22: Same conditions as in Fig. 7.21, except muons from open beauty hadrons are used as input.

Since the fraction of charm and beauty components of the muon signals in data are unknown, we cannot combine the efficiency matrix of muons from charm and that of muons from beauty together. Our second test is to understand whether we can use the efficiency matrix built with one single component to correct the distribution of total muon signals. This test presented at the simulation level is shown in Fig. 7.22 and 7.23. In Fig. 7.22, we implemented the same correction matrix as used in the first test to correct muons from open beauty hadrons in the ideal simulation with PYTHIA ATLAS tuning. We find some deviations between the corrected results and the input distributions in this case. These deviations appear in the low p_{t} region and the situation can be improved with a p_{t} cut. This indicates that, in the high p_{t} region, the efficiency correction with our strategy is not only reliable but also insensitive with the input signal p_{t} shape used to build the correction matrix. Then, we mix the charm and botto components of the signal muons together with the fractions given by the PYTHIA ATLAS tuning, and implement the correction again with the same matrix used in Fig. 7.22, as the results shown in Fig. 7.23. These results confirm once more that, if the corrected results are insensitive with the input shapes to build the correction matrix, in the p_{t} region ($p_{\mathrm{t}} > 2$ GeV/c) we

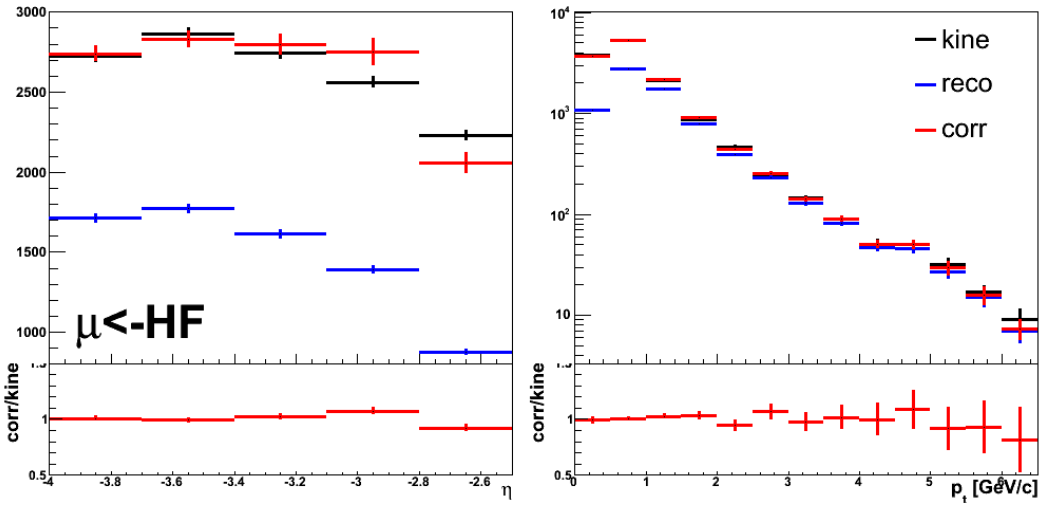

Figure 7.23: Same conditions as in Fig. 7.21, except taht total muon signals from both open charm and beauty hadrons are used as input.

can use the correction matrix build with the single component of signal muons to correct the total spectrum of muon from both open charm and beauty hadrons.

7.4.3 Systematic Uncertainty in Data

Finally, we tested the efficiency correction in data, and estimate the systematic uncertainty on the efficiency correction. The main aim of this test is to understand how the corrected results in data are sensitive to the efficiency matrices built with different p_{t} and η shapes of muon signals.

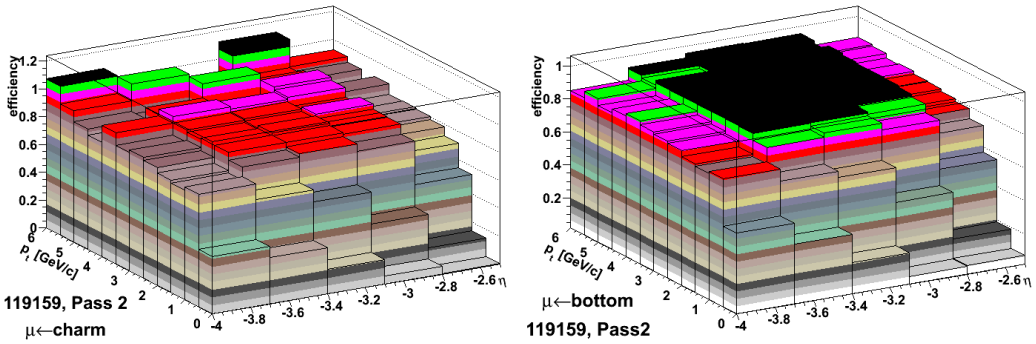

Figure 7.24: The efficiency correction matrices made by muons from charm (left) and muons from beauty (right) with the inputs of HvQMNR predictions. The realistic detector configurations corresponding to run 119159 in LHC10c1 are used for these simulations.

In this case, we proceed as follows:

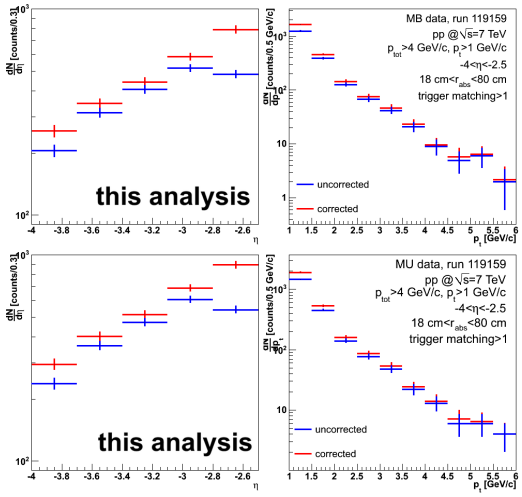

Figure 7.25: Results of efficiency correction in run 119159 from LHC10c1 for minimum bias data (up) and muon triggered data (down), respectively. The efficiency matrix is built with muons from charm with the corresponding realistic detector configurations, as shown in left plot of Fig. 7.24.

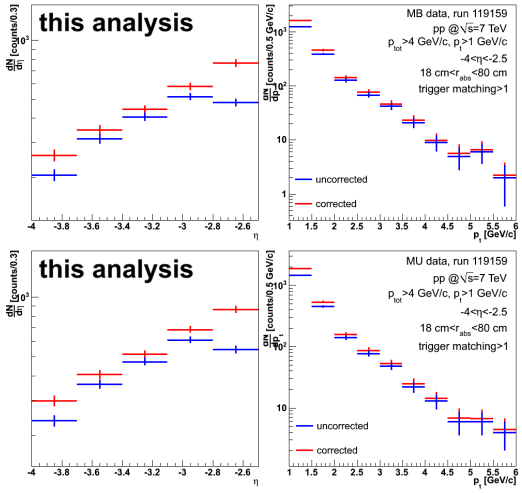

Figure 7.26: Results of efficiency correction in run 119159 from LHC10c1 for minimum bias data (up) and muon triggered data (down), respectively. The efficiency matrix is built with muons from beauty with the corresponding realistic detector configurations, as shown in right plot of Fig. 7.24.

1. create the efficiency matrices for both muons from charm and muons from beauty, respectively, with the realistic detector configurations for a given run (here run 119159 in LHC10c1 is used), as shown in Fig. 7.24;

2. use these two efficiency matrices to correct the corresponding data, as shown in Fig. 7.25 and 7.26; in these figures, the correction is presented for minimum bias events and muon triggered events, respectively; also during the corrections, all the analysis cuts are applied to build the correction matrices and to the data;

3. compare the corrected results with these two independent correction matrices, as shown in Fig. 7.27, and estimate the systematic uncertainty on the efficiency correction according to the differences between the corrected results with different correction matrices.

The results from the comparison shown in Fig. 7.27 are summarized in Tab. 7.4 and 7.5 for the minimum bias triggered data and muon triggered data, respectively. In these tables, we get the value of the ratio between the corrected results from these two independent correction matrices for minimum bias events (Tab. 7.4) and muon trigger events (Tab. 7.5), respectively. Note that the values in the p_t region where the statistical fluctuations are large, are removed. Then we calculate the mean of these ratios and the deviations between their values and the mean. Finally, we found that the results in both minimum bias events and muon triggered events

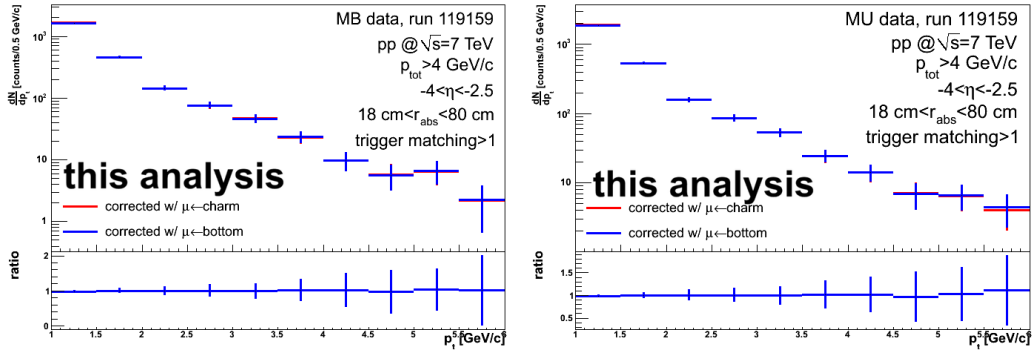

Figure 7.27: Comparison of the corrected results in run 119159 from LHC10c1 with the correction matrices build by muons from charm (left plot of Fig. 7.24) and that with muons from bottom (right plot of Fig. 7.24), for the minimum bais triggered data (left) and muon triggered data (right), respectively.

p_{t} [GeV/c]	$2-2.5$	$2.5-3$	$3-3.5$	$3.5-4$	$4-4.5$	$4.5-5$	mean
ratio	1.00	1.01	1.01	0.99	1.02	1.02	1.01
deviation	1%	0	0	1%	1%	1%	–

Table 7.4: The ratio of the corrected results with two independent correction matrices for run 119159 from LHC10c1 for the minimum bias triggered events extracted from lower panel in left plot of Fig. 7.27 in some given p_{t} regions.

p_{t} [GeV/c]	$2-2.5$	$2.5-3$	$3-3.5$	$3.5-4$	$4-4.5$	$4.5-5$	mean
ratio	1.00	1.01	1.01	0.99	1.02	1.02	1.01
deviation	1%	0	0	1%	1%	1%	–

Table 7.5: Ratio of the corrected results with two independent correction matrices in run 119159 from LHC10c1 for the muon triggered events extracted from lower panel in right plot of Fig. 7.27 in some given p_{t} regions.

are almost the same, the maximum deviation is 1%. This 1% deviation is the estimated systematic uncertainty on the efficiency correction. Recent studies [308], using higher statistics data sample, give an upper limit for the systematic uncertainty on efficiency correction of 0.8%. These results allow to conclude that the uncertainty on the efficiency correction is small and can be neglected.

In addition, according to the structure of the tracking chambers of the MUON spectrometer, the mis-alignment also affects the reconstructed p_{t} spectrum. Due to the mis-alignment, the tracks with opposite charges will shift to opposite directions in the p_{t} spectrum with respect to their real p_{t} values. The understanding of the misalignment depends on the real shape of the p_{t} spectrum and also on the real ratio between positive and negative tracks. But it is impossible to know it before

the correction of the mis-alignment. Normally, the decoupling of the mis-alignment from data is carried out via the iterative steps [293]. In our correction procedure, as we saw, the corrected results in data are insensitive with the input p_t shapes used for building the correction matrices. This indicates that the misalignment do not affect too much our interesting p_t region for what concerns the efficiency correction. In this case, instead of the further correction for the mis-alignment, we consider the estimated uncertainty in our final systematic uncertainty, of $1\% \times p_t$ with the unit of p_t in "GeV/c". In addition, there will be a 5% systematic uncertainty for the detector response which should be also included in the final systematic uncertainty. This value was obtained by comparing the values of trigger and tracking efficiencies extracted from data and simulations.

7.5 Comparison with FONLL Predictions

One of the motivations of the open heavy flavour production cross section measurement is to test the pQCD calculations. In this regard, it is important to compare the measured results with the theoretical predictions. As mentioned in Sec. 2.1.3.2, the FONLL calculations is one of the reasonable predictions for the open heavy flavour production since it overcomes the divergence at high p_t by the re-summation of the pQCD series in the high p_t region by matching the pQCD NLO calculations with the calculations from fragmentation function formalism. To test the pQCD framework, we are going to compare our results with the FONLL predictions. Moreover, in order to ensure that this comparison is done properly, the uncertainties on FONLL predictions should also be considered.

7.5.1 Error Propagation for FONLL Predictions

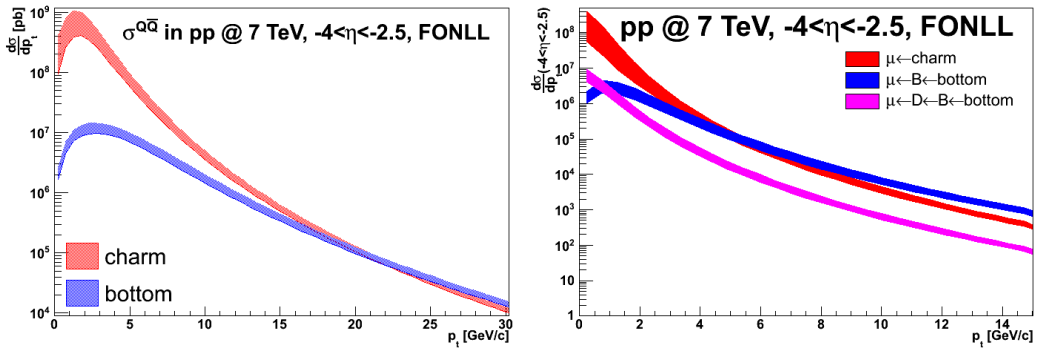

Figure 7.28: The production cross sections of heavy quark pairs (left) and muons from heavy quark decays (right) from FONLL predictions in $-4 < \eta < -2.5$, in pp collisions at $\sqrt{s} = 7$ TeV.

The production cross sections of $c\bar{c}$ and $b\bar{b}$ in the acceptance of the ALICE MUON spectrometer ($-4 < \eta < -2.5$) in pp collisions at $\sqrt{s} = 7$ TeV are shown in

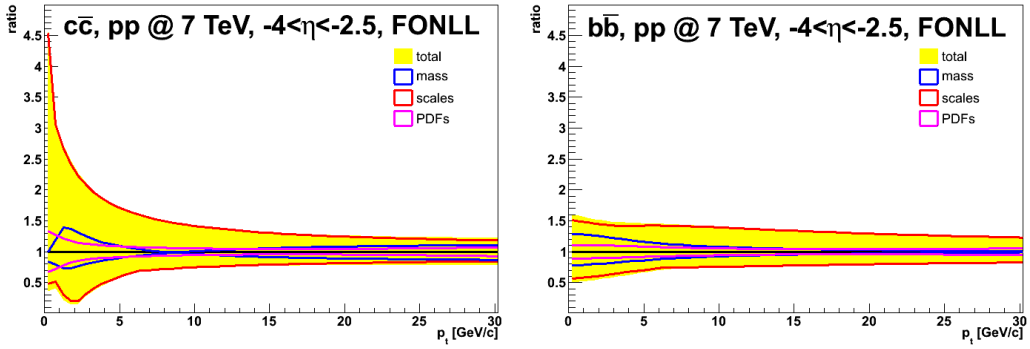

Figure 7.29: The rescaled ratios of production cross sections with respect to the central values for $c\bar{c}$ (left) and $b\bar{b}$ (right) from FONLL predictions in $-4 < \eta < -2.5$, in pp collisions at $\sqrt{s} = 7$ TeV.

Fig. 7.28 (left panel). As shown in Eq. (2.1), the calculation of the heavy flavour production cross section depends on the input quark mass, the chosen PDF and the used values of the renormalization and factorization scales, μ_R and μ_F. Each of them will introduce an uncertainty on the predictions of the production cross section of heavy quarks. In the results shown in Fig. 7.28 (left panel), the central values are obtained by using $\mu_R = \mu_F = \mu_0 = \sqrt{p_t^2 + m_Q^2}$ with the charm quark mass $m_c = 1.5$ GeV/c^2 and bottom quark mass $m_b = 4.75$ GeV/c^2. The uncertainties on quark masses are estimated by setting the ranges of 1.3 GeV/$c^2 < m_c < 1.7$ GeV/c^2 for charm quarks and 4.5 GeV/$c^2 < m_b < 5.0$ GeV/c^2 for bottom quarks. The uncertainty on the QCD scales are given by varying μ_R and μ_F independently with the following conditions:

$$\begin{aligned} &\frac{1}{2}\mu_0 < \mu_R,\ \mu_F < 2\mu_0, \\ &\frac{1}{2} < \mu_R/\mu_F < 2, \end{aligned} \tag{7.29}$$

to optimize the accuracy of the pQCD predictions [309]. The uncertainty on PDFs is given by different sets of inputs from CTEQ 6. The rescaled production cross sections with respect to the central values for charm and bottom quarks are shown in left and right plots of Fig. 7.29, respectively, with the different sources of uncertainties. In this figure, one can see that, by comparing with the uncertainties from the quark masses and PDFs, the uncertainty from QCD scales is the largest one in the whole p_t region.

By considering the fragmentation and semi-muonic decay with appropriate branching ratio, we get the p_t-differential production cross section at muon level, as shown in Fig. 7.28 (right panel). There are three kinds of muon sources: muons from charm quarks, muons from bottom quarks and the muons from the indirect decay of bottom quarks. In order to simplify the description in this section, we named these three kinds of muons as charm μ, bottom μ and feed down μ, respectively.

The uncertainties at quark level should be propagated at the muon level and the additional uncertainty on the fragmentation process should also be included. But as shown in Fig. 2.5, due to the hard fragmentation of heavy quarks, the uncertainty on the fragmentation with different kinds of fragmentation functions is very small, and by comparing with the other uncertainty sources it is negligible. In this case, the results for different kinds of muons shown in Fig. 7.28 (right panel) only include the same uncertainty sources at quark level.

For the comparison with data, we should add the production cross sections of these three kinds of muons together. This will allow to get the results for muons from both open charm hadron and open bottom hadron decays. The uncertainty on these three kinds of muon sources are not independent and cannot be propagated quadratically. To propagate the uncertainties correctly, the following steps are used:

1. both the bottom μ and feed down μ originate from bottom quarks, the parameters of these two sources cannot be changed independently;

2. add the central values of the production cross section of these three kind of muons together to get the central value of the production cross section for muons from open heavy flavour decays;

3. fix the other parameters in order to get the central cross section value, then vary m_{c} and m_{b} independently. For both m_{c} and m_{b} one can choose three different values, this will give 9 kinds of combinations, the maximum and minimum differences between these 9 combinations and the central cross section value give the upper and lower uncertainties from the quark masses, $\sigma^{\mathrm{max}}_{\mathrm{mass}}$ and $\sigma^{\mathrm{min}}_{\mathrm{mass}}$;

4. similarly to the procedure just discussed, one changes the QCD scales independently for muons from charm and those from bottom (the bottom μ and feed down μ) while keeping the other parameters unchanged, in order to estimate the upper and lower uncertainties from the QCD scales, $\sigma^{\mathrm{max}}_{\mathrm{scales}}$ and $\sigma^{\mathrm{min}}_{\mathrm{scales}}$. For each case, there are 7 combinations of μ_{R} and μ_{F} which satisfy the conditions of Eq. (7.29):

$$\begin{aligned}
\mu_{\mathrm{R}} &= \mu_0, \quad \mu_{\mathrm{F}} = \mu_0, \\
\mu_{\mathrm{R}} &= 0.5\mu_0, \quad \mu_{\mathrm{F}} = 0.5\mu_0, \\
\mu_{\mathrm{R}} &= 2\mu_0, \quad \mu_{\mathrm{F}} = 2\mu_0, \\
\mu_{\mathrm{R}} &= 2\mu_0, \quad \mu_{\mathrm{F}} = \mu_0, \\
\mu_{\mathrm{R}} &= \mu_0, \quad \mu_{\mathrm{F}} = 2\mu_0, \\
\mu_{\mathrm{R}} &= \mu_0, \quad \mu_{\mathrm{F}} = 0.5\mu_0, \\
\mu_{\mathrm{R}} &= 0.5\mu_0, \quad \mu_{\mathrm{F}} = \mu_0.
\end{aligned} \tag{7.30}$$

   Finally by combining the charm and bottom together, we can get a total 49 combinations for the QCD scales by mixing the QCD scales;

5. the upper and lower uncertainties from PDFs, $\sigma^{\mathrm{max}}_{\mathrm{PDFs}}$ and $\sigma^{\mathrm{min}}_{\mathrm{PDFs}}$, are propagated quadratically;

After all above steps, the upper and lower uncertainties on the production cross sections of muons from heavy flavour decays are obtained by adding quadratically the corresponding uncertainties on quark masses, QCD scales and PDFs.

7.5.2 Results of the Comparison

After this short discussion about the uncertainty propagation in FONLL predictions, we present the comparison between data and FONLL predictions.

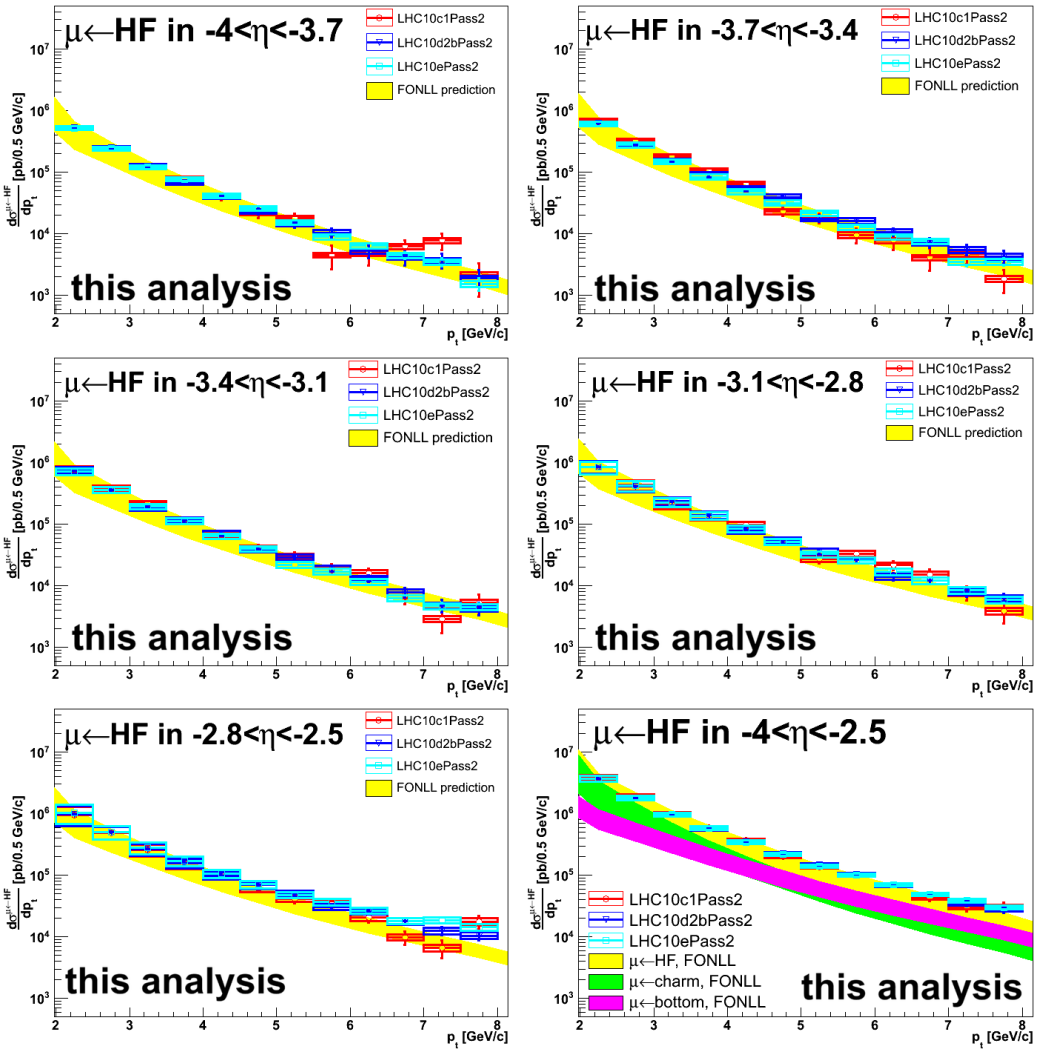

Figure 7.30: The corrected p_{t}-differential production cross sections of muons from open heavy flavour decays in LHC10c1, LHC10c2 and LHC10e, in different η regions. The results are compared with the FONLL predictions. In each run period, only the muon triggered data are used.

Fig. 7.30 and 7.31 show the p_{t} and η differential production cross section of muons from open heavy flavours decays, respectively. The p_{t}-differential produc-

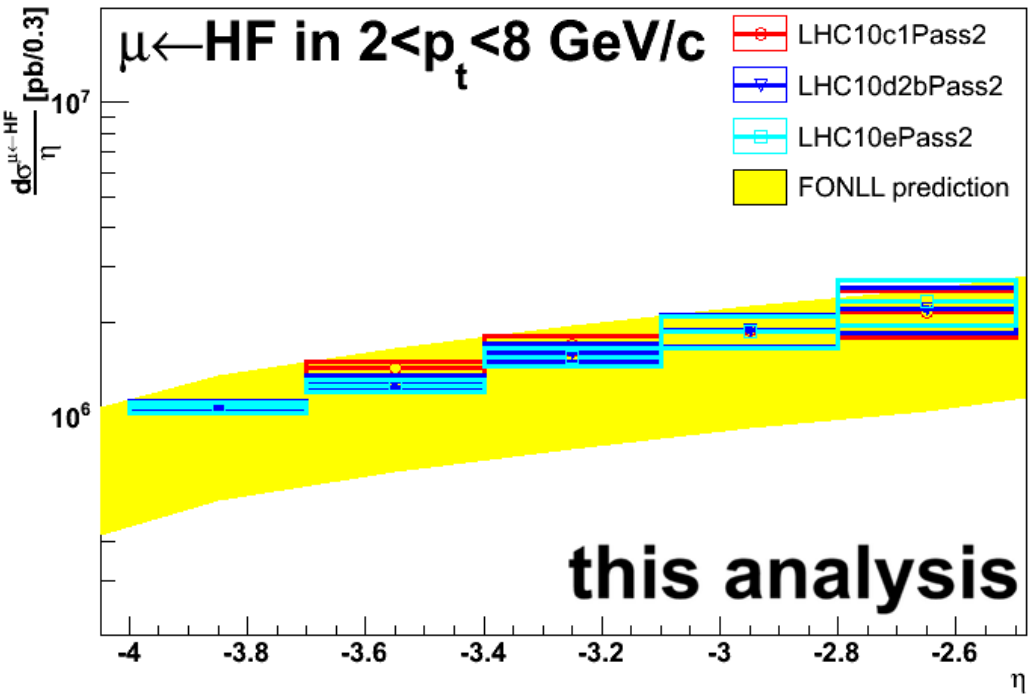

Figure 7.31: The corrected η-differential production cross section of muons from open heavy flavour decays in LHC10c1, LHC10c2 and LHC10e, in $p_{\rm t} > 2$ GeV/c. The result are compared with the FONLL predictions. In each run period, only the muon triggered data are used.

tion cross sections are shown in different η regions. The results are from LHC10c1, LHC10d2b and LHC10e by using the muon triggered data. They are corrected via the strategy introduced in Sec. 7.4.1, with the correction matrices shown in Fig. 7.20 for LHC10c1 and LHC10d2b as examples, the correction matrix for LHC10e is created via the same procedure used for LHC10c1 and LHC10d2b but with the realistic detector simulations for LHC10e. The systematic uncertainty in data, at present, just includes the one on background subtraction as discussed in Sec. 7.3.5. This error is propagated bin by bin quadratically by using the Eq. (7.23) and (7.24). The $p_{\rm t}$-differential production cross sections from different pseudo-rapidity bins (the first five plots in Fig. 7.30) are added together to get the production cross section in the total acceptance $-4 < \eta < -2.5$ (the last plot in the bottom right of Fig. 7.30), and to integrate the results in each pseudo-rapidity region to obtain the η-differential production cross section depicted in Fig. 7.31. The uncertainties in FONLL predictions are calculated according to the strategy presented in Sec. 7.5.1. In these two figures, one can notice that in the $p_{\rm t}$ range up to 8 GeV/c, the measured differential cross sections of muons from heavy flavours decays from different run periods agree well within uncertainties both as a function of $p_{\rm t}$ and η. They also agree with FONLL predictions within experimental and theoretical uncertainties.

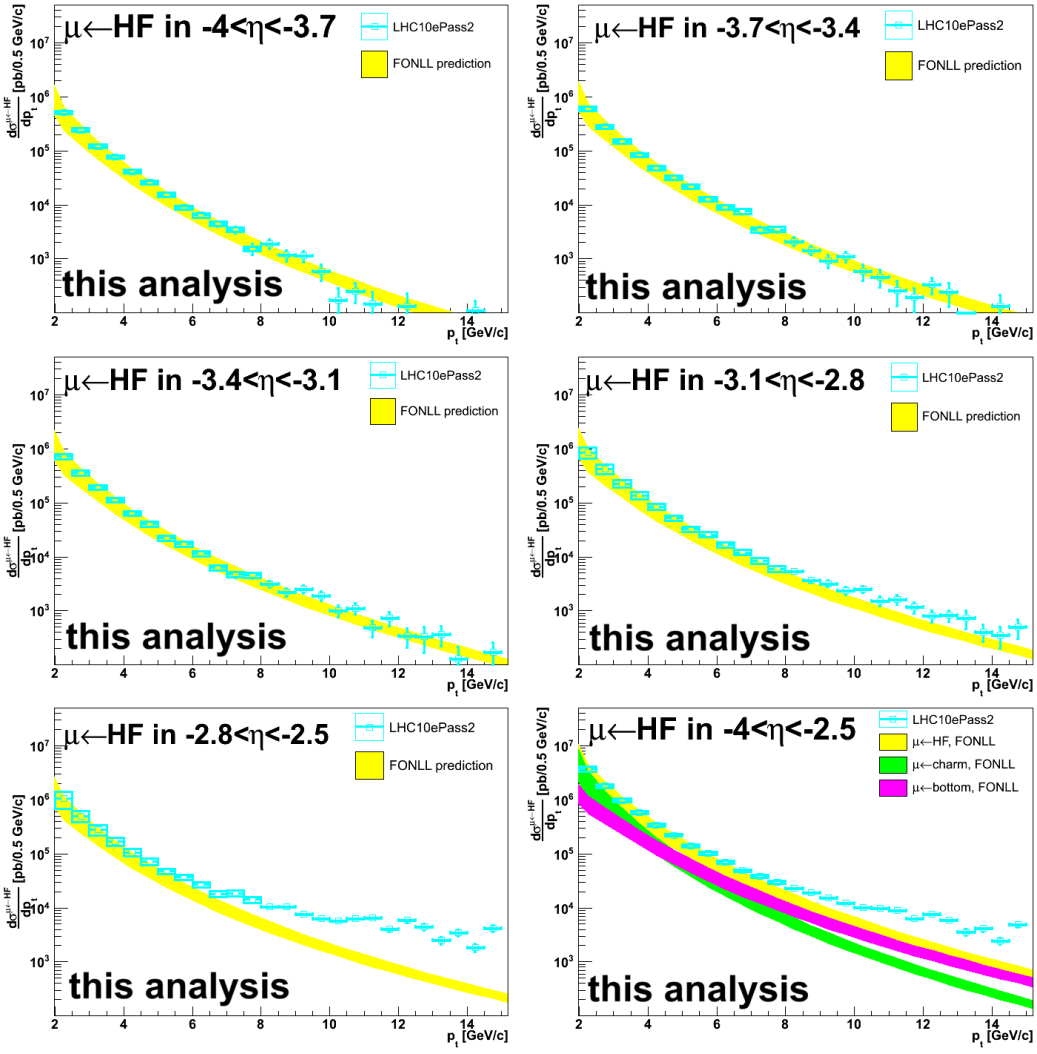

Figure 7.32: Similar as Fig. 7.30, but the comparison with FONLL predictions is presented for LHC10e data, with p_{t} measured up to 15 GeV/c.

Of course, we (indeed my bosses) are not satisfied if we just stop here. As shown in Tab. 7.1, the statistics of the muon triggered events in LHC10e is three times higher than the total statistics from LHC10c1 and LHC10d2b together. With LHC10e period, we can perform the measurements in a higher p_{t} region, up to 15 GeV/c, as shown in Fig. 7.32. Same analysis cuts, as in Fig. 7.30, are applied. One can notice that, in the high p_{t} region, the data are not reproduced by the FONLL predictions. By comparing the data with FONLL predictions in Fig. 7.32, we can notice that:

- in the total acceptance, $-4 < \eta < -2.5$, the results in data are higher than those from FONLL predictions in the high p_{t} region, $p_{\mathrm{t}} \gtrsim 8$ GeV/c;
- the disagreements between data and FONLL predictions mainly come from

the η regions close to the mid-rapidity region, $-3.2 < \eta < -2.8$ and $-2.8 < \eta < -2.5$, and increase with p_t;

- the disagreement between data and theoretical predictions become smaller when $|\eta|$ increases.

Up to now, it is difficul to conclude about the origin of the problem and if it comes from our measurements or from the FONLL predictions. From our side, we can check the data. Anyhow, the systematic trends in the disagreements give hints for checking the data.

7.6 Beam Induced Backgroud Rejection

According to the trends in the differences between the experimental measurements and the FONLL predictions, we started to check some distributions in each pseudo-rapidity region and we attributed the differences between data and FONLL to the beam induced background. The first justification of the beam induced background rejection is based on the fact that the extrapolation of reconstructed parameters of muon tracks to the primary vertex is incorrect for background tracks produced far away from the primary vertex, during the track reconstruction (Sec. 3.4.4.3). This incorrect extrapolation can introduce some correlation relations between the track kinematics variables. This is due to the **Coulomb-Multi-Scattering** (**CMS**) between the tracks and the material in the front absorber. At final, we developed a cut based on the behaviour of the Coulomb-Multi-Scattering to cut off the beam induced background.

7.6.1 Additional Background component in the High p_t Region

For the understanding of the differences between data and FONLL predictions in the high p_t region presented in Fig. 7.32, we first plotted the mean values of DCA and tracking χ^2 as a function of p_t in different pseudo-rapidity regions, as shown in Fig. 7.33.

Fig. 7.33 (left panel) presents the mean DCA values as a function of p_t and for the five pseudo-rapidity regions for the muon triggered data of LHC10e and with the muon selection cuts listed in this plot. The DCA (Distance of Closest Approach), introduced in Sec. 3.4.4.3, is defined as the closest distance between the primary vertex and the track calculated according to the track parameters after the energy loss correction in the front absorber (but before to relate the track parameter to the primary vertex). According to this definition, a large value of DCA can be due to following reasons:

- the production point of particles related to a given recontructed track is far from the primary vertex, as for primary muons or beam shield induced particles (as shown in left plot of Fig. 6.11);

- large scattering angles for the tracks inside the front absorber, as low p_t tracks.

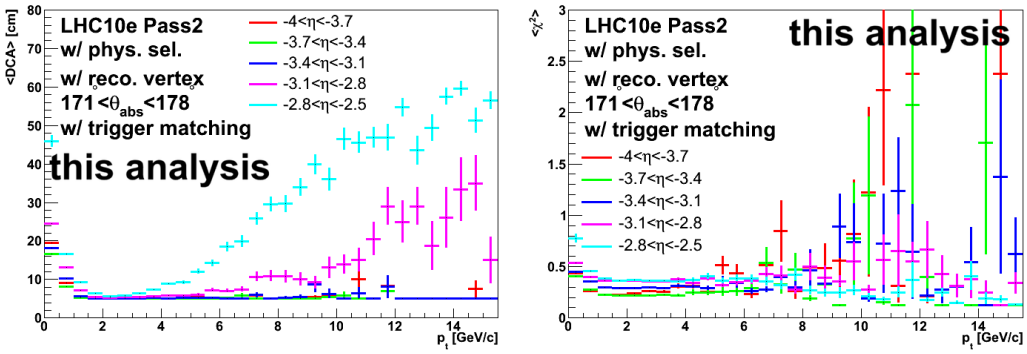

Figure 7.33: The mean values of DCA (left) and tracking χ^2 (right) for reconstructed tracks versus p_t bin in five pseudo-rapidity regions. The results are obtained from the muon triggered events in LHC10e with the muon selection cuts.

In the left plot of Fig. 7.33, we can see that, in the last two η bins, $-3.1 < \eta < -2.8$ and $-2.8 < \eta < -2.5$, the mean values of DCA (<DCA>) increase with p_t in the high p_t region, while the <DCA> in the first three η bins is smaller and insensitive with p_t in the high p_t region. The disagreements between data and FONLL predictions in the last two η bins, as shown in Fig. 7.32, are consistent with the existence of a new background source, with large DCA values, that was not considered (or becomes important) in the high p_t region for the last two η bins. As a consequence, the model underestimates the experimental results. Since this background is located in the high p_t region, the associated large DCA values should not be attributed to large scatterings of the primary and/or secondary muons in the front absorber (this effect mainly affects the track in the low p_t region). To confirm that these background tracks are produced by physics particles, we further check the mean values of the tracking χ^2 ($< \chi^2 >$) distributions under the same conditions as for <DCA> distributions, as in Fig. 7.33 (right panel). We find that, in the high p_t region for all pseudo-rapidity bins, the $< \chi^2 >$ does not increase, indicating that these background tracks are not fake tracks created by the tracking algorithm and they are from physics particles.

After excluding all possible contributions for this kind of background, we conclude that this background comes from the beam shield induced particles (see also Fig. 6.11). Since these particles are not produced in the simulations, we did not pay sufficient attention to them during our former analysis! Also, because the reconstructed kinematics observables are not correct after extrapolation of track parameters to the primary vertex, the p_t distribution does not follow the expected trend, since the beam induced background becomes very important in the high p_t region, where the yield of physical tracks is strongly suppressed according to their power law distribution (Eq. (5.1)).

7.6.2 Kinematics Combination

Now, our main task is to cut off this beam induced background. In order to find an appropriate observable to isolate this background, we start by considering a very simple case. For a physical track produced at (or close to) the primary vertex, without taking into account multi-scattering in the front absorber, $\theta_{\rm abs}$ is approximated to the polar angle $\theta_{\rm pol}$ and it satisfies the following relation:

$$\eta = -\frac{1}{2}\ln(\tan\frac{\theta_{\rm pol}}{2}) \approx -\frac{1}{2}\ln(\tan\frac{\theta_{\rm abs}}{2}). \tag{7.31}$$

For bean induced tracks, $\theta_{\rm abs}$ is calculated according to the radius of the tracks at the end of the front absorber $R_{\rm abs}$, as defined in Sec. 6.3.2. But after relating the track parameters of the beam induced background to the primary vertex, the absolute values of their polar angle is reduced, this increases their absolute η values and the relation in Eq. (7.31) cannot be applied.

7.6.2.1 $\eta - \theta_{\rm abs}$ Correlation

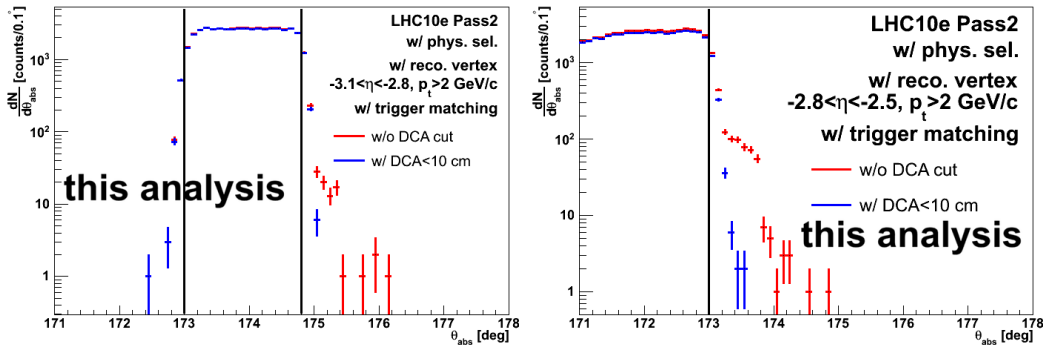

Figure 7.34: $\theta_{\rm abs}$ distributions in $-3.1 < \eta < -2.8$ (left) and in $-2.8 < \eta < -2.5$ (right) from the muon triggered data in LHC10e with the muon selection cuts. The results (red lines) are compared with the ones with DCA$<$ 10 cm (blue lines) in each η region.

In order to test what we thought is right or not, we compare in Fig. 7.34, the $\theta_{\rm abs}$ distributions without (red line) and with (blue lines) an additional cut of DCA$<$ 10 cm after the muon selection cuts, in $-3.1 < \eta < -2.8$ (left) and in $-2.8 < \eta < -2.5$ (right), where the effect from the beam induced background is large in the high $p_{\rm t}$ region. The analysis is done with the muon triggered data in LHC10e. In the $\theta_{\rm abs}$ distributions without the additional DCA cut, we can see that, there is always a fraction of tracks outside the corresponding η acceptance, as shown by the bound made with the back lines calculated according to Eq. (7.31), indicating that these tracks do not satisfy the relation in Eq. (7.31). If these tracks are beam induced tracks, they should also have large DCA values. Then we roughly add a cut of DCA$<$ 10 cm (blue lines in Fig. 7.34), and found that almost all of the tracks

outside the corresponding η acceptance are rejected. This results confirms what was just mentioned: the beam induced background tracks have large DCA values and do not satisfy the relation in Eq. (7.31) due to the incorrect extrapolation of their track parameters to the primary vertex.

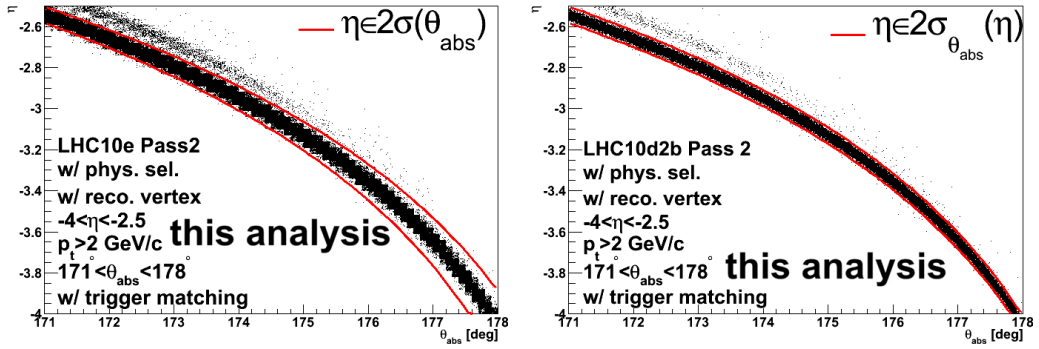

Figure 7.35: The distribution of $\eta - \theta_{\rm abs}$ combination from muon triggered events in LHC10e (left) and LHC10d2b (right) with the selection cuts in $p_{\rm t} > 2$ GeV/c, see text for more details.

In this case, the beam induced background tracks will have a different $\eta - \theta_{\rm abs}$ correlation with respect to the other tracks. This is shown in Fig. 7.35, when we present the $\eta - \theta_{\rm abs}$ distribution with the muon track selection cuts in $p_{\rm t} > 2$ GeV/c by using the muon triggered data in LHC10e (left) and LHC10d2b (right). In this figure, one can clearly distinguish two components in both data samples: one component following the relation in Eq. (7.31) and another component which do not follow this relation and which is mainly located in the η region where the beam induced background is large. The second component, now we can confirm confidently, is the one produced by the beam induced background. To define the cut for the background component region in Fig. 7.35, we go back to the relation in Fig. 7.35. If there is no scattering for the tracks in the front absorber, according to the definitions of $\theta_{\rm pol}$ and $\theta_{\rm abs}$ by using the small angle approximation, we have:

$$\begin{aligned} \theta_{\rm abs} \approx \tan\theta_{\rm abs} &= \frac{R_{\rm abs}}{L_{\rm abs}}, \\ \theta_{\rm pol} \approx \tan\theta_{\rm pol} &= \frac{R_{\rm abs}}{L_{\rm abs} + v_{\rm z}}, \end{aligned} \tag{7.32}$$

where, $R_{\rm abs}$ is the radius of the track position at the end of front absorber and $L_{\rm abs} = 505$ cm is the distance between the end of the front absorber and the origin of the ALICE global coordinate system, as defined in Sec. 6.3.2, $v_{\rm z}$ is the position of the primary vertex along the z-axis (beam direction) in the ALICE global coordinate system. To get Eq. (7.31) we assume $v_{\rm z} = 0$, but in data $v_{\rm z}$ is a distribution as shown in left plot of Fig. 6.5. Therefore, we defined $\sigma_\theta(\eta)$ as:

$$\sigma_\theta(\eta) = \theta_{\rm abs} - \theta_{\rm pol} = \frac{R_{\rm abs}}{L_{\rm abs}} - \frac{R_{\rm abs}}{L_{\rm abs} + v_{\rm z}} = \theta_{\rm pol}(\eta)\frac{v_{\rm z}}{L_{\rm abs}}, \tag{7.33}$$

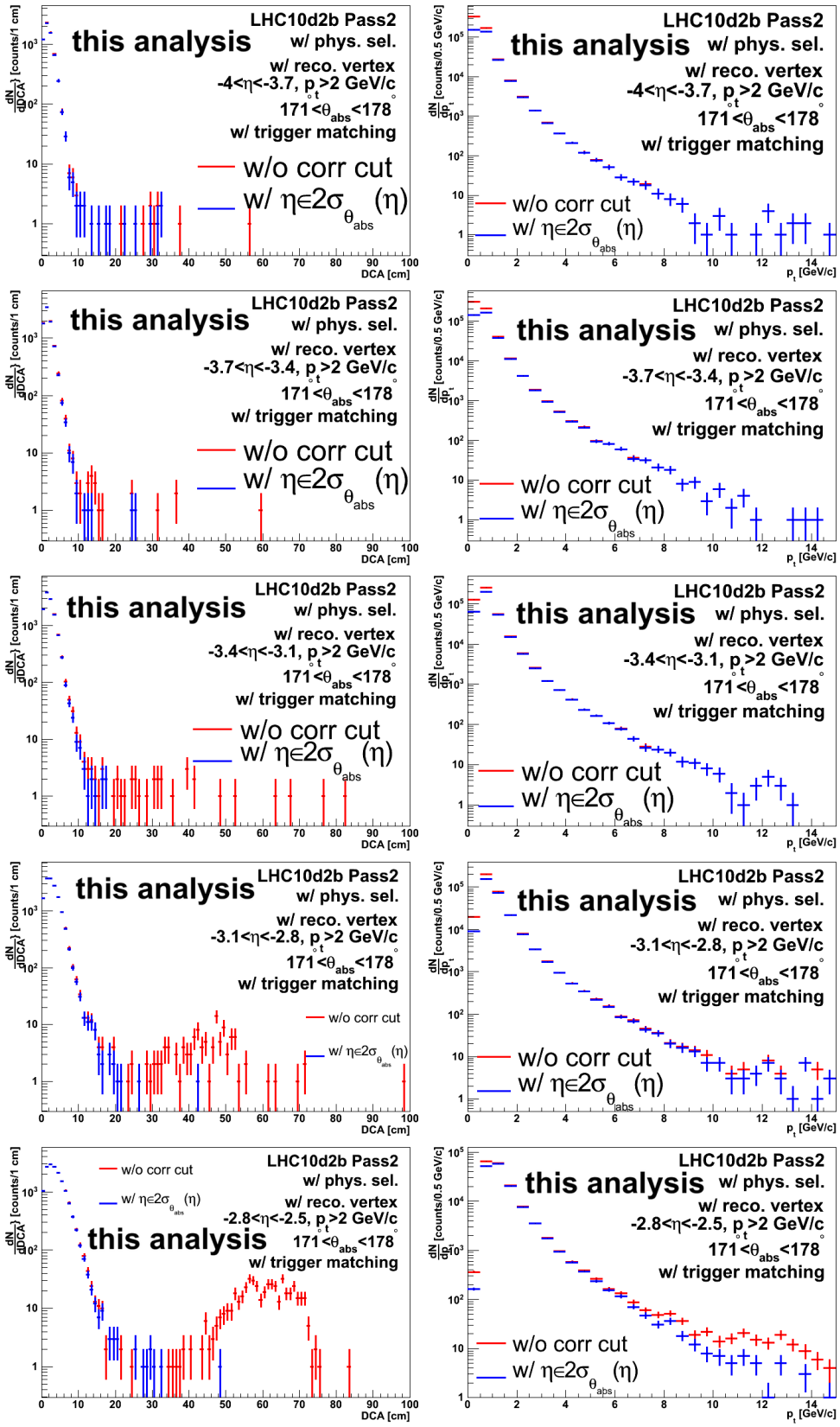

Figure 7.36: DCA (in $p_t > 2$ GeV/c, left column) and p_t (right column) distributions without (red lines) and with (blue lines) the combination cut defined in Eq. (7.34) in five pseudo-rapidity bins. The results are from the muon triggered data in LHC10d2b with the muon selection cuts.

by using $\eta = -2.5$ and $v_z = 10$ cm. Finally, we cut η in $2\sigma_\theta(\eta)$:

$$-\ln(\tan\frac{\theta_{\rm plo}+2\sigma_\theta(\eta)}{2}) < \eta < -\ln(\tan\frac{\theta_{\rm plo}-2\sigma_\theta(\eta)}{2}). \quad (7.34)$$

This cut is shown by the two red curves in Fig. 7.35, and it allows for a good separation of the beam induced background component from the other components.

7.6.2.2 Test of the Correlation Cut

To study the effects of the correlation cut defined in Eq. (7.34), first, as shown in Fig. 7.36, we plot the DCA (left column) and $p_{\rm t}$ (right column) distributions in the five pseudo-rapidity bins without (red lines) and with (blue lines) this combination cut by using the data from the muon triggered events in LHC10d2b with muon selection cuts. The results concerning the DCA distributions are shown in the range $p_{\rm t} > 2$ GeV/c.

After the combination cut, the beam induced background is rejected very effectively, in particular in the last three η bins, $-3.4 < \eta < -3.1$, $-3.1 < \eta < -2.8$ and $-2.8 < \eta < -2.5$. The structures, due the beam induced background, located in the region with large DCA values, disappear after applying the combination cut. The right column of Fig. 7.36 shows the corresponding $p_{\rm t}$ distributions. One can observe that, after the correlation cut, the $p_{\rm t}$ distribution is strongly improved, in particular in the last two η bins.

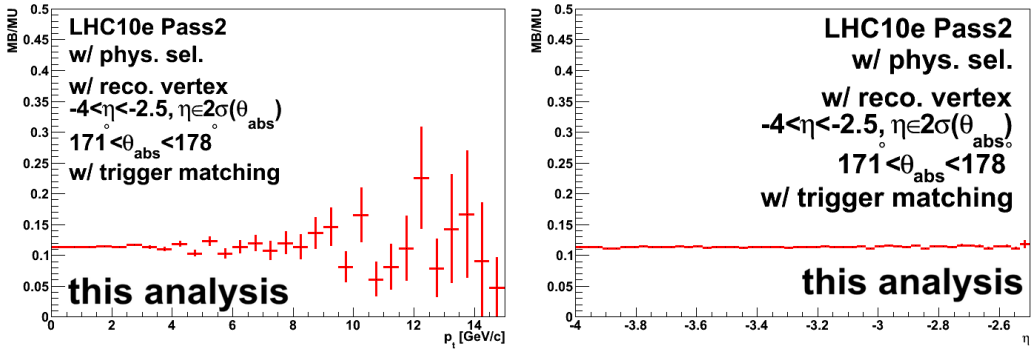

Figure 7.37: The ratios of the track multiplicity with the muon selection cuts plus the additional combination cut in minimum bias events to that in muon triggered events as a function of $p_{\rm t}$ (left) and η (right). The results are gotten from LHC10e.

Another aspect that we can see in the right column of Fig. 7.36 is that, the combination cut not only improves the $p_{\rm t}$ spectrum in the high $p_{\rm t}$ region but also rejects a fraction of tracks which are from the beam induced background in the low $p_{\rm t}$ region. As mentioned in Sec. 7.2.2.2, the normalization of the muon triggered events is done by using the ratio of the track multiplicities after the muon selection cuts in minimum bias events to that in muon triggered events $N_{\rm trk}^{\rm MB}/N_{\rm trk}^{\rm MU}$, Eq. (7.22). Since the combination cut modifies the $p_{\rm t}$ spectrum in both low and high $p_{\rm t}$ regions,

LHC10e w/ muon selection cuts	$N_{\rm trk}^{\rm MB}$	$N_{\rm trk}^{\rm MU}$	$N_{\rm trk}^{\rm MB}/N_{\rm trk}^{\rm MU}$
no combination cut	760520	6695576	11.3585%
w/ combination cut	705230	6206360	11.363%

Table 7.6: The number of reconstructed track in the MUON spectrometer with the muon selection cuts in both minimum bias events and muon trigger events, together with the corresponding ratios. The results are gotten with LHC10e data and shown with and without the additional combination cut defined in Eq. (7.34).

after implementing this cut, we should check if the used normalization scenario is still valid, that is to say if this ratio is still independent on $p_{\rm t}$ and η, as shown in the lower panels of Fig. 7.6 and 7.7. The results are displayed in Fig. 7.37 for data from LHC10e period. According to the results shown in this figure, the normalization procedure of the muon triggered events is still valid with the combination cut. Also, as shown in Tab. 7.6, the number of reconstructed track in the MUON spectrometer with the muon selection cuts from both minimum bias events and muon trigger events, and corresponding ratios are presented without and with the combination cut defined in Eq. (7.34). The value of $N_{\rm trk}^{\rm MB}/N_{\rm trk}^{\rm MU}$ is unchanged before and after the combination cut. A fraction of tracks is removed by the combination cut in both minimum bias eveets and muon trigger events with respect to the results without this cut, but the final ratios are not changed after applying this cut. This means that the nomalized results will not be affected by this additional combination cut. The modification of the measured spectrum in the low $p_{\rm t}$ region, will also affect the normalization of the background gotten from the models, Eq. (7.27). Since the combination cut removes the beam induced background which is not reproduced by simulations, this effect, indeed, will improve the background normalization procedure. Also, since this cut removes the beam induced background and according to Fig. 7.36 this cut has no effect on the muon yield from heavy flavours decays (our signal) in $p_{\rm t} > 2$ GeV/c: we should not consider the correction of this cut in our interesting $p_{\rm t}$ region ($p_{\rm t} > 2$ GeV/c).

Now, we implement the combination cut defined in Eq. (7.34) to data as well as the muon selection cuts, and measure the production cross sections of muon from open heavy flavours decays again, as shown in Fig. 7.38. This figure is similar to the one in Fig. 7.32: we just apply the additional combination cut to the selected muon tracks. By comparing the results in Fig. 7.38 and that in Fig. 7.32, we can see that, with the beam induced background rejected by the combination cut, the production cross sections of muons from open heavy flavour decays in data are in agreement with that from FONLL predictions up to $p_{\rm t} = 15$ GeV/c, in all of the η regions.

Up to now, we found an additional beam induced background, which strongly affects the high $p_{\rm t}$ region and should be rejected from data. This can be successfully done with the combination cut.

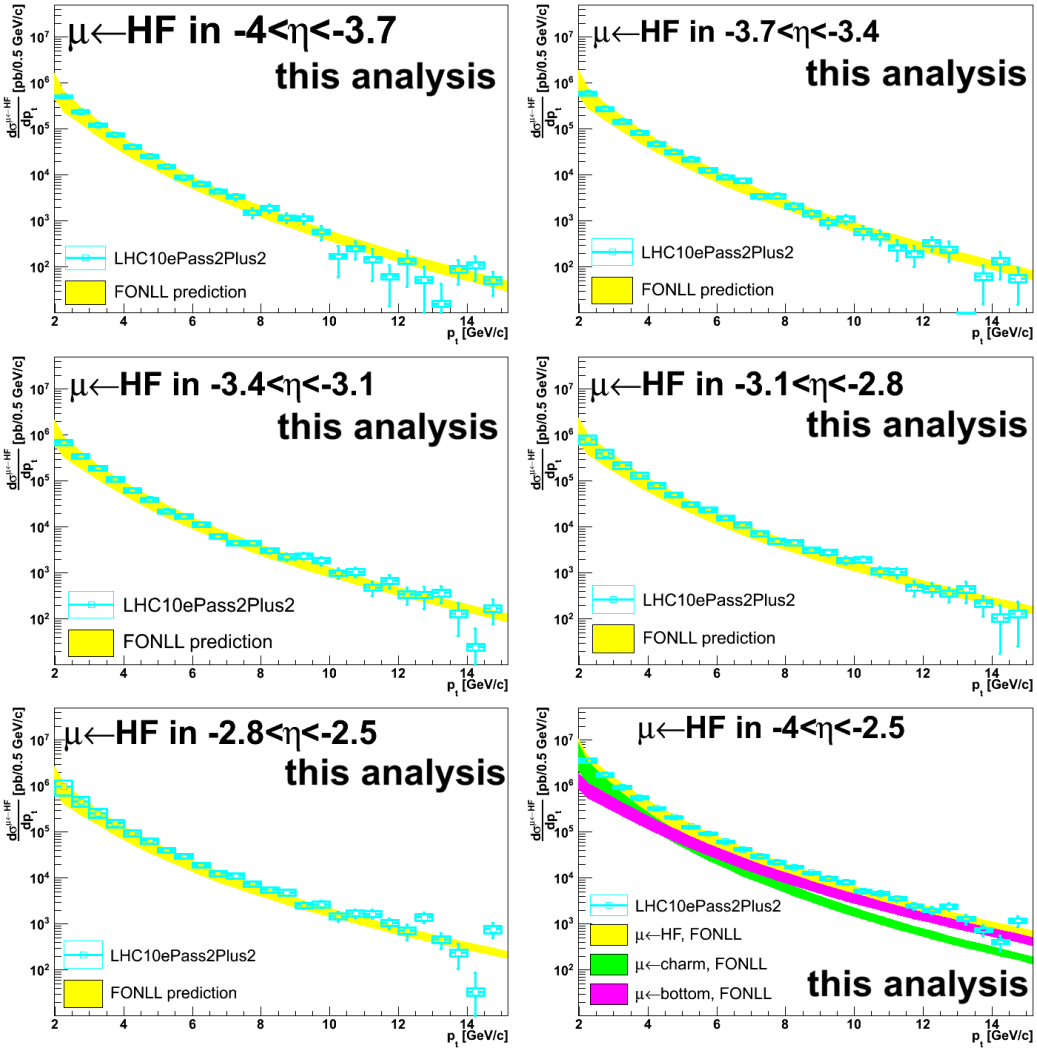

Figure 7.38: Similar as Fig. 7.32, but the results are gotton with the additional combination cut defined in Eq. (7.34).

7.6.2.3 Correlation Cut Optimization

Let us discuss the assumptions used to develop the combination cut in Eq. (7.34). Without considering the v_z spread and multi-scattering effects of the tracks in the front absorber, we get $\theta_{\rm pol} \approx \theta_{\rm abs}$, as in Eq. (7.31). By considering the v_z spread but still without multi-scattering effect, the polar angle can be approximated as Eq. (7.32). But, indeed, with multi-scattering effects, the approximation in Eq. (7.32) does not give the real value of the polar angle. The difference between this approximation and the polar angle reflects the Coulomb-Multi-Scattering effect for tracks in the front absorber. Then we re-define this angle as $\theta_{\rm CMS}$,

$$\theta_{\rm CMS} = \pi - \arctan \frac{R_{\rm abs}}{L_{\rm abs} + v_z}, \tag{7.35}$$

in the ALICE global coordinate system. By using the correlation between $\eta - \theta_{\rm CMS}$ instead of the $\eta - \theta_{\rm abs}$ combination, we avoid the $v_{\rm z}$ spread effect, and as shown in Fig. 7.39. By comparing with the $\eta - \theta_{\rm abs}$ correlation in Fig. 7.35, the $\eta - \theta_{\rm CMS}$ combination separates the beam induced background more clearly.

Since the $\eta - \theta_{\rm CMS}$ combination separates the beam induced background according to the Coulomb-Multi-Scattering effects, we should implement a cut using this correlation. With Coulomb-Multi-Scatterings, the **Root Mean Square** (**RMS**) of the scattering angle $\theta_{\rm RMS}$ as a function of the incident particle momentum [310] is:

$$\theta^{\rm RMS} = \frac{13.6\ {\rm MeV}}{\beta cp} z\sqrt{x/X_0}[1 + 0.038\ln(x/X_0)], \tag{7.36}$$

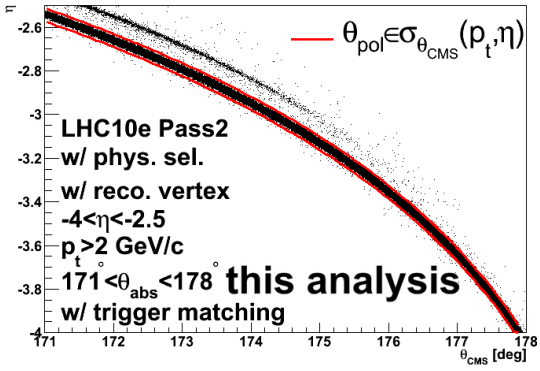

Figure 7.39: Same as the left panel of Fig. 7.35, but with the correlation between η and $\theta_{\rm CMS}$ as defined in Eq. (7.35), see text for more details.

where, p, βc and z are the momentum, velocity and charge number of the incident particle, and x/X_0 is the thickness of the scattering medium in radiation lengths. During track reconstruction, multi-scattering effects in the front absorber are corrected with the Badier-Branson correction, as mentioned in Sec. 3.4.4.3. In this case, multi-scattering effects are approximated by one equivalent scattering at the place of the so-called Branson plane. In case of the muon track reconstruction, the Branson plane position is very close to the end of front absorber. By approximating the Branson plane position to the end of front absorber and with $x/X_0 \simeq 60$ (Tab. 3.2), after calculations [311] according to Eq. (7.36), the difference between $\theta_{\rm pol}$ and $\theta_{\rm CMS}$ due to the multi-scattering effects can be expressed as:

$$\sigma_{\rm CMS}(p_{\rm t}, \eta) = \frac{0.06\ {\rm GeV}/c}{p_{\rm t}}[\pi - \theta_{\rm pol}(\eta)]. \tag{7.37}$$

It depends on both $p_{\rm t}$ and η ($\theta_{\rm pol}$). By using $\sigma_{\rm CMS}(p_{\rm t}, \eta)$ in Eq. (7.37) instead of the $2\sigma_\theta(\eta)$ in Eq. (7.34) we get the bounds as shown by the red curves in Fig. 7.39, which are used as the cuts to separate the beam induced component from the total $\eta - \theta_{\rm CMS}$ distribution.

Another adavntage of the new $\eta - \theta_{\rm CMS}$ correlation is that, it separates the beam induced background from the total combination distribution more clearly and it improves the cut efficiency in the low $p_{\rm t}$ region ($0 < p_{\rm t} < 2$ GeV/c). Fig. 7.40 shows the $\eta - \theta_{\rm CMS}$ distributions in $0 < p_{\rm t} < 0.5$ GeV/c (left column), 0.5 GeV/c $< p_{\rm t} < 1$ GeV/c (middle column) and 1 GeV/c $< p_{\rm t} < 2$ GeV/c (right column) from the data of muon trigger events in LHC10e (upper plots) and from the simulation of

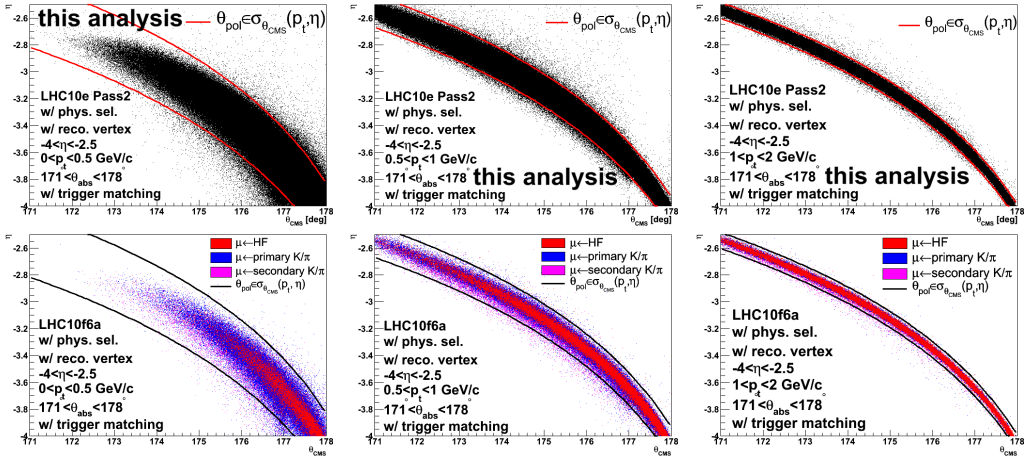

Figure 7.40: The $\eta - \theta_{\rm CMS}$ distributions in $0 < p_{\rm t} < 0.5$ GeV/c (left column), 0.5 GeV/c $< p_{\rm t} <$ 1 GeV/c (middle column) and 1 GeV/c $< p_{\rm t} <$ 2 GeV/c (right column) from the data of muon trigger events in LHC10e (upper plots) and from the simulation of LHC10f6a based on PYTHIA Perugia-0 tuning (lower plots). The results are shown together with the cuts defined in Eq. (7.37) as the bound curves and are obtained after the muon selection cuts in both data and simulations.

LHC10f6a based on PYTHIA Perugia-0 tuning (lower plots). All the results in this figure are obtained after the muon selection cuts. The bounds in each plot show the cut defined in Eq. (7.37) for the $\eta - \theta_{\rm CMS}$ correlation. According to the simulation results, we can find that cutting off the beam induced background via the $\eta - \theta_{\rm CMS}$ correlation in the low $p_{\rm t}$ region does not remove the other muon sources in the total distribution, in particular the muons from open heavy flavour decays.

We have presented the advantages of using the $\eta - \theta_{\rm CMS}$ correlation to get rid of the $v_{\rm z}$ spread effect and to just consider the difference produced by the multi-scattering effects. We also think if we can start with the multi-scattering as described in Eq. (7.36) directly to reject the beam induced background. A complementary method is presented in the following.

7.6.3 Study of $p\times$DCA Observable

From Eq. (7.36), one can deduce that:

$$p \times \theta^{\rm RMS} = \text{const}, \tag{7.38}$$

with $\beta \simeq 1$ for high energy muon tracks. With the small angle approximation, for tracks produced at or close to the primary vertex, we have:

$$\text{DCA} \propto \theta_{\rm scattering}, \tag{7.39}$$

where $\theta_{\rm scattering}$ is the scattering angle for tracks inside the front absorber. Then, Eq. (7.38) can be written in an alternative form as,

$$\sigma(p \times \text{DCA}) \equiv p \times \text{DCA}^{\rm RMS} = \text{const}. \tag{7.40}$$

From Eq. (7.40) on can deduce that, for the tracks produced at or close to the primary vertex, their momentum (p) times the RMS in their DCA distribution, defined as $\sigma(p \times \mathrm{DCA})$, is a constant and does not depend on any other variable. According to this property, the $p\times$DCA distribution of muons from open heavy flavour decays is expected different from the other sources and could be used to reject the background in the inclusive moun spectrum, in particular the beam induced background.

7.6.3.1 $p\times$DCA Calibration

Before the calculation of $p\times$DCA, it is very important to clarify the meaning of each term inside it.

In Eq. (7.36), the momentum p corresponds to the one for the incident particle when it is suffering scatterings, we denote this momentum as p_{CMS}. The final momentum that we obtained for the reconstructed track is corrected for the energy loss in the front absorber and is related to the position of primary vertex, we denote it as p_{vtx}. Due to the energy loss nside the front absorber for the tracks produced at or close to the primary vertex, before they suffer the scattering effects, indeed we have,

$$p_{\mathrm{trk}} < p_{\mathrm{CMS}} < p_{\mathrm{vtx}}, \tag{7.41}$$

where, p_{trk} is the track momentum reconstructed in the tracking chambers without any correction. To calculate the $p\times$DCA correctly, we introduce the following estimate:

$$p_{\mathrm{CMS}} \simeq \frac{1}{2}(p_{\mathrm{trk}} + p_{\mathrm{vtx}}). \tag{7.42}$$

Now, let us consider the DCA term. The DCA that we used is the one in the transverse plane (the plane perpendicular to the beam direction),

$$\mathrm{DCA} = \sqrt{\mathrm{DCA}_x^2 + \mathrm{DCA}_y^2}, \tag{7.43}$$

where, DCA_x and DCA_y are the x and y components of DCA in the transverse plane in the ALICE global coordinate system, respectively, and they are determined according to the position of v_{z}. In this case, to decrease the bias due to the approximation in Eq. (7.39), first, we do following correction:

$$\mathrm{DCA}_{x,\mathrm{vtx}} = \mathrm{DCA}_x - v_x, \qquad \mathrm{DCA}_{y,\mathrm{vtx}} = \mathrm{DCA}_y - v_y, \tag{7.44}$$

where v_{x} and v_{y} are the x and y positions of the primary vertex.

After the correction for the primary vertex position, the distributions of $\mathrm{DCA}_{x,\mathrm{vtx}}$ and $\mathrm{DCA}_{y,\mathrm{vtx}}$ with the muon selection cuts for muon trigger data in LHC10e are shown in the left and right plots of Fig. 7.41, respectively. One can notice that the mean value of $\mathrm{DCA}_{x,\mathrm{vtx}}$ and $\mathrm{DCA}_{y,\mathrm{vtx}}$ are not zero. This is due to the fact that the vertex from tracks is globally shifted from the nominal position due to the global mis-alignment of the tracking chambers of the MUON spectrometer. To avoid this misalignment effect, we correct it as:

$$\begin{aligned} \mathrm{DCA}_{x,\mathrm{cor}} &= \mathrm{DCA}_{x,\mathrm{vtx}} - < \mathrm{DCA}_{x,\mathrm{vtx}} >, \\ \mathrm{DCA}_{y,\mathrm{cor}} &= \mathrm{DCA}_{y,\mathrm{vtx}} - < \mathrm{DCA}_{y,\mathrm{vtx}} >, \end{aligned} \tag{7.45}$$

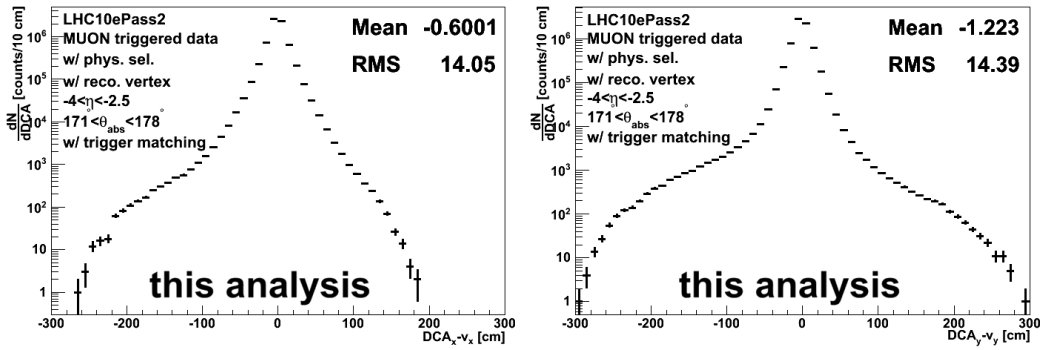

Figure 7.41: The $\mathrm{DCA}_{x,\mathrm{vtx}}$ (left) and $\mathrm{DCA}_{y,\mathrm{vtx}}$ (right) distributions with the muon selection cuts for the muon trigger events in LHC10e.

when calculating the $p\times$DCA, and get,

$$\mathrm{DCA}_{\mathrm{cor}} = \sqrt{\mathrm{DCA}^2_{x,\mathrm{cor}} + \mathrm{DCA}^2_{y,\mathrm{cor}}}. \tag{7.46}$$

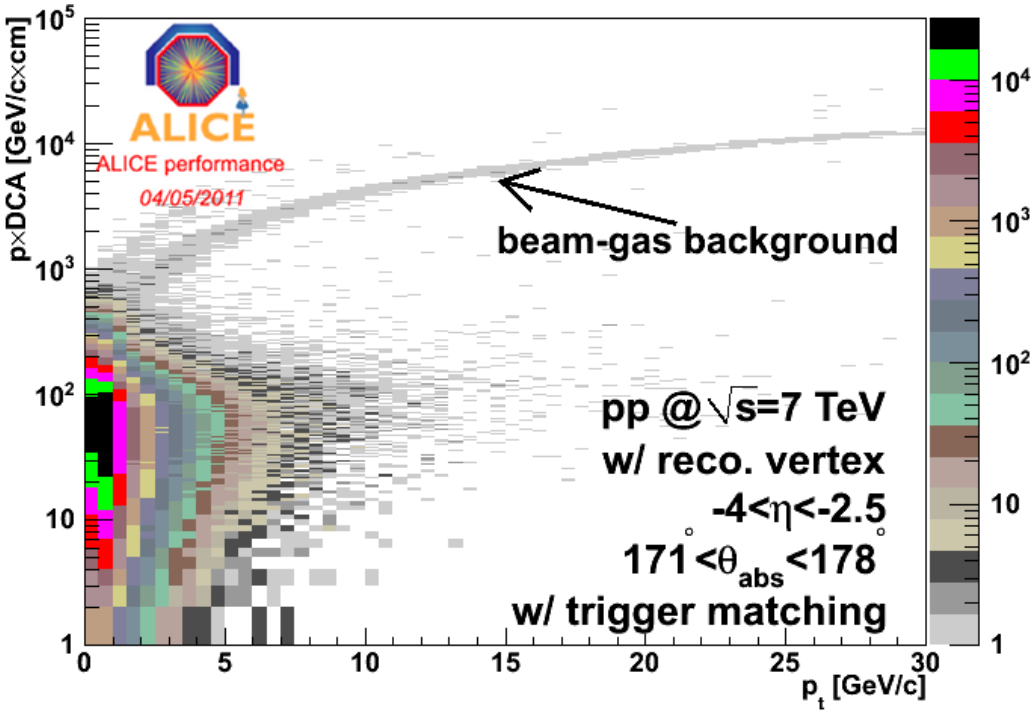

Figure 7.42: $p\times$DCA ($p\mathrm{DCA}_{\mathrm{calib}}$ as defined in Eq. (7.47)) versus p_{t} for muon trigger data in LHC10e. The muon selection cuts are applied.

After all of these calibration steps, the final $p\times$DCA for the muon tracks is calculated as,

$$p\mathrm{DCA}_{\mathrm{calib}} \equiv p_{\mathrm{CMS}} \times \mathrm{DCA}_{\mathrm{corr}}, \tag{7.47}$$

with $p_{\rm CMS}$ and $\rm DCA_{corr}$ defined in Eq. (7.42) and (7.46), respectively. Fig. 7.42 shows the distribution of the correlation between $p_{\rm t}$ and the calibrated $p\times$DCA ($p\rm DCA_{calib}$) defined in Eq. (7.47), $p\rm DCA_{calib}$ *vs.* $p_{\rm t}$, for muon trigger data from LHC10e, with the muon selection cuts. We can notice that the behavior of the beam induced background is very different from that for other sources. Most of tracks (in particular, muons from open heavy flavour decays) satisfy the relation of Eq. (7.40) controlled by the Coulomb-Multi-Scattering effects (Eq. (7.36)) and their $p\rm DCA_{calib}$ values are in the RMS range defined in Eq. (7.40). But this relation is not valid for the beam induced background. In $p_{\rm t} > 2$ GeV/c, the $p\rm DCA_{calib}$ value of the beam induced background is far away from the central value determined by Eq. (7.40), as shown in Fig. 7.42. Instead of the $\eta - \theta_{\rm abs}$ or $\eta - \theta_{\rm CMS}$ combination, the $p\times$DCA is another interesting variable to cut off the beam induced background and it can be used in a more straightforward way than the previous observables.

7.6.3.2 Test of $p\times$DCA Cut

To simplify the notations, in the following, if there no special declaration, we just use $p\times$DCA to express the calibrated result $p\rm DCA_{calib}$ defined in Eq. (7.47).

As shown in Fig. 7.42, $p\times$DCA is a powerful variable to separate the beam induced background. Before to implement this observable to remove the beam induced background, we should study it in detail. According to Eq. (7.36), the value of $\sigma(p\times\rm DCA)$ defined in Eq. (7.40) depends on the property of the scattering medium. Fig. 6.12 shows that, the material of the front absorber is different in $171^{\circ} < \theta_{\rm abs} < 177^{\circ}$ and $177^{\circ} < \theta_{\rm abs} < 178^{\circ}$ (the values of $\theta_{\rm abs}$ listed in Fig. 6.12 are converted to those in the ALICE global coordinate system). In this case, the extraction of the value for $\sigma(p \times \rm DCA)$ in data should be presented in two $\theta_{\rm abs}$ regions, independently. This is done by fitting the calibrated $p\times$DCA (calculated via Eq. (7.47)) distributions with,

$$x \cdot \exp[-(\frac{x - x_0}{\sigma})^2], \tag{7.48}$$

where x_0 and σ^2 are the mean and variance of the Gaussian distribution (as defined in Eq. (5.3) already), in $171^{\circ} < \theta_{\rm abs} < 177^{\circ}$ and $177^{\circ} < \theta_{\rm abs} < 178^{\circ}$, respectively. We define the Gaussian σ obtained from the fit as the measured $\sigma(p\times\rm DCA)$ in data, and denote it as $\sigma_{\rm meas}(p \times \rm DCA)$. Tab. 7.7 shows the values of $\sigma_{\rm meas}(p \times \rm DCA)$ in $171^{\circ} < \theta_{\rm abs} < 177^{\circ}$ and $177^{\circ} < \theta_{\rm abs} < 178^{\circ}$ from the muon trigger events in LHC10e with the muon selection cuts. Then, the obtained values of $\sigma_{\rm meas}(p \times$

LHC10e w/ muon selection cuts	$171^{\circ} < \theta_{\rm abs} < 177^{\circ}$	$177^{\circ} < \theta_{\rm abs} < 178^{\circ}$
$\sigma_{\rm meas}(p \times \rm DCA)$	63 GeV/$c\times$cm	120 GeV/$c\times$cm

Table 7.7: The values of $\sigma_{\rm meas}(p \times \rm DCA)$ in $171^{\circ} < \theta_{\rm abs} < 177^{\circ}$ and $177^{\circ} < \theta_{\rm abs} < 178^{\circ}$ from the muon triggered events in LHC10e with the muon selection cuts.

DCA), as shown in Tab. 7.7, should be corrected for the mis-alignment of the track momentum. During our analysis, we applied this correction in a very simple way by parameterizing the uncertainty of the track momentum p on mis-alignment as $0.4 \cdot p$ [312], and we get,

$$\sigma(p \times \mathrm{DCA}) = \sqrt{\sigma^2_{\mathrm{meas}}(p \times \mathrm{DCA}) + (0.4 \cdot p)^2}. \tag{7.49}$$

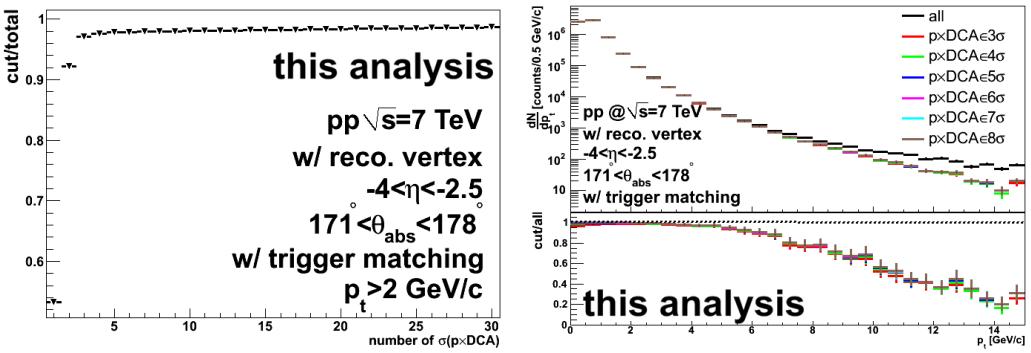

Figure 7.43: Left: the ratio between the number of tracks in $N \cdot \sigma(p \times \mathrm{DCA})$ cut and the total number of tracks as a function of N in $p_{\mathrm{t}} > 2$ GeV/c. Right: the p_{t} distributions in $N \cdot \sigma(p \times \mathrm{DCA})$ with various values of N, the ratios between the p_{t} distributions with and without the $p \times \mathrm{DCA}$ cut are shown in the lower panel. All the results are from muon trigger events in LHC10e with the muon selection cuts.

After the correction of $\sigma(p \times \mathrm{DCA})$, as defined in Eq. (7.49), we are going to cut the $p\times$DCA distribution in $N \cdot \sigma(p \times \mathrm{DCA})$, where N is the number of $\sigma(p \times \mathrm{DCA})$. In order to determine the coefficient N, first, we perform the test shown Fig. 7.43 (left panel). In this plot, we show the ratio between the number of tracks with $N \cdot \sigma(p \times \mathrm{DCA})$ cut and the total number of tracks as a function of N in $p_{\mathrm{t}} > 2$ GeV/c from the muon trigger events in LHC10e with the muon selection cuts. We observe that this ratio saturates at $N \simeq 5$. This indicates that, in $N \gtrsim 5$ the p_{t} spectrum does not depend on N, in $p_{\mathrm{t}} > 2$ GeV/c. In order to understand into more detail this result, we plot the p_{t} distributions in $N \cdot \sigma(p \times \mathrm{DCA})$ with various values of N and the ratio between these distributions and the one without the $p\times$DCA cut in Fig. 7.43 (right panel). The results are obtained from the same data sample as the one used in Fig. 7.43 (left panel). One observes that, by comparison with the p_{t} spectrum without the $p\times$DCA cut, there is a suppression due to the rejection of the beam induced background in the high p_{t} region. Also, the p_{t} spectrum is almost unchanged when varying N in the range 3 to 8. According to these results, we can conclude that the $p\times$DCA cut removes the beam induced background very efficiently in the high p_{t} region and the results are stable by varying the cut with the number of $\sigma(p \times \mathrm{DCA})$, N, in a large range.

To get our final results, together with the muon selection cuts, defined in Sec. 6.4, we introduce the additional $p\times$DCA cut in $5 \cdot \sigma(p \times \mathrm{DCA})$ for the beam induced background rejection.

As in Sec. 7.6.2.2, before to implement the cut of $p\times$DCA in $5\cdot\sigma(p\times\text{DCA})$ in data, there still are two issues that need to be investigated:

- check if this cut will affect the normalization of the muon trigger events (Eq. (7.22));
- check if this cut will change the correction efficiency, as discussed in Sec. 7.4.

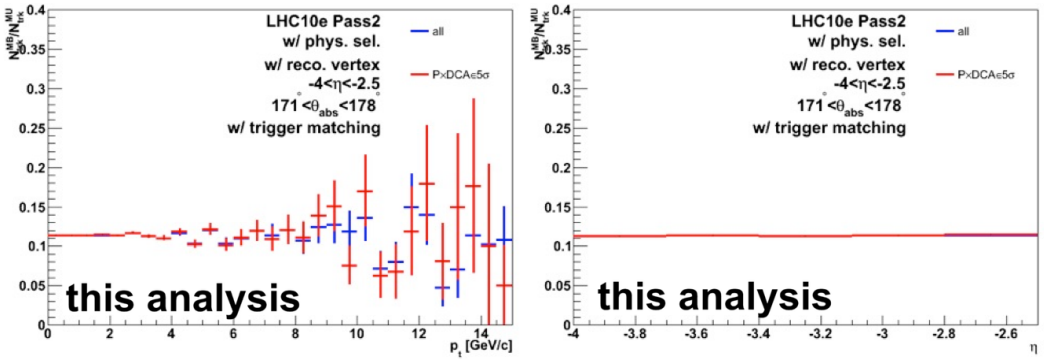

Figure 7.44: Similar as Fig. 7.37, but instead of implementing the $\eta-\theta_{\text{abs}}$ cut, the additional cut $p\times$DCA in $5\cdot\sigma(p\times\text{DCA})$ is used. The results are also compared with those without the $p\times$DCA cut.

The first issue could be checked quickly by making a similar ratio as that shown in Fig. 7.37 but by using the $p\times$DCA cut instead of the $\eta-\theta_{\text{abs}}$ cut. These results are shown in Fig. 7.44. The ratio between muon tracks in minimum bias events and muon trigger events, $N_{\text{trk}}^{\text{MB}}/N_{\text{trk}}^{\text{MU}}$, as a function of p_{t} (left) and η (right) in LHC10e is displayed just with the muon selection cuts (blue lines) and with the additional $p\times$DCA (red lines). The conclusion is similar to the one obtained from results in Fig. 7.37: with the additional $p\times$DCA cut in $5\cdot\sigma(p\times\text{DCA})$, the value of $N_{\text{trk}}^{\text{MB}}/N_{\text{trk}}^{\text{MU}}$ does not depend on pt or η. Moreover, it is also consistent with the one without the $p\times$DCA cut. This means that, similarly to the $\eta-\theta_{\text{abs}}$ cut, the $p\times$DCA does not affect the normalization of the muon trigger events (Eq. (7.22)).

To study the second issue, we make the ratio between the p_{t} distribution with the $p\times$DCA cut in $5\cdot\sigma(p\times\text{DCA})$ and the one without this cut for different muon track sources in the simulations, with the muon selection cuts. These results are shown in Fig. 7.45 for LHC10f6, PhoJet simulation (left) and LHC10f6a, PYTHIA simulation with Perugia-0 tuning (right). According to these results, a $p\times$DCA in $5\cdot\sigma(p\times\text{DCA})$ does not affect muons from open heavy flavour decays (our signal) and primary muons. A small fraction of secondary muons is removed by this cut. In this case, both the primary muon background estimate, as mentioned in Sec. 7.3.2, and the efficiency correction in Sec. 7.4 are not affeected by this new cut. Since this cut removes a fraction of the secondary muon component, in particular in the low p_{t} region, the normalization of the primary muon background (Sec. 7.3.3) and the systematic uncertainty estimate on the background subtraction as shown

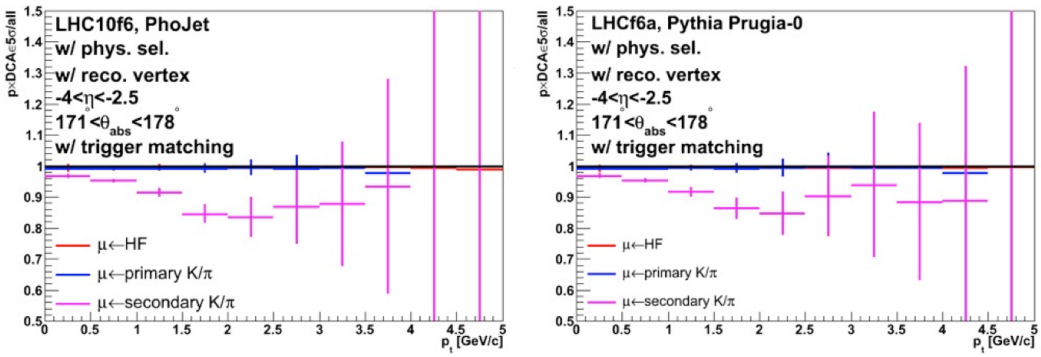

Figure 7.45: Ratio between the p_{t} distributions with $p\times$DCA cut in $5\cdot\sigma(p\times\mathrm{DCA})$ and without this cut for different muon track sources from simulation from LHC10f6 (left) and LHC10f6a (right). The muon selection cuts are implemented.

in Tab. 7.3 should be corrected accordingly by varying the yield of the secondary muons in the Monte-Carlo. As mentioned in Tab. 7.3, the systematic uncertainty on the background normalization has already been corrected by this $p\times$DCA cut. For the final analysis, what we need to do, is to update the normalization of the background in data with the new $p\times$DCA cut.

7.6.3.3 Optimization of $\sigma(p\times\mathrm{DCA})$ in the high p_{t} region

To reject the beam induced background, we implemented the $5\cdot\sigma(p\times\mathrm{DCA})$ calculated according to Eq. (7.49). As shown in Fig. 7.43 (right panel), this cut works fine in our interesting p_{t} region ($2<p_{\mathrm{t}}<15$ GeV/c). But in our incoming analysis (*eg.* the $\mathrm{W}^{\pm}$ boson study), we should investigate the $p\times$DCA cut in a much higher p_{t} region ($p_{\mathrm{t}}\simeq 25\sim 50$ GeV/c, [313]). As the uncertainty on the mis-alignment is $1\%\times p_{\mathrm{t}}$, it will have a strong effect for the $p\times$DCA in this very high p_{t} region. In this case, we cannot treat the mis-alignment effect as in Eq. (7.49). Also, presently, the value of $p\times$DCA is not only affected by the momentum resolution from the mis-alignment but also by the DCA resolution. To do the full correction of the $\sigma(p\times\mathrm{DCA})$, the DCA resolution should also be considered.

In this respect, in [314], the correction of $\sigma(p\times\mathrm{DCA})$ has been updated by considering the effect from both mis-alignment and DCA resolution. In the following, we just give a short summary of the procedure.

According to Eq. (7.47), the full resolution of $p\times$DCA should be,

$$\mathrm{d}(p\mathrm{DCA}_{\mathrm{calib}})\approx(\Delta p_{\mathrm{CMS}})\times\mathrm{DCA}_{\mathrm{calib}}+p_{\mathrm{CMS}}\times(\Delta\mathrm{DCA}_{\mathrm{calib}}). \tag{7.50}$$

The first term in the right side of Eq. (7.50), $(\Delta p_{\mathrm{CMS}})\times\mathrm{DCA}_{\mathrm{calib}}$, corresponds to the uncertainty on the momentum resolution for $p\times$DCA. To illustrate this effect, the following approximation is used,

$$\frac{\sigma_p}{p}\approx\frac{\Delta p}{p}, \tag{7.51}$$

where $\Delta p/p$ is estimated via,

$$p\Delta_{\rm s} = \frac{\Delta p}{p - \Delta p} \tag{7.52}$$

with the momentum resolution $\Delta_{\rm s}$ coming from the sagitta for the track momentum determination during the reconstruction procedure, as in the example shown in Fig. 3.12. Then, assuming that the relation in Eq. (7.52) is also valid for the $p_{\rm CMS}$ defined in Eq. (7.42) we get,

$$\frac{\Delta p_{\rm CMS}}{p_{\rm CMS}} = \frac{p_{\rm CMS}\Delta_{\rm s}}{1 + p_{\rm CMS}\Delta_{\rm s}}. \tag{7.53}$$

With the input from Eq. (7.53), the $p_{\rm CMS}$ now, is corrected as,

$$p_{\rm align} = p_{\rm CMS} - \Delta p_{\rm CMS} = \frac{p_{\rm CMS}}{1 + p_{\rm CMS}\Delta_{\rm s}}, \tag{7.54}$$

to avoid to overestimate the momentum due to the misalignment. With this correction, the requirement of,

$$p_{\rm align} \times {\rm DCA}_{\rm calib} < N \cdot \sigma_{\rm meas}(p \times {\rm DCA}), \tag{7.55}$$

becomes:

$$p_{\rm CMS} \times {\rm DCA}_{\rm calib} < N \cdot (1 + p_{\rm CMS}\Delta_{\rm s}) \cdot \sigma_{\rm meas}(p \times {\rm DCA}). \tag{7.56}$$

Hence we have

$$(\Delta p_{\rm CMS}) \times {\rm DCA}_{\rm calib} = (1 + p_{\rm CMS}\Delta_{\rm s}) \cdot \sigma_{\rm meas}(p \times {\rm DCA}). \tag{7.57}$$

To obtain the second term in the right side of Eq. (7.50), $p_{\rm CMS} \times (\Delta{\rm DCA}_{\rm calib})$, which includes the effect of the DCA resolution, the following approximation is considered: for a given primary vertex position, the DCA resolution could be estimated by the resolution on track slope $\Delta_{\rm k}$. Under the zero order approximation (assuming that the mean value of the vertex position is at the origin of the ALICE global coordinate system), one can get,

$$p_{\rm CMS} \times (\Delta{\rm DCA}_{\rm calib}) = p_{\rm CMS} \times (L_{\rm trk} \cdot \Delta_{\rm k}), \tag{7.58}$$

where $L_{\rm trk} = 535$ cm is the distance between the origin of ALICE global coordinate system and the first tracking chamber of the MUON spectrometer.

By adding the two parts of the $p\times$DCA resolution in the right side of Eq. (7.50) together quadratically, according to the estimate from Eq. (7.57) and (7.58), finally, one can obtain the optimized $p\times$DCA cut as:

$$p_{\rm CMS} \times {\rm DCA}_{\rm calib} < N \cdot \sigma_{\rm corr}(p \times {\rm DCA}), \tag{7.59}$$

with,

$$\sigma_{\rm corr}(p \times {\rm DCA}) = \sqrt{[(1 + p_{\rm CMS} n \cdot \Delta_{\rm s})\sigma_{\rm meas}(p \times {\rm DCA})]^2 + (p_{\rm CMS} L_{\rm trk}\Delta_{\rm k})^2}, \tag{7.60}$$

where, n is introduced to cut off the momentum resolution in $n \cdot \Delta_{\rm s}$, normally one can set $n \simeq N$.

7.7 Results

Based on the previous discussion, it is time to summarize our analysis and to show the final results.

7.7.1 Summary of the Analysis Strategy

To obtain the production cross section of muons from open heavy flavour (charm and bottom quarks) decays, we adopt the following strategy.

1. Event trigger selection:
   - muon triggered events, which have a large statistics of muon tracks, the analysis is based on this data sample;
   - minimum bias triggered events, used for the normalization of the muon trigger events and also for cross checking the results gotten from muon trigger events.
2. Physics selection: rejects a part of the beam gas background from physics events.
3. Data quality assurance: rejects the bad runs which are not suitable for the physics analysis, *eg.* runs in which a large part of detector cells or front-end electronics is missing during the data taking or runs with high pile-up, since the correction of these events should be done very carefully and sometimes it could introduce large bias in the final results.
4. Muon track selection:
   - rejects the tracks from the events without the reconstructed primary vertex, this ensures that the kinematics of muons from open heavy flavour decays is correct;
   - $-4 < \eta < -2.5$, the acceptance cut, can reject part of the background produced far from the primary vertex;
   - $171^{\circ} < \theta_{\rm abs} < 178^{\circ}$, avoid the effects from different materials in the front absorber;
   - requiring that the reconstructed muon track is matched with the one in the muon trigger, allows to reject punch through hadrons and part of the beam induced backgound;
   - $p\times$DCA$< 5 \cdot \sigma(p \times \text{DCA})$, rejects the beam induced background.

   All the above selections for events and muon tracks except the $p\times$DCA cut are called as the muon selection cuts in the previous sections. Now, with the additional $p\times$DCA cut we called them the **Standard Muon Cuts**.
5. Subtraction of the background from primary muons in the data after the standard cuts according to Monte-Carlo simulations.

6. The efficiency correction and the normalization (conversion of yields into cross sections). After this step, the final results can be compared to theoretical predictions.

The systematic uncertainties in the above analysis steps include the following sources:

- background subtraction, from 5% to 35%, depending on $p_{\rm t}$ and η as summarized in Tab. 7.3;
- detector response, 5% in the data sample used in this analysis;
- residual mis-alignment, $1\% \times p_{\rm t}$;
- luminosity measurement for the normalization, 3.5% (not included in the final uncertainty values).

7.7.2 Final Results

The measured differential production cross section of muons from heavy flavour decays as a function of $p_{\rm t}$ in five (pseudo)-rapidity regions are shown in Fig. 7.46. Note that η and y are identical for muons in the acceptance of the spectrometer, and in pp the results are symmetric with respect to η $(y) = 0$. The results will be presented as a function of y with positive values. The error bars (which are smaller than symbols in most of the $p_{\rm t}$ and y bins) represent the statistical uncertainties. The boxes correspond to the systematic uncertainties. The systematic uncertainty on $\sigma_{\rm pp}^{\rm MB}$ at $\sqrt{s} = 7$ TeV measurement is not included in the uncertainty boxes. The results are compared to FONLL predictions (gray curve and shaded band for the systematic uncertainty) as discussed in Sec. 7.5.1. The uncertainty bands from FONLL predictions are the envelope of the resulting cross sections. The ratios between data and FONLL predictions are shown in Fig. 7.47. A good description by the FONLL predictions of the data is observed within uncertainties, in all of the rapidity regions. The measured production cross sections are systematically larger than the central values of the model predictions.

By adding the results in Fig. 7.46 in each rapidity bin according to Eq. (7.23) and (7.24), we get the results in Fig. 7.48. They show the measured differential production cross sections of muons from heavy flavour decays as a function of $p_{\rm t}$ in the rapidity region $2.5 < y < 4$ (left) and as a function of y in the range $2 < p_{\rm t} < 12$ GeV/c (right). The lower panels present the ratios between data and the central values of FONLL predictions. The results show again a good agreement with FONLL predictions. The ratio data over central value of FONLL calculations as a function of $p_{\rm t}$ is about 1.3. This is consistent with the ALICE measurements of the $p_{\rm t}$-differential production cross sections of D mesons [225] in the central rapidity region. The CMS and ATLAS Collaborations made complementary measurements of the heavy flavour production, with electrons and/or muons measured at mid-rapidity in pp collisions at $\sqrt{s} = 7$ TeV [315, 316]. The production of muons from beauty decays, measured by the CMS Collaboration in $|\eta| < 2.1$ and at high pt ($p_{\rm t} > 6$ GeV/c),

exhibits a similar agreement with NLO pQCD calculations within uncertainties: the data points lie in the upper limit of the model predictions. The results from the ATLAS Collaboration concerning the production of muons and electrons from heavy flavour decays in $|\eta| < 2$ (excluding $1.37 < |\eta| < 1.52$) and in the region $7 < p_{\mathrm{t}} < 27$ GeV/c are also consistent with FONLL calculations. The theoretical charm and beauty components are also displayed in Fig. 7.48. According to these predictions, the muon contribution from beauty decays is expected to dominate in the range of $p_{\mathrm{t}} \lesssim 6$ GeV/c. In this region, it represents about 62% of the heavy flavour decay muon cross section.

A paper related to the work presented in this chapter has been pubulished in **Physics Letters B** for the ALICE collaboration, it can be found Appendix A.

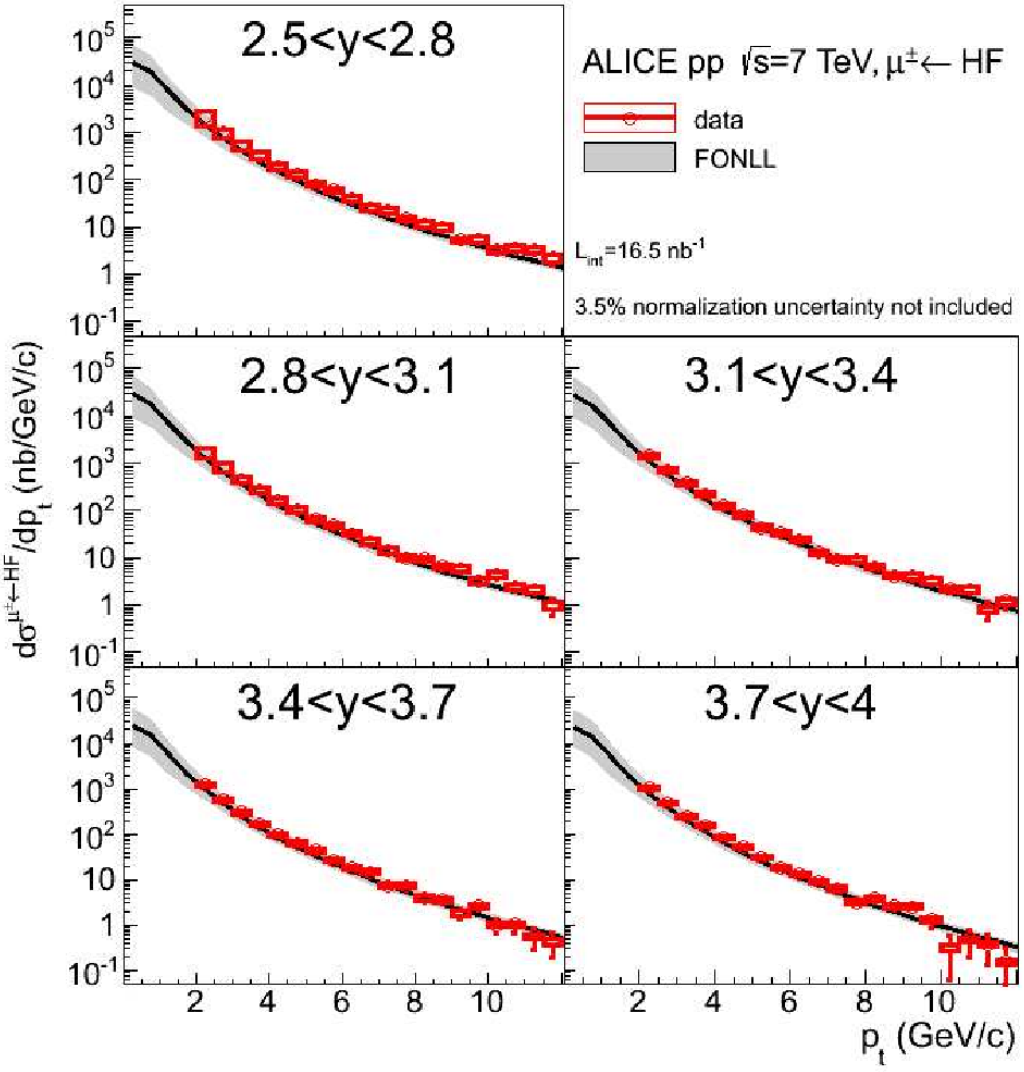

Figure 7.46: The p_{t}-differential production cross section of muons from open heavy flavour decays in pp collisions at $\sqrt{s} = 7$ TeV in five rapidity regions. The analysis is based on the muon triggered data in LHC10e. The gray bands show the predictions from the FONLL predictions. These results are published in Ref. [317].

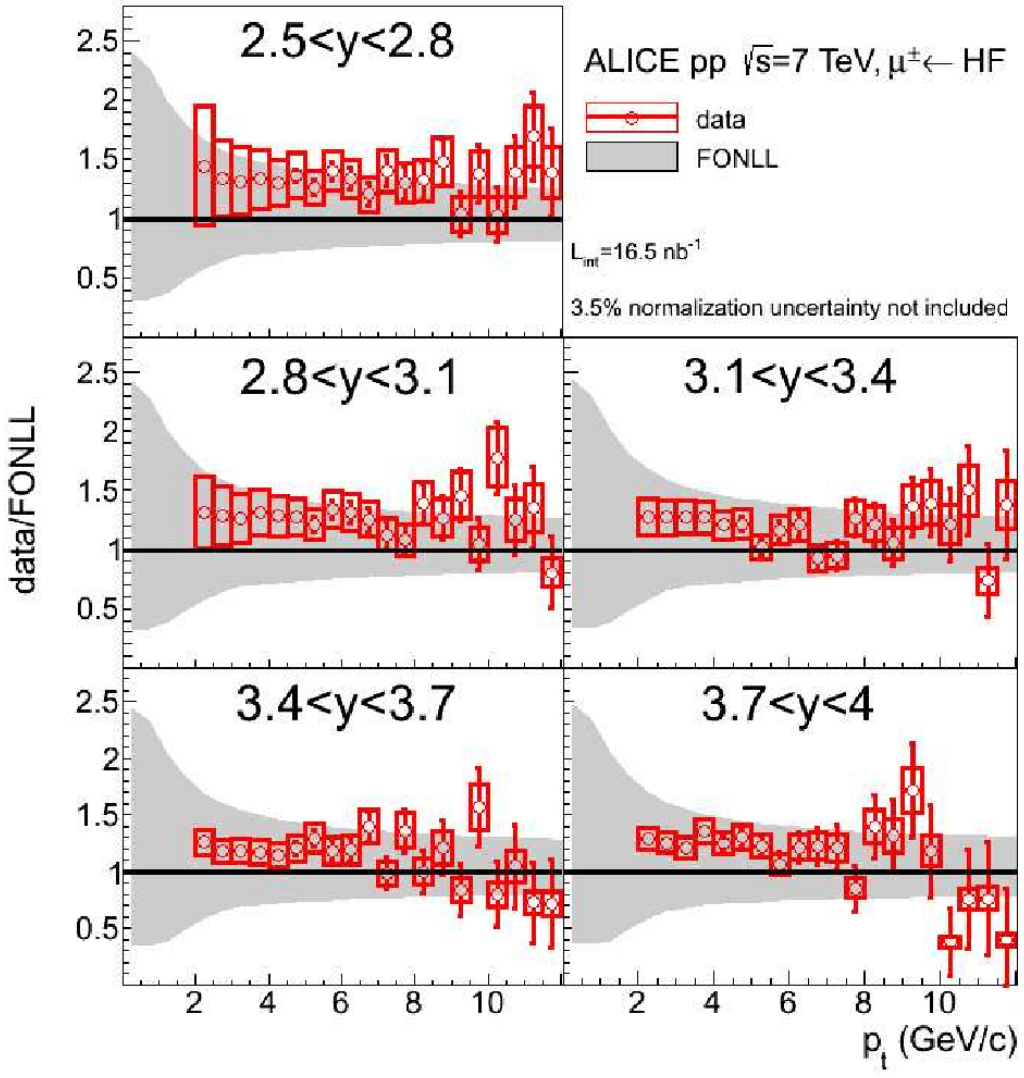

Figure 7.47: The ratio between the measured results in data and the central value of the FONLL predictions, as shown in Fig. 7.46, in five rapidity regions, with the re-scaled errors. These results are published in Ref. [317].

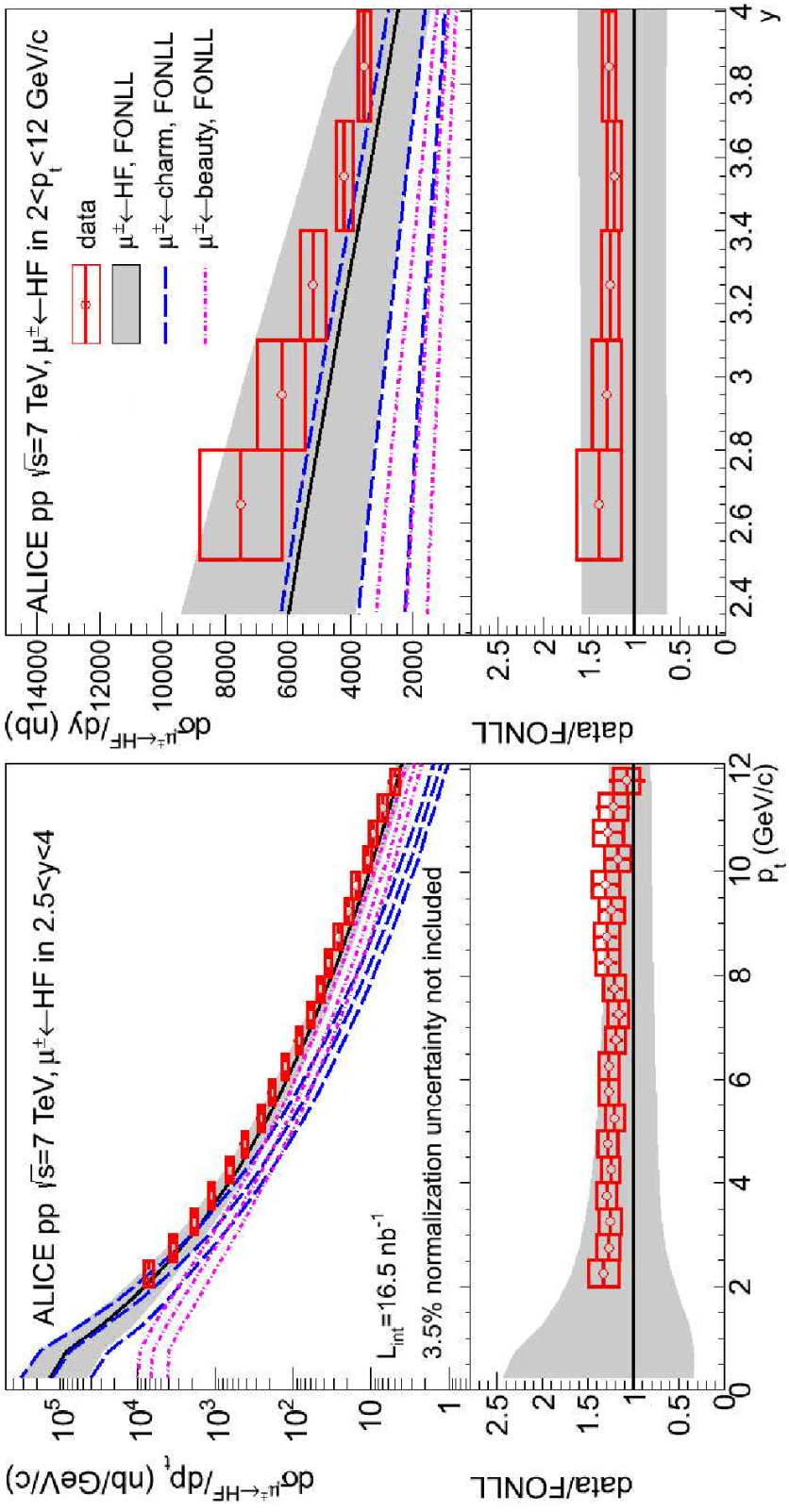

Figure 7.48: The differential production cross sections of muons from open heavy flavour decays as a function of p_t in $2.5 < y < 4$ (left) and as a function of rapidity y in $2 < p_t < 12$ GeV/c (right). The analysis is based on the muon triggered data in LHC10e. The comparison with the FONLL predictions is also presented. As in Fig. 7.47, the lower panels show the ratio between the measured cross sections and central values of the FONLL predictions, with the re-scaled systematical uncertainties. These results are published in Ref. [317].

7.8 Discussion

Up to now, we finished all the steps in the analysis strategy and we obtained the results concerning the measurement of the cross section of muons from open heavy flavour decays. In this section, we discuss two additional items related to this analysis:

- the estimate of the single muon background based on data;
- the charm and bottom component separation.

7.8.1 Data Based Background Estimate

As mentioned in Sec. 7.3.2, Monte-Carlo studies show that primary muons are mainly muons from charged kaon and pion decays. But indeed, this component also includes muons from the muonic decays of low mass resonances (η, ρ, ω, ϕ, *etc.*), quarkonium (J/Ψ, Υ, *etc.*), baryons and hyperons. Instead of estimating the primary muon background based on the Monte-Carlo, one can also reproduce the yield of primary muons according to the measured spectra of their mother particles in data, as an alternative way. In the high $p_{\rm t}$ region ($p_{\rm t} > 2$ GeV/c), in addition to the muons from charged K/π decays, the $\mu^-\mu^+ \leftarrow$ J/Ψ also represents a visible fraction in the total yield of primary muons. In this section, we are going to discuss the primary muon component estimate according to the spectra of charged K/π and J/Ψ measured in ALICE in the mid-rapidity region. A comparison with the previous results, as those shown in Fig. 7.46 and 7.48, will be presented.

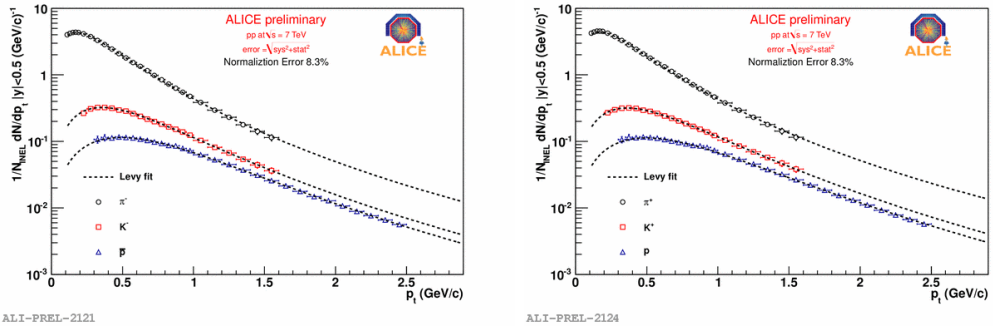

Figure 7.49: The measured spectra of π^-, $K^-$and $\overline{\rm p}$ (left), and π^+, $K^+$and p (right) in central rapidity region ($|y| < 0.5$) in pp collisions at $\sqrt{s} = 7$ TeV with ALICE. All the results are fitted by the Lévy function, see the text for more details.

We start with the charged K/π spectra measured in pp collisions at $\sqrt{s} = 7$ TeV in the central rapidity region $|y| < 0.5$ from ALICE, as shown in Fig. 7.49. All these

spectra are fitted with the Lévy function,

$$\frac{1}{N^{\rm ev}}\frac{{\rm d}^2N}{{\rm d}p_{\rm t}{\rm d}y}|_{|y|<0.5} = \frac{1}{N^{\rm ev}}\frac{{\rm d}N}{{\rm d}y}|_{|y|<0.5} \times\frac{(n-1)(n-2)}{nC[nC+m_0(n-2)]}p_{\rm t}(1+\frac{m_{\rm t}-m_0}{nC})^{-n}, \tag{7.61}$$

where, m_0 is the mass in the rest frame and $m_0 \simeq 0.1396$ GeV/c^2 for $\pi^{\pm}$, $m_0 \simeq 0.4937$ GeV/c^2 for $\rm K^{\pm}$; $m_t = \sqrt{m_0^2+p_{\rm t}^2}$ is the transverse mass; n, C and the normalization factor $1/N^{\rm ev}\cdot{\rm d}N/{\rm d}y$ are the parameters obtained from the fit, for charged K/π. The values are listed in Tab. 7.8. Then, we extrapolate the charged

Lévy fit	π^+	π^-	$\rm K^+$	$\rm K^-$
$1/N^{\rm ev}\cdot{\rm d}N/{\rm d}y$	2.27501	2.25188	0.27939	0.27893
n	5.59591	5.91166	6.59587	6.43006
C (GeV)	0.11614	0.12176	0.19547	0.19545

Table 7.8: Values of the parameters in Lévy function (Eq. (7.61)) obtained by fitting the charged K/π spectra shown in Fig. 7.49.

K/π spectra from central rapidity region to forward rapidity region by parameterizing the rapidity dependence as [318]:

$$\frac{1}{N^{\rm ev}}\frac{{\rm d}^2N}{{\rm d}p_{\rm t}{\rm d}y} = \frac{1}{N^{\rm ev}}\frac{{\rm d}N}{{\rm d}p_{\rm t}{\rm d}y}|_{y=0}\times\exp(-\frac{y^2}{2\sigma_y^2}), \tag{7.62}$$

where σ_y is the extrapolation factor, and the term $1/N^{\rm ev}{\rm d}N/{\rm d}y|_{y=0}$ can be estimated according to Eq. (7.61). By fitting the ratio of the charged K/π spectra in different bins in the forward region to that in the central rapidity region and according to different Monte-Carlo predictions, we obtained $\sigma_y \simeq 3.32$ [319].

With all above inputs, we can use the parameterization formula given by Eq. (7.62) to generate the spectrum of muons from charged K/π decays in the acceptance of the muon spectrometer via simulations with realistic detector configurations and by considering the proper decay branching ratio and the decay kinematics.

Concerning the estimate of muons from J/Ψ decays, we used the inputs of measured prompt J/Ψ spectra in pp collisions at $\sqrt{s} = 7$ TeV from LHCb [320], as shown in the left plot of Fig. 7.50. As for charged K/π spectra, we used these distributions as the inputs of the simulation with realistic detector configuration, and obtain the muon spectra from the prompt J/Ψ decays in different η regions as shown in the right plot of Fig. 7.50. The ratio between the normalized spectra of muons from prompt J/Ψ decay and the inclusive muon spectrum after the normalization are shown in the lower panel of this plot. According to these results, the fraction of muons from prompt J/Ψ decay is $\lesssim 5\%$ of the total inclusive muon yield in $p_{\rm t} > 2$ GeV/c.

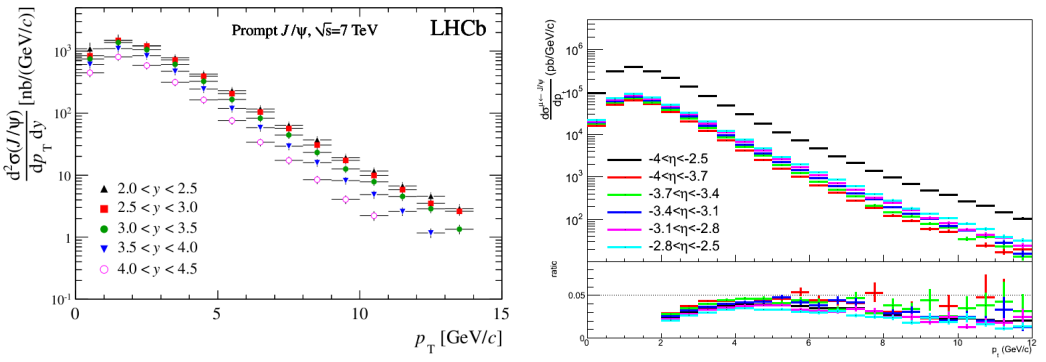

Figure 7.50: Left: the prompt J/Ψ spectra measured in pp collisions at $\sqrt{s} = 7$ TeV from LHCb [320]. Right: the normalized p_{t}-differential spectra of muons from the prompt J/Ψ decay according to the prompt J/Ψ distributions from LHCb (left plot) in different η regions; the ratio between the spectra of muons from the prompt J/Ψ decay and the normalized inclusive muon spectrum measured in pp collisions at $\sqrt{s} = 7$ TeV with the ALICE muon spectrometer is shown in the lower panel of this plot.

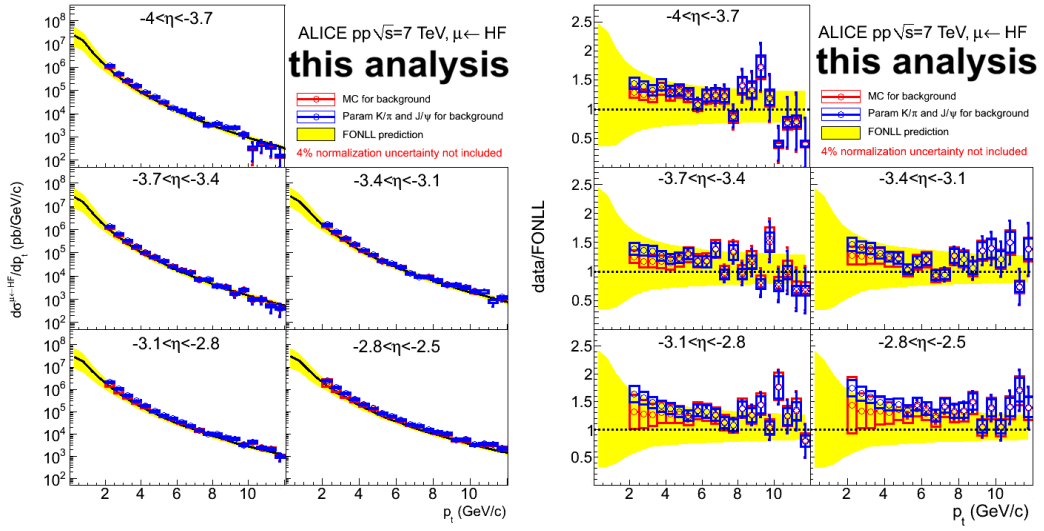

Figure 7.51: Left: Comparison between the results in Fig. 7.46 and those with the background subtraction via the parameterized K/π and J/Ψ distributions measured in data. Right: similar as Fig. 7.47, the ratios between the production cross sections of muons from heavy flavour decays measured in data and the central values of the FONLL predictions.

After subtraction of the estimated muon yield from the parameterized K/π and J/Ψ decays from the data, with the proper normalization, we can get the results in Fig. 7.51 and 7.52. These results are labeled as "Param K/π and J/Ψ for back-

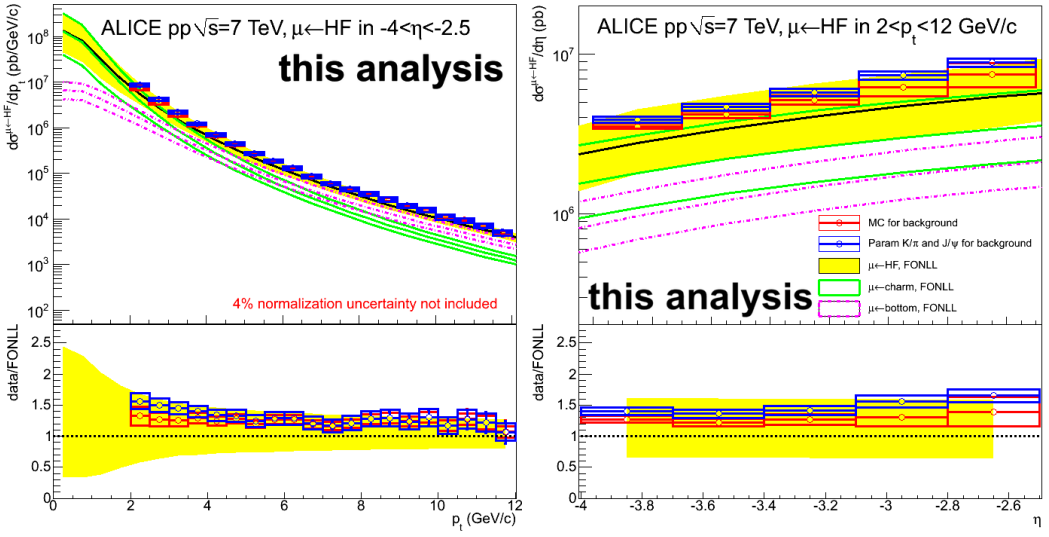

Figure 7.52: Similar as Fig. 7.48, but the production cross section of muons from heavy flavour decays based on the background estimate via the parameterized K/π and J/Ψ distributions are added at here.

ground" and shown in blue. The systematic uncertainty in these results include the one from the σ_y estimate in Eq. (7.50) which is gotten by varying the value of σ_y from different models [321], the $1\% \times p_t$ from the misalignment and the 5% on detector response. The results from our previous method labeled as "MC for background" and shown in red are also presented in Fig. 7.51 and 7.52 for comparison. These results were obtained around August of 2011, and at that time the systematic uncertainty on the normalization was estimated as 4% as presented in this two figures. One can find that the results from the parameterized background are a little bit higher than our previous results in low p_t region ($2 < p_t < 4$ GeV/c). A possible explanation is that within the scenario of the parameterized background, we do not include all the sources of primary muons. For instance, the contribution of muons from low mass resonances and baryons cannot be ignored. But in the high p_t region ($p_t > 4$ GeV/c), the two methods give similar results within uncertainties. Anyhow, the results from the method with the parameterized background are presented as a cross check for our published results which are shown in Fig. 7.46, 7.47 and 7.48, and also as a validation of the published results, in particular in the high p_t region.

7.8.2 Charm and Bottom Component Separation

After the measurement of the production cross section of muons from heavy flavour decays, it is worth to try to separate the charm and bottom components, as mentioned in Sec. 5.3.1. Indeed, we did this test during Summer 2010 with data from LHC10d2b [322].

For this test, we follow the strategy discussed in Sec. 5.3.1. We separate the

charm and bottom components via the combined fit according to Eq. (5.9). But instead of initializing the single muon shape functions f_c and f_b from models, here we do the initialization according to data:

1. subtract the estimated background in the inclusive muon spectrum with the muon selection cuts;
2. initialize f_c and f_b in low p_t region ($3 < p_t < 6$ GeV/c) and high p_t region ($6 < p_t < 15$ GeV/c), respectively;
3. with the initalized shape functions, we presented the combined fit in the muon spectrum after the background subtraction;
4. by comparing the results from the combined fit and those from the HvQMNR predictions we found $\sim 9\%$ deviation between data and the predictions.

But at that time the $p\times$DCA cut was not developed and the beam induced background introduced a bias in the results, in particular in the high p_t region. In this case, we do not present the results from this test. But it is worth to present an outlook concerning the implementation of the combined fit in data:

- our test is positive since it shows that it is possible to separate the charm and bottom components in data via the combined fit;
- instead doing the initialization of the shape functions from models, we can also try to initialize the shape functions directly with data;
- the mis-alignment effect should be treated very carefully, in particular in the high p_t region;
- we also need to develop a proper way to estimate and control the systematic uncertainty in the combined fit.

Chapter 8

Heavy Flavour Suppression in Pb–Pb Collisions at $\sqrt{s_{\mathrm{NN}}} = 2.76$ TeV

In this chapter we focus on the measurement of the nuclear modification factor R_{AA} of muons from open heavy flavour decays in Pb–Pb collisions at $\sqrt{s_{\mathrm{NN}}} = 2.76$ TeV in order to investigate heavy-quark in-medium energy-loss in the Quark Gluon Plasma (QGP) expected to be formed in heavy-ion collisions.

Data analysis in Pb–Pb collisions is for many items such as trigger selection, data quality assurance, event and muon track selections and efficiency correction, similar to that in pp collisions as described in the previous chapters. We begin with a description of the data sample used and of the event and muon track selections. We mainly emphasize the points which are particular to Pb–Pb collisions.

This study is based on the LHC10h data period which took place in the end of 2010 during the first LHC heavy-ion run. The analysis of this data sample started in December 2010, when the first reconstruction pass was achieved.

The whole analysis is separated into three different stages which took place in three different time periods. In each of these stages, the data samples used are different.

Dec. 2010–**Mar.** 2011 in this stage, the analysis was based on the first reconstruction pass (pass 1) of LHC10h. Around 70 runs have been used at most. The aim was to study the centrality determination and to optimize the cuts, in particular for fake track rejection.

Apr. 2011–**May** 2011 the analysis concerned the LHC10h second reconstruction pass (pass 2). In this second reconstruction pass, the parameters for muon track reconstruction have been optimized in order to reduce the fraction of fake tracks and to improve the momentum resolution, in particular in the high p_{t} region. The results of the data quality assurance (QA) analysis became available during this analysis. According to the QA results, there were 94 runs available for the single muon analysis. At that time, the centrality selection and the normalization factors in different centrality classes were made available by the corresponding analyzers. The main purpose of the analysis at this step was to obtain preliminary results on the inclusive muon nuclear modification factors (R_{AA} and R_{CP}) to be presented at the Quark Matter conference in May 2011.

From autumn of 2011 on we completed the analysis on the Grid of the total 94 runs in LHC10h pass 2 which were validated by the muon QA selections in order to accumulate as much statistics as possible [1]. From the software side, both the physics selection and the centrality selection were fine-tuned. In particular, the centrality QA was added in the official centrality selection. The final data sample used was also required to satisfy the QA selection for the centrality determination. The ultimate goal at this step was to obtain the final results on the $R_{\rm AA}$ of muons from open heavy flavour decays for publication.

8.1 Event Trigger Selection

As for the analysis of pp data, the selection of physics-collision events and of QA events should be applied for Pb–Pb data. The event QA for muon analysis in Pb–Pb collisions is similar to that of pp collisions. It follows the same standard mentioned in Sec. 7.1.1. For the physics-collision event selection, there are two trigger classes implemented in the LHC10h period, the minimum-bias trigger and the high-multiplicity trigger. In the following, we explain the difference between the event-trigger selection in Pb–Pb collisions and in pp collisions.

8.1.1 Trigger Classes

In Pb–Pb collisions, the minimum bias trigger is only fired when two bunches have been detected in both sides of the ALICE detector. This is similar to the situation in pp collisions. However, the conditions for the trigger decision in minimum-bias Pb–Pb collisions takes into account the much larger multiplicity of produced particles compared to pp collisions.

In the early stage of data taking, with low luminosity, the minimum-bias events in Pb–Pb collisions are flagged by three different trigger classes:

CMBS2A-B-NOPF-ALL & **CMBS2C-B-NOPF-ALL** at least two hits are found in the SPD and each SPD layer should include at least one hit ("**S2**"), plus at least one cell fired in V0A or V0C;

CMBAC-B-NOPF-ALL there is at least one cell fired in both V0A and V0C.

Note that in pp collisions, the minimum-bias trigger requires at least one cell fired in the whole SPD without condition on the layer fired. The string "NOPF" means that no past and future protection in implemented and "ALL" is the name of the trigger cluster described in Sec. 6.1. What is similar to pp collisions is that, in Pb–Pb collisions, one also requires that at least two detectors should be fired out of the three trigger detectors (SPD, V0A and V0C). This condition is called **2-out-of-3**.

[1] Depending on the status of the Grid, some sub-jobs fail. To improve the statistics, we have to re-submit the failed sub-jobs several times until a given fraction (*eg.* 95%) of statistics is collected.

With increasing luminosity, the 2-out-of-3 condition is not sufficient to separate the physics-collision events and the beam-gas background. Therefore the **3-out-of-3** condition, which requires that all of the three trigger detectors are fired with at least 2 hits in different layers of SPD plus at least one cell fired in V0A and V0C, is applied. The corresponding trigger class is **CMBACS2-B-NOPF-ALL**.

Then, all the above hardware-level triggers have to be reproduced again at both hardware and software levels with the detector calibration, after event reconstruction, to avoid the response and noise of the front-end electronics. Furthermore, the V0 leading time and the background identification are implemented to reject the residual beam-gas background. This procedure is called as the **Physics Selection**, as mentioned in Sec. 6.2.1.

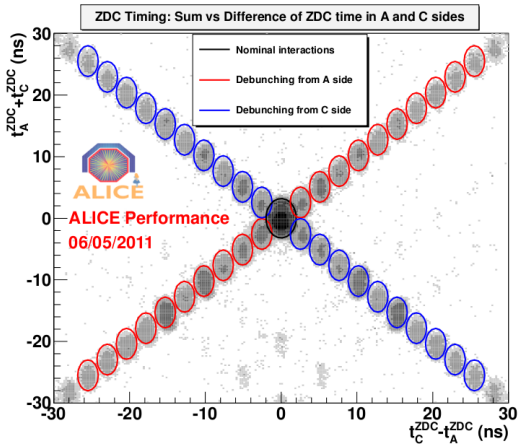

Figure 8.1: The correlation between the corrected TDC timing of ZDC C−A and that of ZDC C+A. The results are obtained from minimum bias triggered events. The tails corresponding to the de-bunching collisions are shown in the plot.

8.1.2 De-bunching

In Pb–Pb collisions, and differently to pp collisions, there are two additional backgrounds, the electromagnetic (**EM**) events and the so called "de-bunching collisions". The ZDC plays a major role in the rejection of these two backgrounds. As the electromagnetic interaction is much weaker than the strong interaction, the deposited energy in the collisional region in EM events is much smaller than that from inelastic strong interactions. In another words, the spectator nucleons, which can be detected by the ZDC, will take a large fraction of the injection energy in EM events. The additional cut on the ZDC trigger bit is used to reject this background.

De-bunching collisions are produced via the following mechanism: in each 25 ns bunch crossing time, there are 10 packets usually but only one is populated. However, some ions can jump in a different packet and induce collisions. We call this kind of collisions as the "de-bunching collisions". The displacement of primary vertex corresponding to these collisions in the z direction can be estimated as,

$$\Delta v_z = 2.5 \text{ ns}/2 \times c \simeq 37.5 \text{ cm}, \tag{8.1}$$

where $c \simeq 3 \cdot 10^8$ m/s is the light speed. The detection of these collisions is strongly biased because they can take place far away from the ALICE detector. The left and right elements of ZDC-ZN and ZDC-ZP (see Sec. 3.3 for the details), called "**ZDC**

A" and "**ZDC C**", which are placed far from the ALICE central detectors (116 m), deliver higher timing difference resolution than the VZERO detector. Fig. 8.1 shows the correlation between the corrected TDC timing of ZDC C−A and that of ZDC C+A. The results are obtained from minimum-bias triggered events with the CMBACS2 trigger class under the 3-out-of-3 trigger condition. The "normal" collision events are located around the centre of this distribution and the tails (as labeled in this figure) result from de-bunching events. Thes events are characterized by a large time asymmetry between ZDC C and ZDC A. According to these results, further cuts in the combination of ZDC timing is implemented in the physics selection of Pb–Pb collisions to reject de-bunching collisions.

8.1.3 Selection Results

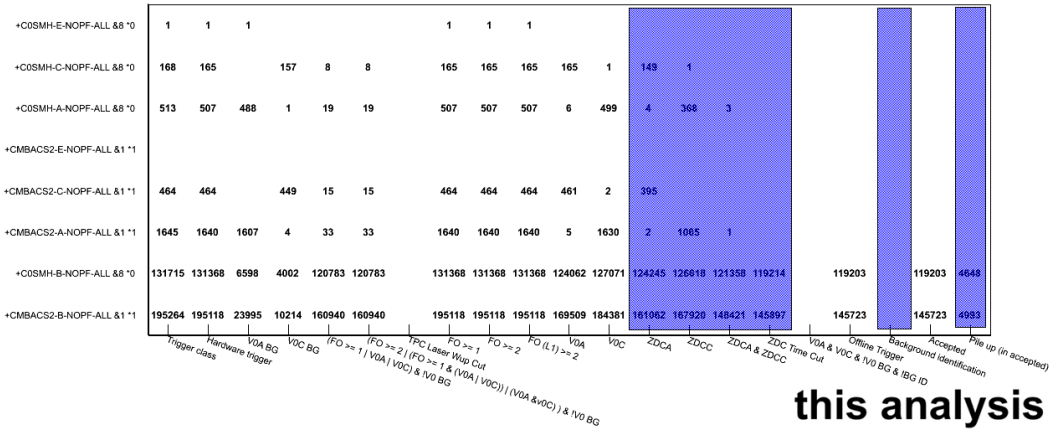

Figure 8.2: Event statistics table in physics selection of run 139036 in LHC10h pass 2, with AliRoot version v5-02-02-AN.

Fig. 8.2 shows the statistics table of run 139036 in LHC10h pass 2. The results are obtained with AliRoot version v5-02-02-AN [2]. By comparing this table to the event statistics table for pp collisions shown in Fig. 6.4, there are three different points to be mentioned:

- the "ZDC A & ZDC C" cut is used to reject the EM events in Pb–Pb collisions according to the energy taken by the spectator nucleons;
- the ZDC timing cut, as shown in Fig. 8.1, is implemented to cut off de-bunching collisions;
- there is no background identified event (third column from the right). This indicates that the beam-gas background in LHC10h is negligible thanks to the

[2]The physics selection has continuously been developed and/or optimized according to the data taking conditions, and the layout of the statistics table from the physics selection has also been slightly modified from one version of AliRoot to another.

much lower luminosity compared to pp runs ($\mathfrak{L} = 1.3 \cdot 10^{25}$ cm^{-2}s^{-1} for the Pb–Pb collisions in LHC10h and $\mathfrak{L} = 0.6 \sim 1.2 \cdot 10^{29}$ cm^{-2}s^{-1} in pp collisions).

The last column in the right side of Fig. 8.2 shows the counted pile-up events via the pile-up vertex identification method as introduced in Sec. 7.1.3.1. Finally, the trigger class **C0SMH-B-NOPF-ALL** corresponds to the high-multiplicity trigger. It is a sub-sample of the minimum-bias trigger which requires, in addition, that 100 hits are found in the SPD outer layer. In the following analysis, we only use the minimum bias triggered events.

8.2 Centrality Determination

There are usually two kinds of approaches to determine the event centrality in data. One, based on the definition presented in Sec. 1.4.2.1, consists in binning the event multiplicity distribution according to the total integral. Another way is to measure the number of spectator nucleons. In ALICE, the first approach can rely on the charged particle multiplicity reconstructed in central barrel, the SPD tracklets, the FMD multiplicity or the VZERO amplitude. The number of spectators $N_{\rm spec}$, used in the second approach, can be determined by the total energy deposited $E_{\rm ZDC}$ in ZDC-ZN and ZDC-ZP via

$$E_{\rm ZDC} = \sqrt{s_{\rm NN}} \times N_{\rm spec}, \tag{8.2}$$

with $\sqrt{s_{\rm NN}} = 2.76$ TeV in the present case. The centrality selection based on these methods are provided "officially" in ALICE. In our analysis, we use the centrality determined in the framework of the first approach according to the VZERO amplitude.

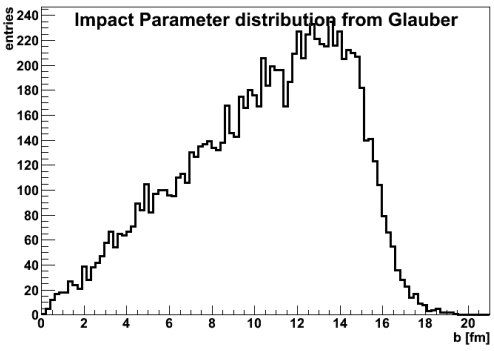

Figure 8.3: The impact parameter distriubtion in Pb–Pb collisions.

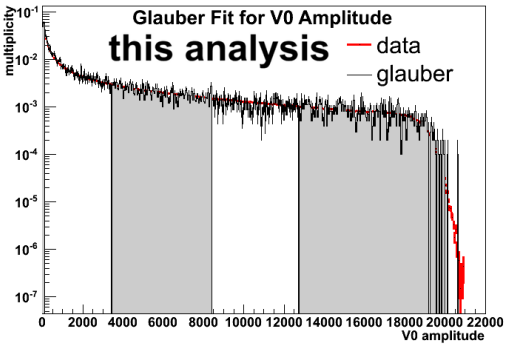

Figure 8.4: An example of DoubleNBD grid fitting to the VZERO amplitude.

In the following we illustrate how to implement the first centrality determination approach. A short description for using the ZDC deposition energy is also given.

8.2.1 VZERO Amplitude

In order to use the VZERO amplitude to determine the event centrality, one should first correct the gain saturation in each VZERO cell. Then the event multiplicity (refered to as VZERO amplitude) distribution similar as the one in Fig. 1.9 can be obtained. By binning this distribution according to the fraction of the total integral, the centrality classes for each event are determined. In the further analysis, the estimate of $< N_{\rm part} >$ and $< N_{\rm coll} >$ is very important for normalizing the events in a given centrality class. In ALICE, the values of $< N_{\rm part} >$ and $< N_{\rm coll} >$ are obtained using the Glauber model to reproduce the event multiplicity distribution via the following steps:

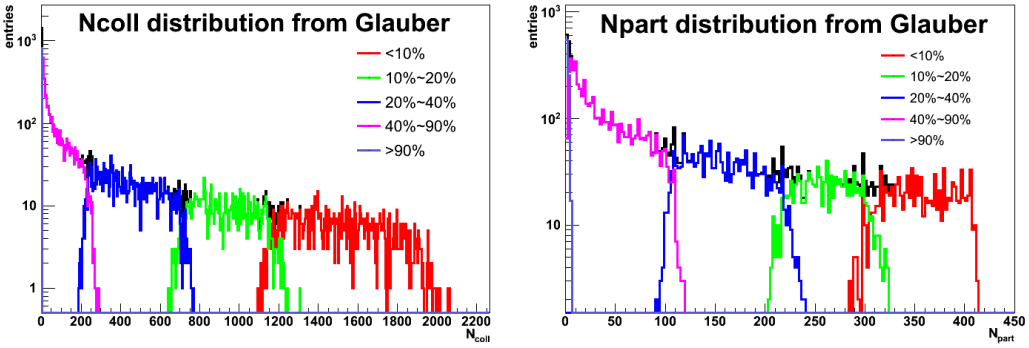

Figure 8.5: The $N_{\rm coll}$ (left) and $N_{\rm part}$ (right) distributions in different centrality classes obtained from the multiplicity distribution in Fig. 8.4.

1. under the assumption of a random distribution of the impact parameter $\vec{b}$, each of the surface element $\mathrm{d}^2\vec{b}$ becomes:

$$\mathrm{d}^2\vec{b} = b\mathrm{d}\phi\mathrm{d}b \rightarrow \pi\mathrm{d}b^2, \tag{8.3}$$

   and has the identical weight with respect to other surface elements. This property gives an uniform distribution of b^2. According to this, the impact parameter distribution in Pb–Pb collisions is obtained as in Fig. 8.3;

2. using the b distribution in Fig. 8.3 as input, Pb–Pb collisions are simulated via Monte-Carlo with the Glauber model under the optical limit approximation [50];

3. the values of $N_{\rm coll}$ and $N_{\rm part}$ are given for each simulated event via a Monte-Carlo approach, and assuming $\sigma_{\rm NN}^{\rm inel} = 64$ mb at $\sqrt{s_{\rm NN}} = 2.76$ TeV. Then the multiplicity of a given event is modeled as,

$$\mathrm{mult} = \frac{1-\beta}{2} \cdot M(N_{\rm part}) + \beta \cdot M(N_{\rm coll}), \tag{8.4}$$

where the parameter β is the fraction of hard processes, which satisfy the $N_{\rm coll}$ scaling, in the total binary collisions. The function $M(N)$ is expressed as,

$$M(N) = \sum_{i=1}^{N} n_i, \tag{8.5}$$

each n_i in Eq. (8.5) is sampled according to the probability given by the **Double Negative Binomial Distribution** (**DoubleNBD**) [323],

$$P(n_i) = \text{DoubleNBD}(k_1, m_1, k_2, m_2, \alpha), \tag{8.6}$$

where k_i and m_i $(i = 1, 2)$ are the input parameters for each NBD, α gives the weight between two NBDs as,

$$\text{DoubleNBD}(k_1, m_1, k_2, m_2, \alpha) = \alpha\text{NBD}(k_1, m_1) + (1-\alpha)\text{NBD}(k_2, m_2); \tag{8.7}$$

by collecting a large sample of the simulation events with the given value of the 6 parameters, k_1, m_1, k_2, m_2, α and β, the multiplicity distribution is obtained according to Eq. (8.4);

4. by varying the values of all of these 6 parameters and re-do all the above steps, one can obtain a set of multiplicity distributions, called the **DoubleNBD Grid**, given by the Glauber model;

5. after normalization of each distribution on the DoubleNBD grid, the χ^2 between the distributions on the DoubleNBD grid and the measured event multiplicity distribution in data (*eg.* the distribution of SPD tracklets or VZERO amplitude) can be calculated. The simulated multiplicity distribution with the minimum value of χ^2 corresponds to the best fit on the DoubleNBD grid to data. Fig. 8.4 shows an example of this fit with $k_1 = 3$, $m_1 = 4$, $k_2 = 2$, $m_2 = 11$, $\alpha = 0.4$ and $\beta = 0.13$. The total multiplicity distribution are separated in four regions which correspond to four centrality classes $0 - 10\%$, $10 - 20\%$, $20 - 40\%$ and $40 - 90\%$;

6. by cutting the multiplicity bins obtained in Fig. 8.4 according to $N_{\rm coll}$ and $N_{\rm part}$, the corresponding distributions in each centrality classes are obtained, as shown in Fig. 8.5; then the values of $< N_{\rm coll} >$ and $< N_{\rm part} >$ in different centrality classes can be extracted from the corresponding distributions.

All the above results were obtained at the end of 2010 just after the reconstruction of the LHC10h pass 1 data. Then the ALICE Collaboration did a more detailed study applying all above steps to LHC10h pass 2 data, and published the results in [324].

ALICE also allows to determine the centrality via the SPD tracklets, the number of clusters in the inner or outer layer of SPD, the TPC tracks and the FMD multiplicity. The strategy is almost the same as that mentioned above, in the example using the VZERO amplitude. The combinations of VZERO amplitude *vs.* FMD multiplicity and that *vs.* SPD tracklets are used for the centrality determination too, under the assumption of the VZERO amplitude is proportional to the FMD multiplicity and to the SPD tracklets.

8.2.2 $E_{\rm ZEM}$ *vs.* $E_{\rm ZDC}$

An alternative way to determine the centrality class is to use the correlation between the energy deposit in ZDC-ZEM ($E_{\rm ZEM}$ and $E_{\rm ZDC}$) defined in Eq. (8.2). The underlying assumptions are: in the most central collisions, $E_{\rm ZEM}$ reaches its maximum value and $E_{\rm ZDC}$ is very low since $N_{\rm spec}$ detected in ZDC-ZN and ZDC-ZP is small. Starting from these central collisions and following the shape of the correlation, b (or $N_{\rm spec}$) increases as the collisions become more and more peripheral. In this way, it is possible to separate the centrality classes according to the well defined percentiles of the total hadronic cross section:

$$x_i \times \sigma = \int_0^{b_i} {\rm d}b \frac{{\rm d}\sigma}{{\rm d}b} = \int_{E_{{\rm ZDC},i}} {\rm d}E_{\rm ZDC} \int_{E_{{\rm ZEM},i}} {\rm d}E_{\rm ZEM} \frac{{\rm d}^2\sigma}{{\rm d}E_{\rm ZDC}{\rm d}E_{\rm ZEM}}, \tag{8.8}$$

where i refers to the selected region in $E_{\rm ZDC}$–$E_{\rm ZEM}$ plane, which corresponds to $0 < b < b_i$, and x_i is the fraction of total (inelastic) hadronic cross section. Fig. 8.6 shows the correlation between ZEM amplitude ($\propto E_{\rm ZEM}$) and $E_{\rm ZDC}$. The four centrality bins in this figure are determined by the VZERO amplitude, but in principle this also can be done by cutting the fraction of the total cross section in the correlation as described in Eq. (8.8). The advantage of using the $E_{\rm ZDC}$ *vs.* $E_{\rm ZEM}$ correlation to determine the centrality classes is that, by applying cuts on the correlation distribution, one can get $< E_{\rm ZDC} >$ in different centrality classes. By using Eq. (8.2) the values of $< N_{\rm spec} >$ are obtained as a function of the collision centrality. Then, according to the relation:

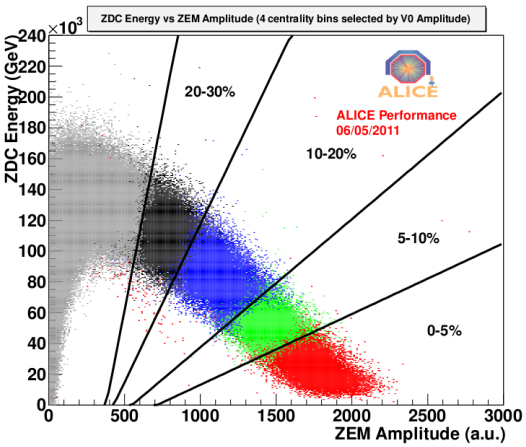

Figure 8.6: The combination distribution of corrected ZEM amplitude and $E_{\rm ZDC}$. The results are obtained from minimum-bias triggered events in LHC10h pass 2. The four centrality bins are selected with the VZERO amplitude.

$$N_{\rm part} = A - N_{\rm spec}, \tag{8.9}$$

with the atomic number $A = 208$ for Pb and $< N_{\rm part} >$ can be estimated in each centrality class. This can be used to correct the results obtained from the method mentioned in Sec. 8.2.1 which uses the VZERO amplitude, the FMD multiplicity *etc.*, where $< N_{\rm part} >$ is given by Glauber model. This improves the accuracy on the centrality determination and the estimated values of $< N_{\rm part} >$ and $< N_{\rm coll} >$.

8.2.3 Centrality QA

ALICE delivers the centrality determination methods discussed above via the official **Centrality Selection** framework. This framework has been updated from summer 2011 on by adding the centrality QA selection in order to decrease the bias in the centrality determination. The selection is classified into two sets of cuts:

- cuts the vertex quality,
  - $|v_z| < 10$ cm, this cut removes the events far from the the ALICE central detectors. Indeed, the signals from the detectors used for the centrality determination could be biased by these events and introduce uncertainties in the centrality calibration;
  - number of vertex contributor ≥ 1. As the multiplicity in Pb–Pb collisions is much higher than that in pp collisions, this cut does not make sense for most of the events. However the residual beam gas interaction which could be identified as ultra-peripheral collisions can be rejected by this cut;
- the correlation cuts used to reject pile-up and beam gas events. The definition of the event centrality is based on the event multiplicity distribution, as introduced in Sec. 1.4.2.1. Both pile-up and beam gas events strongly bias the event multiplicity distribution and are responsible for uncertainties in the centrality determination; the correlation cut on a few σ in the correlation of VZERO amplitude *vs.* SPD tracklets, TPC tracks and E_{ZDC} is used to reject this background. The basic assumptions to implement these cuts are that the VZERO amplitude is proportional to the SPD tracklets and the TPC tracks, and the relation between VZERO amplitude and E_{ZDC} is comparable to that of E_{ZEM} *vs.* E_{ZDC}, as shown in Fig. 8.6.

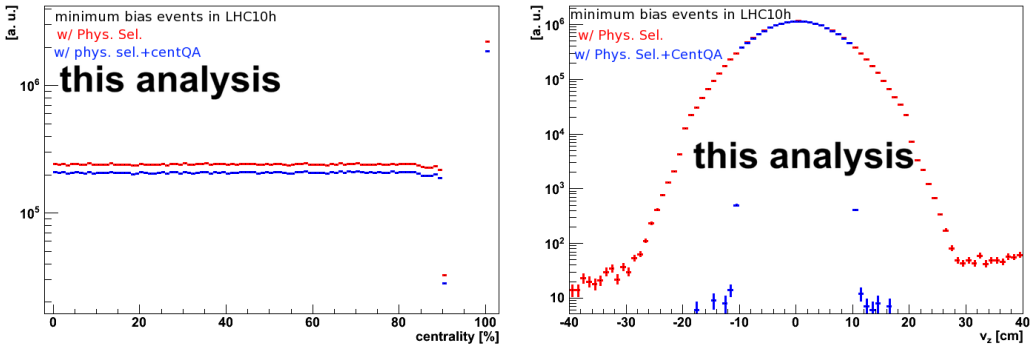

Figure 8.7: The event distribution as a function of centrality (left) and v_z distribution (right) in LHC10h pass 2. The results are obtained from minimum-bias trigger events. In both cases, the red histogram shows the results after the physics selection and the blue one shows the results with the additional centrality QA selection.

The event distribution as a function of centrality and the v_z distribution are shown in the left and right plots of Fig. 8.7, respectively. These results are obtained from the minimum-bias events in LHC10h pass 2. The red histograms are the results after the physics selection and the blue ones are the results with the additional centrality QA selection. In the left plot of Fig. 8.7, the centrality is determined via the VZERO amplitude. One can see that, for centralities up to 90%, both the event distribution and the efficiency of the centrality QA are quite stable. Due to the vertex quality cuts, the width of the v_z is largely decreased after the centrality QA selection, as shown in the right plot of Fig. 8.7.

8.2.4 Centrality Scaling Factors

centrality class	$< N_{\rm part} >$	$< N_{\rm coll} >$	$< T_{\rm AA} >$ (mb^{-1})
$0-10\%$	356.5 ± 3.6	1502.7 ± 169.9	23.4797 ± 0.972587
$10-20\%$	260.5 ± 4.4	923.26 ± 99.6	14.4318 ± 0.573289
$20-40\%$	157.3 ± 3.4	438.8 ± 43.9	6.85556 ± 0.283436
$40-60\%$	68.76 ± 2.4	128.2 ± 12.7	2.0039 ± 0.112462
$60-80\%$	22.57 ± 1.05	26.82 ± 2.46	0.419123 ± 0.0334287
$40-80\%$	45.5 ± 2.05	77.1 ± 8.0	1.20451 ± 0.071843

Table 8.1: Mean values of number of participants ($< N_{\rm part} >$), number of binary collisions ($< N_{\rm coll} >$) and nuclear overlap function ($< T_{\rm AA} >$) in six centrality classes from Glauber model. Results are offered by ALICE officially.

Finally, we list in Tab. 8.1 the mean values of number of participants ($< N_{\rm part} >$), number of binary collisions ($< N_{\rm coll} >$) and nuclear overlap function ($< T_{\rm AA} >$) in six centrality classes which will be used in the following analysis (these values are available officially in ALICE). $\sigma^{\rm inel}_{\rm NN} = 64$ mb is used as the input to the Glauber model to obtain these results. The $< T_{\rm AA} >$ is defined as

$$< T_{\rm AA} >= m \cdot T_{\rm AB}, \tag{8.10}$$

where m and $T_{\rm AB}$ are defined in Eq. (2.16) and (2.22), respectively. Then, with Eq. (2.24) one can get:

$$< T_{\rm AA} >=< N_{\rm coll} > /\sigma^{\rm inel}_{\rm NN}. \tag{8.11}$$

According to Eq. (8.11), instead of the $< N_{\rm coll} >$, $< T_{\rm AA} >$ can also be used for the normalization of Pb–Pb related observables. The advantage to use $< T_{\rm AA} >$ is that, the determination of $< N_{\rm coll} >$ depends on the input value of $\sigma^{\rm inel}_{\rm NN}$ for the Glauber model. The ratio in Eq. (8.11) can cancel part of the bias caused by the input $\sigma^{\rm inel}_{\rm NN}$ value. In the following analysis we use $< T_{\rm AA} >$ to calculate the nuclear modification factors of muons.

8.3 Track Selection

After the above discussion on the data selection at the event level, we discuss in the following the muon track selection in Pb–Pb events. We start with some typical distributions and a revised study of the effect of the $p\times$DCA cut. A summary of the analysis cuts and the event statistics will be given at the end of this section.

8.3.1 Typical Distributions

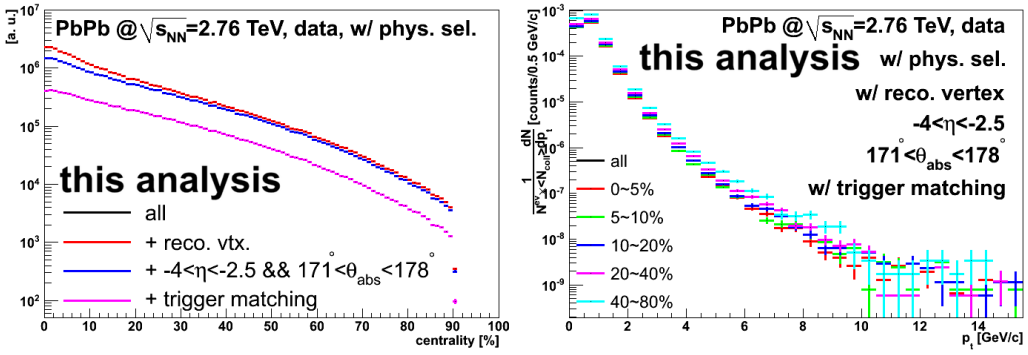

Figure 8.8: Left: muon track multiplicity distribution as a function of centrality. Right: normalized $p_{\rm t}$ distribution of muon tracks in different centrality classes. The results are obtained with the muon selection cuts listed in each plot and from LHC10h pass 2 data analyzed in April 2011.

Following the discussion in Sec. 6.3, a first set of cuts should be implemented on the muon tracks, for Pb–Pb events which pass the physics selection and centrality QA selection. These are the muon selection cuts listed in Sec. 6.4. With the centrality determined according to the ALICE official centrality selection framework, different distributions of selected muon tracks can be obtained.

Two typical distributions are shown in Fig. 8.8: the muon track multiplicity distribution as a function of centrality (left), and the $p_{\rm t}$ distribution of muon tracks in different centrality classes normalized by the corresponding $< N_{\rm coll} >$ (right). The results are obtained from LHC10h pass 2 data with the selection cuts listed in the plots. These results were presented during April 2011. The centrality QA was not included in the ALICE official centrality selection framework at that time.

In the left plot of Fig. 8.8 one can see that:

- the fraction of tracks removed by the acceptance cut ($-4 < \eta < -2.5$ and $171^{\circ} < \theta_{\rm abs} < 178^{\circ}$) is larger in central collisions than in peripheral collisions. This is due to the higher detector occupancy due to the larger event multiplicity in central collisions. There are more fake tracks which can be partly removed by the acceptance cuts in central collisions than in the peripheral collisions;

- the tracking–trigger matching efficiency is almost independent of centrality after the acceptance cuts. This indicates that the status of the muon trigger is stable whatever the occupancy;

- the results shown in this plot and the distributions at event level shown in the left plot of Fig. 8.7 illustrate that there is a bad efficiency of the centrality determination for centrality$\gtrsim 90\%$. In order to cope with that, we focus our physics analysis in the $0-80\%$ centrality class in the following.

By comparing the normalized $p_{\rm t}$ distributions of the selected muon tracks in different centrality classes, as shown in the right plot of Fig. 8.8, one can notice that the spectra are more suppresed in central than in peripheral collisions. This phenomenon is expected since the parton in-medium quenching strength increases with the collision centrality.

We have already repeated in this thesis many many times that the study of the quenching of heavy flavours is very interesting. In this chapter, we are going to show how to measure the suppression of open heavy flavours in the semi-muonic decay channel. Although the time to finish writing this thesis in order to deliver it on time to the referees is now limited, under the name of **SCIENCE**, I will forget the referee issue, and explain how we achieve this final goal step by step rigorously, using our usual style!

8.3.2 Fake Tracks

As previously discussed, the evolution of the efficiency of the acceptance cuts with the collision centrality is due to the corresponding evolution of the fraction of fake tracks outside the muon spectrometer acceptance which are rejected by these acceptance cuts. This arises another question: what about fake tracks inside the acceptance of the muon spectrometer?

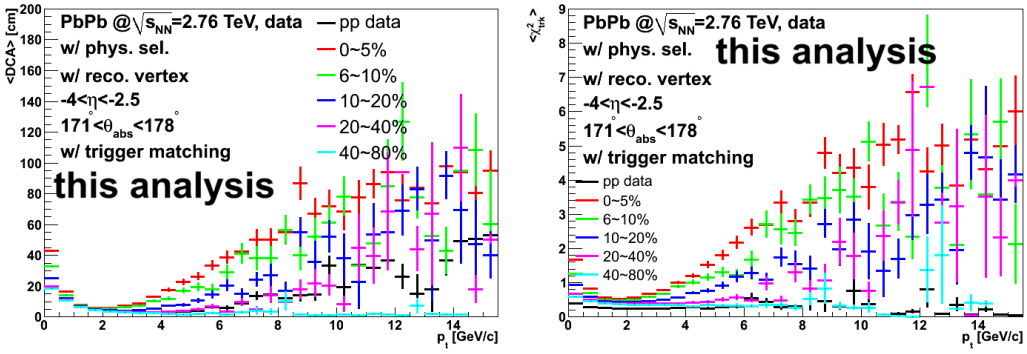

Figure 8.9: The mean values of DCA (left) and tracking χ^2 (right) as a function of $p_{\rm t}$ in different centrality classes. The results are obtained from LHC10h pass 2 data with the muon selection cuts. The corresponding results from pp collisions at $\sqrt{s}=7$ TeV (from LHC10e pass 2) are also shown.

To get some first feelings about fake tracks in Pb–Pb collisions, we present the results conerning the mean values of DCA and tracking χ^2 as a function of $p_{\rm t}$ in different centrality classes obtained from the LHC10h pass 2 data, in the left and right plots of Fig. 8.9, respectively. In this figure, we can see that:

- in the most peripheral collisions (centrality $40-80\%$ here), both the <DCA> and tracking $<\chi^2>$ are independent on $p_{\rm t}$;
- when the centrality of the collision increases, both <DCA> and tracking $<\chi^2>$ increase with $p_{\rm t}$ and the slopes of this increase become larger;
- by looking at tracking $<\chi^2>$ in pp collisions, as shown in the right plot of Fig. 8.9 (or the right plot of Fig. 7.33), we can see that this tracking $<\chi^2>$ does not depend on $p_{\rm t}$. Therefore, the increase of both <DCA> and tracking $<\chi^2>$ in central Pb–Pb collisions should be attributed to a new background source which is not present in pp collisions. This new source of background consists of fake tracks which are induced by the high detector occupancy in central Pb–Pb collisions.

Now, we can confirm that, after the muon selection cuts, there is still a fraction of fake tracks located in the high $p_{\rm t}$ region inside the acceptance of muon spectrometer. This fraction of fake tracks is larger in central collisions. A second question then arises: how to cut off this annoying background?

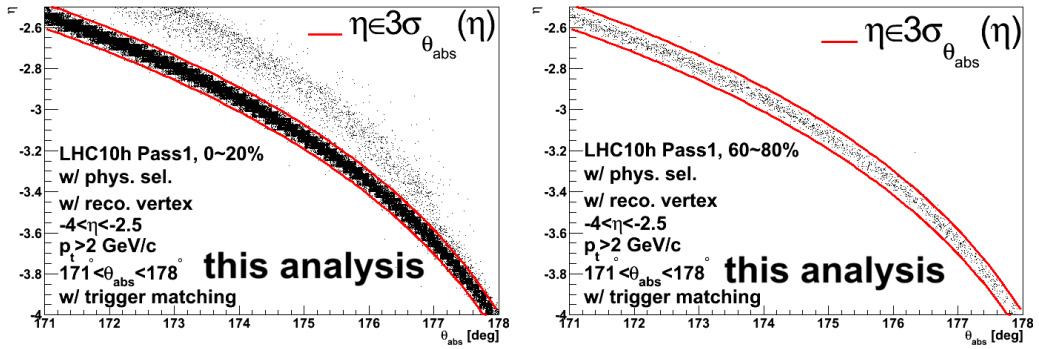

Figure 8.10: The $\eta-\theta_{\rm abs}$ correlation of muon tracks with the selection cuts from LHC10h pass 1 in the centrality classes $0-20\%$ (left) and $60-80\%$ (right), respectively. The red lines show the 3σ limit of the correlation calculated according to Eq. (7.34).

Do not worry, we always can find some ideas! From the left plot of Fig. 8.9, we can see that fake tracks show the same behavior in DCA distribution in the high $p_{\rm t}$ region as the beam-gas background in pp collisions. As shown in Sec. 7.6.2.1, the correlation of $\eta-\theta_{\rm abs}$ allows to clearly distinguish the beam-gas background from other tracks. Our first idea is then to see whether this correlation can also be used to distinguish fake tracks from other single muon sources. The left and right plots of Fig. 8.10 show this correlation for muon tracks with the selection cuts in centrality

classes $0-20\%$ and $60-80\%$. The 3σ limit of the correlation is shown by the red lines, calculated according to Eq. (7.34). As expected, the fake tracks are separated from other tracks by the $\eta-\theta_{\rm abs}$ correlation, as shown in the left plot of Fig. 8.10, in central Pb–Pb collisions. The right plot of Fig. 8.10 shows the correlation in peripheral collisions where the fraction of fake tracks is negligible. The correlation between real tracks is defined by Eq. (7.31) and these real tracks are contained in the 3σ band. The results from Sec. 7.6.3 have shown that the component which can be separated via the $\eta-\theta_{\rm abs}$ correlation can also be cut off by the $p\times$DCA cut. We implement in the following the $p\times$DCA cut in Pb–Pb collisions with the $p\times$DCA calibration.

8.3.3 $p\times$DCA in Pb–Pb Collisions

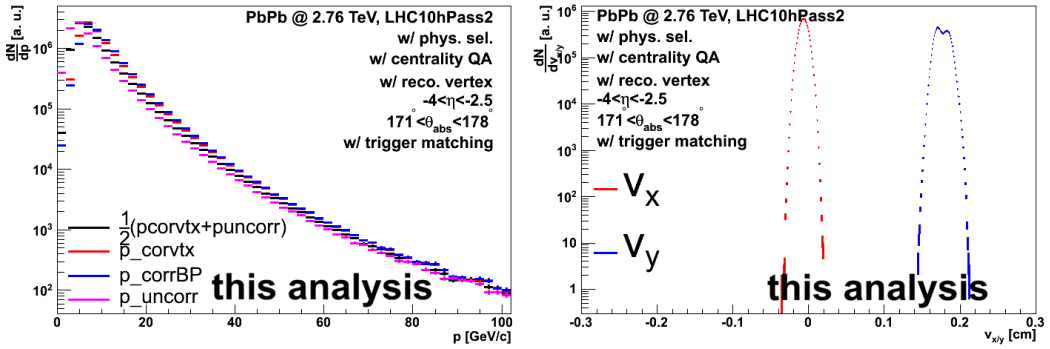

Figure 8.11: Left: the momentum distributions of muon tracks at different reconstruction steps as labeled in the plot. The $p_{\rm CMS}$ observable defined in Eq. (7.42) is also shown in this plot (black histogram). Right: the v_x and v_y distributions used to correct the DCA$_x$ and DCA$_y$, as defined in Eq. (7.44). All the distributions are obtained from LHC10h pass 2 data with the selection cuts listed in the plots.

Concerning the calibration of $p\times$DCA in Pb–Pb collisions, we follow the same strategy as in pp collisions as mentioned in Sec. 7.6.3.1. Some control plots used for the calibration are shown in Fig. 8.11 and 8.12.

The left plot of Fig. 8.11 shows the momentum distribution of muon tracks reconstructed in the tracking stations, after the Branson plane correction, and with the final correction relative to the primary vertex in purple, blue and red (labeled as $p_{\rm uncorr}$, $p_{\rm corrBP}$ and $p_{\rm corvtx}$, respectively). The results are obtained from LHC10h pass 2 data with the muon selection cuts listed in the plot. The $p_{\rm CMS}$ distribution used for the calculation of the pDCA$_{\rm calib}$ (defined in Eq. (7.47)) is also shown in this plot as the black histogram. The right plot of Fig. 8.11 shows the v_x and v_y of muon tracks used for the DCA$_x$ and DCA$_y$ correction. These are obtained under the same conditions as the left plot. By correcting the DCA$_x$ and DCA$_y$ distributions, shown by the red histograms in the left and right plots of Fig. 8.12, with the input vertex distributions in the right plot of Fig. 8.11 according to Eq. (7.44), we get the

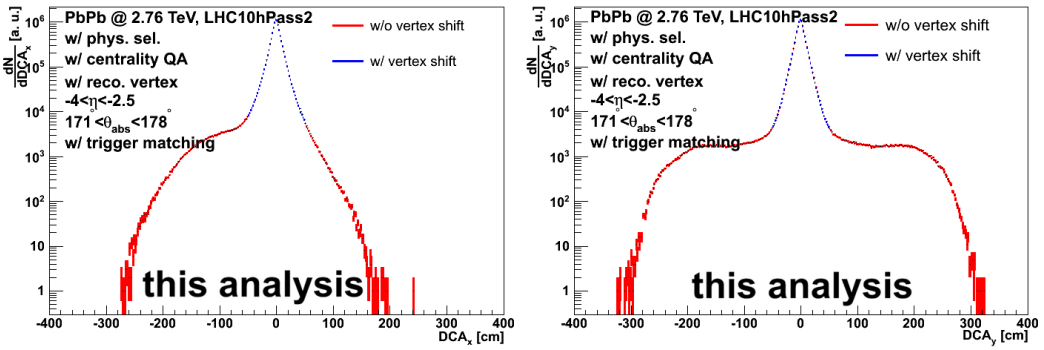

Figure 8.12: The distributions of DCA_x (left) and DCA_y (right) without the correction of the vertex position (red histograms) and with the vertex correction (blue histograms), according to Eq. (7.44) and with the inputs of v_x and v_y distributions from the right plot of Fig. 8.11.

blue histograms in Fig. 8.12 corresponding to the corrected DCA_x (left) and DCA_y (right) distributions, respectively.

One can notice that, in the left plot of Fig. 8.12, the DCA_x distribution is asymmetric. This phenomenon has already been observed in pp collisions, as shown in the left plot of Fig. 7.41. At that time, to reduce the bias on $< \mathrm{DCA}_{x/y,\mathrm{vtx}} >$ (defined in Eq. (7.44)) estimate, we extract the values in the region of DCA$<$ 100 cm. What is different between Pb–Pb collisions and pp collisions here is that, Pb–Pb collisions have different centrality classes. So we would like to check how this asymmetric structure in the DCA_x distribution affects the $< \mathrm{DCA}_{x,\mathrm{vtx}} >$ estimate in different centrality classes.

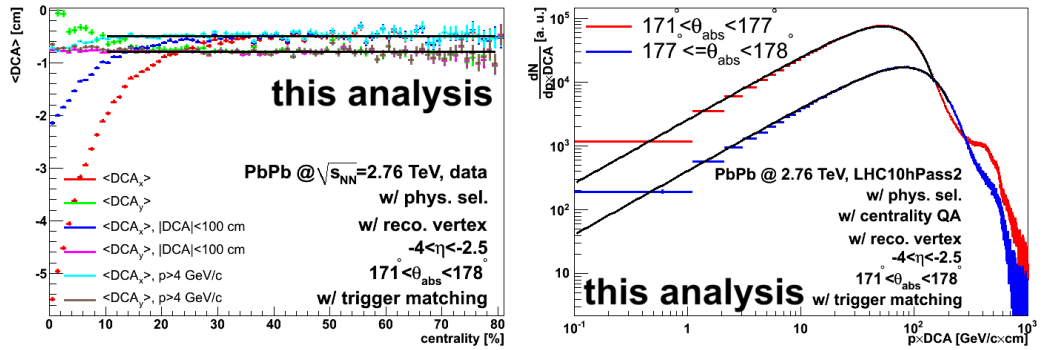

Figure 8.13: Left: $< \mathrm{DCA}_{x/y,\mathrm{vtx}} >$ with different selection conditions. Right: fits of the $p\mathrm{DCA}_{\mathrm{calib}}$ in two different θ_{abs} regions according to the function in Eq. (7.48). The results are obtained from LHC10h pass 2 data with the selection conditions listed in the plots.

The evolution of $< \mathrm{DCA}_{x/y,\mathrm{vtx}} >$ with the collision centrality is shown in the left plot of Fig. 8.13. In this plot we can see that:

- $< \mathrm{DCA}_{y,\mathrm{vtx}} >$ slightly decreases in peripheral collisions and is constant in central collisions;
- with the cuts $|\mathrm{DCA}| < 100$ cm or $p > 4$ GeV/c, $< \mathrm{DCA}_{y,\mathrm{vtx}} >$ is uniform in all centrality bins;
- similarly to $< \mathrm{DCA}_{y,\mathrm{vtx}} >$, the $< \mathrm{DCA}_{x,\mathrm{vtx}} >$ is constant versus centrality for centralities $\gtrsim 20\%$, but in the most central collisions its values increases with centrality. The two cuts implemented here, can partly restore the $< \mathrm{DCA}_{x,\mathrm{vtx}} >$ as a constant in the whole centrality region.

Finally, we can conclude that the deviation of $< \mathrm{DCA}_{x/y,\mathrm{vtx}} >$ results from the soft tracks originating from multi-scatterings in the front absorber. The asymmetric structure in the DCA distributions is due to a non-uniform material structure versus azimuthal angle in the front absorber.

To avoid the bias on the $p\times$DCA calibration, we extract the $< \mathrm{DCA}_{x/y,\mathrm{vtx}} >$ values by fitting their distributions in centrality$> 20\%$ with a straight lines (shown by the black line in the left plot of Fig. 8.13).

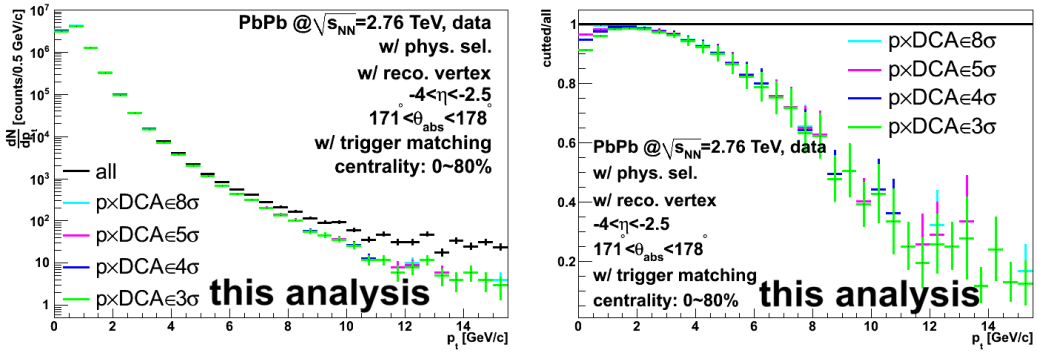

Figure 8.14: The left and right plots are similar to the upper and lower plots in the right plot of Fig. 7.43. The results are here obtained from LHC10h pass 2 data.

Up to now, we obtain all the inputs for the $p\times$DCA calibration. The fitting results of the $p\mathrm{DCA}_{\mathrm{calib}}$ in $171^\circ < \theta_{\mathrm{abs}} < 177^\circ$ and $177^\circ < \theta_{\mathrm{abs}} < 178^\circ$ according to Eq. (7.48) are shown in the right plot of Fig. 8.13. After these fits the values

LHC10h pass 2 w/ muon selection cuts	$171^\circ < \theta_{\mathrm{abs}} < 177^\circ$	$177^\circ < \theta_{\mathrm{abs}} < 178^\circ$
$\sigma_{\mathrm{meas}}(p \times \mathrm{DCA})$	60.69 GeV/$c\times$cm	101.53 GeV/$c\times$cm

Table 8.2: The values of $\sigma_{\mathrm{meas}}(p \times \mathrm{DCA})$ in $171^\circ < \theta_{\mathrm{abs}} < 177^\circ$ and $177^\circ < \theta_{\mathrm{abs}} < 178^\circ$ in LHC10h pass 2 data extracted from the fit presented in the right plot of Fig. 8.13.

of $\sigma_{\mathrm{meas}}(p \times \mathrm{DCA})$ in these two regions are obtained. They are listed in Tab. 8.2.

Then, following the same strategy as the one in pp collisions, we should validate the number of $\sigma_{\rm meas}(p \times {\rm DCA})$ used to separate fake tracks from other tracks.

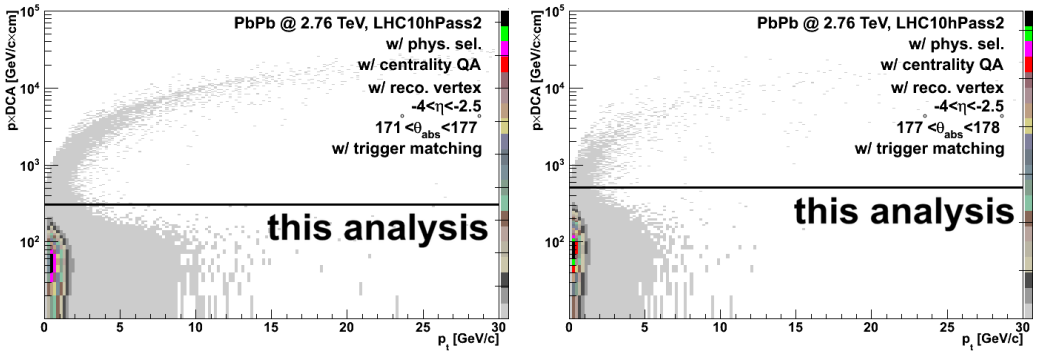

Figure 8.15: The correlation of $p{\rm DCA}_{\rm calib}$ *vs.* $p_{\rm t}$ in $171^{\circ} < \theta_{\rm abs} < 177^{\circ}$ (left) and $177^{\circ} < \theta_{\rm abs} < 178^{\circ}$ (right) from LHC10h pass 2 data with the muon selection cuts. The black lines correspond to $5\sigma_{\rm meas}(p \times {\rm DCA})$ obtained from the fits in the right plot of Fig. 8.13.

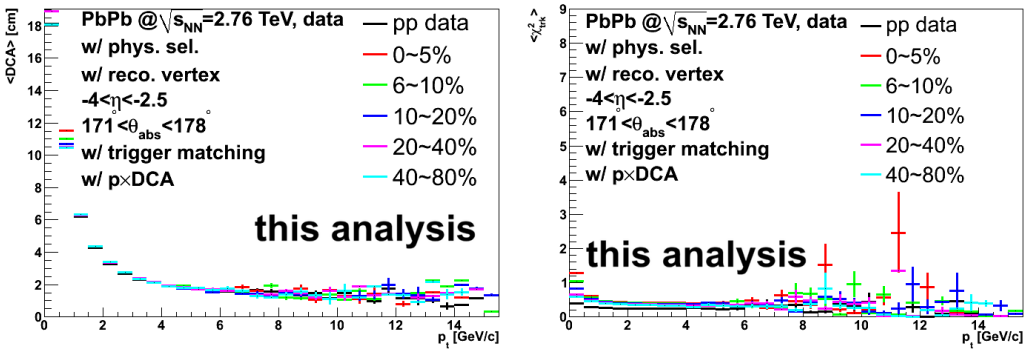

Figure 8.16: Similar as Fig. 8.9, but the results are obtained with the additional $p\times$DCA cut in $5\sigma_{\rm meas}(p \times {\rm DCA})$.

As shown in the upper and lower panels of the right plot of Fig. 7.43, we show, for Pb–Pb collisions, the $p_{\rm t}$ distribution of selected muons with different numbers of $\sigma_{\rm meas}(p \times {\rm DCA})$ cut and the ratio between this distribution and the one without the $p\times$DCA cut in the left and right plots of Fig. 8.14, respectively. As it was the case for pp collisions and according to the results in Fig. 8.14, a cut on $p\times$DCA of $5\sigma_{\rm meas}(p \times {\rm DCA})$ is sufficient for our analysis. The $p{\rm DCA}_{\rm calib}$ *vs.* $p_{\rm t}$ correlation in Pb–Pb collisions for LHC10h pass 2 data, in $171^{\circ} < \theta_{\rm abs} < 177^{\circ}$ and $177^{\circ} < \theta_{\rm abs} < 178^{\circ}$ with the black lines corresponding to $5\sigma_{\rm meas}(p \times {\rm DCA})$ cuts are shown in the left and right plots of Fig. 8.15, respectively. We can see that, the fake tracks and other muon sources are clearly separated by this $5\sigma_{\rm meas}(p \times {\rm DCA})$ cut. In order to get more confidence in our $p\times$DCA study in Pb–Pb collisions, finally we add the additional $p\times$DCA cut in $5\sigma_{\rm meas}(p \times {\rm DCA})$ in the distributions in Fig. 8.9, and the

results are shown in the left and right plots of Fig. 8.16. We see that after the cut on p×DCA, the <DCA> and tracking $< \chi^2 >$ distributions as a function of p_t are similar, in all centrality classes to the ones in pp collisions (where there is no fake tracks) with the same muon selection cut conditions. This strongly confirms that the p×DCA cut successfully rejects the fake tracks in Pb–Pb collisions.

8.3.4 Statistics Summary

Now, it is time to make a summary of the muon data sample selection in Pb–Pb collisions with the corresponding statistics that we used for our final analysis.

Firstly, the selection at event level can be classified into three parts:

event trigger selection as there is no muon trigger used to collect the LHC10h data, the minimum-bias trigger events with the 2-out-of-3 or 3-out-of-3 conditions correspond to the default data sample for our analysis;

physics selection the principle of the physics selection is almost the same as that in pp collisions, the additional ZDC timing cut is used to reject the de-bunching and EM background;

centrality selection it includes two parts,

- centrality QA, this is used to remove events far from the center of ALICE barrel detectors and pile-up events, and beam gas to reduce the bias in the centrality determination,
- choosing events in centrality region $0 - 80\%$ to ensure a good efficiency of the centrality determination.

The selection at track level is similar to that used in pp collisions. We just add the requirement that the reconstructed vertex is included inside the centrality QA selection already. We combine all above conditions together and called them as the standard muon selection in Pb–Pb collisions.

cut	all	+centQA	$+0 - 80\%$
No. of events	23894769	20507552	16595117

Table 8.3: Event statistics in LHC10h pass 2 used for the final analysis.

cut	all	+centQA	$+0 - 80\%$	$+\eta$ cut	$+\theta_{\text{abs}}$ cut	+trM
No. of events	47928319	41110737	41005680	32008436	30879884	10271205

Table 8.4: Muon track statistics in LHC10h pass 2 used for the final analysis.

The statistics at event and track levels used for our final analysis with different selection cuts is listed in Tab. 8.3 and 8.4, respectively. The results are obtained from the minimum bias trigger events in LHC10h pass 2 data analyzed during September

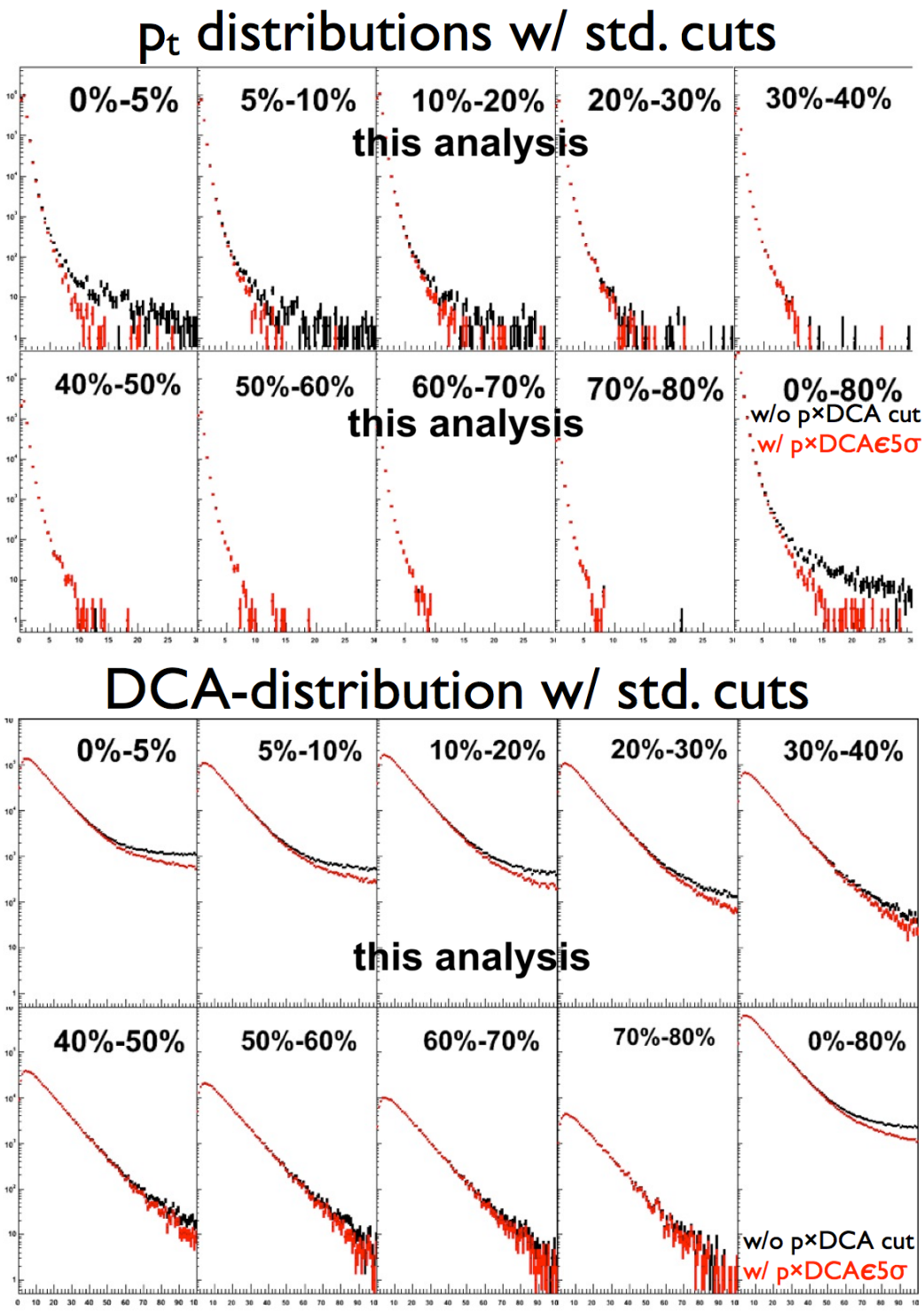

Figure 8.17: The p_{t} (upper) and DCA (lower) distributions of muon tracks with the standard selection cuts in different centrality classes. The results are obtained from LHC10h pass 2 data which is used for our final analysis. The distributions without the $p\times$DCA cut and those with $p\times$DCA cut are compared.

2011. Thanks to the low beam injection luminosity during this data taking period, the pile-up effect is negligible (and the centrality QA selection removes almost all pile-up events). Therefore the pile-up correction is not implemented in the Pb–Pb analysis for the event normalization.

Finally, the $p_{\rm t}$ and DCA distributions of muon tracks with the standard selection cuts in different centrality regions are shown in the upper and lower plots of Fig. 8.17, respectively. The results are obtained from LHC10h pass 2 data used for our final analysis. The distributions without the $p\times$DCA cut and those with $p\times$DCA cuts are compared.

8.4 Reference from pp Collisions

After the above discussion of issues related to the selection of the data sample, now, we can focus on the measurement of muons from heavy flavour decays. Differently from the analysis in pp collisions, it took us a very long time to fix the final strategy of get the physics results in Pb–Pb collisions. We first describe our physics goal and what inputs are needed.

Our final aim is to get the nuclear modification factor of muons from open heavy flavour decays in the acceptance of the muon spectrometer ($-4 < \eta < -2.5$) in Pb–Pb collisions at $\sqrt{s_{\rm NN}} = 2.76$ TeV (based on the LHC10h pass 2 data),

$$R_{\rm AA}^{\mu\leftarrow{\rm HF}}(p_{\rm t}) = \frac{1}{< T_{\rm AA} >} \times \frac{1}{N^{\rm ev}} \times \frac{1}{\varepsilon_{\rm AA}} \times \frac{{\rm d}N_{\rm AA}^{\mu\leftarrow{\rm HF}}/{\rm d}p_{\rm t}}{{\rm d}\sigma_{\rm pp}^{\mu\leftarrow{\rm HF}}/{\rm d}p_{\rm t}}, \tag{8.12}$$

where: $N^{\rm ev}$, $\varepsilon_{\rm AA}$ and ${\rm d}N_{\rm AA}^{\mu\leftarrow{\rm HF}}/{\rm d}p_{\rm t}$ are the number of events, the correction efficiency and the uncorrected spectrum of muons from open heavy flavour decays in a given centrality class in Pb–Pb collisions. The value of $< T_{\rm AA} >$ is obtained from Tab. 8.1 according to the chosen centrality class; ${\rm d}\sigma_{\rm pp}^{\mu\leftarrow{\rm HF}}/{\rm d}p_{\rm t}$ is the production cross section of muons from open heavy flavour decays at $\sqrt{s} = 2.76$ TeV. Before going to Pb–Pb data, we are going to mention in this section how we get the reference term ${\rm d}\sigma_{\rm pp}^{\mu\leftarrow{\rm HF}}/{\rm d}p_{\rm t}$ in pp collisions.

Similarly to the analysis of Pb–Pb data, there are also three important periods to get the ${\rm d}\sigma_{\rm pp}^{\mu\leftarrow{\rm HF}}/{\rm d}p_{\rm t}$.

Dec. 2010–May to 2011 during this time, the pass 2 data of pp collisions at $\sqrt{s} = 2.76$ TeV was not available (the pass 1 data of pp collisions at $\sqrt{s} = 2.76$ TeV has been available in the beginning of 2011). To get the reference of ${\rm d}\sigma_{\rm pp}^{\mu\leftarrow{\rm HF}}/{\rm d}p_{\rm t}$ in pp collisions at $\sqrt{s} = 2.76$ TeV, we have interpolated the measured production cross section of muons from heavy flavour decays in pp collisions at $\sqrt{s} = 7$ TeV, as shown in Fig. 7.48, to this lower collision energy, via a scaling factor obtained from the FONLL calculations;

End of 2011 when the pp data at $\sqrt{s} = 2.76$ TeV became available, we have extracted ${\rm d}\sigma_{\rm pp}^{\mu\leftarrow{\rm HF}}/{\rm d}p_{\rm t}$ at this energy using the method implemented at $\sqrt{s} = 7$ TeV. A that time simulations from only one model (PYTHIA

Perugia-0 tuning) with realistic detector configurations were available. In order to estimate the background, and especially the corresponding systematic uncertainty, we need at least two model predictions. Therefore, at that time, in order to get an additional model prediction, we have scaled the results from the PHOJET simulations at $\sqrt{s} = 7$ TeV to this lower energy for the background estimation.

Beginning of 2012 the simulations with realistic detector configurations according to both PYTHIA Perugia-0 and PHOJET for pp collisions at $\sqrt{s} = 2.76$ TeV have been completed. We have therefore implemented the full strategy as we did for pp collisions at $\sqrt{s} = 7$ TeV to get $\mathrm{d}\sigma_{\mathrm{pp}}^{\mu\leftarrow\mathrm{HF}}/\mathrm{d}p_{\mathrm{t}}$. This is used to calculate our final result: the R_{AA} of muons from heavy flavour decays.

In the following, we give a short review of results from each of period.

8.4.1 Energy Interpolation

The basic principle to get the production cross section at $\sqrt{s} = 2.76$ TeV from that at $\sqrt{s} = 7$ TeV via the energy interpolation is expressed as:

$$\frac{\mathrm{d}\sigma_{\mathrm{pp}}^{\mu\leftarrow\mathrm{HF}}}{\mathrm{d}p_{\mathrm{t}}}|_{2.76\ \mathrm{TeV}} = \mathrm{interpF}(\frac{2.76\ \mathrm{TeV}}{7\ \mathrm{TeV}}) \times \frac{\mathrm{d}\sigma_{\mathrm{pp}}^{\mu\leftarrow\mathrm{HF}}}{\mathrm{d}p_{\mathrm{t}}}|_{7\ \mathrm{TeV}}, \tag{8.13}$$

where $\mathrm{d}\sigma_{\mathrm{pp}}^{\mu\leftarrow\mathrm{HF}}/\mathrm{d}p_{\mathrm{t}}|_{7\ \mathrm{TeV}}$ is obtained from data in pp collisions at $\sqrt{s} = 7$ TeV, as shown in Fig. 7.48, with the interpolation factor from the FONLL calculations [3],

$$\mathrm{interpF}(\frac{2.76\ \mathrm{TeV}}{7\ \mathrm{TeV}}) = \frac{\mathrm{d}\sigma_{\mathrm{pp}}^{\mu\leftarrow\mathrm{HF}}/\mathrm{d}p_{\mathrm{t}}|_{2.76\ \mathrm{TeV}}}{\mathrm{d}\sigma_{\mathrm{pp}}^{\mu\leftarrow\mathrm{HF}}/\mathrm{d}p_{\mathrm{t}}|_{7\ \mathrm{TeV}}}|_{\mathrm{FONLL}}. \tag{8.14}$$

As listed in Fig. 7.29, there are three main sources of uncertainties in the FONLL calculations: the quark masses, the QCD scaling factors and the PDFs. So, the key point is to propagate these uncertainties to the predicted production cross sections of muons from heavy flavour decays at these two energies correctly via the ratio of the interpolation factor Eq. (8.14).

In Fig. 7.29, one can see that the uncertainty on the PDFs is very small for both charm and beauty and can be neglected. To calculate the uncertainties on the interpolation factor, we only take into account the propagation of the uncertainties on the quark masses and on the QCD scales. Then, the error propagation procedure is very similar to what was discussed in Sec. 7.5.1:

1. estimate the uncertainties on the quark masses and the QCD scales, σ_{mass} and σ_{scales}, independently;

[3] Indeed, what we get from FONLL calculations is the production cross section of muons from heavy flavour decays at $\sqrt{s} = 2.75$ TeV. We use this result to estimate the corresponding cross section at $\sqrt{s} = 2.76$ TeV. The difference in the results between these two energies, in principle is negligible.

2. add them together quadratically to get the final uncertainty:

$$\sigma_{\mathrm{interF}} = \sqrt{\sigma^2_{\mathrm{mass}} + \sigma^2_{\mathrm{scales}}}. \tag{8.15}$$

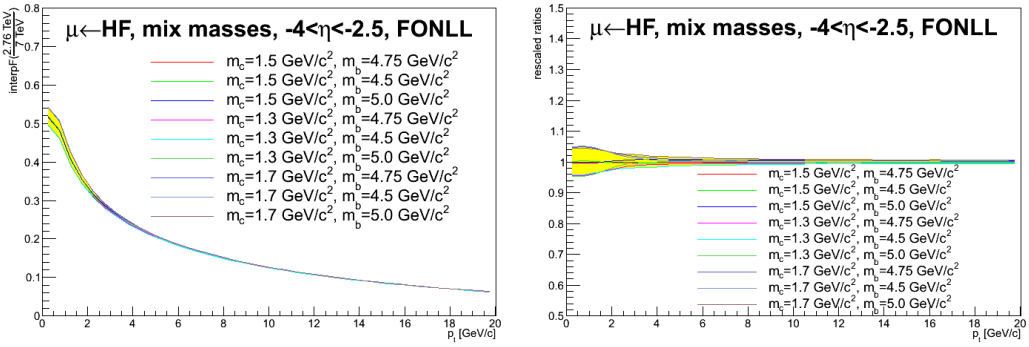

Figure 8.18: Left: the interpolation factor for scaling the production cross section of muons from heavy flavour decays from pp collisions at $\sqrt{s} = 7$ TeV to that at $\sqrt{s} = 2.76$ TeV via FONLL calculations. The results are obtained by fixing $\mu_{\mathrm{F}} = \mu_{\mathrm{R}} = \mu_0$, and by varying the masses of charm and beauty quarks in the 9 combinations listed in the plot. The yellow band shows the envelope of the results obtained with all mass combinations. Right: the re-scaled results from the left side plot according to the one with $m_{\mathrm{c}} = 1.5$ GeV/c^2 and $m_{\mathrm{b}} = 4.75$ GeV/c^2. The yellow band shows the envelope of these re-scaled results. It corresponds to the relative uncertainty of the interpolation factor from quark masses.

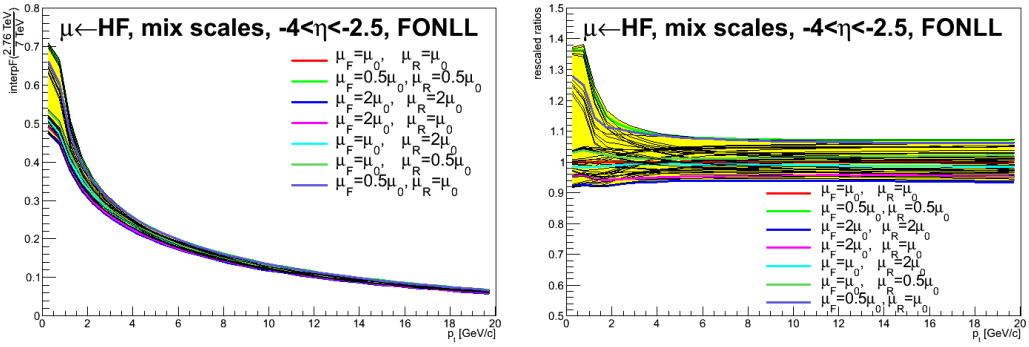

Figure 8.19: As in Fig. 8.18, the results are obtained by fixing $m_{\mathrm{c}} = 1.5$ GeV/c^2 and $m_{\mathrm{b}} = 4.75$ GeV/c^2 and by varying the QCD scales in the corresponding 49 combinations. The color lines show the results for charm and beauty choices the with different values of the QCD scales.

To obtain the uncertainty on the interpolation factor from the quark masses, we fix the QCD scales as $\mu_{\mathrm{F}} = \mu_{\mathrm{R}} = \mu_0$ with the value $\mu_0 = \sqrt{p_{\mathrm{t}}^2 + m_{\mathrm{Q}}^2}$ for

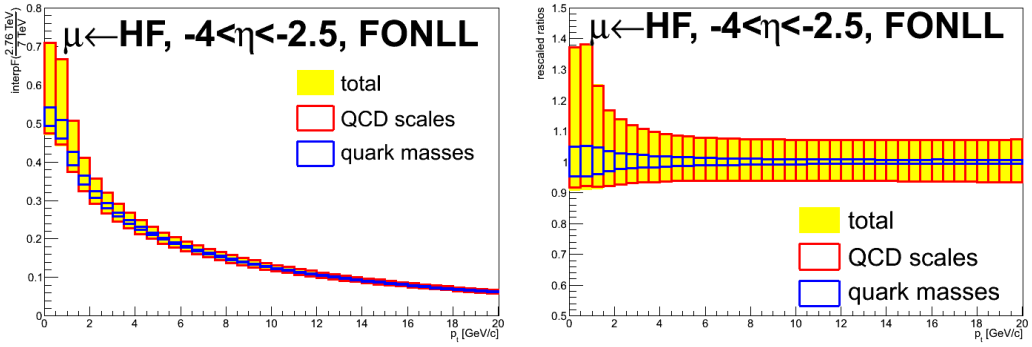

Figure 8.20: The interpolation factor (left) and its re-scaled ratio (right), with the uncertainties on the quark masses and the QCD scales obtained from Fig. 8.18 and Fig. 8.19, respectively. The total uncertainty calculated according to Eq. (8.15) is also shown.

both charm and beauty. Then we use the masses of charm and beauty quarks in the 9 combinations listed in Fig. (8.18) to calculate the interpolation factor in Eq. (8.15). The results from different quark mass combinations are shown in the left plot of Fig. (8.18), the yellow band shows the envelope of the results from all different mass combinations. By re-scaling these results according to the ones with $m_{\rm c} = 1.5$ GeV/c^2 and $m_{\rm b} = 4.75$ GeV/c^2, we get the results in the right plot of Fig. (8.18). The yellow band shows the envelope of these re-scaled results. It corresponds to the relative uncertainty on the interpolation factor from the quark masses.

Similarly to what we have done to obtain the uncertainty on the interpolation factor from the quark masses, to get the uncertainty from the QCD scales, we fix the values of the quark masses to $m_{\rm c} = 1.5$ GeV/c^2 and $m_{\rm b} = 4.75$ GeV/c^2 for charm and beauty, respectively. Then, we vary the values of the QCD scales in the total 49 combinations as mentioned in Sec. 7.5.1 and calculate the corresponding interpolation factor. The results are shown in the left plot of Fig. 8.19. In the right plot of Fig. 8.19 the re-scaled results according to the one with $\mu_{\rm F} = \mu_{\rm R} = \mu_0$ for both charm and beauty are shown. The yellow band shows the envelope of these re-scaled results. It corresponds to the relative uncertainty on the interpolation factor from the QCD scales.

We now consider the uncertainties on the interpolation factor from the quark masses and the QCD scales obtained from Fig. (8.18) and Fig. 8.19, respectively, and add them together according to Eq. (8.15). The results with the total uncertainties are shown in the left plot of Fig. 8.20. The central value of the interpolation factor in this plot is obtained by choosing $m_{\rm c} = 1.5$ GeV/c^2 and $m_{\rm b} = 4.75$ GeV/c^2 and $\mu_{\rm F} = \mu_{\rm R} = \mu_0$. The re-scaled results according to this central value are shown in the right plot of Fig. 8.20.

With the inputs of $\mathrm{d}\sigma_{\mathrm{pp}}^{\mu\leftarrow\mathrm{HF}}/\mathrm{d}p_{\mathrm{t}}|_{7\ \mathrm{TeV}}$ from Fig. 7.48 and the interpolation factor from the left plot of Fig. 8.20 from Eq. (8.13), $\mathrm{d}\sigma_{\mathrm{pp}}^{\mu\leftarrow\mathrm{HF}}/\mathrm{d}p_{\mathrm{t}}|_{2.76\ \mathrm{TeV}}$ is obtained via this energy interpolation procedure. It is shown by the red curve in Fig. 8.21. The systematic uncertainty on this cross section is shown by the red boxes. It includes the uncertainty on $\mathrm{d}\sigma_{\mathrm{pp}}^{\mu\leftarrow\mathrm{HF}}/\mathrm{d}p_{\mathrm{t}}|_{7\ \mathrm{TeV}}$ and the one from the interpolation factor as shown in Fig. 8.20. The black curve in this figure shows the production cross section of inclusive muons in data [4]. The difference between $\mathrm{d}\sigma_{\mathrm{pp}}^{\mu\leftarrow\mathrm{HF}}/\mathrm{d}p_{\mathrm{t}}|_{2.76\ \mathrm{TeV}}$ and the production cross section of inclusive muons indicates the contribution from the background (blue curve). The systematic uncertainty on the estimated background (blue boxes) only includes the one from $\mathrm{d}\sigma_{\mathrm{pp}}^{\mu\leftarrow\mathrm{HF}}/\mathrm{d}p_{\mathrm{t}}|_{2.76\ \mathrm{TeV}}$.

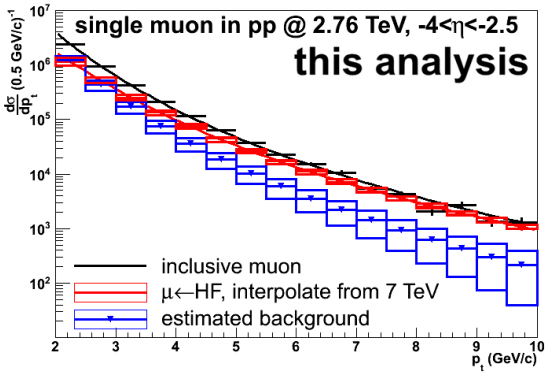

Figure 8.21: The $\mathrm{d}\sigma_{\mathrm{pp}}^{\mu\leftarrow\mathrm{HF}}/\mathrm{d}p_{\mathrm{t}}|_{2.76\ \mathrm{TeV}}$ calculated according to Eq. (8.13) (in red) and compared with the inclusive muon production cross section in data (in black). See text for more details.

A more detail study of the energy interpolation for the heavy flavour production can be found in Ref. [325].

8.4.2 Reference from pp Data at 2.76 TeV

The data sample we used to obtain the $\mathrm{d}\sigma_{\mathrm{pp}}^{\mu\leftarrow\mathrm{HF}}/\mathrm{d}p_{\mathrm{t}}|_{2.76\ \mathrm{TeV}}$ is LHC11a pass 2. After the data QA selection for muon analysis, there are 18 runs to be used. The used statistics at the event and muon track level in minimum bias trigger and muon-trigger data are summarized in Tab. 8.5 and Tab. 8.6, respectively.

trigger type	w/o cut	+Phys. Sel.	+Reco. Vtx.
MB trigger	34961767	34666268	31517941
MU trigger	8820393	8670397	8345001

Table 8.5: The event statistics in the used LHC11a data sample.

Similarly to what we did in pp collisions at $\sqrt{s} = 7$ TeV, the final results are obtained from muon trigger events and minimum-bias events are used to normalize muon-trigger events according to Eq. (7.22). In Tab. 8.6 the muon selection cuts (Sel. cuts) are defined in Sec. 6.4 as usual and the $p\times$DCA is cut at $5 \cdot \sigma$.

At the end of 2011, only the simulations with the PYTHIA Perugia-0 tuning

[4] The pp collisions at $\sqrt{s} = 2.76$ TeV data are introduced in Sec. 8.4.2. The correction strategy to get this result will be mentioned in Sec. 8.6.1.

trigger type	w/o cut	+Sel. cuts	+p×DCA
MB trigger	516933	147746	146989
MU trigger	5162369	4326614	4305063

Table 8.6: The muon-track statistics in the used LHC11a data sample.

using realistic detector configurations for LHC11a was available. Two scenarios were used to get the production cross section of muons from open heavy flavour decays via the method implemented in pp collisions at $\sqrt{s} = 7$ TeV [326]:

scenario 1: estimate the background using only the PYTHIA simulation and shift the central value of the spectrum after the background subtraction with the estimated systematic error on the background subtraction in pp collisions at $\sqrt{s} = 7$ TeV (Tab. 7.3);

scenario 2: scale the background from PHOJET simulation at $\sqrt{s} = 7$ TeV to $\sqrt{s} = 2.76$ TeV according to the ratio between the spectra of decay muons from PYTHIA simulations at $\sqrt{s} = 2.76$ TeV and $\sqrt{s} = 7$ TeV. Then perform the background subtraction with the PYTHIA simulation at $\sqrt{s} = 2.76$ TeV and this scaled background.

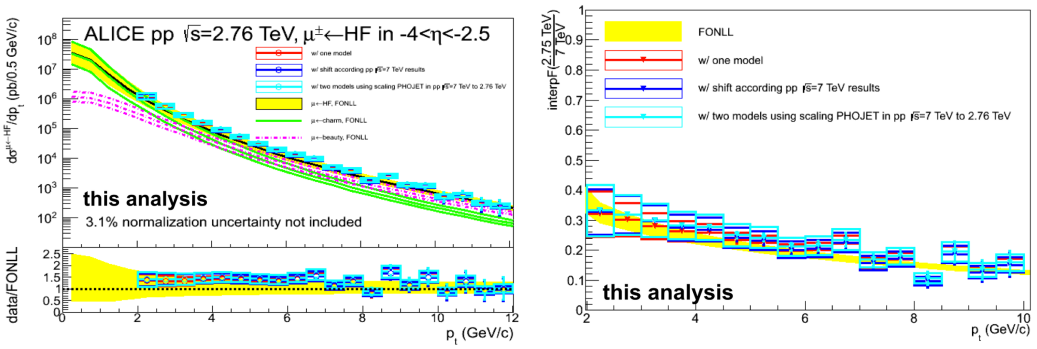

Figure 8.22: Left: production cross section of muons from heavy flavour decays in pp collisions at $\sqrt{s} = 2.76$ TeV from LHC11a. This was obtained at the end of 2011 according the two scenarios described in the text. The results are also compared with the ones using the energy interpolation (red curve in Fig. 8.21) and FONLL predictions. Right: the ratio between the production cross section of muons from heavy flavour decays in pp collisions at $\sqrt{s} = 2.76$ TeV in the left side plot and that obtained in pp collisions at $\sqrt{s} = 7$ TeV (shown in Fig. 7.48). The interpolation factor in the left plot of Fig. 8.20 using the FONLL calculations is also presented for comparison.

The production cross sections of muons from heavy flavour decays in pp collisions at $\sqrt{s} = 2.76$ TeV extracted from LHC11a data according to above scenario 1 and

scenario 2 are shown in the left plot of Fig. 8.22. They are labeled "w/ one model" and "w/ two models", respectively. The results from the energy interpolation (red curve in Fig. 8.21), labeled as "w/ shift from 7 TeV", is also compared with the FONLL predictions. One can see that, within errors, the results from the three methods are in agreement and are also consistent with the FONLL predictions. This can be seen more clearly from the re-scaled ratios according to the central value of FONLL predictions shown in the lower panel of this plot. Furthermore, we have computed the ratio between these results and the production cross section of muons from heavy flavour decays in pp collisions at $\sqrt{s} = 7$ TeV (Fig. 7.48) and compared them with FONLL predictions (the interpolation factor in the left plot of Fig. 8.20). As expected, a very good agreement is found with FONLL predictions.

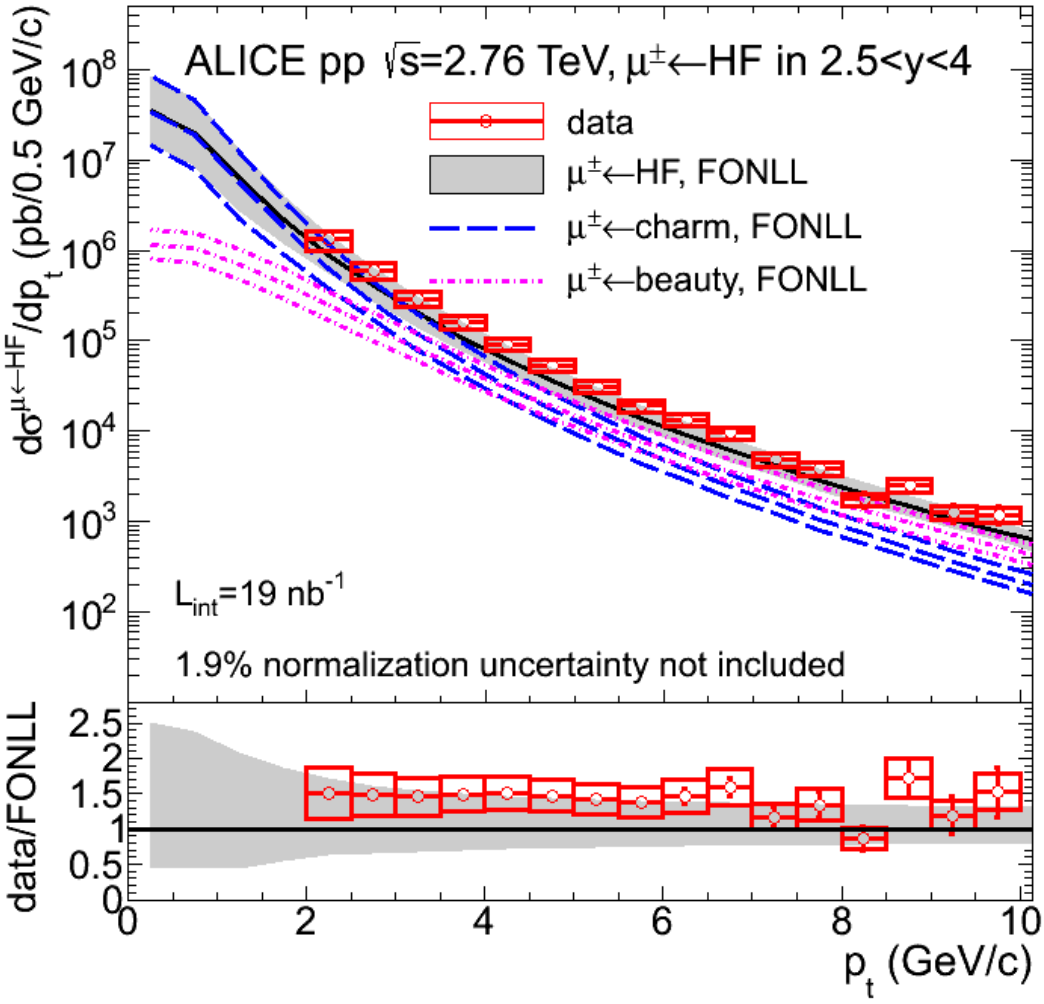

Figure 8.23: The production cross sections of muons from heavy flavour decays in pp collisions at $\sqrt{s} = 2.76$ TeV from LHC11a. The background is estimated according to both PYTHIA and PHOJET simulations with realistic detector configurations.

The PHOJET simulation with realistic detector configuration of LHC11a became available in the beginning of 2012. With this new simulation plus the one from PYTHIA Perugia-0 we have repeated the complete analysis strategy that we have applied to pp collisions at $\sqrt{s} = 7$ TeV and got, in the same conditions, the production cross sections of muons from heavy flavour decays in pp collision at $\sqrt{s} = 2.76$ TeV. This is shown in Fig. 8.23. The sources of the systematic uncertainties shown by the red boxes are the same as those listed in Sec. 7.7.1. The value of these uncertainties are:

- background subtraction: $\sim 13\%$ from model and $5-20\%$ from transport code depending on $p_{\rm t}$;
- detector response: 3%;
- residual mis-alignment: $1\% \times p_{\rm t}$;
- luminosity measurement (normalisation): 1.9% (not included in the red boxes in Fig. 8.23).

This result will be used in Eq. (8.12) to calculate the final results for the $R_{\rm AA}$ of muons from open heavy flavour decays in Pb–Pb collisions at $\sqrt{s_{\rm NN}} = 2.76$ TeV.

8.5 Background Estimate

After having obtained the denominator $\mathrm{d}\sigma_{\rm pp}^{\mu\leftarrow\rm HF}/\mathrm{d}p_{\rm t}$ in Eq. (8.12), to calculate the $R_{\rm AA}$ of muons from open heavy flavour decays in Pb–Pb collisions at $\sqrt{s_{\rm NN}} = 2.76$ TeV in Sec. 8.4, we need now to consider the numerator $1/\varepsilon_{\rm AA} \times \mathrm{d}N_{\rm AA}^{\mu\leftarrow\rm HF}/\mathrm{d}p_{\rm t}$. This corresponds to the corrected spectrum of muons from open heavy flavour decays a given centrality class in Pb–Pb collisions at $\sqrt{s_{\rm NN}} = 2.76$ TeV. We start by describing the challenges to obtain this term and the solutions we finally found. They do not only affect our analysis strategy but also determine the way to correct the Pb–Pb data for efficiency.

8.5.1 Strategy

In Pb–Pb collisions, the main challenge is to get the corrected $p_{\rm t}$ spectrum of muons from open heavy flavour decays $1/\varepsilon_{\rm AA} \times \mathrm{d}N_{\rm AA}^{\mu\leftarrow\rm HF}/\mathrm{d}p_{\rm t}$, in Eq. (8.12), for all centrality classes. Similarly to the approach used in pp collisions, this term can be obtained as

$$\frac{1}{\varepsilon_{\rm AA}} \times \mathrm{d}N_{\rm AA}^{\mu\leftarrow\rm HF}/\mathrm{d}p_{\rm t} = \frac{1}{\varepsilon_{\rm AA}} \times (\mathrm{d}N_{\rm AA}^{\rm incl\ \mu}/\mathrm{d}p_{\rm t} - \mathrm{d}N_{\rm AA}^{\rm bkg}/\mathrm{d}p_{\rm t}), \tag{8.16}$$

with the uncorrected inclusive muon spectrum $\mathrm{d}N_{\rm AA}^{\rm incl\ \mu}/\mathrm{d}p_{\rm t}$ and the uncorrected background spectrum $\mathrm{d}N_{\rm AA}^{\rm bkg}/\mathrm{d}p_{\rm t}$ in a given centrality class in Pb–Pb data. In pp collisions, the background spectrum (mainly primary muons) is estimated using different Monte-Carlo models. The same strategy to estimate the background in Pb–Pb collisions cannot be implemented since the quenching effects in Pb–Pb collisions

are unknown in the forward rapidity region and therefore are not well described by any kind of model. In addition, the uncertainty on cold nuclear effects also induces bias in the simulations.

We should find an alternative way to estimate the background in Pb–Pb collisions. The basic idea to estimate the background in Pb–Pb collisions is to use the cocktail-data based which is introduced in Sec. 7.8.1:

- as discussed during the analysis of pp collisions, in the high $p_{\rm t}$ region, the background is almost only constituted of primary muons which mainly come from kaon and pion decays;
- if we use the measured spectra of kaons and pions in the ALICE central barrel, we can extrapolate them to the forward region and reproduce their decay muon spectra.

The general idea for this is:

1. using the similar steps as in Sec. 7.8.1, extrapolate the K/π spectra in pp collisions measured in ALICE central barrel to the forward rapidity via Eq. (7.62);
2. in Pb–Pb collisions, by assuming,
$$R_{\rm AA}^{\rm K/\pi}(p_{\rm t}, y) = n_y \times R_{\rm AA}^{\rm K/\pi}(p_{\rm t}, y = 0), \tag{8.17}$$
where factor n_y describes the differences of the quenching effect between the central and forward rapidities, one can get,
$$\begin{aligned}
&\frac{1}{N_{\rm AA}^{\rm ev}} \cdot \frac{{\rm d}^2 N_{\rm AA}^{\rm K/\pi}}{{\rm d}p_{\rm t}{\rm d}y} \\
=&< N_{\rm coll} > \times R_{\rm AA}^{\rm K/\pi}(p_{\rm t}, y) \times \frac{1}{N_{\rm pp}^{\rm ev}} \cdot \frac{{\rm d}^2 N_{\rm pp}^{\rm K/\pi}}{{\rm d}p_{\rm t}{\rm d}y} \\
=&n_y \times < N_{\rm coll} > \times R_{\rm AA}^{\rm K/\pi}(p_{\rm t}, y = 0) \times \frac{1}{N_{\rm pp}^{\rm ev}} \cdot \frac{{\rm d}N_{\rm pp}^{\rm K/\pi}}{{\rm d}p_{\rm t}}|_{y=0} \times \exp[-\frac{1}{2}(\frac{y}{\sigma_y})^2] \\
=&n_y \times \frac{1/N_{\rm AA}^{\rm ev} \cdot {\rm d}N_{\rm AA}^{\rm K/\pi}/{\rm d}p_{\rm t}|_{y=0}}{1/N_{\rm pp}^{\rm ev} \cdot {\rm d}N_{\rm pp}^{\rm K/\pi}/{\rm d}p_{\rm t}|_{y=0}} \times \frac{1}{N_{\rm pp}^{\rm ev}} \cdot \frac{{\rm d}N_{\rm pp}^{\rm K/\pi}}{{\rm d}p_{\rm t}}|_{y=0} \times \exp[-\frac{1}{2}(\frac{y}{\sigma_y})^2] \\
=&n_y \times \frac{1}{N_{\rm AA}^{\rm ev}} \cdot \frac{{\rm d}N_{\rm AA}^{\rm K/\pi}}{{\rm d}p_{\rm t}}|_{y=0} \times \exp[-\frac{1}{2}(\frac{y}{\sigma_y})^2];
\end{aligned} \tag{8.18}$$
3. finally, the background spectra of muons from K/π decays in pp and Pb–Pb collisions can be obtained by implementing the decay processes K/$\pi \to \mu$ in Monte-Carlo by considering the effect of the front absrober of the muon spectrometer,
$$\frac{1}{N_{\rm AA(pp)}^{\rm ev}} \frac{{\rm d}N_{\rm AA(pp)}^{\mu \leftarrow {\rm K}/\pi}}{{\rm d}p_{\rm t}}|_{-4<\eta<-2.5} = \frac{1}{N_{\rm AA(pp)}^{\rm ev}} \int_{\Delta\eta} {\rm d}\eta \frac{{\rm d}^2 N_{\rm AA(pp)}^{\mu \leftarrow {\rm K}/\pi}}{{\rm d}p_{\rm t}{\rm d}\eta} \Leftarrow \frac{1}{N_{\rm AA(pp)}^{\rm ev}} \frac{{\rm d}^2 N_{\rm AA(pp)}^{\rm K/\pi}}{{\rm d}p_{\rm t}{\rm d}y}. \tag{8.19}$$

8.5.2 Inputs from Data

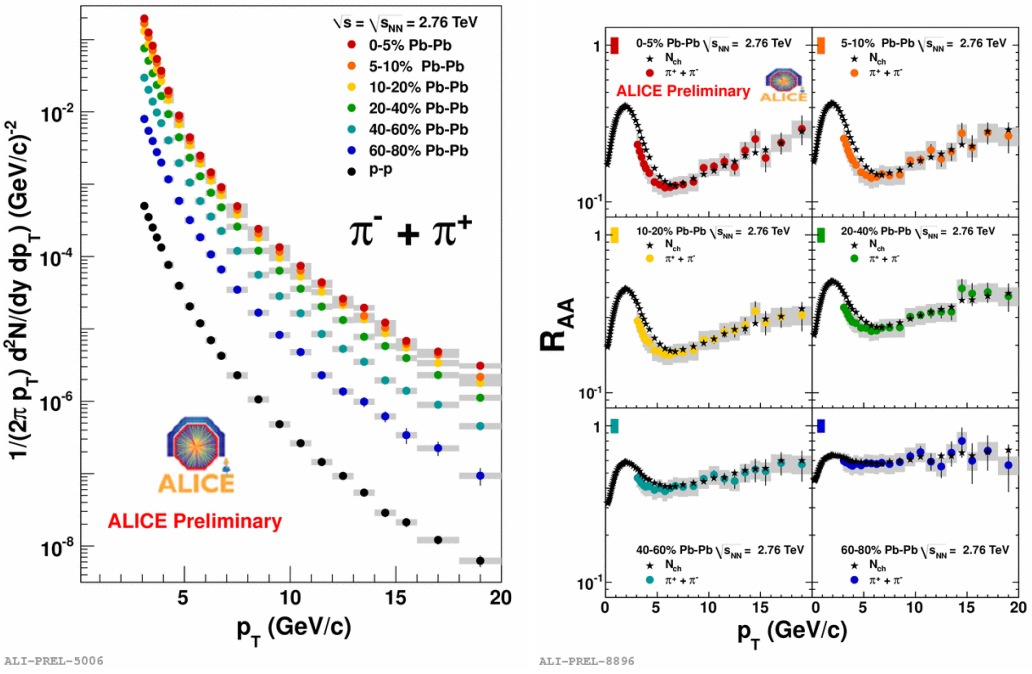

Figure 8.24: Left: the p_{t} spectra of charged pions measured in ALICE central barrel in different centrality bins in Pb–Pb collisions at $\sqrt{s_{\mathrm{NN}}} = 2.76$ TeV. The results are normalized to the number of events and compared with the charged pions spectrum measured in pp collisions under the same conditions. Right: the R_{AA} of charged pions obtained according to the p_{t} spectra in the left plot. The results are compared with the R_{AA} of the measured total charged particles.

As mentioned in our proposal described in Eq. (8.19), we will use the cocktail data based method, which needs as input the charged K/π spectra in mid-rapidity as shown in Eq. (8.18), to estimate the decay muon background in Pb–Pb collisions. The implementation of this procedure started in November 2011. The measurement of kaons and pions in the ALICE central barrel in Pb–Pb collisions at $\sqrt{s_{\mathrm{NN}}} = 2.76$ TeV, available at that time, are presented in Fig. 8.24 and 8.25, respectively.

The left plot of Fig. 8.24 shows the p_{t} spectra of charged pions in different centrality classes from ALICE central barrel in Pb–Pb collisions at $\sqrt{s_{\mathrm{NN}}} = 2.76$ TeV. The results are normalized to the number of events and compared to the p_{t} spectra of charged pions measured in the ALICE central barrel in pp collisions at $\sqrt{s} = 2.76$ TeV. The right plot of Fig. 8.24 shows the charged pion R_{AA} in different centrality classes with the inputs from the left side plot. The R_{AA} of total charged particles is also presented in this plot for comparison. This figure contains the inputs of the cocktail data based on charged pions for all centrality classes that we are interested in.

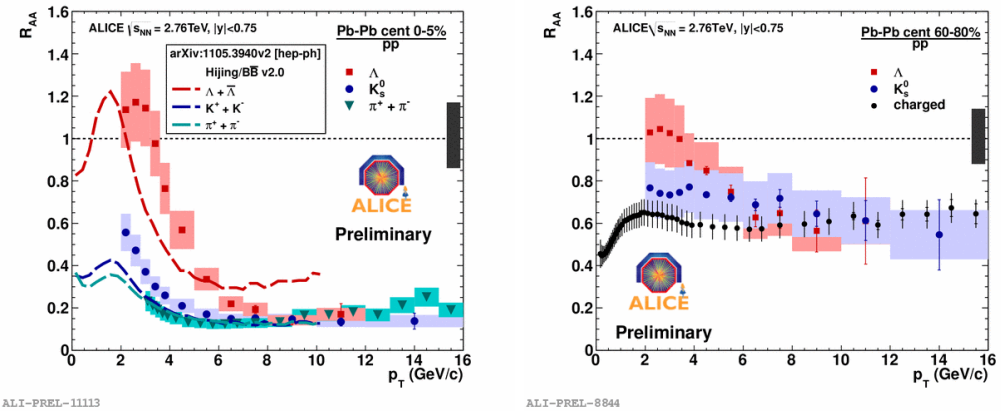

Figure 8.25: $R_{\rm AA}$ of $\rm K^0_s$ measured in $0-5\%$ (left) and $60-80\%$ (right) centrality classes from ALICE central barrel in Pb–Pb collisions at $\sqrt{s_{\rm NN}} = 2.76$ TeV. The results are compared to other charged particles as well as to model predictions as labeled in the plots.

Concerning of the inputs for kaons, as shown in Fig. 8.25, some information is missing.

- Indeed, what we need are the results of charged kaons but at that time only the results of $\rm K^0_s$ were approved. In order to cope with that, we estimate the spectra of charged kaons from those of $\rm K^0_s$ according to:

$$N(\rm K^+) + N(\rm K^-) \simeq 2 \cdot N(\rm K^0_s). \tag{8.20}$$

  This assumption is also used for the comparison of the data with HIJING predictions as shown in the left plot of Fig. 8.25.

- Another limitation from the kaon data is that the results are only available in two centrality classes: $0-5\%$ and $60-80\%$ as shown in the left and right plots of Fig. 8.25, respectively. To overcome this problem, we implemented a modification in the background estimation strategy. This is explained in Sec. 8.5.3.3.

8.5.3 Convert the Spectra of K/π to the Muon Level

With all above inputs using measurements performed in the ALICE central barrel, now we begin to estimate the decay muon background in Pb–Pb collisions according to Eq. (8.19) step by step.

8.5.3.1 Validation of the Rapidity Extrapolation

In the first step of Eq. (8.19), the extrapolation of the measured K/π spectra in Pb–Pb collisions from central to forward rapidities as shown in Eq. (8.18), we

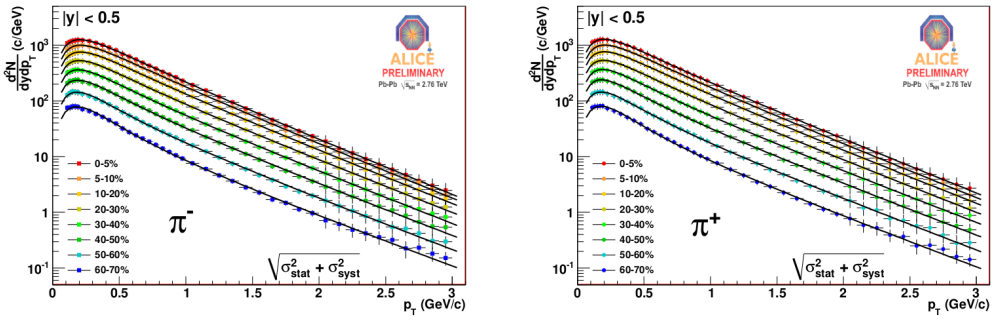

Figure 8.26: The spectra of π^- (left) and π^+ in different centrality classes measured in ALICE central barrel in Pb–Pb collisions at $\sqrt{s_{\rm NN}} = 2.76$ TeV. The results concern the low $p_{\rm t}$ region where thermal production dominants. The Blast-Wave fits for these spectra are also shown in the plots.

assumed that only the quenching effect is different between central to forward rapidities, the Eq. (8.17). In contrary to pp collisions, in Pb–Pb collisions particles can be produced according to:

- partonic scatterings in the early stage of the collisions;
- inside the fireball via the thermal production. This production mechanism dominantes in the low $p_{\rm t}$ region.

The rapidity extrapolation is not valid for the particle produced inside the fireball. Therefore, before considering the extrapolation, we should exclude the $p_{\rm t}$ region where thermal particles are dominant.

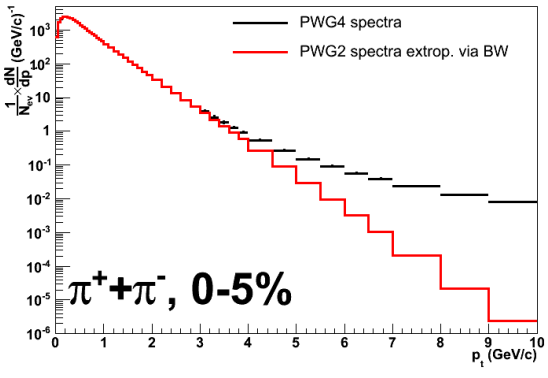

Figure 8.27: The study of thermal charged pions. See text for more details.

Fig. 8.26 shows the π^- and π^+ distributions measured in ALICE central barrel in the low $p_{\rm t}$ region, in the left and right plots, respectively. The results are fitted via the **Blast-Wave** (**BW**) function [327] which describes well the thermal behaviour of particles in the fireball formed in heavy ion collisions. To understand which $p_{\rm t}$ region is dominated by thermal production in the total charged pion spectrum, we add together the fits of π^- and π^+. We then extrapolate these BW fits to the high $p_{\rm t}$ region. After that, we can compare the fit results and those gotten from the left plot of Fig. 8.24. Fig. 8.27 shows one of this comparison for the charged pion spectra in the $0-5\%$ centrality class. We can observe that

thermal pions, which are described by the BW fits (red histogram in Fig. 8.27), dominates in $p_t < 4$ GeV/c. If we convert the pion spectra to decay muons, this p_t threshold will become lower. Therefore, in our cocktail data based strategy of background estimation, the particle spectra extrapolation for $p_t > 4$ GeV/c, via Eq. (8.17), is justified. Our final results will also be presented in this p_t region.

8.5.3.2 Fast Simulation Method

After the validation of the rapidity extrapolation, now, we focus on the second step: obtain the spectra of decay muons in different centrality classes in Pb–Pb collisions. Using the parameterization and generation strategy as in Sec. 7.8.1, will cost a very long CPU time. It is therefore better to implement a faster technique to convert the spectra of kaons and pions to decay muons.

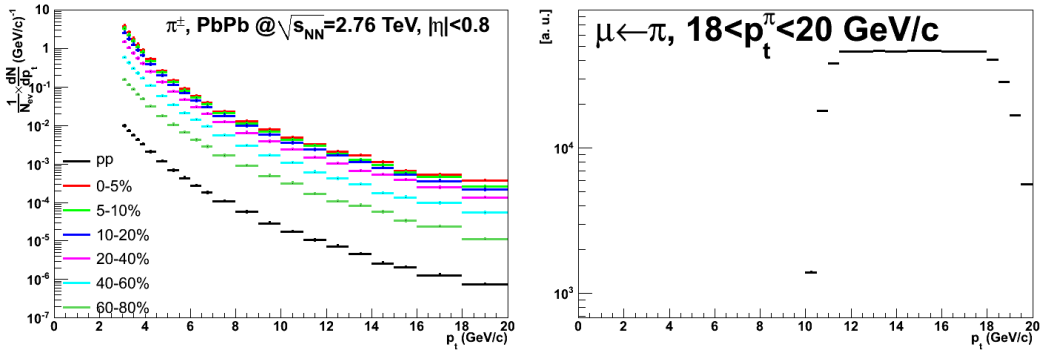

Figure 8.28: Left: the normalized p_t distributions of charged pions in different centrality classes derived from the left plot of Fig. 8.24. Right: the distribution of muons from charged pion decays in $18 < p_t < 20$ GeV/c with a flat p_t distribution of the charged pions as input.

To convert the K/π spectra to those of decay muons, we start with the case of charged pions with $n_y = 1$ (assuming the same quenching at mid-rapidity and forward rapidity), as an example. Using as input the invariant normalized p_t spectra for charged pions, as show in the left plot of Fig. 8.24, we convert them to the normalized p_t distributions of charged pions. The results are shown in the left plot of Fig. 8.28. The general way to convert these p_t distributions of charged pions to those of their decay muons is to parameterize these distributions and implement them in a generator to perform the semi-muonic decay processes via a Monte-Carlo technique. In this case, we should proceed with the generation several times. Because the p_t spectra decrease with p_t according to a power law, if we want to obtain a good statistics in the high p_t region, a large simulation time is required.

An alternative way to do this conversion is to proceed as shown in Fig. 8.29. We first generate a flat p_t distribution of charged pions, (black lines in this plot). After the semi-muonic decay of these pions via Monte-Carlo, we obtain the decay muons from pions in different p_t regions (color lines in this plot). In this Monte-Carlo

simulation, the effect of the front absorber of the muon spectrometer is simulated by applying the cut

$$\rho < 130 \text{ cm}, \tag{8.21}$$

where ρ is the distance between the origin and the muon production point [5]. Then, the normalization of the muon distributions in this plot to a given pion spectrum in the left plot of Fig. 8.28, is done according to the following steps:

1. for each muon we get the transverse momentum of its mother pion p_{t}^{π};
2. weight this muon according to the bin content at $p_{\mathrm{t}} = p_{\mathrm{t}}^{\pi}$ in the given pion spectrum in the left plot of Fig. 8.28, then re-fill it in the muon distribution with the weighted corresponding systematic error shown by the error bars;
3. loop over the above steps for all muons and we get a new muon distribution weighted according to the given pion spectrum;
4. finally, we normalize this weighted muon distribution with the total number of generated mother pions and the decay muon distribution according to a given input pion spectrum from the left plot of Fig. 8.28 is obtained.

With this strategy, we need to run the generation only once. Then we can scale the decay muon distributions according to any input pion spectrum. Also, since we generate the charged pions with a flat p_{t} distribution, it is easy to have a good statistics in the high p_{t} region. This is reflected in the distributions of both the generated pions and the decay muons in Fig. 8.29. One can see that indeed the statistical error bars are negligible in both cases.

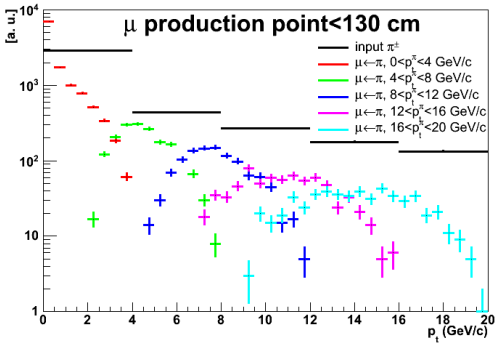

Figure 8.29: The distribution of muons from $\pi^{\pm}$ decays in different mother pions p_{t} regions with a flat p_{t} distribution of the charged pions as input and a cut on the muon production distance of < 130 cm.

In order to fully validate this strategy, an important check has to be done. According to the left plot of Fig. 8.28 (also the left plot of Fig. 8.24), the measured charged pion spectra in ALICE central barrel do not exceed $p_{\mathrm{t}} = 20$ GeV/c, and therefore our scaling too. Pions from the higher p_{t} region still have a chance to decay into muons in our p_{t} region of interest. If we do not consider their contribution

[5] According to Tab. 3.2, the distance between the origin of the beam interaction point and the front absorber is 90 cm. The distance of the mean free path of hadrons in the front absorber is 40 cm. Therefore, only muons coming from pions which decay at a distance less than 130 cm from the interaction point have a chance to pass through the front absorber and to be detected in the muon spectrometer.

there will be a bias in the final scaled muon spectrum. To overcome this issue, first we should define what is our interesting p_t region in the data. According to the upper plot of Fig. 8.17, the statistics in the data can allow to present the physics results up to $p_t = 10$ GeV/c. This is the upper limit of our p_t region. Therefore, we should check that the muons from pion decays with $p_t > 20$ GeV/c will not populate the muon spectrum in $p_t < 10$ GeV/c. This is confirmed by looking at the right plot of Fig. 8.28. Here, only the distribution of muons from pion decays with $18 < p_t < 20$ GeV/c is shown. We can see that there is no muon with $p_t < 10$ GeV/c from pions with $p_t > 18$ GeV/c. This means that if we consider muons with $p_t < 10$ GeV/c, the pion spectra from ALICE central barrel with p_t up to 20 GeV/c can be used to estimate the muon spectra from charged pion decays. By combining the discussion in Sec. 8.5.3.1 and here, the final results will be presented in $4 < p_t < 10$ GeV/c.

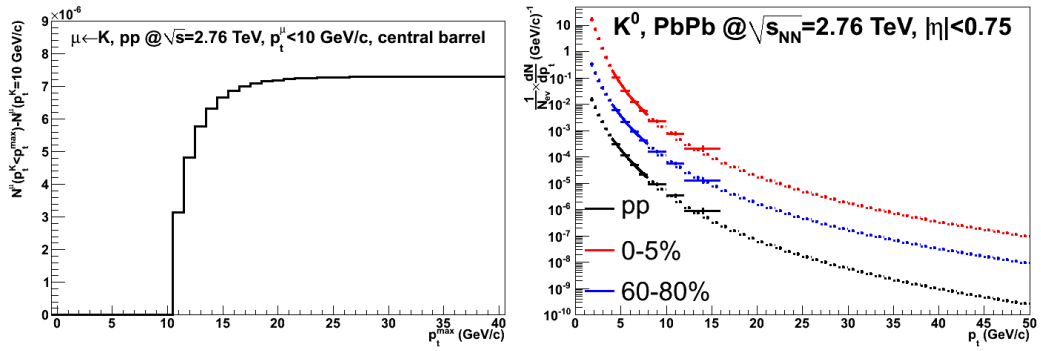

Figure 8.30: Left: the control plot used to get the upper limit of the p_t for the mother kaons. See text for more details. Right: the measured kaon spectra in ALICE central barrel in Pb–Pb collisions at $\sqrt{s_{\rm NN}} = 2.76$ TeV and pp collisions at the same collision energy. The results are extrapolated with a fit using Eq. (1.21).

In principle, the above strategy implemented for pions should be also valid for kaons. As shown in Fig. 8.25, the measured kaon spectra in the ALICE central barrel is limited to $p_t = 16$ GeV/c. One should check if kaons with $p_t > 16$ GeV/c decay to muons with $p_t < 10$ GeV/c. This is studied in the left plot of Fig. 8.30, where we show the difference between the number of muons from kaon decays with $p_t < p_t^{\rm max}$ and those from kaon decays with $p_t < 10$ GeV/c as a function of $p_t^{\rm max}$, with as input a flat kaon p_t distribution. We can see that this difference saturates at $p_t^{\rm max} = 40$ GeV/c. This means kaons with $p_t > 40$ GeV/c do not decay to muons with $p_t < 10$ GeV/c. Furthermore, to validate the conversion strategy we implemented for pions, the input p_t spectra of kaons should at least reach $p_t = 40$ GeV/c. Therefore, we fit the measured p_t spectra of kaons from ALICE central barrel with a power law (Eq. (1.21)), and extrapolate to the higher p_t region, as shown in the right plot of Fig. 8.25.

After implementing all the steps needed for the fast simulation for both pions and kaons, we get the spectra of muons from pion and kaon decays in different

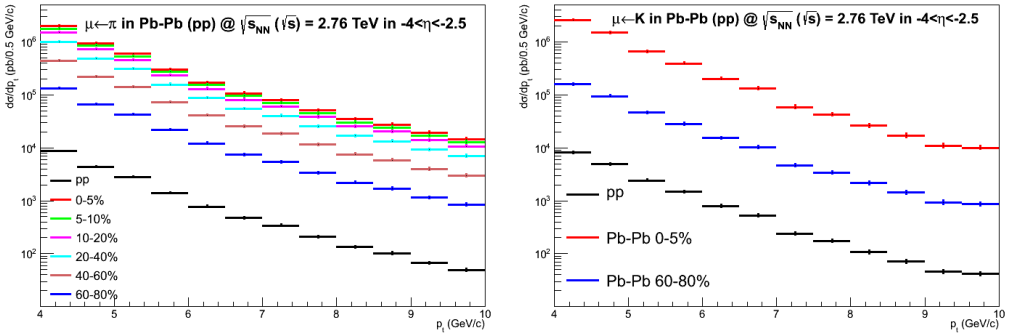

Figure 8.31: Muons from pion (left) and kaon (right) decays in $-4 < \eta < -2.5$, with $\rho < 130$ cm and $n_y = 1$.

centrality classes, as shown in Fig. 8.31. The kaon data from the ALICE central barrel are only available in two centrality regions: $0 - 5\%$ and $60 - 80\%$. In the following, we are going to discuss how to get the spectra of decay muons in all our interested centrality regions.

8.5.3.3 Centrality Extrapolation

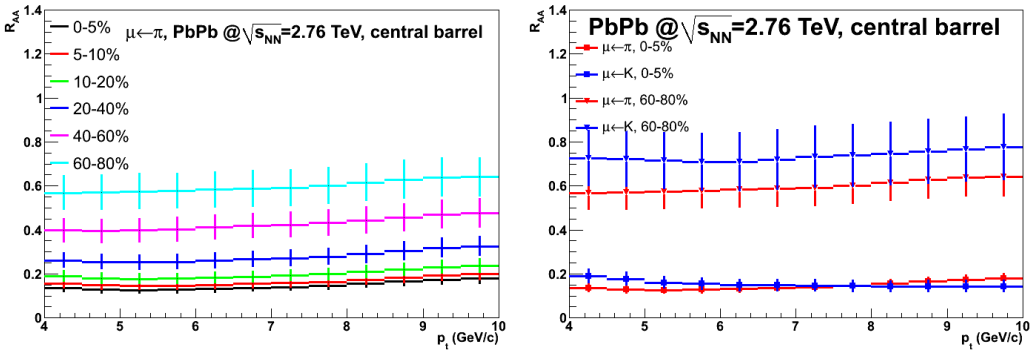

Figure 8.32: Left: the $R_{\rm AA}$ of muons in different centrality classes obtained by converting the charged pion spectra in left plot of Fig. 8.28 to the muon level, the error bars show the systematic uncertainties converted from the mother pion spectra. Right: the $R_{\rm AA}$ of muons from kaon decays in different centrality classes, the results are compared of those from pion decays in the corresponding centrality classes.

In order to find a way to get the spectra of muons from K/π decays in all of the interested centrality regions, here we keep $n_{\rm y} = 1$ and calculate the $R_{\rm AA}$ of muons from pion and kaon decays, respectively. These results are shown in Fig. 8.32. In the right plot of Fig. 8.32, we can see that, in each centrality class, both the trend and the magnitude of the $R_{\rm AA}^{\mu\leftarrow\pi}$ and $R_{\rm AA}^{\mu\leftarrow{\rm K}}$ as a function of $p_{\rm t}$ are different. The observed differences allow us to conclude that it is mandatory to use both pion and kaon data in order to estimate the $R_{\rm AA}$ of muons from pion and kaon decays.

Now we add the $p_{\rm t}$ spectra of muons from pion decays and those from kaon decays in a given centrality class in Pb–Pb collisions and in pp collisions to build the $R_{\rm AA}$ of decay muons [6]. The results are labeled as $R_{\rm AA}^{\mu\leftarrow {\rm K}/\pi}$ in the left plot of Fig. 8.33, for the two centrality classes.

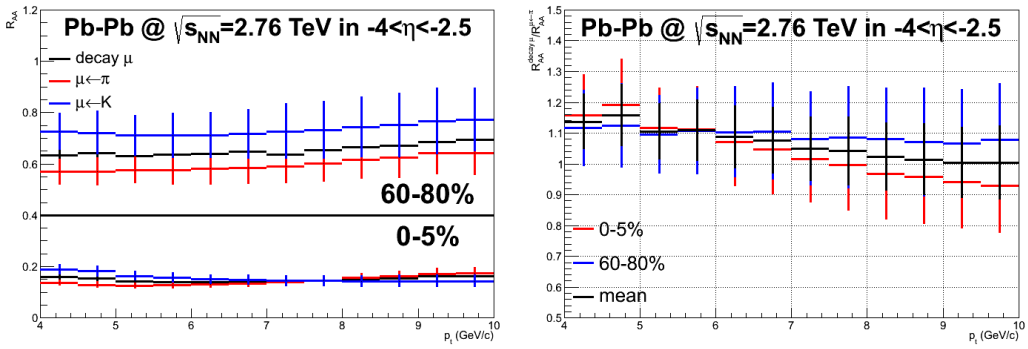

Figure 8.33: Left: the $R_{\rm AA}$ of different sources of decay muons in two different centrality classes as labeled in the plot. The results are obtained after all conversion steps in Sec. 8.5.3.2 with the inputs from Fig. 8.29. Right: the double ratio between $R_{\rm AA}^{\mu\leftarrow\pi}$ and $R_{\rm AA}^{\mu\leftarrow {\rm K}/\pi}$ which is obtained from the left plot in two different centrality classes.

As already mentioned, the kaon data from the ALICE central barrel are only available in two centrality classes. In addition both the magnitude and the trend of $R_{\rm AA}^{\mu\leftarrow\pi}$ and $R_{\rm AA}^{\mu\leftarrow {\rm K}}$ *vs.* $p_{\rm t}$ are different in these two centrality bins. It is therefore difficult to get the $R_{\rm AA}$ of decay muons in all centrality classes. This issue is nevertheless solved according to the results shown in the right plot of Fig. 8.33, where, we present the double ratio between $R_{\rm AA}^{\mu\leftarrow\pi}$ and $R_{\rm AA}^{\mu\leftarrow {\rm K}/\pi}$ (the $R_{\rm AA}$ of decay muons),

$$D_{\rm AA}(p_{\rm t}) = \frac{R_{\rm AA}^{\mu\leftarrow {\rm K}/\pi}(p_{\rm t}, n_y = 1)}{R_{\rm AA}^{\mu\leftarrow\pi}(p_{\rm t}, n_y = 1)}|_{-4<\eta<-2.5}. \tag{8.22}$$

One can see that even if the $R_{\rm AA}$ from different sources of decay muons is different in a given centrality region, this double ratio does not depend strongly on centrality. Therefore WE use the central value of the double ratio as a modification function to get $R_{\rm AA}^{\mu\leftarrow {\rm K}}$ in all centrality classes and to obtain the corresponding $R_{\rm AA}^{\mu\leftarrow {\rm K}/\pi}$. The differences between these two double ratios give the systematic uncertainty on this modification.

[6] One can notice that pion data are measured in $|\eta| < 0.8$ and kaon data are measured in $|\eta| < 0.75$ according to the left plot of Fig. 8.28 and the right plot of Fig. 8.30, respectively. The normalization according to the η bin width is applied before we add muons from kaons and muons from pions together.

Then, the decay muon background to all centrality regions can be scaled as:

$$\begin{aligned}
&\frac{1}{N_{\rm AA}^{\rm ev}}\frac{{\rm d}N_{\rm AA}^{\mu\leftarrow{\rm K}/\pi}}{{\rm d}p_{\rm t}}|_{-4<\eta<-2.5}\\
=&n_y\times\frac{1}{N_{\rm AA}^{\rm ev}}\frac{{\rm d}N_{\rm AA}^{\mu\leftarrow{\rm K}/\pi}}{{\rm d}p_{\rm t}}|_{-4<\eta<-2.5}^{n_y=1}\\
=&n_y\times<N_{\rm coll}>\times[R_{\rm AA}^{\mu\leftarrow{\rm K}/\pi}(p_{\rm t},n_y=1)\times\frac{1}{N_{\rm pp}^{\rm ev}}\frac{{\rm d}N_{\rm pp}^{\mu\leftarrow{\rm K}/\pi}}{{\rm d}p_{\rm t}}]|_{-4<\eta<-2.5}\\
=&n_y\times<N_{\rm coll}>\times D_{\rm AA}\times[R_{\rm AA}^{\mu\leftarrow\pi}(p_{\rm t},n_y=1)\times\frac{1}{N_{\rm pp}^{\rm ev}}\frac{{\rm d}N_{\rm pp}^{\mu\leftarrow{\rm K}/\pi}}{{\rm d}p_{\rm t}}]|_{-4<\eta<-2.5}.
\end{aligned}\tag{8.23}$$

In this procedure the uncertainty on $D_{\rm AA}$ comes from the differences between its mean value and its results in $0-5\%$ and $60-80\%$ centrality classes. Now, the background in Pb–Pb collisions as shown in Eq. (8.19), is recalculated in Eq. (8.23) here, in all centrality bins according to the data inputs. In order to get the output from Eq. (8.23), there are two additional terms, the quenching exptrapolation factor n_y and the decay muon spectrum in pp collisions $1/N_{\rm pp}^{\rm ev}\cdot{\rm d}N_{\rm pp}^{\mu\leftarrow{\rm K}/\pi}/{\rm d}p_{\rm t}|_{-4<\eta<-2.5}$, are required. In the following, we are going to discuss how to obtain these two terms in Sec. 8.5.4 and Sec. 8.5.5, respectively.

8.5.4 Estimate of the Rapidity Extrapolation Factor

Due to the unknow quenching effect in this new LHC energy range, the estimate of the rapidity factor n_y in Eq. (8.23) is another challenge in the analysis. We start to estimate the n_y factor according to some model predictions to get the first feeling. In the final results, we treat the range of the range of n_y, which estimated based on data measurements, as one kind of systematic uncertainty.

8.5.4.1 Rapidity Extrapolation Based on Model Predictions

According to the conclusion in Sec. 8.5.3.2, Eq. (8.23) can be used in the region $4<p_{\rm t}<10$ GeV/c, where the nuclear effects are dominated by the in-medium parton quenching. Therefore the factor n_y in Eq. (8.23) mainly reflects the difference between the energy loss of partons in the central and forward rapidity regions. It can be estimated according to the relation between the $R_{\rm AA}$ and the parton energy loss.

We call ${\rm d}\sigma/{\rm d}p_{\rm t}(E)$ the particle production cross section normalized per binary collision without energy loss. If we only consider the parton quenching effect, the mean energy loss $<\Delta E>$ results in a systematic shift of the particle spectra. Then, with the energy loss, the particle production cross section becomes ${\rm d}\sigma/{\rm d}p_{\rm t}(E+<\Delta E>)$, and the $R_{\rm AA}$ for the hard partons can be estimated as:

$$R_{\rm AA}(p_{\rm t}=E)=\frac{{\rm d}\sigma/{\rm d}p_{\rm t}(E+<\Delta E>)}{{\rm d}\sigma/{\rm d}p_{\rm t}(E)}.\tag{8.24}$$

According to the BDMPS limit [223], we have the following relation:

$$< \Delta E > \propto \alpha_{\rm s} C_{\rm R} < \hat{q} > L^2, \tag{8.25}$$

where $\alpha_{\rm s}$ and $C_{\rm R}$ are the QCD coupling constant and the color Casimir factor, respectively. As discussed in Sec. 1.2.1, L is the path length of the partons inside the QCD medium and $< \hat{q} >$ is the transport coefficient used to describe the mean energy exchange between the partons and the medium. Concerning the parameters in the right side of Eq. (8.25):

- $\alpha_{\rm s}$ depends on the temperature of the hot and dense matter and it does not change in the QCD medium formed in Pb–Pb collisions;
- $C_{\rm R}$ only depends on the parton species as mentioned in Sec. 1.2.1;
- L is related to the overlap region of the two colliding nucleus. Its mean value is also fixed for a given collision centrality class.

In a given collision centrality class, all the above three parameters are fixed and do not depend on the rapidity. Only the value of $< \hat{q} >$ depends on the medium density and is therefore expected to be rapidity dependent.

Under the BDMPS approximation, the difference of $< \Delta E >$ in the central and forward rapidity regions is only reflected via $< \hat{q} >$. We use the factor k to express the ratio between $< \hat{q} >$ in the **Central Barrel** (**CB**) and the **forward** (**FW**) rapidity region and set,

$$< \hat{q}_{\rm CB} >= k \times < \hat{q}_{\rm FW} >, \tag{8.26}$$

where $k > 1$. Since the medium density in the central rapidity region is larger than that in the forward rapidity region, then one can get,

$$< \Delta E_{\rm FW} >= \frac{1}{k} \times < \Delta E_{\rm CB} > . \tag{8.27}$$

Inserting Eq. (8.27) into Eq. (8.24), the factor n_y in Eq. (8.23) can be expressed as:

$$n_{\rm y} = \frac{R_{\rm AA}^{\rm FW}}{R_{\rm AA}^{\rm CB}} = \frac{{\rm d}\sigma/{\rm d}p_{\rm t}(E + < \Delta E > /k)}{{\rm d}\sigma/{\rm d}p_{\rm t}(E + < \Delta E >)}. \tag{8.28}$$

Using the same assumption as in Eq. (1.21),

$$\frac{{\rm d}\sigma}{{\rm d}p_{\rm t}} \propto \frac{1}{p_{\rm t}^m}, \tag{8.29}$$

where $m < 6$ is obtained from the fits to the ALICE charged particle spectra as mentioned in Sec. 1.5.3.2, Eq. (8.28) becomes:

$$\begin{aligned} n_{\rm y} = \frac{R_{\rm AA}^{\rm FW}}{R_{\rm AA}^{\rm CB}} &= \frac{(E + < \Delta E >)^m}{(E + < \Delta E > /k)^m} \\ &= (\frac{k + k \cdot < \Delta E > /E}{k + < \Delta E > /E})^m \\ &< (\frac{k + k \cdot < \Delta E > /E}{1 + < \Delta E > /E})^m = k^m, \end{aligned} \tag{8.30}$$

where in the last relation, we use $k > 1$.

Now, our problem consists to estimate the value of k in Eq. (8.30), according to the difference between the medium density in the central and the forward rapidity regions. To achieve this goal, we follow the assumption used in Ref. [328],

$$< \hat{q} > (\eta) =< \hat{q} > (\eta = 0) \times \frac{\mathrm{d}N_{\mathrm{ch}}/\mathrm{d}\eta}{\mathrm{d}N_{\mathrm{ch}}/\mathrm{d}\eta|_{\eta=0}}, \tag{8.31}$$

and get

$$k = \frac{< \hat{q}_{\mathrm{CB}} >}{< \hat{q}_{\mathrm{FW}} >} \frac{\mathrm{d}N_{\mathrm{ch}}/\mathrm{d}\eta|_{\mathrm{CB}}}{\mathrm{d}N_{\mathrm{ch}}/\mathrm{d}\eta|_{\mathrm{FW}}} \simeq 1.2, \tag{8.32}$$

with the ratio of the charged particle density between the central and the forward rapidity regions predicted by the CGC model [329].

Combining all these equations together, finally we have

$$n_y < k^m \lesssim 1.2^6 \simeq 3, \tag{8.33}$$

which gives the upper limit of the factor n_y in Eq. (8.23). Now we shortly discuss the following three points for Eq. (8.33).

- Our starting point for this estimate is the BDMPS approximation in Eq. (8.25) which is used to describe the hot nuclear effects (quenching) of partons in the QCD medium. However, the input for estimating the k factor is from the CGC theory (Eq. (8.32)) which is derived from cold nuclear effects. Therefore, the final result in Eq. (8.33) not only includes hot nuclear effects but also cold nuclear effects, partly.

- Indeed Eq. (8.33) gives the upper limit of the factor n. According to this upper limit, we set the range of n as:

$$0 < n_{\mathrm{y}} < 3, \tag{8.34}$$

  this range gives the uncertainty of the $R_{\mathrm{AA}}^{\mu\leftarrow\mathrm{K}/\pi}|_{\mathrm{FW}}$ estimate in Eq. (8.17). According to Eq. (8.33), Eq. (8.17) can be also expressed as

$$0 < R_{\mathrm{AA}}^{\mu\leftarrow\mathrm{K}/\pi}|_{\mathrm{FW}} < 3 \times R_{\mathrm{AA}}^{\mu\leftarrow\mathrm{K}/\pi}|_{\mathrm{CB}}, \tag{8.35}$$

  with $R_{\mathrm{AA}}^{\mu\leftarrow\mathrm{K}/\pi}|_{\mathrm{CB}} = R_{\mathrm{AA}}^{\mu\leftarrow\mathrm{K}/\pi}(p_{\mathrm{t}}, y = 0)$ obtained according to the stragtegy mentioned in Sec. 8.5.3.3.

- The upper limit of the factor k is only estimated according to the BDMPS and CGC predictions. Other models could give different predictions. To estimate the full uncertainty on the factor k, we should include predictions from several different kinds of models, and this, in some sense, is an impossible duty. In the left plot of Fig. 8.33, one can see that, in peripheral collisions $(60 - 80\%)$ $R_{\mathrm{AA}}^{\mu\leftarrow\mathrm{K}/\pi}|_{\mathrm{CB}} \simeq 0.65$. Using this value in Eq. (8.35), one can get the upper limit of $R_{\mathrm{AA}}^{\mu\leftarrow\mathrm{K}/\pi}|_{\mathrm{FW}}$ which is ~ 2. This value can, for sure, be considered as a limit for any prediction. For central collisions, there is no hint about the range of

$R_{\rm AA}^{\mu\leftarrow {\rm K}/\pi}|_{\rm FW}$ estimated in Eq. (8.35). To overcome this drawback, we modify Eq. (8.35) as:

$$0 < R_{\rm AA}^{\mu\leftarrow {\rm K}/\pi}|_{\rm FW} < \max\{3 \times R_{\rm AA}^{\mu\leftarrow {\rm K}/\pi}|_{\rm CB}, 1\}. \tag{8.36}$$

The physics meaning of Eq. (8.36) is that, in central collisions where $3 \times R_{\rm AA}^{\mu\leftarrow {\rm K}/\pi}|_{\rm CB} < 1$, we set the range of $R_{\rm AA}^{\mu\leftarrow {\rm K}/\pi}|_{\rm FW}$ as:

$$0 < R_{\rm AA}^{\mu\leftarrow {\rm K}/\pi}|_{\rm FW} < 1, \tag{8.37}$$

this upper and lower limits correspond to the situation where all partons are quenched and there is no quenching for partons, respectively.

8.5.4.2 Rapidity Extrapolation Based on Data Measurements

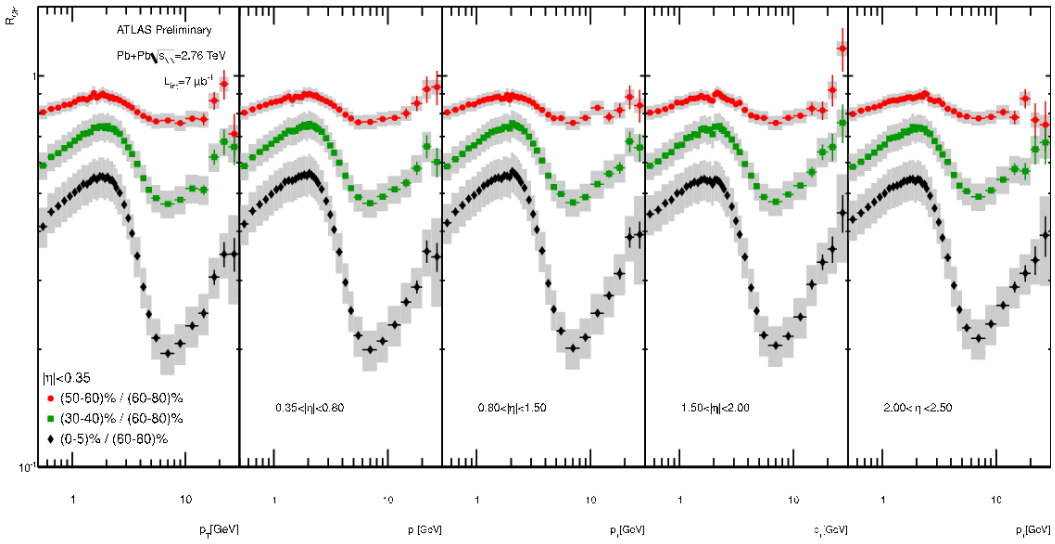

Figure 8.34: $R_{\rm CP}$ extracted from the inclusive charged particle distributions in different η ranges, and three centrality classes $0-5\%$, $30-40\%$ and $50-60\%$ with respect to a common peripheral sample $(60-80\%)$. Statistical errors are shown with vertical lines and the overall systematic uncertainty is shown with gray boxes [330].

In our final results, we estimate the range of factor n_y according to the measured $R_{\rm CP}$ of charged particles in ATLAS [330] up to $\eta = 2.5$, as shown in Fig. 8.34. According to these results, the $R_{\rm CP}$ of charged particles is insenstive to the rapidity up to $\eta = 2.5$, and indicates that the quenching strength from central rapidity region to forward rapidity does not change within uncertainties. In this case, we choose $n_y = 1$ to present the final results and we vary the value of factor n_y within 100%, $0 < n_y < 2$, to estimate the uncertainty of the quenching strength in the forward rapidity region.

8.5.5 Yield of Decay Muons in pp Collisions

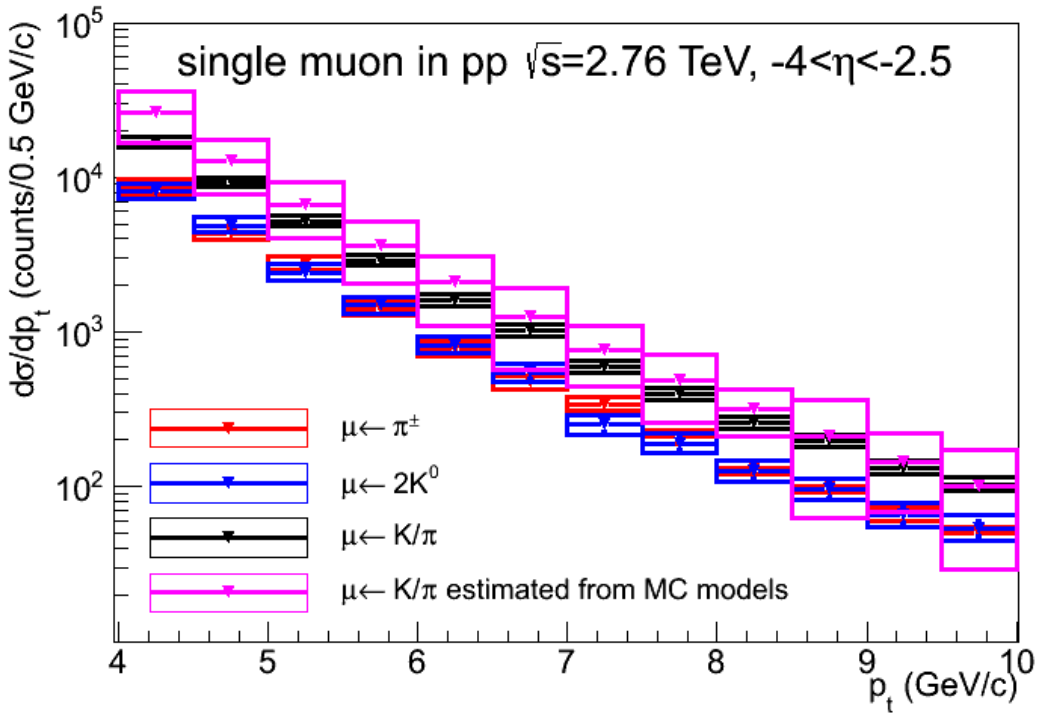

Figure 8.35: The spectra of decay muons normalized at the cross section level in pp collisions at $\sqrt{s} = 2.76$ TeV, see text for more details.

Up to now we get the range of n_y in Eq. (8.23). To finalize the background estimate in Pb–Pb collisions now, we are going to estimate the term of $\mathrm{d}N_{\mathrm{pp}}^{\mu\leftarrow\mathrm{K}/\pi}/\mathrm{d}p_{\mathrm{t}}|_{\mathrm{FW}}$, the corrected spectrum of decay muons in pp collisions at $\sqrt{s} = 2.76$ TeV, in Eq. (8.23).

In principle, we can get $\mathrm{d}N_{\mathrm{pp}}^{\mu\leftarrow\mathrm{K}/\pi}/\mathrm{d}p_{\mathrm{t}}|_{\mathrm{FW}}$ directly by using the strategy mentioned in Sec. 7.8.1 with the input K/π spectra in pp collisions at $\sqrt{s} = 2.76$ TeV from the left plot of Fig. 8.28 and the right plot of Fig. 8.30, respectively. After this procedure, we need to add the further correction of background to get the full term of $1/\varepsilon_{\mathrm{pp}}^{\mathrm{bkg}} \times \mathrm{d}N_{\mathrm{pp}}^{\mu\leftarrow\mathrm{K}/\pi}/\mathrm{d}p_{\mathrm{t}}|_{\mathrm{FW}}$. On another hand, with the strategy mentioned in Sec. 8.5.3.2, using the fast simulation procedure, the output spectra are obtained at the generation level. In other words, they can be treated as the results already corrected by the efficiency. Therefore, we apply a background estimate procedure in pp collisions at $\sqrt{s} = 2.76$ TeV by combining the two strategies mentioned in Sec. 7.8.1 and Sec. 8.5.3.2.

1. Extrapolate the K/π spectra from ALICE central barrel (left plot of Fig. 8.28 and right plot of Fig. 8.30) to the forward rapidity region according to Eq. (7.62). In this equation, $\sigma_y = 1.59 \pm 0.22$ is obtained by fitting the ratios of the charged K/π spectra in the forward region to that in the central

rapidity region according to PYTHIA Perugia-0 and PHOJET simulations in pp collisions at $\sqrt{s} = 2.76$ TeV.

2. Use the extrapolated K/π spectra in the forward region to scale the muons generated with the flat K/π distributions after cutting off the distance between their production point and the collision interaction point (130 cm). An example is shown in Fig. 8.29. The method for the scaling is described in Sec. 8.5.3.2 and Sec. 8.5.3.3, but instead of the one dimension weight in $p_{\rm t}$ implemented in Pb–Pb collisions, here we apply the scaling in both $p_{\rm t}$ and η to describe the acceptance effect of the muon spectrometer [7].

3. Finally, by adding muons from kaon and pion decays together, the decay muon spectrum in pp collisions in the forward region is obtained.

Fig. 8.35 shows the spectra of decay muons obtained according to the above steps, all the results are normalized to the cross section according to data. The spectra of muons from pion and kaon decays are shown in the red and blue histograms, respectively. The spectrum of muons from kaon decays is labeled as "$\mu \leftarrow 2\mathrm{K}^0$" in this figure, this is due to the fact that we used the spectrum of $\mathrm{K}^0_{\rm s}$ to estimate the charged kaon spectra in data as mentioned in Sec. 8.5.2. The yield of the charged kaons in data is given by the yield of $\mathrm{K}^0_{\rm s}$ with a factor of 2 as described in Eq. (8.20). By adding the spectra of muons from pion and kaon decays together, the spectrum of decay muons is obtained, as shown with the black histogram. The systematic errors on all these spectra, shown by the boxes, are propagated from the systematic uncertainties on the input data. For the comparison, the spectrum of decay muons from the two Monte-Carlo simulations, used in Sec. 8.4.2 to get the results of production cross section of muons from heavy flavour decays in Fig. 8.23, is also displayed in this figure. The systematic uncertainties affecting the decay muon spectrum from the Monte-Carlo models come from the model differences and the transport code as illustrated in Sec. 8.5.2. Since the spectrum of decay muons obtained here is at the generation level (we do not implement the reconstruction as mentioned), to compare the results from Monte-Carlo simulations with it, the spectrum of decay muons from Monte-Carlo models are also gotten at the generation level. Indeed, we can see that, the spectrum of decay muons obtained from these two independent methods agree each other quite well, within errors.

8.6 Efficiency and Uncertainty

After the background estimate in Pb–Pb collisions, it is time to present the background subtraction and show the final corrected results. Differently from pp collisions, according to this fast simulation strategy in Sec. 8.5.3.2, the background

[7] As we already mentioned, in Eq. (7.62), the effect of η just plays a role as a scaling factor of the $p_{\rm t}$ spectra. Our final aim is to calculated the $R_{\rm AA}$ in which this scaling factor cancels out. However, to estimate the muon $p_{\rm t}$ spectrum in pp collision this η scaling factor is very important, especially for normalizing the spectrum of decay muons to the data.

spectra of muons from pion and kaon decays in Pb–Pb collisions shown in Fig. 8.31 are corrected automatically, since there is no detection effect in the procedure used to produce the decay muons. In this case, the output from Eq. (8.19) is the second term shown in the right side of Eq. (8.16),

$$\frac{1}{\varepsilon_{\rm AA}} \times {\rm d}N^{\rm bkg}_{\rm AA}/{\rm d}p_{\rm t} = \frac{1}{N^{\rm ev}_{\rm AA(pp)}} \frac{{\rm d}N^{\mu\leftarrow{\rm K}/\pi}_{\rm AA(pp)}}{{\rm d}p_{\rm t}}|_{-4<\eta<-2.5}. \tag{8.38}$$

Inserting the relation Eq. (8.38) back into Eq. (8.16) we can get,

$$\frac{1}{\varepsilon_{\rm AA}} \times {\rm d}N^{\mu\leftarrow{\rm HF}}_{\rm AA}/{\rm d}p_{\rm t} = \frac{1}{\varepsilon_{\rm AA}} \times {\rm d}N^{\rm incl\ \mu}_{\rm AA}/{\rm d}p_{\rm t} - \frac{1}{N^{\rm ev}_{\rm AA}} \frac{{\rm d}N^{\mu\leftarrow{\rm K}/\pi}_{\rm AA}}{{\rm d}p_{\rm t}}|_{-4<\eta<-2.5}. \tag{8.39}$$

Eq. (8.39) means that, in Pb–Pb collisions we should present the efficiency correction of the inclusive muon spectra before the background subtraction. Then the background subtraction and signal efficiency correction procedure described in Eq. (8.16), which have already implemented in the analysis of pp collisions at $\sqrt{s}$ = 7 TeV, cannot be used here. To get the corrected signal spectra in Pb–Pb collisions, the background should be subtracted from the efficiency corrected spectra of inclusive muons. For getting the final results, firstly, we discuss the efficinecy correction of inclusive muons in Pb–Pb collisions.

8.6.1 Efficiency Correction

In principle, in a given centrality class in Pb–Pb collisions, the factors which affect the correction efficiency of muon tracks are the same as those in pp collisions, as listed in the begining of Sec. 7.4. But due to the evolution of the event multiplicity with the collision centrality in Pb–Pb collisions, the occupancy of the tracking and trigger chambers of the muon spectrometer changes with the collision centrality. The change of the occupancy affects the reconstruction efficiency of muon tracks. This is indicated in Fig. 8.9, where we see that, the fraction of fake tracks reconstructed in the muon spectrometer increases as the event centrality increases, and this is attributed to the decrease of the reconstruction efficiency due to the increase of the event multiplicity and detector occupancy when the collisions become more and more central. In this case, differently from that in pp collisions, in Pb–Pb collisions, the correction efficiency is not fixed but evolves with the collision centrality.

Anyhow, as mentioned above, the factors which affect the correction efficiency in Pb–Pb collisions are the same as those in pp collisions. According to this, one direct way to estimate the correction efficiency in different centrality regions in Pb–Pb collisions is to simulate several event samples, and each of them with the input multiplicity corresponding to that in a given centrality region, then the correction efficiency can be obtained by comparing the reconstructed sample with its corresponding input in each centrality region. But the main problem to implement this procedure is that, in principle, the input multiplicity in data in unknown, before the efficiency correction.

On the other hand, according to the performance studies even with the twice input multiplicity predicted by Hijing in central Pb–Pb collisions at $\sqrt{s_{\rm NN}} = 5.5$ TeV, the occupancy of the tracking chambers of muon spectrometer is still not very large and is about 3.5% [221]. In this case, one does not expect strong changes in the efficiency correction of muon tracks, from pp collisions to central of Pb–Pb collisions. Under this expectation, we estimate the efficiency correction in two steps:

- the efficiency correction in pp collisions which is also equivalent to that in peripheral Pb–Pb collisions;
- the evolution of the correction efficiency with the collision centrality in Pb–Pb collisions.

Now we start the efficiency estimate with the efficiency correction of inclusive muons in pp collisions. Here, due to the low occupancy, the correction efficiency, for sure, is insensitive with the particle multiplicity, and the main factor which affects the efficiency correction is the misalignment effect of the detector chambers which depends on the shape of the particle $p_{\rm t}$ distributions. But as mentioned in Sec. 8.5.3, the used statistics in LHC10h data sample, allows to investigate the region $p_{\rm t} < 10$ GeV/c, as shown in Fig. 8.17. In this $p_{\rm t}$ region, the misalignment effect is not very large ($\sim 1\% \times p_{\rm t}$ with $p_{\rm t}$ in unit of GeV/c). Furthermore, as discussed in Sec. 8.5.3.1, Eq. (8.36) which is used to estimate the $R_{\rm AA}$ of decay muons in the forward region can be applied only in $p_{\rm t} > 4$ GeV/c, and the final results will be also presented in this $p_{\rm t}$ region. So, for the efficiency correction, we only need to focus on this $p_{\rm t}$ region, too. As proved in Sec. 7.4.3, the corrected results are insensitive with the input shapes used to build the correction matrices in $p_{\rm t} > 2$ GeV/c. In other words, in our interesting $p_{\rm t}$ region $4 < p_{\rm t} < 10$ GeV/c, if we ignore the misalignment effect for a moment, the efficiency matrix built with one given input $p_{\rm t}$ shape can be used to correct different kinds of particles with different $p_{\rm t}$ shapes in pp collisions. In this case, we build the correction matrix for the inclusive muons with muons from beauty decay from the HvQMNR predictions as the input for pp collisions.

centrality (%)	$0-10$	$10-20$	$20-40$	$40-60$	$40-80$	$60-80$
efficiency ratio	0.966	0.977	0.984	0.99	0.998	1

Table 8.7: The ratios between the efficiency correction of single muons in different centrality regions and the one in $60-80\%$. The results are gotten by embedding the J/Ψ signal in LHC10h data [331].

In the second part of the correction efficiency, the dependence of the collision centrality in Pb–Pb collisions, is estimated by means of the so called embedding technique. The general idea of the embedding is:

1. simulate a sample of events with a given number of signal in each of them;
2. let these signals cross the detectors in the transport code;

3. then merge the simulated hits in the detectors, produced by the input signal, with the detected hits in data event by event to build the so-called embedding event;

4. after the reconstruction of the embedding events as the real data, the reconstruction efficiency for the embedded signal is obtained according to the Monte-Carlo information of the reconstructed input signal in the simulation.

The advantage to use the embedding is that, by merging the simulated hits with those from the real data, the problem of estimating the input multiplicity in data is overcame. Tab. 8.7 shows the ratios between the correction efficiency of single muons in different centrality regions and the one in $60-80\%$, in which the multiplicity is very close to that in pp collisions. The results are gotten by embedding the J/Ψ signal in LHC10h data. As expected, due to the quite low occupancy of the muon spectrometer in central Pb–Pb collisions ($\sim 5\%$), the efficiency from peripheral to central collisions decreases by less than $< 5\%$.

After all, the correction efficiency of the inclusive muons in Pb–Pb collisions is obtained by modifying the efficiency matrix, which is gotten in pp collisions with the input of muons from beauty decays from the HvQMNR predictions, with the ratios in Tab. 8.7 gotten from the embedding of J/Ψ signals in LHC10h data.

8.6.2 Systematic Uncertainty on the Final Results

Finally, by using Eq. (8.39) and Eq. (8.12), the $R_{\rm AA}$ of muons from open heavy flavour decays can be expressed as (in the following the default acceptance is $-4 < \eta < -2.5$):

$$\begin{aligned} R_{\rm AA}^{\mu\leftarrow{\rm HF}} =& \frac{1}{< T_{\rm AA} >} \cdot \frac{1}{N_{\rm AA}^{\rm ev}} \cdot \frac{{\rm d}N_{\rm AA}^{\mu\leftarrow{\rm HF}}/{\rm d}p_{\rm t}}{{\rm d}\sigma_{\rm pp}^{\mu\leftarrow{\rm HF}}/{\rm d}p_{\rm t}} \\ =& \frac{1}{< T_{\rm AA} >} \cdot \frac{1}{N_{\rm AA}^{\rm ev}} \cdot \frac{1}{\varepsilon_{\rm AA}} \times \frac{{\rm d}N_{\rm AA}^{{\rm incl}\ \mu}/{\rm d}p_{\rm t} - {\rm d}N_{\rm AA}^{\rm bkg}/{\rm d}p_{\rm t}}{{\rm d}\sigma_{\rm pp}^{\mu\leftarrow{\rm HF}}/{\rm d}p_{\rm t}} \\ =& \frac{1}{< T_{\rm AA} >} \cdot \frac{1}{N_{\rm AA}^{\rm ev}} \cdot \frac{1}{\varepsilon_{\rm AA}} \times \frac{{\rm d}N_{\rm AA}^{{\rm incl}\ \mu}/{\rm d}p_{\rm t}}{{\rm d}\sigma_{\rm pp}^{\mu\leftarrow{\rm HF}}/{\rm d}p_{\rm t}} - \frac{1}{< T_{\rm AA} >} \cdot \frac{1}{N_{\rm AA}^{\rm ev}} \cdot \frac{{\rm d}N_{\rm AA}^{\mu\leftarrow{\rm K}/\pi}/{\rm d}p_{\rm t}}{{\rm d}\sigma_{\rm pp}^{\mu\leftarrow{\rm HF}}/{\rm d}p_{\rm t}}, \end{aligned} \tag{8.40}$$

where $1/N_{\rm AA}^{\rm ev} \cdot 1/\varepsilon_{\rm AA} \cdot {\rm d}N_{\rm AA}^{{\rm incl}\ \mu}/{\rm d}p_{\rm t}$ is the corrected $p_{\rm t}$ spectrum of inclusive muons measured in a given centrality region in Pb–Pb collisions at $\sqrt{s_{\rm NN}} = 2.76$ TeV, ${\rm d}\sigma_{\rm pp}^{\mu\leftarrow{\rm HF}}/{\rm d}p_{\rm t}$ is the measured production cross section of muons from open heavy flavour decays in pp collisions at $\sqrt{s} = 2.76$ TeV, $1/N_{\rm AA}^{\rm ev} \cdot {\rm d}N_{\rm AA}^{\mu\leftarrow{\rm K}/\pi}/{\rm d}p_{\rm t}$ is the background distribution given by Eq. (8.23). To explain the systematic uncertainty estimation, we define:

$$\begin{aligned} {\rm termA} =& \frac{1}{< T_{\rm AA} >} \times \frac{1}{N_{\rm AA}^{\rm ev}} \times \frac{1}{\varepsilon_{\rm AA}} \times \frac{{\rm d}N_{\rm AA}^{{\rm incl}\ \mu}/{\rm d}p_{\rm t}}{{\rm d}\sigma_{\rm pp}^{\mu\leftarrow{\rm HF}}/{\rm d}p_{\rm t}}, \\ {\rm termB} =& \frac{1}{< T_{\rm AA} >} \times \frac{1}{N_{\rm AA}^{\rm ev}} \times \frac{{\rm d}N_{\rm AA}^{\mu\leftarrow{\rm K}/\pi}/{\rm d}p_{\rm t}}{{\rm d}\sigma_{\rm pp}^{\mu\leftarrow{\rm HF}}/{\rm d}p_{\rm t}}, \end{aligned} \tag{8.41}$$

and Eq. (8.40) becomes,

$$R_{\rm AA}^{\mu\leftarrow{\rm HF}} = {\rm termA} - {\rm termB}. \tag{8.42}$$

Now we describe the uncertainty sources in termA and termB one by one.

The systematic uncertainty on termA includes:

- systematic uncertainty on $< T_{\rm AA} >$ and $\sigma_{\rm NN}^{\rm inel}$ used to normalize ${\rm d}\sigma_{\rm pp}^{\mu\leftarrow{\rm HF}}/{\rm d}p_{\rm t}$. These two sources are independent with $p_{\rm t}$. We put them together and call it as the systematic uncertainty on normalization, $\sigma_{\rm Norm}$;
- systematic uncertainties on $1/N_{\rm AA}^{\rm ev}\cdot {\rm d}N_{\rm AA}^{\rm incl\ \mu}/{\rm d}p_{\rm t}$, they are:
  - misalignment, $1\%\times p_{\rm t}$ ($p_{\rm t}$ in GeV/c),
  - detector response, 3.5%,
  - 1% from the efficiency estimation via embedding;
- systematic uncertainty on ${\rm d}\sigma_{\rm pp}^{\mu\leftarrow{\rm HF}}/{\rm d}p_{\rm t}$, see Sec. 8.4.2.

To understand the sources of systematic uncertainty on termB, firstly, we put Eq. (8.23) in:

$$\begin{aligned}
{\rm termB} &= n_y \times D_{\rm AA}(p_{\rm t})\cdot R_{\rm AA}^{\mu\leftarrow\pi}(p_{\rm t}, n_y=1)\cdot\frac{1}{N_{\rm pp}^{\rm ev}}\cdot\frac{{\rm d}N_{\rm pp}^{\mu\leftarrow{\rm K}/\pi}/{\rm d}p_{\rm t}}{{\rm d}\sigma_{\rm pp}^{\mu\leftarrow{\rm HF}}/{\rm d}p_{\rm t}}\cdot\frac{< N_{\rm coll} >}{< T_{\rm AA} >}\\
&= n_y \times D_{\rm AA}(p_{\rm t})\cdot R_{\rm AA}^{\mu\leftarrow\pi}(p_{\rm t}, n_y=1)\times\frac{1/N_{\rm pp}^{\rm ev}\cdot{\rm d}N_{\rm pp}^{\mu\leftarrow{\rm K}/\pi}/{\rm d}p_{\rm t}\times\sigma_{\rm NN}^{\rm inel}}{{\rm d}\sigma_{\rm pp}^{\mu\leftarrow{\rm HF}}/{\rm d}p_{\rm t}}\\
&= n_y \times D_{\rm AA}(p_{\rm t})\cdot R_{\rm AA}^{\mu\leftarrow\pi}(p_{\rm t}, n_y=1)\cdot\frac{{\rm d}\sigma_{\rm pp}^{\mu\leftarrow{\rm K}/\pi}/{\rm d}p_{\rm t}}{{\rm d}\sigma_{\rm pp}^{\mu\leftarrow{\rm HF}}/{\rm d}p_{\rm t}}.
\end{aligned} \tag{8.43}$$

In Eq. (8.43), we use the definition:

$$< T_{\rm AA} > \equiv \frac{< N_{\rm coll} >}{\sigma_{\rm NN}^{\rm inel}}. \tag{8.44}$$

Now we discuss the systematic uncertainty on each term in Eq. (8.43) one by one.

$D_{\rm AA}$, its systematic uncertainty comes from the differences between its mean value and the values in the central and peripheral collisions, as shown in Fig. 8.33.

$R_{\rm AA}^{\mu\leftarrow\pi}(p_{\rm t}, n_y=1)$, its systematic uncertainty includes,

- systematic uncertainty on the input data from the central barrel, as shown in Fig. 8.24 and Fig. 8.25;
- systematic uncertainty on the rapidity extrapolation, the one on the factor σ_y in Eq. (7.62) and Eq. (8.18), but this uncertainty is cancelled in the ratio;

- in this case the systematic uncertainty on $R_{\rm AA}^{\mu\leftarrow\pi}(p_{\rm t}, n_y = 1)$ only includes the one from the input K/π spectra from the central barrel.

$\mathrm{d}\sigma_{\rm pp}^{\mu\leftarrow{\rm K}/\pi}/\mathrm{d}p_{\rm t}$, the systematic uncertainty includes:

- systematic uncertainty on the input data from the central barrel;
- systematic uncertainty on σ_y for the rapidity extrapolation;
- 15% on the absorber effect estimate in Eq. (8.21) [8].

Of course, in termB the systematic uncertainty on $\mathrm{d}\sigma_{\rm pp}^{\mu\leftarrow{\rm HF}}/\mathrm{d}p_{\rm t}$ is also included.

Note that, Eq. (8.43) does not include $<_{\rm AA}>$ and the uncertainty on $\sigma_{\rm NN}^{\rm inel}$ is canceled in the ratio:

$$\frac{\mathrm{d}\sigma_{\rm pp}^{\mu\leftarrow{\rm K}/\pi}/\mathrm{d}p_{\rm t}}{\mathrm{d}\sigma_{\rm pp}^{\mu\leftarrow{\rm HF}}/\mathrm{d}p_{\rm t}}. \tag{8.45}$$

In this case, termB is independent with the systematic uncertainty on normalization $\sigma_{\rm Norm}$. To treate $\sigma_{\rm Norm}$ in an universal way, we recalculate it as:

$$\sigma_{\rm Norm}^{\rm R} = \frac{\sigma_{\rm Norm}}{\mathrm{termA} - \mathrm{termB}|_{n_y=1}}. \tag{8.46}$$

We use $n_y = 1$ to calculate the central values of the results and the integrated values (in $4 < p_{\rm t} < 10$ GeV/c) are used to calculate the ratios in termA and termB in Eq. (8.46), respectively.

Also, one can see that the term $\mathrm{d}\sigma_{\rm pp}^{\mu\leftarrow{\rm HF}}/\mathrm{d}p_{\rm t}$ is present in both termA and termB. If we propogate the errors on termA and termB independently, the error on $\mathrm{d}\sigma_{\rm pp}^{\mu\leftarrow{\rm HF}}/\mathrm{d}p_{\rm t}$ will be double counted. To avoid this and also for including the uncertainty on the factor n_y, the following strategy is used.

In both differential and integrated $R_{\rm AA}^{\mu\leftarrow{\rm HF}}$ we use $n_y = 1$ to calculate the central values, $R_{\rm AA}^{\mu\leftarrow{\rm HF}}(n_y = 1)$.

In the integrated $R_{\rm AA}^{\mu\leftarrow{\rm HF}}$, the systematic uncertainty on $\mathrm{d}\sigma_{\rm pp}^{\mu\leftarrow{\rm HF}}/\mathrm{d}p_{\rm t}$ is separated from other uncertainty sources and combined with $\sigma_{\rm Norm}^{\rm R}$ (defined in Eq. (8.46)) together and called the "correlated uncertainty". The remaining part of the uncertainty called the "uncorrelated uncertainty" is estimated via the following steps:

1. get the maximum and minimum values of $R_{\rm AA}^{\mu\leftarrow{\rm HF}}$, the $R_{\rm max}$ and $R_{\rm min}$ according to the range of n_y;

2. calculate the value of $R_{\rm AA}^{\mu\leftarrow{\rm HF}}(n_y = 1)$ and the corresponding uncertainties $\sigma_{\rm upper}^{\rm C}$ and $\sigma_{\rm lower}^{\rm C}$ according to all uncorrelated uncertainty sources defined above, the systematic uncertainty on $\mathrm{d}\sigma_{\rm pp}^{\mu\leftarrow{\rm HF}}/\mathrm{d}p_{\rm t}$ was separated from other so there is no double counting in the calculation of $\sigma_{\rm upper}^{\rm C}$ and $\sigma_{\rm lower}^{\rm C}$;

[8] This systematic uncertainty is estimated by varying the cut value in Eq. (8.21) from 110 cm to 150 cm, and it changes the yields of both muons from kaon and pion decays in $\sim 15\%$. But the value of $R_{\rm AA}^{\mu\leftarrow\pi}(p_{\rm t}, n_y = 1)$ does not change while varying the value of this cut.

3. the upper and lower error bars on n_y estimate are,

$$\begin{aligned}\sigma^{\mathrm{Q}}_{\mathrm{upper}} =& R_{\mathrm{max}} - R^{\mu\leftarrow\mathrm{HF}}_{\mathrm{AA}}(n_y = 1)\\ \sigma^{\mathrm{Q}}_{\mathrm{lower}} =& R^{\mu\leftarrow\mathrm{HF}}_{\mathrm{AA}}(n_y = 1) - R_{\mathrm{min}};\end{aligned} \tag{8.47}$$

4. the total uncertainties with respect to the central values are given by the **Central Limit Theorem**,

$$\begin{aligned}\sigma_{\mathrm{upper}} =& \sqrt{(\sigma^{\mathrm{C}}_{\mathrm{upper}})^2 + (\sigma^{\mathrm{Q}}_{\mathrm{upper}})^2}\\ \sigma_{\mathrm{lower}} =& \sqrt{(\sigma^{\mathrm{C}}_{\mathrm{lower}})^2 + (\sigma^{\mathrm{Q}}_{\mathrm{lower}})^2}.\end{aligned} \tag{8.48}$$

For the differential $R^{\mu\leftarrow\mathrm{HF}}_{\mathrm{AA}}(p_{\mathrm{t}})$, the uncertainty on $\mathrm{d}\sigma^{\mu\leftarrow\mathrm{HF}}_{\mathrm{pp}}/\mathrm{d}p_{\mathrm{t}}$ is propagated with $\sigma^{\mathrm{C}}_{\mathrm{upper}}$ and $\sigma^{\mathrm{C}}_{\mathrm{lower}}$ together (also called $\sigma^{\mathrm{C}}_{\mathrm{upper}}$ and $\sigma^{\mathrm{C}}_{\mathrm{lower}}$). For the error propagation, we just use the uncertainty on $\mathrm{d}\sigma^{\mu\leftarrow\mathrm{HF}}_{\mathrm{pp}}/\mathrm{d}p_{\mathrm{t}}$ once, such that there is also no double counting. Then, using Eq. (8.48) we get the p_{t} dependent σ_{upper} and σ_{lower}. Finally, we put the re-calculated systematic uncertainty on normalization defined in Eq. (8.46) independently, as a fraction of percentage with respect to the integrated $R^{\mu\leftarrow\mathrm{HF}}_{\mathrm{AA}}(n_y = 1)$.

8.7 Results

After all these steps, now it is time to show our final results. We start with a short discussion about the inclusive muon R_{CP} then, we focus on the results of R_{AA} of muons from heavy flavour decays in the forward rapidity region.

8.7.1 R_{CP} of Inclusive Muons

With the last input of the correction efficiency, we are ready to get the R_{AA} of muons from open heavy flavour decays. Do not be too excited, cowboys, please come down! As usual, before to present the final results, it is worth to make a short discussion.

The R_{AA} is the ratio between the spectra in Pb–Pb collisions and that in pp collision scaled by the number of binary collisions. If there is no nuclear effect, the value of R_{AA} should be unity. The deviation between the measured values of R_{AA} and unity reflects the nuclear effects. In this case, R_{AA} is a very powerful observable to study the properties of the QCD medium formed in heavy ion collisions by researching how they affect the particles passing through it. We can imagine that, when the collision centrality becomes more and more peripheral, nuclear effects will become and more weak to approach the limiting case: pp collisions where there is no nuclear effect. In these conditions, the nuclear effects can also be reflected by the ratio between the spectra in central collisions and that in a peripheral centrality bin after the normalization with the number of binary collisions in both of them. This ratio is the so called central-to-peripheral ratio (R_{CP}) and can be calculated as:

$$R_{\mathrm{CP}} = \frac{1/T_{\mathrm{AA}} \times \mathrm{d}N/\mathrm{d}p_{\mathrm{t}}|_{\mathrm{central}}}{1/T_{\mathrm{AA}} \times \mathrm{d}N/\mathrm{d}p_{\mathrm{t}}|_{\mathrm{peripheral}}}. \tag{8.49}$$

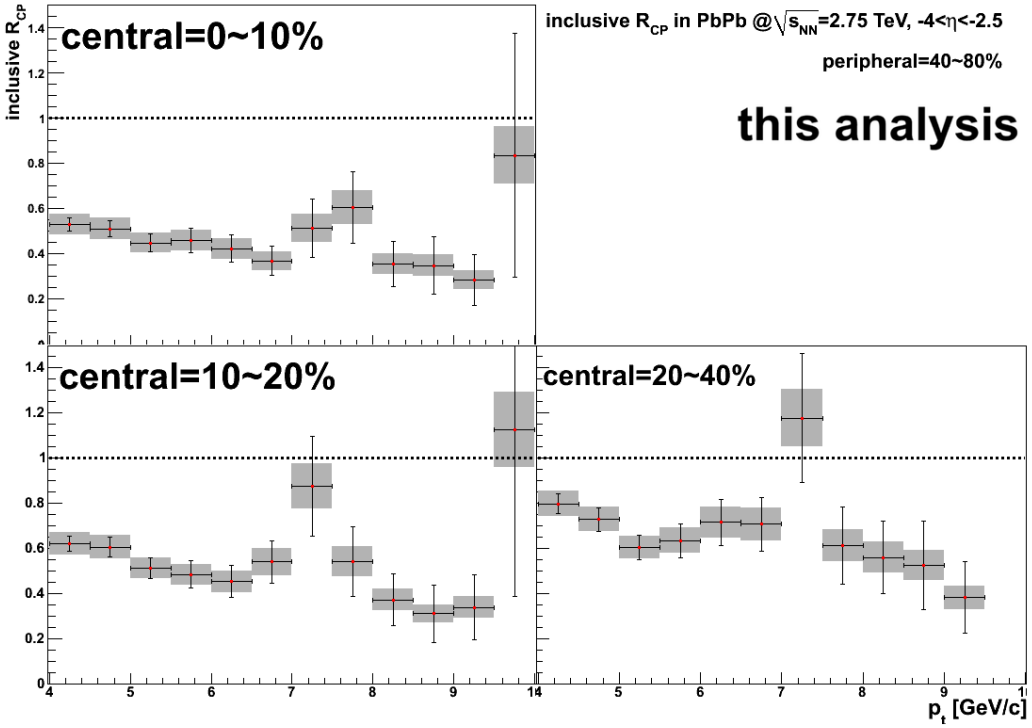

Figure 8.36: R_{CP} of inclusive muons as a function of p_{t} in different centrality regions in Pb–Pb collisions at $\sqrt{s_{\mathrm{NN}}} = 2.76$ TeV. The reference is provided by the centrality region $40 - 80\%$. The results are gotten from LHC10h pass 2 data.

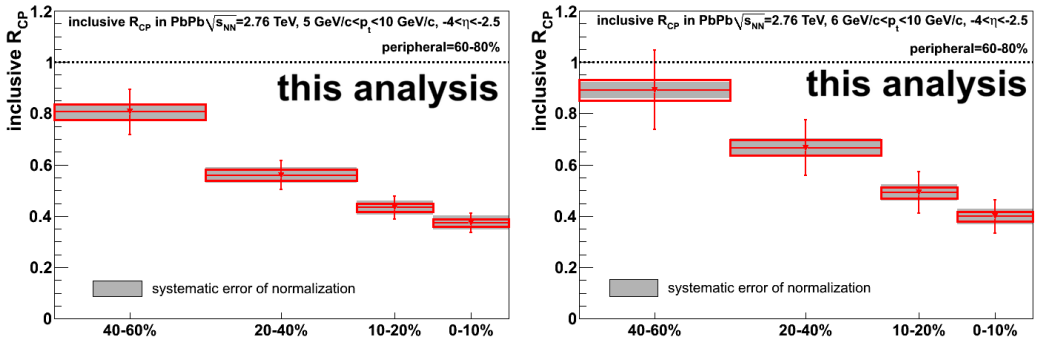

Figure 8.37: R_{CP} of inclusive muons as a function of the centrality percentage in $p_{\mathrm{t}} > 5$ GeV/c (left) and $p_{\mathrm{t}} > 6$ GeV/c (right) in Pb–Pb collisions at $\sqrt{s_{\mathrm{NN}}} = 2.76$ TeV. The reference is the centrality region $60 - 80\%$. The results are gotten from LHC10h pass 2 data.

The advantage of R_{CP} is that, the bias on the detector response and that on the T_{AA} estimate is partly canceled in this ratio.

The p_{t}-differential R_{CP} of inclusive muons after the standard muon selection

cuts in $p_t > 4$ GeV/c and three different centrality bins is shown in Fig. 8.36. Due to the statistics limitation, here the peripheral reference bin is chosen as the centrality class $40-80\%$. The grey boxes present the systematic uncertainties on the inclusive muon p_t spectra: $1\% \times p_t$ on misalignment and 3.5% on detector response. The strong suppression of R_{CP} in the most central collisions $(0-10\%)$ indicates strong quenching effects. The clear increase of the values of the R_{CP} with the centrality percentage indicates that the quenching effects are reduced when the collisions become more and more peripheral.

Alternatively, to investigate the evolution of the values of R_{CP} with the collision centrality more clearly, we present the integrated R_{CP} as a function of the centrality percentage in $p_t > 5$ GeV/c and $p_t > 6$ GeV/c in the left and right plots of Fig. 8.37, repectively. Since we integrated the p_t spectra, the statistics is sufficient to choose the peripheral reference bin as $60-80\%$. Differently from Fig. 8.36, here the systematic uncertainties on the muon p_t spectra are shown as the red boxes and the grey boxes are used to show the systematic uncertainty on T_{AA} listed in Tab. 8.1. The integrated R_{CP} decreases with the centrality percentage and the same conclusion as that of Fig. 8.36 can be made. But, due to the higher p_t cuts than that in Fig. 8.36, the values better reflect the evolution of the suppression for muons from open heavy flavour decays with the collision centrality.

8.7.2 R_{AA} of Muons from Heavy Flavour Decays

The results of R_{AA} as a function of p_t for muons from open heavy flavour decays in centrality classes $0-10\%$ and $40-80\%$ measured in the ALICE muon spectrometer in Pb–Pb collisions at $\sqrt{s_{NN}} = 2.76$ TeV are shown in the left and right plots of Fig. 8.38, respectively. The central values (full symbols) and the p_t dependent asymmetric systematic errors (empty boxes) are gotten according to the above strategy. The vertical error bars are the statistical uncertainty. The relative systematic uncertainty on the normalization is shown as the grep boxes (plotted at $R_{AA} = 1$) in these two given centrality regions. To validate Eq. (8.17) for estimating the nuclear effects of decay muons in the forward region, the results are only shown in $p_t > 4$ GeV/c. In this figure, a larger suppression is observed in central collisions than in peripheral collisions, with no significant p_t dependence within uncertainties.

Fig. 8.39 shows the centrality dependence of the R_{AA} for the muons from open heavy flavour decays in the acceptance of muon spectrometer in $6 < p_t < 10$ GeV/c. The analysis is carried out in five centrality classes from $0-10\%$ to $60-80\%$ listed in the first five rows in Tab. 8.1. The results are depicted as a function of $< N_{part} >$. As in Fig. 8.38, the central values of the results are gotten with $n = 1$. The suppression of forward heavy flavour decay muons exhibits a strong increase with increasing centrality, reaching a factor of about $3-4$ in the 10% most central collisions. This indicates a strong quenching effect of heavy quarks in the QCD medium in the forward rapidity region. In both Fig. 8.38 and Fig. 8.39 the systematic uncertainties are shown as discussed in Sec. 8.6.2.

A paper related to the work presented in this chapter has been published in **Physical Review Letters** and it is in Appendix B.

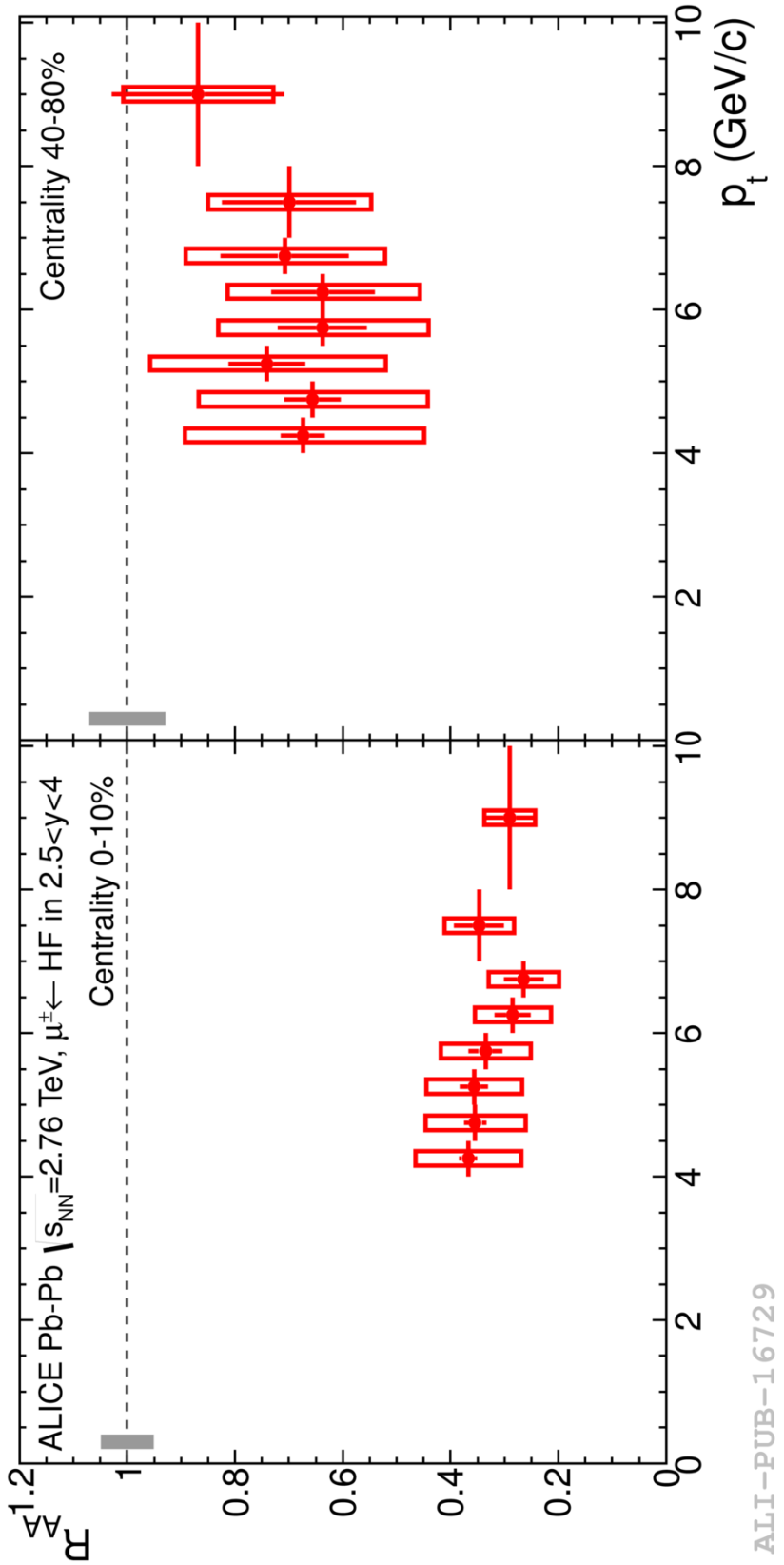

Figure 8.38: R_{AA} as a function of p_t for muons from open heavy flavour decays in centrality classes $0-10\%$ (upper) and $40-80\%$ (lower) measured in ALICE muon spectrometer in Pb–Pb collisions at $\sqrt{s_{NN}} = 2.76$ TeV [332], see the text for more details.

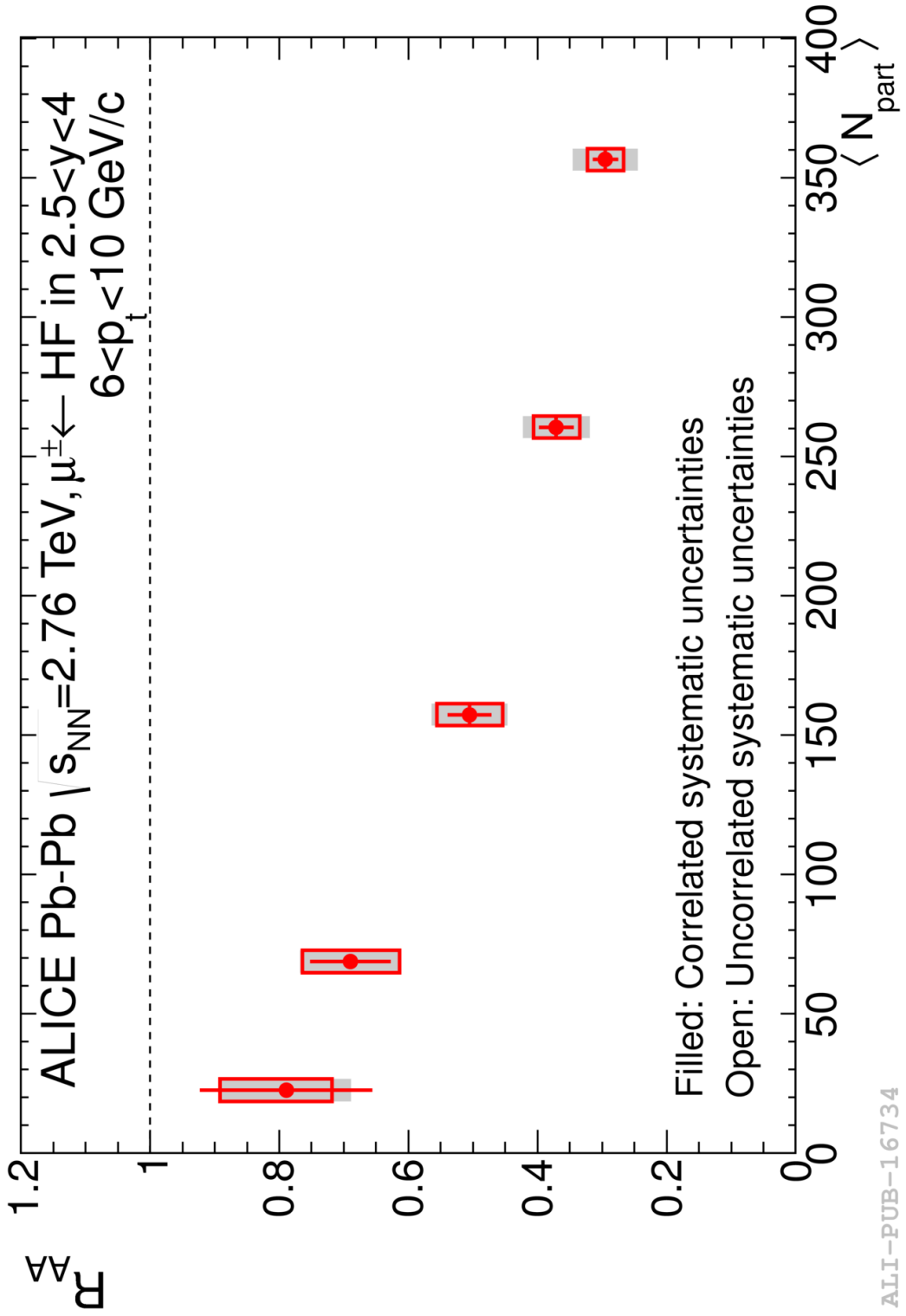

Figure 8.39: R_{AA} of muons from open heavy flavour decays as a function of centrality measured in the acceptance of the ALICE muon spectrometer in Pb–Pb collisions at $\sqrt{s_{NN}} = 2.76$ TeV [332], see the text for more details.

8.7.3 Discussions

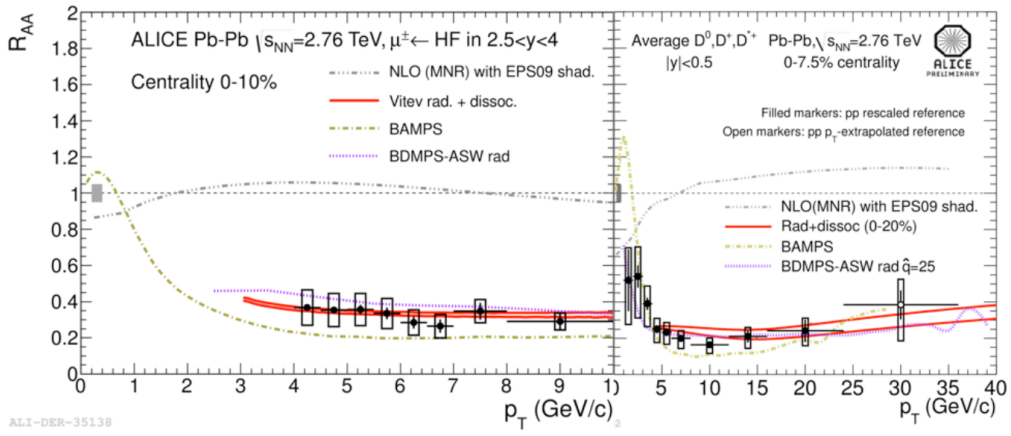

Figure 8.40: Left: $R_{\rm AA}$ of muons from heavy flavour decays as a function of $p_{\rm t}$ for the centrality $0-10\%$, which is extracted from left plot of Fig. 8.38. Right: $R_{\rm AA}$ of D-mesons as a function of $p_{\rm t}$ for the centrality in $0-7\%$ measured in ALICE central barrel ($|\eta| < 0.5$) [333]. Both results are obtained in Pb–Pb collisions at $\sqrt{s_{\rm NN}} = 2.76$ TeV and compared with the model predictions, see the text for more details.

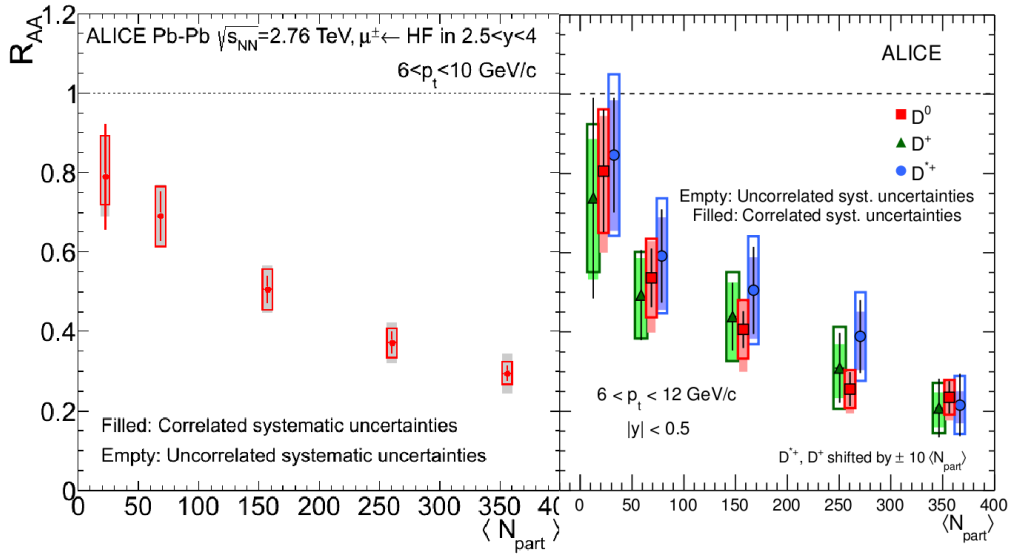

Figure 8.41: Left: $R_{\rm AA}$ of muon from heavy flavour decays as a function of centrality gotten from Fig. 8.39. Right: $R_{\rm AA}$ of D-mesons as a function of centrality measured in ALICE central barrel ($|\eta| < 0.5$) [333]. Both results are shown in $p_{\rm t} > 6$ GeV/c.

To extract more information from these final results, we compared them with

the measured results from ALICE central barrel.

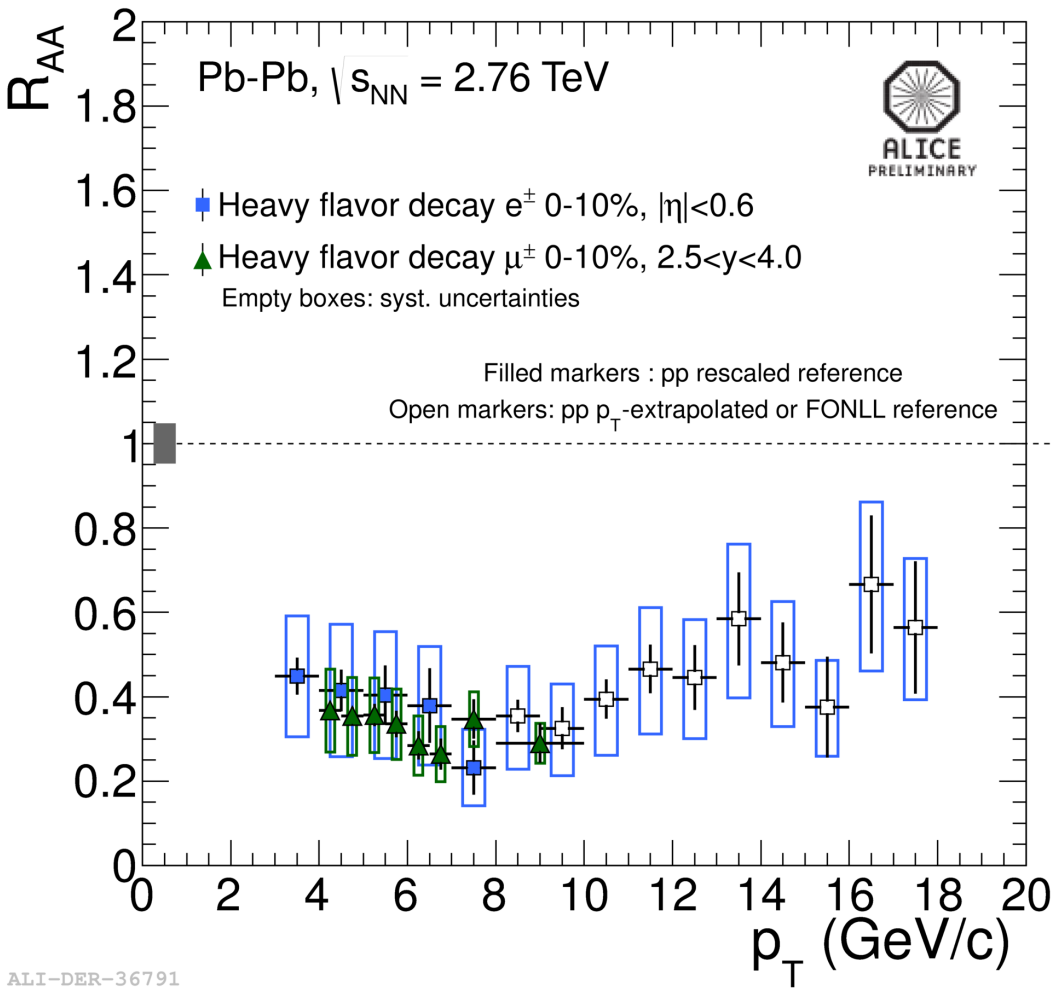

Figure 8.42: R_{AA} of muon from heavy flavour decays as a function of centrality gotten from Fig. 8.39 and that of heavy flavour electrons measured in $|\eta| < 0.6$.

Fig. 8.40 shows the R_{AA} as a function of p_{t} of muons from heavy flavour decays measured in the acceptance of the ALICE muon spectrometer and that of D-mesons measured in ALICE central barrel ($|\eta| < 0.5$) [333]. Both results are obtained in in Pb–Pb collisions at $\sqrt{s_{\mathrm{NN}}} = 2.76$ TeV. Also, different model predictions: "Vitev rad.+dissoc." [334], "BAMPS" [335] and "BDMPS-ASW rad." [222], are compared with both results from heavy flavour muons at forward rapidity and D-mesons at central rapidity. The models implementing radiative energy loss ("BDMPS-ASW") and radiation plus dissociation mechanisms ("Vitev") can describe both muon and D meson data. Within errors, we can find that, the suppresion of heavy flavours at muon level at forward rapidity and that at hadron level at mid-rapidity are consistent. In addition, the predictions from EPS09 [55] shows in Fig. 8.40 indicate that the shadowing effect on heavy flavour production in the forward region is ex-

pected to be small. In Fig. 8.41, we campare the $R_{\rm AA}$ as a function of centrality of muons from heavy flavour decays and that of D-mesons. Both results are shown in $p_{\rm t} > 6$ GeV/c. Even if the associated $p_{\rm t}$ of heavy quarks in these two measurements are not the same, within errors we find again a nice agreement between these two results.

Finally, we make the comparison between the results from forward rapidity and those from central rapidity more directly, as shown in Fig. 8.42. This figure shows the $R_{\rm AA}$ of muons from heavy flavour decays as a function of centrality, gotten from Fig. 8.39, and that of heavy flavour electrons measured in $|\eta| < 0.6$. The $R_{\rm AA}$ is shown in both cases at lepton level. We can clearly find that, these two results are in agreement within errors.

After all of these comparisons, we can conclude that, a strong suppression of high $p_{\rm t}$ muons from heavy flavour decays is observed at forward rapidity, in the most central collisions. The measured suppression is insensitive with $p_{\rm t}$ in $4 < p_{\rm t} < 10$ GeV/c. It is compatible with that of electrons from heavy flavour decays and D-mesons at central rapidity.

Chapter 9

Elliptic Flow of Muons in Pb–Pb Collisions at $\sqrt{s_{\rm NN}} = 2.76$ TeV

The study of the $R_{\rm AA}$ of muons from open heavy flavour decays is described in the previous chapter. But before we go through this chapter, let us go back to the beginning of Chap. 8, where the time schedule for the analysis of $R_{\rm AA}^{\mu\leftarrow{\rm HF}}$ is listed. This schedule shows that there was no activity during the summer of 2011. At that time, I was not in summer vacation but did some analyses for the elliptic flow of inclusive muons in Pb–Pb collisions with the ALICE muon spectrometer. This is what we are going to report about in this chapter. The physics motivations of the flow measurement are described in Sec. 1.4.3.1 and Sec. 2.2.3.4. Our aim here is:

- validate the flow analysis methods for muons at forward region;
- study the background subtraction strategy in the flow analysis in order to obtain the flow of muons from open heavy flavour decays.

The data sample used here is the same as that used for $R_{\rm AA}^{\mu\leftarrow{\rm HF}}$ study: LHC10h pass 2 data which correspond to Pb–Pb collisions at $\sqrt{s_{\rm NN}} = 2.76$ TeV.

The basic issues of the LHC10h pass 2 data (like physics and centrality selections, and muon QA) were discussed in Chap. 8. Here we focus on the elliptic flow analysis of inclusive muons. In the following a short overview of the principles for general flow analysis methods will be discussed first. Then we implement these methods for data analysis after taking into account our experimental constraints. Finally, the strategy for the extraction of the elliptic flow of muons from open heavy flavour decays as well as the outlook of this work will be presented.

9.1 Flow Analysis Methods

The collective flow observables have been measured with data since 1980's. Since then, different flow analysis methods have been developed. Flow analysis methods available in the early days can be classified into two different categories:

- fit the $p_{\rm t}$ or rapidity distributions of the particles of interest by assuming a local thermal equilibrium and a hydrodynamical evolution of the considered system. By doing so, information about the initial conditions, the EOS, the dynamics of the system expansion and the freeze-out temperature *etc.* can be extracted (*eg.* Ref. [327]). This approach, of course, strongly depends on model assumptions;

- the alternative way is based on the study of the azimuthal event shapes from experimental data without any model. Some commonly used methods in this category are directivity tensor [336], three dimensional [337] and two dimensional [338] sphericity analyses.

Nowadays, more flow analysis methods from the second category are available. These can be sorted out into two classes i) calculate the collective flow from definitions and ii) extract the flow signal in data according to the correlation behavior of the flow. Before implementing these methods in data analysis, in the following we will give a short general introduction on their principle.

9.1.1 Event Plane Method

In the **Event Plane** (**EP**) method [339], the collective flow is calculated directly from the data following the definitions in Eq. (1.15) and Eq. (1.16). Some typical issues in flow analysis can be illustrated with this method. So in this introduction, we do not follow the history of the developments for flow analyses, but we start with the event plane method.

9.1.1.1 Event Plane

First, let us go back to Eq. (1.15), and do its Fourier expansion in an alternative way. Generally, the particle invariant spectrum can be written as:

$$E\frac{\mathrm{d}^3N}{\mathrm{d}p^3} = \frac{\mathrm{d}^3N}{p_\mathrm{t}\mathrm{d}p_\mathrm{t}\mathrm{d}y\mathrm{d}\phi} = \frac{\mathrm{d}^2N}{p_\mathrm{t}\mathrm{d}p_\mathrm{t}\mathrm{d}y}\cdot r(p_\mathrm{t},y,\phi), \tag{9.1}$$

where the function $r(p_\mathrm{t},y,\phi)$ should satisfy the normalization condition,

$$\int_0^{2\pi}\mathrm{d}\phi\cdot r(p_\mathrm{t},y,\phi) = 1. \tag{9.2}$$

The Fourier expansion for $r(p_\mathrm{t},y,\phi)$ is:

$$r(p_\mathrm{t},y,\phi) = \frac{1}{2\pi}[1+2\cdot\sum_{n=1}^{\infty}(Q_X(p_\mathrm{t},y,n)\cos n\phi + Q_Y(p_\mathrm{t},y,n)\sin n\phi)], \tag{9.3}$$

where,

$$\begin{aligned} Q_X(p_\mathrm{t},y,n) &= \int_0^{2\pi}\mathrm{d}\phi\cdot r(p_\mathrm{t},y,\phi)\cos n\phi, \\ Q_Y(p_\mathrm{t},y,n) &= \int_0^{2\pi}\mathrm{d}\phi\cdot r(p_\mathrm{t},y,\phi)\sin n\phi. \end{aligned} \tag{9.4}$$

In each phase space of p_t, y and n, one can define the Q-**Vector**:

$$\vec{Q}(p_\mathrm{t},y,n) = \{Q_X(p_\mathrm{t},y,n), Q_Y(p_\mathrm{t},y,n)\} = \{V_n(p_\mathrm{t},y), n\Psi_n\}, \tag{9.5}$$

with

$$\begin{aligned} Q_X(p_\mathrm{t}, y, n) &= V_n(p_\mathrm{t}, y)\cos n\Psi_n, \\ Q_Y(p_\mathrm{t}, y, n) &= V_n(p_\mathrm{t}, y)\sin n\Psi_n. \end{aligned} \tag{9.6}$$

Then, Eq. (9.3) becomes:

$$r(p_\mathrm{t}, y, \phi) = \frac{1}{2\pi}[1 + \sum_{n=1}^{\infty} 2V_n(p_\mathrm{t}, y)\cos n(\phi - \Psi_n)]. \tag{9.7}$$

Finally, putting Eq. (9.7) back into Eq. (9.1), one can get:

$$E\frac{\mathrm{d}^3N}{\mathrm{d}p^3} = \frac{\mathrm{d}^2N}{2\pi p_\mathrm{t}\mathrm{d}p_\mathrm{t}\mathrm{d}y} \cdot [1 + 2V_n(p_\mathrm{t}, y)\cos n(\phi - \Psi_n)]. \tag{9.8}$$

By comparing Eq. (9.8) and Eq. (1.15), one can see that Ψ_n here plays the same role as the reaction plane Ψ_R in Eq. (1.15), and it called the n-th order **Event Plane**. In order to determine the event plane Ψ_n in a given event, the following steps have to be considered:

1. since the number of particles in each event is finite, Eq. (9.4) becomes:

$$\begin{aligned} Q_X(p_\mathrm{t}, y, n) &= \sum_j^M r(p_\mathrm{t}, y, \phi_j)\cos n\phi_j, \\ Q_Y(p_\mathrm{t}, y, n) &= \sum_j^M r(p_\mathrm{t}, y, \phi_j)\sin n\phi_j, \end{aligned} \tag{9.9}$$

   where M is the number of particles used to calculate the Q-vector;

2. according to Eq. (9.6), the n-th order event plane is:

$$\Psi_n = \frac{1}{n} \cdot \arctan \frac{\sum_{j=1}^M r(p_\mathrm{t}, y, \phi_j)\sin n\phi_j}{\sum_{j=1}^M r(p_\mathrm{t}, y, \phi_j)\cos n\phi_j}. \tag{9.10}$$

Similarly to Eq. (1.16), with the calculated event plane for each event according to Eq. (9.10), the collective flow becomes

$$v_n = < \cos n(\phi - \Psi_n) >, \tag{9.11}$$

and it is averaged over both particles and events.

Eq. (9.10) and Eq. (9.11) contain basic principle of the event plane method. Now we are going to discuss some issues related to these two formulae which are also of general interest for all other flow analysis methods.

9.1.1.2 Particles of Interest and Reference Particles

By comparing Eq. (9.8) and Eq. (1.15), one can observe that not only the event plane plays the same role as reaction plane, but also V_n, which can be calculated as

$$V_n(p_t, y) = \sqrt{Q_X^2(p_t, y, n) + Q_Y^2(p_t, y, n)}. \tag{9.12}$$

According to Eq. (9.6), $V_n(p_t, y)$ plays the same role as the n-th order collective flow parameter v_n. The latter is the signal that one wants to extract from data. So, what is the difference between V_n in Eq. (9.8) and v_n in Eq. (9.11) or Eq. (1.16)?

In Sec. 1.4.3.1 we emphasized that, the invariant distribution from Eq. (1.15) is related to the **Particles of Interest** (**POI**) which is the signal. On the other hand, the invariant distribution in Eq. (9.1) concerns the particles used to determine the event plane via Eq. (9.10). Due to the fact that the reaction plane is determined by the collision geometry in the early stage, the measured event plane should be insensitive to the particle sample which is used for its measurement. However, if the event plane is measured using the POI, then the correlations between the POI and the event plane will bias the results for the collective flow. Normally, to avoid this auto-correlation effect, the POI are excluded from the sample of particles which are used to determine the event plane. These particles are called as **Reference Particles** (**RP**).

The POI and RP are two very important concepts in flow analyses. They have to be separated from each other at the beginning in almost all flow analysis methods. The general principle for separating the POI and RP is to consider different particle species and/or kinematical regions. For example, if one wants to measure the flow of charged kaons, the POI will be $K^{\pm}$. One can then choose other particle species for the RP, like charged pions, to determine the event plane. If the POI is all charged particles measured in the central rapidity region, the RP can be chosen as the measured particles at forward rapidities. In these cases, one removes the correlation between the POI and the measured event plane.

Since the event plane is independent on p_t and rapidity, the calculation of the Q-vector in Eq. (9.9) should not be done in each p_t and rapidity regions, and V_n in Eq. (9.12) is generally independent on p_t and rapidity. V_n is the flow of RP and is called **Reference Flow**. It gives the reference direction for calculating the flow of POI [1]. Due to the fact that V_n is independent on p_t and rapidity, in some of the flow analysis methods, it is also named **Integrated Flow** and the flow of POI is named **Differential Flow**.

9.1.1.3 Discussion

For a given event the orientation of the reaction plane Ψ_R is fixed, and should therefore not change with different analysis conditions. A precise value of Ψ_R is difficult to extract from data. On the other hand, the n-th order event plane Ψ_n, which can be measured via final state observables according to Eq. (9.10), plays the

[1] Indeed, in the phase space of Q-vector, this reference direction is the position of event plane.

role of the reaction plane for the n-th order harmonic in the Fourier expansion. This does not mean that the value of $\Psi_{\rm R}$ and that of Ψ_n should be the same. Using Ψ_n instead of $\Psi_{\rm R}$ can be done only if they satisfy the condition:

$$\begin{aligned} &\cos n(\phi - \Psi_{\rm R}) = \cos n(\phi - \Psi_n) \\ \Rightarrow &n(\phi - \Psi_n) + 2k\pi = n(\phi - \Psi_{\rm R}) \\ \Rightarrow &\Psi_n = \Psi_{\rm R} + 2\frac{k}{n}\pi, \end{aligned} \tag{9.13}$$

where both n and k are positive integers. This means that in a given event, the choice of the n-th order event plane is not unique.

Determination of v_n via Lower Order Harmonic The n-th order collective flow can also be calculated with the m-th order event plane if,

$$n = l \cdot m, \tag{9.14}$$

with positive integers l, m and n via:

$$\begin{aligned} v_n =& < \cos n(\phi - \Psi_{\rm R}) > \\ =& < \cos lm(\phi - \Psi_m + 2\frac{k}{m}\pi) > \\ =& < \cos[lm(\phi - \Psi_m) + kl \cdot 2\pi] > \\ =& < \cos lm(\phi - \Psi_m) > . \end{aligned} \tag{9.15}$$

This is general to most of the flow analysis methods. The n-th order differential flow can be calculated with the m-th order of Q-vector or the integrated flow if m and n satisfy the relation Eq. (9.14). However, in most of the flow analysis methods, the uncertainty on the final results increases with the factor l in Eq. (9.14) [2]. To minimize the uncertainty, usually $l = 1$ is used (both the differential flow and the integrated flow have the order of harmonic). The advantage to use the m-th order harmonic to determine the n-th order of flow is that in most of the flow analysis methods, the uncertainty σ and the used statistics M follow [3],

$$\sigma^{\alpha} \propto \frac{1}{M}, \tag{9.16}$$

[2] With the event plane method, the factor l mainly affects the event plane resolution.

[3] The estimate of the systematic uncertainty for different flow analysis methods is very complicated and we will not go through the details. The general sources of uncertainties are:

- fluctuations caused by the finite statistics;
- non-flow correlations like jets, resonance decays *etc.*;
- non-uniform acceptance correlations.

Some of them can be partly removed by implementing cuts in the analysis, like: choose particles with $p_{\rm t}$ less than a given value helps to remove correlations from mini-jets; set a rapidity gap is used to reject correlations from resonance decays. In parallel, correlations due to the non-uniform acceptance can be treated by efficiency corrections.

where α is a positive real number because of the finite number of used particles M per event. Also, the magnitude of flow normally decreases with the harmonic order n, then the relative uncertainty σ/v_n will increase when the harmonic order becomes higher. If the harmonic of the differential flow n is high, and the multiplicity M of RP is not sufficient, then, the lower order harmonic m to determine the n-order flow can be used to decrease the total uncertainty on the final results.

Particle Weights An alternative way, also commonly used in most of the flow analysis methods to reduce the uncertainty on the flow signal, is to apply particule weights. According to its definition, the factor r in Eq. (9.9) should satisfy the normalization condition Eq. (9.2). However, one can find that, even if the factor r is not normalized, it cancels out in the ratio of Eq. (9.10) and this has no effect on the event plane determination. Indeed, the Q-vector is a general observable in different flow analysis methods as it includes the information of both the integrated flow and the orientation of the event plane. Then, according to Eq. (9.6), both Q_X and Q_Y are proportional to V_n. In most of the flow analysis methods, the Q-vector is calculated by using as weight variables which are proportional to V_n in order enhance its magnitude. For instance, in the low p_{t} region, since $v_2 \propto p_{\mathrm{t}}$, p_{t} can be used as a particle weight to calculate the elliptic flow and $r_j = p_{\mathrm{t}}(\phi_j)$. In low-energy collisions, $v_1 \propto \eta$. In this case, $r_j = \eta(\phi_j)$ is used to calculate the directed flow. After the weighting, the Q-vector can always be normalized according to the used weights (in the case of the event plane method, as already mentioned, the normalization factor resulting from the particle weights naturally cancel out in the ratio of Eq. (9.10)). Also, particle weights are not applied to RP to calculate the Q-vector but they also can be used for POI. In the event plane method, with the POI weights w_j, Eq. (9.11) becomes:

$$v_n = \frac{\sum_j w_j \cos n(\phi_j - \Psi_n)}{\sum_j w_j}. \tag{9.17}$$

Event Plane Resolution All above discussions are valid in the context of ideal experimental conditions: fluctuations due to finite number of particles, non-flow correlations and effects related to **Non-Uniform Acceptance** (**NUA**) were not taken into account. In data, the above effects will bias the final results. Therefore, with the event plane method, the event plane determination and Eq. (9.13) are not validate anymore. It becomes:

$$\Psi_n = \Delta\Psi + \Psi_{\mathrm{R}} + 2\frac{k}{n}\pi, \tag{9.18}$$

where $\Delta\Psi$ is the difference between the measured event plane orientation and the real one. It also results a difference between the measured flow,

$$v_n^{\mathrm{meas}} = < \cos n(\phi - \Psi_m) > \tag{9.19}$$

and the real flow,

$$v_n^{\mathrm{real}} = < \cos n(\phi - \Psi_{\mathrm{R}}) > . \tag{9.20}$$

With the relation in Eq. (9.18), one can get:

$$\begin{aligned} v_n^{\rm meas} &= < \cos n(\phi - \Psi_m) > \\ &= < \cos n(\phi - \Psi_{\rm R} - \Delta\Psi) > \\ &= < \cos n(\phi - \Psi_{\rm R}) \cos n\Delta\Psi - \sin n(\phi - \Psi_{\rm R}) \sin n\Delta\Psi > \\ &= < \cos n(\phi - \Psi_{\rm R}) \cos n(\Psi_m - \Psi_{\rm R}) > \\ \Rightarrow v_n^{\rm real} &= \frac{v_n^{\rm meas}}{< \cos n(\Psi_m - \Psi_{\rm R}) >}, \end{aligned} \tag{9.21}$$

with $< \sin n(\phi - \Psi_{\rm R}) >= 0$. $< \cos n(\Psi_m - \Psi_{\rm R}) >$ is called the event plane resolution. Eq. (9.21) shows that to get the real flow, the results using the event plane method should be corrected by the event plane resolution. This correction always increases the measured flow because $\cos n(\Psi_m - \Psi_{\rm R}) < 1$. The methods used to estimate the event plane resolution will be introduced in Sec. 9.3.1.3.

9.1.2 Fit-Q and Scalar Product

The event plane method offers a direct way to calculate the flow according to the definition, but its drawbacks are:

- final results are biased by the event-by-event fluctuations, and have to be corrected by the event plane resolution;
- non-flow correlations are difficult to remove;
- further corrections should be implemented to deal with non-uniform acceptance (NUA) correlations.

The **Fit-Q** (**FQ**) and **Scalar Product** (**SP**) methods are developed to overcome part of the first two drawbacks of the event plane method. In the following, we will make a short description of these two methods. The correction for the NUA will be introduced in Sec. 9.3.1.1.

9.1.2.1 Fit-Q

The starting point of Fit-Q method is to consider a simple case assuming no flow, $V_n = 0$. In this case:

1. according to Eq. (9.6), $Q_X(n) = Q_Y(n) = 0$;
2. however, due to event-by-event fluctuations the values of $Q_X(n)$ and $Q_Y(n)$ are not zero;
3. the distributions of $Q_X(n)$ and $Q_Y(n)$ can then be treated as independent Gaussians with the same width σ according to the **Central Limit Theorem**;

4. the 2 dimension distribution of Q-vector can then be written as:

$$\begin{aligned}\frac{\mathrm{d}^2P}{\mathrm{d}\vec{Q}_n} &= \frac{\mathrm{d}P}{\mathrm{d}Q_X(n)}\cdot\frac{\mathrm{d}P}{\mathrm{d}Q_Y(n)} \\ &= \frac{1}{2\pi\sigma^2}\exp[-\frac{1}{2}(\frac{Q_X(n)}{\sigma})^2]\cdot\exp[-\frac{1}{2}(\frac{Q_Y(n)}{\sigma})^2] \\ &= \frac{1}{2\pi\sigma^2}\exp[-\frac{1}{2}\frac{Q_X^2(n)+Q_Y^2(n)}{\sigma^2}] = \frac{1}{2\pi\sigma^2}\exp[-\frac{1}{2}(\frac{V_n}{\sigma})^2].\end{aligned} \tag{9.22}$$

The last step in Eq. (9.22) shows the V_n distribution when there is no flow. Under such condition, let us calculate the expression of σ. Firstly, we separate σ_X and σ_Y. According to the definition of Eq. (9.9) one get,

$$\sigma_X^2 =< (r_j\cos n\phi_j - < Q_X(n) >)^2 >=< r_j^2\cos^2 n\phi_j > . \tag{9.23}$$

Here, $< Q_X(n) >= 0$ is used. Since the particle weights r_j and azimuthal ϕ_j are independent, Eq. (9.23) becomes:

$$\begin{aligned}\sigma_X^2 &= \frac{1}{M}\sum_j\sum_k \delta_{j,k}r_j^2\cos^2 n\phi_k \\ &= \frac{1}{M}\sum_j r_j^2\sum_k\cos^2 n\phi_k \\ &= M < r_j^2 >< \cos^2 n\phi_j >,\end{aligned} \tag{9.24}$$

where M is the number of particles used to calculate the Q-vector. Similarly, one can have

$$\sigma_Y^2 = M < r_j^2 >< \sin^2 n\phi_j > . \tag{9.25}$$

Then, following the assumption $\sigma_X = \sigma_Y$, one can get:

$$\begin{aligned}\sigma^2 = \sigma_X^2 = \sigma_Y^2 &= \frac{1}{2}(\sigma_X^2+\sigma_Y^2) \\ &= \frac{1}{2}M < r_j^2 > (< \cos^2 n\phi_j > + < \sin^2 n\phi_j >) \\ &= \frac{1}{2}M < r_j^2 >,\end{aligned} \tag{9.26}$$

where the relation,

$$\begin{aligned}&< \cos^2 n\phi_j >=< \sin^2 n\phi_j > \\ =&\frac{1}{2\pi}\int_0^{2\pi}\mathrm{d}n\phi\cos^2 n\phi = \frac{1}{2\pi}\int_0^{2\pi}\mathrm{d}n\phi\sin^2 n\phi = \frac{1}{2}\end{aligned} \tag{9.27}$$

is used in the last step.

By adding the non-vanished flow $\tilde{V}_n$ (here we also use $\tilde{V}_n$ to express the real value of the flow and use V_n to express the measured flow value), the Gaussian σ in Eq. (9.26) will not change. It only shifts the mean value in the V_n distribution Eq. (9.22) from zero to $\tilde{V}_n$. Because V_n is also the norme of Q-vector, the shift in

the mean value of V_n indeed corresponds to the shift of the mean value of Q-vector. We use $\vec{Q}_n = \{V_n, n\Psi_n\}$ to express the measured Q-vector and $\vec{Q}_n^{\mathrm{R}} = \{\tilde{V}_n, n\Psi_{\mathrm{R}}\}$ to express the real Q-vector. Then Eq. (9.22) becomes:

$$\begin{aligned}
&\frac{\mathrm{d}^2P}{\mathrm{d}\vec{Q}_n} = \frac{\mathrm{d}^2P}{V_n \mathrm{d}V_n \mathrm{d}n\Psi_n} \\
=&\frac{1}{2\pi\sigma^2}\exp[-\frac{1}{2}(\frac{\vec{Q}_n - \vec{Q}_n^{\mathrm{R}}}{\sigma})^2] \\
=&\frac{1}{2\pi\sigma^2}\exp[-\frac{1}{2}\frac{V_n^2 + \tilde{V}_n^2 - 2V_n\tilde{V}_n\cos n(\Psi_n - \Psi_{\mathrm{R}})}{\sigma^2}] \\
\Rightarrow&\frac{\mathrm{d}P}{V_n\mathrm{d}V_n} = \int_0^{2\pi}\mathrm{d}n(\Psi_n - \Psi_{\mathrm{R}})\frac{\mathrm{d}^2P}{V_n\mathrm{d}V_n\mathrm{d}n\Psi_n} \\
=&\frac{1}{\sigma^2}\exp[-\frac{V_n^2 + \tilde{V}_n^2}{2\sigma^2}]\cdot \mathrm{I}_0(\frac{V_n\tilde{V}_n}{\sigma^2}),
\end{aligned} \tag{9.28}$$

where $\mathrm{I}_0(x)$ is the modified Bessel function. In data, the real values of the differential flow $\tilde{V}_n(p_{\mathrm{t}}, y)$ can be obtained by fitting the event-by-event V_n distribution in different p_{t} and rapidity windows with Eq. (9.28) and using $\tilde{V}_n$ and σ as the fit parameters.

Since V_n is the norme of Q-vector, this method is named as **Fit-Q** [67]. The advantage of the Fit-Q method, compared to the event plane method, is that it allows to extract the flow signal according to the event-by-event fluctuations and it avoids to apply corrections resulting from the event plane resolution. However, its disadvantages are:

- the RP and POI are not separated. Auto-correlations between the particles used to calculated the Q-vector in each event will bias the final results. Also, if the statistics for the POI is small, the uncertainty from the fit will be large;
- σ in Eq. (9.26) only includes the contribution from the event-by-event fluctuations. Non-flow and NUA correlations need to be further corrected in the final results.

9.1.2.2 Scalar Product

The Scalar Product (SP) method [339] follows the idea of the event plane method. The advantage of this method is that it automatically takes into account (part of) both event-by-event fluctuations and non-flow correlations.

Principle The first step of the scalar product method is to separate the RP in each event into two equivalent sub-events with the same multiplicity. There are two general ways to build the sub-events:

- choose RP in two symmetrical η windows: $[\eta_{\min}, \eta_{\max}]$ and $[-\eta_{\max}, -\eta_{\min}]$ and leave a η gap $\Delta\eta = 2\cdot\eta_{\min}$ between these two sub-events. These kinds of sub-events are called η **sub-events**;

- separate the total RP sample randomly into two sub-samples and assure the same number of particles in each sub-sample. The resulting sub-events are called as **random sub-events**.

In both η sub-events and random sub-events non-flow correlations from jets and resonance decays are (partly) removed. With the not-normalized particle weights r_j in Eq. (9.9), the Q-vector in these two sub-events can be written as:

$$\begin{aligned}\vec{Q}_n^a &= \{\sum_j r_j \cos n\phi_j^a, \sum_j r_j \sin n\phi_j^a\} = \{M^a V_n^a, n\Psi_n^a\} \\ \vec{Q}_n^b &= \{\sum_j r_j \cos n\phi_j^b, \sum_j r_j \sin n\phi_j^b\} = \{M^b V_n^b, n\Psi_n^b\}\end{aligned} \tag{9.29}$$

where, a and b denote the two different sub-events, M^a and M^b are the normalization factors for $\vec{Q}_n^a$ and $\vec{Q}_n^b$, respectively. The total Q-vector is given by:

$$\vec{Q}_n = \vec{Q}_n^a + \vec{Q}_n^b = \{MV_n, n\Psi_n\}, \tag{9.30}$$

where M is the normalization factor of the total Q-vector. As the two sub-events have the same (or very similar) number of particles, we have:

$$\begin{aligned}M^a &\simeq M^b \simeq \frac{1}{2}M \\ V_n^a &\simeq V_n^b \simeq V_n.\end{aligned} \tag{9.31}$$

Then, for each POI, we define another vector $\vec{q}$ as:

$$\vec{q}_n = \{\cos n\phi, \sin n\phi\}, \tag{9.32}$$

with $|\vec{q}_n| = 1$. The average value of the scalar product between $\vec{Q}_n$ and $\vec{q}_n$ over all the POI and events gives:

$$< \vec{Q}_n \cdot \vec{q}_n > = < MV_n \cos n(\phi - \Psi_n) > = < MV_n > v_n^{\rm meas}, \tag{9.33}$$

where the definition in Eq. (9.19) is used in the last step. According to Eq. (9.33), the measured differential flow $v_n^{\rm meas}$ for POI can be obtained when the term $< MV_n >$ is determined from data. According to Eq. (9.31), the term $< MV_n >$ could be extracted via the same average value of the scalar product between $\vec{Q}_n^a$ and $\vec{Q}_n^b$:

$$< \vec{Q}_n^a \cdot \vec{Q}_n^b > = < M^a M^b V_n^a V_n^b \cos n(\Psi_n^a - \Psi_n^b) > . \tag{9.34}$$

By considering the condition in Eq. (9.31), one can get:

$$\begin{aligned}< \vec{Q}_n^a \cdot \vec{Q}_n^b > &= < M^a M^b V_n^a V_n^b >< \cos n(\Psi_n^a - \Psi_n^b) > \\ &\simeq \frac{1}{4} < M^2 V_n^2 >< \cos n(\Psi_n^a - \Psi_n^b) > .\end{aligned} \tag{9.35}$$

By comparing with Eq. (9.33), one can see that there is an additional term $< \cos n(\Psi_n^a - \Psi_n^b) >$ in Eq. (9.35). Now, we are going to discuss what is the meaning of this term:

$$\begin{aligned}< \cos n(\Psi_n^a - \Psi_n^b) > &= < \cos n[(\Psi_n^a - \Psi_{\rm R}) - (\Psi_n^b - \Psi_{\rm R})] > \\ &= < \cos n(\Psi_n^a - \Psi_{\rm R}) >< \cos n(\Psi_n^b - \Psi_{\rm R}) > .\end{aligned} \tag{9.36}$$

Due to the the fact that the difference between Ψ_n^a (Ψ_n^b) and $\Psi_{\rm R}$ are mainly attributed to event-by-event fluctuations, according to Eq. (9.28), the sin terms vanished. If the statistics in the sub-events a and b is large, one can get:

$$\begin{aligned} < \cos n(\Psi_n - \Psi_{\rm R}) > &\simeq < \cos n(\Psi_n^a - \Psi_{\rm R}) > \simeq < \cos n(\Psi_n^b - \Psi_{\rm R}) > \\ &\simeq \sqrt{< \cos n(\Psi_n^a - \Psi_n^b) >}, \end{aligned} \tag{9.37}$$

and indeed, $< \cos n(\Psi_n - \Psi_{\rm R}) >$ is the event plane resolution in Eq. (9.21).

M and V_n being two independent variables, finally, by combining Eq. (9.21), Eq. (9.33) and Eq. (9.35), the real values of the differential flow can be obtained:

$$\begin{aligned} v_n^{\rm real}(p_{\rm t}, y) &= \frac{v_n^{\rm meas}(p_{\rm t}, y)}{< \cos n(\Psi_n - \Psi_{\rm R}) >} \\ &= \frac{v_n^{\rm meas}(p_{\rm t}, y)}{\sqrt{< \cos n(\Psi_n^a - \Psi_n^b) >}} \\ &= \frac{< \vec{Q}_n \cdot \vec{q}_n(p_{\rm t}, y) >}{2\sqrt{< \vec{Q}_n^a \cdot \vec{Q}_n^b >}}. \end{aligned} \tag{9.38}$$

Discussion In the scalar product method, the non-flow correlations are removed by using the sub-events RP. The total event being built according to Eq. (9.30), non-flow correlations are even removed in random sub-events, but these correlations still exist in the total RP sample. In this case, normally, in the scalar product method, we use the η sub-events. On the another hand, the validation of the final results given by Eq. (9.38) depends on the validation of the conditions in Eq. (9.31), in the η sub-events, the event-by-event fluctuations could bias Eq. (9.31). In this case, to select the η sub-events, many cuts should be implemented for the RP to ensure these two sub-events are equivalent.

In addition, the event plane resolution in the scalar product method is estimated via Eq. (9.37). This formula is validated when the statistics in the RP sample is large. The uncertainties in the scalar product method mainly come from the deviation of Eq. (9.37).

Finally, as with the event plane method, one can also implement the particle weights for POI, and the n-th order differential flow could be calculated with m-th order harmonic if m and n satisfy the condition in Eq. (9.14).

9.1.3 Cumulant Methods

This method allows to extract the flow signal from its correlation behaviour. Indeed, the flow reflects the correlation between all POI and the non-flow correlations are only present between a given number of particles. The advantages of the cumulant methods are:

- non-flow effects can be removed order-by-order based on the correlation behaviour;

- event-by-event fluctuations are avoided: there is no need to reconstruct the event plane;

- the correction of the NUA correlations is done numerically in these methods.

The cumulants method that we are going to introduce and the Lee-Yang-Zeroes method which we will present in Sec.9.1.4 belong to this category.

But the drawbacks of these methods are:

- the correlation behaviour is always biased by the statistical uncertainty, the uncertainty of the final results will be larger, if the statistics is not large enough;

- the magnitude of the flow depends on p_{t}, rapidity and collision centrality, the correlation behaviour is also different from one region to another, in order to avoid the bias from the mixing of different correlation behaviours, it is better to divide the phase space in small bins but again, the statistical uncertainty will be larger if the bin size is small.

The basic idea of the cumulants method is to reject the non-flow correlations order-by-order. One can use first the method named **Generating Function Cumulants** (**GFC**) which calculate the cumulants via the numerical interpolation, but in some cases, the final results are unstable since they would be sensitive to the initial conditions of the interpolation. The alternative way is to use the method called Q-**Cumulants** (**QC**), which extracts the cumulants order-by-order according to the measured Q-vector with data.

9.1.3.1 Generating Function Cumulants

Before everything, let us play a small game in mathematics. As illustrated in Sec. 1.4.3.1, with sufficient statistics, we have:

$$< \sin n(\phi - \Psi_{\mathrm{R}}) >= 0, \tag{9.39}$$

and the average is done over both particles and events. Then according to Euler's formula, the layout of the flow definition Eq. (1.16) can be changed as:

$$\begin{aligned} v_n =& < \cos n(\phi - \Psi_{\mathrm{R}}) > \\ =& < \cos n(\phi - \Psi_{\mathrm{R}}) > + i < \sin n(\phi - \Psi_{\mathrm{R}}) > \\ =& < \cos n(\phi - \Psi_{\mathrm{R}}) + i \sin n(\phi - \Psi_{\mathrm{R}}) > \\ =& < e^{in(\phi - \Psi_{\mathrm{R}})} > . \end{aligned} \tag{9.40}$$

In the following, most of the time we will use the definition in Eq. (9.40) to express the flow parameter v_n.

Correlations and Cumulants Let us consider a simplest case: two particle correlations in a given event:

$$< e^{in(\phi_j-\phi_k)} >=< e^{in\phi_j} >< e^{in\phi_k} > +c_n\{2\}. \tag{9.41}$$

In Eq. (9.41), if there is no correlation between particle j and k, $c_n\{2\} = 0$. If we separate the correlations into two parts:

- flow correlations which are present in all particles;
- non-flow correlations which are present only between a given number of particles.

The non-vanished value of $c_n\{2\}$ is due to both of these two kinds of correlations. Furthermore, in case of four particle correlations, we have:

$$\begin{aligned} &< e^{in(\phi_{j1}+\phi_{j2}-\phi_{k1}-\phi_{k2})} > \\ =&< e^{in(\phi_{j1}-\phi_{k1})} >< e^{in(\phi_{j2}-\phi_{k2})} > \\ +&< e^{in(\phi_{j1}-\phi_{k2})} >< e^{in(\phi_{j2}-\phi_{k1})} > +c_n\{4\} \\ =&2 < e^{in(\phi_j-\phi_k)} >^2 +c_n\{4\}, \end{aligned} \tag{9.42}$$

where $c_n\{4\} = 0$ if there is no correlation between the four particles: $j1$, $j2$, $k1$ and $k2$. By considering both flow and non-flow correlations in Eq. (9.42): the non-vanished value of $c_n\{4\}$ still contains the contribution from flow correlations; since the two-particle correlations are included in the term $< e^{in(\phi_j-\phi_k)} >$ already, there is no non-flow correlation up to four particles in $c_n\{4\}$. We define $c_n\{2\}$ as the **n-th order 2-particle correlation cumulant** and $c_n\{4\}$ as the **n-th order 4-particle correlation cumulant**. Following this way, we can define $c_n\{2k\}$ as the **n-th order $2k$-particle correlation cumulant**. In the non-vanished value of $c_n\{2k\}$ the contribution from non-flow correlations up to $2k$ particles is rejected and the contribution from flow correlations are still present. In the limiting case, the non-vanished value of $c_n\{\infty\}$ only includes the contribution of flow correlations and the contribution from all the non-flow correlations are rejected. In this case, we can get the following conclusions:

- there is a relation between $c_n\{2k\}$ and the n-th order flow parameters;
- the non-flow correlations are removed up to $2k$ particles in the final flow results determined according to $c_n\{2k\}$.

In the following, we are going to determine the relation between the cumulants and the flow parameters.

Integrated Flow As with the event plane method and the scalar product method, the first step to get the differential flow of POI in the cumulant method is to use the RP to make a reference flow or integrated flow. So the first task in the cumulant method is to build the relation between the cumulants and the integrated flow. In

the generating function cumulant method [340], the cumulants are generated via a generating function.

In a given event, one can define a function $G_n(z)$ as:

$$G_n(z) = \prod_{j=1}^{M}(1 + \frac{z^* e^{in\phi_j} + z e^{-in\phi_j}}{M}), \tag{9.43}$$

where M is the number of RP in this given event, z is a complex variable and z^* is the complex conjugate of z. It is easy to probe that the function $G_n(z)$ in Eq. (9.43) is a real-valued function [4]. Then the generating function of cumulants is given by:

$$\mathcal{C}_n(z) \equiv M(< G_n(z) >^{1/M} - 1) = \sum_{k,l} \frac{z^{*k} z^l}{k!l!} c_n\{k+l\}, \tag{9.45}$$

where the average of $G_n(z)$ runs over the events with the **SAME** RP multiplicity M, the $c_n\{k+l\}$ are the coefficients of the power expansion series. According to its definition, $\mathcal{C}_n(z)$ is also a real-valued function and all the terms with $k \neq l$ vanish in Eq. (9.45). Then $\mathcal{C}_n(z)$ becomes:

$$\mathcal{C}_n(z) = \sum_{k} \frac{|z|^{2k}}{(k!)^2} c_n\{2k\}. \tag{9.46}$$

By calculating the coefficient $c_n\{2k\}$ in Eq. (9.46) term by term, one can deduce that the $c_n\{2k\}$ coefficient is indeed the defined n-th order $2k$-particle cumulant, this is why $\mathcal{C}_n(z)$ is called as the generating function of cumulants.

As mentioned, $c_n\{2k\}$ includes the information on the flow correlations and is related to the flow parameter. To get this relation, we calculate $\mathcal{C}_n(z)$ in an alternative way. The average of $G_n(z)$ in Eq. (9.45) can be performed in two steps:

1. average over the events with the same value of Ψ_{R};
2. average over the results with different Ψ_{R}.

We denote $< x|\Psi_{\mathrm{R}} >$ as the average of quantity x with fixed value of $\Psi_{\mathrm{R}} >$, then,

$$\begin{aligned} < e^{in\phi_j}|\Psi_{\mathrm{R}} > &=< e^{in(\phi_j - \Psi_{\mathrm{R}}) + in\Psi_{\mathrm{R}}}|\Psi_{\mathrm{R}} > \\ &=< e^{in(\phi_j - \Psi_{\mathrm{R}})}|\Psi_{\mathrm{R}} > e^{in\Psi_{\mathrm{R}}} \\ &= V_n e^{in\Psi_{\mathrm{R}}}, \end{aligned} \tag{9.47}$$

where in the last step, we used the definition in Eq. (9.40) and since we only consider the RP, the term $< e^{in(\phi_j - \Psi_{\mathrm{R}})} >$ gives the integrated flow V_n. Then one can get:

$$< G_n(z)|\Psi_{\mathrm{R}} >= (1 + \frac{z V_n e^{-in\Psi_{\mathrm{R}}} + z^* V_n e^{in\Psi_{\mathrm{R}}}}{M})^M. \tag{9.48}$$

[4] If $sz = x + iy$, with real-values of variables x and y, Eq. (9.43) becomes:

$$G_n(z) = \prod_{j=1}^{M}(1 + \frac{2x\cos n\phi_j + 2y \sin n\phi_j}{M}), \tag{9.44}$$

without any imaginary part.

With large M values to satisfy the condition,

$$\frac{M!}{(M-2k)!} \simeq M^{2k}, \tag{9.49}$$

finally, we have:

$$\begin{aligned} < G_n(z) > &= \int_0^{2\pi} \frac{\mathrm{d}\Psi_\mathrm{R}}{2\pi} < G_n(z)|\Psi_\mathrm{R} > \\ &= \sum_{k=0}^{[M/2]} \frac{M!}{(M-2k)!(k!)^2} (\frac{V_n}{M}|z|)^{2k} \\ &\simeq \mathrm{I}_0(2V_n|z|), \end{aligned} \tag{9.50}$$

and

$$\mathcal{C}_n(z) \simeq M(\mathrm{I}_0^{1/M}(2V_n|z|) - 1) \simeq \ln \mathrm{I}_0(2V_n|z|). \tag{9.51}$$

With the serie expansion of Eq. (9.51) and by comparing the coefficients of the $|z|^{2k}$ terms with those in Eq. (9.46) one by one, one can obtain the relations between the cumulants and flow parameters as:

$$\begin{aligned} V_n^2\{2\} &= c_n\{2\} \\ V_n^4\{4\} &= -c_n\{4\} \\ V_n^6\{6\} &= c_n\{6\}/4 \\ &\vdots \end{aligned} \tag{9.52}$$

where $V_n\{2k\}$ denotes V_n determined via the cumulants of the $2k$-particle correlations $c_n\{2k\}$. Of course, in $V_n\{2k\}$ the non-flow correlations are rejected up to the order of $2k$-particles.

As usual, the particle weights r_j can also be implemented in the calculation of the integrated flow in the generating function cumulant method via:

$$G_n(z) = \prod_{j=1}^{M} [1 + \frac{r_j}{M}(z^* e^{in\phi_j} + z e^{-in\phi_j})]. \tag{9.53}$$

In this case, there will be the same normalization factor from the used particle weights present before the $c_n\{2k\}$ in Eq. (9.46) and the $V_n\{2k\}$ in Eq. (9.51). Finally the relations in Eq. (9.52) will not change, but the results should be normalized with this factor.

Differential Flow Following a similar strategy which has been already used in the event plane and scalar product methods, after getting the integrated flow of RP, the differential flow of POI can be obtained via the following steps:

1. determine the cumulants of the differential flow according to the cumulants of integrated flow;

2. find the relation between the differential cumulants and the corresponding flow parameters.

In the following, we detail this procedure.

To get the differential cumulants, the following generating function is defined:

$$\mathcal{D}_{mn/n}(z) = \frac{< e^{imn\phi} G_n(z) >}{< G_n(z) >}, \tag{9.54}$$

where: ϕ is the azimuthal angle of POI, the function $G_n(z)$ is defined in Eq. (9.43) for the RP, m is an integer and the average over both POI and events. The physics meaning of Eq. (9.54) can be understood as:

- the function $G_n(z)$ is build by the RP and it includes the information of the integrated cumulants or the integrated flow;
- in the numerator, $< e^{imn\phi} G_n(z) >$ relates the POI to the RP, this procedure is quite similar as Eq. (9.11) in the event plane method and Eq. (9.33) in the scalar product method, in this case, the numerator contains the information on the differential cumulants or the differential flow;
- the term $< G_n(z) >$ in the denominator has a similar meaning as the term $< \vec{Q}_n^a \cdot \vec{Q}_n^b >$ in Eq. (9.38) which is used to cancel the effects from the RP in the numerator as well as to correct the event-by-event fluctuations;
- the final ratio of Eq. (9.54) only includes the correlation information of POI;
- according to above discussion, in Eq. (9.54), $m = 1$ allows to determine the n-th order differential flow v_n with the same order of harmonic, $m > 1$ means that we use the lower order harmonic to determine the v_n.

It is worth to notice that, the differential generating function (Eq. (9.54)) can also be understood as the correlations between each POI and several RP, to avoid self-correlations, if a particle (*eg.* the j-th particle) belongs to both POI and RP, its contribution should be removed from $G_n(z)$ in the numerator of Eq. (9.54) by dividing the term $e^{imn\phi_j} G_n(z)$ with $1 + r_j/M(z^* e^{in\phi_j} + z e^{-in\phi_j})$.

In analogy with to Eq. (9.46), the power expansion series of Eq. (9.38),

$$\mathcal{D}_{mn/n}(z) = \sum_k \frac{z^{*k} z^{k+m}}{k!(k+m)!} d'_{mn/n}\{2k+m+1\}, \tag{9.55}$$

the coefficients $d'_{mn/n}\{2k+m+1\}$ should be the differential cumulants for POI. But indeed, $\mathcal{D}_{mn/n}(z)$ is a complex-valued function and $d'_{mn/n}\{2k+m+1\}$ are also complex-valued. In this case, the differential cumulants $d\{2k+m+1\}$ are defined as:

$$d_{mn/n}\{2k+m+1\} = \Re[d'_{mn/n}\{2k+m+1\}]. \tag{9.56}$$

On the other hand, the $\mathcal{D}_{mn/n}(z)$ can be calculated as:

$$\mathcal{D}_{mn/n}(z) = \frac{\int_0^{2\pi} \mathrm{d}\frac{\Psi_\mathrm{R}}{2\pi} < e^{imn\phi} G_n(z) | \Psi_\mathrm{R} >}{< G_n(z) >} \simeq \frac{\mathrm{I}_m(2V_n|z|)}{\mathrm{I}_0(2V_n|z|)} v_{mn}, \tag{9.57}$$

where the approximation in Eq. (9.49) is used in the last step. By comparing the coefficients in terms of $z^{*k}z^{k+m}$ between Eq. (9.55) and Eq. (9.57) and according to the definition of the differential cumulants in Eq. (9.56), one can get:

$$\begin{aligned} v_{n/n}\{2\} &= d_{n/n}\{2\}/V_n \\ v_{n/n}\{4\} &= -d_{n/n}\{4\}/V_n^3 \\ &\vdots \end{aligned} \tag{9.58}$$

when $m = 1$ and

$$\begin{aligned} v_{2n/n}\{3\} &= d_{2n/n}\{3\}/V_n^2 \\ v_{2n/n}\{5\} &= -d_{2n/n}\{5\}/(2V_n^4) \\ &\vdots \end{aligned} \tag{9.59}$$

when $m = 2$. Here, $v_{mn/n}\{2k+m+1\}$ denotes the mn-th order differential flow determined via the n-th order harmonic with the $2k$-particle cumulant.

Also the particle weights w_j for POI can be used to build the differential generating function as:

$$\mathcal{D}_{mn/n}(z) = \frac{< w_j e^{imn\phi_j} G_n(z) >}{< G_n(z) >}, \tag{9.60}$$

and the final results should be normalized according to the used weights. The $p_{\rm t}$ and rapidity dependence of the differential flow $v_{mn/n}\{2k+m+1\}(p_{\rm t}, y)$ can be obtained by computing the differential generating function in Eq. (9.54) or Eq. (9.60) in different $p_{\rm t}$ and rapidity windows.

Discussion To implement the generating function cumulants, there are two conditions that should be satisfied:

- to build the generating function $\mathcal{C}_n(z)$ or $\mathcal{D}_{mn/n}(z)$, it is required that the events should have the same multiplicity of RP, M, and this requirement is satisified by choosing small centrality bin size in the analysis. If this condition is not fulfilled the event-by-event M fluctuations will bias the final results;
- to compute both the integrated flow $V_n\{2k\}$ and the differential flow $v_{mn/n}\{2k+m+1\}(p_{\rm t}, y)$ the value of M should be large enough to satisfy the approximation in Eq. (9.49).

Due to these two requirements, the pre-condition for the implementation of the generating function cumulant method is that the statistics of both RP and POI in data should be large.

Another issue in the generating function cumulant method is that, both the integrated generating function $\mathcal{C}_n(z)$ and the differential generating function $\mathcal{D}_{mn/n}(z)$ depend on the arbitrary complex-valued variable z. In practice, $\mathcal{C}_n(z)$ or $\mathcal{D}_{mn/n}(z)$ is computed via the numerical interpolation with $p_{\rm max} \times q_{\rm max}$ complex-valued points:

$$z_{p,q} = r_0\sqrt{p} \cdot (\cos\frac{2q\pi}{q_{\rm max}} + i\sin\frac{2q\pi}{q_{\rm max}}), \tag{9.61}$$

where $p = 1, 2, \cdots, p_{\max}$ and $q = 0, 1, \cdots, q_{\max} - 1$. In this case, one should change the values of r_0, $p_{\max}$ and $q_{\max}$ to test the stability of the final results. If the final results are sensitive to these initial values of the interpolation, then the generating function cumulant method is not applicable.

The detail of the interpolation and the correction of the NUA correlations can be found in Ref. [341]. The uncertainty estimation in generating function cumulant method is introduced in Ref. [340].

9.1.3.2 Q-Cumulants

One of the problem in the generating function cumulant method is that, if the interpolation procedure is unstable, the method cannot be used. The Q-Cumulant (QC) method [342] is built to overcome this drawback by extracting the cumulants order-by-order via the measured Q-vector in data.

Integrated Cumulants First, as in Eq. (9.40), in Q-cumulant method, the Q-vector in a given event is defined as a complex:

$$Q_n = \sum_{j=1}^{M} e^{in\phi_j}. \tag{9.62}$$

According to this definition, indeed one can find that for a given event, Eq. (9.41) and Eq. (9.42) can be expressed as:

$$\begin{aligned} &< 2_n > \equiv < e^{in(\phi_j - \phi_k)} > = \frac{|Q_n|^2 - M}{M(M-1)}, \\ &< 4_n > \equiv < e^{in(\phi_{j1} + \phi_{j2} - \phi_{k1} - \phi_{k2})} > \\ &\quad = \frac{|Q_n|^4 + |Q_{2n}|^2 - 2\Re[Q_{2n}Q_n^{*2}]}{M(M-1)(M-2)(M-3)} - \frac{4(M-2)|Q_n|^2 - 2M(M-3)}{M(M-1)(M-2)(M-3)}, \end{aligned} \tag{9.63}$$

where M is the number of used RP in this given event. With the definition of Eq. (9.41) and Eq. (9.42), in principle, one can express the cumulants $c_n\{2\}$ and $c_n\{4\}$ with this complex-valued Q-vector. The cumulants come from the average over all the events, and N (j) denotes the number of events (the j-th event in the sample). Finally, one can get:

$$\begin{aligned} c_n\{2\} &= \frac{\sum_{j=1}^{N}(|Q_n|_j^2 - M_j)}{\sum_{j=1}^{N} M_j(M_j - 1)}, \\ c_n\{4\} &= \frac{\sum_{j=1}^{N}(|Q_n|_j^4 + |Q_{2n}|_j^2 - 2\Re[Q_{2n}Q_n^{*2}]_j)}{\sum_{j=1}^{N} M_j(M_j-1)(M_j-2)(M_j-3)} \\ &\quad - \frac{\sum_{j=1}^{N}[4(M_j-2)|Q_n|_j^2 - 2M_j(M_j-3)]}{\sum_{j=1}^{N} M_j(M_j-1)(M_j-2)(M_j-3)} - 2 \cdot c_n^2\{2\}. \end{aligned} \tag{9.64}$$

Following this way, one can calculate the cumulants order-by-order by hand. After getting the sufficient orders of cumulants, then the integrated flow is obtained according to Eq. (9.52).

Particle Labels As mentioned in the generating function cumulants, in Eq. (9.54) or Eq. (9.60), if the particle belongs to both POI and RP, its constribution should be subtracted from function $G_n(z)$ in the numerator when relating this particle to the function $G_n(z)$. To apply the same procedure in Q-cumulants, the POI are labeled into two types:

- all the POI are labeled as the p particles, m_p denotes the total number of POI;
- inside the p particles, the particles which also belong to the RP sample are labeled as q particles, m_q denotes the total number of particles in this subsample.

According to this label rule, one defines the p-vector and q-vector as:

$$p_n \equiv \sum_{j=1}^{m_p} e^{in\phi_j}, \qquad q_n \equiv \sum_{j=1}^{m_q} e^{in\phi_j}. \tag{9.65}$$

In building the differential cumulants, q particles are treated differently from those only labeled as the p particles.

Differential Cumulants The strategy to determine the differential cumulants is the same as that to determine the integrated cumulants: use the re-defined Q-vector from Eq. (9.62) to express the $d'_{mn/n}\{2k+m+1\}$ (or $d_{mn/n}\{2k+m+1\}$) order-by-order by hand. Here, we only show the calculation of $d_{n/n}\{2\}$ as an example.

According to the definition in Eq. (9.55) in a given event, one can get:

$$\begin{aligned} d'_{n/n}\{2\} &= < e^{in(\phi^{\mathrm{POI}}-\phi^{\mathrm{RP}})} > \\ &= \frac{1}{m_p M - m_q} \sum_{j=1}^{m_p} \sum_{k=1,k\neq j}^{M} e^{in(\phi^{\mathrm{POI}}-\phi^{\mathrm{RP}})} \\ &= \frac{p_n Q_n^* - m_q}{m_p M - m_q}. \end{aligned} \tag{9.66}$$

Then the average of this quantity is done over all the events and one gets:

$$d_{n/n}\{2\} = \Re[d'_{n/n}\{2\}] = \Re[\frac{\sum_{j=1}^{N}(p_n Q_n^* - m_q)_j}{\sum_{j=1}^{N}(m_p M - m_q)_j}], \tag{9.67}$$

where N is the total number of events and j denotes the j-th event. Following this way, one can calculate the higher order differential cumulants one by one by hand.

After obtaining both the integrated and the differential cumulants up to a sufficient order, then, the differential flow can be calculated according to the formula as Eq. (9.58) or Eq. (9.59). The p_{t} and rapidity dependence of the differential flow in Q-cumulants can be obtained by determining the p- and q-vectors in Eq. (9.65) in different p_{t} and rapidity windows. The higher orders of both integrated and differential Q-cumulants can be found in Ref. [342] as well as the correlation of the NUA corrections and the uncertainty estimate [5].

[5] During a private communication with one of the developers of Q-cumulants method, A. Bi-

Discussion Indeed, in the Q-cumulant method, both the integrated flow and differential flow are calculated according to the relations derivated from the generating function cumulants method, *eg*. Eq. (9.52) Eq. (9.58) and Eq. (9.59). The only improvement in Q-cumulant method cumulants is that, instead of calculating the cumulants via the numerical interpolation as in generating function cumulants method, in this method, the cumulants are extracted from data order by order. In this case, the cumulant values are more stable in Q-cumulant method than that in generating function cumulant method. Another advantage of the Q-cumulant method is that, to get the average cumulants over all the events, *eg*. Eq. (9.64) and Eq. (9.67), it is not needed that the events have the same multiplicity, then the event-by-event multiplicity fluctuations are also removed in this method.

9.1.4 Lee-Yang-Zeroes Methods

Let us make a short conclusion before to introduce this more recent method.

One kind of important background in the flow signal is what we called the non-flow correlations. It is difficult to remove them in the event plane method. However, by applying analysis cuts one can can partly reduce some non-flow correlations, but each cut could introduce biases in the final results. Also, in the event plane method, one should take care about the event-by-event fluctuations and the NUA correlations. To overcome the drawbacks of the event plane method, in the scalar product method, the non-flow correlations are partly rejected by the η sub-events and the event plane resolution is also corrected automatically. In an alternative way, the cumulant methods extract the flow according to its correlation behaviour. In this case, not only the event-by-event fluctuations can be corrected automatically but also the non-flow correlations are subtracted order-by-order. In addition, the correction of the NUA correlations is implemented in cumulant methods numerically. But the drawback of the cumulants methods is that, to get the higher order of the cumulants in both the GFC method and QC method is very complicated. In the practice, one can only use the finite orders (in principle, at most up to the 8th order) of cumulants to calculate the flow in data.

The **Lee-Yang-Zeroes** (**LYZ**) method is developed to overcome this problem in cumulant methods, the results from the Lee-Yang-Zeroes method are equivalent to the infinite order of cumulants:

$$v_n\{\text{LYZ}\} = v_n\{\infty, \text{GFC/QC}\}. \tag{9.68}$$

In this case, there is no non-flow correlation included in the final results from the Lee-Yang-Zeroes method.

landzic, we learn that, some parts about the NUA correlation and uncertainty estimate of this method have been updated, and all of these updates are available in the **Flow Package** of AliRoot.

9.1.4.1 Lee and Yang's Theory of Phase Transitions

As mentioned many times, the flow represents the correlations between all the particles in a given event and this is quite similar as another phenomenon in the nature: the phase transition. When a phase transition happens, there will be long range correlations between all the particles in the system. In this case, the method used to measure the flow in data could be analogous to the one used to describe the phase transition in statistical physics. The Lee-Yang-Zeroes method is triggered by one of the phase transition theory built by Lee and Yang in 1952. So firstly, we give a brief overview of Lee and Yang's theory.

If one considers the grand canonical partition function, we get

$$\mathcal{G}(\mu) = \sum_{N=0}^{\infty} \mathcal{Z}_N \exp(\frac{\mu N}{k_{\rm B}T}), \tag{9.69}$$

where $\mathcal{Z}_N$ is the canonical partition function for N particles, $k_{\rm B}$ is the Boltzmann's constant, μ and T are the chemical potential and temperature of the system. The grand canonical partition function Eq. (9.69) corresponds to the un-normalized probability of possible states of the system. To normalize Eq. (9.69), one can define the G-function as:

$$G(\mu) = \frac{\mathcal{G}(\mu)}{\mathcal{G}(\mu_{\rm c})} = \sum_{N=0}^{\infty} P_N(\mu_{\rm c}) y^N(\mu). \tag{9.70}$$

Here:

$$P_N(\mu_{\rm c}) = \frac{1}{\mathcal{G}(\mu_{\rm c})} \exp(\frac{\mu_{\rm c} N}{k_{\rm B}T}), \tag{9.71}$$

is the normalized probability of a system with N particles with chemical potential $\mu_{\rm c}$, and

$$y(\mu) = \exp(\frac{\mu - \mu_{\rm c}}{k_{\rm B}T}) \tag{9.72}$$

is the fugacity. In this case, Eq. (9.70) can be written as:

$$G(y) = < y^N > . \tag{9.73}$$

Of course, the G-function in Eq. (9.73) has no zero value when y is a real-valued variable, but with complex-valued y, one can get many zeroes of G-function in the complex plane. Lee and Yang proved that [343]:

- if the phase transition occurs at $\mu_{\rm c}$, the zeroes of G-function in the complex plane will become more and more close to $y = 1$ with the increase of the system volume;
- if there is no phase transition, the zeroes of G-function in the complex plane will not change with the volume of the system.

The above conclusion from Lee and Yang can be briefly understood as follows.

- If there is no phase transition, there are only short range correlations between the particles in the system, and the system can be classified with different clusters with particles having short range correlations between each other. Since the total partition function of the system is the product of the partition functions of the clusters, the zeroes of G-function in Eq. (9.73) are determined by the zeros of those in each cluster. Then the position of zeroes of the G-function for the total system will not change when its volume increases (large number of independent clusters in the system).

- if a phase transition occurs, the short range correlations between the particles in the clusters become the long range correlations between the particles in the whole system. The probability distribution P_N in Eq. (9.70) will widely spread between the volume V of the two phases. With the relation $N \propto V$, y obeys to:

$$\ln y \propto \frac{1}{V}, \tag{9.74}$$

  and this makes the zeroes of G-function in Eq. (9.73) closer and closer to $y = 1$ when the system volume V increases with a phase transition occurring at $\mu = \mu_c$.

As mentioned, both the phase transition and the flow have a similar property: correlations between all particles in the system. According to the theory of Lee and Yang, the phase transition or the correlations between particles is characterized by the distribution of the zeroes of the G-function Eq. (9.73). Following this idea, if one can build a similar G-function according to the final observables in data, the correlations between all particles or flow can also be characterized by the zeroes of that function.

9.1.4.2 Flow Determination with Lee-Yang zeroes

The key point to implement the idea from the phase transition theory of Lee and Yang in the flow analysis is to construct a similar function as the G-function in Eq. (9.73) which includes the information on the correlations between particles in the system.

Integrated Flow In the Lee-Yang-Zeroes method, the generating function of the integrated flow for RP is constructed as:

$$G_n^\theta(z) = < e^{zQ_n^\theta} >, \tag{9.75}$$

where z is a complex-valued variable and the average is over all the used events in the sample. In a given event Q_n^θ is defined as,

$$Q_n^\theta = \sum_{j=1}^{M} r_j \cos n(\phi_j - \theta), \tag{9.76}$$

in which M is the number of used RP in this given event, r_j denotes the particle weights and θ is an arbitrary angle. The Q_n^θ in Eq. (9.75) can be treated as the projection of Q-vector to an arbitrary direction θ. By comparing Eq. (9.75) with Eq. (9.73) one can find that, Q_n^θ has the same role as the number of particles N, and e^z has the same role as the fugacity y; since Q_n^θ is scaled by the number of RP, M, and N is scaled as the system volume V, M is equivalent to V.

To get the relation between $G_n^\theta(z)$ and the integrated flow, first one can consider the following power expansion under the assumption of $|z| \ll 1$ and r_j is normalized:

$$\begin{aligned} \ln < e^{zQ_n^\theta} | \Psi_{\mathrm{R}} > &\simeq z \cdot < Q_n^\theta | \Psi_{\mathrm{R}} > + \mathcal{O}(z^2) \\ &= z V_n \cos n(\theta - \Psi_{\mathrm{R}}) + \mathcal{O}(z^2). \end{aligned} \tag{9.77}$$

By assuming that $\mathcal{O}(z^2)$ is independent on Ψ_{R}, $G_n^\theta(z)$ can be calculated as,

$$\begin{aligned} G_n^\theta(z) =& < e^{zQ_n^\theta} > \\ &= \int_0^{2\pi} \frac{\mathrm{d}\Psi_{\mathrm{R}}}{2\pi} < e^{zQ_n^\theta} | \Psi_{\mathrm{R}} > \\ &\simeq \int_0^{2\pi} \frac{\mathrm{d}\Psi_{\mathrm{R}}}{2\pi} \exp[z V_n \cos n(\theta - \Psi_{\mathrm{R}}) + \mathcal{O}(z^2)] \\ &= e^{\mathcal{O}(z^2)} \mathrm{I}_0(z V_n). \end{aligned} \tag{9.78}$$

On the other hand, as in cumulants method, by expanding $G_n^\theta(z)$ as the power series:

$$\ln G_n^\theta(z) = \sum_{k=1}^{\infty} \frac{z^{2k}}{(2k)!} c_n^\theta\{2k\}, \tag{9.79}$$

and comparing the coefficient $c_n^\theta\{2k\}$ with each z^{2k} term in Eq. (9.78) the integrated flow $V_n\{2k\}$ then, can be extracted order-by-order. The θ dependence of the coefficient $c_n^\theta\{2k\}$ is canceled in the coefficient of term $\mathcal{O}(z^2)$. The final results is independent of θ. Up to now, the function $G_n^\theta(z)$ looks like only as an alternative way to build the integrated cumulant generating function of Eq. (9.43). As mentioned, the expression of $G_n^\theta(z)$ is analogous to the G-function Eq. (9.73), the correlations of all particles, the flow without the non-flow correlations, in principle can be extracted according to the zeroes of $G_n^\theta(z)$.

The correlations of all particles correspond to the coefficient $c_n^\theta\{\infty\}$ in Eq. (9.79). Indeed, by comparing the coefficient of z^{2k} term between Eq. (9.78) and Eq. (9.79) up to $k \to \infty$ [344], one can get,

$$G_n^\theta(ir) = \lim_{k\to\infty} G_n^\theta(z) = e^{\mathcal{O}(z^2)} \mathrm{J}_0(ir V_n^\theta\{\infty\}), \tag{9.80}$$

where $\mathrm{J}_0(x)$ is the zero order Bessel function, $r = \Im z$ is the imaginary part of z [6], $V_n^\theta\{\infty\}$ corresponds to the integrated flow from the infinity order of cumulant $c_n^\theta\{\infty\}$.

To get $V_n^\theta\{\infty\}$ via the Lee-Yang-Zeroes method, the following steps are used:

[6] This is consistent with the further study of Lee and Yang: all zeroes of G-function Eq. (9.73) lie on the imaginary axis [345].

1. with a fixed value of θ, build $G_n^\theta(ir)$ according to Eq. (9.75) in data;
2. plot $|G_n^\theta(ir)|$ as a function of r and determine the first position of **minimum** [7] r_0^θ;
3. since the first zero of $\mathrm{J}_0(x)$ in the imaginary axis is given by $x = i\mathrm{j}_{01} \simeq i2.405$, the $V_n^\theta\{\infty\}$ is determined as:

$$\begin{aligned} r_0^\theta \times V_n^\theta\{\infty\} &= \mathrm{j}_{01} \\ \Rightarrow V_n^\theta\{\mathrm{LYZ}\} \equiv V_n^\theta\{\infty\} &= \frac{\mathrm{j}_{01}}{r_0^\theta} \simeq \frac{2.405}{r_0^\theta}. \end{aligned} \tag{9.81}$$

Differential Flow What is important in the Lee-Yang-Zeroes method is to understand how to implement the conclusions from the Lee and Yang's study of the phase transitions. The whole approach of this method is shown in the case of the integrated flow. With such illustration, the differential flow determination becomes more straightforward.

1. As that in the cumulant methods, one defines a differential generating function as:

$$D_{mn/n}^\theta(z) = < \cos mn(\phi - \theta) e^{zQ_n^\theta} >, \tag{9.82}$$

with the complex-valued variable z. The differential cumulants $d_{mn/n}\{k\}$ can be given by the coefficients of the power expansion:

$$\frac{D_{mn/n}^\theta(z)}{G_n^\theta(z)} = \sum_{k=0}^{\infty} \frac{z^k}{k!} d_{mn/n}\{k\}. \tag{9.83}$$

2. With the same approach for calculating $G_n^\theta(z)$ in Eq. (9.78) under the assumption $|z| \ll 1$ one gets:

$$\lim_{|z|\to 0} \frac{D_{mn/n}^\theta(z)}{G_n^\theta(z)} = \frac{\mathrm{I}_m(zV_n^\theta)}{\mathrm{I}_0(zV_n^\theta)} \cdot v_{mn/n}^\theta, \tag{9.84}$$

where $v_{mn/n}^\theta$ is the differential flow.

3. Compare the coefficients of z^k terms up to $k \to \infty$, the results at the first minimum position r_0^θ of function $|G_n^\theta(ir)|$ then can be gotten as:

$$\begin{aligned} v_{mn/n}^\theta\{\mathrm{LYZ}\} &\equiv v_{mn/n}^\theta\{\infty\} \\ &= V_n^\theta\{\mathrm{LYZ}\} \cdot \frac{\mathrm{J}_1(\mathrm{j}_{01})}{\mathrm{J}_m(\mathrm{j}_{01})} \Re[i^{1-m} \frac{< \cos mn(\phi - \theta) e^{ir_0^\theta Q_n^\theta} >}{< Q_n^\theta e^{ir_0^\theta Q_n^\theta} >}], \end{aligned} \tag{9.85}$$

where $\mathrm{j}_{01} = 2.405$.

[7] The Lee and Yang' theory of phase transitions is used to deal with the statistical system which means that one can treat the number of particles $N \to \infty$ in the system. But in the analysis of flow in data, the finite number of particles and events will make the zeroes slightly off the imaginary axis. So in practice, the position of first minimum of $|G_n^\theta(ir)|$ is used instead of the position of the first zeroe of this function.

9.1.4.3 Discussion

By comparing with Q-cumulants method, the advantage of the Lee-Yang-Zero method is that one does not need to calculate the cumulants order-by-order by hand, it returns the results from the infinity order of cumulants. The following items are worth to notice for implementing this method in data analysis:

- in principle, both the integrated flow and differential flow are insensitive to the arbitrary angle θ, but in practice, normally, the final results are gotten from the average value of the results with several θ values,

$$V_n\{\text{LYZ}\} =< V_n^{\theta}\{\text{LYZ}\} >, \quad v_{mn/n}\{\text{LYZ}\} =< v_{mn/n}^{\theta}\{\text{LYZ}\} >; \tag{9.86}$$

- as with the cumulant methods, the correction of the NUA correlations is implemented in Lee-Yang-Zeroes method numerically;

- to avoid the self-correlation in the differential cumulants, the particles belonging to both RP and POI should be removed from term $e^{ir_0^{\theta}Q_n^{\theta}}$ in the numerator of Eq. (9.85) one by one as those in the generating function cumulant method;

- both the POI and RP can be weighted by the particle weights, and as in all the other methods, the final results should be normalized according to the used particle weights;

- the p_{t} and rapidity dependence of the differential flow is given by Eq. (9.85) in different p_{t} and rapidity windows;

- finally, what important is that, the Lee-Yang-Zeroes method, in principle should be implemented to events having the same impact parameter $|\vec{b}|$, in this case, it is better to choose small centrality bins to implement this method, otherwise, the fluctuations between the collision centralities could bias the results.

Here, Q_n^{θ} in Eq. (9.76) is chosen as a summable function [346], the corresponding results with Q_n^{θ} are labeled as $V_n\{\text{LYZ}, \text{SUM}\}$ and $v_{mn/n}\{\text{LYZ}, \text{SUM}\}$. Alternatively, the Q_n^{θ} can also be defined as a product function [347], the corresponding results withQ_n^{θ} are labeled as $V_n\{\text{LYZ}, \text{PROD}\}$ and $v_{mn/n}\{\text{LYZ}, \text{PROD}\}$. More details about the Lee-Yang zeroes theory are given in Ref. [348]. A practice guide of Lee-Yang-Zeroes method can be found in [349].

By the way, the integrated flow $V_n\{\text{LYZ}\}$ from Lee-Yang-Zeroes method is corrected both for the NUA correlations (numerically) and the non-flow correlations. In this case, one can use $V_n\{\text{LYZ}\}$ to correct the integrated flow from the event plane method, Eq. (9.12), and remove both the NUA correlations and non-flow correlations in the event plane method via a event-by-event weight. This approach is called as **Lee-Yang-Zero Event Plane** (**LYZEP**) method. The detailed illustration of this method is in [350].

9.2 Data Analysis Environment

After this long and boring introduction on different flow analysis methods, we are now going to move to a more interesting thing, the data analysis.

As already mentioned, except for the Fit-Q method, the RP and POI should be defined before the analysis in all other methods introduced in Sec. 9.1. In this analysis, the POI are the inclusive muons detected in the ALICE muon spectrometer at forward rapidities. Since the data sample used for flow studies is the same as that presented in Chap. 8 (LHC10h pass 2 the Pb–Pb collisions at $\sqrt{s_{\rm NN}} = 2.76$ TeV), the event and muon selections here follow the strategy implemented in the analysis discussed in Chap. 8. The first task is to choose the proper RP in order to build the reference for the flow of muons.

9.2.1 Reference Particle Selection

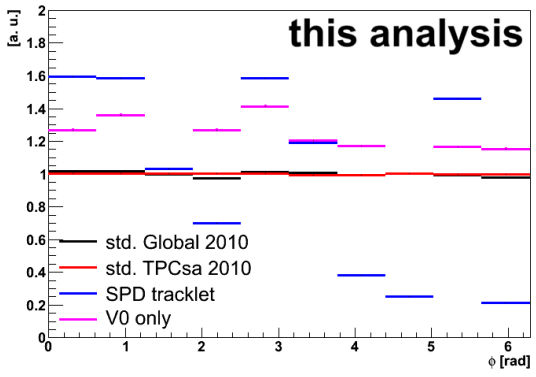

Figure 9.1: The normalized azimuthal distributions of different kinds of RP with the corresponding RP selection cuts or corrections.

In this analysis the POI being the muons in the forward rapidity region, the way to evidence the correlations between the POI and RP is to choose the RP detected in the ALICE central barrel. The corresponding available RP are the SPD tracklets, the global charged tracks reconstructed in the central barrel and the tracks reconstructed with **TPC standalone** (**TPCsa**) [8].

The selection of the SPD tracklets is straightforward and no selection cuts are needed. In case of the global tracks and TPCsa tracks, to ensure the track quality and reject part of the non-flow correlations, several cuts were used. These cuts are provided by people working on flow analyses with central barrel data. They can be classified into three categories:

- the kinematics cuts which are used to reject part of the non-flow correlations. For both global tracks and TPCsa tracks, the kinematics range is set as $0.2 < p_{\rm t} < 5$ GeV/c, $-0.8 < \eta < 0.8$;

- cuts on the reconstruction quality, like the number of used clusters, the $\mathrm{d}E/\mathrm{d}x$ in TPC, minimum and maximum values of tracking χ^2 per cluster *etc.*;

[8] Among the four experiments at the LHC only ALICE is equipped a TPC. This allows to have track reconstruction and PID in a wide $p_{\rm t}$ range and for different particle species.

- the geometrical cuts, like the DCA to the primary vertex, from the kink decays *etc.*. These cuts are used to reject some tracks from particle decays.

The exact values of these cuts are officially set in the flow package of AliRoot. For LHC10h pass 2, they are called **Standard Global Track Cuts 2010** and **Standard TPC Standalone Track Cuts 2010** for global tracks and TPCsa tracks, respectively. After the track selection, we named the corresponding RP **Standard Global Track** and **Standard TPCsa Tracks**.

In Fig. 9.1, the normalized azimuthal distributions of SPD tracklets (in blue), the standard global track (in black) and the standard TPCsa tracks (in red) are shown. One can see that the standard TPCsa tracks have an uniform azimuthal distribution. Therefore, the NUA corrections to standard TPCsa tracks are smaller than for others tracks. For this reason, we choose the standard TPCsa tracks for the RP reconstruction in the flow study of inclusive muons.

As we mentioned in Sec. 8.1.1, there is no muon trigger in LHC10h, and the analysis is based on minimum bias events. In this case, choosing TPCsa tracks as the RP is convenient. In the LHC11h data sample, the muon trigger was added. Since the statistics of single muons in muon triggered events is much larger than that in the minimum bias data sample, in the future, the analysis of the muon flow will use the muon triggered data. However, the TPC is not included in the muon trigger cluster. Therefore, in future analyses, the RP should be provided by another detector (included in the muon trigger cluster) like the VZERO. In order to develop an analysis strategy which we can use in the future, the VZERO amplitude is also used as the RP in this analysis. The normalized distribution of the VZERO amplitude after correction for the gain saturation is also shown in Fig. 9.1. One can observe that this distribution is not quite flat and also has holes. Therefore, in order to use the VZERO amplitude as the RP, one should take care about NUA corrections as well as non-flow correlations since there is an overlap region between the acceptance of the VZERO and that of the muon spectrometer. On the other hand, it is interesting to note that the results with these two kinds of RPs can be checked against each other.

9.2.2 Single Muons in the Flow Package

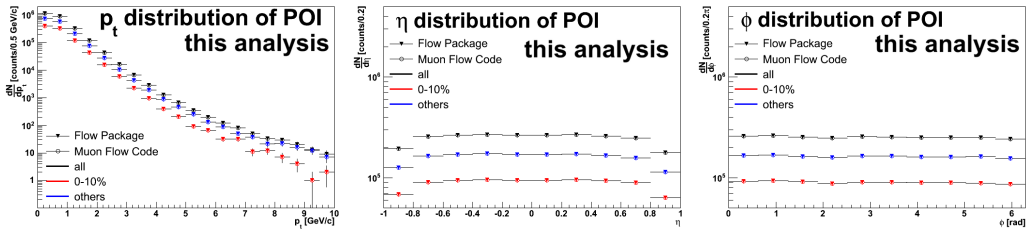

Figure 9.2: The p_{t} (left), η (middle) and ϕ (right) distributions of global tracks without any selection cut.

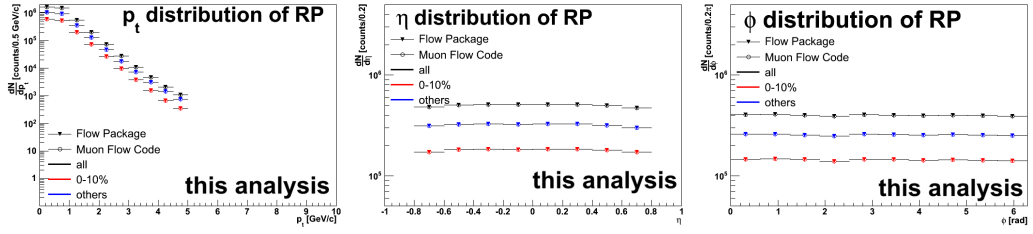

Figure 9.3: The p_{t} (left), η (middle) and ϕ (right) distributions of standard global tracks with the selection cuts.

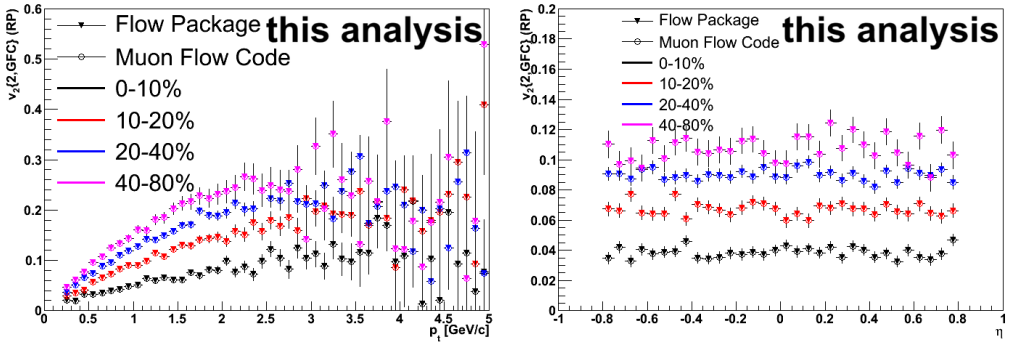

Figure 9.4: The p_{t} (left) and η (right) dependence of v_2 for the RP from second order GFC method.

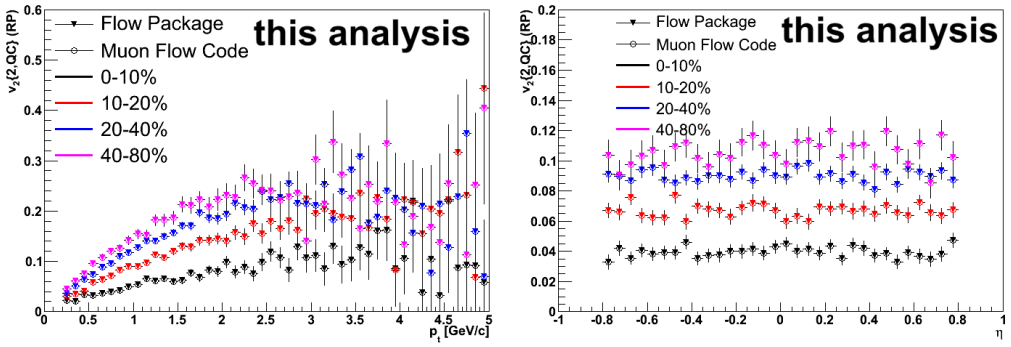

Figure 9.5: The p_{t} (left) and η (right) dependence of v_2 for the RP from the second order QC method.

All algorithms to compute the collective flow with different methods are provided officially in the so-called Flow Package in AliRoot. This package was developed for flow analyses in the ALICE central barrel and the muon selection was not included. To validate our analysis, we built an interface in the flow package in order to select muons with the analysis cuts described in Chap. 8. The flow package is a very complicated code and any modification in this package should be done carefully. In

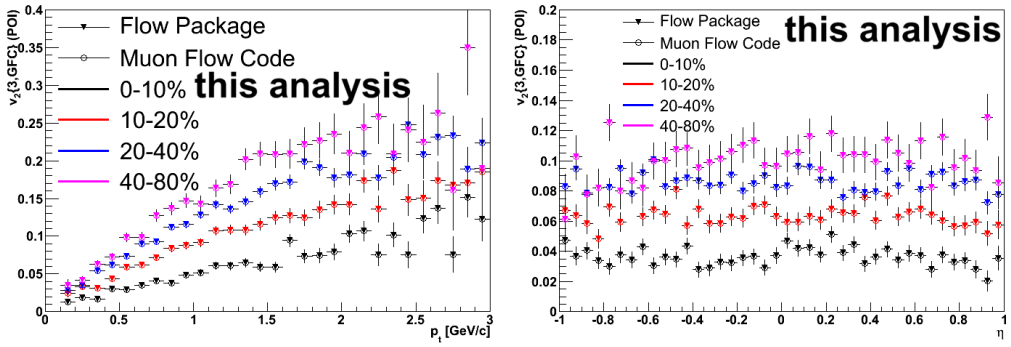

Figure 9.6: The p_t (left) and η (right) dependence of v_2 for the POI from the second order GFC method.

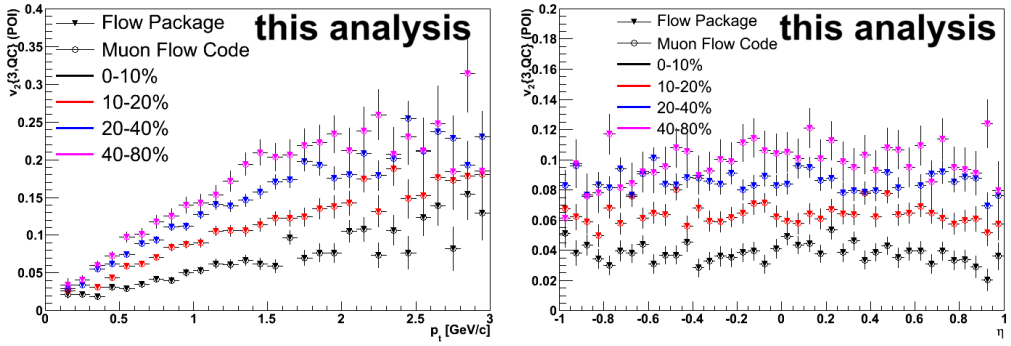

Figure 9.7: The p_t (left) and η (right) dependence of v_2 for the POI from the second order QC method.

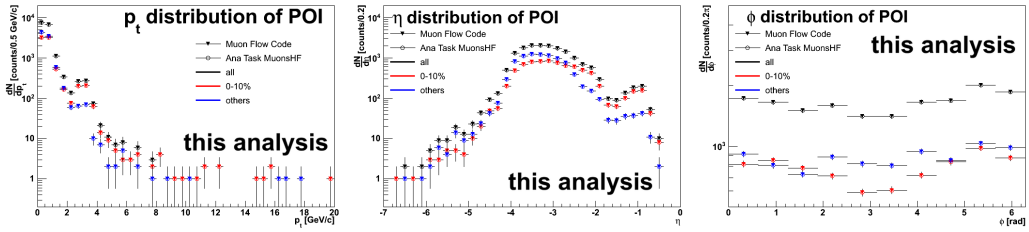

Figure 9.8: The p_t (left), η (middle) and ϕ (right) distributions of muon tracks without any selection cut.

order to validate our developments in the interface, we did a performance test of this new code. The test includes the following three steps.

1. Reproduce the track distributions in the central barrel obtained with the official flow package using the modified flow package with the muon interface. Here we choose the global tracks for the comparison. The global track distributions in central barrel without any cuts and with selection cuts are shown in

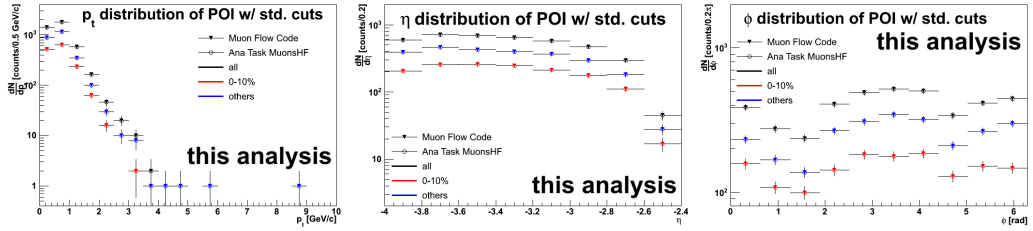

Figure 9.9: The p_{t} (left), η (middle) and ϕ (right) distributions of muon tracks with standard muon selection cuts.

Fig. 9.2 and Fig. 9.3, respectively. In these figures the inverted triangles correspond to results obtained with the official flow package and the open circles (labeled as "Muon Flow Code") are obtained with the updated flow package for the muon flow analysis. To make the comparison as complete as possible, the results are shown for different centrality classes labeled in the figures. One can see that, in all cases, the official flow package and the muon flow code give the same results. This means that the modification of the flow package does not affect the track selection in the flow package.

2. Reproduce the results from official flow package via the muon flow code. At this stage, we show the global tracks in Fig. 9.2 as POI and the standard global tracks with the selection cuts in Fig. 9.3 as RP. Then we compute the elliptic flow via the GFC and the QC methods. The results of the integrated flow from the second order cumulant of GFC and QC methods are shown in Fig. 9.4 and Fig. 9.5, respectively. In each case, the results from the official flow package and the results from the "muon flow code" are compared together. One can see that there is no difference between the results from the two codes. In addition, the corresponding differential flow of the POI is shown in Fig. 9.6 and Fig. 9.7. Again, one can see that the results from the two analysis codes are absolutely the same. We note that these results are not meaningful for physics at this stage since no detail configuration is included. Our aim here is only to test the validity of the modified flow package.

3. Reproduce the muon distributions from the muon analysis code that we introduced in Sec. 4.3.2 via the "muon flow code". The corresponding results are shown in Fig. 9.8 (without any muon selection cut) and Fig. 9.9 (with the standard muon selection cuts used in Chap. 8). By comparing the results from the muon analysis code and that from the "muon flow code", one can see that the "muon flow code" validates all functions of the muon analysis code and ensure that the input inclusive muon distributions for the flow analysis are the same as those used in the analysis presented in Chap. 8.

4. After all of these comparisons, we can conclude that: on one hand, the "muon flow code" can reproduce both the track distributions and the flow results in central barrel from the official flow package; on the other hand, it also

reproduces the muon distributions from the muon analysis code. This validates the "muon flow code".

9.3 Analysis Configuration

After the determination of the RP samples and the validation of the analysis code, we select the SP, GFC, QC and LYZ methods for the analysis. The EP method needs to deal with the corrections of event-plane resolution, non-flow corrections and the NUA corrections and in addition it is difficult to control the bias due to flow fluctuations. However, this is one of the basic methods for flow analysis and it is worth to compare also the results from this method.

9.3.1 Corrections for the Event Plane Method

As mentioned, the implementation of the EP method is straightforward but its underlying corrections are very complicated. The following steps should be considered:

1. the correction of the NUA correlations. This step is also called as event plane flattening;
2. rejection of the non-flow correlations;
3. method implementation;
4. estimation of the event-plane resolution;
5. final results with the correction for the event-plane resolution.

Let us now introduce these steps one by one.

9.3.1.1 Event Plane Flattening

Generally, there are four kinds of popular used methods for event plane flattening:

- weighting method;
- recentering method;
- shifting method;
- mixed-events method.

The details for all these methods are presented in Ref. [339].

As shown in Fig. 9.1, the azimuthal distribution of the standard TPCsa and that of the corrected VZERO amplitude are quite different. We also use different kinds of event-plane flattening strategy. For standard TPCsa RP, we only apply the weighting method and for the corrected VZERO RP, we will combine the weighting method, the recentering method and the shifting method.

Standard TPCsa RP The black curve in the left plot of Fig. 9.10 shows the normalized azimuthal distribution $r(\phi)$ of standard TPCsa tracks. The corresponding ϕ-weight $w(\phi)$ for the event-plane flattening is given by:

$$w(\phi) = \frac{1}{r(\phi)} \cdot \int_0^{2\pi} \frac{\mathrm{d}\phi}{2\pi} r(\phi), \tag{9.87}$$

which is shown by the red histogram in the left plot of Fig. 9.10.

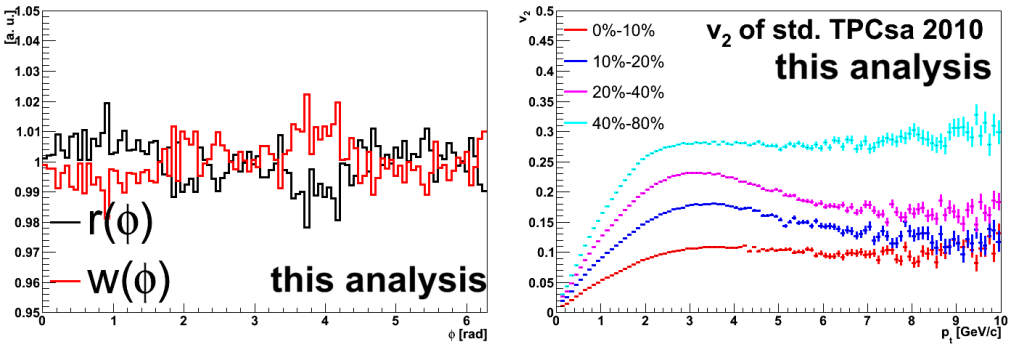

Figure 9.10: Left: the azimuthal distribution and its weight distributions of standard TPCsa tracks. Right: the reference elliptic flow as a function of p_t for standard TPCsa tracks calculated via the EP method according to Eq. (9.12). Results are obtained from LHC10h pass 2 data.

Furthermore, we also implemented the particle weights to deduce the event-by-event fluctuations. As mentioned in Sec. 9.1.1.3, the particle weights are chosen as quantities which are proportional to V_n. The p_t dependence of the reference flow v_2 for standard TPCsa RP is obtained from the EP method via Eq. (9.12) in different centrality regions. This is shown in the right plot of Fig. 9.10. According to these results one can find that, in each centrality region, the reference flow first increases with p_t almost linearly up to $p_\mathrm{t} \simeq 2$ GeV/c, and it saturates when $p_\mathrm{t} \gtrsim 2$ GeV/c. According to this behaviour, we choose the particle weights as a function of p_t as:

$$w(p_\mathrm{t}) = \begin{cases} p_\mathrm{t} & (p_\mathrm{t} < 2 \text{ GeV}/c) \\ 2 & (p_\mathrm{t} > 2 \text{ GeV}/c). \end{cases} \tag{9.88}$$

The final weights r_j for the standard TPCsa RP are given by

$$r_j = w_j(\phi) \times w_j(p_\mathrm{t}). \tag{9.89}$$

Fig. 9.11 shows the 2nd order event plane Ψ_2 distributions for standard TPCsa RP in four different centrality bins as labeled in the figure and obtained with the particle weights defined in Eq. (9.89). One can see that after the event plane flattening with the weighting method, there are still fluctuations in the Ψ_2 distributions. These fluctuations increases as the centrality of the collision increases. In the most central collisions $(0-10\%)$ the fluctuations are of the order of $\sim 10\%$. The results indicate that there is still room for improving the event plane flattening of standard TPCsa RP, *eg.* use ϕ-weight in each centrality bin.

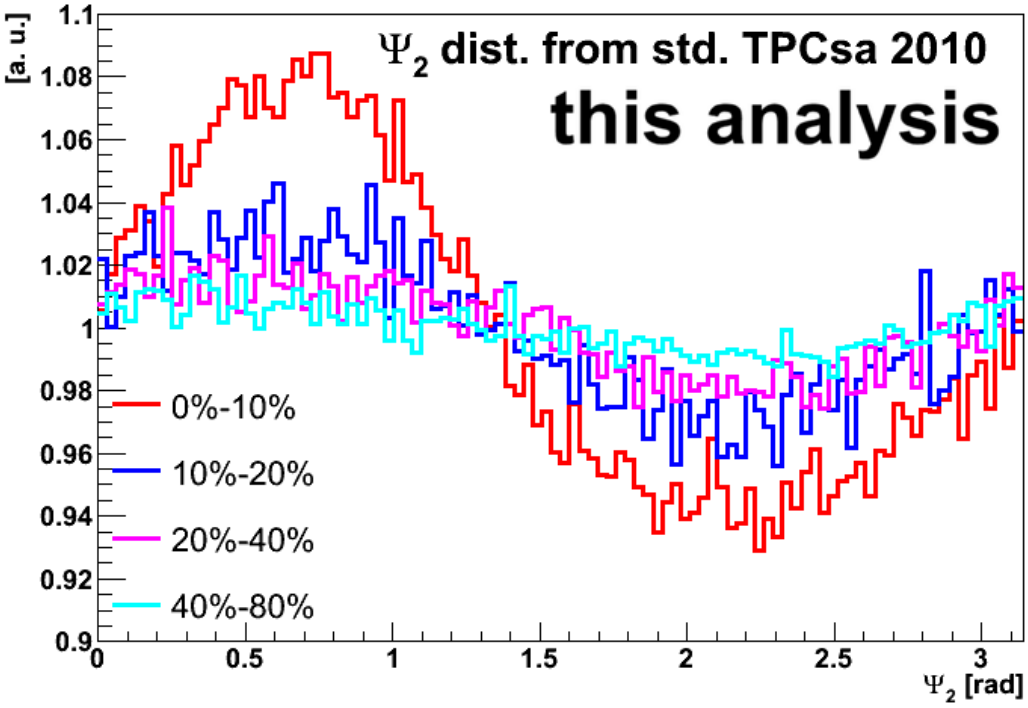

Figure 9.11: The 2nd order event plane Ψ_2 distributions for standard TPCsa RP in different centrality classes obtained with the particle weights defined in Eq. (9.89).

Correction for saturation of the VZERO RP The azimuthal distribution of the corrected VZERO amplitude shown in Fig. 9.1 is not as perfect as that of the standard TPCsa RP. The procedure of event plane flattening for VZERO is indeed more complicated.

Fig. 9.12 shows the distributions of saturation corrected VZERO amplitude as a function of the sector number in different centrality classes. One can see that even after the gain saturation corrections, the fluctuations of the amplitude between different sectors are still very large. The weighting method is here used to smooth these fluctuations. It is built by considering the following items:

1. due to the fact that the VZERO includes two sub-detectors, V0A and V0C, the weighting method should be implemented for these two sub-detectors independently;

2. M_j denotes, in a given event, the corrected VZERO amplitude (Fig. 9.12) for the j-th sector. $M_j^{\rm wgt}$ is the weighted one. It corresponds to the real value of the VZERO amplitude in this sector;

3. $< M_j >$ denotes the mean value of M_j in the events in the same centrality class;

4. $M_j - < M_j >$ gives the fluctuations of M_j in a given event, assuming the

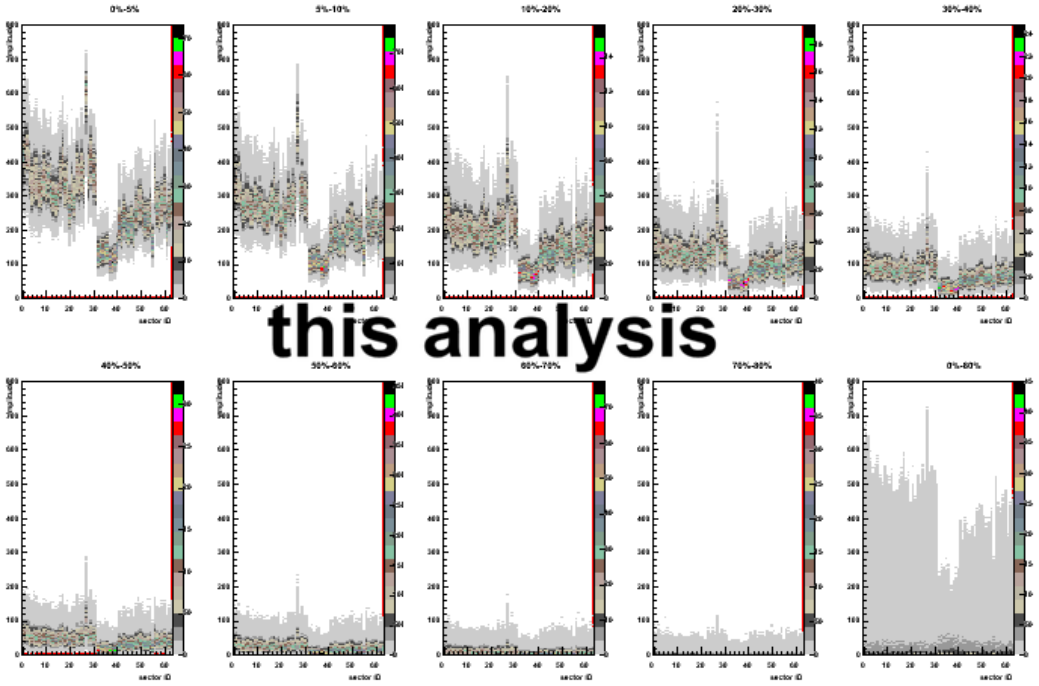

Figure 9.12: The distributions of saturation corrected VZERO amplitude as a function of sector number in different centrality classes.

distribution of $M_j - < M_j >$ is a Gaussian,

$$P_j = A_j \exp[(\frac{M_j - < M_j >}{\sigma_j})^2], \tag{9.90}$$

where A_j is the normalization factor, σ_j is the variance of M_j which is obtained from the data;

5. $< M >$ denotes the mean value of M_j over all the sectors in a given VZERO sub-detector (V0A or V0C) for events in the same centrality class. $M_j^{\rm wgt} - < M >$ gives the fluctuations between different sectors in events with the same centrality;

6. the fluctuations in both $M_j - < M_j >$ and $M_j^{\rm wgt} - < M >$ being caused by the statistical uncertainty, after the normalization, they should have the same probability distribution:

$$\frac{M_j - < M_j >}{\sigma_j} = \frac{M_j^{\rm wgt} - < M >}{\sigma}, \tag{9.91}$$

where σ is the variance of M;

7. finally, the weights to get $M_j^{\rm wgt}$ for the j-th sector are given by:

$$M_j^{\rm wgt} = \frac{M_j - < M_j >}{\sigma_j} \times \sigma + < M > . \tag{9.92}$$

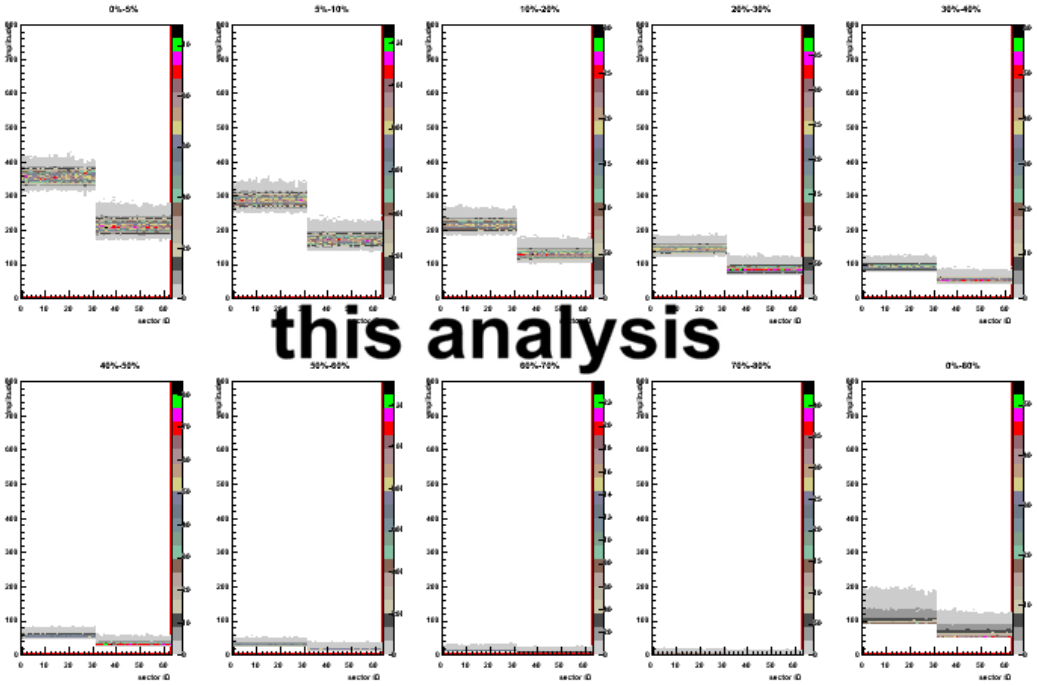

Figure 9.13: The distributions of saturation corrected VZERO amplitude as a function of sector number after the event-by-event weighting according to Eq. (9.92) in different centrality classes.

Fig. 9.13 shows the distributions of the saturation corrected VZERO amplitude as a function of the sector number after the weighting of the amplitude in each sector event-by-event according to Eq. (9.92). The results show that the amplitude distributions are improved by the weighting procedure.

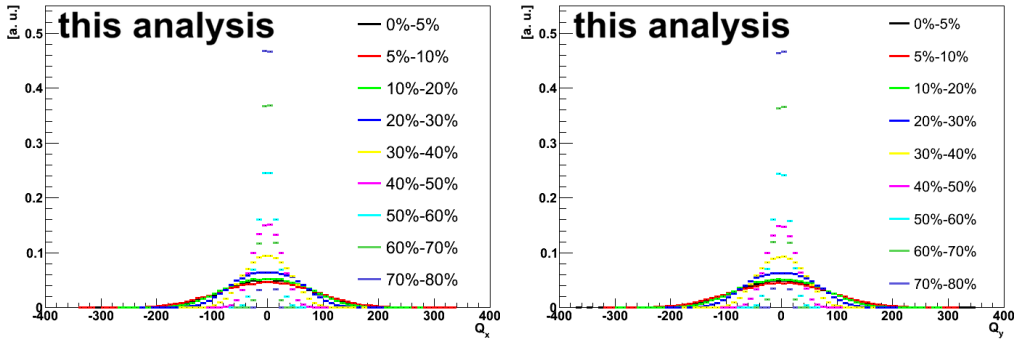

Figure 9.14: The x (left) and y (right) components of 2nd order Q-vector calculated from VZERO amplitude after the weighting. The results are shown in different centrality classes as labeled in the plots.

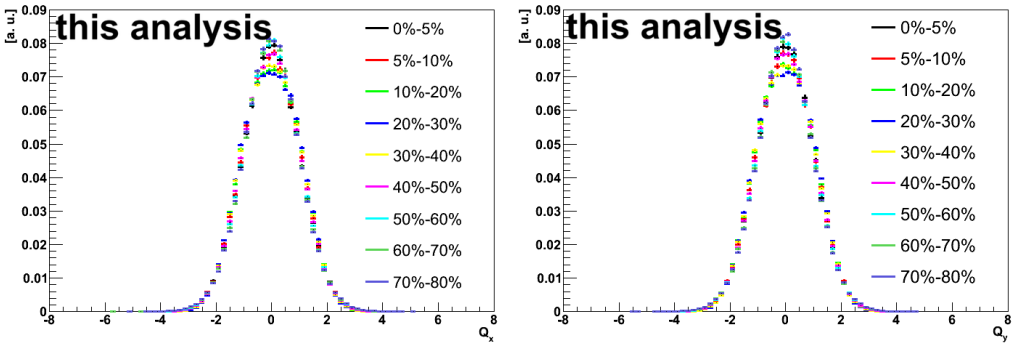

Figure 9.15: The x (left) and y (right) components of 2nd order Q-vector with the re-centering according to Eq. (9.93). The results are shown in different centrality classes as labeled in the plots.

After the weighting, in each event, we correct the Q-vector according to the re-centering method via:

$$\vec{Q}_n^{\mathrm{re-cent}} = \frac{\vec{Q}_n - < \vec{Q}_n >}{\vec{\sigma}(\vec{Q}_n)}, \tag{9.93}$$

where $\vec{Q}_n$ is the Q-vector in a given event calculated after the weighting of the VZERO amplitude and $\vec{Q}_n^{\mathrm{re-cent}}$ denotes the one after the re-centering. $< \vec{Q}_n >$ is the mean value of $\vec{Q}_n$ over the events in the same centrality class. $\vec{\sigma}(\vec{Q}_n)$ is the variance of $\vec{Q}_n$ which is used to correct the event-by-event fluctuations in the Q-vector distributions in each centrality class. The 2nd order Q-vector distributions before and after the re-centering in different centrality classes are shown in Fig. 9.14 and Fig. 9.15, respectively.

After the re-centering of the Q-vector, the event-plane Ψ_n can be calculated according to Eq. (9.10) event-by-event. Then we correct this event plane according to the shifting method:

$$\begin{aligned} \Psi_n^{\mathrm{shifting}} =& \Psi_n + \frac{1}{n} \cdot \sum_{k=1}^{N} \Delta_{kn/n}, \\ \Delta_{kn/n} =& \frac{2}{k}(< \cos kn\Psi_n > \sin kn\Psi_n - \cos kn\Psi_n < \sin kn\Psi_n >), \end{aligned} \tag{9.94}$$

where, $n = 2$ since we focus on the elliptic flow. We choose $N = 10$. The results on the 2nd order event-plane Ψ_2 distributions before and after the shifting according to Eq. (9.94) are compared in Fig. 9.16 in different centrality classes.

After all the correction steps, the final distributions of the event plane built via the VZERO amplitude, (red curves in Fig. 9.16), show a very good uniform trend in all centrality classes.

9.3.1.2 Non-Flow Correlations

Concerning the rejection of non-flow correlations, we proceed as follows.

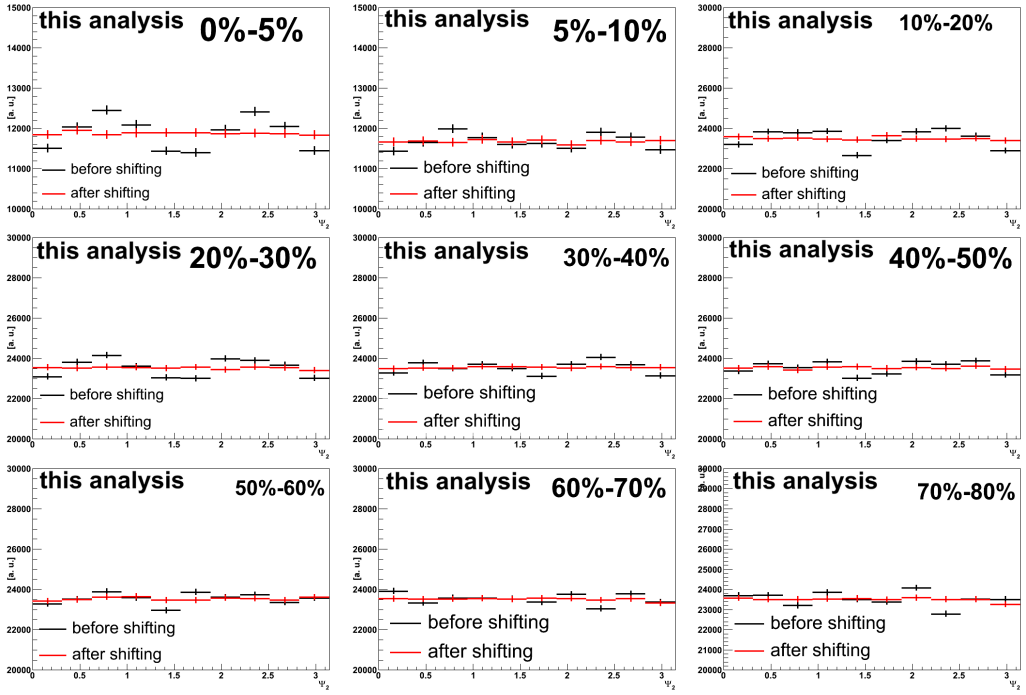

Figure 9.16: The 2nd order event plane Ψ_2 distributions calculated according the Q-vector after the re-centering with Eq. (9.93) in different centrality classes. The results are shown before the shifting (black histograms) and after the shifting according to Eq. (9.94) (red histograms), respectively.

POI the inclusive muons are selected with the standard muon analysis cuts. Since the front absorber allows to reject most of the hadronic component ($> 90\%$), non-flow correlations from mini-jets are negligible in POI compared with the contribution of muons from the resonance decays. The latter is also very small in the distribution of inclusive muons. Therefore non-flow correlations are expected not to have a visible effect in POI.

standard TPCsa RP non-flow correlations from mini-jets are also partly rejected via the $p_{\rm t}$ cuts ($0.2 < p_{\rm t} < 5$ GeV/c). Non-rejected non-flow correlations are difficult to estimate. They remain as a bias in the final results.

VZERO RP there are more cases to be considered:

- in case we can only get the amplitude from each VZERO cell, these correlations are very difficult to separate but part of these can be accounted for via the event plane flattening procedure;
- what is important is that, due the fact that the acceptance of the VZERO and the muon spectrometer partly overlap, there are both near-side and away-side correlations between the muon spectrometer and V0C and V0A, respectively;

- these correlations also bias the results from other methods when using the VZERO for the RP;
- at present, the only way to check the effects from these correlations is to compare the results obtained with the VZERO RP and those from the standard TPC RP. If the differences are small, we just treat this bias as a systematic uncertainty.

9.3.1.3 Event Plane Resolution

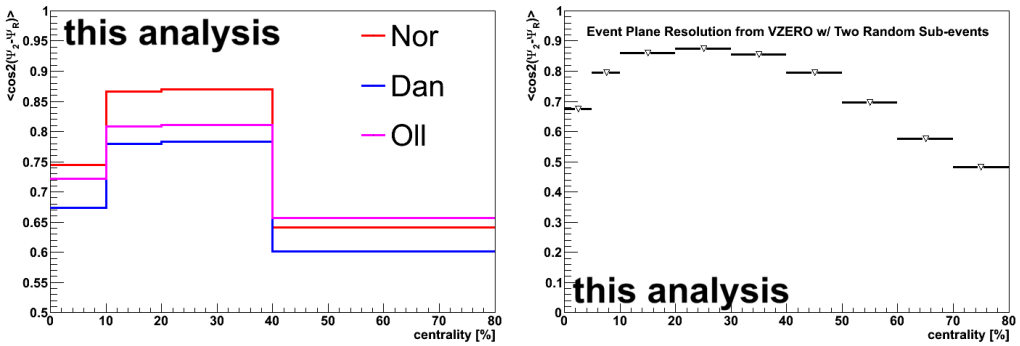

Figure 9.17: The 2nd order event-plane resolution for standard TPCsa RP (left) and VZERO RP (right) as a function of centrality. See text for more details.

One of the most popular method used to estimate the event-plane resolution is based on the event-by-event fluctuations [202, 351]. The procedure is similar to that used to derive Eq. (9.28). To implement this method with data, the following steps are used:

1. in each event, separate the RP into two random sub-events a and b. Then calculate Ψ_2^a and Ψ_2^b event-by-event;
2. calculate $< \cos 2(\Psi_2^a - \Psi_2^b) >$ for events within a same centrality class;
3. solve the following equation:

$$< \cos 2(\Psi_2^a - \Psi_2^b) >= \frac{\pi}{8}\chi^2 e^{-\chi^2/2}[\mathrm{I}_0(\frac{\chi^2}{4}) + \mathrm{I}_1(\frac{\chi^2}{4})]^2, \tag{9.95}$$

   and get the value of χ in each centrality region;
4. the event-plane resolution in a given centrality class is

$$< \cos 2(\Psi_2 - \Psi_\mathrm{R}) >= \frac{\sqrt{\pi}}{2}\chi e^{-\chi^2/2}[\mathrm{I}_0(\frac{\chi^2}{2}) + \mathrm{I}_1(\frac{\chi^2}{2})]. \tag{9.96}$$

Eq. (9.95) and Eq. (9.96) are only valid for the 2nd order harmonic. For other order harmonics, one should follow the procedure in [351] and calculate them by hand.

The left plot in Fig. 9.17 shows the event-plane resolution for standard TPCsa tracks, estimated with the random sub-event technique, as a function of centrality. In this plot, the result labeled as "Oll" is from the standard method using Eq. (9.95) and Eq. (9.96). It is compared to results from another two methods labeled as and "Dan" [336] and "Nor" [339]. In the "Dan" method, the event-plane resolution is estimated as:

$$< \cos n(\Psi_n - \Psi_{\mathrm{R}}) >= \cos \frac{n}{2}(\Psi_n^a - \Psi_n^b). \tag{9.97}$$

The "Nor" method gives the event-plane resolution via [9]:

$$< \cos n(\Psi_n - \Psi_{\mathrm{R}}) >= \sqrt{2 \cdot \cos n(\Psi_n^a - \Psi_n^b)}. \tag{9.99}$$

The right plot in Fig. 9.17 shows the event-plane resolution of the VZERO RP with random sub-events from the standard method in Eq. (9.95) and Eq. (9.96) as a function of centrality. By comparing these results with the corresponding ones from the standard TPCsa RP, we can find that the standard TPCsa RP gives a worse event-plane resolution compared to that from the VZERO RP. This could be due to fluctuations in the event-plane distributions with standard TPCsa RP (Fig. 9.11) which are larger than that from the VZERO RP (Fig. 9.16).

9.3.2 Configurations of Other Methods

Compared to the correction with the EP method, the configurations of other methods are more easier. Thanks to the developers of the Flow Package, the corrections of the NUA correlations for the SP, the GFC and the QC methods, are implemented numerically in AliRoot. The LYZ method does not need to be corrected for NUA correlations. Also, we do not implement the particle weights in the above methods.

Concerning the SP method, its configuration is more straightforward. In this method, the η sub-events are separated as $|\Delta\eta| > 1$ with the standard TPCsa RP. In the case of the VZERO RP, they are separated according to V0A and V0C.

In the following, we will discuss some control plots from the GFC, the QC and the LYZ methods to check if these methods can be used in our analysis.

9.3.2.1 Generating Function Cumulants

As mentioned, the calculation of the cumulants in the GFC method depends on the numerical interpolation of $p_{\max} \times q_{\max}$ complex-value points with the initial value r_0 in Eq. (9.61). The first task in the implementation of the GFC method is to test the stability of the results with different values of r_0. The left plot of Fig. 9.18 shows the $c_2\{2\}$ distribution as a function of centrality with $r_0 = 2.2$, 1 and 4 for standard TPCsa tracks. Despite the values of r_0 change in a large range

[9] Indeed, this method only gives the upper limit of the event-plane resolution,

$$< \cos n(\Psi_n - \Psi_{\mathrm{R}}) >\leq \sqrt{2 \cdot \cos n(\Psi_n^a - \Psi_n^b)}. \tag{9.98}$$

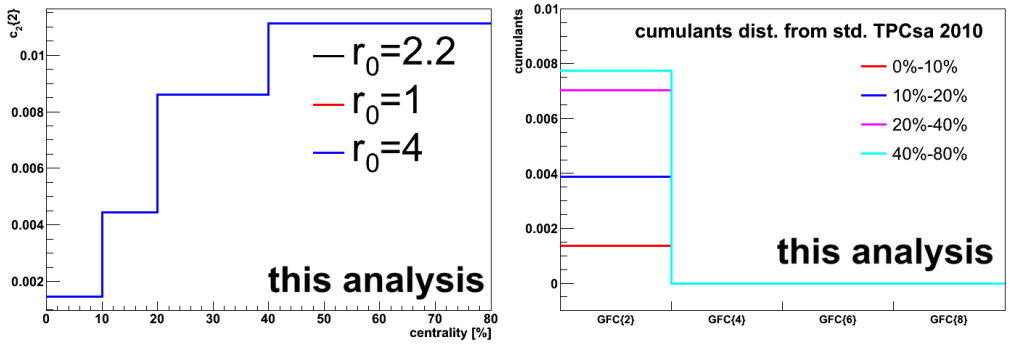

Figure 9.18: Left: the 2nd order integrated cumulant $c_2\{2\}$ distributions as a function of centrality with different values of r_0 as labeled in the plot. Right: the integrated cumulant distribution as a function of the cumulant order in different centrality regions. The results are obtained with the standard TPCsa RP.

($\sim 100\%$), the results of the cumulants are exactly the same. This proves that the GFC method is stable with the standard TPCsa RP.

The right plot of Fig. 9.18 presents the integrated cumulant distribution as a function of the cumulant order in different centrality regions. We can see that, in each centrality region, only the 2nd order of the integrated cumulant $c_2\{2\}$ has a finite value while the others vanish. These results mean that, with this condition, only the 2nd order of integrated cumulants can be used to calculate the differential flow of inclusive muons.

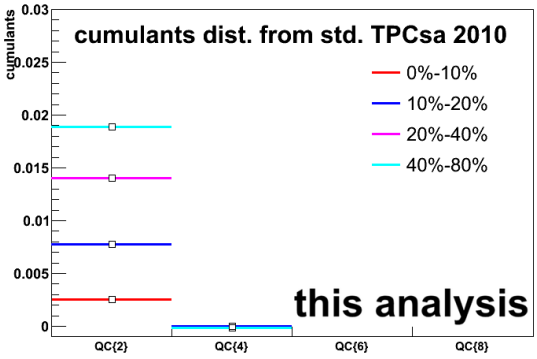

Figure 9.19: The integrated Q-cumulant distributions as a function of the cumulant orders in different centrality classes with the standard TPCsa RP.

We also observe that all order of cumulants vanish with the VZERO RP, despite many different kinds of configurations have been tested. Then, the conclusion for GFC method is that, even the value of cumulants are insensitive with the value of the parameter r_0, they can only be implemented with the standard TPCsa RP and the corresponding differential flow of inclusive muons can only be calculated with the 2nd order cumulants.

9.3.2.2 Q-Cumulants Method

Fig. 9.19 shows the integrated Q-cumulant distribution as a function of the cumulant order in different centrality classes with the standard TPCsa RP. These results show that, in the QC method, the cumulants are validated up to the 4th

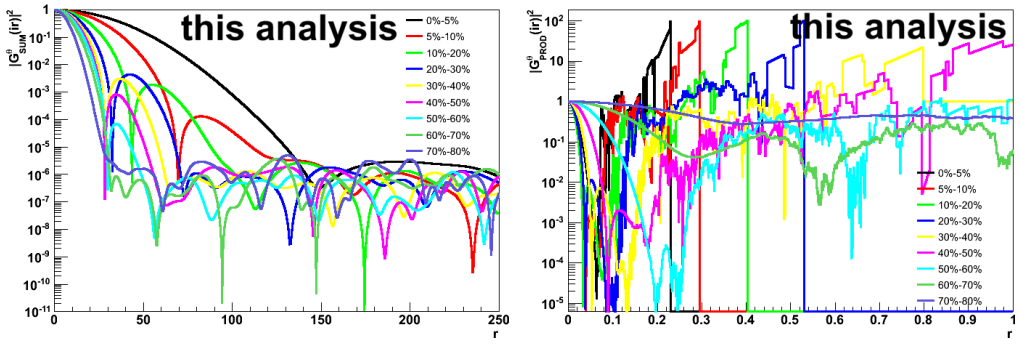

Figure 9.20: $|G_n^\theta(ir)|$ as a function of r with the standard TPCsa RP from sum generating function (left) and product generating function (right), respectively. The results are shown in different centrality regions as labeled in each plot.

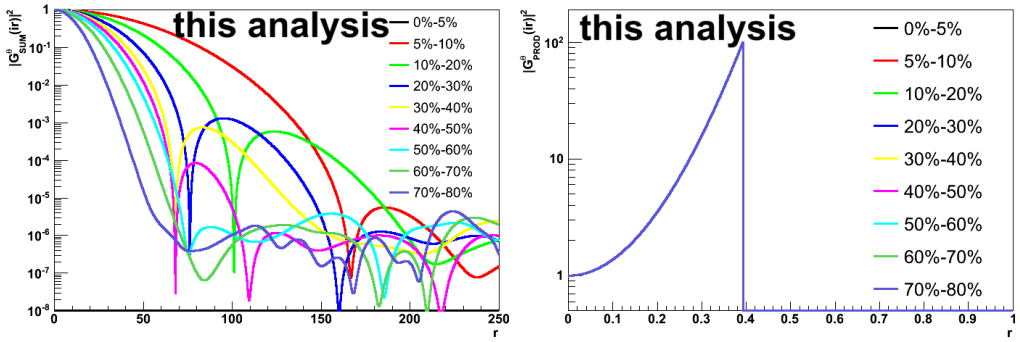

Figure 9.21: The same as Fig. 9.20, but with the VZERO RP.

order with the standard TPCsa RP. Then the corresponding differential flow of the inclusive muons can be determined according to the integrated flow up to this order.

Again, as it is the case with the GFC method, when we use the VZERO RP, all integrated cumulants vanish. In this case, none of the GFC and the QC methods can be used with the VZERO RP. The problem of implementing the cumulants methods with VZERO RP is still under investigation.

9.3.2.3 Lee-Yang-Zeroes Method

In the LYZ method, the integrated flow is determined by the position of the first minimum of $|G_n^\theta(ir)|$. To check if the LYZ method can be used, one should first plot $|G_n^\theta(ir)|$ as a function of r. Fig. 9.20 and Fig. 9.21 show these results with both the standard TPCsa RP and the VZERO RP, respectively, in different centrality regions. In each case, the results from the sum generating function and those from the product generating function are presented. One can see that, with the standard TPCsa RP, both the sum generating function LYZ method and the product generating function LYZ method are validated since there are obvious minimum

positions in each case. With the VZERO RP, clear minima only appear with the sum generating function while with the product generating function there is no minimum and the distributions in all centrality classes are the same. The results show that only the sum generating function LYZ can be implemented with the VZERO RP.

9.4 Results and Discussions

According to the study presented in Sec. 9.3, the status of the different flow analysis methods with the standard TPCsa RP and VZERO RP is summarized in Tab. 9.1 [10].

status	standard TPCsa RP	corrected VZERO RP
$V_2\{\mathrm{EP}\}$	$\surd$	$\surd$
$V_2\{\mathrm{SP}\}$	$\surd$	$\surd$
$V_2\{\mathrm{GFC},2\}$	$\surd$	$\times$
$V_2\{\mathrm{GFC},4\}$	$\times$	$\times$
$V_2\{\mathrm{QC},2\}$	$\surd$	$\times$
$V_2\{\mathrm{QC},4\}$	$\surd$	$\times$
$V_2\{\mathrm{LYZ},\mathrm{SUM}\}$	$\surd$	$\surd$
$V_2\{\mathrm{LYZ},\mathrm{PROD}\}$	$\surd$	$\times$

Table 9.1: The status of the different flow analysis methods with the standard TPCsa RP and the VZERO RP.

9.4.1 Preliminary Results

In all the validated cases in Tab. 9.1: the event plane distribution with standard TPCsa RP is not very flat after the flattening procedure. The GFC method always gives very large error bars [352]. All these issues are still presently under study. In the final results, we exclude these two cases.

In Fig. 9.22, the p_{t}-dependence of v_2 for inclusive muons with different analysis methods and different kinds of RP are compared together in four centrality classes. The LYZ methods, with both sum and product generating functions, are not validated in the most central $(0-10\%)$ and most peripheral $(40-80\%)$ collisions. In the two intermediate centrality bins $(10-20\%$ and $20-40\%)$, the LYZ methods give results very similar to those from the 4th order of QC method. The results from the LYZ and 4th order of QC methods are systematically lower than those from other methods since they allow to reject almost all non-flow correlations. Also, flow fluctuations could be responsible for the observed trends. In all cases, the v_2 from

[10] "$\surd$" means validated and "$\times$" means not validated.

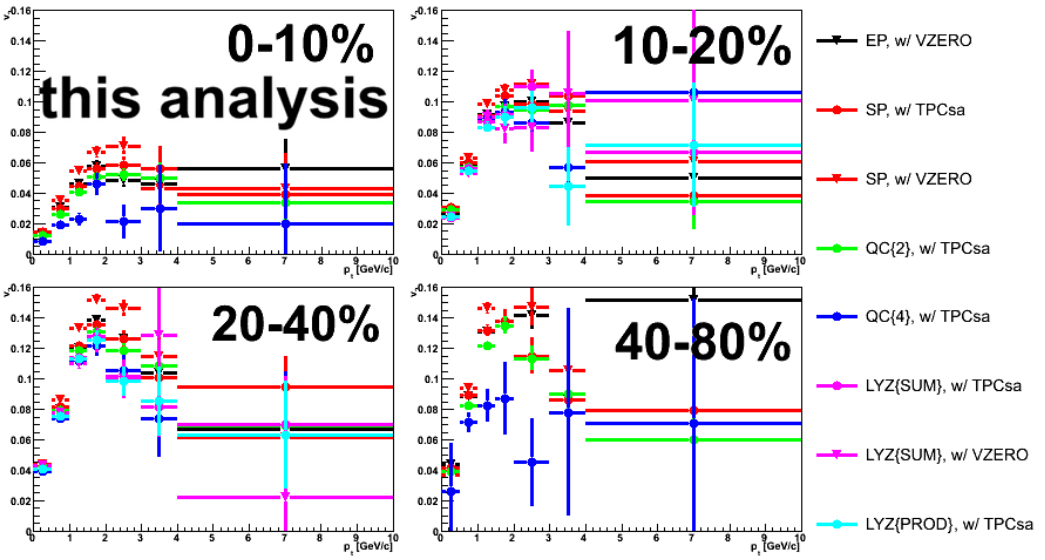

Figure 9.22: The p_{t}-dependence of v_2 for inclusive muons with different analysis methods and different kinds of RP in four centrality classes.

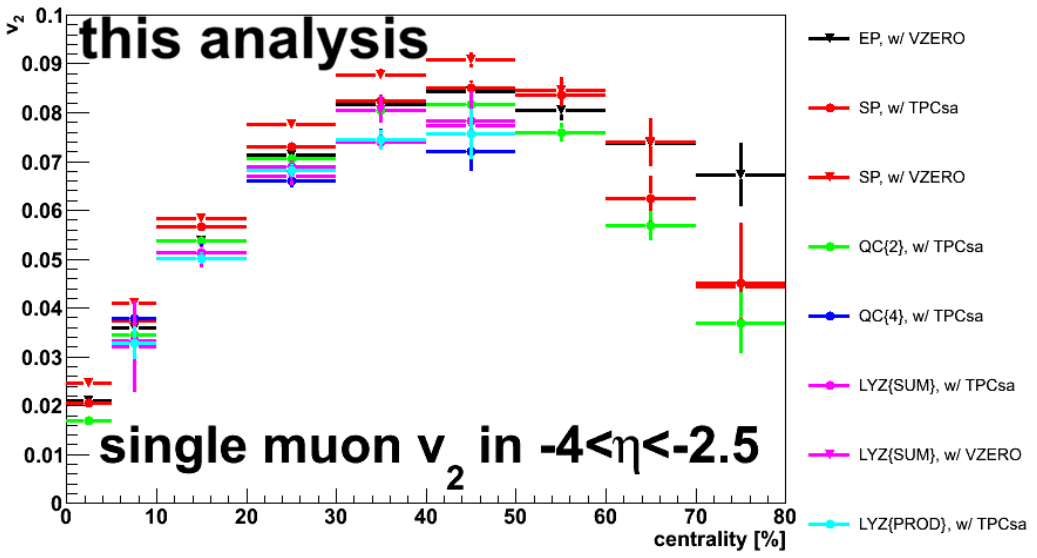

Figure 9.23: The same as Fig. 9.22, but the results are integrated over p_{t} and shown as a function of centrality.

the 2nd order of the QC method gives smaller results than the SP method. This was expected since the 2nd order of the QC method rejects non-flow correlations up to the 2nd order but in the SP method non-flow correlations are only partly rejected via the η sub-events. Within uncertainties, all results from different cases are consistent with each other. We note that the large fluctuations in the high p_{t}

region are due to a lack of statistics.

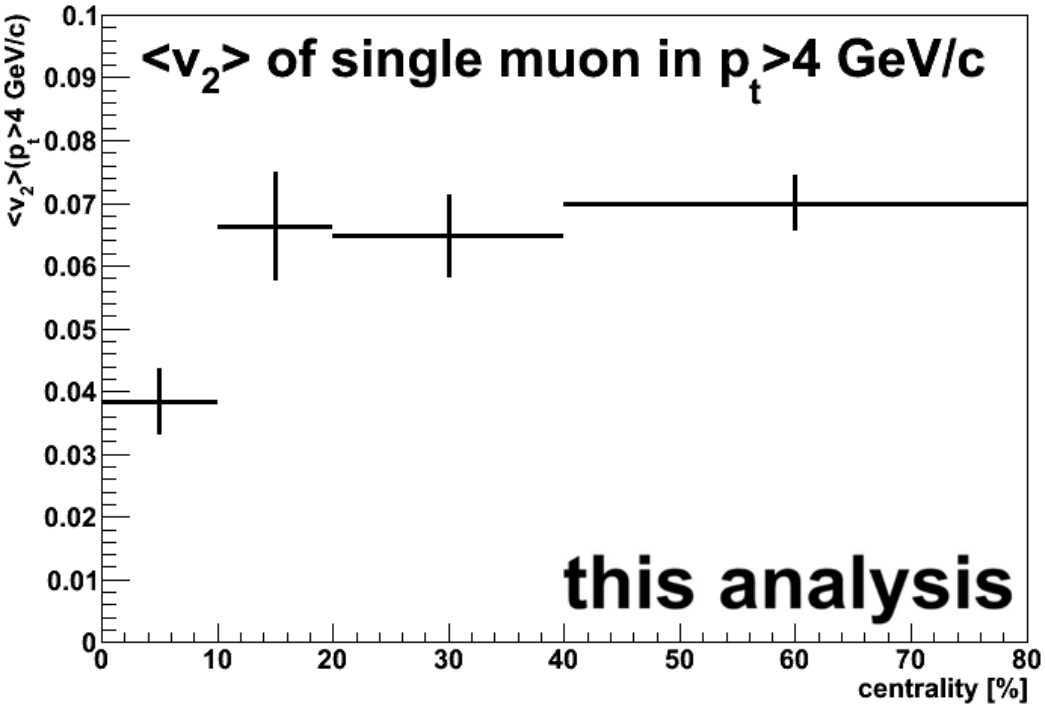

Figure 9.24: The mean values of the results in Fig. 9.23 for $p_{\mathrm{t}} > 4$ GeV/c.

Fig. 9.23 shows the v_2 of inclusive muons integrated over p_{t} and as a function of centrality with different analysis methods and RPs. Results from different cases are similar to those in Fig. 9.22. These results exhibit a systematic trend: from the most central collisions to the most peripheral ones, v_2 increases, reach a maximum value for semi-central collisions, and then decreases. This is due to the fact that v_2 results from the asymmetric pressure gradient in the initial stage of the collisions. In the most central and most peripheral collisions, the asymmetry of the initial system is small and makes the values of v_2 smaller. The systematic trend in the v_2 of inclusive muons in Fig. 9.23 show hints that a thermalized partonic phase was formed in Pb–Pb collisions at $\sqrt{s_{\mathrm{NN}}} = 2.76$ TeV.

The mean values of v_2 in Fig. 9.23 for $p_{\mathrm{t}} > 4$ GeV/c are shown in Fig. 9.24. According to the study presented in Chap. 8, in this high p_{t} region, muons from heavy flavour decays dominate. From this figure, one can see that v_2 does not depend on the collision centrality for centrality classes $> 10\%$. Also, in this high p_{t} region, v_2 is believed to be controlled by the path length dependence of parton energy loss in the QCD medium. To systematically investigate this interesting property, we are going to analyse more statistics from the Pb–Pb data taken in 2011.

9.4.2 Discussion

With the LHC10h pass 2 data, we studied the v_2 of inclusive muons according to the following steps:

1. implementation the muon selection cuts in the flow package;
2. investigation of the strategy for the event-plane flattening, especially for the VZERO RP;
3. test if the different flow analysis methods with both the standard TPCsa RP and the VZERO RP can be applied;
4. extract preliminary results of v_2 for inclusive muons.

Also, there are many outlooks:

- check the results with more statistics using the Pb–Pb data taken in 2011 with muon triggered events;
- investigate whether there is any bias to determine the RP in muon triggered events;
- improve the event-plane flattening for the standard TPCsa RP;
- validate the cumulant methods and the LYZ method with the product generating function for the VZERO RP. This is quite important if the analysis in the future is based on muon triggered events;
- develop the strategy to extract the flow of muons from open heavy flavour decays from the results of inclusive muons.

For what concerns the last item, Fig. 9.24 shows that one possible way is to apply a high p_{t} cut. There could be two possible ways to obtain the results at lower p_{t}:

- use the measured flow of light hadrons and extrapolate it in the acceptance of muon spectrometer to estimate the flow of background muons [353];
- since muons from open heavy flavour decays are mainly located in the low DCA region, the flow measured for DCA larger than a given value could be used to measure the flow from the background muons [354].

According to above two proposals, if the flow from the background muons v_n^{bkg} can be estimated, and if we can know the fraction of background f_{bkg} from other approaches, *eg.* the vertex unfolding method [297, 282], then flow of muons from open heavy flavour decay $v_n^{\mu\leftarrow\mathrm{HF}}$ can be estimated as:

$$v_n^{\mu\leftarrow\mathrm{HF}} = \frac{v_n^{\text{inclusive }\mu} - v_n^{\mathrm{bkg}} \cdot f_{\mathrm{bkg}}}{1 - f_{\mathrm{bkg}}}, \tag{9.100}$$

where $v_n^{\text{inclusive }\mu}$ denotes the flow of inclusive muons as shown in Fig. 9.22 and Fig. 9.23.

Conclusion and Outlooks

In this thesis, after a general introduction on heavy ion collisions and QCD phase transitions, we summarized the motivations for the study of open heavy flavours in nucleon–nucleon, nucleon–nucleus and nucleus–nucleus collisions. In particular, we emphasized the novelties at the LHC energies. Then we gave an overview of:

- the ALICE detector with a detailed description of the forward muon spectrometer;
- the ALICE online and offline frameworks;
- the offline analysis framework (for data and simulations) and, in particular, the software developed for the study of heavy flavours.

After this general introduction on both theoretical and experimental aspects, the work done in this thesis has been presented in five different parts.

First, we have shown a performance study, based on simulation, for the measurement of D- and B-hadron production cross sections via the single muon and the dimuon channels in pp collisions at $\sqrt{s} = 14$ TeV. We have started with an ideal case, without background. We have used a procedure based on a combined fit to separate the single muon and dimuon components from charm and beauty decays from the total single muon $p_{\rm t}$ distribution and dimuon invariant mass distribution, respectively. After that, the $p_{\rm t}$ distribution of open D- and B-hadrons have been obtained by correcting the corresponding (di)muons $p_{\rm t}$ (invariant mass) distributions for the reconstruction efficiency of (di)muons in the ALICE muon spectrometer, the kinematics of the open heavy flavour hadron semi-muonic decays and the decay branching ratios. After normalization to the number of minimum bias events and to the corresponding minimum bias cross section in pp collisions at $\sqrt{s} = 14$ TeV, the $p_{\rm t}$-differential production cross sections of open D- and B-hadrons have been obtained. The systematic uncertainty on the final results mainly come from two parts: a first one from the combined fit to separate the muon components from open charm and beauty hadron decays and a second one from the conversion of the (di)muon $p_{\rm t}$ (invariant mass) distributions to the $p_{\rm t}$-differential spectra at the hadron level. The first uncertainty was estimated by performing combined fits with different fit parameters. The second uncertainty was estimated by comparing results with correction factors from different shapes in order to mimic different model predictions. The reconstructed production cross sections of open heavy flavour hadrons are in very good agreement with the simulation inputs within errors. Furthermore, we discussed the strategy to remove different background sources in the single muon $p_{\rm t}$ distribution. After implementation of the strategy in minimum bias simulations, and background subtraction, we have repeated all above steps and obtained again

a nice agreement between the reconstructed p_{t}-differential production cross section of open heavy flavour hadrons and the input in the minimum bias simulations. The final results show the ability of the ALICE muon spectrometer for reconstructing the production cross section of open D- and B-hadrons via the (di)muon channels. All the strategy used in this work give very important insights for the data analysis.

After this performance study, we have started analyzing the data in pp collisions at $\sqrt{s} = 900$ GeV collected at the end of 2009. This first helped us to understand some features in the data:

- event trigger classes and the detector cluster used to deliver different kinds of event trigger;
- selection of physics events according to the offline physics selection;
- efficiency of the selection of muon tracks.

Furthermore, this study allowed to investigate the performance of the ALICE muon spectrometer for physics analyses:

- reconstruction of muon tracks;
- behaviour of the background components;
- optimization of cuts used to reject the background.

With the findings from the study of this data sample, the incoming physics analysis becomes more straightforward.

The data taken in pp collisions at $\sqrt{s} = 7$ TeV in 2010 offer sufficient statistics for physics analysis. The physics aim at this stage was to measure the production cross section of muons from open heavy flavour decays. We started with the study of the data quality assurance (QA) and muon analysis by means of the ALICE official physics event selection. Other conditions have been implemented at both event and muon track levels in order to reject background not suitable for physics analyses. After the event and the muon track selection, we have investigated the normalization strategy of the selected data sample. As the data sample has been collected with both minimum bias events and muon trigger events, the physics analysis has been validated for both types of events. The strategy for the normalization has been presented for these two samples, separately. What is important in the normalization of minimum bias events is the pile-up correction. We introduced two independent methods for this correction, one is based on applying the cuts of the reconstructed pile-up vertex and another is based on the estimate of the pile-up factor according to the CTP information. The later is more stable than the first one for the data taking period where the pile-up effect is small. As the data taking periods which have the largest pile-up effects are rejected by the QA selection, in the data analysis, we corrected the pile-up effects with CTP information. The key point of the normalization of muon triggered events is to estimate the corresponding number of the minimum bias events for the used muon triggered data sample. Two methods can be used, the CTP scaling method and the multiplicity scaling method. The advantage of the later

is that it avoids to investigate the evolution of the CTP rate for different triggers with the data taking time. In practice, we choose the multiplicity scaling method to normalize the muon triggered events. After understanding all basic conditions, the main part in this work was to subtract the background from the inclusive muon spectrum. We decided to show the results for $p_{\rm t} > 2$ GeV/c since, according to MC simulations the only dominant background component in this region is muons from primary kaon and pion decays. The method used to estimate the yield of this background in data is to get its predicted $p_{\rm t}$ shape from models and normalize it to data. The differences between different models and transport codes give the corresponding systematic uncertainty. After the subtraction of the background and efficiency correction via efficiency matrices built under realistic detector configurations, the $p_{\rm t}$-differential production cross sections of muons from open heavy flavour decays were obtained in five η bins. Then the η-differential production cross section was obtained by integrating the results in these five η bins and the $p_{\rm t}$-differential distribution in the acceptance of the muon spectrometer was obtained by adding the results in the five different η bins. A good agreement has been observed between data and FONLL predictions. Finally, we have also discussed an alternative method to estimate the background. This consists in extrapolating the charged kaon and pion spectra measured in the ALICE central barrel to forward rapidity in order to get the decay muon spectra in the forward region via the MC simulations for the decay kinematics. The results obtained with this background estimate strategy fully agree with the ones from the previous method. The results from these studies give the baseline for investigating nuclear effects on heavy flavour production in heavy-ion collisions as well as for validating pQCD calculations in this new energy regime. This work is published in **Physics Letters B** (see Appendix A).

The first heavy-ion run, Pb–Pb collisions at $\sqrt{s_{\rm NN}} = 2.76$ TeV, took place at the LHC in the end of 2010. This allowed to study the suppression of high-$p_{\rm t}$ muons from open heavy flavour decays, which is thought to result from in-medium energy loss of heavy quarks. After an introduction of the event and track selections in Pb–Pb collisions, in particular of their differences compared to pp collisions, we illustrated the principle of the centrality selection in data with the corresponding centrality QA cuts. Then we focused on the background estimate in Pb–Pb collisions. Due to unknown quenching effects in data which are hard to estimate from simulations, the strategy for the background estimate here is quite different from that in pp collisions. First, we assumed that the quenching strength in the central rapidity region is the same as that at forward rapidity. Under this assumption, we extrapolated the measured $p_{\rm t}$ spectra of kaons and pions in different centrality classes in Pb–Pb collisions from the ALICE central barrel region to the forward rapidity region. We then have built, with fast simulations, the decay muon spectra in the forward region in different centrality classes. At this step, to avoid the lack of input data from the central barrel measurements, we have used the measured yield of $\rm K^0_s$ to estimate the yield of charged kaons, and derived those in all centrality classes using the double ratio between the $R_{\rm AA}$ of decay muons from kaons and pions and that of muons from pion decays, in two centrality classes. After this, the difference

of the quenching strength for charged hadrons between the central barrel and the forward region has been estimated as an uncertainty of 100% (varying the estimated yield of decay muons in different centrality regions from 0 to 100%). The nuclear modification factor $R_{\rm AA}$ of the signal muons has been obtained by dividing the estimated spectra of muons from open heavy flavour decays (which was obtained by subtracting the estimated decay muon background in each centrality class to the corresponding inclusive muon spectrum) by the production cross section of heavy flavour decay muons measured in pp collisions at $\sqrt{s} = 2.76$ TeV (analysed with the same strategy as that implemented for the 7 TeV data). These results show a very clear suppression which increases when the collisions become more and more central. This suppression does not depend on transverse momentum for $p_{\rm t} > 4$ GeV/c. This work is accepted as a publication of **Physical Review Letters** (see Appendix B).

Also, with the Pb–Pb data taken at the end of 2010, we have presented a first measurement of the elliptic flow of inclusive muons. The motivation for this work was to validate different flow analysis methods and to test the strategy for the measurement of the flow of muons from heavy flavour decays. After the introduction of different flow analysis methods, we illustrated our physics requirements. Then, the preliminary results of the inclusive muon flow have been obtained by implementing different flow analysis methods. The results from different method are in good agreement with each other within errors. The results from this study are:

- different flow analysis methods have been systematically tested for muon flow analysis;
- validation of the event plane flattening procedure for the VZERO amplitude;
- the stability of the cumulants methods and the Lee-Yang Zeros method have been investigated;
- according to the results of the elliptic flow for inclusive muons, proposals for getting the flow of muons from open heavy flavour decays have been detailed.

Of course, there are plenty of issues left for coming PhD students:

- in both pp and Pb–Pb collisions, the extraction of muons from open heavy flavour decays is difficult to handle in the $p_{\rm t}$ region where the background level is large (we started at $p_{\rm t} > 2$ GeV/c and $p_{\rm t} > 4$ GeV/c in pp and Pb–Pb collisions, respectively). One of the solution would be to estimate the decay muon components by unfolding the vertex distribution with fits which take into account the decay length of light hadrons. An alternative way to overcome this problem is to study punch through hadrons in the muon spectrometer as follows:
  1. isolate punch through hadrons which are rejected by the matching of the reconstructed tracks with the muon trigger tracks;
  2. after the correction of the front absorber effect and detector efficiency (this step could be quite similar to that implemented in the fast simulation which has been used to estimate the decay muon background in

Pb–Pb collisions), the charged hadron spectra in data in the forward region could be reproduced;

3. use as input this reproduced spectra in the simulations with the realistic detector configurations, then the spectra of both decay muons and secondary muons could be estimated in data;
4. with such a strategy, the measurement of muons from open heavy flavour decays could be done in all the p_{t} range (but one should be careful about the tracking efficiency at low p_{t} due to the 3 GeVc mean energy loss of muon tracks in the front absorber);
5. furthermore, this procedure also should allow us measure the R_{AA} of charged hadrons.

- The background subtraction for muon elliptic flow is not as straightforward as that for identified particles as one should know both the fraction of background and the magnitude of flow of the background. Some proposals on this topic are given in Sec. 9.4.2.

- With the high statistics in both pp and Pb–Pb collisions taken in 2011 and 2012 (until now), we can start to study W physics with the muon spectrometer. The main challenge is not to extract the W signals, but the present momentum resolution in the high p_{t} region that should be improved and a better alignment is needed.

The final words to the young and ambitious researchers: **enjoy life during your PhD career in heavy-ion physics!**

Part IV

Appendix

Appendix A

Publication of "Heavy Flavour decay muon production at forward rapidity in proton–proton collisions at $\sqrt{s} = 7$ TeV"

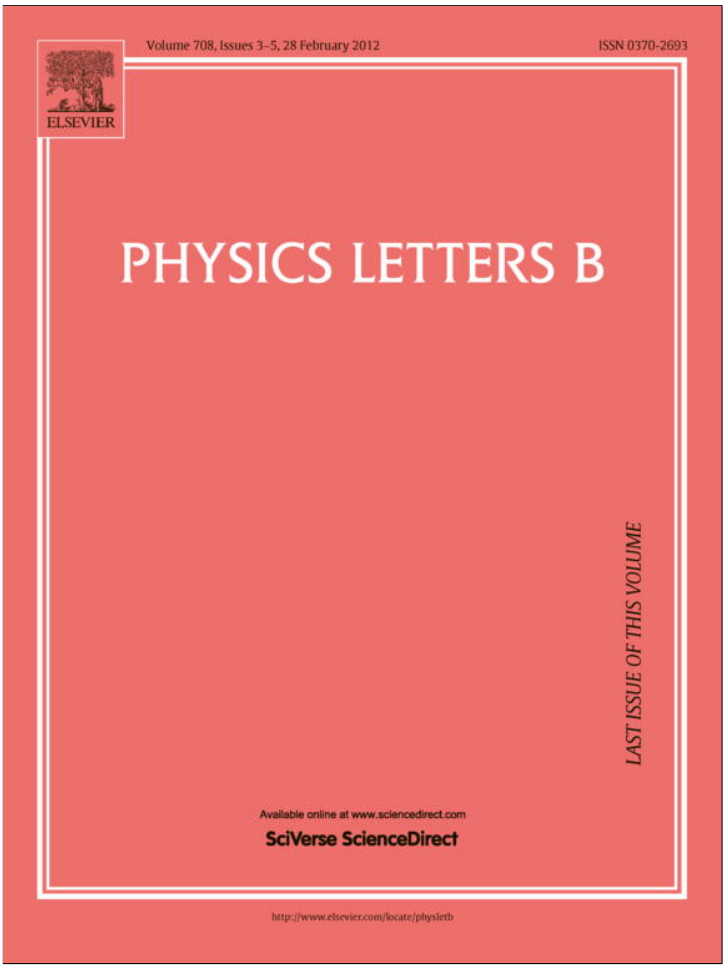

Physics Letters B 708 (2012) 265–275

Contents lists available at SciVerse ScienceDirect

Physics Letters B

www.elsevier.com/locate/physletb

Heavy flavour decay muon production at forward rapidity in proton–proton collisions at $\sqrt{s} = 7$ TeV ☆

ALICE Collaboration

ARTICLE INFO

Article history:
Received 20 January 2012
Accepted 24 January 2012
Available online 28 January 2012
Editor: L. Rolandi

Keywords:
LHC
ALICE experiment
pp collisions
Single muons
Heavy flavour production

ABSTRACT

The production of muons from heavy flavour decays is measured at forward rapidity in proton–proton collisions at $\sqrt{s} = 7$ TeV collected with the ALICE experiment at the LHC. The analysis is carried out on a data sample corresponding to an integrated luminosity $L_{\rm int} = 16.5\ {\rm nb}^{-1}$. The transverse momentum and rapidity differential production cross sections of muons from heavy flavour decays are measured in the rapidity range $2.5 < y < 4$, over the transverse momentum range $2 < p_{\rm t} < 12$ GeV/c. The results are compared to predictions based on perturbative QCD calculations.

1. Introduction

The study of heavy flavour (charm and beauty) production in proton–proton collisions at LHC (Large Hadron Collider) energies provides an important test of perturbative QCD (pQCD) calculations [1,2] in a new energy domain, where unprecedented small Bjorken-x (momentum fraction) values are probed. In the rapidity region $2.5 < y < 4$, charm (beauty) production at $\sqrt{s} = 7$ TeV is expected to be sensitive to x values down to about $6 \cdot 10^{-6}$ ($2 \cdot 10^{-5}$). Important progress has been achieved in the understanding of heavy flavour production at lower energies. In earlier measurements, the beauty production cross section in $\mathrm{p\bar{p}}$ collisions at $\sqrt{s} = 1.8$ TeV measured by the CDF and D0 experiments [3,4] at the FNAL Tevatron, was found to be higher than Next-to-Leading Order (NLO) pQCD predictions [1]. More recent results from the CDF Collaboration [5], for $\mathrm{p\bar{p}}$ collisions at $\sqrt{s} = 1.96$ TeV, are described well by Fixed Order Next-to-Leading Log (FONLL) [6,7] and NLO [8] pQCD calculations. The charm production cross section measured at the FNAL Tevatron [9] is also well reproduced by FONLL [10] and GM-VFN [11] calculations within experimental and theoretical uncertainties, although at the upper limit of the calculations. The PHENIX and STAR Collaborations [12,13] at the RHIC (Relativistic Heavy Ion Collider) measured the production of muons and electrons from heavy flavour decays in pp collisions at $\sqrt{s} = 0.2$ TeV. The upper limit of FONLL pQCD calculations [14] is consistent with the measurement of electrons from heavy flavour decays in the mid-rapidity region, while in the forward rapidity region the production of muons from heavy flavour decays is underestimated by the model calculations. Furthermore, at LHC energies, the ATLAS [15], LHCb [16] and CMS [17,18] Collaborations reported on the measurement of beauty production in pp collisions at $\sqrt{s} = 7$ TeV. The results are consistent with NLO pQCD calculations within uncertainties. A similar agreement with FONLL calculations is also observed for mid-rapidity electrons and muons from heavy flavour decays, measured by the ATLAS experiment [19] in pp collisions at $\sqrt{s} = 7$ TeV. In this respect, it is particularly interesting to perform the measurement of heavy flavour decay muon production in the forward rapidity region at the LHC and compare it with theoretical models.

The investigation of heavy flavour production in pp collisions also constitutes an essential baseline for the corresponding measurements in heavy ion collisions. In the latter, heavy quarks are produced at early stages of the collision and then experience the full evolution of the extremely hot and dense, strongly interacting medium [20,21]. The modification of the heavy flavour transverse momentum distributions measured in heavy ion collisions with respect to those measured in pp collisions is considered as a sensitive probe of this medium [22,23].

Finally, the study of heavy flavour production is also important for the understanding of quarkonium production, both in pp, p–nucleus and nucleus–nucleus collisions [20,21].

The ALICE experiment [24] measures the heavy flavour production at mid-rapidity through the semi-electronic decay channel [25] and in a more direct way through the hadronic D-meson decay channel [26], and at forward rapidity through the semi-muonic decay channel. In this Letter, we present the measurement of differential production cross sections of muons from heavy flavour decays in the rapidity range $2.5 < y < 4$ and transverse momentum range $2 < p_{\rm t} < 12$ GeV/c, with the ALICE muon

☆ © CERN for the benefit of the ALICE Collaboration.

0370-2693/
doi:10.1016/j.physletb.2012.01.063

spectrometer [24], in pp collisions at $\sqrt{s} = 7$ TeV. The results are compared to FONLL pQCD calculations [2,27].

The Letter is organized as follows. Section 2 consists of an overview of the ALICE experiment with an emphasis on the muon spectrometer and a description of data taking conditions. Section 3 is devoted to the analysis strategy: event and track selection, background subtraction, corrections, normalization and determination of systematic uncertainties. Section 4 addresses the experimental results: p_{t}- and y-differential production cross sections of muons from heavy flavour decays at forward rapidity, and comparisons to FONLL pQCD predictions. Conclusions are given in Section 5.

2. The ALICE experiment and data taking conditions

A detailed description of the ALICE detector can be found in [24]. The apparatus consists of two main parts: a central barrel (pseudo-rapidity coverage: $|\eta| < 0.9$) placed in a large solenoidal magnet ($B = 0.5$ T), which measures hadrons, electrons and photons, and a muon spectrometer ($-4 < \eta < -2.5$[1]). Several smaller detectors for global event characterization and triggering are located in the forward and backward pseudo-rapidity regions. Amongst those, the VZERO detector is used for triggering purposes and in the offline rejection of beam-induced background events. It is composed of two scintillator arrays placed at each side of the interaction point and covering $2.8 < \eta < 5.1$ and $-3.7 < \eta < -1.7$. The central barrel detector used in this work for the interaction vertex measurement is the Silicon Pixel Detector (SPD), the innermost part of the Inner Tracking System (ITS). The SPD consists of two cylindrical layers of silicon pixels covering $|\eta| < 2.0$ and $|\eta| < 1.4$ for the inner and outer layer, respectively. The SPD is also used in the trigger logic.

The muon spectrometer detects muons with momentum larger than 4 GeV/c and is composed of two absorbers, a dipole magnet providing a field integral of 3 Tm, and tracking and trigger chambers. A passive front absorber of 10 interaction lengths (λ_{I}), made of carbon, concrete and steel, is designed to reduce the contribution of hadrons, photons, electrons and muons from light hadron decays. A small angle beam shield ($\theta < 2^\circ$), made of tungsten, lead and steel, protects the muon spectrometer against secondary particles produced by the interaction of large-η primary particles in the beam pipe. Tracking is performed by means of five tracking stations, each composed of two planes of Cathode Pad Chambers. Stations 1 and 2 (4 and 5) are located upstream (downstream) of the dipole magnet, while station 3 is embedded inside the dipole magnet. The intrinsic spatial resolution of the tracking chambers is better than 100 μm. Two stations of trigger chambers equipped with two planes of Resistive Plate Chambers each are located downstream of the tracking system, behind a 1.2 m thick iron wall of 7.2 λ_{I}. The latter absorbs most of the hadrons that punch through the front absorber, secondary hadrons produced inside the front absorber and escaping it and low momentum muons ($p < 4$ GeV/c). The spatial resolution of the trigger chambers is better than 1 cm and the time resolution is about 2 ns. Details concerning track reconstruction can be found in [28,29].

The results presented in this publication are based on the analysis of a sample of pp collisions at $\sqrt{s} = 7$ TeV collected in 2010, corresponding to an integrated luminosity of 16.5 nb^{-1}.

The data sample consists of minimum bias trigger events (MB) and muon trigger events (μ-MB), the latter requiring, in addition to the MB trigger conditions, the presence of one muon above a transverse momentum (p_{t}) threshold that reaches the muon trigger system. The MB trigger is defined as a logical OR between the requirement of at least one hit in the SPD and a hit in one of the two VZERO scintillator arrays. It also asks for a coincidence between the signals from the two beam counters, one on each side of the interaction point, indicating the passage of bunches. This corresponds to at least one charged particle in 8 units of pseudo-rapidity. The logic of the μ-MB trigger requires hits in at least three (out of four possible) trigger chamber planes. The estimate of the muon transverse momentum is based on the deviation of the measured track with respect to a straight line coming from the interaction point, in the bending plane (plane measuring the position along the direction perpendicular to the magnetic field). By applying a cut on this deviation, tracks above a given p_{t} threshold are selected. The p_{t} threshold allows the rejection of soft background muons mainly coming from pion and kaon decays, and also to limit the muon trigger rate when high luminosities are delivered at the interaction point. In the considered data taking period, the p_{t} trigger threshold was set to its minimum value of about 0.5 GeV/c and the corresponding muon trigger rate varied between about 40 and 150 Hz. The instantaneous luminosity at the ALICE interaction point was limited to $0.6\text{–}1.2 \cdot 10^{29}$ cm^{-2} s^{-1} by displacing the beams in the transverse plane by 3.8 times the r.m.s. of their transverse profile. In this way, the probability to have multiple MB interactions in the same bunch crossing is kept below 2.5%.

The alignment of the tracking chambers, a crucial step for the single muon analysis, was carried out using the MILLEPEDE package [30], by analyzing tracks without magnetic field in the dipole and solenoidal magnet. The corresponding resolution is about 300 μm in the bending plane, for tracks with $p_{\mathrm{t}} > 2$ GeV/c. With such alignment precision, the relative momentum resolution of reconstructed tracks ranges between about 1% at a momentum of 20 GeV/c and 4% at 100 GeV/c.

3. Data analysis

The single muon analysis was carried out with muon trigger events while, as will be discussed in Section 3.4, minimum bias trigger events were used to convert differential muon yields into differential cross sections. The identification of muons from charm and beauty decays in the forward region is based on the p_{t} distribution of reconstructed tracks. Three main background contributions must be subtracted and/or rejected:

- decay muons: muons from the decay of primary light hadrons including pions and kaons (the main contribution) and other meson and baryon decays (such as J/ψ and low mass resonances η, ρ, ω and ϕ);
- secondary muons: muons from secondary light hadron decays produced inside the front absorber;
- punch-through hadrons and secondary hadrons escaping the front absorber and crossing the tracking chambers, which are wrongly reconstructed as muons.

A Monte Carlo simulation based on the GEANT3 transport code [31,32] and using the PYTHIA 6.4.21 event generator [33,34] (tune Perugia-0 [35]) was performed to obtain the p_{t} distributions of these different contributions. They are displayed in Fig. 1 after all the selection cuts discussed in Section 3.1 were applied. After cuts, the component of muons from heavy flavour decays prevails over the background contribution for $p_{\mathrm{t}} \gtrsim 4$ GeV/c. The simulation results indicate that the hadronic background and the contribution of fake tracks (tracks which are not associated to one single particle crossing the whole spectrometer) are negligible. The component of

[1] The muon spectrometer covers a negative pseudo-rapidity range in the ALICE reference frame. η and y variables are identical for muons in the acceptance of the muon spectrometer, and in pp collisions the physics results are symmetric with respect to η (y) = 0. They will be presented as a function of y, with positive values.

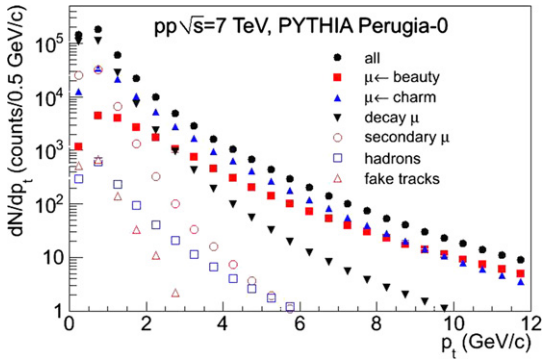

Fig. 1. Transverse momentum distribution of reconstructed tracks in the muon spectrometer after all selection cuts were applied (see Section 3.1 for details). The distributions were obtained from a PYTHIA [33,34] (tune Perugia-0 [35]) simulation of pp collisions at $\sqrt{s} = 7$ TeV. The main sources are indicated in the figure.

muons from $W^{\pm}$ and Z^0 decays, which dominates in the p_t range 30–40 GeV/c [36,19], is not considered in this analysis. This contribution is negligible in the p_t range of interest 2–12 GeV/c.

3.1. Data sample: event and track selection

The data sample used in the physics analysis amounts to $1.3 \cdot 10^7$ μ-MB trigger events. These selected events satisfied the quality criteria on detector conditions during data taking and the analysis quality criteria, which reduced the beam-induced background. This was achieved by using the timing information from the VZERO and by exploiting the correlation between the number of hits and track segments in the SPD. The accepted events have at least one interaction vertex reconstructed from hits correlation in the two SPD layers. The corresponding total number of tracks reconstructed in the muon spectrometer is $7.8 \cdot 10^6$. Various selection cuts were applied in order to reduce the background contributions in the data sample. Tracks were required to be reconstructed in the geometrical acceptance of the muon spectrometer, with $-4 < \eta < -2.5$ and $171^\circ < \theta_{\rm abs} < 178^\circ$, $\theta_{\rm abs}$ being the track polar angle measured at the end of the absorber. These two cuts reject about 9% of tracks. Then, the track candidate measured in the muon tracking chambers was required to be matched with the corresponding one measured in the trigger chambers. This results in a very effective rejection of the hadronic component that is absorbed in the iron wall. This condition is fulfilled for a large fraction of reconstructed tracks since the analysis concerns μ-MB trigger events. The fraction of reconstructed tracks that are not matched with a corresponding one in the trigger system is about 5%. For comparison, in MB collisions this fraction is about 64%. Furthermore, the correlation between momentum and Distance of Closest Approach (DCA, distance between the extrapolated muon track and the interaction vertex, in the plane perpendicular to the beam direction and containing the vertex) was used to remove remaining beam-induced background tracks which do not point to the interaction vertex. Indeed, due to the multiple scattering in the front absorber, the DCA distribution of tracks coming from the interaction vertex is expected to be described by a Gaussian function whose width depends on the absorber material and is proportional to $1/p$. The beam-induced background does not follow this trend and can be rejected by applying a cut on $p \times \mathrm{DCA}$ at 5σ, where σ is extracted from a Gaussian fit to the $p \times \mathrm{DCA}$ distribution measured in two regions in $\theta_{\rm abs}$, corresponding to different materials in the front absorber. This cut removes 0.4% of tracks, mainly located in the high p_t range (in the region $p_t > 4$ GeV/c, this condition rejects about 13% of tracks). After these cuts, the data sample consists of $6.67 \cdot 10^6$ muon candidates.

The measurement of the heavy flavour decay muon production is performed in the region $p_t > 2$ GeV/c where the contribution of secondary muons is expected to be small (about 3% of the total muon yield, see Fig. 1). In such a p_t region the main background component consists of decay muons and amounts to about 25% of the total yield (see Fig. 1).

3.2. Subtraction of the background contribution of decay muons

The subtraction of the background component from decay muons (muons from primary pion and kaon decays, mainly) is based on simulations, using PYTHIA 6.4.21 [33,34] (tune Perugia-0 [35]) and PHOJET 1.12 [37] as event generators. In order to avoid fluctuations due to the lack of statistics in the high p_t region in the Monte Carlo generators, the reconstructed p_t distribution of decay muons, obtained after all selection cuts are applied (Section 3.1), is fitted using

$$\frac{\mathrm{d}N}{\mathrm{d}p_t}^{\mu\leftarrow\mathrm{decay}} = \frac{\mathrm{a}}{(p_t^2 + \mathrm{b})^{\mathrm{c}}}, \tag{1}$$

where a, b and c are free parameters. The fits are performed in five rapidity intervals, in the region $2.5 < y < 4$. The normalization is done assuming that the fraction of decay muons in the data is the same as the one in the simulations, in the region where this component is dominant ($p_t < 1$ GeV/c). Finally, the (fitted) p_t distribution is subtracted from the measured muon p_t distribution. The subtracted p_t distribution is the mean of the p_t distributions from the PYTHIA and PHOJET event generators.

The total systematic uncertainty due to this procedure includes contributions from the model input and the transport code (GEANT3 [31,32]). The former takes into account the shape and normalization of the p_t distribution of decay muons, and the observed difference in the $K^{\pm}/\pi^{\pm}$ ratio as a function of p_t in the mid-rapidity region [38] between ALICE data and simulations. The results show that both PYTHIA (tune Perugia-0) and PHOJET underestimate this ratio by about 20%. The corresponding uncertainty due to this difference between data and simulations is propagated to the muon yield in the forward rapidity region. The effect of the transport code is estimated by varying the yield of secondary muons within 100% in such a way to provide a conservative estimate of the systematic uncertainty on the secondary particle production in the front absorber. The systematic uncertainty from the model input varies from about 7% to 2% as y increases from 2.5 to 4, independently of p_t, while the one from the transport code depends both on y and p_t and ranges from 4% ($3.7 < y < 4$) to a maximum of 34% ($p_t = 2$ GeV/c and $2.5 < y < 2.8$). The corresponding values of these systematic uncertainties as a function of p_t and y are summarized in Table 1. They are added in quadrature in the following.

3.3. Corrections

The extracted yields of muons from heavy flavour decays are corrected for acceptance, reconstruction and trigger efficiencies by means of a simulation modelling the response of the muon spectrometer. The procedure is based on the generation of a large sample of muons from beauty decays by using a parameterization of NLO pQCD calculations [29]. The tracking efficiency takes into account the status of each electronic channel and the residual mis-alignment of detection elements. The evolution of the tracking efficiency over time is controlled by weighting the response of electronic channels as a function of time. The typical value of muon tracking efficiency is about 93%. The efficiencies of the muon trigger chambers are obtained directly from data [28] and employed in the simulations. The typical value of such efficiencies

Table 1
Systematic uncertainties introduced by the procedure used for the subtraction of decay muons. MC and transport refer to the systematic uncertainty due to model input and transport code, respectively. See the text for details.

	MC	Transport						
		p_t (GeV/c)						
		[2.0; 2.5]	[2.5; 3.0]	[3.0; 3.5]	[3.5; 4.0]	[4.0; 4.5]	[4.5; 5.0]	>5.0
$2.5 < y < 2.8$	7%	34%	22%	20%	16%	12%	10%	6%
$2.8 < y < 3.1$	5.5%	22%	18%	14%	12%	10%	8%	6%
$3.1 < y < 3.4$	4.5%	10%	9%	8%	7%		6%	
$3.4 < y < 3.7$	3.0%				6%			
$3.7 < y < 4.0$	2.0%				4%			

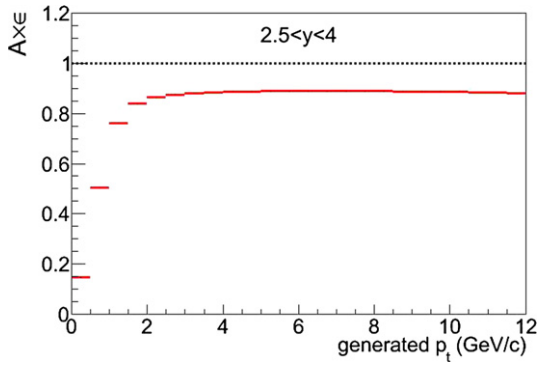

Fig. 2. Acceptance × efficiency as a function of generated p_t, obtained from a simulation of muons from beauty decays.

is about 96%. Fig. 2 shows the resulting acceptance and efficiency ($A \times \varepsilon$) as a function of generated p_t. The global $A \times \varepsilon$ increases significantly up to about 2 GeV/c and tends to saturate at a value close to 90%.

The systematic uncertainty corresponding to the sensitivity of $A \times \varepsilon$ on the input p_t and y distributions was estimated by comparing the results with those from a simulation using muons from charm decays. This amounted to less than 1% and was neglected. The accuracy in the detector modelling introduces a systematic uncertainty estimated to be 5%, by comparing the values of trigger and tracking efficiencies extracted from data and simulations [28].

The distortion of the measured p_t distribution, dominated in the high p_t region by the effect of residual mis-alignment, is also corrected for by introducing in the simulation a residual mis-alignment of the same order of magnitude as in the data. However, this residual mis-alignment is generated randomly. A p_t dependent relative systematic uncertainty on the muon yield of $1\% \times p_t$ (in GeV/c) is considered in order to take into account the differences between the real (unknown) residual mis-alignment and the simulated one. This is a conservative value determined by comparing the reconstructed p_t distribution with or without including the residual mis-alignment.

3.4. Production cross section normalization

The differential production cross section is obtained by normalizing the corrected yields of muons from heavy flavour decays to the integrated luminosity. Since the yields have been extracted using μ-MB trigger events, the differential production cross section is calculated according to

$$\frac{\mathrm{d}^2\sigma_{\mu^\pm\leftarrow\mathrm{HF}}}{\mathrm{d}p_t\,\mathrm{d}y} = \frac{\mathrm{d}^2N_{\mu^\pm\leftarrow\mathrm{HF}}}{\mathrm{d}p_t\,\mathrm{d}y} \times \frac{N^{\mu^\pm}_{\mathrm{MB}}}{N^{\mu^\pm}_{\mu\text{-MB}}} \times \frac{\sigma_{\mathrm{MB}}}{N_{\mathrm{MB}}}, \tag{2}$$

where:

- $\frac{\mathrm{d}^2N_{\mu^\pm\leftarrow\mathrm{HF}}}{\mathrm{d}p_t\,\mathrm{d}y}$ is the p_t- and y-differential yield of muons from heavy flavour decays;
- $N^{\mu^\pm}_{\mathrm{MB}}$ and $N^{\mu^\pm}_{\mu\text{-MB}}$ are the numbers of reconstructed tracks that satisfy the analysis cuts in MB and μ-MB trigger events, respectively;
- N_{MB} is the number of minimum bias collisions corrected as a function of time by the probability to have multiple MB interactions in a single bunch crossing, and σ_{MB} is the corresponding measured minimum bias cross section.

σ_{MB} is derived from the $\sigma_{\text{VZERO-AND}}$ cross section [39] measured with the van der Meer scan method [40]. The VZERO-AND condition is defined as a logical AND between signals in the two VZERO scintillator arrays. Such a combination allows one to reduce the sensitivity to beam-induced background. The $\sigma_{\text{VZERO-AND}}/\sigma_{\mathrm{MB}}$ ratio is the fraction of minimum bias events where the VZERO-AND condition is fulfilled. Its value is 0.87 and it remains stable within 1% over the analyzed data sample. This gives $\sigma_{\mathrm{MB}} = 62.5 \pm 2.2$ (syst.) mb. The statistical uncertainty is negligible, while the 3.5% systematic uncertainty is mainly due to the uncertainty on the beam intensities [41] and on the analysis procedure related to the van der Meer scan of the VZERO-AND signal. Other effects, such as oscillation in the ratio between MB and VZERO-AND counts, contribute less than 1%.

3.5. Summary of systematic uncertainties

The systematic uncertainty on the measurements of the p_t- and y-differential production cross sections of muons from heavy flavour decays accounts for the following contributions discussed in the previous sections:

- background subtraction: from about 5% ($3.7 < y < 4$) to a maximum of 35% ($2.5 < y < 2.8$, $p_t = 2$ GeV/c), see Section 3.2 and Table 1;
- detector response: 5% (Section 3.3);
- residual mis-alignment: $1\% \times p_t$ (Section 3.3);
- luminosity measurement: 3.5% (Section 3.4).

The resulting systematic uncertainty, in the rapidity region $2.5 < y < 4$, varies between 8–14% (the 3.5% systematic uncertainty on the normalization is not included).

4. Results and model comparisons

The measured differential production cross sections of muons from heavy flavour decays as a function of p_t in the rapidity region $2.5 < y < 4$ and as a function of y in the range $2 < p_t < 12$ GeV/c are displayed in Fig. 3 (circles), left and right panels, respectively. The error bars (which are smaller than symbols in most of the p_t and y bins) represent the statistical uncertainties. The boxes correspond to the systematic uncertainties. The

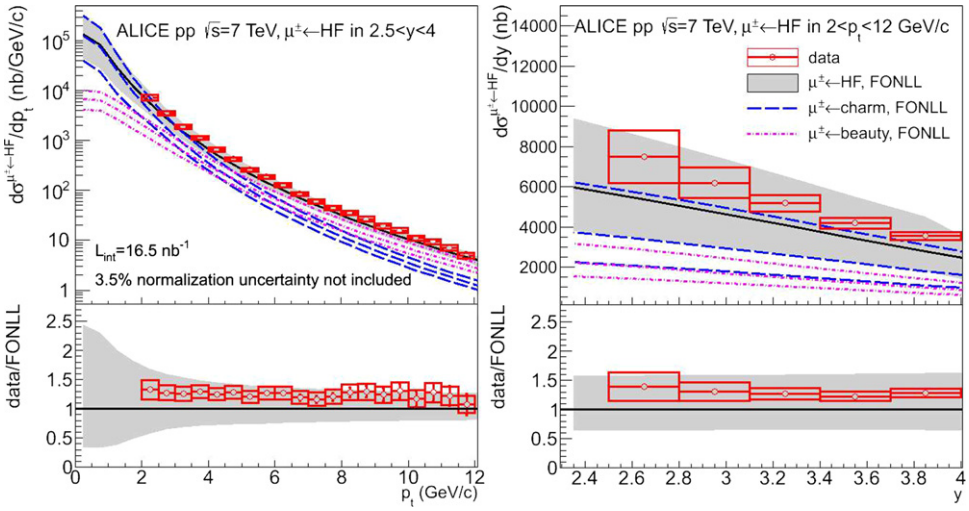

Fig. 3. Left: p_t-differential production cross section of muons from heavy flavour decays in the rapidity range $2.5 < y < 4$. Right: y-differential production cross section of muons from heavy flavour decays, in the range $2 < p_t < 12$ GeV/c. In both panels, the error bars (empty boxes) represent the statistical (systematic) uncertainties. A 3.5% normalization uncertainty is not shown. The solid curves are FONLL calculations and the bands display the theoretical systematic uncertainties. Also shown, are the FONLL calculations and systematic theoretical uncertainties for muons from charm (long dashed curves) and beauty (dashed curves) decays. The lower panels show the corresponding ratios between data and FONLL calculations.

systematic uncertainty on σ_{MB} is not included in the boxes. The results are compared to FONLL predictions [2,27] (black curve and shaded band for the systematic uncertainty). The central values of FONLL calculations use CTEQ6.6 [42] parton distribution functions, a charm quark mass (m_c) of 1.5 GeV/c^2, a beauty quark mass (m_b) of 4.75 GeV/c^2 and the renormalization (μ_R) and factorization (μ_F) QCD scales such that $\mu_R/\mu_0 = \mu_F/\mu_0 = 1$ ($\mu_0 = m_{t,q} = \sqrt{p_t^2 + m_q^2}$). The theoretical uncertainties correspond to the variation of charm and beauty quark masses in the ranges $1.3 < m_c < 1.7$ GeV/c^2 and $4.5 < m_b < 5.0$ GeV/c^2, and QCD scales in the ranges $0.5 < \mu_R/\mu_0 < 2$ and $0.5 < \mu_F/\mu_0 < 2$ with the constraint $0.5 < \mu_F/\mu_R < 2$. The FONLL predictions for muons from beauty decays include the components of muons coming from direct b-hadron decays and from b-hadron decays via c-hadron decays (e.g. $B \to D \to \mu$ channel). The uncertainty band is the envelope of the resulting cross sections. The ratios between data and FONLL predictions are shown in the bottom panels. A good description of the data is observed within uncertainties, for both the p_t distribution (up to 12 GeV/c) and the y distribution (in the p_t range from 2 to 12 GeV/c). The measured production cross sections are systematically larger than the central values of the model predictions. The ratio of data over central values of FONLL calculations as a function of p_t and y is about 1.3 over the whole p_t and y ranges. This is consistent with the ALICE measurements of the p_t-differential production cross sections of D mesons [26] in the central rapidity region. The CMS and ATLAS Collaborations made complementary measurements of the heavy flavour production, with electrons and/or muons measured at mid-rapidity in pp collisions at $\sqrt{s} = 7$ TeV [18,19]. The production of muons from beauty decays, measured by the CMS Collaboration in $|\eta| < 2.1$ and at high p_t ($p_t > 6$ GeV/c), exhibits a similar agreement with NLO pQCD calculations within uncertainties: the data points lie in the upper limit of the model predictions. The results from the ATLAS Collaboration concerning the production of muons and electrons from heavy flavour decays in $|\eta| < 2.0$ (excluding $1.37 < |\eta| < 1.52$) and in the region $7 < p_t < 27$ GeV/c are also consistent with FONLL calculations.

The theoretical charm and beauty components are also displayed in Fig. 3. According to these predictions, the muon contribution from beauty decays is expected to dominate in the range $p_t \gtrsim 6$ GeV/c. In this region, it represents about 62% of the heavy flavour decay muon cross section.

A similar comparison between data and FONLL calculations was performed in five rapidity intervals from $y = 2.5$ to $y = 4$ (Fig. 4, upper panels). The corresponding ratio of data over FONLL predictions is depicted in the lower panels of Fig. 4. The model calculations provide an overall good description of the data up to $p_t = 12$ GeV/c in all rapidity intervals, within experimental and theoretical uncertainties.

5. Conclusions

We have presented measurements of the differential production cross sections of muons from heavy flavour decays in the rapidity range $2.5 < y < 4$ and transverse momentum range $2 < p_t < 12$ GeV/c, in pp collisions at $\sqrt{s} = 7$ TeV with the ALICE experiment. The FONLL pQCD calculations are in good agreement with data within experimental and theoretical uncertainties, although the data are close to the upper limit of the model calculations. Both the p_t and y dependence of the heavy flavour decay muon production cross section is well described by the model predictions. The results provide an important baseline for the study of heavy quark medium effects in nucleus–nucleus collisions.

Acknowledgements

The ALICE Collaboration would like to thank all its engineers and technicians for their invaluable contributions to the construction of the experiment and the CERN accelerator teams for the outstanding performance of the LHC complex.

The ALICE Collaboration would like to thank M. Cacciari for providing the pQCD predictions that are compared to these data.

The ALICE Collaboration acknowledges the following funding agencies for their support in building and running the ALICE detector:

Calouste Gulbenkian Foundation from Lisbon and Swiss Fonds Kidagan, Armenia;

Conselho Nacional de Desenvolvimento Científico e Tecnológico (CNPq), Financiadora de Estudos e Projetos (FINEP), Fundação de Amparo à Pesquisa do Estado de São Paulo (FAPESP);

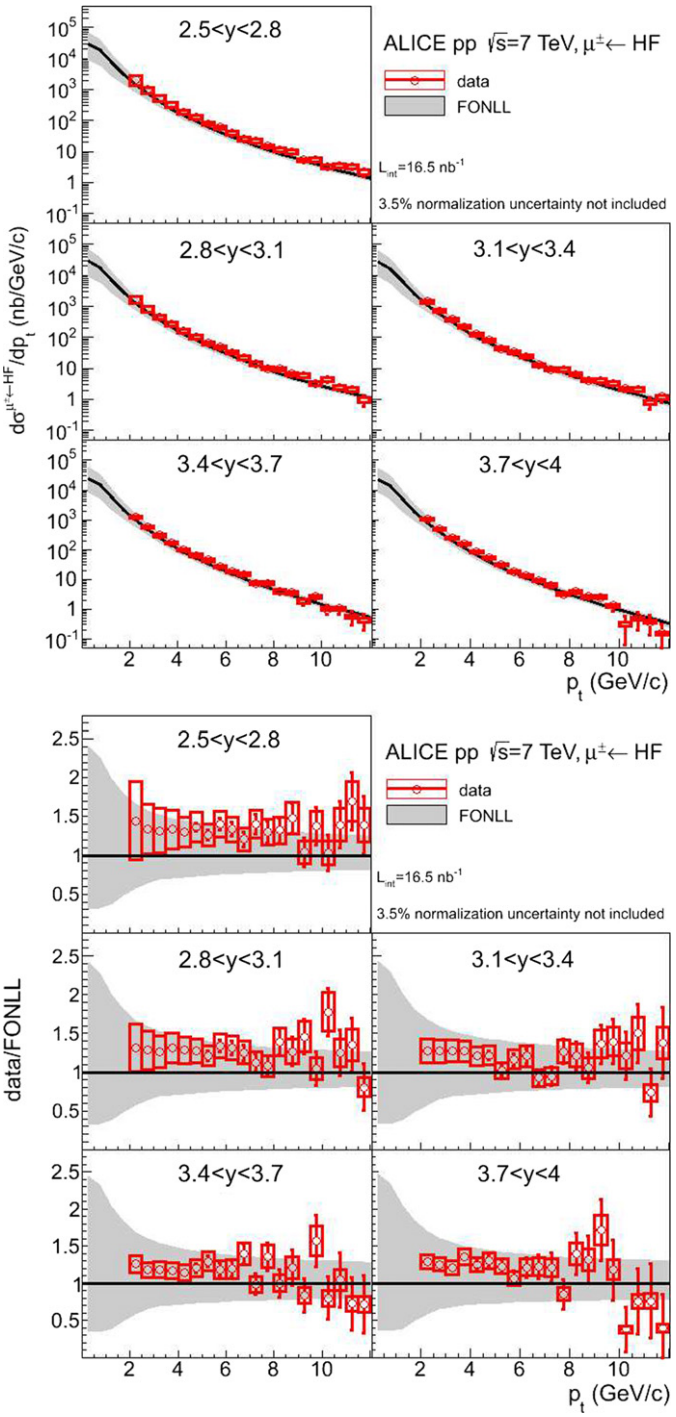

Fig. 4. Upper panel: p_t-differential production cross section of muons from heavy flavour decays in five rapidity regions mentioned in the figures. The error bars (empty boxes) represent the statistical (systematic) uncertainties. A 3.5% normalization uncertainty is not shown. The solid curves are FONLL calculations and the bands display the theoretical systematic uncertainty. Lower panel: ratio between data and FONLL calculations.

National Natural Science Foundation of China (NSFC), the Chinese Ministry of Education (CMOE) and the Ministry of Science and Technology of China (MSTC);

Ministry of Education and Youth of the Czech Republic;

Danish Natural Science Research Council, the Carlsberg Foundation and the Danish National Research Foundation;

The European Research Council under the European Community's Seventh Framework Programme;

Helsinki Institute of Physics and the Academy of Finland;

French CNRS-IN2P3, the 'Region Pays de Loire', 'Region Alsace', 'Region Auvergne' and CEA, France;

German BMBF and the Helmholtz Association;

General Secretariat for Research and Technology, Ministry of Development, Greece;

Hungarian OTKA and National Office for Research and Technology (NKTH);

Department of Atomic Energy and Department of Science and Technology of the Government of India;

Istituto Nazionale di Fisica Nucleare (INFN) of Italy;

MEXT Grant-in-Aid for Specially Promoted Research, Japan;

Joint Institute for Nuclear Research, Dubna;

National Research Foundation of Korea (NRF);

CONACYT, DGAPA, México, ALFA-EC and the HELEN Program (High-Energy physics Latin-American–European Network);

Stichting voor Fundamenteel Onderzoek der Materie (FOM) and the Nederlandse Organisatie voor Wetenschappelijk Onderzoek (NWO), Netherlands;

Research Council of Norway (NFR);

Polish Ministry of Science and Higher Education;

National Authority for Scientific Research – NASR (Autoritatea Naţională pentru Cercetare Ştiinţifică – ANCS);

Federal Agency of Science of the Ministry of Education and Science of Russian Federation, International Science and Technology Center, Russian Academy of Sciences, Russian Federal Agency of Atomic Energy, Russian Federal Agency for Science and Innovations and CERN-INTAS;

Ministry of Education of Slovakia;

Department of Science and Technology, South Africa;

CIEMAT, EELA, Ministerio de Educación y Ciencia of Spain, Xunta de Galicia (Consellería de Educación), CEADEN, Cubaenergía, Cuba, and IAEA (International Atomic Energy Agency);

Swedish Research Council (VR) and Knut & Alice Wallenberg Foundation (KAW);

Ukraine Ministry of Education and Science;

United Kingdom Science and Technology Facilities Council (STFC);

The United States Department of Energy, the United States National Science Foundation, the State of Texas, and the State of Ohio.

Open Access

References

[1] M.L. Mangano, P. Nason, G. Ridolfi, Nucl. Phys. B 373 (1992) 295.
[2] M. Cacciari, M. Greco, P. Nason, JHEP 9805 (1998) 007.
[3] S. Abachi, et al., D0 Collaboration, Phys. Rev. Lett. 74 (1995) 3548;
B. Abbott, et al., D0 Collaboration, Phys. Lett. B 487 (2000) 264;
B. Abbott, et al., D0 Collaboration, Phys. Rev. Lett. 85 (2000) 5068.
[4] F. Abe, et al., CDF Collaboration, Phys. Rev. Lett. 71 (1993) 500;
F. Abe, et al., CDF Collaboration, Phys. Rev. Lett. 71 (1993) 2396;
D. Acosta, et al., CDF Collaboration, Phys. Rev. D 65 (2002) 052005.
[5] D. Acosta, et al., CDF Collaboration, Phys. Rev. D 71 (2005) 032001;
A. Abulencia, et al., CDF Collaboration, Phys. Rev. D 75 (2007) 012010;
T. Aaltonen, et al., CDF Collaboration, Phys. Rev. D 79 (2009) 092003.
[6] M. Cacciari, P. Nason, Phys. Rev. Lett. 89 (2002) 122003.
[7] M. Cacciari, et al., JHEP 0407 (2004) 033.
[8] B.A. Kniehl, et al., Phys. Rev. D 77 (2008) 014011.
[9] D. Acosta, et al., CDF Collaboration, Phys. Rev. Lett. 91 (2003) 241804.
[10] M. Cacciari, P. Nason, JHEP 0309 (2003) 006.
[11] B.A. Kniehl, et al., Phys. Rev. Lett. 96 (2006) 012001.

[12] S.S. Adler, et al., PHENIX Collaboration, Phys. Rev. Lett. 96 (2006) 032001; A. Adare, et al., PHENIX Collaboration, Phys. Rev. Lett. 97 (2006) 252002; S.S. Adler, et al., PHENIX Collaboration, Phys. Rev. D 76 (2007) 092002; A. Adare, et al., PHENIX Collaboration, Phys. Rev. Lett. 103 (2009) 082002.
[13] B.I. Abelev, et al., STAR Collaboration, Phys. Rev. Lett. 98 (2007) 192301; W. Xie, STAR Collaboration, PoS DIS (2010) 182.
[14] M. Cacciari, P. Nason, R. Vogt, Phys. Rev. Lett. 95 (2005) 122001.
[15] J. Kirk, ATLAS Collaboration, PoS (2010) 013.
[16] R. Aaij, et al., LHCb Collaboration, Phys. Lett. B 694 (2010) 209; R. Aaij, et al., LHCb Collaboration, Eur. Phys. J. C 71 (2011) 1645.
[17] V. Khachatryan, et al., CMS Collaboration, Phys. Rev. Lett. 106 (2011) 112001; S. Chatrchyan, et al., CMS Collaboration, Phys. Rev. Lett. 106 (2011) 252001; P. Bellan, CMS Collaboration, arXiv:1109.2003 [hep-ex].
[18] V. Khachatryan, et al., CMS Collaboration, JHEP 1103 (2011) 090.
[19] G. Aad, et al., ATLAS Collaboration, CERN-PH-EP-2011-108, arXiv:1109.0525 [hep-ex].
[20] F. Carminati, et al., ALICE Collaboration, J. Phys. G: Nucl. Part. Phys. 30 (2004) 1517.
[21] B. Alessandro, et al., ALICE Collaboration, J. Phys. G: Nucl. Part. Phys. 32 (2006) 1295.
[22] N. Armesto, et al., Phys. Rev. D 71 (2005) 050427.
[23] M. Djordjevic, M. Gyulassy, S. Wicks, Phys. Rev. Lett. 94 (2005) 112301; A.D. Frawley, T. Ullrich, R. Vogt, Phys. Rep. 462 (2008) 125.
[24] K. Aamodt, et al., ALICE Collaboration, JINST 3 (2008) S08002.
[25] A. Dainese, et al., ALICE Collaboration, J. Phys. G: Nucl. Part. Phys. 38 (2011) 124032, and references therein.
[26] B. Abelev, et al., ALICE Collaboration, arXiv:1111.1553 [hep-ex].
[27] M. Cacciari, S. Frixione, N. Houdeau, M.L. Mangano, P. Nason, G. Ridolfi, CERN-PH-TH/2011-227.
[28] K. Aamodt, et al., ALICE Collaboration, Phys. Lett. B 704 (2011) 442.
[29] L. Aphecetche, et al., ALICE Internal Note ALICE-INT-2009-044, https://edms.cern.ch/document/1054937/1.
[30] V. Blobel, C. Kleinwort, arXiv:hep-ex/0208021.
[31] R. Brun, et al., GEANT3 User Guide, CERN, Data Handling Division DD/EE/841, 1985.
[32] R. Brun, et al., CERN Program Library Long Write-up, W5013, GEANT Detector Description and Simulation Tool, 1994.
[33] T. Sjöstrand, Comput. Phys. Commun. 82 (1994) 74.
[34] T. Sjöstrand, S. Mrenna, P. Skands, JHEP 0605 (2006) 026.
[35] P.Z. Skands, Phys. Rev. D 82 (2010) 074018.
[36] Z. Conesa del Valle, et al., ALICE Collaboration, Eur. Phys. J. C 49 (2007) 149.
[37] R. Engel, J. Ranft, S. Roesler, Phys. Rev. D 52 (1995) 1459.
[38] M. Chojnacki, et al., ALICE Collaboration, J. Phys. G: Nucl. Part. Phys. 38 (2011) 124074.
[39] M. Gagliardi, et al., ALICE Collaboration, arXiv:1109.5369 [hep-ex]; B. Abelev, et al., ALICE Collaboration, Measurement of inelastic, single and double diffraction cross sections in proton–proton collisions at LHC with ALICE, in preparation; L. Aphecetche, et al., ALICE-SCIENTIFIC-NOTE-2011-001.
[40] S. van der Meer, ISR-PO/68-31, KEK68-64.
[41] A. Alici, et al., CERN-ATS-Note-2011-016 PERF.
[42] P.M. Nadolsky, et al., Phys. Rev. D 78 (2008) 013004.

ALICE Collaboration

B. Abelev [69], J. Adam [34], D. Adamová [74], A.M. Adare [120], M.M. Aggarwal [78], G. Aglieri Rinella [30], A.G. Agocs [60], A. Agostinelli [19], S. Aguilar Salazar [56], Z. Ahammed [116], N. Ahmad [14], A. Ahmad Masoodi [14], S.U. Ahn [64,37], A. Akindinov [46], D. Aleksandrov [89], B. Alessandro [95], R. Alfaro Molina [56], A. Alici [96,30,9], A. Alkin [2], E. Almaráz Aviña [56], T. Alt [36], V. Altini [28,30], S. Altinpinar [15], I. Altsybeev [117], C. Andrei [71], A. Andronic [86], V. Anguelov [83], J. Anielski [54], C. Anson [16], T. Antičić [87], F. Antinori [100], P. Antonioli [96], L. Aphecetche [102], H. Appelshäuser [52], N. Arbor [65], S. Arcelli [19], A. Arend [52], N. Armesto [13], R. Arnaldi [95], T. Aronsson [120], I.C. Arsene [86], M. Arslandok [52], A. Asryan [117], A. Augustinus [30], R. Averbeck [86], T.C. Awes [75], J. Äystö [38], M.D. Azmi [14], M. Bach [36], A. Badalà [97], Y.W. Baek [64,37], R. Bailhache [52], R. Bala [95], R. Baldini Ferroli [9], A. Baldisseri [12], A. Baldit [64], F. Baltasar Dos Santos Pedrosa [30], J. Bán [47], R.C. Baral [48], R. Barbera [24], F. Barile [28], G.G. Barnaföldi [60], L.S. Barnby [91], V. Barret [64], J. Bartke [104], M. Basile [19], N. Bastid [64,*], B. Bathen [54], G. Batigne [102], B. Batyunya [59], C. Baumann [52], I.G. Bearden [72], H. Beck [52], I. Belikov [58], F. Bellini [19], R. Bellwied [110], E. Belmont-Moreno [56], G. Bencedi [60], S. Beole [26], I. Berceanu [71], A. Bercuci [71], Y. Berdnikov [76], D. Berenyi [60], C. Bergmann [54], D. Berzano [95], L. Betev [30], A. Bhasin [81], A.K. Bhati [78], L. Bianchi [26], N. Bianchi [66], C. Bianchin [22], J. Bielčík [34], J. Bielčíková [74], A. Bilandzic [73], S. Bjelogrlic [45], F. Blanco [7], F. Blanco [110], D. Blau [89], C. Blume [52], M. Boccioli [30], N. Bock [16], A. Bogdanov [70], H. Bøggild [72], M. Bogolyubsky [43], L. Boldizsár [60], M. Bombara [35], J. Book [52], H. Borel [12], A. Borissov [119], S. Bose [90], F. Bossú [30,26], M. Botje [73], S. Böttger [51], B. Boyer [42], P. Braun-Munzinger [86], M. Bregant [102], T. Breitner [51], T.A. Browning [84], M. Broz [33], R. Brun [30], E. Bruna [120,26,95], G.E. Bruno [28], D. Budnikov [88], H. Buesching [52], S. Bufalino [26,95], K. Bugaiev [2], O. Busch [83], Z. Buthelezi [80], D. Caballero Orduna [120], D. Caffarri [22], X. Cai [40], H. Caines [120], E. Calvo Villar [92], P. Camerini [20], V. Canoa Roman [8,1], G. Cara Romeo [96], W. Carena [30], F. Carena [30], N. Carlin Filho [107], F. Carminati [30], C.A. Carrillo Montoya [30], A. Casanova Díaz [66], M. Caselle [30], J. Castillo Castellanos [12], J.F. Castillo Hernandez [86], E.A.R. Casula [21], V. Catanescu [71], C. Cavicchioli [30], J. Cepila [34], P. Cerello [95], B. Chang [38,123], S. Chapeland [30], J.L. Charvet [12], S. Chattopadhyay [90], S. Chattopadhyay [116], M. Cherney [77], C. Cheshkov [30,109], B. Cheynis [109], E. Chiavassa [95], V. Chibante Barroso [30], D.D. Chinellato [108], P. Chochula [30], M. Chojnacki [45], P. Christakoglou [73,45], C.H. Christensen [72], P. Christiansen [29], T. Chujo [114], S.U. Chung [85], C. Cicalo [93], L. Cifarelli [19,30], F. Cindolo [96], J. Cleymans [80], F. Coccetti [9], J.-P. Coffin [58], F. Colamaria [28], D. Colella [28], G. Conesa Balbastre [65], Z. Conesa del Valle [30,58], P. Constantin [83], G. Contin [20], J.G. Contreras [8], T.M. Cormier [119], Y. Corrales Morales [26], P. Cortese [27], I. Cortés Maldonado [1], M.R. Cosentino [68,108], F. Costa [30], M.E. Cotallo [7], E. Crescio [8], P. Crochet [64], E. Cruz Alaniz [56], E. Cuautle [55], L. Cunqueiro [66], A. Dainese [22,100], H.H. Dalsgaard [72], A. Danu [50], K. Das [90], I. Das [90,42], D. Das [90], A. Dash [48,108], S. Dash [41,95], S. De [116], A. De Azevedo Moregula [66], G.O.V. de Barros [107], A. De Caro [25,9], G. de Cataldo [94],

J. de Cuveland [36], A. De Falco [21], D. De Gruttola [25], H. Delagrange [102], E. Del Castillo Sanchez [30], A. Deloff [101], V. Demanov [88], N. De Marco [95], E. Dénes [60], S. De Pasquale [25], A. Deppman [107], G. D Erasmo [28], R. de Rooij [45], D. Di Bari [28], T. Dietel [54], C. Di Giglio [28], S. Di Liberto [99], A. Di Mauro [30], P. Di Nezza [66], R. Divià [30], Ø. Djuvsland [15], A. Dobrin [119,29], T. Dobrowolski [101], I. Domínguez [55], B. Dönigus [86], O. Dordic [18], O. Driga [102], A.K. Dubey [116], L. Ducroux [109], P. Dupieux [64], A.K. Dutta Majumdar [90], M.R. Dutta Majumdar [116], D. Elia [94], D. Emschermann [54], H. Engel [51], H.A. Erdal [32], B. Espagnon [42], M. Estienne [102], S. Esumi [114], D. Evans [91], G. Eyyubova [18], D. Fabris [22,100], J. Faivre [65], D. Falchieri [19], A. Fantoni [66], M. Fasel [86], R. Fearick [80], A. Fedunov [59], D. Fehlker [15], L. Feldkamp [54], D. Felea [50], G. Feofilov [117], A. Fernández Téllez [1], R. Ferretti [27], A. Ferretti [26], J. Figiel [104], M.A.S. Figueredo [107], S. Filchagin [88], R. Fini [94], D. Finogeev [44], F.M. Fionda [28], E.M. Fiore [28], M. Floris [30], S. Foertsch [80], P. Foka [86], S. Fokin [89], E. Fragiacomo [98], M. Fragkiadakis [79], U. Frankenfeld [86], U. Fuchs [30], C. Furget [65], M. Fusco Girard [25], J.J. Gaardhøje [72], M. Gagliardi [26], A. Gago [92], M. Gallio [26], D.R. Gangadharan [16], P. Ganoti [75], C. Garabatos [86], E. Garcia-Solis [10], I. Garishvili [69], J. Gerhard [36], M. Germain [102], C. Geuna [12], M. Gheata [30], A. Gheata [30], B. Ghidini [28], P. Ghosh [116], P. Gianotti [66], M.R. Girard [118], P. Giubellino [30], E. Gladysz-Dziadus [104], P. Glässel [83], R. Gomez [106], E.G. Ferreiro [13], L.H. González-Trueba [56], P. González-Zamora [7], S. Gorbunov [36], A. Goswami [82], S. Gotovac [103], V. Grabski [56], L.K. Graczykowski [118], R. Grajcarek [83], A. Grelli [45], A. Grigoras [30], C. Grigoras [30], V. Grigoriev [70], S. Grigoryan [59], A. Grigoryan [121], B. Grinyov [2], N. Grion [98], P. Gros [29], J.F. Grosse-Oetringhaus [30], J.-Y. Grossiord [109], R. Grosso [30], F. Guber [44], R. Guernane [65], C. Guerra Gutierrez [92], B. Guerzoni [19], M. Guilbaud [109], K. Gulbrandsen [72], T. Gunji [113], R. Gupta [81], A. Gupta [81], H. Gutbrod [86], Ø. Haaland [15], C. Hadjidakis [42], M. Haiduc [50], H. Hamagaki [113], G. Hamar [60], B.H. Han [17], L.D. Hanratty [91], A. Hansen [72], Z. Harmanova [35], J.W. Harris [120], M. Hartig [52], D. Hasegan [50], D. Hatzifotiadou [96], A. Hayrapetyan [30,121], S.T. Heckel [52], M. Heide [54], H. Helstrup [32], A. Herghelegiu [71], G. Herrera Corral [8], N. Herrmann [83], K.F. Hetland [32], B. Hicks [120], P.T. Hille [120], B. Hippolyte [58], T. Horaguchi [114], Y. Hori [113], P. Hristov [30], I. Hřivnáčová [42], M. Huang [15], S. Huber [86], T.J. Humanic [16], D.S. Hwang [17], R. Ichou [64], R. Ilkaev [88], I. Ilkiv [101], M. Inaba [114], E. Incani [21], P.G. Innocenti [30], G.M. Innocenti [26], M. Ippolitov [89], M. Irfan [14], C. Ivan [86], A. Ivanov [117], V. Ivanov [76], M. Ivanov [86], O. Ivanytskyi [2], A. Jachołkowski [30], P.M. Jacobs [68], L. Jancurová [59], H.J. Jang [63], S. Jangal [58], M.A. Janik [118], R. Janik [33], P.H.S.Y. Jayarathna [110], S. Jena [41], R.T. Jimenez Bustamante [55], L. Jirden [30], P.G. Jones [91], H. Jung [37], W. Jung [37], A. Jusko [91], A.B. Kaidalov [46], V. Kakoyan [121], S. Kalcher [36], P. Kaliňák [47], M. Kalisky [54], T. Kalliokoski [38], A. Kalweit [53], K. Kanaki [15], J.H. Kang [123], V. Kaplin [70], A. Karasu Uysal [30,122], O. Karavichev [44], T. Karavicheva [44], E. Karpechev [44], A. Kazantsev [89], U. Kebschull [62,51], R. Keidel [124], S.A. Khan [116], P. Khan [90], M.M. Khan [14], A. Khanzadeev [76], Y. Kharlov [43], B. Kileng [32], D.J. Kim [38], T. Kim [123], S. Kim [17], S.H. Kim [37], M. Kim [123], J.S. Kim [37], J.H. Kim [17], D.W. Kim [37], B. Kim [123], S. Kirsch [36,30], I. Kisel [36], S. Kiselev [46], A. Kisiel [30,118], J.L. Klay [4], J. Klein [83], C. Klein-Bösing [54], M. Kliemant [52], A. Kluge [30], M.L. Knichel [86], K. Koch [83], M.K. Köhler [86], A. Kolojvari [117], V. Kondratiev [117], N. Kondratyeva [70], A. Konevskikh [44], A. Korneev [88], C. Kottachchi Kankanamge Don [119], R. Kour [91], M. Kowalski [104], S. Kox [65], G. Koyithatta Meethaleveedu [41], J. Kral [38], I. Králik [47], F. Kramer [52], I. Kraus [86], T. Krawutschke [83,31], M. Krelina [34], M. Kretz [36], M. Krivda [91,47], F. Krizek [38], M. Krus [34], E. Kryshen [76], M. Krzewicki [73,86], Y. Kucheriaev [89], C. Kuhn [58], P.G. Kuijer [73], P. Kurashvili [101], A.B. Kurepin [44], A. Kurepin [44], A. Kuryakin [88], S. Kushpil [74], V. Kushpil [74], H. Kvaerno [18], M.J. Kweon [83], Y. Kwon [123], P. Ladrón de Guevara [55], I. Lakomov [42,117], R. Langoy [15], C. Lara [51], A. Lardeux [102], P. La Rocca [24], C. Lazzeroni [91], R. Lea [20], Y. Le Bornec [42], S.C. Lee [37], K.S. Lee [37], F. Lefèvre [102], J. Lehnert [52], L. Leistam [30], M. Lenhardt [102], V. Lenti [94], H. León [56], I. León Monzón [106], H. León Vargas [52], P. Lévai [60], X. Li [11], J. Lien [15], R. Lietava [91], S. Lindal [18], V. Lindenstruth [36], C. Lippmann [86,30], M.A. Lisa [16], L. Liu [15], P.I. Loenne [15], V.R. Loggins [119], V. Loginov [70], S. Lohn [30], D. Lohner [83], C. Loizides [68], K.K. Loo [38], X. Lopez [64], E. López Torres [6], G. Løvhøiden [18], X.-G. Lu [83], P. Luettig [52], M. Lunardon [22], J. Luo [40,64], G. Luparello [45], L. Luquin [102], C. Luzzi [30], R. Ma [120], K. Ma [40], D.M. Madagodahettige-Don [110], A. Maevskaya [44], M. Mager [53,30], D.P. Mahapatra [48], A. Maire [58], M. Malaev [76], I. Maldonado Cervantes [55], L. Malinina [59,i], D. Mal'Kevich [46], P. Malzacher [86], A. Mamonov [88], L. Manceau [95], L. Mangotra [81], V. Manko [89], F. Manso [64], V. Manzari [94], Y. Mao [65,40], M. Marchisone [64,26], J. Mareš [49], G.V. Margagliotti [20,98], A. Margotti [96], A. Marín [86], C. Markert [105], I. Martashvili [112], P. Martinengo [30],

M.I. Martínez [1], A. Martínez Davalos [56], G. Martínez García [102], Y. Martynov [2], A. Mas [102], S. Masciocchi [86], M. Masera [26], A. Masoni [93], L. Massacrier [109,102], M. Mastromarco [94], A. Mastroserio [28,30], Z.L. Matthews [91], A. Matyja [102], D. Mayani [55], C. Mayer [104], J. Mazer [112], M.A. Mazzoni [99], F. Meddi [23], A. Menchaca-Rocha [56], J. Mercado Pérez [83], M. Meres [33], Y. Miake [114], A. Michalon [58], L. Milano [26], J. Milosevic [18,ii], A. Mischke [45], A.N. Mishra [82], D. Miśkowiec [86,30], C. Mitu [50], J. Mlynarz [119], A.K. Mohanty [30], B. Mohanty [116], L. Molnar [30], L. Montaño Zetina [8], M. Monteno [95], E. Montes [7], T. Moon [123], M. Morando [22], D.A. Moreira De Godoy [107], S. Moretto [22], A. Morsch [30], V. Muccifora [66], E. Mudnic [103], S. Muhuri [116], H. Müller [30], M.G. Munhoz [107], L. Musa [30], A. Musso [95], B.K. Nandi [41], R. Nania [96], E. Nappi [94], C. Nattrass [112], N.P. Naumov [88], S. Navin [91], T.K. Nayak [116], S. Nazarenko [88], G. Nazarov [88], A. Nedosekin [46], M. Nicassio [28], B.S. Nielsen [72], T. Niida [114], S. Nikolaev [89], V. Nikolic [87], V. Nikulin [76], S. Nikulin [89], B.S. Nilsen [77], M.S. Nilsson [18], F. Noferini [96,9], P. Nomokonov [59], G. Nooren [45], N. Novitzky [38], A. Nyanin [89], A. Nyatha [41], C. Nygaard [72], J. Nystrand [15], A. Ochirov [117], H. Oeschler [53,30], S. Oh [120], S.K. Oh [37], J. Oleniacz [118], C. Oppedisano [95], A. Ortiz Velasquez [55], G. Ortona [30,26], A. Oskarsson [29], P. Ostrowski [118], I. Otterlund [29], J. Otwinowski [86], K. Oyama [83], K. Ozawa [113], Y. Pachmayer [83], M. Pachr [34], F. Padilla [26], P. Pagano [25], G. Paić [55], F. Painke [36], C. Pajares [13], S. Pal [12], S.K. Pal [116], A. Palaha [91], A. Palmeri [97], V. Papikyan [121], G.S. Pappalardo [97], W.J. Park [86], A. Passfeld [54], B. Pastirčák [47], D.I. Patalakha [43], V. Paticchio [94], A. Pavlinov [119], T. Pawlak [118], T. Peitzmann [45], M. Perales [10], E. Pereira De Oliveira Filho [107], D. Peresunko [89], C.E. Pérez Lara [73], E. Perez Lezama [55], D. Perini [30], D. Perrino [28], W. Peryt [118], A. Pesci [96], V. Peskov [30,55], Y. Pestov [3], V. Petráček [34], M. Petran [34], M. Petris [71], P. Petrov [91], M. Petrovici [71], C. Petta [24], S. Piano [98], A. Piccotti [95], M. Pikna [33], P. Pillot [102], O. Pinazza [30], L. Pinsky [110], N. Pitz [52], F. Piuz [30], D.B. Piyarathna [110], M. Płoskoń [68], J. Pluta [118], T. Pocheptsov [59,18], S. Pochybova [60], P.L.M. Podesta-Lerma [106], M.G. Poghosyan [30,26], K. Polák [49], B. Polichtchouk [43], A. Pop [71], S. Porteboeuf-Houssais [64], V. Pospíšil [34], B. Potukuchi [81], S.K. Prasad [119], R. Preghenella [96,9], F. Prino [95], C.A. Pruneau [119], I. Pshenichnov [44], S. Puchagin [88], G. Puddu [21], A. Pulvirenti [24,30], V. Punin [88], M. Putiš [35], J. Putschke [119,120], E. Quercigh [30], H. Qvigstad [18], A. Rachevski [98], A. Rademakers [30], S. Radomski [83], T.S. Räihä [38], J. Rak [38], A. Rakotozafindrabe [12], L. Ramello [27], A. Ramírez Reyes [8], R. Raniwala [82], S. Raniwala [82], S.S. Räsänen [38], B.T. Rascanu [52], D. Rathee [78], K.F. Read [112], J.S. Real [65], K. Redlich [101,57], P. Reichelt [52], M. Reicher [45], R. Renfordt [52], A.R. Reolon [66], A. Reshetin [44], F. Rettig [36], J.-P. Revol [30], K. Reygers [83], L. Riccati [95], R.A. Ricci [67], T. Richert [29], M. Richter [18], P. Riedler [30], W. Riegler [30], F. Riggi [24,97], M. Rodríguez Cahuantzi [1], K. Røed [15], D. Rohr [36], D. Röhrich [15], R. Romita [86], F. Ronchetti [66], P. Rosnet [64], S. Rossegger [30], A. Rossi [22], F. Roukoutakis [79], P. Roy [90], C. Roy [58], A.J. Rubio Montero [7], R. Rui [20], E. Ryabinkin [89], A. Rybicki [104], S. Sadovsky [43], K. Šafařík [30], P.K. Sahu [48], J. Saini [116], H. Sakaguchi [39], S. Sakai [68], D. Sakata [114], C.A. Salgado [13], J. Salzwedel [16], S. Sambyal [81], V. Samsonov [76], X. Sanchez Castro [55,58], L. Šándor [47], A. Sandoval [56], S. Sano [113], M. Sano [114], R. Santo [54], R. Santoro [94,30], J. Sarkamo [38], E. Scapparone [96], F. Scarlassara [22], R.P. Scharenberg [84], C. Schiaua [71], R. Schicker [83], H.R. Schmidt [86,115], C. Schmidt [86], S. Schreiner [30], S. Schuchmann [52], J. Schukraft [30], Y. Schutz [30,102], K. Schwarz [86], K. Schweda [86,83], G. Scioli [19], E. Scomparin [95], R. Scott [112], P.A. Scott [91], G. Segato [22], I. Selyuzhenkov [86], S. Senyukov [27,58], J. Seo [85], S. Serci [21], E. Serradilla [7,56], A. Sevcenco [50], I. Sgura [94], A. Shabetai [102], G. Shabratova [59], R. Shahoyan [30], S. Sharma [81], N. Sharma [78], K. Shigaki [39], M. Shimomura [114], K. Shtejer [6], Y. Sibiriak [89], M. Siciliano [26], E. Sicking [30], S. Siddhanta [93], T. Siemiarczuk [101], D. Silvermyr [75], G. Simonetti [28,30], R. Singaraju [116], R. Singh [81], S. Singha [116], T. Sinha [90], B.C. Sinha [116], B. Sitar [33], M. Sitta [27], T.B. Skaali [18], K. Skjerdal [15], R. Smakal [34], N. Smirnov [120], R. Snellings [45], C. Søgaard [72], R. Soltz [69], H. Son [17], J. Song [85], M. Song [123], C. Soos [30], F. Soramel [22], I. Sputowska [104], M. Spyropoulou-Stassinaki [79], B.K. Srivastava [84], J. Stachel [83], I. Stan [50], I. Stan [50], G. Stefanek [101], G. Stefanini [30], T. Steinbeck [36], M. Steinpreis [16], E. Stenlund [29], G. Steyn [80], D. Stocco [102], M. Stolpovskiy [43], K. Strabykin [88], P. Strmen [33], A.A.P. Suaide [107], M.A. Subieta Vásquez [26], T. Sugitate [39], C. Suire [42], M. Sukhorukov [88], R. Sultanov [46], M. Šumbera [74], T. Susa [87], A. Szanto de Toledo [107], I. Szarka [33], A. Szostak [15], C. Tagridis [79], J. Takahashi [108], J.D. Tapia Takaki [42], A. Tauro [30], G. Tejeda Muñoz [1], A. Telesca [30], C. Terrevoli [28], J. Thäder [86], D. Thomas [45], J.H. Thomas [86], R. Tieulent [109], A.R. Timmins [110], D. Tlusty [34], A. Toia [36,30], H. Torii [39,113], L. Toscano [95], F. Tosello [95], T. Traczyk [118], D. Truesdale [16], W.H. Trzaska [38], T. Tsuji [113], A. Tumkin [88], R. Turrisi [100], T.S. Tveter [18], J. Ulery [52], K. Ullaland [15], J. Ulrich [62,51], A. Uras [109], J. Urbán [35], G.M. Urciuoli [99], G.L. Usai [21],

M. Vajzer [34,74], M. Vala [59,47], L. Valencia Palomo [42], S. Vallero [83], N. van der Kolk [73], P. Vande Vyvre [30], M. van Leeuwen [45], L. Vannucci [67], A. Vargas [1], R. Varma [41], M. Vasileiou [79], A. Vasiliev [89], V. Vechernin [117], M. Veldhoen [45], M. Venaruzzo [20], E. Vercellin [26], S. Vergara [1], D.C. Vernekohl [54], R. Vernet [5], M. Verweij [45], L. Vickovic [103], G. Viesti [22], O. Vikhlyantsev [88], Z. Vilakazi [80], O. Villalobos Baillie [91], L. Vinogradov [117], A. Vinogradov [89], Y. Vinogradov [88], T. Virgili [25], Y.P. Viyogi [116], A. Vodopyanov [59], S. Voloshin [119], K. Voloshin [46], G. Volpe [28,30], B. von Haller [30], D. Vranic [86], G. Øvrebekk [15], J. Vrláková [35], B. Vulpescu [64], A. Vyushin [88], V. Wagner [34], B. Wagner [15], R. Wan [58,40], Y. Wang [83], D. Wang [40], Y. Wang [40], M. Wang [40], K. Watanabe [114], J.P. Wessels [30,54], U. Westerhoff [54], J. Wiechula [115], J. Wikne [18], M. Wilde [54], G. Wilk [101], A. Wilk [54], M.C.S. Williams [96], B. Windelband [83], L. Xaplanteris Karampatsos [105], H. Yang [12], S. Yang [15], S. Yasnopolskiy [89], J. Yi [85], Z. Yin [40], H. Yokoyama [114], I.-K. Yoo [85], J. Yoon [123], W. Yu [52], X. Yuan [40], I. Yushmanov [89], C. Zach [34], C. Zampolli [96,30], S. Zaporozhets [59], A. Zarochentsev [117], P. Závada [49], N. Zaviyalov [88], H. Zbroszczyk [118], P. Zelnicek [30,51], I.S. Zgura [50], M. Zhalov [76], X. Zhang [64,40], Y. Zhou [45], D. Zhou [40], F. Zhou [40], X. Zhu [40], A. Zichichi [19,9], A. Zimmermann [83], G. Zinovjev [2], Y. Zoccarato [109], M. Zynovyev [2]

[1] *Benemérita Universidad Autónoma de Puebla, Puebla, Mexico*
[2] *Bogolyubov Institute for Theoretical Physics, Kiev, Ukraine*
[3] *Budker Institute for Nuclear Physics, Novosibirsk, Russia*
[4] *California Polytechnic State University, San Luis Obispo, CA, United States*
[5] *Centre de Calcul de l'IN2P3, Villeurbanne, France*
[6] *Centro de Aplicaciones Tecnológicas y Desarrollo Nuclear (CEADEN), Havana, Cuba*
[7] *Centro de Investigaciones Energéticas Medioambientales y Tecnológicas (CIEMAT), Madrid, Spain*
[8] *Centro de Investigación y de Estudios Avanzados (CINVESTAV), Mexico City and Mérida, Mexico*
[9] *Centro Fermi – Centro Studi e Ricerche e Museo Storico della Fisica "Enrico Fermi", Rome, Italy*
[10] *Chicago State University, Chicago, IL, United States*
[11] *China Institute of Atomic Energy, Beijing, China*
[12] *Commissariat à l'Energie Atomique, IRFU, Saclay, France*
[13] *Departamento de Física de Partículas and IGFAE, Universidad de Santiago de Compostela, Santiago de Compostela, Spain*
[14] *Department of Physics Aligarh Muslim University, Aligarh, India*
[15] *Department of Physics and Technology, University of Bergen, Bergen, Norway*
[16] *Department of Physics, Ohio State University, Columbus, OH, United States*
[17] *Department of Physics, Sejong University, Seoul, South Korea*
[18] *Department of Physics, University of Oslo, Oslo, Norway*
[19] *Dipartimento di Fisica dell'Università and Sezione INFN, Bologna, Italy*
[20] *Dipartimento di Fisica dell'Università and Sezione INFN, Trieste, Italy*
[21] *Dipartimento di Fisica dell'Università and Sezione INFN, Cagliari, Italy*
[22] *Dipartimento di Fisica dell'Università and Sezione INFN, Padova, Italy*
[23] *Dipartimento di Fisica dell'Università 'La Sapienza' and Sezione INFN, Rome, Italy*
[24] *Dipartimento di Fisica e Astronomia dell'Università and Sezione INFN, Catania, Italy*
[25] *Dipartimento di Fisica 'E.R. Caianiello' dell'Università and Gruppo Collegato INFN, Salerno, Italy*
[26] *Dipartimento di Fisica Sperimentale dell'Università and Sezione INFN, Turin, Italy*
[27] *Dipartimento di Scienze e Tecnologie Avanzate dell'Università del Piemonte Orientale and Gruppo Collegato INFN, Alessandria, Italy*
[28] *Dipartimento Interateneo di Fisica 'M. Merlin' and Sezione INFN, Bari, Italy*
[29] *Division of Experimental High Energy Physics, University of Lund, Lund, Sweden*
[30] *European Organization for Nuclear Research (CERN), Geneva, Switzerland*
[31] *Fachhochschule Köln, Köln, Germany*
[32] *Faculty of Engineering, Bergen University College, Bergen, Norway*
[33] *Faculty of Mathematics, Physics and Informatics, Comenius University, Bratislava, Slovakia*
[34] *Faculty of Nuclear Sciences and Physical Engineering, Czech Technical University in Prague, Prague, Czech Republic*
[35] *Faculty of Science, P.J. Šafárik University, Košice, Slovakia*
[36] *Frankfurt Institute for Advanced Studies, Johann Wolfgang Goethe-Universität Frankfurt, Frankfurt, Germany*
[37] *Gangneung-Wonju National University, Gangneung, South Korea*
[38] *Helsinki Institute of Physics (HIP) and University of Jyväskylä, Jyväskylä, Finland*
[39] *Hiroshima University, Hiroshima, Japan*
[40] *Hua-Zhong Normal University, Wuhan, China*
[41] *Indian Institute of Technology, Mumbai, India*
[42] *Institut de Physique Nucléaire d'Orsay (IPNO), Université Paris-Sud, CNRS-IN2P3, Orsay, France*
[43] *Institute for High Energy Physics, Protvino, Russia*
[44] *Institute for Nuclear Research, Academy of Sciences, Moscow, Russia*
[45] *Nikhef, National Institute for Subatomic Physics and Institute for Subatomic Physics of Utrecht University, Utrecht, Netherlands*
[46] *Institute for Theoretical and Experimental Physics, Moscow, Russia*
[47] *Institute of Experimental Physics, Slovak Academy of Sciences, Košice, Slovakia*
[48] *Institute of Physics, Bhubaneswar, India*
[49] *Institute of Physics, Academy of Sciences of the Czech Republic, Prague, Czech Republic*
[50] *Institute of Space Sciences (ISS), Bucharest, Romania*
[51] *Institut für Informatik, Johann Wolfgang Goethe-Universität Frankfurt, Frankfurt, Germany*
[52] *Institut für Kernphysik, Johann Wolfgang Goethe-Universität Frankfurt, Frankfurt, Germany*
[53] *Institut für Kernphysik, Technische Universität Darmstadt, Darmstadt, Germany*
[54] *Institut für Kernphysik, Westfälische Wilhelms-Universität Münster, Münster, Germany*
[55] *Instituto de Ciencias Nucleares, Universidad Nacional Autónoma de México, Mexico City, Mexico*
[56] *Instituto de Física, Universidad Nacional Autónoma de México, Mexico City, Mexico*
[57] *Institut of Theoretical Physics, University of Wroclaw, Poland*

[58] Institut Pluridisciplinaire Hubert Curien (IPHC), Université de Strasbourg, CNRS-IN2P3, Strasbourg, France
[59] Joint Institute for Nuclear Research (JINR), Dubna, Russia
[60] KFKI Research Institute for Particle and Nuclear Physics, Hungarian Academy of Sciences, Budapest, Hungary
[61] Kharkiv Institute of Physics and Technology (KIPT), National Academy of Sciences of Ukraine (NASU), Kharkov, Ukraine
[62] Kirchhoff-Institut für Physik, Ruprecht-Karls-Universität Heidelberg, Heidelberg, Germany
[63] Korea Institute of Science and Technology Information, South Korea
[64] Laboratoire de Physique Corpusculaire (LPC), Clermont Université, Université Blaise Pascal, CNRS-IN2P3, Clermont-Ferrand, France
[65] Laboratoire de Physique Subatomique et de Cosmologie (LPSC), Université Joseph Fourier, CNRS-IN2P3, Institut Polytechnique de Grenoble, Grenoble, France
[66] Laboratori Nazionali di Frascati, INFN, Frascati, Italy
[67] Laboratori Nazionali di Legnaro, INFN, Legnaro, Italy
[68] Lawrence Berkeley National Laboratory, Berkeley, CA, United States
[69] Lawrence Livermore National Laboratory, Livermore, CA, United States
[70] Moscow Engineering Physics Institute, Moscow, Russia
[71] National Institute for Physics and Nuclear Engineering, Bucharest, Romania
[72] Niels Bohr Institute, University of Copenhagen, Copenhagen, Denmark
[73] Nikhef, National Institute for Subatomic Physics, Amsterdam, Netherlands
[74] Nuclear Physics Institute, Academy of Sciences of the Czech Republic, Řež u Prahy, Czech Republic
[75] Oak Ridge National Laboratory, Oak Ridge, TN, United States
[76] Petersburg Nuclear Physics Institute, Gatchina, Russia
[77] Physics Department, Creighton University, Omaha, NE, United States
[78] Physics Department, Panjab University, Chandigarh, India
[79] Physics Department, University of Athens, Athens, Greece
[80] Physics Department, University of Cape Town, iThemba LABS, Cape Town, South Africa
[81] Physics Department, University of Jammu, Jammu, India
[82] Physics Department, University of Rajasthan, Jaipur, India
[83] Physikalisches Institut, Ruprecht-Karls-Universität Heidelberg, Heidelberg, Germany
[84] Purdue University, West Lafayette, IN, United States
[85] Pusan National University, Pusan, South Korea
[86] Research Division and ExtreMe Matter Institute EMMI, GSI Helmholtzzentrum für Schwerionenforschung, Darmstadt, Germany
[87] Rudjer Bošković Institute, Zagreb, Croatia
[88] Russian Federal Nuclear Center (VNIIEF), Sarov, Russia
[89] Russian Research Centre Kurchatov Institute, Moscow, Russia
[90] Saha Institute of Nuclear Physics, Kolkata, India
[91] School of Physics and Astronomy, University of Birmingham, Birmingham, United Kingdom
[92] Sección Física, Departamento de Ciencias, Pontificia Universidad Católica del Perú, Lima, Peru
[93] Sezione INFN, Cagliari, Italy
[94] Sezione INFN, Bari, Italy
[95] Sezione INFN, Turin, Italy
[96] Sezione INFN, Bologna, Italy
[97] Sezione INFN, Catania, Italy
[98] Sezione INFN, Trieste, Italy
[99] Sezione INFN, Rome, Italy
[100] Sezione INFN, Padova, Italy
[101] Soltan Institute for Nuclear Studies, Warsaw, Poland
[102] SUBATECH, Ecole des Mines de Nantes, Université de Nantes, CNRS-IN2P3, Nantes, France
[103] Technical University of Split FESB, Split, Croatia
[104] The Henryk Niewodniczanski Institute of Nuclear Physics, Polish Academy of Sciences, Cracow, Poland
[105] The University of Texas at Austin, Physics Department, Austin, TX, United States
[106] Universidad Autónoma de Sinaloa, Culiacán, Mexico
[107] Universidade de São Paulo (USP), São Paulo, Brazil
[108] Universidade Estadual de Campinas (UNICAMP), Campinas, Brazil
[109] Université de Lyon, Université Lyon 1, CNRS/IN2P3, IPN-Lyon, Villeurbanne, France
[110] University of Houston, Houston, TX, United States
[111] University of Technology and Austrian Academy of Sciences, Vienna, Austria
[112] University of Tennessee, Knoxville, TN, United States
[113] University of Tokyo, Tokyo, Japan
[114] University of Tsukuba, Tsukuba, Japan
[115] Eberhard Karls Universität Tübingen, Tübingen, Germany
[116] Variable Energy Cyclotron Centre, Kolkata, India
[117] V. Fock Institute for Physics, St. Petersburg State University, St. Petersburg, Russia
[118] Warsaw University of Technology, Warsaw, Poland
[119] Wayne State University, Detroit, MI, United States
[120] Yale University, New Haven, CT, United States
[121] Yerevan Physics Institute, Yerevan, Armenia
[122] Yildiz Technical University, Istanbul, Turkey
[123] Yonsei University, Seoul, South Korea
[124] Zentrum für Technologietransfer und Telekommunikation (ZTT), Fachhochschule Worms, Worms, Germany

* Corresponding author.
E-mail address: nicole.bastid@clermont.in2p3.fr (N. Bastid).
[i] Also at: M.V. Lomonosov Moscow State University, D.V. Skobeltsyn Institute of Nuclear Physics, Moscow, Russia.
[ii] Also at: "Vinča" Institute of Nuclear Sciences, Belgrade, Serbia.

Appendix B

Publication of "Production of muons from heavy flavour decays at forward rapidity in pp and Pb–Pb collisions at $\sqrt{s_{\mathrm{NN}}} = 2.76$ TeV"

Production of Muons from Heavy Flavor Decays at Forward Rapidity in pp and Pb-Pb Collisions at $\sqrt{s_{NN}} = 2.76$ TeV

B. Abelev *et al.**
(ALICE Collaboration)

(Received 4 June 2012; published 13 September 2012)

The ALICE Collaboration has measured the inclusive production of muons from heavy-flavor decays at forward rapidity, $2.5 < y < 4$, in pp and Pb-Pb collisions at $\sqrt{s_{NN}} = 2.76$ TeV. The p_t-differential inclusive cross section of muons from heavy-flavor decays in pp collisions is compared to perturbative QCD calculations. The nuclear modification factor is studied as a function of p_t and collision centrality. A weak suppression is measured in peripheral collisions. In the most central collisions, a suppression of a factor of about 3–4 is observed in $6 < p_t < 10$ GeV/c. The suppression shows no significant p_t dependence.

DOI: 10.1103/PhysRevLett.109.112301 PACS numbers: 25.75.Cj, 13.20.−v

The study of ultrarelativistic heavy ion collisions is aimed at investigating the properties of strongly interacting matter in the extreme conditions of high temperature and energy density expected to be reached. Under such conditions, quantum chromodynamics (QCD) calculations on the lattice predict the formation of a deconfined partonic phase, the quark-gluon plasma, and chiral symmetry is restored [1]. Heavy quarks (charm and beauty), abundantly produced at the Large Hadron Collider (LHC), are sensitive probes of the properties of the quark-gluon plasma. Because of their large masses, they are created mainly in hard scattering processes during the early stage of the collision and subsequently interact with the hot and dense medium. In particular, measurement of open heavy-flavor hadrons may probe the energy density of the system through the mechanism of in-medium energy loss of heavy quarks. The in-medium effects are usually quantified by means of the nuclear modification factor R_{AA} of the transverse momentum (p_t) distribution. Using the nuclear overlap function from the Glauber model [2], R_{AA} can be expressed as

$$R_{AA}(p_t) = \frac{1}{\langle T_{AA} \rangle} \times \frac{dN_{AA}/dp_t}{d\sigma_{pp}/dp_t}, \quad (1)$$

where $\langle T_{AA} \rangle$ is the average nuclear overlap function in a given centrality class. The term dN_{AA}/dp_{t} is the p_t-differential yield in nucleus-nucleus (AA) collisions, while $d\sigma_{pp}/dp_t$ is the p_t-differential inclusive cross section in pp collisions. The value of R_{AA} is unity for hard probes if no nuclear modification is present. A R_{AA} value smaller than unity can arise from partonic energy loss as well as other nuclear effects. According to QCD, the radiative energy loss of gluons should be larger than that of quarks, and due to the dead cone effect [3–6], heavy quark energy loss should be further reduced with respect to that of light quarks. The contribution from other interaction mechanisms, for instance collisional energy loss [7,8], in-medium fragmentation, recombination, and coalescence [9–11], could also lead to a modification of heavy-flavor hadron p_t distributions in AA collisions. Finally, initial state effects [12,13] could complicate the interpretation of any deviation from unity of the R_{AA} in terms of energy loss effects, particularly in the low p_t region. The study of p-A collisions is required to quantify the role of initial state effects. The PHENIX and STAR Collaborations have reported a strong suppression of electrons from heavy-flavor decays at midrapidity, in central Au-Au collisions at $\sqrt{s_{NN}} = 200$ GeV at RHIC [14–17]. The PHENIX Collaboration also measured a significant suppression of muons from heavy-flavor decays at forward rapidity in central Cu-Cu collisions at $\sqrt{s_{NN}} = 200$ GeV [18]. Recently, a significant suppression of D mesons [19] and J/ψ's from B decays [20] was measured at midrapidity in central Pb-Pb collisions at $\sqrt{s_{NN}} = 2.76$ TeV by ALICE and CMS at the LHC, respectively. A complementary measurement of heavy-flavor suppression at forward rapidity, at the same energy, is of great interest in order to provide new constraints on models which aim at describing the nuclear modification factor as partonic energy loss.

In this Letter, we report the first measurement at the LHC of the production of muons from heavy-flavor decays at forward rapidity ($2.5 < y < 4$), with the ALICE experiment [21], in pp and Pb-Pb collisions at $\sqrt{s_{NN}} = 2.76$ TeV. The measured p_t-differential inclusive cross section of muons from heavy-flavor decays in pp collisions at $\sqrt{s} = 2.76$ TeV is compared to perturbative QCD (pQCD) calculations. In-medium effects are investigated by means of the nuclear modification factor as a function of

*Full author list given at the end of the article.

p_t in $4 < p_t < 10$ GeV/c, and as a function of collision centrality in $6 < p_t < 10$ GeV/c.

The ALICE experiment is described in detail in [21]. The apparatus is composed of a central barrel (pseudorapidity coverage $|\eta| < 0.9$), a muon spectrometer ($-4 < \eta < -2.5$ [22]), and a set of detectors for global collision characterization and triggering located in the forward and backward pseudorapidity regions. The two scintillator arrays (VZERO), covering the $2.8 < \eta < 5.1$ and $-3.7 < \eta < -1.7$, are used for triggering, centrality determination, and background removal. The two zero degree calorimeters (ZDC), located at ± 114 m from the interaction point, are used in offline rejection of background events. The silicon pixel detector (SPD), a two-layer central barrel that constitutes the innermost part of the inner tracking system, is included in the trigger logic. The SPD provides also the interaction vertex reconstruction. The muon spectrometer consists of a 10 interaction length (λ_I) passive front absorber, a beam shield, an iron wall, a 3 T m dipole magnet, and a set of tracking and trigger chambers. Tracking is performed by means of five stations of cathode pad chambers, with the third station inside the dipole magnet. The tracking system is supplemented by two trigger stations of resistive plate chambers, behind a 1.2 m thick iron wall with thickness $7.2\lambda_I$. The latter absorbs hadrons that punch through the front absorber, as well as secondary hadrons produced inside it and low momentum muons, mainly from pion and kaon decays.

The Pb-Pb data were collected during the 2010 run. The rate of hadronic collisions was about 100 Hz, corresponding to a luminosity of 1.3×10^{25} cm^{-2} s^{-1}. The results presented in this Letter are based on the analysis of minimum bias (MB) trigger events. The MB trigger required the following conditions: a signal in at least two pixel chips in the outer layer of the SPD and a signal on each VZERO detector. The beam-induced background was reduced by using the timing information from the VZERO and ZDC detectors, and by exploiting the correlation between the number of hits and track segments in the SPD. Moreover, a minimal energy deposit in the ZDC was required in order to reject electromagnetic interactions. Finally, only events with an interaction vertex within ± 10 cm from the center of the detector along the beam line were analyzed. Pb-Pb collisions were classified according to their degree of centrality by means of the sum of the amplitudes of the signals in the VZERO detectors, as described in [23,24]. The analysis was limited to the 80% most central events for which the MB trigger was fully efficient. This leads to a data sample of 16.6×10^6 Pb-Pb collisions which, in the following, will be divided into five centrality classes: 0–10%, 10%–20%, 20%–40%, 40%–60%, and 60%–80% [the two last bins will be grouped together for the study of $R_{AA}(p_t)$]. The corresponding integrated luminosity is $L_{\rm int} = 2.71 \pm 0.09\ \mu$b^{-1}. The values of the mean number of participating nucleons and mean nuclear overlap function are given in Table I. They were determined with the Glauber Monte Carlo simulation assuming an inelastic nucleon-nucleon cross section of 64 mb [23]. The strategy of cuts applied to reconstructed tracks is similar to the one used for pp collisions [25]. Various selection cuts were used in order to improve the purity of the data sample. Tracks were required to be reconstructed in the geometrical acceptance of the muon spectrometer. A track candidate measured in the muon tracking chambers was then required to be matched with the corresponding track measured in the trigger chambers. This results in a very effective rejection of the hadronic background that is absorbed in the iron wall. Furthermore, the correlation between the momentum and the distance of closest approach (distance between the extrapolated muon track and the interaction vertex in the plane perpendicular to the beam direction and containing the vertex) was used to remove the remaining beam-induced background tracks that do not point to the interaction vertex and fake tracks (tracks not associated to one single particle crossing the spectrometer). After these selections, the data sample consists of 10×10^6 muon candidates. The R_{AA} measurement of muons from heavy-flavor decays will be performed at highp_t ($p_t > 4 - 6$ GeV/c) where the main background component consists of muons from primary pion and kaon decays. The Pb-Pb distributions are corrected for acceptance and for tracking and trigger efficiency ($A\epsilon$) using the procedure described in [25]. The global $A\epsilon$ is close to 80% for $p_t > 4$ GeV/c. The dependence of the trigger and tracking efficiency on the detector occupancy, which is correlated with the collision centrality, was evaluated by means of the embedding procedure [26]. A decrease of the efficiency of about $4\% \pm 1\%$ is observed in the 10% most central collisions.

The R_{AA} of muons from heavy-flavor decays in the forward rapidity region is calculated according to Eq. (1), which can be written as

$$R_{AA}^{\mu^\pm \leftarrow \rm HF}(p_t) = \frac{1}{\langle T_{AA} \rangle} \times \frac{dN_{\rm PbPb}^{\mu^\pm}/dp_t - dN_{\rm PbPb}^{\mu^\pm \leftarrow \pi^\pm, K^\pm}/dp_{\rm t}}{d\sigma_{pp}^{\mu^\pm \leftarrow \rm HF}/dp_t}, \quad (2)$$

TABLE I. Mean number of participating nucleons ($\langle N_{\rm part} \rangle$) and mean nuclear overlap function ($\langle T_{AA} \rangle$) for different centrality classes, expressed in percentiles of the hadronic Pb-Pb cross section.

Centrality	$\langle N_{\rm part} \rangle$	$\langle T_{AA} \rangle$ (mb^{-1})
0–10%	357 ± 4	23.48 ± 0.97
10%–20%	261 ± 4	14.43 ± 0.57
20%–40%	157 ± 3	6.85 ± 0.28
40%–60%	69 ± 2	2.00 ± 0.11
60%–80%	23 ± 1	0.42 ± 0.03
40%–80%	46 ± 2	1.20 ± 0.07

where $dN^{\mu^\pm}_{\rm PbPb}/dp_t$ and $dN^{\mu^\pm\leftarrow\pi^\pm,K^\pm}_{\rm PbPb}/dp_t$ are the inclusive muon and charged pion and kaon decay muon p_t distributions at forward rapidity in Pb-Pb collisions, respectively.

The pp reference, $d\sigma^{\mu^\pm\leftarrow{\rm HF}}_{pp}/dp_t$, was obtained from the analysis of muon-triggered events collected during a pp run at $\sqrt{s} = 2.76$ TeV, in March 2011, with integrated luminosity of 19 nb^{-1} after event selection cuts. The analysis technique from the event and track selection to the normalization is the same as that described in [25]. Figure 1 shows the measured p_t-differential inclusive cross section of muons from heavy-flavor decays in the kinematic region $2.5 < y < 4$ and $2 < p_t < 10$ GeV/c. In the range $p_t > 4$ GeV/c ($p_t > 6$ GeV/c), regions of interest for the $R^{\mu^\pm\leftarrow{\rm HF}}_{AA}(p_t)$ measurement, the contribution of muons from primary light hadron decays (mainly primary pion and kaon decays) that was subtracted amounts to about 19% (12%) of the total yield. The error bars are statistical uncertainties. The open boxes represent the systematic uncertainties varying from 15% to 24%, depending on p_t. This includes the contributions from background subtraction (ranging from a maximum of about 24% at $p_t = 2$ GeV/c to 14% at $p_t = 10$ GeV/c), detector response (3%), and residual misalignment of tracking chambers (1% $\times$ p_t, in GeV/c). The systematic uncertainty on the minimum bias pp cross section (1.9%), used in the normalization, is not shown. The data are compared to fixed order next-to-leading log (FONLL) pQCD predictions [27,28] (curve, with shaded band for the uncertainty). The ratio between data and FONLL calculations is also shown. The measured p_t-differential inclusive cross section of muons from heavy-flavor decays is well reproduced by the calculations within experimental and theoretical uncertainties, although at the upper limit of the predictions. A similar agreement between heavy-flavor results and pQCD calculations was also reported in pp collisions at $\sqrt{s} = 7$ TeV in the four LHC experiments and at lower energies at the FNAL Tevatron and at the RHIC (see [25] and references therein). The contributions of muons from charm and beauty decays from the FONLL calculations are displayed separately in Fig. 1. According to these predictions, the component of muons from beauty decays exceeds that of muons from charm decays for $p_t \gtrsim 6$ GeV/c.

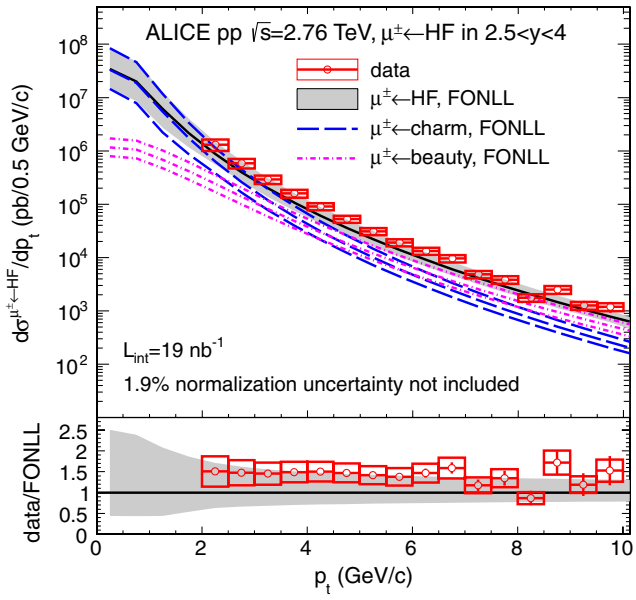

FIG. 1 (color online). Transverse momentum differential inclusive cross section of muons from heavy-flavor decays in $2.5 < y < 4$, in pp collisions at $\sqrt{s} = 2.76$ TeV. The vertical error bars (open boxes) are the statistical (systematic) uncertainties. The solid curve and the band show FONLL [27,28] calculations and theoretical uncertainties, respectively. The FONLL calculations are also reported for muons from charm (long dashed curves) and beauty (dot-dashed curves) decays, separately. The lower panel shows the ratio between data and FONLL calculations.

The p_t distribution of muons from heavy-flavor decays in Pb-Pb collisions at forward rapidity is obtained by subtracting the muon background component (mainly muons from primary pion and kaon decays) from the corrected inclusive muon p_t-differential distribution. The presence of unknown nuclear effects, in particular, medium-induced parton energy loss at forward rapidity, prevents subtraction of this contribution by means of Monte Carlo simulations, as was done in pp collisions [25]. Hence, the contribution of muons from primary $\pi^\pm$ and $K^\pm$ decays at forward rapidity in Pb-Pb collisions was estimated by extrapolating to forward rapidity ($2.5 < y < 4$) the p_t distributions of pions and kaons measured at central rapidity ($|y| < 0.8$) in pp and Pb-Pb collisions [29] and generating the corresponding p_t distributions of decay muons with a simulation of the decay kinematics and of the front absorber. For the rapidity extrapolation, it was assumed that the suppression of pions and kaons is independent of rapidity up to $y = 4$. This assumption is motivated by the observation, made by the ATLAS Collaboration, that the central-to-peripheral nuclear modification factor of charged hadrons does not show any η dependence up to $\eta = 2.5$ within uncertainties [30]. The systematic uncertainty introduced by this assumption was conservatively estimated by varying $R^{\pi^\pm,K^\pm}_{AA}(p_t)$ from 0 (full suppression) up to 2 times its value. The entire background-estimation procedure is detailed in the following.

The p_t distribution of pions and kaons at forward rapidity in Pb-Pb collisions in a given centrality range is expressed as

$$dN^{\pi^\pm,K^\pm}_{\rm PbPb}/dp_t = \langle T_{AA}\rangle (d\sigma^{\pi^\pm,K^\pm}_{pp}/dp_t)[R^{\pi^\pm,K^\pm}_{AA}(p_t)]_{y=0}. \quad (3)$$

The midrapidity pion and kaon p_t distributions measured in pp collisions were extrapolated to forward rapidity using [31]:

$$d^2N_{pp}^{\pi^\pm,K^\pm}/dp_t dy = [d^2N_{pp}^{\pi^\pm,K^\pm}/dp_t dy]_{y=0} \exp\left(\frac{-y^2}{2\sigma_y^2}\right), \quad (4)$$

with $\sigma_y = 3.18$. The latter is the average of the values obtained with the PYTHIA [32] and PHOJET [33] event generators. Equation (4) assumes that the shape of the p_t distribution is independent of y. However, results from the BRAHMS Collaboration suggest a small dependence at large rapidities [34], but the effect is expected to be negligible in the analysis due to the small amount of muons from pion and kaon decays in the p_t range of interest (see below).

Then, the muon p_t distributions in $2.5 < y < 4$ in pp and Pb-Pb collisions were obtained by means of fast simulations using the resultant pion and kaon p_t distributions as input. The effect of the front absorber was taken into account by considering only pions and kaons that decay before reaching a distance corresponding to one interaction length in the absorber.

The input charged pion p_t distributions were measured up to $p_t = 20$ GeV/c for all centrality classes used in the analysis. The kaon p_t distributions were determined only at low p_t. Therefore, the K^0_S p_t distributions, measured up to 16 GeV/c were used, considering that $N(K^+) + N(K^-) = 2N(K^0_S)$. A further extrapolation up to 40 GeV/c, by means of a power law fit, was needed. In addition, the K^0_S p_t distributions were measured only for the 0–5% and 60%–80% centrality classes. As a consequence, the p_t distributions of muons from pion and kaon decays at forward rapidity were determined only in these two centrality classes. For the other centrality classes used in this analysis (Table I), the $dN_{\rm PbPb}^{\mu^\pm\leftarrow\pi^\pm,K^\pm}/dp_t$ distributions were obtained by scaling the $R_{AA}^{\mu^\pm\leftarrow\pi^\pm}(p_t)$ with the double ratio $R_{AA}^{\mu^\pm\leftarrow\pi^\pm,K^\pm}(p_t)/R_{AA}^{\mu^\pm\leftarrow\pi^\pm}(p_t)$ which was found to be the same in the 0–5% and 60%–80% centrality classes, within a maximum variation of 9% included in the systematic uncertainty.

This procedure allowed us to estimate $dN_{\rm PbPb}^{\mu^\pm\leftarrow\pi^\pm,K^\pm}/dp_t$ and then to deduce the nuclear modification of muons from heavy-flavor decays at forward rapidity according to Eq. (2). The background contribution to the muon p_t distribution increases with decreasing p_t. Hence, in order to limit the systematic uncertainty on its subtraction, R_{AA} was computed for $p_t > 4$ GeV/c where this component is 7% (11%) of the total muon yield in central (peripheral) collisions.

The systematic uncertainties on the R_{AA} of muons from heavy-flavor decays originate from the pp reference, the corresponding Pb-Pb yields, and the average nuclear overlap function. The systematic uncertainty on the pp reference, previously discussed, is about 15%–17% for $p_t > 4$ GeV/c. The systematic uncertainty on the yields of muons from heavy-flavor decays in Pb-Pb includes contributions from the following: (1) the inclusive muon yields in Pb-Pb collisions, about 6%–10%, containing the systematic uncertainty on the detector response (3.5%), the residual misalignment (1% × p_t, in GeV/c) and the centrality dependence of the efficiency determined with the embedding procedure (1%); (2) the yields of muons from primary pion and kaon decays in pp collisions at forward rapidity, about 17%, due to the systematic uncertainty on the input midrapidity distributions, the extrapolation procedure (σ_y parameter), and the absorber effect (pion and kaon mean free path in the absorber); (3) the $R_{AA}^{\mu^\pm\leftarrow\pi^\pm}(p_t)$, about 14%–17%, due to the systematic uncertainty on the input midrapidity pion p_t distributions; (4) the $R_{AA}^{\mu^\pm\leftarrow\pi^\pm,K^\pm}(p_t)/R_{AA}^{\mu^\pm\leftarrow\pi^\pm}(p_t)$ double ratio, up to 9% at $p_t = 10$ GeV/c; (5) the unknown suppression at forward rapidity for muons from primary pion and kaon decays. As mentioned, a conservative systematic uncertainty was considered by varying $R_{AA}^{\pi^\pm,K^\pm}(p_t)$ from 0 to 2 times its value, with the additional condition that the upper limit does not exceed unity. Finally, the systematic uncertainty on the normalization includes the 1.9% uncertainty on the minimum bias cross section measurement in pp collisions and the uncertainty of 4.3% (centrality class 0–10%) to 7.3% (centrality class 60%–80%) on $\langle T_{AA}\rangle$.

Figure 2 presents the R_{AA} of muons from heavy-flavor decays in $2.5 < y < 4$, as a function of p_t in central (0–10%, left) and peripheral (40%–80%, right) collisions. The vertical error bars are the statistical uncertainties. The p_t-dependent systematic uncertainties are displayed by the open boxes and include all the contributions previously discussed, except the normalization uncertainty that is displayed at $R_{AA} = 1$. A larger suppression is observed in central collisions than in peripheral collisions, with no significant p_t dependence within uncertainties.

The centrality dependence of the R_{AA} of muons from heavy-flavor decays was studied in the range $6 < p_t < 10$ GeV/c where the contribution of muons from B decays becomes dominant in pp collisions according to the central value of the FONLL calculations: in particular, it amounts

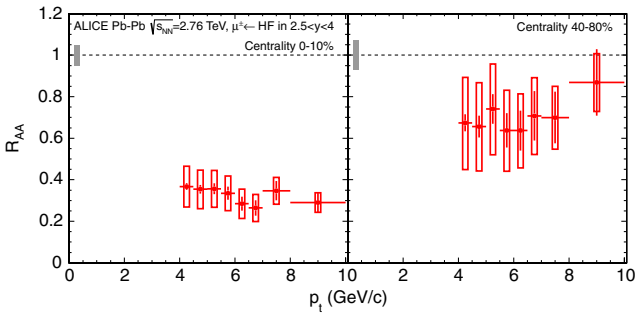

FIG. 2 (color online). R_{AA} of muons from heavy-flavor decays in $2.5 < y < 4$ as a function of p_t, in the 0–10% (left) and 40%–80% (right) centrality classes, in Pb-Pb collisions at $\sqrt{s_{NN}} = 2.76$ TeV. Vertical bars (open boxes) represent the statistical (systematic) uncertainty. The filled box centered at $R_{AA} = 1$ is the normalization uncertainty. Horizontal bars show the bin widths.

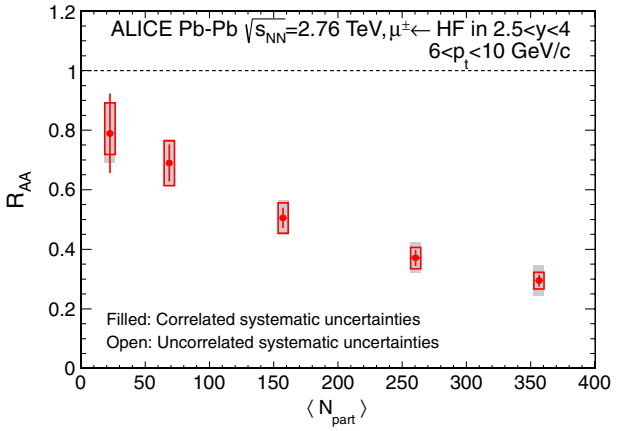

FIG. 3 (color online). R_{AA} of muons from heavy-flavor decays as a function of the mean number of participating nucleons, in $2.5 < y < 4$ and $6 < p_t < 10$ GeV/c. The horizontal bars indicate the uncertainty on $\langle N_{\text{part}} \rangle$.

to about 58% and 68% at $p_t = 6$ and 10 GeV/c, respectively, (Fig. 1). The analysis was carried out in five centrality classes from 0–10% to 60%–80% (Table I). The resulting R_{AA} is displayed as a function of $\langle N_{\text{part}} \rangle$ in Fig. 3. The contribution to the total systematic uncertainty, which is fully correlated between centrality classes (filled boxes), including the pp reference and normalization, is displayed separately from the remaining uncorrelated systematic uncertainty (open boxes). The R_{AA} of muons from heavy-flavor decays at forward rapidity exhibits a strong suppression with increasing centrality, reaching a factor of about 3–4 in the 10% most central collisions.

The ALICE Collaboration has measured the production of prompt D mesons in $2 < p_t < 16$ GeV/c at midrapidity ($|y| < 0.5$) [19] and the CMS Collaboration reported on that of nonprompt J/ψ from beauty decays, in $6.5 < p_t < 30$ GeV/c and $|y| < 2.4$ [20]. The corresponding suppression of D mesons and J/ψ from beauty decays in those studies is similar to that reported here for muons from heavy-flavor decays, although in a different p_t and rapidity region.

In conclusion, we have reported on the first measurement of the production of high-p_t muons from heavy-flavor decays at forward rapidity, in pp and Pb-Pb collisions at $\sqrt{s_{NN}} = 2.76$ TeV with the ALICE detector. FONLL pQCD calculations describe well the pp data within experimental and theoretical uncertainties, with the data being close to the upper limit of the model predictions. The R_{AA} of high-p_t muons from heavy-flavor decays indicates a clear suppression increasing towards the most central collisions. The measured suppression is almost independent of p_t, in the region $4 < p_t < 10$ GeV/c. These results provide clear evidence for large in-medium effects for heavy quarks in central Pb-Pb collisions at $\sqrt{s_{NN}} = 2.76$ TeV. The forthcoming p-Pb collisions will complement these measurements, by providing insight into the possible contribution of initial nuclear matter effects, although those are expected to be less important in the high p_t region studied here.

The ALICE Collaboration would like to thank all its engineers and technicians for their invaluable contributions to the construction of the experiment and the CERN accelerator teams for the outstanding performance of the LHC complex. The ALICE Collaboration acknowledges the following funding agencies for their support in building and running the ALICE detector: Calouste Gulbenkian Foundation from Lisbon and Swiss Fonds Kidagan, Armenia; Conselho Nacional de Desenvolvimento Científico e Tecnológico (CNPq), Financiadora de Estudos e Projetos (FINEP), Fundação de Amparo à Pesquisa do Estado de São Paulo (FAPESP); National Natural Science Foundation of China (NSFC), the Chinese Ministry of Education (CMOE) and the Ministry of Science and Technology of China (MSTC); Ministry of Education and Youth of the Czech Republic; Danish Natural Science Research Council, the Carlsberg Foundation and the Danish National Research Foundation; The European Research Council under the European Community's Seventh Framework Programme; Helsinki Institute of Physics and the Academy of Finland; French CNRS-IN2P3, the "Region Pays de Loire," "Region Alsace," "Region Auvergne," and CEA, France; German BMBF and the Helmholtz Association; General Secretariat for Research and Technology, Ministry of Development, Greece; Hungarian OTKA and National Office for Research and Technology (NKTH); Department of Atomic Energy and Department of Science and Technology of the Government of India; Istituto Nazionale di Fisica Nucleare (INFN) of Italy; MEXT Grant-in-Aid for Specially Promoted Research, Japan; Joint Institute for Nuclear Research, Dubna; National Research Foundation of Korea (NRF); CONACYT, DGAPA, México, ALFA-EC and the HELEN Program (High-Energy physics Latin-American—European Network); Stichting voor Fundamenteel Onderzoek der Materie (FOM) and the Nederlandse Organisatie voor Wetenschappelijk Onderzoek (NWO), Netherlands; Research Council of Norway (NFR); Polish Ministry of Science and Higher Education; National Authority for Scientific Research—NASR (Autoritatea Naţională pentru Cercetare Ştiinţifică—ANCS); Federal Agency of Science of the Ministry of Education and Science of Russian Federation, International Science and Technology Center, Russian Academy of Sciences, Russian Federal Agency of Atomic Energy, Russian Federal Agency for Science and Innovations and CERN-INTAS; Ministry of Education of Slovakia; Department of Science and Technology, South Africa; CIEMAT, EELA, Ministerio de Educación y Ciencia of Spain, Xunta de Galicia (Consellería de Educación), CEADEN, Cubaenergía, Cuba, and IAEA (International Atomic Energy Agency); Swedish

Research Council (VR) and Knut & Alice Wallenberg Foundation (KAW); Ukraine Ministry of Education and Science; United Kingdom Science and Technology Facilities Council (STFC); the United States Department of Energy, the United States National Science Foundation, the State of Texas, and the State of Ohio.

[1] F. Karsch, J. Phys. Conf. Ser. **46**, 122 (2006), and references therein.
[2] M. L. Miller, K. Reygers, S. Sanders, and P. Steinberg, Annu. Rev. Nucl. Part. Sci. **57**, 205 (2007).
[3] Y. L. Dokshitzer and D. E. Kharzeev, Phys. Lett. B **519**, 199 (2001).
[4] M. Djordjevic and M. Gyulassy, Nucl. Phys. **A733**, 265 (2004).
[5] B-W. Zhang, E. Wang, and X-N. Wang, Phys. Rev. Lett. **93**, 072301 (2004).
[6] N. Armesto, C. A. Salgado, and U. A. Wiedemann, Phys. Rev. D **69**, 114003 (2004).
[7] M. G. Mustafa, Phys. Rev. C **72**, 014905 (2005).
[8] S. Wicks, W. Horowitz, M. Djordjevic, and M Gyulassy, Nucl. Phys. **A783**, 493 (2007).
[9] A. Adil and I. Vitev, Phys. Lett. B **649**, 139 (2007).
[10] V. Greco, C. M. Ko, and R. Rapp, Phys. Lett. B **595**, 202 (2004).
[11] H. van Hees, V. Greco, and R. Rapp, Phys. Rev. C **73**, 034913 (2006).
[12] D. Kharzeev, E. Levin, and L. McLerran, Phys. Lett. B **561**, 93 (2003).
[13] N. Armesto, J. Phys. G **32**, R367 (2006).
[14] K. Adcox *et al.* (PHENIX Collaboration), Phys. Rev. Lett. **88**, 192303 (2002).
[15] S. S. Adler *et al.* (PHENIX Collaboration), Phys. Rev. Lett. **94**, 082301 (2005); Phys. Rev. Lett. **96**, 032301 (2006).
[16] A. Adare *et al.* (PHENIX Collaboration), Phys. Rev. Lett. **98**, 172301 (2007); Phys. Rev. C **84**, 044905 (2011).
[17] B. I. Abelev *et al.* (STAR Collaboration), Phys. Rev. Lett. **98**, 192301 (2007); **106**, 159902 (2011)].
[18] A. Adare *et al.* (PHENIX Collaboration), Phys. Rev. C **86**, 024909 (2012).
[19] B. Abelev *et al.* (ALICE Collaboration), arXiv:1203.2160 [J. High Energy Phys. (to be published)].
[20] S. Chatrchyan *et al.* (CMS Collaboration), J. High Energy Phys. 05 (2012) 063.
[21] K. Aamodt *et al.* (ALICE Collaboration), JINST **3**, S08002 (2008).
[22] In the ALICE reference frame, the muon spectrometer covers a negative η range and consequently a negative y range. The results are presented with a positive y notation.
[23] K. Aamodt *et al.* (ALICE Collaboration), Phys. Rev. Lett. **106**, 032301 (2011).
[24] K. Aamodt *et al.* (ALICE Collaboration), Phys. Lett. B **696**, 30 (2011).
[25] B. Abelev *et al.* (ALICE Collaboration), Phys. Lett. B **708**, 265 (2012).
[26] B. Abelev *et al.* (ALICE Collaboration), Phys. Rev. Lett. **109**, 072301 (2012).
[27] M. Cacciari, M. Greco, and P. Nason, J. High Energy Phys. 05 (1998) 007.
[28] M. Cacciari, S. Frixione, N. Houdeau, M. L. Mangano, P. Nason, G. Ridolfi, arXiv:1205.6344.
[29] H. Appelshäuser (ALICE Collaboration), J. Phys. G **38**, 124014 (2011).
[30] A. Milov (ATLAS Collaboration), J. Phys. G **38**, 124113 (2011).
[31] S. S. Adler (PHENIX Collaboration), Phys. Rev. D **76**, 092002 (2007).
[32] T. Sjöstrand, S. Mrenna, and P. Skands, J. High Energy Phys. 05 (2006) 026.
[33] R. Engel, J. Ranft, and S. Roesler, Phys. Rev. D **52**, 1459 (1995).
[34] L. Arsene *et al.* (BRAMHS Collaboration), Phys. Rev. Lett. **93**, 242303 (2004).

B. Abelev,[1] J. Adam,[2] D. Adamová,[3] A. M. Adare,[4] M. M. Aggarwal,[5] G. Aglieri Rinella,[6] A. G. Agocs,[7] A. Agostinelli,[8] S. Aguilar Salazar,[9] Z. Ahammed,[10] A. Ahmad Masoodi,[11] N. Ahmad,[11] S. A. Ahn,[12] S. U. Ahn,[13,14] A. Akindinov,[15] D. Aleksandrov,[16] B. Alessandro,[17] R. Alfaro Molina,[9] A. Alici,[18,19] A. Alkin,[20] E. Almaráz Aviña,[9] J. Alme,[21] T. Alt,[22] V. Altini,[23] S. Altinpinar,[24] I. Altsybeev,[25] C. Andrei,[26] A. Andronic,[27] V. Anguelov,[28] J. Anielski,[29] C. Anson,[30] T. Antičić,[31] F. Antinori,[32] P. Antonioli,[18] L. Aphecetche,[33] H. Appelshäuser,[34] N. Arbor,[35] S. Arcelli,[8] A. Arend,[34] N. Armesto,[36] R. Arnaldi,[17] T. Aronsson,[4] I. C. Arsene,[27] M. Arslandok,[34] A. Asryan,[25] A. Augustinus,[6] R. Averbeck,[27] T. C. Awes,[37] J. Äystö,[38] M. D. Azmi,[11] M. Bach,[22] A. Badalà,[39] Y. W. Baek,[13,14] R. Bailhache,[34] R. Bala,[17] R. Baldini Ferroli,[19] A. Baldisseri,[40] A. Baldit,[13] F. Baltasar Dos Santos Pedrosa,[6] J. Bán,[41] R. C. Baral,[42] R. Barbera,[43] F. Barile,[23] G. G. Barnaföldi,[7] L. S. Barnby,[44] V. Barret,[13] J. Bartke,[45] M. Basile,[8] N. Bastid,[13] S. Basu,[10] B. Bathen,[29] G. Batigne,[33] B. Batyunya,[46] C. Baumann,[34] I. G. Bearden,[47] H. Beck,[34] I. Belikov,[48] F. Bellini,[8] R. Bellwied,[49] E. Belmont-Moreno,[9] G. Bencedi,[7] S. Beole,[50] I. Berceanu,[26] A. Bercuci,[26] Y. Berdnikov,[51] D. Berenyi,[7] A. A. E. Bergognon,[33] D. Berzano,[17] L. Betev,[6] A. Bhasin,[52] A. K. Bhati,[5] J. Bhom,[53] L. Bianchi,[50] N. Bianchi,[54] C. Bianchin,[55] J. Bielčík,[2] J. Bielčíková,[3] A. Bilandzic,[56,47] S. Bjelogrlic,[57] F. Blanco,[58] F. Blanco,[49] D. Blau,[16] C. Blume,[34] M. Boccioli,[6] N. Bock,[30] S. Böttger,[59] A. Bogdanov,[60] H. Bøggild,[47] M. Bogolyubsky,[61] L. Boldizsár,[7] M. Bombara,[62] J. Book,[34] H. Borel,[40] A. Borissov,[63] S. Bose,[64] F. Bossú,[50] M. Botje,[56] B. Boyer,[65] E. Braidot,[66] P. Braun-Munzinger,[27] M. Bregant,[33] T. Breitner,[59] T. A. Browning,[67] M. Broz,[68] R. Brun,[6] E. Bruna,[50,17] G. E. Bruno,[23] D. Budnikov,[69] H. Buesching,[34] S. Bufalino,[50,17] K. Bugaiev,[20]

O. Busch,[28] Z. Buthelezi,[70] D. Caballero Orduna,[4] D. Caffarri,[55] X. Cai,[71] H. Caines,[4] E. Calvo Villar,[72] P. Camerini,[73] V. Canoa Roman,[74,75] G. Cara Romeo,[18] F. Carena,[6] W. Carena,[6] N. Carlin Filho,[76] F. Carminati,[6] C. A. Carrillo Montoya,[6] A. Casanova Díaz,[54] J. Castillo Castellanos,[40] J. F. Castillo Hernandez,[27] E. A. R. Casula,[77] V. Catanescu,[26] C. Cavicchioli,[6] C. Ceballos Sanchez,[78] J. Cepila,[2] P. Cerello,[17] B. Chang,[38,79] S. Chapeland,[6] J. L. Charvet,[40] S. Chattopadhyay,[10] S. Chattopadhyay,[64] I. Chawla,[5] M. Cherney,[80] C. Cheshkov,[6,81] B. Cheynis,[81] V. Chibante Barroso,[6] D. D. Chinellato,[82] P. Chochula,[6] M. Chojnacki,[57] S. Choudhury,[10] P. Christakoglou,[56,57] C. H. Christensen,[47] P. Christiansen,[83] T. Chujo,[53] S. U. Chung,[84] C. Cicalo,[85] L. Cifarelli,[8,6] F. Cindolo,[18] J. Cleymans,[70] F. Coccetti,[19] F. Colamaria,[23] D. Colella,[23] G. Conesa Balbastre,[35] Z. Conesa del Valle,[6] P. Constantin,[28] G. Contin,[73] J. G. Contreras,[74] T. M. Cormier,[63] Y. Corrales Morales,[50] P. Cortese,[86] I. Cortés Maldonado,[75] M. R. Cosentino,[66] F. Costa,[6] M. E. Cotallo,[58] E. Crescio,[74] P. Crochet,[13] E. Cruz Alaniz,[9] E. Cuautle,[87] L. Cunqueiro,[54] A. Dainese,[55,32] H. H. Dalsgaard,[47] A. Danu,[88] D. Das,[64] I. Das,[65] K. Das,[64] S. Dash,[89] A. Dash,[82] S. De,[10] G. O. V. de Barros,[76] A. De Caro,[90,19] G. de Cataldo,[91] J. de Cuveland,[22] A. De Falco,[77] D. De Gruttola,[90] H. Delagrange,[33] A. Deloff,[92] V. Demanov,[69] N. De Marco,[17] E. Dénes,[7] S. De Pasquale,[90] A. Deppman,[76] G. D. Erasmo,[23] R. de Rooij,[57] M. A. Diaz Corchero,[58] D. Di Bari,[23] T. Dietel,[29] S. Di Liberto,[93] A. Di Mauro,[6] P. Di Nezza,[54] R. Divià,[6] Ø. Djuvsland,[24] A. Dobrin,[63,83] T. Dobrowolski,[92] I. Domínguez,[87] B. Dönigus,[27] O. Dordic,[94] O. Driga,[33] A. K. Dubey,[10] L. Ducroux,[81] P. Dupieux,[13] M. R. Dutta Majumdar,[10] A. K. Dutta Majumdar,[64] D. Elia,[91] D. Emschermann,[29] H. Engel,[59] H. A. Erdal,[21] B. Espagnon,[65] M. Estienne,[33] S. Esumi,[53] D. Evans,[44] G. Eyyubova,[94] D. Fabris,[55,32] J. Faivre,[35] D. Falchieri,[8] A. Fantoni,[54] M. Fasel,[27] R. Fearick,[70] A. Fedunov,[46] D. Fehlker,[24] L. Feldkamp,[29] D. Felea,[88] B. Fenton-Olsen,[66] G. Feofilov,[25] A. Fernández Téllez,[75] A. Ferretti,[50] R. Ferretti,[86] J. Figiel,[45] M. A. S. Figueredo,[76] S. Filchagin,[69] D. Finogeev,[95] F. M. Fionda,[23] E. M. Fiore,[23] M. Floris,[6] S. Foertsch,[70] P. Foka,[27] S. Fokin,[16] E. Fragiacomo,[96] U. Frankenfeld,[27] U. Fuchs,[6] C. Furget,[35] M. Fusco Girard,[90] J. J. Gaardhøje,[47] M. Gagliardi,[50] A. Gago,[72] M. Gallio,[50] D. R. Gangadharan,[30] P. Ganoti,[37] C. Garabatos,[27] E. Garcia-Solis,[97] I. Garishvili,[1] J. Gerhard,[22] M. Germain,[33] C. Geuna,[40] A. Gheata,[6] M. Gheata,[88,6] B. Ghidini,[23] P. Ghosh,[10] P. Gianotti,[54] M. R. Girard,[98] P. Giubellino,[6] E. Gladysz-Dziadus,[45] P. Glässel,[28] R. Gomez,[99] A. Gonschior,[27] E. G. Ferreiro,[36] L. H. González-Trueba,[9] P. González-Zamora,[58] S. Gorbunov,[22] A. Goswami,[100] S. Gotovac,[101] V. Grabski,[9] L. K. Graczykowski,[98] R. Grajcarek,[28] A. Grelli,[57] C. Grigoras,[6] A. Grigoras,[6] V. Grigoriev,[60] A. Grigoryan,[102] S. Grigoryan,[46] B. Grinyov,[20] N. Grion,[96] P. Gros,[83] J. F. Grosse-Oetringhaus,[6] J.-Y. Grossiord,[81] R. Grosso,[6] F. Guber,[95] R. Guernane,[35] C. Guerra Gutierrez,[72] B. Guerzoni,[8] M. Guilbaud,[81] K. Gulbrandsen,[47] T. Gunji,[103] A. Gupta,[52] R. Gupta,[52] H. Gutbrod,[27] Ø. Haaland,[24] C. Hadjidakis,[65] M. Haiduc,[88] H. Hamagaki,[103] G. Hamar,[7] B. H. Han,[104] L. D. Hanratty,[44] A. Hansen,[47] Z. Harmanova,[62] J. W. Harris,[4] M. Hartig,[34] D. Hasegan,[88] D. Hatzifotiadou,[18] A. Hayrapetyan,[6,102] S. T. Heckel,[34] M. Heide,[29] H. Helstrup,[21] A. Herghelegiu,[26] G. Herrera Corral,[74] N. Herrmann,[28] B. A. Hess,[105] K. F. Hetland,[21] B. Hicks,[4] P. T. Hille,[4] B. Hippolyte,[48] T. Horaguchi,[53] Y. Hori,[103] P. Hristov,[6] I. Hřivnáčová,[65] M. Huang,[24] T. J. Humanic,[30] D. S. Hwang,[104] R. Ichou,[13] R. Ilkaev,[69] I. Ilkiv,[92] M. Inaba,[53] E. Incani,[77] G. M. Innocenti,[50] P. G. Innocenti,[6] M. Ippolitov,[16] M. Irfan,[11] C. Ivan,[27] V. Ivanov,[51] M. Ivanov,[27] A. Ivanov,[25] O. Ivanytskyi,[20] A. Jachołkowski,[6] P. M. Jacobs,[66] H. J. Jang,[12] S. Jangal,[48] M. A. Janik,[98] R. Janik,[68] P. H. S. Y. Jayarathna,[49] S. Jena,[89] D. M. Jha,[63] R. T. Jimenez Bustamante,[87] L. Jirden,[6] P. G. Jones,[44] H. Jung,[14] A. Jusko,[44] A. B. Kaidalov,[15] V. Kakoyan,[102] S. Kalcher,[22] P. Kaliňák,[41] T. Kalliokoski,[38] A. Kalweit,[106] K. Kanaki,[24] J. H. Kang,[79] V. Kaplin,[60] A. Karasu Uysal,[6,107] O. Karavichev,[95] T. Karavicheva,[95] E. Karpechev,[95] A. Kazantsev,[16] U. Kebschull,[59] R. Keidel,[108] P. Khan,[64] M. M. Khan,[11] S. A. Khan,[10] A. Khanzadeev,[51] Y. Kharlov,[61] B. Kileng,[21] D. W. Kim,[14] M. Kim,[14] M. Kim,[79] S. H. Kim,[14] D. J. Kim,[38] S. Kim,[104] J. H. Kim,[104] J. S. Kim,[14] B. Kim,[79] T. Kim,[79] S. Kirsch,[22] I. Kisel,[22] S. Kiselev,[15] A. Kisiel,[6,98] J. L. Klay,[109] J. Klein,[28] C. Klein-Bösing,[29] M. Kliemant,[34] A. Kluge,[6] M. L. Knichel,[27] A. G. Knospe,[110] K. Koch,[28] M. K. Köhler,[27] A. Kolojvari,[25] V. Kondratiev,[25] N. Kondratyeva,[60] A. Konevskikh,[95] A. Korneev,[69] R. Kour,[44] M. Kowalski,[45] S. Kox,[35] G. Koyithatta Meethaleveedu,[89] J. Kral,[38] I. Králik,[41] F. Kramer,[34] I. Kraus,[27] T. Krawutschke,[28,111] M. Krelina,[2] M. Kretz,[22] M. Krivda,[44,41] F. Krizek,[38] M. Krus,[2] E. Kryshen,[51] M. Krzewicki,[27] Y. Kucheriaev,[16] C. Kuhn,[48] P. G. Kuijer,[56] I. Kulakov,[34] J. Kumar,[89] P. Kurashvili,[92] A. B. Kurepin,[95] A. Kurepin,[95] A. Kuryakin,[69] V. Kushpil,[3] S. Kushpil,[3] H. Kvaerno,[94] M. J. Kweon,[28] Y. Kwon,[79] P. Ladrón de Guevara,[87] I. Lakomov,[65] R. Langoy,[24] S. L. La Pointe,[57] C. Lara,[59] A. Lardeux,[33] P. La Rocca,[43] C. Lazzeroni,[44] R. Lea,[73] Y. Le Bornec,[65] M. Lechman,[6] S. C. Lee,[14] K. S. Lee,[14] G. R. Lee,[44] F. Lefèvre,[33] J. Lehnert,[34] L. Leistam,[6] M. Lenhardt,[33] V. Lenti,[91] H. León,[9] M. Leoncino,[17] I. León Monzón,[99] H. León Vargas,[34] P. Lévai,[7] J. Lien,[24] R. Lietava,[44] S. Lindal,[94]

V. Lindenstruth,[22] C. Lippmann,[27,6] M. A. Lisa,[30] L. Liu,[24] P. I. Loenne,[24] V. R. Loggins,[63] V. Loginov,[60] S. Lohn,[6] D. Lohner,[28] C. Loizides,[66] K. K. Loo,[38] X. Lopez,[13] E. López Torres,[78] G. Løvhøiden,[94] X.-G. Lu,[28] P. Luettig,[34] M. Lunardon,[55] J. Luo,[71] G. Luparello,[57] L. Luquin,[33] C. Luzzi,[6] R. Ma,[4] K. Ma,[71] D. M. Madagodahettige-Don,[49] A. Maevskaya,[95] M. Mager,[106,6] D. P. Mahapatra,[42] A. Maire,[28] M. Malaev,[51] I. Maldonado Cervantes,[87] L. Malinina,[46,*] D. Mal'Kevich,[15] P. Malzacher,[27] A. Mamonov,[69] L. Manceau,[17] L. Mangotra,[52] V. Manko,[16] F. Manso,[13] V. Manzari,[91] Y. Mao,[71] M. Marchisone,[13,50] J. Mareš,[112] G. V. Margagliotti,[73,96] A. Margotti,[18] A. Marín,[27] C. A. Marin Tobon,[6] C. Markert,[110] I. Martashvili,[113] P. Martinengo,[6] M. I. Martínez,[75] A. Martínez Davalos,[9] G. Martínez García,[33] Y. Martynov,[20] A. Mas,[33] S. Masciocchi,[27] M. Masera,[50] A. Masoni,[85] L. Massacrier,[81,33] M. Mastromarco,[91] A. Mastroserio,[23,6] Z. L. Matthews,[44] A. Matyja,[45,33] D. Mayani,[87] C. Mayer,[45] J. Mazer,[113] M. A. Mazzoni,[93] F. Meddi,[114] A. Menchaca-Rocha,[9] J. Mercado Pérez,[28] M. Meres,[68] Y. Miake,[53] L. Milano,[50] J. Milosevic,[94,†] A. Mischke,[57] A. N. Mishra,[100] D. Miśkowiec,[27,6] C. Mitu,[88] J. Mlynarz,[63] B. Mohanty,[10] A. K. Mohanty,[6] L. Molnar,[6] L. Montaño Zetina,[74] M. Monteno,[17] E. Montes,[58] T. Moon,[79] M. Morando,[55] D. A. Moreira De Godoy,[76] S. Moretto,[55] A. Morsch,[6] V. Muccifora,[54] E. Mudnic,[101] S. Muhuri,[10] M. Mukherjee,[10] H. Müller,[6] M. G. Munhoz,[76] L. Musa,[6] A. Musso,[17] B. K. Nandi,[89] R. Nania,[18] E. Nappi,[91] C. Nattrass,[113] N. P. Naumov,[69] S. Navin,[44] T. K. Nayak,[10] S. Nazarenko,[69] G. Nazarov,[69] A. Nedosekin,[15] M. Niculescu,[88,6] B. S. Nielsen,[47] T. Niida,[53] S. Nikolaev,[16] V. Nikolic,[31] S. Nikulin,[16] V. Nikulin,[51] B. S. Nilsen,[80] M. S. Nilsson,[94] F. Noferini,[18,19] P. Nomokonov,[46] G. Nooren,[57] N. Novitzky,[38] A. Nyanin,[16] A. Nyatha,[89] C. Nygaard,[47] J. Nystrand,[24] A. Ochirov,[25] H. Oeschler,[106,6] S. Oh,[4] S. K. Oh,[14] J. Oleniacz,[98] C. Oppedisano,[17] A. Ortiz Velasquez,[83,87] G. Ortona,[50] A. Oskarsson,[83] P. Ostrowski,[98] J. Otwinowski,[27] K. Oyama,[28] K. Ozawa,[103] Y. Pachmayer,[28] M. Pachr,[2] F. Padilla,[50] P. Pagano,[90] G. Paić,[87] F. Painke,[22] C. Pajares,[36] S. Pal,[40] S. K. Pal,[10] A. Palaha,[44] A. Palmeri,[39] V. Papikyan,[102] G. S. Pappalardo,[39] W. J. Park,[27] A. Passfeld,[29] B. Pastirčák,[41] D. I. Patalakha,[61] V. Paticchio,[91] A. Pavlinov,[63] T. Pawlak,[98] T. Peitzmann,[57] H. Pereira Da Costa,[40] E. Pereira De Oliveira Filho,[76] D. Peresunko,[16] C. E. Pérez Lara,[56] E. Perez Lezama,[87] D. Perini,[6] D. Perrino,[23] W. Peryt,[98] A. Pesci,[18] V. Peskov,[6,87] Y. Pestov,[115] V. Petráček,[2] M. Petran,[2] M. Petris,[26] P. Petrov,[44] M. Petrovici,[26] C. Petta,[43] S. Piano,[96] A. Piccotti,[17] M. Pikna,[68] P. Pillot,[33] O. Pinazza,[6] L. Pinsky,[49] N. Pitz,[34] D. B. Piyarathna,[49] M. Płoskoń,[66] J. Pluta,[98] T. Pocheptsov,[46] S. Pochybova,[7] P. L. M. Podesta-Lerma,[99] M. G. Poghosyan,[6,50] K. Polák,[112] B. Polichtchouk,[61] A. Pop,[26] S. Porteboeuf-Houssais,[13] V. Pospíšil,[2] B. Potukuchi,[52] S. K. Prasad,[63] R. Preghenella,[18,19] F. Prino,[17] C. A. Pruneau,[63] I. Pshenichnov,[95] S. Puchagin,[69] G. Puddu,[77] J. Pujol Teixido,[59] A. Pulvirenti,[43,6] V. Punin,[69] M. Putiš,[62] J. Putschke,[63,4] E. Quercigh,[6] H. Qvigstad,[94] A. Rachevski,[96] A. Rademakers,[6] S. Radomski,[28] T. S. Räihä,[38] J. Rak,[38] A. Rakotozafindrabe,[40] L. Ramello,[86] A. Ramírez Reyes,[74] S. Raniwala,[100] R. Raniwala,[100] S. S. Räsänen,[38] B. T. Rascanu,[34] D. Rathee,[5] K. F. Read,[113] J. S. Real,[35] K. Redlich,[92,116] P. Reichelt,[34] M. Reicher,[57] R. Renfordt,[34] A. R. Reolon,[54] A. Reshetin,[95] F. Rettig,[22] J.-P. Revol,[6] K. Reygers,[28] L. Riccati,[17] R. A. Ricci,[117] T. Richert,[83] M. Richter,[94] P. Riedler,[6] W. Riegler,[6] F. Riggi,[43,39] B. Rodrigues Fernandes Rabacal,[6] M. Rodríguez Cahuantzi,[75] A. Rodriguez Manso,[56] K. Røed,[24] D. Rohr,[22] D. Röhrich,[24] R. Romita,[27] F. Ronchetti,[54] P. Rosnet,[13] S. Rossegger,[6] A. Rossi,[6,55] C. Roy,[48] P. Roy,[64] A. J. Rubio Montero,[58] R. Rui,[73] E. Ryabinkin,[16] A. Rybicki,[45] S. Sadovsky,[61] K. Šafařík,[6] R. Sahoo,[118] P. K. Sahu,[42] J. Saini,[10] H. Sakaguchi,[119] S. Sakai,[66] D. Sakata,[53] C. A. Salgado,[36] J. Salzwedel,[30] S. Sambyal,[52] V. Samsonov,[51] X. Sanchez Castro,[48] L. Šándor,[41] A. Sandoval,[9] S. Sano,[103] M. Sano,[53] R. Santo,[29] R. Santoro,[91,6,19] J. Sarkamo,[38] E. Scapparone,[18] F. Scarlassara,[55] R. P. Scharenberg,[67] C. Schiaua,[26] R. Schicker,[28] C. Schmidt,[27] H. R. Schmidt,[105] S. Schreiner,[6] S. Schuchmann,[34] J. Schukraft,[6] Y. Schutz,[6,33] K. Schwarz,[27] K. Schweda,[27,28] G. Scioli,[8] E. Scomparin,[17] R. Scott,[113] P. A. Scott,[44] G. Segato,[55] I. Selyuzhenkov,[27] S. Senyukov,[86,48] J. Seo,[84] S. Serci,[77] E. Serradilla,[58,9] A. Sevcenco,[88] A. Shabetai,[33] G. Shabratova,[46] R. Shahoyan,[6] N. Sharma,[5] S. Sharma,[52] S. Rohni,[52] K. Shigaki,[119] M. Shimomura,[53] K. Shtejer,[78] Y. Sibiriak,[16] M. Siciliano,[50] E. Sicking,[6] S. Siddhanta,[85] T. Siemiarczuk,[92] D. Silvermyr,[37] C. Silvestre,[35] G. Simatovic,[87,31] G. Simonetti,[6] R. Singaraju,[10] R. Singh,[52] S. Singha,[10] V. Singhal,[10] T. Sinha,[64] B. C. Sinha,[10] B. Sitar,[68] M. Sitta,[86] T. B. Skaali,[94] K. Skjerdal,[24] R. Smakal,[2] N. Smirnov,[4] R. J. M. Snellings,[57] C. Søgaard,[47] R. Soltz,[1] H. Son,[104] M. Song,[79] J. Song,[84] C. Soos,[6] F. Soramel,[55] I. Sputowska,[45] M. Spyropoulou-Stassinaki,[120] B. K. Srivastava,[67] J. Stachel,[28] I. Stan,[88] I. Stan,[88] G. Stefanek,[92] T. Steinbeck,[22] M. Steinpreis,[30] E. Stenlund,[83] G. Steyn,[70] J. H. Stiller,[28] D. Stocco,[33] M. Stolpovskiy,[61] K. Strabykin,[69] P. Strmen,[68] A. A. P. Suaide,[76] M. A. Subieta Vásquez,[50] T. Sugitate,[119] C. Suire,[65] M. Sukhorukov,[69] R. Sultanov,[15] M. Šumbera,[3] T. Susa,[31] A. Szanto de Toledo,[76] I. Szarka,[68] A. Szczepankiewicz,[45] A. Szostak,[24] M. Szymanski,[98] J. Takahashi,[82] J. D. Tapia Takaki,[65] A. Tauro,[6] G. Tejeda Muñoz,[75] A. Telesca,[6] C. Terrevoli,[23]

J. Thäder,[27] D. Thomas,[57] R. Tieulent,[81] A. R. Timmins,[49] D. Tlusty,[2] A. Toia,[22,6] H. Torii,[103] L. Toscano,[17] D. Truesdale,[30] W. H. Trzaska,[38] T. Tsuji,[103] A. Tumkin,[69] R. Turrisi,[32] T. S. Tveter,[94] J. Ulery,[34] K. Ullaland,[24] J. Ulrich,[121,59] A. Uras,[81] J. Urbán,[62] G. M. Urciuoli,[93] G. L. Usai,[77] M. Vajzer,[2,3] M. Vala,[46,41] L. Valencia Palomo,[65] S. Vallero,[28] N. van der Kolk,[56] P. Vande Vyvre,[6] M. van Leeuwen,[57] L. Vannucci,[117] A. Vargas,[75] R. Varma,[89] M. Vasileiou,[120] A. Vasiliev,[16] V. Vechernin,[25] M. Veldhoen,[57] M. Venaruzzo,[73] E. Vercellin,[50] S. Vergara,[75] R. Vernet,[122] M. Verweij,[57] L. Vickovic,[101] G. Viesti,[55] O. Vikhlyantsev,[69] Z. Vilakazi,[70] O. Villalobos Baillie,[44] A. Vinogradov,[16] L. Vinogradov,[25] Y. Vinogradov,[69] T. Virgili,[90] Y. P. Viyogi,[10] A. Vodopyanov,[46] K. Voloshin,[15] S. Voloshin,[63] G. Volpe,[23,6] B. von Haller,[6] D. Vranic,[27] G. Øvrebekk,[24] J. Vrláková,[62] B. Vulpescu,[13] A. Vyushin,[69] V. Wagner,[2] B. Wagner,[24] R. Wan,[71,48] M. Wang,[71] D. Wang,[71] Y. Wang,[28] Y. Wang,[71] K. Watanabe,[53] M. Weber,[49] J. P. Wessels,[6,29] U. Westerhoff,[29] J. Wiechula,[105] J. Wikne,[94] M. Wilde,[29] G. Wilk,[92] A. Wilk,[29] M. C. S. Williams,[18] B. Windelband,[28] L. Xaplanteris Karampatsos,[110] C. G. Yaldo,[63] Y. Yamaguchi,[103] H. Yang,[40] S. Yang,[24] S. Yasnopolskiy,[16] J. Yi,[84] Z. Yin,[71] I.-K. Yoo,[84] J. Yoon,[79] W. Yu,[34] X. Yuan,[71] I. Yushmanov,[16] C. Zach,[2] C. Zampolli,[18] S. Zaporozhets,[46] A. Zarochentsev,[25] P. Závada,[112] N. Zaviyalov,[69] H. Zbroszczyk,[98] P. Zelnicek,[59] I. S. Zgura,[88] M. Zhalov,[51] X. Zhang,[71,13] H. Zhang,[71] F. Zhou,[71] D. Zhou,[71] Y. Zhou,[57] J. Zhu,[71] J. Zhu,[71] X. Zhu,[71] A. Zichichi,[8,19] A. Zimmermann,[28] G. Zinovjev,[20] Y. Zoccarato,[81] M. Zynovyev,[20] and M. Zyzak[34]

(ALICE Collaboration)

[1]*Lawrence Livermore National Laboratory, Livermore, California, USA*
[2]*Faculty of Nuclear Sciences and Physical Engineering, Czech Technical University in Prague, Prague, Czech Republic*
[3]*Nuclear Physics Institute, Academy of Sciences of the Czech Republic, Řež u Prahy, Czech Republic*
[4]*Yale University, New Haven, Connecticut, USA*
[5]*Physics Department, Panjab University, Chandigarh, India*
[6]*European Organization for Nuclear Research (CERN), Geneva, Switzerland*
[7]*KFKI Research Institute for Particle and Nuclear Physics, Hungarian Academy of Sciences, Budapest, Hungary*
[8]*Dipartimento di Fisica dell'Università and Sezione INFN, Bologna, Italy*
[9]*Instituto de Física, Universidad Nacional Autónoma de México, Mexico City, Mexico*
[10]*Variable Energy Cyclotron Centre, Kolkata, India*
[11]*Department of Physics Aligarh Muslim University, Aligarh, India*
[12]*Korea Institute of Science and Technology Information, Daejeon, South Korea*
[13]*Laboratoire de Physique Corpusculaire (LPC), Clermont Université, Université Blaise Pascal, CNRS–IN2P3, Clermont-Ferrand, France*
[14]*Gangneung-Wonju National University, Gangneung, South Korea*
[15]*Institute for Theoretical and Experimental Physics, Moscow, Russia*
[16]*Russian Research Centre Kurchatov Institute, Moscow, Russia*
[17]*Sezione INFN, Turin, Italy*
[18]*Sezione INFN, Bologna, Italy*
[19]*Centro Fermi—Centro Studi e Ricerche e Museo Storico della Fisica "Enrico Fermi", Rome, Italy*
[20]*Bogolyubov Institute for Theoretical Physics, Kiev, Ukraine*
[21]*Faculty of Engineering, Bergen University College, Bergen, Norway*
[22]*Frankfurt Institute for Advanced Studies, Johann Wolfgang Goethe-Universität Frankfurt, Frankfurt, Germany*
[23]*Dipartimento Interateneo di Fisica 'M. Merlin' and Sezione INFN, Bari, Italy*
[24]*Department of Physics and Technology, University of Bergen, Bergen, Norway*
[25]*V. Fock Institute for Physics, St. Petersburg State University, St. Petersburg, Russia*
[26]*National Institute for Physics and Nuclear Engineering, Bucharest, Romania*
[27]*Research Division and ExtreMe Matter Institute EMMI, GSI Helmholtzzentrum für Schwerionenforschung, Darmstadt, Germany*
[28]*Physikalisches Institut, Ruprecht-Karls-Universität Heidelberg, Heidelberg, Germany*
[29]*Institut für Kernphysik, Westfälische Wilhelms-Universität Münster, Münster, Germany*
[30]*Department of Physics, The Ohio State University, Columbus, Ohio, United States*
[31]*Rudjer Bošković Institute, Zagreb, Croatia*
[32]*Sezione INFN, Padova, Italy*
[33]*SUBATECH, Ecole des Mines de Nantes, Université de Nantes, CNRS-IN2P3, Nantes, France*
[34]*Institut für Kernphysik, Johann Wolfgang Goethe-Universität Frankfurt, Frankfurt, Germany*
[35]*Laboratoire de Physique Subatomique et de Cosmologie (LPSC), Université Joseph Fourier, CNRS-IN2P3, Institut Polytechnique de Grenoble, Grenoble, France*
[36]*Departamento de Física de Partículas and IGFAE, Universidad de Santiago de Compostela, Santiago de Compostela, Spain*

[37]Oak Ridge National Laboratory, Oak Ridge, Tennessee, United States
[38]Helsinki Institute of Physics (HIP) and University of Jyväskylä, Jyväskylä, Finland
[39]Sezione INFN, Catania, Italy
[40]Commissariat à l'Energie Atomique, IRFU, Saclay, France
[41]Institute of Experimental Physics, Slovak Academy of Sciences, Košice, Slovakia
[42]Institute of Physics, Bhubaneswar, India
[43]Dipartimento di Fisica e Astronomia dell'Università and Sezione INFN, Catania, Italy
[44]School of Physics and Astronomy, University of Birmingham, Birmingham, United Kingdom
[45]The Henryk Niewodniczanski Institute of Nuclear Physics, Polish Academy of Sciences, Cracow, Poland
[46]Joint Institute for Nuclear Research (JINR), Dubna, Russia
[47]Niels Bohr Institute, University of Copenhagen, Copenhagen, Denmark
[48]Institut Pluridisciplinaire Hubert Curien (IPHC), Université de Strasbourg, CNRS-IN2P3, Strasbourg, France
[49]University of Houston, Houston, Texas, United States
[50]Dipartimento di Fisica Sperimentale dell'Università and Sezione INFN, Turin, Italy
[51]Petersburg Nuclear Physics Institute, Gatchina, Russia
[52]Physics Department, University of Jammu, Jammu, India
[53]University of Tsukuba, Tsukuba, Japan
[54]Laboratori Nazionali di Frascati, INFN, Frascati, Italy
[55]Dipartimento di Fisica dell'Università and Sezione INFN, Padova, Italy
[56]Nikhef, National Institute for Subatomic Physics, Amsterdam, Netherlands
[57]Nikhef, National Institute for Subatomic Physics and Institute for Subatomic Physics of Utrecht University, Utrecht, Netherlands
[58]Centro de Investigaciones Energéticas Medioambientales y Tecnológicas (CIEMAT), Madrid, Spain
[59]Institut für Informatik, Johann Wolfgang Goethe-Universität Frankfurt, Frankfurt, Germany
[60]Moscow Engineering Physics Institute, Moscow, Russia
[61]Institute for High Energy Physics, Protvino, Russia
[62]Faculty of Science, P.J. Šafárik University, Košice, Slovakia
[63]Wayne State University, Detroit, Michigan, USA
[64]Saha Institute of Nuclear Physics, Kolkata, India
[65]Institut de Physique Nucléaire d'Orsay (IPNO), Université Paris-Sud, CNRS-IN2P3, Orsay, France
[66]Lawrence Berkeley National Laboratory, Berkeley, California, USA
[67]Purdue University, West Lafayette, Indiana, USA
[68]Faculty of Mathematics, Physics and Informatics, Comenius University, Bratislava, Slovakia
[69]Russian Federal Nuclear Center (VNIIEF), Sarov, Russia
[70]Physics Department, University of Cape Town, iThemba LABS, Cape Town, South Africa
[71]Hua-Zhong Normal University, Wuhan, China
[72]Sección Física, Departamento de Ciencias, Pontificia Universidad Católica del Perú, Lima, Peru
[73]Dipartimento di Fisica dell'Università and Sezione INFN, Trieste, Italy
[74]Centro de Investigación y de Estudios Avanzados (CINVESTAV), Mexico City and Mérida, Mexico
[75]Benemérita Universidad Autónoma de Puebla, Puebla, Mexico
[76]Universidade de São Paulo (USP), São Paulo, Brazil
[77]Dipartimento di Fisica dell'Università and Sezione INFN, Cagliari, Italy
[78]Centro de Aplicaciones Tecnológicas y Desarrollo Nuclear (CEADEN), Havana, Cuba
[79]Yonsei University, Seoul, South Korea
[80]Physics Department, Creighton University, Omaha, Nebraska, USA
[81]Université de Lyon, Université Lyon 1, CNRS/IN2P3, IPN-Lyon, Villeurbanne, France
[82]Universidade Estadual de Campinas (UNICAMP), Campinas, Brazil
[83]Division of Experimental High Energy Physics, University of Lund, Lund, Sweden
[84]Pusan National University, Pusan, South Korea
[85]Sezione INFN, Cagliari, Italy
[86]Dipartimento di Scienze e Innovazione Tecnologica dell'Università del Piemonte Orientale and Gruppo Collegato INFN, Alessandria, Italy
[87]Instituto de Ciencias Nucleares, Universidad Nacional Autónoma de México, Mexico City, Mexico
[88]Institute of Space Sciences (ISS), Bucharest, Romania
[89]Indian Institute of Technology, Mumbai, India
[90]Dipartimento di Fisica 'E.R. Caianiello' dell'Università and Gruppo Collegato INFN, Salerno, Italy
[91]Sezione INFN, Bari, Italy
[92]Soltan Institute for Nuclear Studies, Warsaw, Poland
[93]Sezione INFN, Rome, Italy
[94]Department of Physics, University of Oslo, Oslo, Norway
[95]Institute for Nuclear Research, Academy of Sciences, Moscow, Russia
[96]Sezione INFN, Trieste, Italy

[97]Chicago State University, Chicago, Illinois, USA
[98]Warsaw University of Technology, Warsaw, Poland
[99]Universidad Autónoma de Sinaloa, Culiacán, Mexico
[100]Physics Department, University of Rajasthan, Jaipur, India
[101]Technical University of Split FESB, Split, Croatia
[102]Yerevan Physics Institute, Yerevan, Armenia
[103]University of Tokyo, Tokyo, Japan
[104]Department of Physics, Sejong University, Seoul, South Korea
[105]Eberhard Karls Universität Tübingen, Tübingen, Germany
[106]Institut für Kernphysik, Technische Universität Darmstadt, Darmstadt, Germany
[107]Yildiz Technical University, Istanbul, Turkey
[108]Zentrum für Technologietransfer und Telekommunikation (ZTT), Fachhochschule Worms, Worms, Germany
[109]California Polytechnic State University, San Luis Obispo, California, USA
[110]The University of Texas at Austin, Physics Department, Austin, Texas, USA
[111]Fachhochschule Köln, Köln, Germany
[112]Institute of Physics, Academy of Sciences of the Czech Republic, Prague, Czech Republic
[113]University of Tennessee, Knoxville, Tennessee, USA
[114]Dipartimento di Fisica dell'Università "La Sapienza" and Sezione INFN, Rome, Italy
[115]Budker Institute for Nuclear Physics, Novosibirsk, Russia
[116]Institut of Theoretical Physics, University of Wroclaw
[117]Laboratori Nazionali di Legnaro, INFN, Legnaro, Italy
[118]Indian Institute of Technology Indore (IIT), Indore, India
[119]Hiroshima University, Hiroshima, Japan
[120]Physics Department, University of Athens, Athens, Greece
[121]Kirchhoff-Institut für Physik, Ruprecht-Karls-Universität Heidelberg, Heidelberg, Germany
[122]Centre de Calcul de l'IN2P3, Villeurbanne, France

*Also at M. V. Lomonosov Moscow State University, D. V. Skobeltsyn Institute of Nuclear Physics, Moscow, Russia.
†Also at "Vinča" Institute of Nuclear Sciences, Belgrade, Serbia.

Bibliography

[1] Stephen Hawking. *A Brief History of Time*. Bantam Dell Publishing Group, 1988. (Cited on page 3.)

[2] Albert Einstein. Zur Elektrodynamik bewegter Körper. *Annalen der Physik*, 17:891, 1905. (Cited on page 3.)

[3] W. Heisenberg. Über quantentheoretische umdeutung kinematischer und mechanischer Beziehungen. *Zeitschrift für Physik*, 33:879–893, 06 1925. (Cited on page 3.)

[4] M. Born and P. Jordan. Zur Quantenmechanik. *Zeitschrift für Physik*, 34:858–888, 09 1925. (Cited on page 3.)

[5] M. Born and W. Heisenberg. Zur Quantenmechanik II. *Zeitschrift für Physik*, 35:557–615, 11 1925. (Cited on page 3.)

[6] Richard Feynman. *The Principle of Least Action in Quantum Mechanics*. PhD thesis, Princeton University, 1942. (Cited on page 3.)

[7] E. Rutherford. The Scattering of α and β Particles by Matter and the Structure of the Atom. *Philos. Mag.*, 6:21, 1911. (Cited on page 3.)

[8] R. Gatto. *Scale And Conformal Symmetry In Hadron Physics*, page 139. John Wiley And Sins Inc., 1973. (Cited on page 3.)

[9] Chen-Ning Yang and Robert L. Mills. Conservation of Isotopic Spin and Isotopic Gauge Invariance. *Phys. Rev.*, 96:191–195, 1954. (Cited on page 4.)

[10] J. Goldstone. Field Theories with Superconductor Solutions. *Nuovo Cimento*, 19:154–164, 1961. (Cited on page 4.)

[11] Yoichiro Nambu. Quasiparticles and Gauge Invariance in the Theory of Superconductivity. *Phys. Rev.*, 117:648–663, 1960. (Cited on page 4.)

[12] Jeffrey Goldstone, Abdus Salam, and Steven Weinberg. Broken Symmetries. *Phys. Rev.*, 127:965–970, 1962. (Cited on page 4.)

[13] Peter W. Higgs. Broken Symmetries and the Masses of Gauge Bosons. *Phys. Rev. Lett.*, 13:508–509, 1964. (Cited on page 4.)

[14] Steven Weinberg. A Model of Leptons. *Phys. Rev. Lett.*, 19:1264–1266, 1967. (Cited on page 5.)

[15] A. Salam. *Elementary Particle Theory*, page 367. Almquist and Wiksells, Stockholm, 1969. (Cited on page 5.)

[16] H. Fritzsch, Murray Gell-Mann, and H. Leutwyler. Advantages of the Color Octet Gluon Picture. *Phys. Lett.*, B47:365–368, 1973. Introduces the term 'color'. (Cited on page 5.)

[17] Standard Model. http://en.wikipedia.org/wiki/Standard_Model, 11 2011. (Cited on pages xvii and 5.)

[18] F.J. Hasert, H. Faissner, W. Krenz, J. Von Krogh, D. Lanske, et al. SEARCH FOR ELASTIC MUON-NEUTRINO ELECTRON SCATTERING. *Phys. Lett.*, B46:121–124, 1973. (Cited on page 6.)

[19] F. J. Hasert et al. Observation of Neutrino Like Interactions Without Muon Or Electron in the Gargamelle Neutrino Experiment. *Phys. Lett.*, B46:138–140, 1973. (Cited on page 6.)

[20] F. J. Hasert et al. Observation of Neutrino Like Interactions without Muon or Electron in the Gargamelle Neutrino Experiment. *Nucl. Phys.*, B73:1–22, 1974. (Cited on page 6.)

[21] Georges Aad et al. Observation of a new particle in the search for the Standard Model Higgs boson with the ATLAS detector at the LHC. *Phys. Lett. B*, [arXiv:1207.7214] 2012. (Cited on page 6.)

[22] Serguei Chatrchyan et al. Observation of a new boson at a mass of 125 GeV with the CMS experiment at the LHC. *Phys. Lett. B*, [arXiv:1207.7235] 2012. (Cited on page 6.)

[23] G. Dissertori and G. P. Salam. Quantum Chromodynamics. *J. Phys. G*, 37(7A):114, 07 2010. (Cited on pages 6 and 7.)

[24] P. Braun-Munzinger and J. Wambach. Colloquium: Phase diagram of strongly interacting matter. *Rev. Mod. Phys.*, 81:1031–1050, 2009. (Cited on page 7.)

[25] T. van Ritbergen, J.A.M. Vermaseren, and S.A. Larin. The Four loop beta function in quantum chromodynamics. *Phys. Lett.*, B400:379–384, 1997. (Cited on page 8.)

[26] M. Czakon. The Four-loop QCD beta-function and anomalous dimensions. *Nucl. Phys.*, B710:485–498, 2005. (Cited on page 8.)

[27] Y. Schroder and M. Steinhauser. Four-loop decoupling relations for the strong coupling. *JHEP*, 0601:051, 2006. (Cited on page 8.)

[28] K.G. Chetyrkin, Johann H. Kuhn, and Christian Sturm. QCD decoupling at four loops. *Nucl. Phys.*, B744:121–135, 2006. (Cited on page 8.)

[29] D.J. Gross and Frank Wilczek. Ultraviolet Behavior of Nonabelian Gauge Theories. *Phys. Rev. Lett.*, 30:1343–1346, 1973. (Cited on page 8.)

[30] H.David Politzer. Reliable Perturbative Results for Strong Interactions? *Phys. Rev. Lett.*, 30:1346–1349, 1973. (Cited on page 8.)

[31] Siegfried Bethke. Experimental tests of asymptotic freedom. *Prog. Part. Nucl. Phys.*, 58:351–386, 2007. (Cited on pages xvii and 8.)

[32] Christian S. Fischer and Reinhard Alkofer. Nonperturbative propagators, running coupling and dynamical quark mass of Landau gauge QCD. *Phys. Rev.*, D67:094020, 2003. (Cited on pages xvii, 8 and 9.)

[33] Guido Altarelli. *The Development of Perturbative QCD*, chapter 6, page 290. Workd Scientific Publishing Co. Pre. Ltd., 1994. (Cited on page 9.)

[34] Simon Hands. The Phase Diagram of QCD. *Contemp. Phys.*, 42:209–225, 2001. (Cited on pages xvii, 9, 12 and 15.)

[35] John Bardeen, L.N. Cooper, and J.R. Schrieffer. Theory of superconductivity. *Phys. Rev.*, 108:1175–1204, 1957. (Cited on page 9.)

[36] K. Langfeld, H. Markum, R. Pullirsch, C.D. Roberts, and S.M. Schmidt. Concerning the quark condensate. *Phys. Rev.*, C67:065206, 2003. (Cited on page 9.)

[37] Christian S. Fischer. Infrared properties of QCD from Dyson-Schwinger equations. *J. Phys.*, G32:R253–R291, 2006. (Cited on page 10.)

[38] John B. Kogut. A Review of the Lattice Gauge Theory Approach to Quantum Chromodynamics. *Rev. Mod. Phys.*, 55:775, 1983. (Cited on page 11.)

[39] Szabolcs Borsanyi, Gergely Endrodi, Zoltan Fodor, Antal Jakovac, Sandor D. Katz, et al. The QCD equation of state with dynamical quarks. *JHEP*, 1011:077, 2010. (Cited on pages xvii, 11 and 12.)

[40] Frithjof Karsch. Lattice QCD at High Temperature and Density. *Lect. Notes Phys.*, 583:209, 2002. (Cited on page 11.)

[41] Andrea Dainese. *Charm production and in-medium QCD energy loss in nucleus–nucleus collisions with ALICE. A performance study.* PhD thesis, UNIVERSITA DEGLI STUDI DI PADOVA, 2003. (Cited on pages xviii, xix, xx, 11, 36, 49 and 66.)

[42] A. Chodos, R. L. Jaffe, K. Johnson, Charles B. Thorn, and V. F. Weisskopf. A New Extended Model of Hadrons. *Phys. Rev.*, D9:3471–3495, 1974. (Cited on page 13.)

[43] P. Braun-Munzinger and J. Stachel. Probing the phase boundary between hadronic matter and the quark-gluon-plasma in relativistic heavy ion collisions. *Nucl. Phys.*, A606:320–328, 1996. (Cited on page 13.)

[44] Stefan B. Ruester, Verena Werth, Michael Buballa, Igor A. Shovkovy, and Dirk H. Rischke. The phase diagram of neutral quark matter: Self-consistent treatment of quark masses. *Phys. Rev.*, D72:034004, 2005. (Cited on page 13.)

[45] S. Gupta, X. Luo, B. Mohanty, H. G. Ritter, and N. Xu. Scale for the phase diagram of quantum chromodynamics. *Science*, 332(6037):1525, 06 2011. (Cited on page 14.)

[46] P. Coles and F. Lucchin. *Cosmology: The Origin and Evolution of Cosmic Structure*. John Wiley And Sons Ltd., 2002. (Cited on page 14.)

[47] J. D. Bjorken. Highly Relativistic Nucleus-Nucleus Collisions: The Central Rapidity Region. *Phys. Rev.*, D27(1):140–151, 1983. (Cited on pages 14 and 23.)

[48] J. P. Blaizot and Alfred H. Mueller. The Early Stage of Ultrarelativistic Heavy Ion Collisions. *Nucl. Phys.*, B289:847, 1987. (Cited on page 14.)

[49] Carsten Greiner, Dirk-Hermann Rischke, Horst Stoecker, and Peter Koch. The Creation of Strange Quark Matter Droplets as a Unique Signature for Quark - Gluon Plasma Formation in Relativistic Heavy Ion Collisions. *Phys. Rev.*, D38:2797–2807, 1988. (Cited on page 14.)

[50] Michael L. Miller, Klaus Reygers, Stephen J. Sanders, and Peter Steinberg. Glauber modeling in high energy nuclear collisions. *Ann. Rev. Nucl. Part. Sci.*, 57:205–243, 2007. (Cited on pages xvii, 16 and 234.)

[51] Roy J. Glauber. Quantum Optics and Heavy Ion Physics. *Nucl. Phys.*, A774:3–13, 2006. (Cited on page 17.)

[52] Asher Shor and Ronald S. Longacre. Effects of Secondary Interactions in Proton–Nucleus and Nucleus–Nucleus Collisions Using the HIJET Event Generator. *Phys. Lett.*, B218:100, 1989. (Cited on page 17.)

[53] Nestor Armesto. Nuclear shadowing. *J. Phys. G*, G32:R367–R394, 2006. (Cited on page 17.)

[54] Kari J. Eskola, Hannu Paukkunen, and Carlos A. Salgado. An Improved global analysis of nuclear parton distribution functions including RHIC data. *JHEP*, 0807:102, 2008. (Cited on pages 17 and 52.)

[55] K.J. Eskola, H. Paukkunen, and C.A. Salgado. EPS09: A New Generation of NLO and LO Nuclear Parton Distribution Functions. *JHEP*, 0904:065, 2009. (Cited on pages 17, 52 and 282.)

[56] Ivan Vitev. Initial state parton broadening and energy loss probed in d+Au at RHIC. *Phys. Lett.*, B562:36–44, 2003. (Cited on page 17.)

[57] Francois Gelis, Edmond Iancu, Jamal Jalilian-Marian, and Raju Venugopalan. The Color Glass Condensate. *Ann. Rev. Nucl. Part. Sci.*, 60:463–489, 2010. (Cited on page 17.)

[58] V. N. Gribov and L. N. Lipatov. Deep inelastic e p scattering in perturbation theory. *Sov. J. Nucl. Phys.*, 15:438–450, 1972. (Cited on pages 18 and 34.)

[59] Guido Altarelli and G. Parisi. Asymptotic Freedom in Parton Language. *Nucl. Phys.*, B126:298, 1977. (Cited on page 18.)

[60] Yuri L. Dokshitzer. Calculation of the Structure Functions for Deep Inelastic Scattering and e^-e^+ Annihilation by Perturbation Theory in Quantum Chromodynamics. *Sov. Phys. JETP*, 46:641–653, 1977. (Cited on pages 18 and 35.)

[61] L. N. Lipatov. Reggeization of the Vector Meson and the Vacuum Singularity in Nonabelian Gauge Theories. *Sov. J. Nucl. Phys.*, 23:338–345, 1976. (Cited on page 18.)

[62] E. A. Kuraev, L. N. Lipatov, and Victor S. Fadin. The Pomeranchuk Singularity in Nonabelian Gauge Theories. *Sov. Phys. JETP*, 45:199–204, 1977. (Cited on page 18.)

[63] I. I. Balitsky and L. N. Lipatov. The Pomeranchuk Singularity in Quantum Chromodynamics. *Sov. J. Nucl. Phys.*, 28:822–829, 1978. (Cited on page 18.)

[64] Hans-Joachim Drescher and Yasushi Nara. Eccentricity fluctuations from the color glass condensate at RHIC and LHC. *Phys. Rev.*, C76:041903, 2007. (Cited on page 18.)

[65] Javier L. Albacete and Yuri V. Kovchegov. Solving high energy evolution equation including running coupling corrections. *Phys. Rev.*, D75:125021, 2007. (Cited on page 18.)

[66] Sheng-qin Feng, Feng Liu, and Lian-shou Liu. Thermal equilibrium and nonuniform longitudinal flow in relativistic heavy ion collisions. *Phys. Rev.*, C63:014901, 2001. (Cited on page 19.)

[67] S. Voloshin and Y. Zhang. Flow study in relativistic nuclear collisions by Fourier expansion of Azimuthal particle distributions. *Z. Phys.*, C70:665–672, 1996. (Cited on pages 19 and 293.)

[68] J. D. Bjorken. Energy Loss of Energetic Partons in Quark-Gluon Plasma: Possible Extinction of High p_t Jets in Hadron-Hadron Collisions. FERMILAB-PUB-82-059-THY, 1982. (Cited on page 20.)

[69] Eric Braaten and Markus H. Thoma. Energy loss of a heavy quark in the quark-gluon plasma. *Phys. Rev.*, D44:2625–2630, 1991. (Cited on page 21.)

[70] A. Peshier. The QCD collisional energy loss revised. *Phys. Rev. Lett.*, 97:212301, 2006. (Cited on page 21.)

[71] B. G. Zakharov. Parton energy loss in an expanding quark-gluon plasma: Radiative vs collisional. *JETP Lett.*, 86:444–450, 2007. (Cited on page 21.)

[72] Stephane Peigne and Andre Peshier. Collisional energy loss of a fast heavy quark in a quark-gluon plasma. *Phys. Rev.*, D77:114017, 2008. (Cited on page 21.)

[73] Miklos Gyulassy and Michael Plumer. Jet Quenching in Dense Matter. *Phys. Lett.*, B243:432–438, 1990. (Cited on page 21.)

[74] Xin-Nian Wang and Miklos Gyulassy. Gluon shadowing and jet quenching in A+A collisions at $\sqrt{s_{\rm NN}}$ GeV. *Phys. Rev. Lett.*, 68:1480–1483, 1992. (Cited on page 21.)

[75] R. Baier, Yuri L. Dokshitzer, Alfred H. Mueller, S. Peigne, and D. Schiff. Radiative energy loss and $p_{\rm t}$-broadening of high energy partons in nuclei. *Nucl. Phys.*, B484:265–282, 1997. (Cited on page 21.)

[76] M. Gyulassy, P. Levai, and I. Vitev. Reaction operator approach to non-Abelian energy loss. *Nucl. Phys.*, B594:371–419, 2001. (Cited on pages 21, 31 and 55.)

[77] Urs Achim Wiedemann. Gluon radiation off hard quarks in a nuclear environment: Opacity expansion. *Nucl. Phys.*, B588:303–344, 2000. (Cited on page 21.)

[78] R. Baier, Yuri L. Dokshitzer, Alfred H. Mueller, S. Peigne, and D. Schiff. The Landau-Pomeranchuk-Migdal effect in QED. *Nucl. Phys.*, B478:577–597, 1996. (Cited on page 21.)

[79] Carlos A. Salgado and Urs Achim Wiedemann. Calculating quenching weights. *Phys. Rev.*, D68:014008, 2003. (Cited on pages 21, 55 and 56.)

[80] Sangyong Jeon and Guy D. Moore. Energy loss of leading partons in a thermal QCD medium. *Phys. Rev.*, C71:034901, 2005. (Cited on page 21.)

[81] Simon Turbide, Charles Gale, Sangyong Jeon, and Guy D. Moore. Energy loss of leading hadrons and direct photon production in evolving quark-gluon plasma. *Phys. Rev.*, C72:014906, 2005. (Cited on page 21.)

[82] Simon Wicks, William Horowitz, Magdalena Djordjevic, and Miklos Gyulassy. Elastic, inelastic, and path length fluctuations in jet tomography. *Nucl. Phys.*, A784:426–442, 2007. (Cited on pages 21, 26 and 57.)

[83] Ben-Wei Zhang and Xin-Nian Wang. Multiple parton scattering in nuclei: Beyond helicity amplitude approximation. *Nucl. Phys.*, A720:429–451, 2003. (Cited on page 21.)

[84] A. Majumder, R. J. Fries, and Berndt Muller. Photon bremsstrahlung and diffusive broadening of a hard jet. *Phys. Rev.*, C77:065209, 2008. (Cited on page 21.)

[85] Juan Martin Maldacena. The large N limit of superconformal field theories and supergravity. *Adv. Theor. Math. Phys.*, 2:231–252, 1998. (Cited on page 21.)

[86] P. Kovtun, D. T. Son, and A. O. Starinets. Viscosity in strongly interacting quantum field theories from black hole physics. *Phys. Rev. Lett.*, 94:111601, 2005. (Cited on pages 21, 28 and 62.)

[87] Hong Liu, Krishna Rajagopal, and Urs Achim Wiedemann. Wilson loops in heavy ion collisions and their calculation in AdS/CFT. *JHEP*, 03:066, 2007. (Cited on page 21.)

[88] Jorge Casalderrey-Solana and Carlos A. Salgado. Introductory lectures on jet quenching in heavy ion collisions. *Acta Phys. Polon.*, B38:3731–3794, 2007. (Cited on page 21.)

[89] R. Arnaldi et al. J/Ψ suppression in In–In collisions at 158 GeV/nucleon. *Nucl. Phys.*, A783:261–268, 2007. (Cited on page 22.)

[90] C. Spieles et al. Modelling J/Ψ production and absorption in a microscopic nonequilibrium approach. *Phys. Rev.*, C60:054901, 1999. (Cited on page 23.)

[91] Sourendu Gupta and Helmut Satz. Final state J/Ψ suppression in nuclear collisions. *Phys. Lett.*, B283:439–445, 1992. (Cited on page 23.)

[92] M. C. Abreu et al. Evidence for deconfinement of quarks and gluons from the J/Ψ suppression pattern measured in Pb Pb collisions at the CERN-SPS. *Phys. Lett.*, B477:28–36, 2000. (Cited on pages xvii and 23.)

[93] T. Matsui and H. Satz. J/ψ Suppression by Quark-Gluon Plasma Formation. *Phys. Lett.*, B178:416, 1986. (Cited on page 23.)

[94] Johann Rafelski and Berndt Muller. Strangeness Production in the Quark-Gluon Plasma. *Phys. Rev. Lett.*, 48:1066, 1982. (Cited on page 23.)

[95] Kristin Fanebust Hetland et al. Results on hyperon production from NA57. *J. Phys.*, G28:1607–1614, 2002. (Cited on pages xvii and 24.)

[96] S. S. Adler et al. Suppressed π^0 production at large transverse momentum in central Au+Au collisions at $\sqrt{s_{\rm NN}}$ GeV. *Phys. Rev. Lett.*, 91:072301, 2003. (Cited on pages xvii, 25 and 26.)

[97] J. Adams et al. Evidence from d+Au measurements for final-state suppression of high $p_{\rm t}$ hadrons in Au+Au collisions at RHIC. *Phys. Rev. Lett.*, 91:072304, 2003. (Cited on pages xvii and 26.)

[98] K. J. Eskola, H. Honkanen, C. A. Salgado, and U. A. Wiedemann. The fragility of high-p_t hadron spectra as a hard probe. *Nucl. Phys.*, A747:511–529, 2005. (Cited on page 26.)

[99] John Adams et al. Pion, kaon, proton and anti-proton transverse momentum distributions from p+p and d+Au collisions at $\sqrt{s_{NN}} = 200$ GeV. *Phys. Lett.*, B616:8–16, 2005. (Cited on pages xvii and 27.)

[100] J. Adams et al. Identified hadron spectra at large transverse momentum in p+p and d+Au collisions at $\sqrt{s_{NN}} = 200$ GeV. *Phys. Lett.*, B637:161–169, 2006. (Cited on pages xvii and 27.)

[101] B. I. Abelev et al. Identified baryon and meson distributions at large transverse momenta from Au+Au collisions at $\sqrt{s_{NN}} = 200$ GeV. *Phys. Rev. Lett.*, 97:152301, 2006. (Cited on pages xvii, 26 and 27.)

[102] P. Abreu et al. $\pi^{\pm}$, $K^{\pm}$, p and $\overline{p}$ production in $Z^0 \to q\overline{q}$, $Z^0 \to b\overline{b}$, $d\overline{d}$, $s\overline{s}$. *Eur. Phys. J.*, C5:585–620, 1998. (Cited on pages xvii and 27.)

[103] Rudolph C. Hwa and C. B. Yang. Recombination of shower partons at high p_t in heavy-ion collisions. *Phys. Rev.*, C70:024905, 2004. (Cited on pages xvii, 26 and 27.)

[104] R. J. Fries, Berndt Muller, C. Nonaka, and S. A. Bass. Hadron production in heavy ion collisions: Fragmentation and recombination from a dense parton phase. *Phys. Rev.*, C68:044902, 2003. (Cited on pages xvii, 26 and 27.)

[105] S. Albino, B. A. Kniehl, and G. Kramer. Fragmentation functions for light charged hadrons with complete quark flavour separation. *Nucl. Phys.*, B725:181–206, 2005. (Cited on page 26.)

[106] Markus D. Oldenburg. Scaling of anisotropic flow in the picture of quark coalescence. *J. Phys. G*, G31:S437–S442, 2005. (Cited on pages xvii, 27 and 28.)

[107] Huichao Song, Steffen A. Bass, and Ulrich Heinz. Viscous QCD matter in a hybrid hydrodynamic+Boltzmann approach. *Phys. Rev.*, C83:024912, 2011. (Cited on page 28.)

[108] Huichao Song, Steffen A. Bass, Ulrich Heinz, Tetsufumi Hirano, and Chun Shen. Hadron spectra and elliptic flow for 200 AGeV Au+Au collisions from viscous hydrodynamics coupled to a Boltzmann cascade. *Phys. Rev.*, C83:054910, 2011. (Cited on pages xviii, 28 and 29.)

[109] S. Afanasiev et al. Systematic Studies of Elliptic Flow Measurements in Au+Au Collisions at $\sqrt{s_{NN}} = 200$ GeV. *Phys. Rev.*, C80:024909, 2009. (Cited on pages xviii and 29.)

[110] J. Adams et al. Azimuthal anisotropy in Au+Au collisions at $\sqrt{s_{NN}} = 200$ GeV. *Phys. Rev.*, C72:014904, 2005. (Cited on pages xviii and 29.)

[111] J. Schukraft. Heavy ions at the LHC: Physics perspectives and experimental program. *Pramana*, 57:345–354, 2001. (Cited on pages xxxvii and 30.)

[112] B Abelev et al. Charged-particle multiplicity density at mid-rapidity in central Pb–Pb collisions at $\sqrt{s_{\rm NN}} = 2.76$ TeV. *Phys. Rev. Lett.*, 105:252301, 2010. (Cited on pages xviii, 29 and 30.)

[113] K. Aamodt et al. Two-pion Bose-Einstein correlations in central Pb–Pb collisions at $\sqrt{s_{\rm NN}} = 2.76$ TeV. *Phys. Lett.*, B696:328–337, 2011. (Cited on pages xviii, 29 and 30.)

[114] K Aamodt et al. Elliptic flow of charged particles in Pb–Pb collisions at 2.76 TeV. *Phys. Rev. Lett.*, 105:252302, 2010. (Cited on pages xviii and 31.)

[115] W.A. Horowitz and Miklos Gyulassy. Quenching and Tomography from RHIC to LHC. *J. Phys. G*, G38:124114, 2011. * Temporary entry *. (Cited on pages xviii, xx, 31, 32 and 65.)

[116] R. Hanbury Brown and R. Q. Twiss. A New Type of Interferometer for Use in Radio Astronomy. *Phil. Mag.*, 45:663–682, 1954. (Cited on page 29.)

[117] R. Hanbury Brown and R. Q. Twiss. A Test of a New Type of Stellar Interferometer on Sirius. *Nature*, 178:1046, 1956. (Cited on page 29.)

[118] Harvey B. Meyer. Transport properties of the quark-gluon plasma from lattice QCD. *Nucl. Phys.*, A830:641C–648C, 2009. (Cited on page 31.)

[119] J.J. Aubert et al. Experimental Observation of a Heavy Particle J. *Phys. Rev. Lett.*, 33:1404–1406, 1974. Technical report 96. (Cited on page 33.)

[120] J.E. Augustin et al. Discovery of a Narrow Resonance in e^+e^- Annihilation. *Phys. Rev. Lett.*, 33:1406–1408, 1974. (Cited on page 33.)

[121] E.G. Cazzoli, A.M. Cnops, P.L. Connolly, R.I. Louttit, M.J. Murtagh, et al. Evidence for $\Delta S = -\Delta Q$ Currents or Charmed Baryon Production by Neutrinos. *Phys. Rev. Lett.*, 34:1125–1128, 1975. (Cited on page 33.)

[122] G. Goldhaber, F. Pierre, G.S. Abrams, M.S. Alam, A. Boyarski, et al. Observation in e^+e- Annihilation of a Narrow State at 1865 MeV/c^2 Decaying to Kπ and K$\pi\pi\pi$. *Phys. Rev. Lett.*, 37:255–259, 1976. (Cited on page 33.)

[123] I. Peruzzi, M. Piccolo, G.J. Feldman, H.K. Nguyen, J. Wiss, et al. Observation of a Narrow Charged State at 1876 MeV/c^2 Decaying to an Exotic Combination of K$\pi\pi$. *Phys. Rev. Lett.*, 37:569–571, 1976. (Cited on page 33.)

[124] S.W. Herb, D.C. Hom, L.M. Lederman, J.C. Sens, H.D. Snyder, et al. Observation of a Dimuon Resonance at 9.5 GeV in 400 GeV Proton–Nucleus Collisions. *Phys. Rev. Lett.*, 39:252–255, 1977. (Cited on page 33.)

[125] M. Basile et al. Evidence for a New Particle with Naked 'BEAUTY' and for its Associated Production in High-Energy pp Interactions. *Nuovo Cim. Lett.*, 31:97, 1981. (Cited on page 33.)

[126] S. Behrends et al. Observation of Exclusive Decay Modes of B Flavored Mesons. *Phys. Rev. Lett.*, 50:881–884, 1983. (Cited on page 33.)

[127] John C. Collins, Davison E. Soper, and George F. Sterman. Heavy Particle Production in High-Energy Hadron Collisions. *Nucl. Phys.*, B263:37, 1986. (Cited on page 33.)

[128] CTEQ. http://cteq.org. webpage, 06 2011. (Cited on page 35.)

[129] M Cinausero et al. ALICE: Physics performance report, volume I. *J. Phys.*, G30:1517–1763, 2004. (Cited on pages xviii and 36.)

[130] Nicola Carrer and Andrea Dainese. Charm and beauty production at LHC. Technical report, CERN, 2003. (Cited on pages xviii and 36.)

[131] H. L. Lai and W. K. Tung. Charm production and parton distributions. *Z. Phys.*, C74:463–468, 1997. (Cited on page 35.)

[132] A. Dainese, R. Vogt, M. Bondila, K. J. Eskola, and V. J. Kolhinen. D-meson enhancement in p p collisions at the LHC due to nonlinear gluon evolution. *J. Phys.*, G30:1787–1799, 2004. (Cited on pages xviii and 37.)

[133] ALICE Collaboration. ALICE: Physics Performance Report, Volume II. *J. Phys. G: Nucl. Part. Phys.*, 32:1295, 2006. (Cited on pages 37, 75, 86 and 124.)

[134] K. J. Eskola, H. Honkanen, V. J. Kolhinen, Jian-wei Qiu, and C. A. Salgado. Nonlinear corrections to the DGLAP equations in view of the HERA data. *Nucl. Phys.*, B660:211–224, 2003. (Cited on page 38.)

[135] K. J. Eskola, V. J. Kolhinen, and R. Vogt. Enhancement of charm quark production due to nonlinear corrections to the DGLAP equations. *Phys. Lett.*, B582:157–166, 2004. (Cited on page 38.)

[136] George F. Sterman. Summation of Large Corrections to Short Distance Hadronic Cross-Sections. *Nucl. Phys.*, B281:310, 1987. (Cited on page 38.)

[137] S. Catani and L. Trentadue. Resummation of the QCD Perturbative Series for Hard Processes. *Nucl. Phys.*, B327:323, 1989. (Cited on page 38.)

[138] Sean Fleming. Soft Collinear Effective Theory: An Overview. *PoS*, EFT09:002, 2009. (Cited on page 38.)

[139] Nikolaos Kidonakis, Eric Laenen, Sven Moch, and Ramona Vogt. Sudakov resummation and finite order expansions of heavy quark hadroproduction cross-sections. *Phys. Rev.*, D64:114001, 2001. (Cited on page 38.)

[140] P. Nason, S. Dawson, and R.Keith Ellis. The One Particle Inclusive Differential Cross-Section for Heavy Quark Production in Hadronic Collisions. *Nucl. Phys.*, B327:49–92, 1989. (Cited on pages 39 and 42.)

[141] Matteo Cacciari and Mario Greco. Large p_{T} hadroproduction of heavy quarks. *Nucl. Phys.*, B421:530–544, 1994. (Cited on page 39.)

[142] Matteo Cacciari, Mario Greco, and Paolo Nason. The p_{T} spectrum in heavy flavor hadroproduction. *JHEP*, 9805:007, 1998. (Cited on page 40.)

[143] Alfred H. Mueller. Cut Vertices and their Renormalization: A Generalization of the Wilson Expansion. *Phys. Rev.*, D18:3705, 1978. (Cited on page 40.)

[144] John C. Collins, Davison E. Soper, and George F. Sterman. Soft Gluons and Factorization. *Nucl.Phys.*, B308:833, 1988. (Cited on page 40.)

[145] J.D. Bjorken. Properties of Hadron Distributions in Reactions Containing Very Heavy Quarks. *Phys. Rev.*, D17:171–173, 1978. (Cited on page 41.)

[146] Mahiko Suzuki. Fragmentation of Hadrons from Heavy Quark Partons. *Phys. Lett.*, B71:139, 1977. (Cited on page 41.)

[147] V.G. Kartvelishvili, A.K. Likhoded, and V.A. Petrov. On the Fragmentation Functions of Heavy Quarks Into Hadrons. *Phys. Lett.*, B78:615, 1978. (Cited on page 41.)

[148] M.G. Bowler. $e^{-}e+$ Production of Heavy Quarks in the String Model. *Z. Phys.*, C11:169, 1981. (Cited on page 41.)

[149] C. Peterson, D. Schlatter, I. Schmitt, and Peter M. Zerwas. Scaling Violations in Inclusive e+ e- Annihilation Spectra. *Phys. Rev.*, D27:105, 1983. (Cited on page 41.)

[150] P. D. B. Collins and T. P. Spiller. The Fragmentation of Heavy Quarks. *J. Phys.*, G11:1289, 1985. (Cited on page 41.)

[151] Michelangelo L. Mangano, Paolo Nason, and Giovanni Ridolfi. Heavy quark correlations in hadron collisions at next-to-leading order. *Nucl. Phys.*, B373:295–345, 1992. (Cited on pages xviii, xx, 41, 62, 63 and 124.)

[152] J. Baines, S.P. Baranov, O. Behnke, J. Bracinik, M. Cacciari, et al. Heavy quarks (Working Group 3): Summary Report for the HERA-LHC Workshop Proceedings. arXiv:hep-ph/0601164, 01 2006. (Cited on pages xviii, xx, 41, 62, 63 and 131.)

[153] C. Albajar et al. Beauty Production at the CERN Proton - anti-Proton Collider. 1. *Phys. Lett.*, B186:237–246, 1987. (Cited on page 42.)

[154] C. Albajar et al. Beauty production at the CERN $\mathrm{p\overline{p}}$ collider. *Phys. Lett.*, B256:121–128, 1991. Revised version. (Cited on pages 42 and 134.)

[155] P. Nason, S. Dawson, and R. Keith Ellis. The Total Cross-Section for the Production of Heavy Quarks in Hadronic Collisions. *Nucl. Phys.*, B303:607, 1988. (Cited on page 42.)

[156] F. Abe et al. A Measurement of the B meson and b quark cross-sections at $\sqrt{s} = 1.8$ TeV using the exclusive decay $B^{\pm} \to J/\Psi K^{\pm}$. *Phys. Rev. Lett.*, 68:3403–3407, 1992. (Cited on page 42.)

[157] Alan D. Martin, R.G. Roberts, W.James Stirling, and R.S. Thorne. Parton distributions: A New global analysis. *Eur. Phys. J.*, C4:463–496, 1998. (Cited on page 43.)

[158] H.L. Lai et al. Global QCD analysis of parton structure of the nucleon: CTEQ5 parton distributions. *Eur. Phys. J.*, C12:375–392, 2000. (Cited on pages 43 and 123.)

[159] S. Abachi et al. Inclusive μ and B quark production cross-sections in $p\overline{p}$ collisions at $\sqrt{s} = 1.8$ TeV. *Phys. Rev. Lett.*, 74:3548–3552, 1995. (Cited on page 43.)

[160] B. Abbott et al. The $b\overline{b}$ production cross section and angular correlations in $p\overline{p}$ collisions at $\sqrt{s} = 1.8$ TeV. *Phys. Lett.*, B487:264–272, 2000. (Cited on pages 43 and 134.)

[161] D. Acosta et al. Measurement of the J/ψ meson and b-hadron production cross sections in $p\overline{p}$ collisions at $\sqrt{s} = 1960$ GeV. *Phys. Rev.*, D71:032001, 2005. (Cited on pages xviii, 43 and 90.)

[162] M. Cacciari, S. Frixione, M.L. Mangano, P. Nason, and G. Ridolfi. QCD analysis of first b cross-section data at 1.96-TeV. *JHEP*, 0407:033, 2004. (Cited on pages xviii and 43.)

[163] D. Acosta et al. Measurement of prompt charm meson production cross sections in $p\overline{p}$ collisions at $\sqrt{s} = 1.96$ TeV. *Phys. Rev. Lett.*, 91:241804, 2003. (Cited on pages xix, 43 and 44.)

[164] Matteo Cacciari and Paolo Nason. Charm cross-sections for the Tevatron Run II. *JHEP*, 0309:006, 2003. (Cited on pages xix, 43 and 44.)

[165] Bernd A. Kniehl, G. Kramer, and B. Potter. Testing the universality of fragmentation functions. *Nucl. Phys.*, B597:337–369, 2001. ISSN 0418-9833. (Cited on pages xix and 44.)

[166] A. Adare et al. Measurement of high-p_T single electrons from heavy-flavor decays in p+p collisions at $\sqrt{s} = 200$ GeV. *Phys. Rev. Lett.*, 97:252002, 2006. (Cited on pages xix, 44 and 45.)

[167] Matteo Cacciari, Paolo Nason, and Ramona Vogt. QCD predictions for charm and bottom production at RHIC. *Phys. Rev. Lett.*, 95:122001, 2005. (Cited on pages xix, 44 and 45.)

[168] H. Agakishiev et al. High p_T non-photonic electron production in p+p collisions at $\sqrt{s} = 200$ GeV. *Phys. Rev.*, D83:052006, 2011. (Cited on pages xix and 45.)

[169] K. Adcox et al. Measurement of single electrons and implications for charm production in Au+Au collisions at $\sqrt{s} = 130$ GeV. *Phys. Rev. Lett.*, 88:192303, 2002. (Cited on page 44.)

[170] S. S. Adler et al. Centrality dependence of charm production from single electrons measurement in Au+Au collisions at $\sqrt{s} = 200$ GeV. *Phys. Rev. Lett.*, 94:082301, 2005. (Cited on page 44.)

[171] M. M. Aggarwal et al. Measurement of the Bottom contribution to non-photonic electron production in p+p collisions at $\sqrt{s} = 200$ GeV. *Phys. Rev. Lett.*, 105:202301, 2010. (Cited on page 45.)

[172] Michelangelo L. Mangano, Paolo Nason, and Giovanni Ridolfi. Fixed target hadroproduction of heavy quarks. *Nucl. Phys.*, B405:507–535, 1993. (Cited on pages 46 and 189.)

[173] Elena Bruna. *Open charm measurements via hadronic decay channels in the ALICE experiment.* PhD thesis, UNIVERSITA DEGLI STUDI DI TORINO, 2007. (Cited on page 47.)

[174] Roger Woods and David S. Saxon. Diffuse Surface Optical Model for Nucleon-Nuclei Scattering. *Physical Review*, 95:577–578, 07 1954. (Cited on page 47.)

[175] K. J. Eskola, R. Vogt, and X. N. Wang. Nuclear overlap functions. *Int. J. Mod. Phys.*, A10:3087–3090, 1995. (Cited on page 48.)

[176] R. J. Glauber and G. Matthiae. High-energy scattering of protons by nuclei. *Nucl. Phys.*, B21:135–157, 1970. (Cited on page 48.)

[177] Yi-Fei Zhang. Open charm hadron measurement in p+p and Au+Au collisions at $\sqrt{s_{NN}} = 200$ GeV in STAR. *J. Phys.*, G38:124142, 2011. (Cited on pages xix, 48 and 49.)

[178] Michele Arneodo. Nuclear effects in structure functions. *Phys. Rept.*, 240:301–393, 1994. (Cited on page 50.)

[179] P.R. Norton. The EMC effect. *Rept. Prog. Phys.*, 66:1253–1297, 2003. (Cited on page 50.)

[180] A. Bodek and J.L. Ritchie. Fermi Motion Effects in Deep Inelastic Lepton Scattering from Nuclear Targets. *Phys. Rev.*, D23:1070, 1981. (Cited on page 50.)

[181] K.J. Eskola, V.J. Kolhinen, and C.A. Salgado. The Scale dependent nuclear effects in parton distributions for practical applications. *Eur. Phys. J.*, C9:61–68, 1999. (Cited on pages 50 and 51.)

[182] K.J. Eskola, V.J. Kolhinen, and P.V. Ruuskanen. Scale evolution of nuclear parton distributions. *Nucl. Phys.*, B535:351–371, 1998. (Cited on page 50.)

[183] M. Hirai, S. Kumano, and M. Miyama. Determination of nuclear parton distributions. *Phys. Rev.*, D64:034003, 2001. (Cited on page 50.)

[184] M. Gluck, E. Reya, and A. Vogt. Parton distributions for high-energy collisions. *Z. Phys.*, C53:127–134, 1992. (Cited on page 51.)

[185] H.L. Lai, J. Huston, S. Kuhlmann, Fredrick I. Olness, Joseph F. Owens, et al. Improved parton distributions from global analysis of recent deep inelastic scattering and inclusive jet data. *Phys. Rev.*, D55:1280–1296, 1997. (Cited on page 51.)

[186] M. Hirai, S. Kumano, and T.-H. Nagai. Determination of nuclear parton distribution functions and their uncertainties in next-to-leading order. *Phys. Rev.*, C76:065207, 2007. (Cited on page 52.)

[187] D. de Florian and R. Sassot. Nuclear parton distributions at next-to-leading order. *Phys. Rev.*, D69:074028, 2004. (Cited on pages xix and 52.)

[188] Alberto Accardi, N. Armesto, M. Botje, S.J. Brodsky, B. Cole, et al. Hard probes in heavy ion collisions at the LHC: pdfs, shadowing and pA collisions. arXiv:hep-ph/0308248, 2004. (Cited on pages xix and 54.)

[189] K.J. Eskola, H. Honkanen, V.J. Kolhinen, Jian-wei Qiu, and C.A. Salgado. Nonlinear corrections to the DGLAP equations: Looking for the saturation limits. arXiv:hep-ph/0302185, 2003. Contribution to CERN Yellow Report on Hard Probes in Heavy Ion Collisions at the LHC. (Cited on page 52.)

[190] D. Kharzeev and K. Tuchin. Open charm production in heavy ion collisions and the color glass condensate. *Nucl. Phys.*, A735:248–266, 2004. (Cited on pages xx, 53, 65 and 66.)

[191] L. Apanasevich, C. Balazs, C. Bromberg, J. Huston, A. Maul, et al. k_{T} effects in direct photon production. *Phys. Rev.*, D59:074007, 1999. (Cited on page 53.)

[192] G. F. Xu, D. C. Zhou, and W. C. Xiang. Gluon radiation outside a finite cone. *Indian J. Phys.*, 85(6):953–957, 06 2011. (Cited on page 53.)

[193] R. Baier, Yuri L. Dokshitzer, Alfred H. Mueller, and D. Schiff. Angular dependence of the radiative gluon spectrum and the energy loss of hard jets in QCD media. *Phys. Rev.*, C60:064902, 1999. (Cited on page 54.)

[194] Yuri L. Dokshitzer and D.E. Kharzeev. Heavy quark colorimetry of QCD matter. *Phys. Lett.*, B519:199–206, 2001. (Cited on page 55.)

[195] Magdalena Djordjevic and Miklos Gyulassy. The Ter-Mikayelian effect on QCD radiative energy loss. *Phys. Rev.*, C68:034914, 2003. (Cited on pages xix, 55 and 56.)

[196] Nestor Armesto, Carlos A. Salgado, and Urs Achim Wiedemann. Medium induced gluon radiation off massive quarks fills the dead cone. *Phys. Rev.*, D69:114003, 2004. (Cited on page 55.)

[197] M. L. Ter-Mikayelian. *High-Energy Electromagnetic Processes in Condensed Media*. John Wiley & sons, New York, 1972. (Cited on page 55.)

[198] X. M. Zhang, Y. Zhu, Y. C. He, and D. C. Zhou. Dead Cone Effect of Charm Quark Radiation. *High Energy Phys. & Nucl. Phys.*, 31(1):43–47, 01 2007. (Cited on page 55.)

[199] Magdalena Djordjevic and Miklos Gyulassy. Heavy quark radiative energy loss in QCD matter. *Nucl. Phys.*, A733:265–298, 2004. (Cited on page 56.)

[200] X. M. Zhang, D. C. Zhou, and W. C. Xiang. Dead Cone Effect of Heavy Quark in Medium. *International Journal of Modern Physics E*, 16(7 & 8):2123–2129, 2007. (Cited on page 56.)

[201] Manuel Calderon de la Barca Sanchez. Heavy Flavor Production in STAR. arXiv:nucl-ex/0608028, 2006. (Cited on pages xix and 56.)

[202] A. Adare et al. Heavy Quark Production in p+p and Energy Loss and Flow of Heavy Quarks in Au+Au Collisions at $\sqrt{s_N N}$ = 200 GeV. *Phys. Rev.*, C84:044905, 2011. (Cited on pages xx, xxi, 56, 58, 60, 62, 71 and 322.)

[203] Munshi G. Mustafa. Energy loss of charm quarks in the quark-gluon plasma: Collisional versus radiative. *Phys. Rev.*, C72:014905, 2005. (Cited on pages 57 and 63.)

[204] A. Adare et al. Measurement of Bottom versus Charm as a Function of Transverse Momentum with Electron-Hadron Correlations in p+p Collisions at $\sqrt{s}$ = 200 GeV. *Phys. Rev. Lett.*, 103:082002, 2009. (Cited on page 58.)

[205] Guy D. Moore and Derek Teaney. How much do heavy quarks thermalize in a heavy ion collision? *Phys. Rev.*, C71:064904, 2005. (Cited on page 58.)

[206] H. van Hees, M. Mannarelli, V. Greco, and R. Rapp. Nonperturbative heavy-quark diffusion in the quark-gluon plasma. *Phys. Rev. Lett.*, 100:192301, 2008. (Cited on pages 58 and 61.)

[207] Cheuk-Yin Wong. Heavy quarkonia in quark gluon plasma. *Phys. Rev.*, C72:034906, 2005. (Cited on page 59.)

[208] Azfar Adil and Ivan Vitev. Collisional dissociation of heavy mesons in dense QCD matter. *Phys. Lett.*, B649:139–146, 2007. (Cited on page 59.)

[209] Su Houng Lee, Kazuaki Ohnishi, Shigehiro Yasui, In-Kwon Yoo, and Che-Ming Ko. Λ(c) enhancement from strongly coupled quark-gluon plasma. *Phys. Rev. Lett.*, 100:222301, 2008. (Cited on page 59.)

[210] P.B. Gossiaux, R. Bierkandt, and J. Aichelin. Tomography of a quark gluon plasma at RHIC and LHC energies. *Phys. Rev.*, C79:044906, 2009. (Cited on page 59.)

[211] Dmitri E. Kharzeev. Universal upper bound on the energy of a parton escaping from the strongly coupled quark-gluon matter. arXiv:0806.0358, 2008. (Cited on page 59.)

[212] S. Batsouli, S. Kelly, M. Gyulassy, and J.L. Nagle. Does the charm flow at RHIC? *Phys. Lett.*, B557:26–32, 2003. (Cited on pages xx and 60.)

[213] Denes Molnar and Miklos Gyulassy. New solutions to covariant nonequilibrium dynamics. *Phys. Rev.*, C62:054907, 2000. (Cited on page 60.)

[214] Denes Molnar. Charm elliptic flow from quark coalescence dynamics. *J. Phys. G*, G31:S421–S428, 2005. (Cited on page 61.)

[215] Denes Molnar and Sergei A. Voloshin. Elliptic flow at large transverse momenta from quark coalescence. *Phys.Rev.Lett.*, 91:092301, 2003. (Cited on page 61.)

[216] Zi-wei Lin and Denes Molnar. Quark coalescence and elliptic flow of charm hadrons. *Phys. Rev.*, C68:044901, 2003. (Cited on page 61.)

[217] V. Greco, C.M. Ko, and R. Rapp. Quark coalescence for charmed mesons in ultrarelativistic heavy ion collisions. *Phys. Lett.*, B595:202–208, 2004. (Cited on page 61.)

[218] Bin Zhang, Lie-Wen Chen, and Che-Ming Ko. Charm elliptic flow at RHIC. *Phys. Rev.*, C72:024906, 2005. (Cited on page 61.)

[219] Xin-Nian Wang. pQCD based approach to parton production and equilibration in high-energy nuclear collisions. *Phys. Rept.*, 280:287–371, 1997. (Cited on page 61.)

[220] Ralf Rapp and Hendrik van Hees. Heavy Quark Diffusion as a Probe of the Quark-Gluon Plasma. arXiv:0803.0901 [hep-ph], 2008. (Cited on page 61.)

[221] ALICE Collaboration. ALICE: Physics Performance Report, Volume I. *J. Phys. G: Nucl. Part. Phys.*, 30(11):1517, 2004. (Cited on pages xx, 62, 75 and 272.)

[222] Nestor Armesto, Andrea Dainese, Carlos A. Salgado, and Urs Achim Wiedemann. Testing the color charge and mass dependence of parton energy loss with heavy-to-light ratios at RHIC and CERN LHC. *Phys. Rev.*, D71:054027, 2005. (Cited on pages xx, 63, 64 and 282.)

[223] R. Baier, Yuri L. Dokshitzer, Alfred H. Mueller, and D. Schiff. Medium induced radiative energy loss: Equivalence between the BDMPS and Zakharov formalisms. *Nucl. Phys.*, B531:403–425, 1998. (Cited on pages 64 and 266.)

[224] B. Abelev. Measurement of charm production at central rapidity in proton–proton collisions at $\sqrt{s} = 2.76$ TeV. *JHEP*, 1207:191, 2012. (Cited on pages xx, 67 and 68.)

[225] B. Abelev et al. Measurement of charm production at central rapidity in proton–proton collisions at $\sqrt{s} = 7$ TeV. *JHEP*, 1201:128, 2012. (Cited on pages xx, 67 and 219.)

[226] Betty Abelev et al. D_s meson production at central rapidity in proton–proton collisions at *sqrts* = 7 TeV. arXiv: 1208.1948, 2012. (Cited on page 68.)

[227] Alessandro Grelli. D meson nuclear modification factor in Pb–Pb collisions at $\sqrt{s_{NN}} = 2.76$ TeV, using the 2011 data sample. ALICE-INT-ANA-284, 06 2012. (Cited on pages xxi and 68.)

[228] K. Aamodt et al. Suppression of Charged Particle Production at Large Transverse Momentum in Central Pb–Pb Collisions at $\sqrt{s_{NN}} = 2.76$ TeV. *Phys. Lett.*, B696:30–39, 2011. (Cited on pages xxi and 68.)

[229] Antonio Ortiz Velasquez. High p_T Spectra and R_{AA} using the Time Projection Chamber dE/dx. ALICE-INT-ANA-232, 08 2012. (Cited on pages xxi and 68.)

[230] Francesco Prino. Measurement of D meson v_2 in Pb–Pb collisions at $\sqrt{s_{NN}} = 2.76$ TeV. ALICE-INT-ANA-046, 07 2012. (Cited on pages xxi, 68 and 69.)

[231] Betty Abelev et al. Anisotropic flow of charged hadrons, pions and (anti-)protons measured at high transverse momentum in Pb–Pb collisions at $\sqrt{s_{NN}} = 2.76$ TeV. arXiv:1205.5761, 2012. (Cited on pages xxi, 68 and 69.)

[232] Betty Abelev et al. Measurement of electrons from semileptonic heavy-flavour hadron decays in pp collisions at $\sqrt{s} = 7$ TeV. arXiv:1205.5423, 2012. (Cited on pages xxi and 69.)

[233] S. Chekanov et al. Measurement of charm fragmentation ratios and fractions in photoproduction at HERA. *Eur. Phys. J.*, C44:351–366, 2005. (Cited on pages xxi, 70 and 71.)

[234] Betty Abelev et al. Measurement of electrons from beauty hadron decays in pp collisions at *sqrts* = 7 TeV. arXiv:1208.1902, 2012. (Cited on pages xxi, 70 and 71.)

[235] Shingo Sakai. Measurement of Heavy Flavor Electron R_{AA} in Pb–Pb collisions at $\sqrt{s_{NN}} = 2.76$ TeV. ALICE-INT-ANA-285, 07 2012. (Cited on pages xxi and 71.)

[236] H. J. Specht. Experimental aspects of heavy ion physics at LHC energies. CERN-90-10-v-2, 1990. (Cited on page 75.)

[237] ALICE Collaboration. The ALICE experiment at the CERN LHC. 2008 JINST 3 S08002, 2008. (Cited on pages xxii, xxxvii, 77, 81, 89, 103, 106 and 108.)

[238] The LEP experiments. http://public.web.cern.ch/public/en/research/LEPExp-en.html. (Cited on page 75.)

[239] ALICE Collaboration. ALICE Inner Tracking System (ITS): Technical Design Report. CERN-LHCC-99-012, 1999. (Cited on page 79.)

[240] ALICE Collaboration. Alignment of the ALICE Inner Tracking System with cosmic-ray tracks. arXiv:1001.0502v3, 01 2010. (Cited on page 79.)

[241] ALICE Collaboration. ALICE time projection chamber: Technical Design Report. CERN-LHCC-2000-001, 2001. (Cited on page 79.)

[242] ALICE Collaboration. ALICE transition-radiation detector: Technical Design Report. CERN-LHCC-2001-021, 2001. (Cited on page 80.)

[243] ALICE Collaboration. ALICE: a transition radiation detector for electron identification within the ALICE central detector - an addendum to the Technical Proposal. CERN-LHCC-99-013, 1999. (Cited on page 80.)

[244] ALICE Collaboration. ALICE Time-Of-Flight system (TOF): Technical Design Report. CERN-LHCC-2000-012, 2000. (Cited on page 80.)

[245] ALICE Collaboration. ALICE Time-Of Flight system (TOF): addendum to the technical design report. CERN-LHCC-2002-016, 2002. (Cited on page 80.)

[246] ALICE Collaboration. ALICE high-momentum particle identification: Technical Design Report. CERN-LHCC-98-019, 1998. (Cited on page 80.)

[247] ALICE Collaboration. Technical design report of the photon spectrometer. CERN-LHCC-99-004, 1999. (Cited on page 80.)

[248] ALICE Figure Repository. http://aliceinfo.cern.ch/Figure, 2012. (Cited on pages xxi and 81.)

[249] ALICE Collaboration. ALICE electromagnetic calorimeter: addendum to the ALICE technical proposal,. CERN-LHCC-2006-014, 2006. (Cited on page 81.)

[250] R. Fruhwirth. Application of Kalman filtering to track and vertex fitting. *Nucl. Instrum. Meth.*, A262:444–450, 1987. (Cited on page 82.)

[251] ALICE Collaboration. ALICE Zero-Degree Calorimeter (ZDC): Technical Design Report. CERN-LHCC-99-005, 1999. (Cited on page 87.)

[252] ALICE Collaboration. ALICE Photon Multiplicity Detector (PMD): Technical Design Report. CERN-LHCC-99-032, 1999. (Cited on page 87.)

[253] ALICE Collaboration. ALICE forward detectors: FMD, T0 and V0: Technical Design Report. CERN-LHCC-2004-025, 2004. (Cited on page 87.)

[254] ALICE Collaboration. ALICE dimuon forward spectrometer: Technical Design Report. CERN-LHCC-99-022, 1999. (Cited on page 90.)

[255] ALICE Collaboration. ALICE dimuon forward spectrometer: addendum to the Technical Design Report. CERN-LHCC-2000-046, 2000. (Cited on page 90.)

[256] Philippe Crochet et al. Electron-Muon Coincidence as a Measure of Charm and Bottom with ALICE. ALICE-INT-2000-01, 2000. (Cited on pages 90 and 144.)

[257] A. Sansoni. Quarkonia production at CDF. *Nucl. Phys.*, A610:373c–385c, 1996. (Cited on page 90.)

[258] F. Guerin et al. ALICE Muon Trigger Performance. ALICE-INT-2006-002, 2006. (Cited on pages 91, 101, 138 and 155.)

[259] R. Guernane et al. Machine induced Background in the ALICE Muon Trigger System in p–p Data taking. ALICE-INT-2003-041, 2003. (Cited on page 91.)

[260] D. K. Swoboda et al. Results from the ALICE dipole magnet commissioning. *IEEE Trans. Appl. Sup.*, 16:1696, 2006. (Cited on page 93.)

[261] J. Peyre, B. Genolini, and J. Pouthas. A Full-Scale Prototype for the Tracking Chambers of the ALICE Muon Spectrometer. Part I: Mechanics, Anode and Cathode Plane Design, Assembly and Construction. ALICE-INT-1998-28, 1998. (Cited on page 95.)

[262] A. Behrens and C. Lasseur. Positioning strategy, metrology and survey in ALICE. ALICE-INT-2008-018, 2008. (Cited on page 95.)

[263] A. Grigoryan et al. The Geometry Monitoring System of the ALICE Dimuon Spectrometer - Overview. ALICE-INT-2005-009, 2005. (Cited on page 96.)

[264] A. Zinchenko et al. A new approach to cluster finding and hit reconstruction in muon chambers of ALICE. ALICE-INT-2003-006. (Cited on page 96.)

[265] F. Guerin. *Sonde muonique et instrumentation associeé pour l'étude du plasma de quarks et de gluons dans l'expérience ALICE*. PhD thesis, Université Blaise Pascal, 2006. (Cited on page 102.)

[266] ALICE collaboration. ALICE trigger data-acquisition high-level trigger and control system: Technical Design Report. CERN-LHCC-2003-062. (Cited on page 103.)

[267] D Evans et al. The ALICE central trigger processor. CERN 2005-038, 2005. (Cited on page 103.)

[268] A Bhasin et al. Recent developements on the ALICE central trigger processor. CERN 2007-001, 2007. (Cited on page 103.)

[269] B. G. Taylor. Timing distribution at the LHC. CERN-2002-003, 2002. (Cited on page 104.)

[270] S. Baron et al. Status of the TTC upgrade. CERN-2007-001, 2007. (Cited on page 104.)

[271] P. Buncic et al. The architecture of the AliEn system. Proceedings of the Computing in High Energy Physics (CHEP 2004), Interlaken, Switzerland, 2004. (Cited on page 106.)

[272] T. Alt et al. The ALICE high level trigger. *J. Phys.*, G30:S1097–S1100, 2004. (Cited on page 107.)

[273] ALICE Collaboration. Technical Design Report of the Computing. CERN-LHCC-2005-018, 2005. (Cited on pages xxii and 110.)

[274] http://www.cern.ch/MONARC. (Cited on page 111.)

[275] http://aliweb.cern.ch/Offline/Activities/Analysis/CAF/index.html. (Cited on page 111.)

[276] P. Saiz et al. AliEn - ALICE environment on the GRID. *Nucl. Instrum. Meth.*, A502:437–440, 2003. (Cited on page 112.)

[277] http://www.cs.wisc.edu/condor/classad. (Cited on page 112.)

[278] I. C. Legrand et al. MonALISA: an agent based, dynamic service system to monitor, control and optimize grid based applications. http://cdsweb.cern.ch/record/865735, 2004. (Cited on page 112.)

[279] http://www.cern.ch/ALICE/Projects/offline/aliroot/Welcome.html. (Cited on page 112.)

[280] http://root.cern.ch. (Cited on page 114.)

[281] M. Ballintijn, R. Brun, F. Rademakers, and G. Roland. Distributed parallel analysis framework with PROOF. http://root.cern.ch/twiki/bin/view/ROOT/PROOF. (Cited on page 115.)

[282] L. Manceau. *Mesure de la section efficace de production des hadrons lourds avec le spectrométre á muons d'ALICE au LHC.* PhD thesis, Université Blaise Pascal, 2010. (Cited on pages xxii, 116 and 329.)

[283] Zaida Conesa DEL Valle. *Performance of the ALICE muon spectrometer: Weak boson production and measurement in heavy-ion collisions at LHC*. PhD thesis, Universite de Nantes, 12 2007. (Cited on page 118.)

[284] R. Guernane, P. Crochet, A. Morsch, and E. Vercellin. Measuring the b-Meson Production Cross Section in 5.5 TeV Pb–Pb Collisions Using Semileptonic Decay Muons. ALICE-INT-2005-018, 2005. (Cited on page 123.)

[285] L. Manceau et al. Performance of ALICE muon spectrometer for measurement of B-hadron & D-hadron production cross sections in pp collisions at $\sqrt{s}$ = 14 TeV. ALICE-INT-2010-004, 2010. (Cited on pages 123 and 140.)

[286] L. Manceau et al. Performance of ALICE muon spectrometer for measurement of B-hadron and D-hadron production cross sections in pp collisions at $\sqrt{s}$ = 14 TeV via single muons. ALICE-INT-2011-XXX, 2011. (Cited on page 123.)

[287] GEANT Detector Description and Simulation Tool. CERN Program Library Long Writeup W5013, 1994. (Cited on page 123.)

[288] Torbjorn Sjostrand, Leif Lonnblad, and Stephen Mrenna. PYTHIA 6.2: Physics and manual. arXiv:hep-ph/0108264, 2001. (Cited on page 123.)

[289] C. Buttar, S. Dittmaier, V. Drollinger, S. Frixione, A. Nikitenko, et al. Les houches physics at TeV colliders 2005, standard model and Higgs working group: Summary report. arXiv:hep-ph/0604120, 2006. (Cited on page 123.)

[290] J.F. Amundson, Oscar J.P. Eboli, E.M. Gregores, and F. Halzen. Quantitative tests of color evaporation: Charmonium production. *Phys. Lett.*, B390:323–328, 1997. (Cited on page 124.)

[291] M. Bedjidian et al. CERN Yellow Report. CERN-2004-009, 2004. (Cited on page 124.)

[292] Bo Andersson, G. Gustafson, G. Ingelman, and T. Sjostrand. Parton Fragmentation and String Dynamics. *Phys. Rept.*, 97:31–145, 1983. (Cited on page 124.)

[293] Z. Conesa. Efficiency determination strategy in the ALICE muon spectrometer. ALICE-INT-2009-005, 2009. (Cited on pages 125 and 195.)

[294] C. Albajar et al. Measurement of the Bottom Quark Production Cross-Section in Proton - anti-Proton Collisions at $\sqrt{s}$ = 0.63 TeV. *Phys. Lett.*, B213:405, 1988. (Cited on page 134.)

[295] F. Abe et al. Measurement of the bottom quark production cross-section using semileptonic decay electrons in $p\overline{p}$ collisions at $\sqrt{s}$ = 1.8 TeV. *Phys. Rev. Lett.*, 71:500–504, 1993. (Cited on page 134.)

[296] L. Aphecetche et al. Numerical Simulations and Offline Reconstruction of the Muon Spectrometer of ALICE. ALICE-INT-2009-044, 2009. (Cited on page 140.)

[297] D. Stocco. *Development of the ALICE Muon Spectrometer: preparation for data taking and heavy flavor measurement*. PhD thesis, UNIVERSITA DEGLI STUDI DI TORINO, 2008. (Cited on pages 142, 143 and 329.)

[298] A. Morsch and D. Stocco. Separation of the Decay-Background and Heavy Flavour components of the Single-Muon Spectrum. ALICE-INT-2006-027, 2006. (Cited on page 142.)

[299] J. E. Gaiser. *Charmonium Spectroscopy from Radiative Decays of the J/Ψ and Ψ'*. PhD thesis, Stanford University, 1982. (Cited on page 144.)

[300] Fritz W. Bopp, R. Engel, and J. Ranft. Rapidity gaps and the PHOJET Monte Carlo. arXiv:hep-ph/9803437, 1998. (Cited on page 145.)

[301] E. Bruna, A. Dainese, M. Masera, and Prino F. Vertex reconstruction for proton-proton collisions in ALICE. ALICE-INT-2009-018, 2009. (Cited on pages 149 and 151.)

[302] Michele Floris et al. Physics Event Selection in the 2009 data @ 900 GeV. talk in ALICE Physics Forum, 01 2010. (Cited on page 149.)

[303] http://alimonitor.cern.ch/configuration. (Cited on page 162.)

[304] Ken Oyama. Cross section normalization in proton–proton collisions at $\sqrt{s} =$ 2.76 TeV and 7 TeV, with ALICE at LHC. arXiv:1107.0692, 2011. (Cited on page 172.)

[305] John Allison et al. Geant4 developments and applications. *IEEE Trans. Nucl. Sci.*, 53:270, 2006. (Cited on page 187.)

[306] Alfredo Ferrari, Paola R. Sala, Alberto Fasso, and Johannes Ranft. Fluka: a multi-particle transport code. CERN–2005–010. (Cited on page 187.)

[307] X. M. Zhang. Efficiency Correction for Single Muons. presentation in ALICE-PWG3-MUON meeting, 2010 Jun 12. (Cited on page 191.)

[308] Jiebin Luo. Update on efficiency correction for single muons. ALICE-PWG3-MUON meeting, 2010 Oct 04. (Cited on page 194.)

[309] M. Cacciari, S. Frixione, M. L. Mangano, P. Nason, and G. Ridolfi. The $t\bar{t}$ cross-section at 1.8 TeV and 1.96 TeV: A study of the systematics due to parton densities and scale dependence. *JHEP*, 04:068, 2004. (Cited on page 196.)

[310] Peter Sonderegger. Fiber Calorimeters: Dense, Fast, Radiation Resistant. *Nucl.Instrum.Meth.*, A257:523, 1987. (Cited on page 209.)

[311] X. M. Zhang. Single Muon Analysis – Q & A time. ALICE-PWG3-MUON meeting, 2011 Mar 30. (Cited on page 209.)

[312] P. Pillot and D. Stocco. Study of Cuts on Single Muons. ALICE-PWG3-MUON meeting, 20 Apr. 2011. (Cited on page 214.)

[313] Zaida Conesa DEL Valle et al. Production of $W^{\pm}$ vector bosons in p+p and Pb+Pb collisions at LHC energies: $W^{\pm}$ detection in the ALICE muon spectrometer. ALICE-INT-2006-021, 09 2006. (Cited on page 216.)

[314] D. Stocco. Update on the code for standard mon cuts. ALICE-PWG3-MUON meeting, 12 Dec. 2011. (Cited on page 216.)

[315] Vardan Khachatryan et al. Inclusive b-hadron production cross section with muons in pp collisions at $\sqrt{s} = 7$ TeV. *JHEP*, 1103:090, 2011. (Cited on page 219.)

[316] Georges Aad et al. Measurements of the electron and muon inclusive cross-sections in proton–proton collisions at $\sqrt{s} = 7$ TeV with the ATLAS detector. *Phys.Lett.*, B707:438–458, 2012. (Cited on page 219.)

[317] Betty Abelev et al. Heavy flavour decay muon production at forward rapidity in proton–proton collisions at $\sqrt{s} = 7$ TeV. *Phys. Lett.*, B708:265–275, 2012. (Cited on pages xxix, 221, 222 and 223.)

[318] S.S. Adler et al. Measurement of Single Muons at Forward Rapidity in p+p Collisions at $\sqrt{s_{\rm NN}} = 200$ GeV and Implications for Charm Production. *Phys. Rev.*, D76:092002, 2007. (Cited on page 225.)

[319] X. M. Zhang. Parameterization & Extrapolation of $K^{\pm}/\pi^{\pm}$ Spectra From Central Barrel to Forward Region in pp collisions @ 7 TeV. ALICE-PWG3-MUON meeting, 29 Jun 2011. (Cited on page 225.)

[320] R. Aaij et al. Measurement of J/ψ production in pp collisions at $sqrts = 7$ TeV. *Eur. Phys. J.*, C71:1645, 2011. (Cited on pages xxix, 225 and 226.)

[321] Jiebin Luo and X. M. Zhang. Subtraction of $\mu \leftarrow$primary K/π using $K^{\pm}/\pi^{\pm}$ spectra from central barrel in pp @ 7 TeV and Measurement of heavy flavour production. ALICE-PWG3-MUON meeting, 17 Aug 2011. (Cited on page 227.)

[322] X. M. Zhang. Single Muon Analysis: Update. ALICE-PWG3-MUON meeting, 21 Jun 2010. (Cited on page 227.)

[323] Negative binomial distribution. http://en.wikipedia.org/wiki/Negative_binomial_distribution. (Cited on page 235.)

[324] K. Aamodt et al. Centrality dependence of the charged-particle multiplicity density at mid-rapidity in Pb–Pb collisions at $\sqrt{s_{\rm NN}} = 2.76$ TeV. *Phys. Rev. Lett.*, 106:032301, 2011. (Cited on page 235.)

[325] R. Averbeck, N. Bastid, Z. Conesa del Valle, P. Crochet, A. Dainese, et al. Reference heavy flavour cross sections in pp collisions at $\sqrt{s} = 2.76$ TeV, using a pQCD-driven $\sqrt{s}$-scaling of ALICE measurements at $\sqrt{s} = 7$ TeV. arXiv:1107.3243, 2011. (Cited on page 252.)

[326] Jiebin Luo. Single muons in pp collisions at 2.76 TeV. ALICE-PWG3-MUON meeting, 09 Jan 2012. (Cited on page 253.)

[327] Ekkard Schnedermann, Josef Sollfrank, and Ulrich W. Heinz. Thermal phenomenology of hadrons from 200 A/GeV S+S collisions. *Phys. Rev.*, C48:2462–2475, 1993. (Cited on pages 259 and 285.)

[328] Z. Conesa del Valle, A. Dainese, H.-T. Ding, G. Martinez Garcia, and D.C. Zhou. Effect of heavy-quark energy loss on the muon differential production cross-section in Pb–Pb collisions at $\sqrt{s_{\rm NN}} = 5.5$ TeV. *Phys. Lett.*, B663:202–208, 2008. (Cited on page 267.)

[329] Dmitri Kharzeev, Eugene Levin, and Marzia Nardi. Color glass condensate at the LHC: Hadron multiplicities in pp, pA and AA collisions. *Nucl. Phys.*, A747:609–629, 2005. (Cited on page 267.)

[330] ATLAS Collaboration. Measurement of the centrality dependence of charged particle spectra and $R_{\rm CP}$ in lead–lead collisions at $\sqrt{s_{\rm NN}} = 2.76$ TeV with the ATLAS detector at the LHC. ATLAS-CONF-2011-079, 06 2011. (Cited on pages xxxiii and 268.)

[331] P. Pillot. Private communication, 02 2012. (Cited on pages xxxviii and 272.)

[332] B. Abelev et al. Production of muons from heavy flavor decays at forward rapidity in pp and pb–pb collisions at $\sqrt{s_{\rm NN}} = 2.76$ tev. *Phys. Rev. Lett.*, 109:112301, Sep 2012. (Cited on pages xxxiii, 279 and 280.)

[333] B. Abelev et al. Suppression of high transverse momentum D mesons in central Pb–Pb collisions at $\sqrt{s_{\rm NN}} = 2.76$ TeV. arXiv:1203.2160, 03 2012. (Cited on pages xxxiv, 281 and 282.)

[334] Yuncun He, Ivan Vitev, and Ben-Wei Zhang. $\mathcal{O}(\alpha_{\rm s}^3)$ Analysis of Inclusive Jet and di-Jet Production in Heavy Ion Reactions at the Large Hadron Collider. *Phys. Lett.*, B713:224–232, 2012. (Cited on page 282.)

[335] O Fochler, J Uphoff, Z Xu, and C Greiner. Jet quenching and elliptic flow at the rhic and the lhc within a pqcd-based partonic transport model. *Journal of Physics G: Nuclear and Particle Physics*, 38(12):124152, 2011. (Cited on page 282.)

[336] P. Danielewicz and G. Odyniec. Transverse Momentum Analysis of Collective Motion in Relativistic Nuclear Collisions. *Phys. Lett.*, B157:146–150, 1985. (Cited on pages 286 and 323.)

[337] P. Danielewicz and M. Gyulassy. Jacobian Free Global Event Aanaysis. *Phys. Lett.*, B129:283–288, 1983. (Cited on page 286.)

[338] Jean-Yves Ollitrault. Anisotropy as a signature of transverse collective flow. *Phys. Rev.*, D46:229–245, 1992. (Cited on page 286.)

[339] Arthur M. Poskanzer and S.A. Voloshin. Methods for analyzing anisotropic flow in relativistic nuclear collisions. *Phys. Rev.*, C58:1671–1678, 1998. 19 pages with one figure. Some equations corrected Journal-ref: Phys. Rev. C, 1 Sept 1998. (Cited on pages 286, 293, 315 and 323.)

[340] Nicolas Borghini, Phuong Mai Dinh, and Jean-Yves Ollitrault. Flow analysis from multiparticle azimuthal correlations. *Phys. Rev.*, C64:054901, 2001. (Cited on pages 298 and 302.)

[341] Nicolas Borghini, Phuong Mai Dinh, and Jean-Yves Ollitrault. Flow analysis from cumulants: A Practical guide. arXiv:nucl-ex/0110016, 2001. (Cited on page 302.)

[342] Ante Bilandzic, Raimond Snellings, and Sergei Voloshin. Flow analysis with cumulants: direct calculations. *Phys. Rev.*, C83:044913, 2011. (Cited on pages 302 and 303.)

[343] Chen-Ning Yang and T. D. Lee. Statistical theory of equations of state and phase transitions. I: Theory of condensation. *Phys. Rev.*, 87:404–409, 1952. (Cited on page 305.)

[344] N. G. van Kampen. *Stochastic Processes in Physics and Chemistry*. North-Holland, Amsterdam, 1981. (Cited on page 307.)

[345] T. D. Lee and Chen-Ning Yang. Statistical theory of equations of state and phase transitions. II: Lattice gas and Ising model. *Phys. Rev.*, 87:410–419, 1952. (Cited on page 307.)

[346] R.S. Bhalerao, N. Borghini, and J.Y. Ollitrault. Genuine collective flow from Lee-Yang zeroes. *Phys. Lett.*, B580:157–162, 2004. (Cited on page 309.)

[347] N. Borghini and J.Y. Ollitrault. Directed flow at RHIC from Lee-Yang zeroes. *Nucl. Phys.*, A742:130–143, 2004. (Cited on page 309.)

[348] R.S. Bhalerao, N. Borghini, and J.Y. Ollitrault. Analysis of anisotropic flow with Lee-Yang zeroes. *Nucl. Phys.*, A727:373–426, 2003. 32 pages, 7 eps figures, RevTeX Report-no: Saclay-T03/098,TIFR/TH/03-15. (Cited on page 309.)

[349] N. Borghini, R.S. Bhalerao, and J.Y. Ollitrault. Anisotropic flow from Lee-Yang zeroes: A Practical guide. *J. Phys. G*, G30:S1213–S1216, 2004. (Cited on page 309.)

[350] Ante Bilandzic, Naomi van der Kolk, Jean-Yves Ollitrault, and Raimond Snellings. Event-plane flow analysis without non-flow effects. *Phys. Rev.*, C83:014909, 2011. (Cited on page 309.)

[351] Jean-Yves Ollitrault. On the measurement of azimuthal anisotropies in nucleus–nucleus collisions. arXiv:nucl-ex/9711003, 1997. (Cited on page 322.)

[352] X. M. Zhang. Inclusive Muon Flow. ALICE-PWG3-MUON meeting, 2011 Jun 29, 06 2011. (Cited on page 326.)

[353] X. M. Zhang. Inclusive Muon Flow. ALICE-PWG3-MUON meeting, 2010 Jul 07. (Cited on page 329.)

[354] X. M. Zhang. Measurement of $\mathrm{d}^2\sigma^{\mu\leftarrow\mathrm{HF}}/\mathrm{d}p_\mathrm{t}\mathrm{d}\eta$ in pp collisions at $\sqrt{s} = 7$ TeV and Single Muon Elliptic Flow Estimation in Pb–Pb Collisions at $\sqrt{s_\mathrm{NN}} = 2.76$ TeV. ALICE Week, 08 2011. (Cited on page 329.)

Publication List

Direct Contributions

1. B. Abelev $\cdots$ X. Zhang $\cdots$ (ALICE Collaboration), **Prodution of Muons from Heavy Flavor Decays at Forward Rapidity in pp collisions at $\sqrt{s_{NN}} = 2.76$ TeV**, *Phys. Rev. Lett.* ***109*** *(2012) 112301.*

2. B. Abelev $\cdots$ X. Zhang $\cdots$ (ALICE Collaboration), **Heavy flavour decay muon production at forward rapidity in proton–proton collisions at $\sqrt{s} = 7$ TeV**, *Phys. Lett.* ***B708*** *(2012) 265.*

3. X. Zhang for ALICE Collaboration, **Heavy flavour production in the semi-muonic channel at forward rapidity in pp collisions at $\sqrt{s} = 7$ TeV and Pb–Pb collisions at $\sqrt{s_{NN}} = 2.76$ TeV with ALICE**, *Journal of Physics G: Nuclear and Particle Physics* ***38*** *(2011) 124067.*

4. X. Zhang, W. Xiang, and D. Zhou, **Medium temperature dependence of quark energy loss**, *Indian J. Phys.* ***85*** *(2011) 1125.*

5. X. Zhang *et al.*, **Measurement of (di)muons from heavy flavour decay in pp collisions at 14 TeV with ALICE at the LHC**, *Chinese Physics C* ***34*** *(2010) 1538.*

6. X. Zhang, D. Zhou, and W. Xiang, **Dead cone effect of heavy quark in medium**, *International Journal of Modern Physics E* ***16*** *(2007) 2123.*

7. X. Zhang, Y. Zhu and Y. He, **Dead cone effect of charm quark radiation**, *High Energy Phys. & Nucl. Phys.* ***31*** *(2007) 43.*

8. X. Zhang for ALICE Collaboration, **Heavy Flavour Physics with the ALICE Muon Spectrometer at the LHC**, *Pos(Bormio 2011) 030 (2011).*

9. R. Averbeck, N. Bastid, Z. Conesa del Valle, P. Crochet, A. Dainese, and X. Zhang, **Reference heavy flavour cross sections in pp collisions at $\sqrt{s} = 2.76$ TeV, using a pQCD-driven $\sqrt{s}$-scaling of ALICE measurements at $\sqrt{s} = 7$ TeV**, *[arXiv:1107.3243v2] (2011).*

10. L. Manceau, X. Zhang **et al.**, **Performance of ALICE muon spectrometer for measurement of B-hadron and D-hadron production cross sections in pp collisions at $\sqrt{s} = 14$ TeV via single muons**, *ALICE-INT-2011-XXX (2011).*

As Member of ALICE

I have 22 additional publications as member of ALICE until April 2012.

Acknowledgments

There are many persons that I would like to thank for various reasons.

First, I would like to thank my supervisors Nicole Bastid and Philippe Crochet at LPC Clermont-Ferrand and, Daicui Zhou at IOPP Wuhan in China who gave me the opportunity to work alternately in France and China, in the ALICE Collaboration on very exciting topics during my Master thesis and PhD thesis. Their support, guidance and availability deserve my deepest gratitude. Their experience and personal qualities have been of great influence for me both on professional and personal aspects. Also, I would like to thank Nicole and Philippe for carefully reading my PhD manuscript and for the detailed corrections.

Many thanks to Daicui, Nicole and Philippe who had many times manage to kindly arrange lunches and dinners for me when I did not had time to cook by myself.

I am grateful to B. Erazmus, G. Martinez Garcia, X. Cai, H. Chen and Y. Ma for accepting to be the referees of my PhD thesis and for their useful comments and corrections which improved the manuscript.

I am also grateful to A. Andronic, F. Antinori, L. Aphecetche, N. Armesto, R. Arnaldi, A. Bilandzic, Z. Conesa del Valle, A. Dainese, P. Dupieux, S. Grigoryan, J. Klay, X. Lopez, L. Manceau, R.-R. Ma, A. Mischke, A. Morsch, J.-Y. Ollitrault, P. Pillot, P. Rosnet, A. Rossi, F. Prino, J. Schukraft, E. Scomparin, R. Snellings, D. Stocco, R. Tieulent, R. Turrisi, E. Vercellin, B. Vulpescu, X. Wang, Y. Wang, N. Xu, H. Yang, Z.-B.Ying and B.-W. Zhang for useful suggestions and stimulating discussions.

Many thanks to my friends and classmates J. Ba, J. Bai, Z. Chang, R. Chen, L. Dan, H.-T. Ding, X.-Z. Fang, Y.-C. He, Y.-F. Hou, S. Li, Y.-T. Lin, J. Liu, D.-H. Luo, J.-B. Luo, Z.-H. Ma, Y.-X. Mao, Z. Ruan, M.-G. Song, L. Tan, R.-Z. Wan, C. Wang, D. Wang, F. Wang, M.-L. Wang, S. Wang, T.-F. Wang, Y. Wei, C.-Z. Xiang, W.-C. Xiang, X. Xiao, G.-F. Xu, W.-Z. Xu, X.-B. Yuan, F. Zhang, Y.-H. Zhang, Z.-Q. Zhang, Y.-T. Zhao, F.-C. Zhou, J. Zhou, Y. Zhou, H.-S. Zhu, J. Zhu, J.-H. Zhu, X.-R. Zhu and Y. Zhu who helped me a lot during my studies and in daily life.

I am giving a special mention to my girlfriend Ting Xiao for the tenderness, encouragement and support during the preparation of my PhD thesis, although if we have often been several thousand kilometers away.

Last, I would like to thank my parents, my young sister as well my girlfriend's parents for their understanding and their support.

All my apologies for the people I may have forgotten.

Xiaoming ZHANG

May 10, 2012

Clermont-Ferrand

Résumé

Les calculs de chromodynamique quantique prédisent, dans des conditions extrêmes de température et de densité d'énergie, la formation d'une phase de matière dans laquelle on assisterait au déconfinement des hadrons en un plasma de quarks et gluons. Les collisions d'ions lourds ultra-relativistes ont pour objectif principal l'étude des propriétés de ce milieu. Les saveurs lourdes (charme et beauté) sont produites principalement lors de processus durs aux premiers instants de la collision puis interagissent avec le milieu produit. Par conséquent, la mesure de ces saveurs lourdes ouvertes devrait permettre d'extraire des informations concernant le système créé aux premiers instants de la collision. Cette thèse est dédiée à l'étude des saveurs lourdes ouvertes dans les collisions pp et Pb–Pb avec les muons simples mesurés aux rapidités avant avec le spectromètre à muons d'ALICE. Les performances du spectromètre à muons pour la mesure des saveurs lourdes ouvertes, via les (di)-muons, dans les collisions pp et l'analyse des premières collisions pp à $\sqrt{s} = 900$ GeV avec pour objectif la compréhension de la réponse du détecteur sont d'abord présentées. La section efficace différentielle de production des muons issus de la désintégration des saveurs lourdes ouvertes est mesurée dans les collisions pp à $\sqrt{s} = 7$ TeV et 2.76 TeV. Un bon accord avec les prédictions FONLL (Fixed Order Next-to-Leading Log) est obtenu pour les deux énergies. Le facteur de modification nucléaire, $R_{\rm AA}$, des muons issus de la désintégration des saveurs lourdes ouvertes, illustrant la perte d'énergie des quarks lourds dans le milieu, est mesuré dans les collisions Pb–Pb à $\sqrt{s_{\rm NN}} = 2.76$ TeV. Dans les collisions centrales $(0 - 10\%)$, une importante suppression des taux de production des muons issus de la désintégration des saveurs lourdes ouvertes est mise en évidence. Le "flow" elliptique, v_2, des muons issus de la désintégration des saveurs lourdes ouvertes apporte des informations concernant les processus de thermalisation des quarks lourds et les effets de perte d'énergie. Ce "flow" elliptique des muons simples est extrait en utilisant plusieurs méthodes.

Mots clés : LHC, ALICE, collisions pp, collisions d'ions lourds ultra-relativistes, muons, production de saveurs lourdes, facteur de modification nuclaire, "flow" elliptique, calculs pQCD.

Abstract

According to quantum chromodynamics (QCD) calculations, at extreme conditions of temperature and energy density the formation of a deconfined medium, the Quark-Gluon Plasma (QGP), is expected. Ultra-relativistic heavy-ion collisions aim at investigating the properties of such strongly-interacting matter. Heavy quarks (charm and beauty) are of particular interest since they are expected to be produced mainly in hard scattering processes during the early stage of the collision and subsequently interact with the hot and dense medium. Therefore, the measurement of open heavy flavours should provide essential information on the properties of the system formed at the early stage of heavy-ion collisions. This thesis work is devoted to the study of open heavy flavours in pp and Pb–Pb collisions via single muons with the ALICE forward muon spectrometer. It starts with the performance study of the muon spectrometer for the measurement of open heavy flavour production in pp collisions via (di-)muons and, the analysis of first pp collisions at 900 GeV to understand the response of the apparatus. The differential production cross section of muons from heavy-flavour decays is measured in pp collisions at $\sqrt{s} = 7$ and 2.76 TeV. A good agreement between data and FONLL (Fixed Order Next-to-Leading Log) predictions is obtained at the two colliding energies, within uncertainties. The nuclear modification factor, $R_{\rm AA}$, of muons from heavy-flavour decays, which illustrates the heavy quark in-medium energy loss, is measured in Pb–Pb collisions at $\sqrt{s_{\rm NN}} = 2.76$ TeV. In the most 10% central Pb–Pb collisions, a strong suppression of the yield of muons from heavy-flavour decays is observed. The elliptic flow, v_2, of muons from heavy-flavour decays is believed to shed light on the thermalization processes of heavy quarks and on the path length dependence of heavy quark in-medium energy loss. Finally, the elliptic flow of inclusive muons is extracted with different flow analysis methods.

Keywords: LHC, ALICE, pp collisions, ultra-relativistic heavy-ion collisions, single muons, heavy-flvour production, nuclear modification factor, elliptic flow, pQCD calculations.